AD-A216 448

ON LOAN. PLEASE RETURN AS
SOON AS POSSIBLE.

The Royal Society of Chemistry
Faraday Division

SYMPOSIUM 24

ORIENTATION AND POLARISATION EFFECTS IN REACTIVE COLLISIONS

Order of Papers

Alignment Measurements in Orbitally Selective Collision-induced Fluorescence

Daniel M. Segal* and Keith Burnett

Clarendon Laboratory, University of Oxford, Parks Road, Oxford OX1 3PU

The results of an experiment in which the polarization of collisionally redistributed near-resonant light was monitored has been analysed. If the incident light is polarized the fluorescent light may also be, with its degree of polarization depending on the collision dynamics. The experimental results have been analysed using a model in which the collision complex is treated as a transient quasi-molecule. In this model the atom-perturber complex is excited directly into a molecular orbital which rotates through the collision. The complex then decouples and the atom radiates at a later time. The rotation experienced during the collision accounts for the depolarization of the light. A knowledge of the interatomic potentials for the system under study is necessary for a quantitative application of the theory. The 2537 Å ($^3P_1$-$^1S_0$) line in Hg perturbed by Kr was chosen for the present work since the interatomic potentials for this system are well documented. It is shown that the primitive form of the decoupling radius model is inadequate to account for the experimental results quantitatively. Extensions and modifciations to the model that overcome some of these difficulties are discussed. The results highlight the poor orbital selectivity attainable in this type of experiment when the molecular potentials do not separate sufficiently rapidly as the collision partners approach one another.

1. Introduction

Orbitally selective collisions and reactions have received a great deal of attention in recent years. The studies most closely related to the discussion here are those involving energy transfer in alkaline earths[1,2] and the photochemistry of Hg in van der Waals complexes.[3] A central question in these studies is how atomic orbitals evolve into their molecular counterparts. We want to know for example if selection of asymptotic atomic states leads to a selective population of molecular states.

Using a tunable laser one can excite collisions before or after they cross the boundary between a region of small interatomic distances, in which the molecular picture holds, and a region of larger interatomic separations in which the partners act as free atoms. This is the type of experiment we shall analyse below.

Grosser[4] discussed in detail the conflict between the atomic and molecular pictures of $^1S_1$-$^1P_1$ atom-atom collisions. The disagreement between the two pictures becomes apparent when one considers the angular momentum of the states involved. When the interaction between the collision partners is small the motion should resemble that of free atoms, and the angular momentum vectors should remain fixed in space. However, when the interaction between the pair is strong a molecular picture is appropriate and it is the projection of the angular momentum vectors onto the internuclear axis that should be conserved. This axis rotates by 180° in a collision. The two pictures are therefore in severe conflict.

Grosser pointed out that when one chooses to approach a problem of this type using molecular eigenfunctions (Σ and Π states for the $^1P_1$-$^1S_0$ transition he considered) a Σ-Π coupling term becomes important at large r and Λ is not conserved in this region.

The coupling term can be regarded as being due to Coriolis forces exerted on the electrons in the frame of the rotating axis. These Coriolis forces will always be present; however, at small r they will be negligible in comparison to the forces which couple the wavefunction to the molecular axis.

The strength of the coupling of the electronic angular momentum to the molecular axis at a given r is represented by the Σ,Π potential difference. The molecular picture becomes inappropriate when this coupling is comparable to the Coriolis coupling between the Σ and Π states.

A utilitarian method of dealing with this problem in semiclassical calculations is to define a radius $R_{\rm L}$ within which the molecular picture holds rigorously and outside of which the atomic picture is used. In an experiment in which an excited atom undergoes collisions $R_{\rm L}$ is the 'locking radius', *i.e.* the interatomic separation at which the atoms are considered to lock together to form a rigid molecule which then rotates through the collision. We shall discuss this approach in the context of the experiments we have performed. However, we have monitored the polarization of fluorescence emitted by an atom after absorption during a collision. Under such circumstances one would normally expect excitation to occur directly to an axis-coupled molecular state. For this type of experiment then $R_{\rm L} = R_{\rm dc}$ is a radius at which the partners decouple to their asymptotic atomic states when the collision is completed. The utility of this approach hinges on how abruptly in r the changeover occurs. This in turn depends on the evolution in r of the Σ-Π potential difference. A method pertinent to our experiment and based on the idea of a decoupling radius has been described by Lewis *et al.*[5] Fig. 1 illustrates

(a)

(b)

(c)
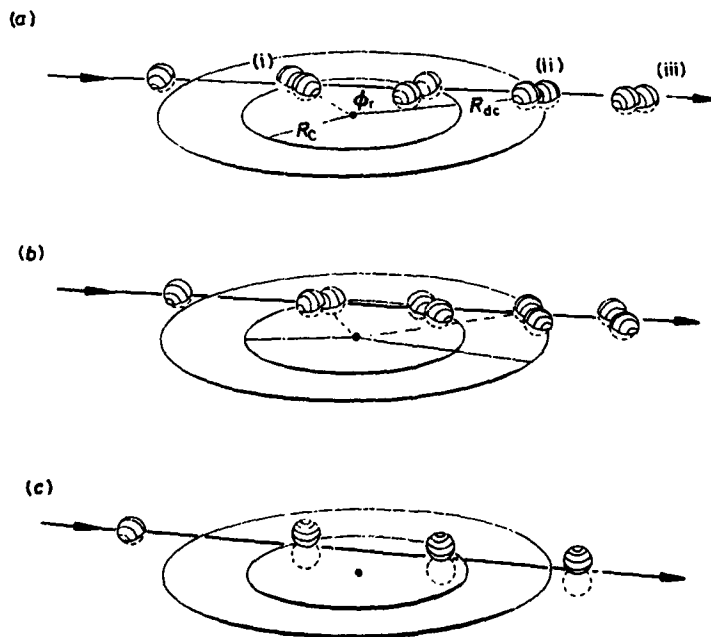
Fig. 1. Orbital reorientation during a collision. The time evolution of the molecular orbitals is illustrated from (i) the point of absorption at $R_{\rm C}$, the Condon point to (ii) the point of decoupling at $R_{\rm dc}$, for the three cases of excitation to (*a*) the Σ state, (*b*) the Π^+ state and (*c*) the Π^- state. Radiative decay occurs at point (iii). The reorientation angle $\phi_{\rm r}$ is equal to $\phi + \theta_{\rm a}$. Note route (*c*) causes no reorientation so that the Π state is overall less depolarizing.

the essential features of the model. The central result is an expression for the detuning dependent atomic alignment as a function of the amount of reorientation (given by the angle ϕ) experienced during the collision and the angle θ_α, where the subscript α can be either Σ or Π. This result is then averaged over impact parameters and velocities.

The average over impact parameters is transformed into an average over θ_α. Explicitly we use

$$\langle \cdots \rangle_{av} = \tfrac{1}{2} \int_{-\pi/2}^{\pi/2} \cos \theta_\alpha \, d\theta_\alpha \langle \cdots \rangle. \tag{1}$$

It is possible to express the polarization of the fluorescence in a form dependent on only R_α/R_{dc} and $\cos \theta_\alpha$. Once the average over θ_α has been accomplished the polarisation can be expressed as a function of $X_\alpha \equiv R_\alpha/R_{dc}$ alone:[6]

$$P = \frac{15 + 15X_\Pi + X_\Pi^2 + g(\Delta\omega)9X_\Sigma^2}{55 + 5X_\Pi + 3X_\Pi^2 + g(\Delta\omega)(25 + 3X_\Sigma^2)}. \tag{2}$$

In this expression $g(\Delta\omega)$ is the probability of exciting the Σ state relative to exciting a Π state. A classical form for this function is found by noting that the probability of absorption at ω is given by the simple quasistatic result,

$$I(\omega) = \frac{n_0 4\pi R_\alpha^2}{|dV/dR|_{R_\alpha}}. \tag{3}$$

The usual Boltzmann factor is missing as a result of neglecting the full integration over velocities (using an average velocity only). $g(\Delta\omega)$ can then be written as

$$g(\Delta\omega) = R_\Sigma^2 \left(\left. \frac{dV}{dR} \right|_{R_\Sigma} \right)^{-1} \left[R_\Pi^2 \left(\left. \frac{dV}{dR} \right|_{R_\Pi} \right)^{-1} \right]^{-1} \tag{4}$$

The polarization P_Π, measured when excitation is *via* the Π curve only, is obtained by letting $g(\Delta\omega) \rightarrow 0$. Conversely P_Σ is obtained by letting $g(\Delta\omega) \rightarrow \infty$. A range for P_α can be deduced by letting $X_\alpha \rightarrow 1$ and 0 as limiting cases. It should be noted that there is hardly any overlap between the ranges

$$0 < P_\Sigma(\%) < 32$$
$$27 < P_\Pi(\%) < 62. \tag{5}$$

If the excitation takes place to only one potential-energy curve the polarization of the fluorescence will label it uniquely as a Σ or Π curve. The dependence of the polarization of the fluorescence on the shape of the potentials enters the problem in two ways: directly, through $R_\alpha(\Delta\omega)$ and indirectly through the expression $g(\Delta\omega)$ which weights the P_Σ and P_Π contributions.

For any model based on the idea of a decoupling radius to be useful, a sensible way of choosing R_{dc} must be found. Grosser investigated the problem by writing down coupled equations for the probability amplitudes of assumed molecular eigenfunctions. He started with an eigenfunction of pure Σ character at large r and integrated his equations to smaller r. Initially as r decreases the state begins to take on a certain amount of Π character. At small r when the Coriolis term becomes negligible the solutions for the probability amplitudes begin to oscillate about a mean value. In this region Λ is conserved. The onset of such oscillations is an indication that the transition zone between the atomic and molecular regions has been reached. Using the condition that the Coriolis coupling be comparable to the Σ-Π potential difference he was able to find an analytical form for R_{dc} when $V_\Sigma - V_\Pi$ can be written as an inverse power law in r. His result is given by

$$R_{dc} = \left| \frac{\Delta C_n}{(n-1)\hbar \bar{v}} \right|^{1/n-1} \tag{6}$$

for $V_\Sigma - V_\Pi = \Delta C_n / r^n$. Lewis *et al.* choose to define R_{dc} through

$$\frac{1}{\hbar}|V_\Sigma(R_{dc}) - (V_\Pi(R_{dc})| = \frac{1}{\tau_c} \qquad (7)$$

on the grounds that $\hbar/t_c$ is the smallest energy separation that the collision can discern.

In an experimental test of the decoupling radius model in a system for which the potentials are well known R_{dc} acts as the only parameter which need be adjusted to fit the data. The model will be deemed a success if a good fit to the data can be achieved with a single R_{dc} which is independent of impact parameter and velocity.

In this paper we will analyse our experimental results for Hg $^3P_1$-$^1S_0$ interacting with a bath of Kr perturbers. The experimental procedure has been described elsewhere.[7] Previous polarization-monitored collisional redistribution experiments have been conducted by Alford *et al.*[8] for the case of a $J = 0 \rightarrow 1$ transition in Sr and Ba perturbed by the rare gases and by Kroop and Behmenburg[9] for the $J = \frac{1}{2} \rightarrow \frac{3}{2}$ case in Na perturbed by Ar. To perform a quantitative test of redistribution theory, in particular the decoupling radius model, a system must be studied for which the interatomic potentials are well known. The comparison between theory and the Ba and Sr experiments has been hampered by a lack of knowledge about the interatomic potentials for these systems. While good potentials are available for the Na-Ar molecule the interpretation of the results in terms of a simple model for the collision is complicated by the presence of fine structure.

The availability of interatomic potentials for the Hg(2537 Å)-Kr $J = 0 \rightarrow 1$ system (*e.g.* Grycuk and Czerwosz,[10] Fuke *et al.*[11]) is the reason for its choice as the subject of our study. Section 2 discusses the potentials put forward by these authors and proposes a set of composite potentials for use in our analysis. In section 3 we present the results of our calculation based on this model and contrast these with previous work in the field. In section 4 we discuss the reasons behind the failure of the model for the system studied. We suggest the type of analysis necessary to get good agreement for our experimental case. In section 5 we draw our conclusions and comment on implications for the prospect of orbital selectivity in this type of interaction.

2. Interatomic Potentials for Hg–Kr

2.1. General Remarks

Many of the polarization-monitored collisional redistribution experiments performed to date have dealt with the case of a $^1P_1$-$^1S_0$ transition and the corresponding p_x, p_y and p_z orbitals of the molecular picture. The decoupling radius model is formulated by Lewis *et al.* for this system. We now examine the complications that arise in the case of the Hg 2537 Å intercombination line ($^3P_1$-$^1S_0$).

With the breakdown of L-S coupling the only good quantum number for the atomic angular momentum is J. Similarly, in the molecular picture, Λ (projection of orbital angular momentum on the internuclear axis) is no longer a good quantum number and only $\Omega = \Lambda + \Sigma$ is conserved. (Σ is the projection of total spin on the internuclear axis.)

In the atomic case, transforming from the $|LSM_LM_S\rangle$ basis to the $|JM\rangle$ basis is achieved through

$$|JM\rangle = \sum_{M_L, M_S} |LSM_LM_s\rangle\langle LSM_LM_s|JM\rangle$$

$$= \sum_{M_L, M_s} \begin{pmatrix} L & S & J \\ M_L & M_s & -M \end{pmatrix} \frac{(2J+1)^{1/2}}{(-1)^{L-S+M}} |LSM_LM_S\rangle. \qquad (8)$$

We now identify the z axis as the internuclear line and make the substitutions $M \equiv \Omega$, $M_L \equiv \Lambda$ and $M_S \equiv \Sigma$. For the $\Omega = 0$ case this gives

$$|J = 1, \Omega = 0\rangle = \sqrt{3}\left\{ \begin{pmatrix} 1 & 1 & 1 \\ 0 & 0 & 0 \end{pmatrix} |\Lambda = 0, \Sigma = 0\rangle \right.$$

$$+ \begin{pmatrix} 1 & 1 & 1 \\ -1 & 1 & 0 \end{pmatrix} |\Lambda = -1, \Sigma = 1\rangle$$

$$\left. + \begin{pmatrix} 1 & 1 & 1 \\ 1 & -1 & 0 \end{pmatrix} |\Lambda = 1, \Sigma = -1\rangle \right\}. \tag{9}$$

Since the first of the three Wigner $3-j$ symbols is zero this yields an expression in terms of $|\Lambda| = 1$ states. For the $\Omega = 1$ case we find

$$|J = 1, \Omega = 1\rangle = -\sqrt{3}\left\{ \begin{pmatrix} 1 & 1 & 1 \\ 1 & 0 & 1 \end{pmatrix} |\Lambda = 1, \Sigma = 0\rangle \right.$$

$$\left. + \begin{pmatrix} 1 & 1 & 1 \\ 0 & 1 & 1 \end{pmatrix} |\Lambda = 0, \Sigma = 1\rangle \right\} \tag{10}$$

giving an expansion in $\Lambda = 1$ and $\Lambda = 0$ states. The state $|J = 1, \Omega = 0\rangle$ is thus expressed as a sum over Π states alone, whilst the state $|J = 1, \Omega = 1\rangle$ contains a mixture of Σ and Π states. The labels of the molecular states for Hg-Kr can be assigned as X $^1 0^+$ ($\Omega = 0$) for the ground state and A $^3 0^+$ ($\Omega = 0$) and B $^3 1$ ($\Omega = \pm 1$) for the excited states (*i.e.* Hund's coupling case C.)

We are now in a position to make some qualitative remarks about the interatomic potentials for Hg-RG systems when the rare-gas atom is in its $^1 S_0$ ground state.[3] The B state has two degenerate components with $\Omega = \pm 1$. These states contain an admixture of Σ component and since it is Λ that governs the electrostatic interactions these states will become repulsive at larger r than the A state. Furthermore, in the region where the r^{-6} term dominates the B state is more attractive than the A state. The result is a shallower potential well for the B state than for the A state and a resulting curve-crossing as shown in fig. 2.

The ground state is a Σ state and is expected to have a fairly shallow well. However, in the ground state the electrons are closely bound and valence repulsion sets in at smaller r than for the excited states. The ground-state well is therefore deeper than the well in the B state and occurs at smaller r. From the general shape of the potentials we expect the red wing of the absorption line to be dominated by a single satellite associated with the minimum in the B-state difference potential.

2.2. Proposed Potentials

Fuke *et al.* arrive at potential-energy curves for Hg 2537 Å interacting with krypton through an analysis of their experimental vibrational spectrum for HgKr van der Waals molecules. (They were unable to resolve the rotational structure.) They performed a vibration-only RKR analysis and compared it with a Birge-Sponer analysis. The agreement between the two analyses was good for the B state but only partial for the A state. Their experimental data for the ground state were limited. Grycuk and Czerwosz performed a temperature-dependent lineshape experiment and used the data-inversion technique described by Hedges *et al.*[12] Their data complements those of Fuke *et al.* by providing reliable ground-state and A-state potentials.
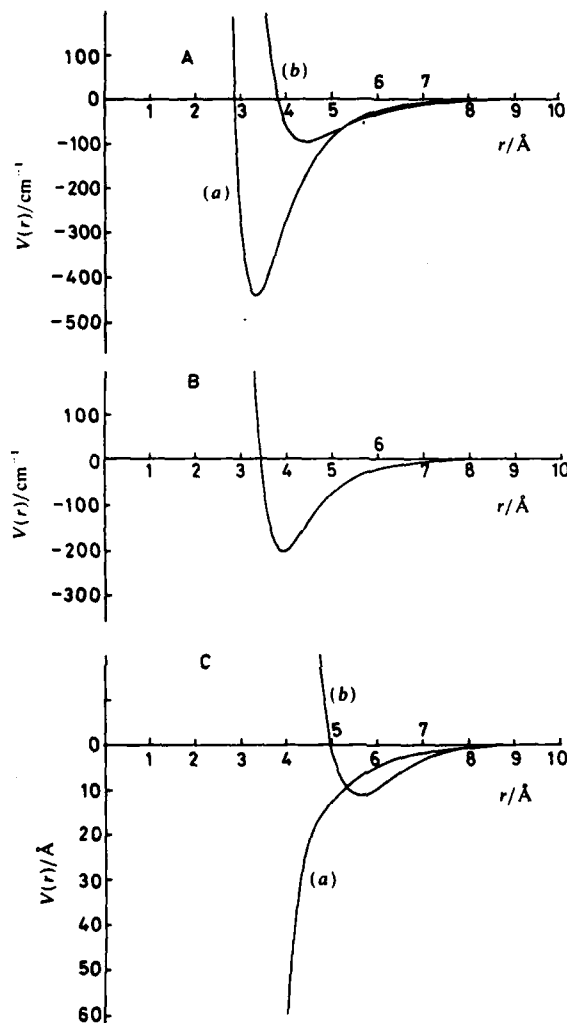
Fig. 2. Composite potentials based on ref. (10) and (11). (A) (*a*) A state, (*b*) B state; (B) X state; (C) (*a*) ΔV_A, (*b*) ΔV_B.

For use in calculations based on the decoupling radius model we are primarily interested in the difference potentials. Since we propose to use ground- and excited-state potentials from different sources care must be taken to check that the B-state difference potential is sensible. Taking the potentials as they stand gives a B-state difference potential with a well depth of only *ca.* 2 cm^{-1}. This is obviously not commensurate with the appearance of the red-wing satellite at *ca.* 12 cm^{-1}. Fuke *et al.* calculated r_m for their B state by using a simulated FCF program to calculate the difference between r_m for their ground and excited states. If we are to use the Grycuk and Czerwosz ground state we must amend the value of r_m for the B state accordingly. With this change the difference potential exhibits a 11.5 cm^{-1} minimum. The potentials to be used are summarized in table 1 and are shown in fig. 2.

Table 1. Summary of potentials used in analysis

state	ε/cm^{-1}	ω_e/cm^{-1}	$\omega_e x_e/cm^{-1}$	$r_m/Å$	α	β	form
$X\,^1 0^+$	200			3.95	11	18	M.S.
$A\,^3 0^+$	438.1			3.35	7.84	4.11	M.S.
$B\,^3 1$	95	11.3	0.32	4.45			Morse

The data of Grycuk and Czerwosz were taken for the $A\,^3 0^+$ state. For convenience of manipulation during calculations, a Maitland–Smith function was fitted to these data.

3. Analysis

3.1 Previous Application of the locking-radius Molecular Model

We now present an analysis of our experimental results using the decoupling radius model of Lewis *et al.* For the sake of comparison we will first outline some of the features of the analysis performed by Alford *et al.* of their results for Sr–RG systems. Fig. 3 shows a comparison between their experimental results for Sr–Ar and some theoretical curves based on this model. Lewis *et al.* calculated polarization curves for several trial potential forms. (Information about the potentials for this system was obtained from lineshape experiments by Carlsten *et al.*[13] and by Harima *et al.*[14]). They first assumed van der Waals r^{-6} potentials for the ground and excited states and calculated the dashed curves in fig. 3. [$g(\Delta\omega)$ was set at either 0 or ∞ and the hypothetical limiting cases of pure Σ and pure Π excitation were calculated.] They assessed their curves as follows. They pointed out that the polarization is initially intermediate between Σ and Π and falls off with roughly the correct slope. The polarization then dips more steeply towards the Σ-only curve at around $\Delta\bar{\nu} = 10$–$20\,cm^{-1}$. The lineshape experiments of
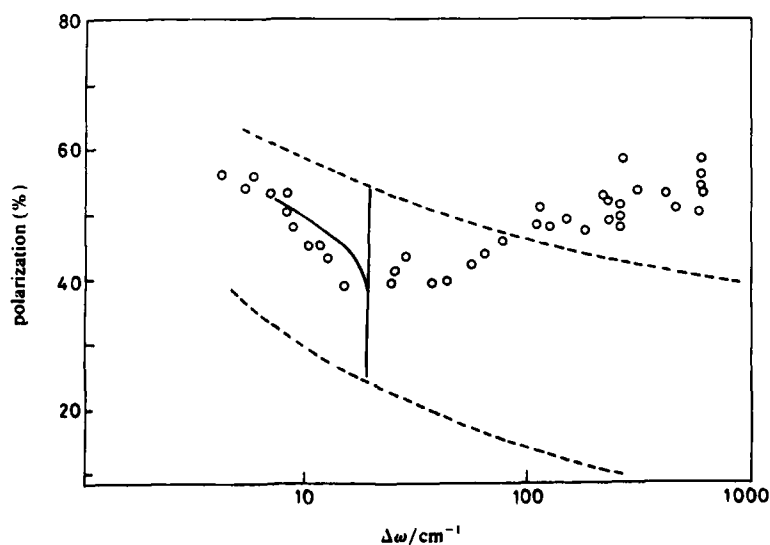
Fig. 3. Polarization redistribution spectrum for the red wing of Sr–Ar. The full curve is the theory[5] using Lennard–Jones potentials in the decoupling-radius model, while the dashed curves assume van der Waals potentials and treat the hypothetical cases of pure Σ and pure Π excitation.

Carlsten *et al.* and Harima *et al.* show a diffuse near-wing satellite, indicating a minimum in one of the difference potentials with a depth of *ca.* 20 cm^{-1}. General arguments would suggest that the minimum is likely to occur in the Σ difference curve rather than in the Π. Lewis *et al.* take the extra decrease in polarization noted in this region to be due to the enhancement of Σ excitation resulting from the satellite.

Once the position of the satellite has been passed the polarization climbs to a value close to that predicted by the Π curve. The polarization then increases to even higher values than those predicted. Lewis *et al.* suggest that the disagreement in this region is due to bent trajectory effects. In order to test eqn (2) directly for a system with potential minima Lewis *et al.* went on to describe the potentials using the Lennard–Jones form capable of producing the known satellites. (An extreme red-wing satellite, attributed to a minimum in the Π difference potential was apparent at *ca.* 1000 cm^{-1}.)

Insertion of these potentials into the decoupling radius model yielded the full curve of fig. 3. The curve reproduces the near-wing polarization reasonably well up to the position of the satellite. The cusp in the curve is due to the classical singularity in the lineshape at this position. After the cusp the full curve reverts to the Π-only curve. Just as a semiclassical analysis removes the singularity in the lineshape, the use of a similar analysis to define $g(\Delta\omega)$ would remove the sharp cusp in the polarization curve. Bieniek[15] has performed such an analysis.

3.2. Mercury–Krypton Analysis

3.2.1. *Impact-limit Polarization*

Omont *et al.*[16] applied quantum-mechanical impact theory to the problem of collisional redistribution. Ballagh and Cooper[17] used the results of Omont *et al.* to derive explicit expressions for the angular and frequency dependence of radiation scattered by a spatially degenerate atom undergoing collisions. Applying this theory to our experimental geometry the polarization P of the fluorescence can be related to the collisional width γ_c and alignment destroying rate $\gamma_c^{(2)}$ through

$$P = \frac{6(\gamma_c/\gamma_c^{(2)}) - 3}{6(\gamma_c/\gamma_c^{(2)}) - 1}. \tag{11}$$

Values of γ_c and $\gamma_c^{(2)}$ are related to the nominal cross-sections σ_R and $\sigma^{(2)}$, respectively, through $\gamma = n_p \bar{v} \sigma$ where n_p is the number density of perturbers and $\bar{v}$ is the mean velocity. Values of σ_R and $\sigma^{(2)}$ for Hg–Kr reported by various authors are tabulated by Lewis.[18]

Substituting the resulting γ_c and $\gamma_c^{(2)}$ values into eqn (11) gives an impact-limit polarization of 82 ± 5%. Taking an estimate of the collisional duration as *ca.* 2.6 ps and using the validity criterion for impact theory we find that the boundary of the impact region occurs at *ca.* 2 cm^{-1} for Hg–Kr. Our experimental results do not extend closer to line centre than 5 cm^{-1} and hence we do not probe the impact region properly. However, an extrapolation of the trend shown in our data suggests that the agreement between the calculated impact polarization and that which can be inferred experimentally is quite good. This agreement lends confidence in the method of correcting for spurious depolarizing effects described elsewhere.[7]

This rather high polarization is due to the relatively low value of $\gamma_c^{(2)}$ for the Hg(2357 Å)–Kr interaction. This arises from the fact that the A- and B-state difference potentials are not well separated in the region of interest. The failure of these curves to separate as well as the analogous Σ and Π potentials in the case of a $^1P_1$–$^1S_0$ transition can be understood by examining the make-up of the A and B states in terms of their Λ components. As we have shown the A state is made up entirely of Π states, whilst the

B state contains a mixture of Σ and Π states. The electrostatic difference between collisions proceeding along the A and B states is therefore not as pronounced as it is in the single–singlet case where the states are of pure Σ and Π character.

3.2.2. Choice of R_{dc}

A simple way of estimating R_{dc} would be to use $\sigma^{(2)} = \pi R_{dc}^2$. Using an average value of $\sigma^{(2)}$ taken from Lewis gives $R_{dc} = 6.1$ Å. Applying the criterion for R_{dc} used by Lewis *et al.* and using the proposed potentials gives $R_{dc} \approx 6.5$ Å. At this point certain difficulties can be noted in attempting to apply the decoupling-radius model to the Hg ($^3P_1$-$^1S_0$)-Kr system.

Note that the maximum energy difference between the A and B states is *ca.* 5 cm^{-1}, which is not markedly greater than our estimate of the energy separation at which the states decouple. It is in precisely such a situation that the concept of a well defined decoupling radius loses its validity. A physical picture based on the decoupling-radius model is that the atomic orbitals never lock tightly to the molecular axis, but merely slew under the influence of the molecular forces. Such a process is badly modelled by the use of a locking radius, no matter how small that radius is chosen to be (given that R_α should remain smaller than R_{dc} throughout the region of interest). Under such circumstances the decoupling-radius model as it stands will always predict more reorientation than actually occurs. It is interesting to compare the maximum polarization (62% for Σ excitation when $R_{dc} = R_\Sigma$) permitted by the decoupling-radius model with calculations for the impact-limit polarization. In a system for which the model is truly applicable one would expect these two polarizations to be in rough agreement. In the case of Ba–Ar the impact limit was found to be $68 \pm 2\%$. Since the corresponding value for Hg–Kr of 82% is much higher than this the model will be unable without modification to give a sufficiently high polarization in the near quasistatic wing to be asymptotically compatible with the impact value.

3.2.3. Red-wing Polarization Curve

We have performed an analysis for Hg–Kr similar to that of Lewis *et al.* for Sr–Ar. In our case, however, the potentials used were far more reliable than those available for the Sr–Ar case. For convenience we have fitted the A-state data to a modified Maitland–Smith function. This was achieved by fixing ε and r_m at the values given by Grycuk and Czerwosz and allowing the α and β parameters to vary to achieve a best fit to the data. Since our red-wing polarization data covered the detuning range 5–40 cm^{-1}, only the lineshape data points lying in this region were included in the fitting procedure. The optimum values were found to be $\alpha = 7.84$ and $\beta = 4.11$. With all the states determined by analytical forms it was easy to differentiate the difference potentials for insertion into $g(\Delta\omega)$. The difference potentials $\Delta V_\alpha(R)$ were inverted numerically to give $R_\alpha(\Delta\omega)$ for substitution into the decoupling-radius model. A complication arises when there is an extremum apparent in a given difference potential. When this happens the function $R_\alpha(\Delta\omega)$ is double-valued and the equation defining $g(\Delta\omega)$ is only valid for single-valued $R_\alpha(\Delta\omega)$. In order to proceed we make the approximation that excitation to the outer Condon point is prevalent and neglect the inner Condon point. This is a reasonable approximation for a number of reasons. For a given detuning the slope of the difference potential is always greater for the inner Condon point than for the outer one. Since the weighting of the contribution of a particular Condon point is inversely proportional to the slope of the difference potential the inner point will always contribute less for the usual asymmetric well. The inner Condon point will also lose out by virtue of the R_α^2 term in the quasistatic formula. These arguments become progressively less valid as the minimum in the potential is approached; however, in this region the difference

in the reorientation experienced after excitation at one Condon point or the other becomes small.

The meaning of the Σ and Π labels in eqn (1)-(5) must now be clarified. These labels draw a distinction between laser excitation to a molecular 'angular momentum' state with $J = 1$ and excitation to a state with $J = 0$. Eqn (1)-(5) were developed in the context of a $^1P_1$-$^1S_0$ transition in which $J \equiv \Lambda$ is a good angular momentum quantum number. In the case of a $^3P_1$-$^1S_0$ transition $J \equiv \Omega$ is the relevant angular momentum
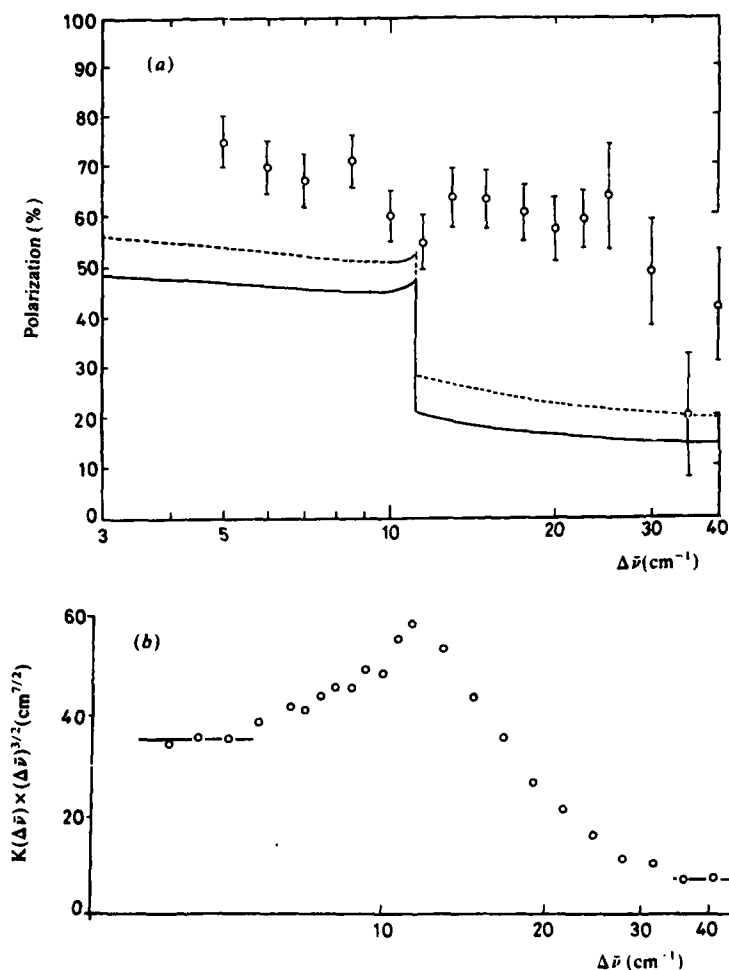
Fig. 4. Polarization redistribution spectrum for the red wing of $Hg(^3P_1$-$^1S_0)$-Kr. (*a*) Measured polarizations are higher than predicted by the simple decoupling-radius model. This results from the proximity of the interatomic difference potentials in the region of interest. The polarization drops in the far wing to a value in better agreement with the theory (- - -) $R_{dc} = 5.5$ Å, (———) $R_{dc} = 6.5$ Å. (*b*) Sketch of the satellite taken from the data of ref. (10). The curves in (*a*) are the results of the primitive decoupling-radius model with a purely classical satellite. An analysis based on the model proposed by Bieniek[15] would use the true form of the satellite, removing the sharp cusp in the polarization curve.

Table 2. Blue-wing Polarization data

$\Delta \bar{\nu}/\mathrm{cm}^{-1}$	polarization (%)
20	65 ± 14
123	76 ± 11

quantum number. Consequently, it is necessary to rewrite eqn (1)-(5) with the labels Σ and Π replaced with $\Omega = 0$ and $\Omega = 1$, respectively.

With these changes made we see that the $A(\Omega = 0)$ state, which is a superposition of $\Lambda = 1(\Pi)$ states, actually behaves like the more depolarizing state of expression (5). The $B(\Omega = 1)$ state, which is a superposition of $\Lambda = 1$ and 0, (Π and Σ) acts as the less depolarizing state.

The result is that as the satellite in the B state is approached we see enhancement of excitation to a *less* depolarizing state. After the satellite has been passed the polarization collapses to the value prescribed by excitation to the more depolarizing A state alone.

Fig. 4 shows the results of our calculation superimposed on our experimental data for various values of R_{dc}. As anticipated, the curve for $R_{dc} = 6.5$ Å lies well below the experimental data. The theoretical curve shows the expected classical cusp similar to that shown in fig. 3 but reversed in direction. Curves with $R_{dc} < 6.5$ Å appear to give better agreement than that for $R_{dc} = 6.5$ Å; however, such curves should be approached with caution for low detunings since they contain components for which $R_{\alpha} > R_{dc}$ which is outside the region of validity of eqn (2). These curves can be expected to give a reasonable fit to the further wing where $R_{\alpha} < R_{dc}$ despite the low value of R_{dc}. The polarization is seen to hold up well after the position of the satellite, but does eventually drop to a value in agreement with the theoretical curves.

3.2.4. *Blue Wing*

Insufficient signal was available to perform a systematic detuning experiment in the blue wing. Furthermore, the exact form of the interatomic difference potential in the blue wing is not known. We can, however, make a comment on the limited data available. These data points were taken at detunings corresponding to the peaks of the two strongest satellites at $\Delta\omega = 20$ and 123 cm^{-1}. Grycuk and Czerwosz discussed the possible origin of these satellites, concluding that the distant satellite is of the usual variety and is associated with an extremum in the difference potential. They suggest that the near satellite is due to bound–free transitions from high-lying vibrational levels in the ground state.

We can be sure that the only potentials to which excitation can occur in the blue wing is the B^{3}1 state. Whilst lack of information on the exact form of the potential prevents us from calculating the polarization at $\Delta\omega = 123$ cm^{-1}, we note that since excitation occurs entirely to the less-depolarizing B state the polarization should be relatively high. This is borne out by the experimental measurement (see table 2).

4. Beyond the Decoupling-radius Molecular Model

4.1. Validity of Approximations

It is apparent that the theory used to analyse our data is incapable of giving a good account of the experimental results. We must therefore address the approximations made in formulating the theory and decide which of these is likely to break down in the case of the Hg(^{3}P$_1$-^{1}S$_0$)-Kr interaction. The approximations made are as follows:

The atoms are taken to follow *classical trajectories* and to be excited *quasistatically* at Condon points. The model also assumes that this excitation occurs *independently* to the $\Omega = 0$ and $\Omega = 1$ states. The atoms are then taken to undergo *adiabatic reorientation* until a fixed *decoupling radius* is reached. The last three points essentially assume that there is no mixing of the molecular states either at excitation, during the rotation or after decoupling. The following sections examine the validity of these assumptions in turn.

4.2. Classical Trajectories and Quasistatic Excitation

The assumption of classical trajectories breaks down if the de Broglie wavelength of the 'particle' (or reduced mass μ in the centre-of-mass frame) is of the order of a typical scale length for the interatomic potential. For the Hg–Kr thermal collisions at room temperature we find $\lambda = 0.19$ Å. The minima in the A, B and X potentials occur at *ca.* 4 Å, which can be taken as a measure of the scale of the potential. The assumption of classical trajectories is therefore a good for the collisions we have studied. If any discrepancy occurs as a result of this assumption it will occur near the turning points where dV/dR is large, *i.e.* the potential changes appreciably over a de Broglie wavelength. Also related to the classical-path assumption is the question of the angular momentum of the collisions or equivalently the rotational energy-level spacing. It can be shown that the rotational angular momentum quantum number $l \approx 100$ for the collisions we have been considering. At such high values of l the system can be described quite accurately classically.

The condition for quasistatic excitation is well fulfilled for $Hg(^3P_1-^1S_0)$–Kr at the detunings investigated. However, clasical quasistatic theory fails to predict the correct form for the satellite. Bieniek[15] proposed a modification of the model that deals with the satellite semiclassically, thus smoothing out the cusp in fig. 3.

4.3. Excitation Reorientation and Decoupling

The work of Hertel *et al.*[19] and Grosser has shown the concept of a locking radius to be useful when the potentials involved separate rapidly. As has been discussed, the concept is not useful when the potentials remain close together over a large region of R. Since this is the case for $Hg(^3P_1-^1S_0)$–Kr we now discuss ways in which the theory could be amended to take account of this problem. Since the model is based on the three processes of excitation, rotation and decoupling we examine these three processes in turn.

The decoupling-radius model assumes that, at excitation, dipoles of either pure $\Omega = 0$ or pure $\Omega = 1$ character are created. Excitation therefore occurs to states with the well defined wavefunctions Ψ_0 (pointing along the molecular axis) or Ψ_1 (at right angles to the molecular axis). In an exact quantum-mechanical treatment of this aspect, excitation occurs to a state whose wavefunction is a linear superposition of these two wavefunctions, $\Psi = C_1\Psi_1 + C_0\Psi_0$. In a perturbation approach C_1 and C_0, which control the admixture of the states involved, are inversely proportional to the energy difference between the states. When, as in our case, excitation occurs at points where the energy separation of the states is small, the correct form of the wavefunction must be used. In the inexact treatment of the decoupling-radius model it is assumed that the Ψ_1 and Ψ_0 wavefunctions rotate adiabatically, that is the rotation does not induce transitions between the two states. These wavefunctions are therefore independent solutions of the Schrödinger equation. In reality the proximity in energy of the two states will lead to further mixing between them during the collision. In order to describe this situation we must solve a pair of coupled equations.

In the exact method it is unnecessary to introduce the concept of a decoupling radius since the behaviour at all R is take care of automatically once the correct form of the wavefunction is used.

In summary, the effects of assuming quasistatic excitation and classical trajectories are either negligible or can be allowed for by making the reasonably simple amendments to the model. Far more serious difficulties arise, for our system, from the assumptions of incoherent excitation, adiabatic reorientation and the use of a decoupling radius. The next step would therefore be to retain the former approximations but to treat the excitation and reorientation processes as described above. It is possible to treat the entire problem quantum-mechanically,[20] Work along these lines is under way at present in this laboratory. The drawback of the full quantum-mechanical calculation is that it does not lend itself to simple physical interpretation.

5. Conclusions

The choice of $Hg(^3P_1-^1S_0)$-Kr as a system worthy of study has been supported throughout by the availability of the interatomic potentials, allowing quantitative tests of theory. However, even the qualitative features of our polarization curve differ from those of the corresponding curve for $Sr(^P_1-^1S_0)$-Ar. The chief qualitative feature in that system was the dip in the polarization near the minimum in the Σ difference potential. It has been shown that in the case of $Hg(^3P_1-^1S_0)$-Kr this trend is reversed and we see an enhancement of the polarization near the minimum in the $\Omega = 1$ difference potential. Just as this qualitative feature allowed Alford *et al.* to label the potential curves definitively as Σ and Π we are able, through this work, to label the $Hg(^3P_1-^1S_0)$-Kr potentials definitively as $\Omega = 0$ and $\Omega = 1$.

One aim of this work was to provide a test of the decoupling radius model. It would be unfair to attribute the failure of our analysis of section 3 to account for our data to the general inadequacy of the theory used. The problem clearly lies in the fact tha some of the underlying assumptions of the model are invalid for a system such as ours in which the $\Omega = 0-\Omega = 1$ potential difference is small.

The model as it stands has therefore not been tested in a region where it can be expected to be adequate. An alternative approach to performing such a test would be to conduct experiments to elucidate the interatomic potentials for Sr-RG and Ba-RG systems since for these systems the polarization data available in the literature are excellent. Such experiments are difficult to perform but have been proposed and are being pursued by other experimenters in the field.

It is arguable that once the stated aim of testing the model had been achieved the logical next step would have been to examine systems for which the validity criteria of the inherent approximations are less well satisfied. In order that such a model be worthy of pursuit it should be widely applicable and should survive, with little modification, reasonable changes in the system studied. The purpose of examining such marginal systems would be to test the range of applicability of the decoupling-radius model. $Hg(^3P_1-^1S_0)$-Kr is just such a marginal system, and our results bring into sharp focus the model's limitations.

Another way of viewing our results is to note that when the decoupling radius is very small (or when it is impossible to define R_{dc} at all meaningfully) the degree of orbital selectivity atainable is poor. This is borne out by the generally high polarizations we have measured. While the system studied may be ideal for testing quantum-mechanical redistribution theory it is unsuited to the exposition of pronounced stereochemical features.

References

1 M. O. Hale, I. V. Hertel S. R. Leone, *Phys. Rev. Lett.*, 1984, **53**, 2296.
2 W. Bussert and S. R. Leone, *Chem. Phys. Lett.*, 1987, **138**, 269; 276.
3 M. C. Duval, O. D. D'Azy, W. H. Breckenridge, C. Jouvet and B. Soep, *J. Chem. Phys.*, 1986, **85**, 6324.
4 J. Grosser, *J. Phys. B*, 1981, **14**, 1449.
5 E. L. Lewis, M. Harris, W. J. Alford, J. Cooper and K. Burnett, *J. Phys. B*, 1983, **16**, 553.
6 N. Andersen, in XII Summer School on Quantum Optics, ed. J. Fiutak and J. Mizerski (World Scientific Publishers, 1985).
7 D. Segal, *Thesis* (University of London, 1988).
8 W. J. Alford, N. Andersen, K. Burnett and J. Cooper, *Phys. Rev. A*, 1984, **30**, 2366.
9 V. Kroop and W. Behmenburg, *Z. Phys. A*, 1980, **294**, 299.
10 Grycuk and E. Czerwosz, *Physica C*, 1981, **106**, 431.
11 Fuke, T. Saito and K. Kaya, *J. Chem. Phys.*, 1984, **81**, 2591.
12 R. E. M. Hedges, D. R. Drummond and A. Gallagher, *Phys. Rev. A*, 1972, **6**, 1519.
13 J. L. Carlsten, A. Szöke and M. G. Raymer, *Phys. Rev. A*, 1977, **15**, 1029.
14 Harima, Y. Fukuzo, K. Tachibana dn Y. Urano, *J. Phys. B*, 1981, **14**, 3069.
15 R. J. Bieniek, *Phys. Rev. A*, 1987, **35**, 3663.
16 A. Omont, E. W. Smith and J. Cooper, *Astrophys. J.* 1972, **175**, 185: 1973, **182**, 283.
17 R. J. Ballagh and J. Cooper, *Astrophys. J.*, 1977, **213**, 479.
18 E. L. Lewis, *Phys. Rep.*, 1980, **58**, 1.
19 I. V. Hertel, H. Schmidt, A. Bähring and E. Meyer, *Rep. Prog. Phys.*, 1985, **48**, 375.
20 P. S. Julienne and F. H. Mies, *Phys. Rev. A*, 1986, **34**, 3792.

Alignment Effects involving Multiple Pathways: Electronic Energy Transfer of Sr 5s6p $^1P_1$ with Rare Gases

Laurie J. Kovalenko, Ruth L. Robinson and Stephen R. Leone*†

Joint Institute for Laboratory Astrophysics, National Bureau of Standards and University of Colorado, Departments of Chemistry and Physics, University of Colorado, Boulder, Colorado 80309-0440, U.S.A.

Orbital alignment effects and branching fractions have been measured for collisionally induced electronic energy transfer from the Sr 5s6p $^1P_1$ state to seven near-resonant states: 5s6p $^3P_{2,1,0}$, 4d5p $^1D_2$ and 4d5p $^3F_{4,3,2}$. The measurements were carried out in a crossed-beam experiment using a pulsed, linearly polarized laser which propagates perpendicular to the initial average relative velocity vector of the collision partners. The results show remarkably high specificity in both the formation of product states and the alignment effects into each state. With He as a collision partner, formation of the $^3F_3$ state shows a preference for the laser polarization parallel to the collision axis; formation of the $^3P_1$ state shows no alignment dependence, whereas the $^3P_0$ state shows a strong preference (4:1) for the perpendicular polarization. All other states are preferentially formed with the perpendicular laser polarization. In addition, the branching fractions produced by collisions with He are highly non-statistical. With Xe, the branching fractions approach those of a statistical distribution, suggesting a strong interaction; however, alignment preferences are still discernible for individual states. Despite the complexity and large number of curve-crossing possibilities in this multistate system, several highly selective crossings are inferred from the observed alignment effects. Specific alignment preferences are discussed in terms of symmetry and energy considerations.

Alignment and orientation effects in inelastic collisions of atoms are of keen interest to experimentalists and theorists alike. Detailed summaries of previous work are provided in the reviews of Hertel *et al.*[1] and Campbell *et al.*[2] Low collision energy, crossed-beam experiments with rare-gas atom collision partners are among some of the simplest alignment-dependent processes for which accurate theoretical treatment is possible. They are studied using polarized lasers to prepare the initial collision alignment. Several studies are notable. Hale *et al.*,[3,4] Neuschäfer *et al.*[5] and Bussert *et al.*[6] studied the Ca–rare-gas spin-changing system. Devdariani and Zagrebin[7] performed a semi-classical Langau–Zener curve-crossing analysis, while Pouilly and Alexander[8] investigated full quantum-mechanical calculations for this system. Düren and Hasselbrink[9] studied alkali-metal atoms using circularly polarized light to prepare the initial collision orientation and analysed their results quantum-mechanically. Manders *et al.*[10,11] analysed the alignment dependence of fine-structure-changing collisions for the excited Ne** + He system. They also developed quantum-mechanical[11] and semiclassical[12] treatments of the alignment preference.

One difficulty in treating these collision systems theoretically is the lack of good potential-energy curves. The spectroscopy of stable, low-temperature collision complexes[13] is one approach which offers excellent promise for an experimental determination of the potential-energy curves. Transient collisional probing of the energy-transfer
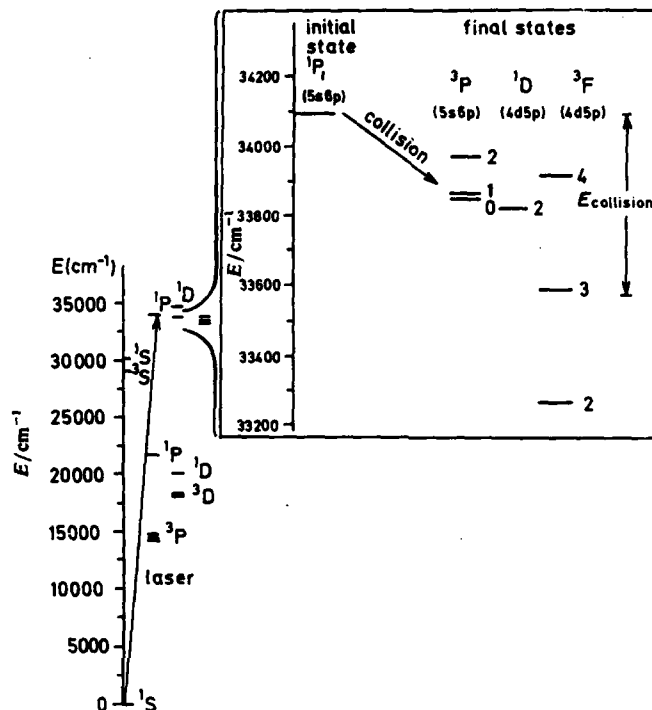
Fig. 1. Relevant strontium energy levels [ref. (16)]. The laser prepares the initial 5s6p ^{1}P$_1$ state as shown at the left. Collisions with rare-gas atoms result in energy transfer to the seven near-resonant states, as shown in the enlarged region at the right. The average collision energy for He is noted.

systems by wind absorption and emission is yet another way to interrogate the alignment effects.[14]

In an initial study of the Sr 5s6p ^{1}P$_1$–rare-gas system[15] it was found that several collisionally produced states have very different alignment effects. This was surprising given the complexity and number of curve-crossings in the energetically accessible region. In this contribution we present a detailed study of the alignment effects and branching fractions for most of the individual states produced upon collision of Sr 5s6p ^{1}P$_1$ with He and Xe. The mean collision energies are 529 cm^{-1} with He and 631 cm^{-1} for Xe. All seven of the collisionally produced states that are observed lie lower in energy than the initial state; the total energy spread of these levels is 832 cm^{-1}, as shown in Fig. 1. Despite the large density of states in the region, highly non-statistical population distributions and large alignment effects are observed for many states. The results are interpreted by an analysis of the symmetry and energy of the molecular states in the crossing region.

Experimental

The experimental apparatus is similar to that described previously[6] with the following modifications: a monochromator is used to resolve individual fine-structure states, photon counting is used to detect fluorescence from collisionally produced states since

the signals through the monochromator are much weaker, and Helmholtz coils are used
to shield the effect of the earth's magnetic field by a factor of 4.

The basic apparatus is as follows (see fig. 2). Three mutually perpendicular beams
intersect at the centre of the chamber: the strontium-atom beam emerges from a pinhole
in an oven located behind the chamber and travels out from the plane of the paper; the
rare-gas beam emerges from the pulsed valve above the chamber and travels down; the
pulsed, linearly polarized u.v. laser beam passes from right to left, going through a
polarization rotator before entering the chamber. The linearly polarized laser prepares
Sr atoms in the 6^1P_1 state with the p orbital aligned along the direction of laser
polarization. Sr is a particularly suitable atom for alignment studies since 93% of its
natural occurring isotopes have a nuclear spin of zero; thus the p orbital remains
space-fixed in the absence of external forces. The initial alignment of the p orbital is
chosen by rotating the polarization of the laser with a double Fresnel rhomb polarization
rotator. Subsequent collision with rare-gas atoms results in population of a number of
near-resonant states: $^3P_{2,1,0}$, $^3F_{4,3,2}$, and $^1D_2$. There is no fluorescence observed from
the $^1D_2$ state located $629\ cm^{-1}$ higher in energy than the initial $^1P_1$ state. Fluorescence
is observed from the $^1S_0$ state located $3507\ cm^{-1}$ below the initial $^1P_1$ state; however,
this fluorescence is seen even in the absence of the rare gas, indicating that this state is
populated by cascade fluorescence. Two fibre bundles are used to collect the fluorescence
simultaneously from both the initial laser-prepared $^1P_1$ state and a collisionally populated
state. Fluorescence entering the larger fibre bundle at the left is used to detect the initial
$^1P_1$ state. Fluorescence entering the smaller fibre bundle at the right is resolved to detect
individual product state transitions. Signals are analysed as a function of laser polariz-
ation angle using time-gated photon counting for the states populated by energy transfer,
and time-gated boxcar integration for the initial $^1P_1$ state.
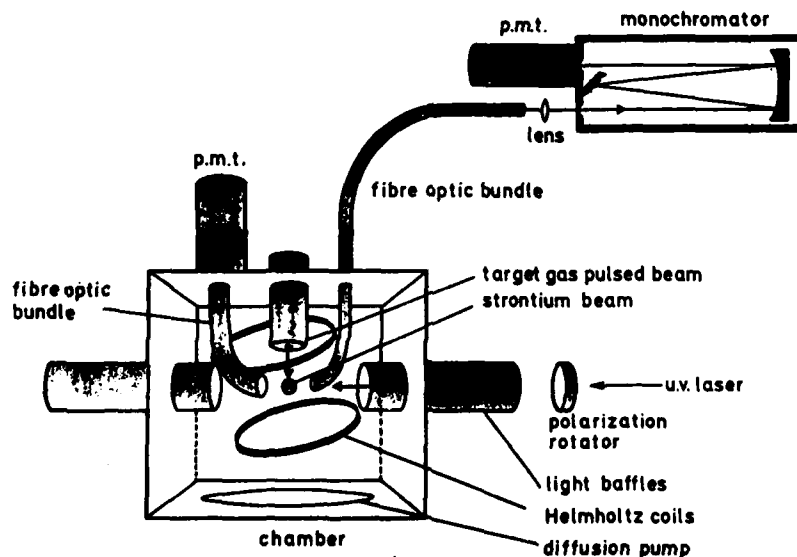
Fig. 2. Schematic diagram of the experimental apparatus. Three mutually perpendicular beams
intersect at the center of the chamber. The Sr beam emerges from a pinhole in an oven located
behind the chamber; the rare-gas beam emerges from the pulsed beam valve above the chamber;
the pulsed linearly polarized laser beam passes through a polarization rotator before entering the
chamber. Two fibre bundles simultaneously collect fluorescence from both the intial state and
the collisionally populated states.

The effusive Sr-atom beam is continuous and emanates from a 1 mm diameter hole in a 953 K nozzle, which is connected to a separately heated 813 K oven located behind the chamber. After 8 mm the Sr beam passes through a 2 mm diameter skimmer; after another 27 mm it encounters the interaction region where the Sr density is 2×10^{10} atoms cm^{-3} and the velocity is 445 m s^{-1}.

The He (or Xe) beam emerges from a pulsed valve at the top of the chamber and after 18 mm crosses the Sr beam perpendicularly with an angular spread determined by the laser beam diameter of 4 mm. With a nozzle diameter of 150 μm and a backing pressure of 80 kPa for helium (37 kPa for xenon), the rare-gas density is 5×10^{14} atoms cm^{-3} (2×10^{14} atoms cm^{-3} for Xe) and the velocity is 1.76×10^3 m s^{-1} (300 m s^{-1} for Xe). Thus the mean relative collision velocities are calculated to be 1.82×10^3 m s^{-1} with He and 536 m s^{-1} for Xe, corresponding to collision energies of 66 and 78 meV, respectively. The angle between the initial relative velocity vector and the horizontal Sr beam is 75° for He (33° for Xe). We note, however, that the *ca.* 200 ns long collection gate times were taken in the early time region of the *ca.* 1 ms long gas pulse, where signals from the collisionally produced states were maximized and the magnetic field due to the pulsed valve was minimized, rather than in the more central region of the pulse, which is more characterizable. Thus the rare-gas beam density and velocity in the actual experiments may differ from the calculated values stated above.

The pulsed, linearly polarized laser beam from a frequency-doubled dye laser travels through a polarization rotator and crosses at right angles to the two atomic beams. The laser beam wavelength is 293 nm, the diameter is 4 mm, the energy is typically 200 μJ per pulse, the temporal width is 5 ns and the frequency width is 0.1 cm^{-1}.

Helmholtz coils are used to shield the earth's magnetic field by a factor of four. The residual weak magnetic field has a negligible effect on the alignment of the initially prepared p orbital, owing to its short (65 ns) lifetime. The present measurement of the Sr 6^1P_1 lifetime agrees with a previous laser fluorescence measurement[17] of 65 ns. These measurements differ from the value of 110 ns reported by Schwenz and Leone.[18] The 110 ns measurement may be suspect since the Sr gas density was at least 100 times larger than that in the present measurement; thus radiation trapping may be responsible for the longer lifetime obtained earlier.

Two fibre bundles, one of diameter 1 cm and the other 7 mm, are located 2 cm from the interaction region. They are used to monitor simultaneously the fluorescence signals from the initially prepared $^1P_1$ state and the collisionally produced state. Total fluorescence is observed without angular or polarization analysis. Light entering the larger fibre bundle passes through a cut-off filter to block scattered laser light, a bandpass filter to select the $^1P_1$ transition at 717 nm to a $^1D_2$ state, and is detected by the photomultiplier (PMT). A boxcar-gated signal averager then integrates the signal, which is either directly displayed with a strip-chart recorder or digitized. This signal is proportional to the number of atoms in the initial $^1P_1$ state and is used for normalization. A 6% variation of the fluorescence with laser-polarization angle is seen for the initially prepared state, as expected from the position of the fibre bundle, the solid angle of collection and the fact that a P-D transition is only partially polarized.

The much weaker fluorescence signals from the collisionally produced states are detected by photon counting. Light entering the smaller fibre bundle passes through a lens to match the $f/\#$ of the monochromator. The $\frac{1}{2}$ m monochromator selects a transition from a collisionally produced state and the signal is detected by a PMT, amplified, discriminated and counted. A typical gate time is 200 ns with a delay time of 25–50 ns after the laser pulse. We note that this may affect the branching fractions if the lifetimes differ among the states. A spherical mirror, not shown in fig. 2, is mounted opposite the smaller fibre bundle and used to increase the signal intensity from the collisionally produced states. The signal is proportional to the number of atoms in each collisionally produced state. No anisotropy of fluorescence from the collisionally produced states was observed.

Typically 1000 laser pulses at 10 Hz are averaged for each experimental point. Since each spectrum takes 10 h, fluorescence intensities are normalized to the $^1P_1$ signal to correct for drifts in laser intensity and Sr-beam density. No correction for rare-gas beam density is necessary. For the alignment measurements, fluorescence intensities are measured with the rare-gas beam on and off. These are then subtracted. Alignment curves are typically run three times each; one was run six times and two only once. For the shorter-time alignment experiments, it was not necessary to normalize to the $^1P_1$ signal, nor was it necessary to correct for rare-gas beam density.

Results

The linearly polarized laser prepares the initial Sr 6 $^1P_1$ p orbital along the direction of polarization. Since 93% of the naturally occurring isotopes of Sr have no nuclear spin, the p orbital for these atoms remains space-fixed in the absence of external forces. The initial alignment of the p orbital is characterized by the angle, β, between the polarization vector, **E**, and the initial relative velocity vector, *v*. For example, the angle $\beta = 90°$ prepares the p orbital perpendicular to the initial relative velocity vector. Thus β is related to the angle between the laser polarization and the horizontal Sr beam, θ_{lab}, by the equation $\beta = \theta_{lab} - 75°$ for collisions with He ($\beta = \theta_{lab} - 33°$ with Xe).

Two kinds of experiments are considered below: (*a*) emission spectra of the collisionally produced states and (*b*) alignment effects for most of the collisionally produced states.

(*a*) Emission Spectra

Fig. 3 shows typical emission spectra of the states produced by collision of Sr 5s6p $^1P_1$ with both He and Xe, where the Sr p orbital is prepared with the laser polarization perpendicular to the initial relative velocity vector. This polarization was chosen to maximize the weakest fluorescence signals. Only the strongest emission line from most states is displayed. With He as the collision partner, negligible emission is seen from the $^3F_2$ state, indicating a relatively small probability of excitation, most likely because of the large energy discrepancy from $^1P_1$ (see fig. 1). With Xe as the collision partner, very different collisionally produced state populations are seen, most likely due to the much stronger interaction potentials overall. Fluorescence intensities are normalized to the $^1P_1$ signal to correct for drift in the laser intensity and Sr-beam density.

The relative fluorescence intensities for He as compared with Xe for all observed spectral emission peaks are given in table 1, where averages of the fluorescence intensities for the perpendicular and parallel laser polarizations are reported. The unresolved emission peak from $^3P_{2,1}$ is also included. The $^1D_2$ emission peak which neighbours the $^3F_4$ peak at 640.7 nm is assumed to be of negligible intensity compared to the $^3F_4$ peak since it was not seen in the compilation of spectral lines by Reader and Corliss.[19] The intensities in the table are normalized so that their sum is equal to 100. Very different relative populations are seen for He compared to Xe; *e.g.* He produces much more $^3P_2$ excitation, while Xe produces more $^3F_4$ and $^3F_2$.

For further insight into the mechanisms of the collisional transfer, we estimate branching fractions from the relative intensities of the collisionally produced states and make a qualitative comparison with a statistical distribution. To relate the above fluorescence intensities to populations, we sum all fluorescence intensities with the same initial state. This total intensity should be proportional to the number of atoms in that initial state.[20a] The relative contribution of $^3P_2$ and $^3P_1$ to the fluorescence intensity of the unresolved $^3P_{2,1}$ peak was estimated using the measured intensities of the other multiplet peaks and fluorescence data from Reader and Corlis.[19] The latter was found to agree well with relative multiplet intensities calculated from pure Russell-Saunders coupling.[20b] We make the assumption that the major fluorescence pathways are $^3P \rightarrow ^3D$,
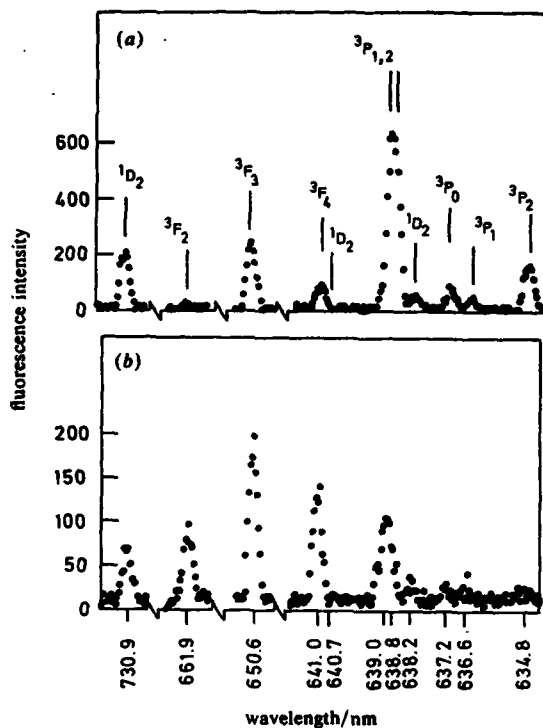
Fig. 3. Emission spectra induced by collisional transfer from Sr 6^1P_1: fluorescence intensity *vs.* wavelength with (*a*) He as collision partner and (*b*) Xe as collision partner. Initial states of the transitions are indicated above the peaks in (*a*); wavelengths of the transitions are indicated below the spectrum in (*b*). The laser is polarized perpendicular to the initial relative velocity vector.

$^1D \rightarrow ^1D$, ^3D and $^3F \rightarrow ^3D$. This is reasonable since both intercombination lines and infrared transitions are expected to be relatively weak; the latter is weak because of the ν^{-3} dependence. We also must assume that the lifetimes of all seven collisionally populated states are approximately the same, since the specific gate width and delay used in our experiments may introduce a sampling bias. A crude fluorescence-lifetime measurement of groups of states suggests that this is a reasonable assumption. From these assumptions, estimates of the branching fractions into various states for both He and Xe as collision partners are shown in fig. 4, along with a statistical population distribution based on relative degeneracies for comparison. The population distribution for collision with Xe approaches much more closely that of a statistical distribution than the result for He. This suggests that the strongly polarizable Xe mixes the product states more completely. It should be noted that previous results for the branching fractions with Kr as the collision partner are also very close to statistical.[18]

(*b*) Alignment Effects

Qualitatively different alignment effects are readily observed for many of the collisionally produced states, as assessed from spectra taken with different laser polarizations. Fig. 5(*a*) shows two scans of the $^3P_0$ and $^3P_1$ peaks with He as the collision partner, first

Table 1. Relative fluorescence intensities for collisional transfer
from Sr 5s6p $^1P_1$

transition from collisionally produced state	λ nm	collision partner[a]	
		helium	xenon
$^3P_{2,1}{}^{b} \rightarrow {}^3D_{3,2}$	638.8	36.8 ± 0.9	17.7 ± 1
	639.0		
$^3P_2 \rightarrow {}^3D_2$	634.8	8.6 ± 0.5	1.5 ± 0.8
$\rightarrow {}^3D_1$	632.4	—[c]	—[c]
$^3P_1 \rightarrow {}^3D_1$	636.6	2.1 ± 0.2	2.1 ± 1.0
$^3P_0 \rightarrow {}^3D_1$	637.2	2.9 ± 0.3	2.4 ± 1.0
$^3F_4 \rightarrow {}^3D_3$	641.0	4.0 ± 0.3	20.0 ± 1.1
$^3F_3 \rightarrow {}^3D_2$	650.6	28.6 ± 0.8	29.0 ± 1.3
$\rightarrow {}^3D_3$	654.9	3.8 ± 0.3	4.0 ± 0.6
$^3F_2 \rightarrow {}^3D_1$	661.9	0.6 ± 0.6	9.9 ± 0.8
$\rightarrow {}^3D_2$	664.5	—[c]	3.4 ± 0.5
$\rightarrow {}^3D_1$	669.0	—[c]	—[c]
$^1D_2 \rightarrow {}^1D_2$	730.9	10.4 ± 0.5	7.6 ± 0.7
$\rightarrow {}^3D_1$	638.2	2.1 ± 0.3	2.4 ± 0.5
$\rightarrow {}^3D_2$	640.7	—[c]	—[c]
$\rightarrow {}^3D_3$	644.8	—[d]	—[d]

[a] Normalized to 100. [b] The unresolved peak for $^3P_{2,1}$ is included. [c] No fluorescence observed. [d] Not resolved; assumed negligible.
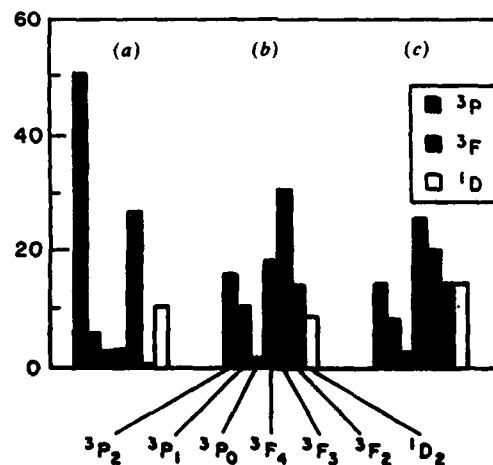
Fig. 4. Approximate collisionally produced state populations. Three distributions of relative state populations are given: (*a*) the distribution produced with He, (*b*) that with Xe and (*c*) a statistical distribution. Each population distribution is normalized to 100.
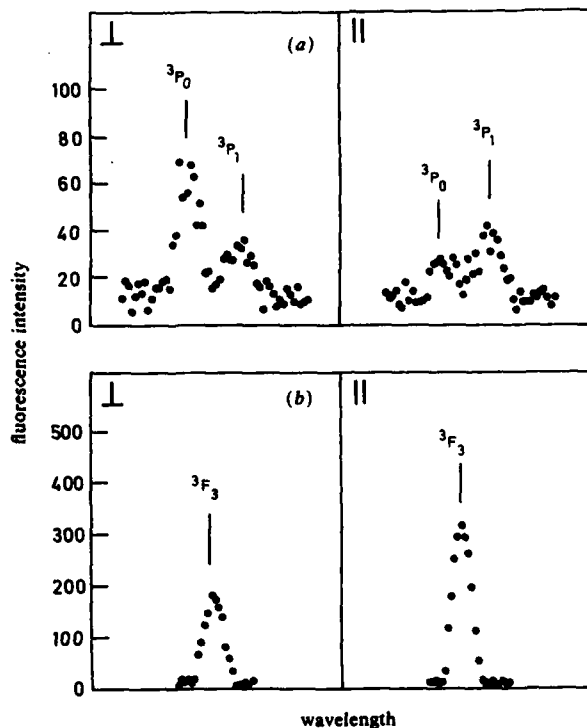
Fig. 5. Qualitatively different alignment effects for He as the collision partner. (*a*) Emission spectrum of transitions originating from the ^{3}P$_1$ and ^{3}P$_0$ states with the laser polarization perpendicular ($\perp$) and parallel ($\parallel$) to the intial relative velocity vector. (*b*) The same as in (*a*) only now the transition is from the ^{3}F$_3$ state.

with the laser polarization perpendicular to the relative velocity vector, then with the parallel laser polarization. It is clear that the ^{3}P$_0$ state is preferentially populated by collision when the laser polarization is perpendicular to the initial relative velocity vector, while the ^{3}P$_1$ state shows little preference. Fig. 5(*b*) shows the opposite alignment effect for the ^{3}F$_3$ state, which is preferentially produced with a parallel laser polarization. In these spectral scans, the fluorescence intensities are normalized to the ^{1}P$_1$ signal to correct for drifts in laser intensity and Sr-beam density.

More quantitative measurements of the alignment effects are made for each state by monitoring the fluorescence intensity at a fixed monochromator wavelength as a function of angle, β, between the laser polarization and the initial relative velocity vector, as shown in fig. 6. Measurements at each angle are taken both with and without the rare-gas beam. Fig. 6 shows the difference between the respective fluorescence signals. Because the stability of the laser and atom beam densities is good over the duration of these experiments, no further normalization was necessary. Most sets of data consist of three independent runs which are averaged together. The error bars show the standard deviation of several measurements taken at one angle. A least-squares fit is made to the data with the functional form

$$I(\beta) = (I_{max} + I_{min})/2 + [(I_{max} - I_{min})/2] \cos[2(\beta - \beta_{max})]$$
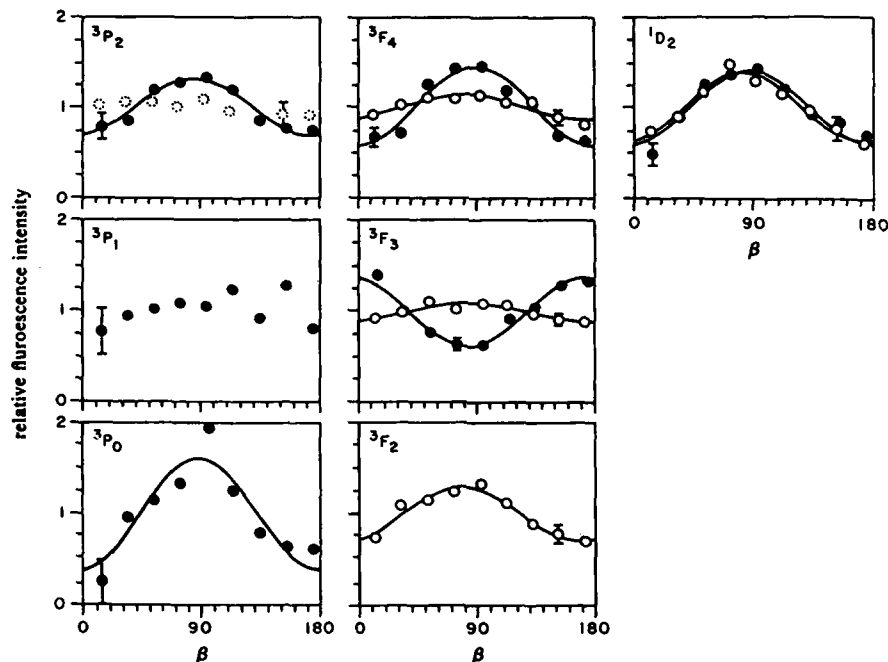
Fig. 6. Alignment effects: relative fluorescence intenstiy vs. angle, β, between the polarization of the laser and the initial average relative velocity vector of the collision partners. The solid lines are least-squares fits to the theoretically expected form. The dotted circles are for the unresolved emission from the sum of the $^3P_1$ and $^3P_2$ states for Xe. ●, He; ○, Xe.

where $I(\beta)$ is the measured intensity of fluorescence at the angle β between the laser polarization and the relative velocity vector. The values of I_{max}, I_{min} and β_{max} are extracted from the least-squares fit. The ratio of I_{max}/I_{min} and β_{max} are given in table 2. For easy comparison between different collisionally produced states, we show in fig. 6 the data and the fit for the 'normalized' relative fluorescence intensity, $I_{rel}(\beta)$, which is obtained by dividing the observed fluorescence intensity by the average fluorescence intensity:

$$I_{rel}(\beta) = 2I(\beta)/(I_{mux} + I_{min})$$

$$= 1 + [(I_{max} - I_{min})/(I_{max} + I_{min})] \cos [2(\beta - \beta_{max})].$$

The strong emission peaks for $^3P_1$ and $^3P_2$ at 639.0 and 638.8 nm, respectively, were not resolved. Rather, the alignment effects for these two states with He as a collision partner were measured using the well resolved peaks at 636.6 and 634.8 nm, respectively. In the case of Xe as the collision partner these latter spectral features were too weak to be measured, so only the alignment effect for the combined $^3P_{2,1}$ emission peak was measured, as indicated by the dotted data points for the $^3P_2$ state in fig. 6. The analyses to determine the alignment effects for the $^3P_{2,1}$ emission peak produced with Xe and the $^3P_1$ peak produced with He gave values of β_{max} nearer to 45°. Since there is no physical basis for such a result, we conclude there to be no discernible alignment preference, as noted in table 2.

Table 2. Summary of alignment effects and angle of maximum fluorescence intensity for Sr 5s6p $^1P_1$ transfer

collisionally produced state	preferred laser polarization	I_{max}/I_{min}	$\beta_{max}{}^a$
	helium as collision partner		
$^3P_2$	$\perp$	1.91 ± 0.14	85.6 ± 2.9
$^3P_1$	none discernible[b]	—	—
$^3P_0$	$\perp$	4.09 ± 1.56	89.0 ± 5.5
$^3F_4$	$\perp$	2.48 ± 0.25	90.0 ± 2.7
$^3F_3$	$\parallel$	2.25 ± 0.18	-6.65 ± 2.6
$^3F_2$	—[c]	—	—
$^1D_2$	$\perp$	2.37 ± 0.29	88.4 ± 3.5
	xenon as collision partner		
$^3P_{2,1}$	none discernible[b]	—	—
$^3P_0$	—[c]	—	—
$^3F_4$	$\perp$	1.31 ± 0.07	82.6 ± 5.4
$^3F_3$	$\perp$	1.21 ± 0.05	82.4 ± 5.4
$^3F_2$	$\perp$	2.22 ± 0.18	79.9 ± 2.8
$^1D_2$	$\perp$	2.18 ± 0.16	83.0 ± 2.4

^{a} β_{max} is the angle between the laser polarization and the initial relative velocity vector. ^{b} Fluorescence signal observed. ^{c} Fluorescence signal too weak.
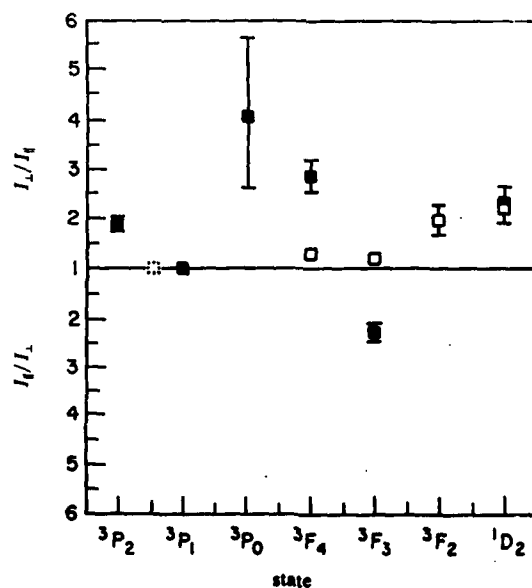
Fig. 7. Summary of alignment data: the ratio of maximum-to-minimum fluorescence intensity is shown for each collisionionally produced state. States showing no preference for either polarization have a ratio of 1. States which prefer perpendicular laser polarization have their ratio plotted above the line; those which prefer parallel laser polarization are below the line. The dotted square corresponds to the measurement with Xe using the unresolved $^3P_{2,1}$ peak. ■, He; □, Xe.

We note that the maximum fluorescence intensity is not at exactly $\beta = 0$ or 90°, but at slightly smaller angles. This may be attributed to an incorrect characterization of our atomic beams, to momentum transfer from the rare-gas beam to the Sr that occurs before the laser pulse, or to a strong dependence of the cross-section on velocity, which might skew the angle away from that anticipated.

A complete summary of the observed alignment effects is given both in table 2 and in fig. 7. The size of the effects are characterized in fig. 7 by the ratio of maximum-to-minimum fluorescence intensity; the vertical axis on the plot in fig. 7 also displays which laser polarization results in the most fluorescence. Points above the horizontal line marked unity represent a higher cross-section for perpendicular laser polarization; points below the line have a higher cross-section for parallel polarization. The dotted square point for xenon lying between the $^3P_1$ and $^3P_2$ states corresponds to the measurement using the unresolved $^3P_{2,1}$ peak.

Discussion

For low-collision-energy systems such as ours, a molecular picture of the collision process is expected to be appropriate when the atoms are close to each other.[2] Two molecular states, $\Pi(\Omega = 1)$ and $\Sigma(\Omega = 0^+)$, correlate to the initial 6 $^1P_1$ atomic state, while 21 molecular states correlate to the final seven atomic states,[21] as shown in table 3. Energy transfer is expected to occur most readily by radial coupling via avoided crossings between adiabatic molecular potential-energy curves of the same value of Ω, which can be correlated with various initial and final atomic states. In the absence of such radial coupling, weaker angular coupling between states differing in Ω by ±1 would then be expected to dominate.[22] The actual mechanism, however, depends on the nature of the diabatic potentials, the non-adiabatic couplings, the relative velocity, the impact parameter and the initial state prepared. Although relevant potential-energy curves are not yet available, we can make significant progress in interpreting the results from symmetry and energy considerations.

Experimentally the system is prepared at large internuclear separation with the Sr p orbital along the polarization vector of the laser. Preparation of an atomic orbital

Table 3. Adiabatic correlation of atomic states, in order of decreasing energy, with molecular states

atomic states	molecular states (Ω)				
initial state					
$^1P_1$ [a]				1 (Π)	$0^+(\Sigma)$
final states					
$^3P_2$			2	1	0^-
$^3F_4$	4	3	2	1	0^-
$^3P_1$ [b]				1	0^+
$^3P_0$ [c]					0^-
$^1D_2$			2	1	0^-
$^3F_3$ [b]		3	2	1	0^+
$^3F_2$			2	1	0^-

[a] The intial atomic state correlates to two molecular states: $\Omega = 0^+$ corresponding to a Σ alignment of the p orbital with respect to the internuclear axis, and $\Omega = 1$ corresponding to a Π alignment. [b] Only these two final atomic states correlate to molecular states with the same value of Ω as the $^1P_1$ state. [c] This is the only final state which does not correlate to a molecular state with the same value of Ω as the $^1P_1$ Π state.

with the laser polarization parallel to the initial relative velocity vector results in an asymptotic Σ molecular state, while preparation by the perpendicular polarization results in an asymptotic Π molecular state. We note that since the $^1P_1$ state is free from both fine and hyperfine interactions, and since the effect of external magnetic fields is negligible within the lifetime of the state, the orbital should retain its initial alignment at large internuclear distances.

An important consideration is whether the p orbital maintains its molecular alignment as the atoms approach. This depends on the impact parameter, the anisotropy of the electrostatic interaction and the relative velocity. An impact parameter of zero results in perfect preservation of molecular alignment at the distance of closest approach (*e.g.* Σ remains Σ), while all impact parameters large enough so that there is negligible interaction between the atoms result in a reversal of the initial molecular alignment at the distance of closest approach (*e.g.* Σ becomes Π).

Since this experiment averages over impact parameter, the most relevant question is whether the prepared molecular alignment of the p orbital is maintained for those collisions which contribute the most to the transition probability. If the main contribution to the transition probability occurs at small internuclear separation, or if it requires a large radial velocity, then only small impact parameter collisions will be successful in causing the transition. In this case, the collisions which would be effective in producing transitions would most likely preserve the initial molecular alignment as the atoms approach each other. If the main contribution to transition probability occurs at large internuclear separation, the initial molecular alignment might be somewhat preserved if the anisotropy of the electrostatic interaction and thus the propensity to 'lock' the orbital occurs at even larger R. The concept of a locking radius, however, is not fully agreed upon,[1,2,8,23] (We also note that several results which are seemingly contradictory to expectation have been interpreted on the basis of reversal of initial molecular alignment for large-impact-parameter collisions.[2])

Maunders *et al.*[10,12] and others[1,2,4,6] have successfully used the above picture with preservation of initial molecular alignment to interpret many experimental results, such as the collisional energy transfer in the Ne**-He system. However, Alexander and Pouilly[23] have interpreted their quantum-mechanical calculations with an alternative picture involving an indeterminate orbital alignment. We choose here to interpret the present results, which show strong alignment effects, by assuming preservation of initial molecular alignment. In the absence of known potential-energy curves, we do not attempt to guess the mechanism for the preservation. Nevertheless, excellent agreement between the observed and expected alignment dependences is obtained, suggesting that molecular alignment preservation may be a good picture in this case.

(a) Interpretation of Results with Helium

Table 3 shows the values of Ω for all the molecular states which correlate to the eight initial and final atomic Sr states arranged in decreasing order of energy. It can immediately be seen that there are only two final states, $^3P_1$ and $^3F_3$, which correlate to molecular states with the 0^+ value of Ω, which is the value of the molecular state corresponding to the Σ alignment of the Sr $^1P_1$ p orbital. Experimentally, it should be noted that these are also the only two states which do not show a preference for perpendicular laser polarization with He. We also immediately see that only one final state, $^3P_0$, correlates to a molecular state whose value of Ω (0^-) differs from that of both initial molecular states (1 and 0^+). By conservation of reflection symmetry[24] the 0^- molecular state cannot couple directly, either radially or angularly, to the 0^+ molecular state corresponding to the Σ alignment; however, it can couple to the $\Omega = 1$ state through angular coupling. This symmetry constraint appears to be a powerful predictive tool, since experimentally the $^3P_0$ state shows strong preference for the perpendicular laser polarization as expected.

Thus, many of the observed results with He are correctly anticipated if the above molecular picture and molecular alignment preservation concept are valid. The perpendicular laser polarization prepares a p orbital aligned perpendicular to the initial relative velocity vector, which correlates primarily to the Π molecular state, enabling radial coupling to the nearby $^3P_2$ state. The 0^+ component of the $^1P_1$ state can only form the $^3P_2$ state through angular coupling. The large branching fraction into the $^3P_2$ state for He and the strong preference for perpendicular alignment corroborate this picture. Preference production of the $^3P_2$ state has also been seen in analogous cases of energy transfer, such as Cd,[25a] Ba,[25b] and Hg.[26] Multiple avoided crossings with the many other states of the same value of $\Omega = 1$ would also distribute population among those states with perpendicular preferences. The notable exception is the $^3F_3$ state, which is discussed below. The smaller branching fractions for $^3F_4$ and $^1D_2$ indicate less effective coupling, while their slightly larger alignment effect may be a result of crosssings at smaller internuclear separation. This may not be unreasonable given the larger energy gap of $^3F_4$ and $^1D_2$ from the $^1P_1$. The $^3F_2$ state, which is the furthest away in energy, is not significantly populated at all, possibly indicating the absence of an effective avoided crossing. Only one state, $^3P_0$, cannot have an avoided crossing with either initial component of $^1P_1$. As mentioned above, although reflection symmetry prohibits the $^3P_0$ state from coupling directly to the 0^+ state, angular couplings may enable the transition between $\Omega = 1$ and 0^-; this may be reponsible for the very large perpendicular alignment effect. We note that Alexander and Pouilly[23] also predict a prefernece for perpendicular polarization to form this state in the analogous Ca system, based on their alternative description of the collision process.

Parallel laser polarization prepares a p orbital aligned along the initial relative velocity vector, which correlates to the Σ molecular state. This enables radial coupling primarily to either of the two $\Omega = 0^+$ molecular states that correlate to the $^3F_3$ and $^3P_1$ atomic states. Thus it may not be surprising that all the atomic states except these two show a preference for the perpendicular laser polarization. The large branching fraction into the $^3F_3$ state, despite its distance from the initial atomic state and its strong preference for parallel laser polarization, suggests a very effective coupling through an avoided crossing with the initial Σ state. A simple intuitive picture of the molecular state correlations[21] suggests that the 0^+ state correlating to the $^3F_3$ state has more Σ character and thus may be more repulsive than the 0^+ state correlating to the $^3P_1$ atomic state, which has more Π character. This might result in a primary avoided crossing of the initial Σ state with the $^3F_3$ state; a secondary avoided crossing may occur between the $^3P_1$ and $^3F_3$ states at larger R. The lack of discernible alignment preference for the $^3P_1$ state may indicate relatively equal coupling to both initial states in this case.

(*b*) Interpretation of Results with Xe

The above discussion using molecular-state symmetries and relative-state energies holds equally well for Xe as the collision partner; yet there are obvious differences in the results with Xe. Adiabatic molecular potential-energy curves with the heavier rare gases will have qualitatively different appearances than those with the light He, owing to the more polarizable nature of the heavy rare gas. The well depths may be much deeper and thus contain more avoided curve-crossings, which will mix the product states more fully; the avoided crossings may also occur at larger internuclear distances, which are accessed by large impact parameter collisions, thus changing the degree of preservation of initial molecular alignment. It may therefore intuitively be expected that the branching fractions will tend to be more statistical, and the alignment effects may not be as large. Indeed, this is what is observed. A statistical population distribution has also been seen in the Sr-Kr system.[18] In addition, the relative velocity for collision with Xe is much lower in our experiment than that for He. This may change the non-adiabatic coupling

between the molecular states. The reversal of the direction of the alignment effect for the $^3F_3$ state between He and Xe, where perpendicular polarization is preferred with Xe, while parallel polarization is preferred with He, may indicate in the Xe case an accessible avoided crossing between the $\Omega = 1$ curves.

We emphasize that the above interpretations are not unique; without relevant potential-energy curves, several explanations can be proposed. Therefore, potential-energy curves for this system and further theoretical work will be most important to be obtained.

Conclusion

Despite the high density of atomic states for this system, large selectivitives in both the branching fractions and alignment effects for several states are observed. The results have been interpreted using symmetry and energy considerations in a molecular picture with preservation of molecular alignment in the collision. Potential-energy curves, perhaps obtained by a van der Waals molecule spectroscopy experiment on the complex Sr–Xe, would be very useful in determining the pathways and curve-crossings responsible for the observed selectivity.

References

1 I. V. Hertel, H. Schmidt, A. Bähring and E. Meyer, *Rep. Prog. Phys.*, 1985, **48**, 375.
2 E. E. B. Campbell, H. Schmidt and I. V. Hertel, *Adv. Chem. Phys.*, 1988, **72**, 37.
3 O. Hale and S. R. Leone, *J. Chem. Phys.*, 1983, **79**, 3352.
4 M. O. Hale, I. V. Hertel and S. R. Leone, *Phys. Tev. Lett.*, 1984, **53**, 2296.
5 D. Neuschäfer, M. O. Hale, I. V. Hertel and S. R. Leone, in *Electronic and Atomic Collisions, XIV ICPEAC*, ed. D. C. Lorents, W. E. Meyerhof and J. R. Peterson (North Holland, Amsterdam, 1986), p. 586.
6 W. Bessert, D. Neuschäfer and S. R. Leone, *J. Chem. Phys.*, 1987, **87**, 3833.
7 A. Z. Devdariani and A. L. Zagregin, *Chem. Phys. Lett.*, 1986, **131**, 197.
8 B. Pouilly and M. H. Alexander, *J. Chem. Phys.*, 1987, **86**, 4790.
9 R. Düren and E. Hasselbrink, *J. Chem. Phys.*, 1986, **85**, 1880.
10 M. P. I. Manders, J. P. J. Driessen, H. C. W. Beijerinck and B. J. Verhaar, *Phys. Rev. Lett.*, 1986, **57**, 1577; 1986, **57**, 2472; M. P. I. Manders, W. M. Ruyten, F. v.d. Beucken, J. P. J. Driessen, W. J. T. Veugelers, P. H. Kramer, E. J. D. Vredenbreght, W. B. M. van Hoek, G. J. Sandker, H. C. W. Beijerinck and B. J. Verhaar, *J. Chem. Phys.*, 1988, submitted.
11 M. P. I. Manders, J. P. J. Driessen, H. C. W. Beijerinck and B. J. Verhaar, *Phys. Rev. A*, 1988, in press.
12 M. P. I. Manders, W. B. M. van Hoek, E. J. D. Vredenbregt, G. J. Sandker, H. C. W. Beijerinck and B. J. Verhaar, *Phys. Rev. A*, 1988, submitted.
13 K. Fuke, T. Saito and K. Kaya, *J. Chem. Phys.*, 1986, **81**, 2591; K. Yamanouchi, J. Fukuyama, H. Horiguchi and S. Tsuchiya, *J. Chem. Phys.*, 1986, **85**, 1806; M-C. Duval, O. B. D'Azy, W. H. Breckenridge, C.Jouvet and B. Soep, *J. Chem. Phys.*, 1986, **85**, 6324.
14 K. C. Lin, P. D. Kleiber, J. X. Wang, W. C. Stwalley and S. R. Leone, *J. Chem. Phys.*, 1988, in press.
15 W. Bussert and S. R. Leone, *Chem. Phys. Lett.*, 1987, **138**, 276.
16 C. E. Moore, *Atomic Energy Levels, National Standard Reference Data Science*, NBS Monograph 35 (1971).
17 G. Jönsson, C. Levinson, A. Persson and C.-G. Wahlström, *Z. Phys. A*, 1984, **316**, 255.
18 R. W. Schwenz and S. R. Leone, *Chem. Phys. Lett.*, 1987, **133**, 433.
19 J. Reader and C. H. Corliss, *Wavelengths and Transition Probabilities for Atoms and Atomic Ions* (NBS Monograph, 1980).
20 H. G. Kuhn, in *Atomic Spectra* (Academic Press, New York, 2nd edn, 1969), chap. 3, (*a*) pp. 170–172, (*b*) pp. 190–192.
21 G. Herzberg, in *Molecular Spectra and Molecular Structure* (Van Nostrand Reinhold, New York, 2nd edn, 1950), vol. 1, chap. 6, pp. 315–320.
22 E. E. Nikitin in *Theory of Elementary Atomic and Molecular Processes in Gases*, transl. M. J. Kearsley (Clarendon Press, Oxford, 1974), chap. 3, pp. 99–147.

23 M. H. Alexander abd B. Pouilly, in *Selectivity in Chemical Reactions*, ed. J. C. Whitehead (D. Reidel, Boston, 1988), p. 265.
24 R. T. Pack and J. O. Horschfelder, *J. Chem. Phys.*, 1968, **49**, 4009.
25 (*a*) W. H. Breckenridge and O. K. Malmin, *J. Chem. Phys.*, 1981, **74**, 3307;
   (*b*) W. H. Breckenridge and C. N. Merrow, *J. Chem. Phys.*, 1988, **88**, 2329.
26 A. B. Callear and K. Du, *Chem. Phys.*, 1987, **113**, 73.

Differential Scattering of Na(³P) from HF:
Reactive and Non-reactive Processes

R. Düren,* S. Milošević,† U. Lackschewitz and H. J. Waldapfel
*Max-Planck-Institut für Strömungsforschung Göttingen, D-3400 Göttingen,
Bunsenstraße 10, Federal Republic of Germany*

Double differential cross-sections for the scattering of a laser-excited Na
beam from an HF beam have been measured at collision energies between
0.29 and 0.86 eV. To the observed quantity ground-state collisions contribute
with non-reactive events, and excited-state collisions contribute with reactive
and non-reactive events. Therefore the analysis of the data allows us to
determine sound estimates for characteristics of the potential-energy surfaces
and the dynamics of the reaction. The effect of alignment of the attacking
atom has also been studied. Our results show that this influence is small
(2.5%) and is connected with the non-reactive channels.

Judging from the number of publications, reactions of alkali-metal atoms with hydrogen
halide molecules have attracted great interest in experiments on theory. So far most of
the experimental work referred to the electronic ground state of the alkali-metal atom,
but the effect of translational,[1-4] vibrational[4-6] and rotational[5-7] energy upon the reaction
has been studied. It is only recently that also the influence of electronic excitation of
the alkali-metal atom has been investigated.[8-10] The evaluation and interpretation of
these data is not at all settled, but the solution can be sought now, as quantum-chemical
work becomes available. Indeed, a fair amount of data for ground state[11-13] and
excited-state interaction[14-16] has appeared. Based on these results from quantum
chemistry, the dynamics of these processes have been studied theoretically.[17-19] As a
common result a reaction path associated with a non-adiabatic transition, a model well
known in non-reactive processes, may be considered to be established.

In our work we have concentrated on Na colliding with HF. This system appeared
to be a suitable candidate to serve as a model for this type of interaction, allowing easy
access to the electronically excited state in experiments and reliable results in quantum
chemistry with reasonable effort. The energetics of this reaction are shown in fig. 1:
The ground-state reaction is seen to be endothermic by *ca.* 0.89 eV,[20] which is not
surmounted by the collision energy (in our experiment this varies between 0.29 and
0.86 eV). With the energy of the photon (2.01 eV) and the translational energy this
changes to an exothermic reaction. It should be noted from fig. 1 that other channels
can be safely neglected. Even though these data are not too well established in the
literature, we can consider these estimates to be sound, anticipating one of our results,
namely that our time-of-flight results show no indications of these channels. Three
points of our experimental work may deserve special emphasis: (1) we measure double
differential cross-sections (energy- and angle-resolved) to obtain by this measurement
(as demonstrated through the years of beam work with elastic and inelastic processes)
the highest available information. (2) We evaluate not only the reactive part of these
cross-sections, but the non-reactive part as well. These latter measurements with their
well resolved structures (*e.g.* from rainbow scattering) are used to determine correspond-
ing characteristic data of the entrance side of the reaction. (3) The polarization of the

† Permanent address: Institute of Physics, University of Zagreb, Yugoslavia.
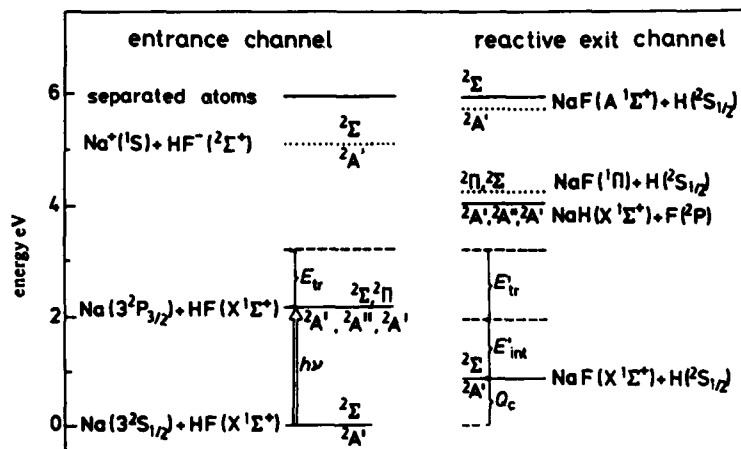
Fig. 1. Energetics of the interaction of ground-state Na and electronically excited Na with HF.

exciting laser light allows us to select the alignment of the initial state. A new method has been developed[21] to discriminate between the dependence of reactive and the non-reactive contribution to the measured signal upon the polarization.

Experimental

The experimental apparatus has been described in some detail before[10,22] and a brief summary may be sufficient. The Na and the HF beams cross each other at right angles, defining a scattering volume of $3 \times 1.5 \times 1.5$ mm^3. The Na beam is produced as a seeded beam allowing, by the variation of the temperature, the pressure and the carrier gas (He, H$_2$, Ne), a velocity variation between 1500 and 4500 m s^{-1}, which leads to collision energies between 0.14 and 1.1 eV (E_{CM}). The width of the velocity distribution varies between 15 and 20%. This beam is well collimated ($\delta\theta = 0.5°$) to allow proper (Doppler-free) excitation of the atoms. The HF beam is produced in a multichannel oven, placed 10 mm from the scattering volume, which leads to a substantial angular divergence ($\delta\theta = 35°$). This angullar divergence and the velocity distribution do not contribute too much to the net resolution of the apparatus owing to the comparably low mean velocity of HF. The detector rotates around the scattering volume in an in-plane arrangement. It consists of a rhenium wire as ionizer (by surface ionization), followed by a quadrupole mass spectrometer. The wire is kept at a temperature of 1650 K, which was chosen to yield equal and 100% ionization efficiency for Na and NaF.[23] At this temperature the residence time on the wire is short enough ($\leqslant 1$ μs) for time-of-flight measurements. The excitation of the Na atoms is performed with a single-mode c.w. dye laser, tuned to the hyperfine transition Na(3 ^{2}S$_{1/2}$, $F = 2$) $\leftrightarrow$ Na(3 ^{2}P$_{3/2}$, $F = 3$). The efficiency of this excitation is between 20 and 25%.[24]

Measurements

The measured cross-sections presented below were obtained with this basic machine in different modes of operation, differing by the kind of preparation and/or detection.

(1) Total Differential Cross-section for the Ground State

These measurements were performed by switching the primary beam on and off, recording the total number of scattered particles, *i.e.* Na and NaF (if present) as a function

of the scattering angle. These results do not discriminate between non-reactive and reactive events. The purpose of these results is to obtain eventual structures in the cross-sections, with a correlation to the channels, provided by other, time-resolved, measurements discussed below [see (3)].

(2) Total Differential Cross-sections for the Excited State

As above, the scattered particles were not selected with respect to their flight time. The Measurement was again achieved by lock-in technique, but this time the chopping was performed by switching the laser (and consequently the population of the excited state) on and off. From this measurement again structures in the cross-sections were obtained, with the correlation to channels provided, as discussed below [see (4)].

(3) Double Differential Cross-sections for the Ground State

To check the validity of the assumption that the ground-state reaction is endothermic, a pseudo-random chopper was installed to modulate the primary beam. Standard techniques of beam work, registration in a multichannel analyser and cross-correlation, is applied to obtain the double differential cross-section. No reactive signal was detected and hence the cross-sections obtained in a measurement, as described above [see (1)] were attributed to ground state non-reactive scattering only.

(4) Double Differential Cross-sections for the Excited States

For this measurement the intensity of the exciting laser was modulated with a pseudo-random sequence by means of a Pockels cell with subsequent polarizer. This led to a modulation of the population of the excited state and yielded with standard techniques of data-acquisition the non-reactive and the reactive differential cross-section.[10,25]

(5) Time-resolved Excited-state Polarization-dependent Cross-sections

By removing the polarizer after the Pockels cell and by careful adjustment of the voltages at the Pockels cell and the laser beam's geometry, the polarization dependence was measured again, applying then standard techniques to the measured spectra. This measurement yields, at the same time, very accurate polarization differences (owing to the high speed of chopping) and this quantity is selective with respect to the non-reactive and the reactive channels.[21]

Results

Fig. 2 shows one of the measurements of the total differential cross-section with laser on, laser off and the difference signal. In addition, the reactive total differential cross-section, obtained by integrating the time-resolved measurements (discussed below), is given for comparison. The pattern of the cross-section shows a first maximum at $\Theta \approx 12°$ (laboratory) and another at $\Theta = 60°$ (laboratory) for both laser on and off. The extrema in the difference signal are at positions different from these with laser on and laser off. This indicates that two patterns are hidden in the laser on signal, which is due to ground state and excited state scattering. The maximum at 60° in the laboratory is identified as orbiting in accordance with the nominal Newton diagram and vanishes, as it should, with increasing collision energy, yielding another maximum at finite angles instead. The ambiguity concerning the two patterns in the laser-on signal is resolved in the measurement of the ground-state cross-section, shown in fig. 3. As we have mentioned, at high energies no indication for reaction could be found and the total measurements represent

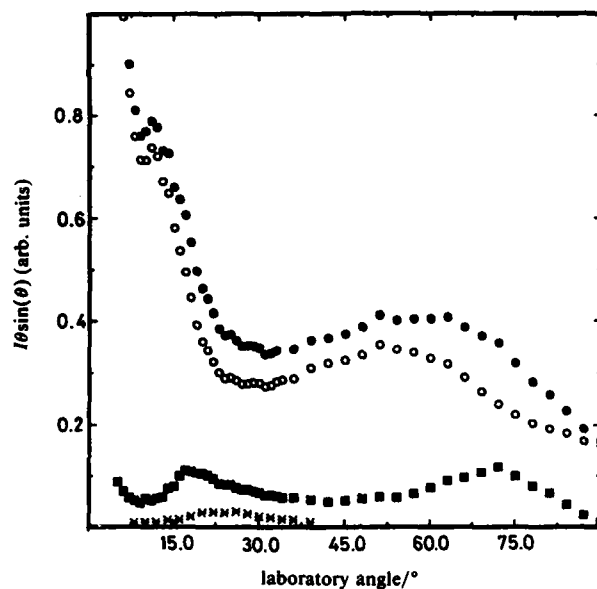*Differential scattering of* Na(^{3}P) *from* HF

Fig. 2. Total differential cross-section for the interaction of Na with HF at a collision energy of 286 meV: ○, laser off; ●, laser on; ■, difference laser on/off; ×, reactive cross-section.
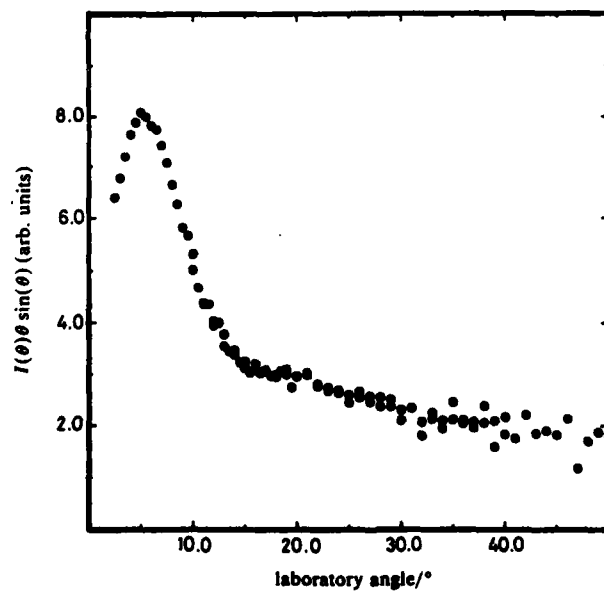

Fig. 3. Total differential cross-section for the interaction of ground-state Na with HF at a collision energy of 147 meV.

the non-reactive cross-section. This result shows clearly another maximum at 7° and an indication of a second maximum at 20°. The latter has been verified by measurements at higher energies.

Measurements of which we have given the two examples, were performed at a number of collision energies, all leading *mutatis mutandis* to the same results. These can be used as a common basis for an evaluation. This was achieved without complicated data reduction: the observed pattern was directly converted to its centre-of-mass counterpart by rescaling the angles with the help of the most probable Newton diagrams.

A feature of this system is given by the observation that the reactive cross-section is small compared with the non-reactive cross-section for all energies. This means that reactive events are a small perturbation to the non-reactive events and that the latter can be evaluated to a first approximation by neglecting reaction. In particular, this has the consequence that structures such as rainbow maxima can be treated as unperturbed. Trying to do so, another complication arises, namely that the rotational and the collisional characteristic times are nearly equal for our system. As a consequence, no proper discrimination between averaging target or static target applies. On the other hand, the HF molecule is highly anisotropic and in this situation a double rainbow, reflecting the scattering from the two ends of the target, may still be visible.[26] Simplifying these complications further, but expressing strong reservations herewith, we evaluate the observed positions as rainbow angles with the simple relation $\Theta_R = 2e/E$, which yields values for a 'well depth' e (with known collision energy E). Note that the values obtained in this way should not be taken as exact values for the true well depth of the potential for Na approaching the HF in the linear configuration. This can be seen in the IOS approximation, where the cross-section is the $(\sin \gamma)$ weighted average of cross-sections, calculated for fixed orientation with a corresponding angle-independent potential. Clearly the competition between the averaging and the actual rainbow structure eventually determines a structured envelope with positions of extrema which in general will not be equal to these, corresponding to a collinear approach, even though they will clearly be correlated. In summary, it seems to be a good approach to think of these values as an average of the well depth within one or other hemisphere of the molecule. A summary of all the observed positions of maxima is given in fig. 4, where the reciprocal observed angles (in the CM system) are plotted *versus* the collision energy. Clearly the points are seen to lie on lines through the origin, indicating that an interpretation of these maxima as rainbow-like is acceptable. From the slope of these lines we obtained the values of 'well depths' given in table 1.

Fig. 5 shows measured time-of-flight spectra at a collision energy of 286 meV for various scattering angles. At low scattering angles the spectra are seen to exhibit two well resolved maxima. The first (high) peaks correspond to non-reactive scattering and the sequence of their amplitudes with increasing angle properly reflects the rainbow scattering, discussed above. The broad late maximum is due to reactive scattering, which vanishes for large angles. All these results and the identification as non-reactive and reactive parts are in agreement with the nominal Newton diagram.

Compared to the total differential cross-sections discussed above and the non-reactive part in the time-resolved cross-section the reactive part needs a more sophisticated evaluation. We chose to simulate the laboratory distribution by forward convolution of parametrized centre-of-mass distribution as a product of angular and energy distributions:

$$\frac{\mathrm{d}^2\sigma}{\mathrm{d}w\,\mathrm{d}E}(\vartheta, E'_{int}) \sim \frac{\mathrm{d}\sigma}{\mathrm{d}w}(\vartheta)P(E'_{int}).$$

The distributions of the beams, required for the forward convolution, have been obtained by measuring the Na distribution and applying a distribution for HF, measured in another laboratory,[5] modified for our arrangement. Note that the resolution of the
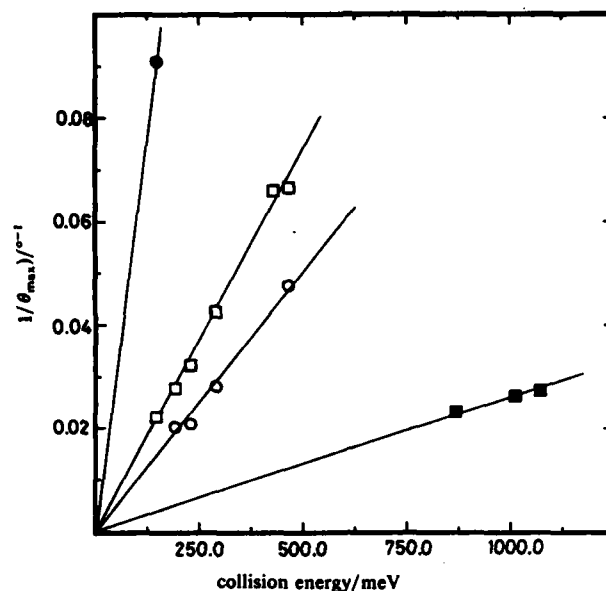
Fig. 4. Reciprocal positions of maxima observed in the differential cross-section *versus* the collision energy.

reactive and non-reactive parts is good enough to achieve the best fit to the reactive part without problems.

The best-fit results for three energies as centre-of-mass distributions are shown in fig. 6. (A) shows the angular part, while (B) shows the distribution of internal energies. Three results are given with each figure: the full line (best fit) and broken lines (variations) are still acceptably in agreement with the experiment. One example of a best fit is shown in fig. 5 as well for the reactive part as a full line. These results show pronounced forward scattering in the angular part at low energies, which has a tendency to wash out to isotropic scattering at high energies. In the energy part a comparably broad distribution is observed, reaching from low to high values with averages of $\langle E_{int} \rangle = 0.57$, 0.77 and 0.99 eV for the three energies given.

The polarization dependence of the cross-sections was measured twice. First a 'total' measurement was performed, where the degree of polarization for alignment parallel and perpendicular to the atomic beam was determined. The result is a weak dependence, varying substantially with the scattering angle between −2.5 and +2.5% from small to large angles, including a structure with two zeros. This measurement leads to an ambiguity: *since the detector does not discriminate between Na and NaF the question*

Table 1. Results of a simplified evaluation of observed maxima in the cross-sections to yield averaged values of the well depth (see text) and comparison with the calculated well depth, ε^a

ground-state interaction			p-state interaction		
ε_{s1}/meV	ε_{s2}/meV	ε_{s2}/meV	ε_{p1}/meV	ε_{p2}/meV	ε_{p2}/meV
17 ± 2	65 ± 1	80	92 ± 3	337 ± 5	500

^{a} From ref. (16), considering a linear approach of Na to FH (from the F side).
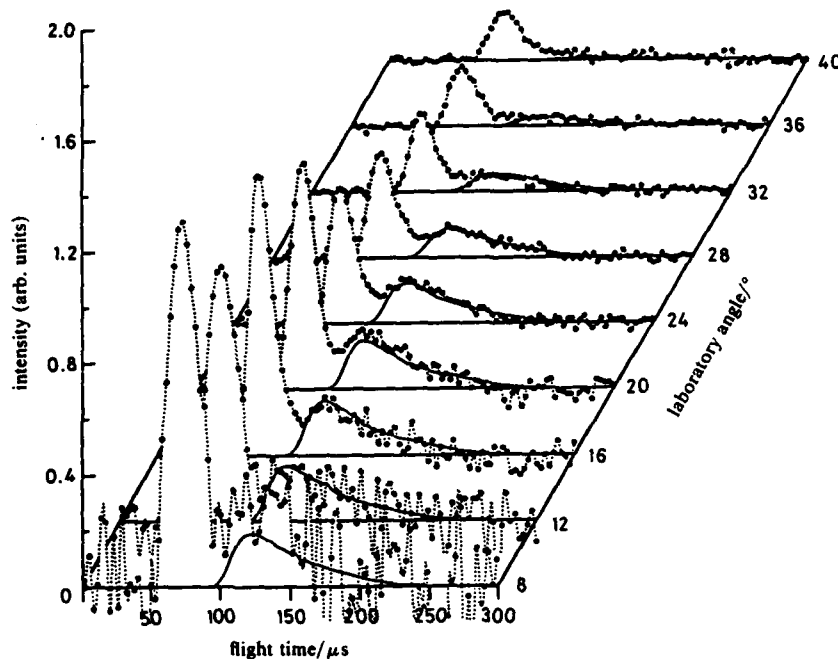
Fig. 5. Double differential cross-section for the scattering of Na(3S) and Na(3P) from HF as time-of-flight spectra at a collision energy of 286 meV. $\theta_{CM} = 14.5°$, $\theta_L = 34.1°$.

is open whether this observed effect refers to the non-reactive or to the reactive contribution to the signal. This ambiguity can be resolved by combining time-of-flight and polarization measurements in the manner described above. We find then that at the rainbow angle, where the polarization dependence of the total signal is the highest, this influence is exclusively due to the non-reactive part.

From angle- and energy-resolved measurements we have finally estimated the integral reactive cross-section by integrating the measured data in the same way as in ref. (3). The result of this estimate yields values between 1 and 2 $Å^2$ in the energy range 0.2–1 eV. A tendency for a linear increase with increasing energy is inferred from the data, but the large errors in this estimate preclude a firm statement on this.

Discussion

To gain further insight into the reaction, the recent quantum-chemical calculations for the alkali-metal–hydrogen halide reactions with excited alkali-metal states[14–16] provide a solid basis. Accordingly the reaction to yield the alkali-metal halide molecule is more or less endothermic for the ground state and exothermic in the excited state. The interaction in the excited state leads to a substantial well in the entrance channel. If reaction occurs, it has to proceed through a non-adiabatic transition, in which the entrance surface for the electronically excited state is coupled to the ground-state surface of the exit channel. The transition region is defined by some bent geometry with a more or less pronounced conical intersection. At the same time as this transition strong distortions of the electronic arrangement, associated with electron jumps, occur.

Some of these general statements can also be inferred directly from the experimental findings, as we have pointed out above, discussing and interpreting our results. These
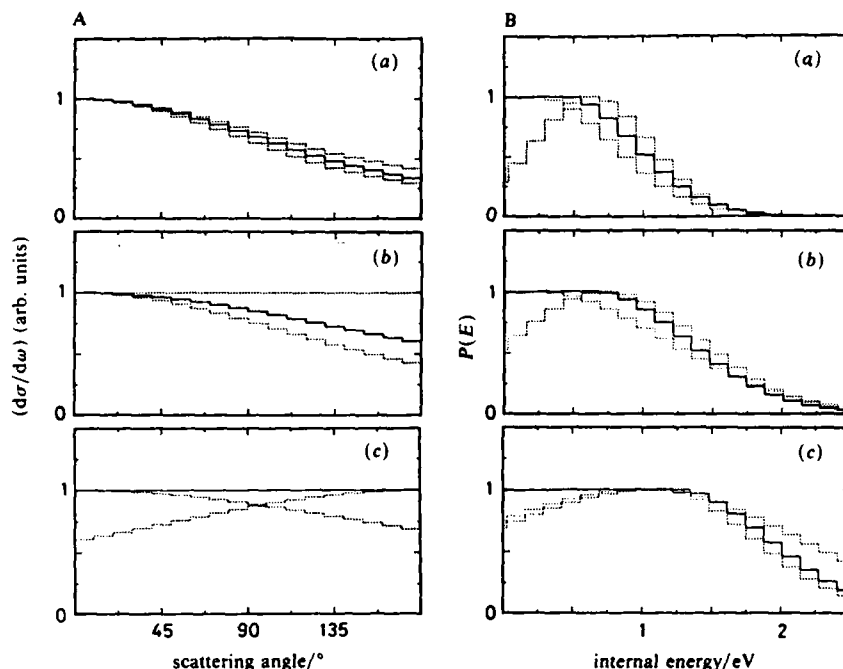
Fig. 6. Centre-of-mass differential cross-sections, obtained from forward convolution and best fit to the experimental cross-sections; (A) angular distribution, (B) distribution of internal energy. Collision energies (a) 286, (b) 555 and (c) 857 meV.

can be substantiated by comparison with the calculations of Sevin *et al.*[16], which were performed independently of our experiments for the same system. Even though dynamical calculations on this surface have not yet been performed, we can already point to some very satisfying features of agreement.

First, we consider our non-reactive results and the 'well depths', associated with the observed rainbow scattering. Recalling the precautions that we attach to our values, concerning a given geometry for the interaction, we compare the experimental values with those, given in ref. (16) for the linear configuration, especially with Na approaching from the F side to the HF molecule (table 1). We consider this agreement to be a satisfying confirmation of the calculation, especially since the deviations are in the expected direction, namely that the apparent well depth in our experiment is smaller than that in the linear configuration. (Another available calculation[13], which was performed for the ground state, yields a value of only $\varepsilon_{s2} = 110$ meV.) Unfortunately, well depths for the approach from the H-side have not been reported and therefore a comparison cannot be given.

Concerning the reactive channel, the comparison with the calculation remains more qualitative. First, we notice an integral reactive cross section, which is small (*ca.* 1 Å^2), *i.e.* much smaller than the non-reactive (gas kinetic) cross-section. This observation, which is reasonable for a transition due to a conical intersection, confirms this qualitative aspect. Nevertheless, a dynamic calculation is required to test this comparison quantitatively. Then we find, confirming the calculation, that no other exit channels other than the electronic ground state of NaF are observed. Similarly a high internal excitation of

the NaF product, deduced from the calculation,[16] is also found in the experiment. This finding agrees well with an early downhill[27] surface, but this assumption leads to difficulties with the observed angular distributions. Obviously it is difficult to assess the validity of this simplification for the actual complicated transition region and a confirmation or rejection of quantitative results cannot be given at this stage.

To summarize this discussion, we hope to have shown that some of our experimental findings agree quite well with the calculated surface of Sevin *et al.*[16] Other findings are predicted here which have not been reported in the calculation, but they should be available in principle. A third class of our results cannot be compared with the very simple means applied so far in our evaluation. They will be tested with appropriate dynamical calculations in the near future.

References

1   K. Lacmann and D. R. Herschbach, *Chem. Phys. Lett.*, 1970, **6**, 106.
2   I. G. Pruett, F. R. Grabiner and P. R. Brooks, *J. Chem. Phys.*, 1975, **63**, 1173.
3   C. H. Becker, P. Casavecchia, P. W. Tiedemann, J. J. Valenhuie and Y. T. Lee, *J. Chem. Phys.*, 1980, **73**, 2833.
4   F. Heismann and H. J. Loesch, *Chem. Phys.*, 1982, **64**, 43.
5   M. Hoffmeister, L. Potthast and H. J. Loesch, *Chem. Phys.*, 1983, **78**, 369.
6   H. H. Dispert, M. W. Geis and P. R. Brooks, *J. Chem. Phys.*, 1979, **70**, 5317.
7   B. A. Blackwell, J. C. Polanyi and J. J. Swan, *Chem. Phys.*, 1978, **30**, 299.
8   M. F. Vernon, H. Schmidt, P. S. Weiss, M. H. Covinsky and Y. T. Lee, *J. Chem. Phys.*, 1986, **84**, 5580.
9   R. Düren, U. Lackschewitz, S. Milošević, H. Panknin and N. Schirawski, *Chem. Phys. Lett.*, 1988, **143**, 45; 1988, **145**, 358.
10 R. Düren, U. Lackschewitz and S. Milošević, *Chem. Phys.*, in press.
11 M. M. L. Chen and H. F. Schäfer III, *J. Chem. Phys.*, 1980, **72**, 4376.
12 Y. Zeivi, M. Shapiro and E. Pollack, *Chem. Phys.*, 1981, **60**, 239.
13 M. Paniagua, J. M. Garcia de la Vega, J. R. Alvarez Collado, J. G. Sanz, J. M. Alvarino and A. Lagana, *J. Mol. Struct.*, 1986, **142**, 525.
14 G. G. Balint-Kurti and R. N. Yardeley, *Faraday Discuss. Chem. Soc.*, 1976, **61**, 77.
15 M. M. Gallo and D. R. Yarkony, *J. Chem. Phys.*, 1987, **86**, 4990.
16 A. Sevin, P. C. Hiberty and J. M. Lefour, *J. Am. Chem. Soc.*, 1987, **109**, 1845.
17 A. Sevin and P. Chaquin, *Chem. Phys.*, 1985, **93**, 49.
18 R. K. Preston and J. G. Tully, *J. Chem. Phys.*, 1971, **54**, 4297.
19 B. Lepetit, J. M. Launay, M. Le Dourneuf and F. X. Gadea, *Chem. Phys.*, 1987, **117**, 17.
20 For this we use a recent value of the dissociation energy of NaF: 5.0 ± 0.1 eV from S. R. Langhoff, C. W. Bauschlicher and H. Partridge, *J. Chem. Phys.*, 1986, **84**, 1687.
21 R. Düren, U. Lackschewitz and S. Milošević, in preparation.
22 R. Düren, W. Gröger, E. Hasselbrink and R. Liedtke, *J. Chem. Phys.*, 1981, **74**, 6806.
23 H. Kawano and F. M. Page, *Int. J. Mass Spectrom. Ion Phys.*, 1983, **50**, 1.
24 Details and further references are reviewed in: R. Düren, in *Atomic and Molecular Beam Methods*, ed. G. Scoles (Clarendan Press, Oxford, 1988), vol. 1.
25 R. Düren, W. Gröger and R. Liedtke, *Rev. Sci. Instr.*, 1985, **56**, 377.
26 U. Buck, F. Gestermann and H. Pauly, *Chem. Phys.*, 1980, **50**, 217.
27 M. H. Mok and J. C. Polanyi, *J. Chem. Phys.*, 1969, **51**, 1451; D. S. Perry, J. C. Polanyi and C. W. Wilson Jr, *Chem. Phys.*, 1974, **3**, 317.

Orientational and Spin–orbital Dependence of Interatomic Forces

Vincenzo Aquilanti,* Giorgio Liuti, Fernando Pirani and Franco Vecchiocattivi

Dipartimento di Chimica, Università di Perugia, 06100 Perugia, Italy

The representation of weak interactions of open-shell atoms as effective anisotropic potentials is discussed. Examples, mainly from recent molecular-beam studies of collisions of magnetically orientated atoms in P states, prove that the spherically averaged component of the interactions follows systematics established for closed-shell van der Waals forces. Data are being collected to unravel similar systematic trends for the anisotropic component of the interactions.

1. Introduction

As a preliminary to a full understanding of the role that spin–orbit and orientation effects due to open-shell electronic clouds play in a variety of kinetic phenomena, it is interesting to focus attention on how these effects are manifest in interatomic forces. Open-shell atoms exert even with closed-shell systems anisotropic interactions which can be probed by spectroscopic or scattering techniques. Also, when a molecule is photodissociated the polarization and orientation of the fragments is determined by the anisotropy of the forces. Since we restrict our attention to weak forces of the van der Waals type, it is especially from scattering experiments that the most valuable information on these interactions has been recently obtained, in particular through the possibility of controlling by magnetic fields the sub-levels of open-shell atoms.

In this paper, after briefly reviewing in section 2 the experimental background, we discuss in section 3 the representation of the van der Waals interactions of open-shell atoms as an expansion in spherical harmonics. In section 4 the spherical averages of the interactions for several systems recently investigated are examined and shown to follow the systematics already established for interactions between closed-shell systems. In section 5 trends that are emerging for the anisotropic part of the interactions are discussed. Discussion and conclusions follow in section 6. Since some examples considered in this paper involve ion–atom interactions, in the Appendix the previously established systematic trends for size and strength of atom–atom forces are shown to be extendable to systems involving ions.

2. Experimental Background

The study of weak interactions involving open-shell atoms is of great importance to assess the role of anisotropy in determining the strength, range and shape of the intermolecular forces involved.[1,3] Specifically such studies provide insight on the influence of spin–orbit and electronic angular momenta on the long-range part of potential-energy surfaces. These surfaces are of interest not only for all kinetic processes where intramultiplet mixing and polarization phenomena are explicitly observed, but also for understanding orientation and alignment effects in reactive collisions when dominated by anisotropy at long range. Also, they can be profitably used in dealing with several microscopic and macroscopic phenomena up to the chemically important processes of flames, plasmas, laser systems and atmospheric chemistry.

1

Collision dynamics studied by molecular-beam techniques coupled with magnetic analysis of atomic sub-levels have proved to be among the most powerful tools to obtain quantitative information on open-shell weak intermolecular forces.[1,4] Significant results from beam experiments involving scattering of fluorine, oxygen and nitrogen atoms by several atoms and molecules have been obtained in this laboratory and reported extensively elsewhere.[1-5]

Similar information has also been obtained by laser-selection of excited atom sub-levels in full-collision[6] and half-collision experiments:[7] the laser-polarized light can be used to prepare the excited atom in well defined sub-states[8] or to quench selectively the sub-levels of an excited metastable state.[9]

Finally, the spectroscopy of simple diatomic rare-gas ions can provide interesting information about the energy and symmetry of molecular states which are a manifestation of the anisotropy of the interaction.[10]

3. Representation of Interatomic Forces

In the following the collision theory needed to obtain information on the interaction is presented and discussed, and the connection is outlined between the asymptotic energy levels of the separated atoms and the adiabatic molecular states.

3.1. Collision Theory

The general theory needed to interpret the experiments mentioned above and to obtain information on the interactions involved has been given[11] and reviewed elsewhere.[1,3a]

In fig. 1 an intuitive picture is given of the fact that the potential for the interaction between a closed-shell atom with a P-state atom or a diatomic molecule can be represented in both cases by formally using the same potential expansion, in Legendre polynomials in these cases.

Close-coupling equations for treating collisions of a $^1S_0$ atom with another atom having non-zero internal angular momentum L and spin S have been given by Reid and Dalgarno,[12a] who considered explicitly a ^2P alkali-metal atom and expanded the electrostatic interaction of the outer electron in Legendre polynomials, leading in this case to a spherical part, V_0, and to an anisotropy, V_2. Later, Mies[12b] considered an equivalent approach where, however, the electrostatic interaction was represented by the more familiar potentials V_Σ and V_Π, where Σ and Π are $\Lambda = 0$ and 1, respectively, and Λ is the projection of L on the interatomic axis. The relationships between the two representations of the electrostatic interactions are in this case simply

$$V_0 = \tfrac{1}{3}(V_\Sigma + 2V_\Pi) \quad \text{and} \quad V_2 = \tfrac{5}{3}(V_\Sigma - V_\Pi).$$

(a)   (b)
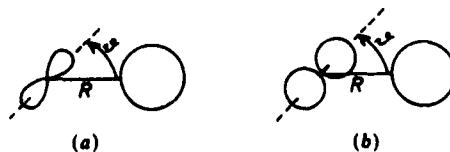
Fig. 1. Showing that the electrostatic interaction of a closed-shell atom with a diatomic molecule and a P-state atom can both be represented by a Legendre expansion, assuming the molecule as a rigid rotor and describing the atom by the symmetry of its electronic cloud. Note that in the latter case only two terms in the expansion need be included. (a) $V(R, \theta) = V_0(R) + V_2(R)P_2(\cos \theta)$, (b) $V(R, \theta) = V_0(R) + \Sigma V(R)P_\lambda(\cos \theta)$.

Both approaches can be generalized to any L,[11a] and the relationship between expansions has been established to be

$$V_\Lambda = \sum_\lambda \langle L0, \lambda 0 | L0 \rangle \langle L\Lambda, \lambda 0 | L\Lambda \rangle V_\lambda$$

or inversely

$$V_\lambda = \sum_\Lambda [(2\lambda + 1) \langle L\Lambda, \lambda 0 | L\Lambda \rangle / (2L + 1) \langle L0, \lambda 0 | L0 \rangle] V_\Lambda$$

where $\lambda = 0$ and 2 only for $L = 1$ (P atoms), or 0, 2, 4 for $L = 2$ (D atoms) and so on. Further generalizations along these lines are possible, both representations being useful: while the one in Λ is directly related to the spectroscopic conventions, the other exploits the fact that we are actually dealing with non-spherical interactions, and is more in the line of collision theory. A phenomenology of these representations is presented in fig. 2.

To describe both the rovibrational states of a diatom or a collision at an energy E sufficiently low to involve only one electronic state (typically the lowest), only the fine-structure components of the open-shell atom need be included in a close-coupling expansion: the multichannel Schrödinger equation at total angular momentum J can be written in matrix notation

$$\left(-\frac{\hbar^2}{2\mu} I \frac{d^2}{dR^2} + U^J(R) \right) \vec{\psi} = E\vec{\psi} \tag{1}$$

where μ is the reduced mass and the potential-energy matrix U^J, which is not diagonal (non-adiabatic representation), is the sum of three contributions depending on the intermolecular distance R:

$$U^J(R) = V_{so}(R) + V_{el}(R) + V_{rot}(R). \tag{2}$$

The fine-structure components are split asymptotically by the spin–orbit interaction of the open-shell atom, V_{so}; the electrostatic interaction between atoms, V_{el}, which is relatively short-ranged, and the centrifugal term, V_{rot}, both describe the collision effects. The dependence of these terms on the interatomic distance is markedly different: V_{so} varies slowly at long range, V_{el} dies out exponentially and V_{rot} decays as R^{-2}.

Eqn (1) provides a unified description of bound and scattering states. When atoms have spin S, which will be assumed to be conserved and coupled to L to give the atomic angular momentum j, following an approach originally suggested within a semiclassical context,[1,11] five alternative representations have been developed for eqn (1), corresponding to the familiar Hund's cases for the spectroscopy of rotating diatomic molecules. This approach provides the different coupling schemes for the angular momenta involved in open-shell atom collisions according to the relative importance of the three terms appearing in eqn (2).[1,11]

Specifically, when V_{el} is lower than both V_{rot} and V_{so}, Hund's case (e) is operative and the good quantum numbers are the atomic angular momentum j and the nuclear orbital angular momentum l; if V_{rot} is much smaller than the other two terms, Hund's cases (c) and (a) are possible. For case (c), where $V_{el} < V_{so}$, the good quantum numbers are j and its projection Ω along the internuclear axis; for the case (a), where $V_{el} > V_{so}$, the good quantum numbers are the projection Λ of the electronic angular momentum L on the internuclear axis and Ω. Finally, when V_{so} is lower than both V_{el} and V_{rot}, Hund's case (b) is present if $V_{rot} < V_{el}$, where the good quantum numbers are K, the total angular momentum without the spin, and Λ, whereas when $V_{rot} > V_{el}$, Hund's case (d) operates with l and K as good quantum numbers.

Typical collision events start from case (e), which corresponds to the separated atoms, and evolve towards the molecular cases (a) or (b) through case (c), if the spin–orbit term is large, and through case (d) in the opposite situation. A similar picture, with proper sequences of coupling cases, applies to the description of vibrations of rotating molecules.
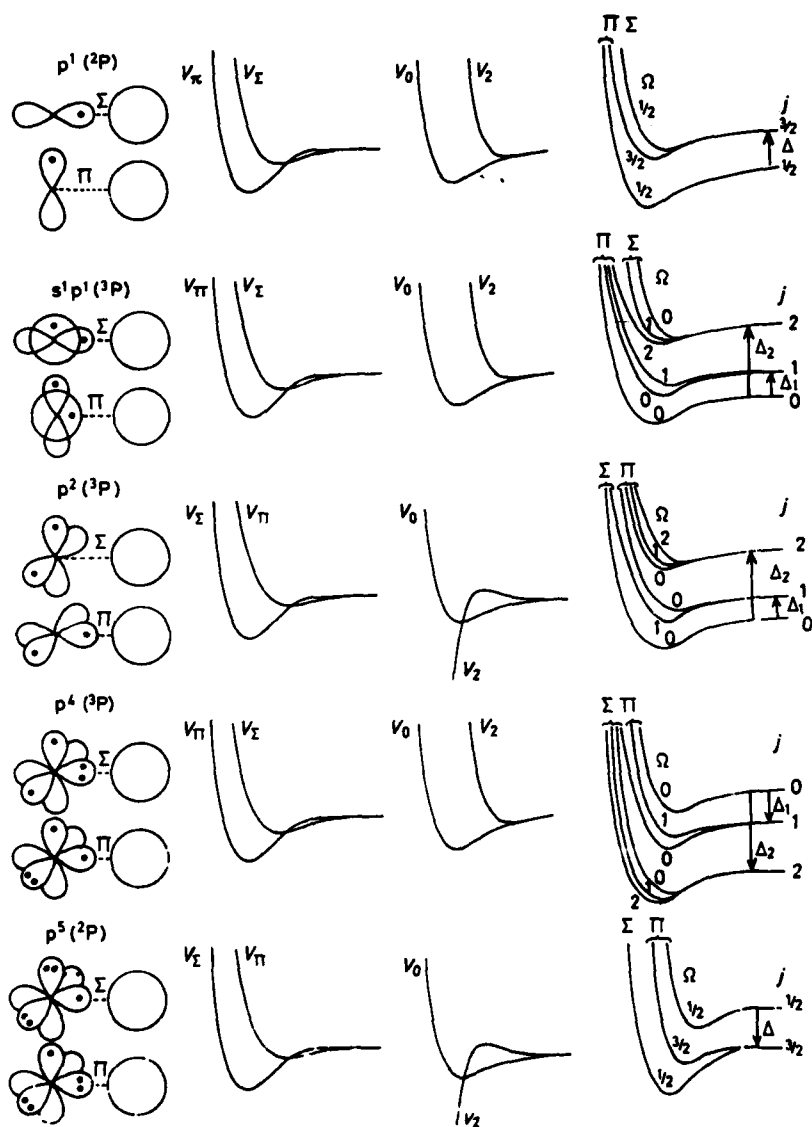
Fig. 2. For typical electronic cloud distributions of open-shell atoms illustrated in the first column, the qualitative behaviour of V_Σ and V_Π interactions with closed-shell systems can be anticipated (second column). The corresponding V_0 (spherical or isotropic interaction) and V_2 (anisotropy) are shown in the third column. The final column shows qualitatively the effective adiabatic interactions, where account is taken of the atomic spin-orbit splitting.

For most of the open-shell atoms considered here the spin–orbit term is relatively large, except for excited lighter alkali-metal atoms, and only Hund's cases (c) and (a) need be considered in describing the collision dynamics at thermal energy.[11b,13] Also, significant information on the interactions is obtained only for those ranges which are probed by the collision: in a classical picture, they occur at relatively small impact parameters: for these conditions the V_{rot} term is negligible compared to both V_{el} and V_{so}.

We can clarify this aspect with an example. Let us consider the collision between halogen atom (^2P_j) with a closed-shell particle: when the collision occurs at large impact parameter, the centrifugal term is dominant and the two collision partners retain their individuality [Hund's case (e) or separated-atom case]. When we consider impact parameters and distances shorter, the V_{rot} term decreases, while V_{el} increases and V_{so} is still larger than V_{el}. In this case the electrostatic interaction succeeds in orientating j with respect the internuclear axis but maintaining the spin–orbit coupled [Hund's case (c) or diatomic case]. Considering impact parameters and distances even shorter the V_{el} term becomes dominant. In this case the electrostatic interaction is so strong as to decouple the spin–orbit and orientate the electronic angular momentum L along the internuclear axis [Hund's case (a) or molecular case].

Therefore a scattering event (or a vibration) can be considered to take place along adiabatic effective potential energy curves $V_{|j\Omega\rangle}$ and eqn (1) can be written in the adiabatic representation as

$$\left[-\frac{\hbar^2}{2\mu}\left(I\frac{d}{dR}+P(R)\right)^2+V(R)+\frac{l(l+1)}{2\mu R^2}I\right]\vec{\psi}=E\vec{\psi} \qquad (3)$$

where the centrifugal term is approximated by a diagonal centrifugal barrier corresponding to an effective orbital angular momentum l.

The diagonal matrix $V(R)$, obtained by diagonalizing V_{el} and V_{so} defines effective adiabatic potential-energy curves $V_{|j\Omega\rangle}$ and the matrix $P(R)$ the non-adiabatic coupling term between them. Explicit formulae for the $P(R)$ matrix elements are reported elsewhere:[2b,3] they allow modifications of the adiabatic curves due to non-adiabatic effects to be taken into account. In most of the cases considered these effects are small.[2b,3]

3.2. Adiabatic Molecular States and Correlation Diagrams

For Hund's cases (a) and (c), which are those to be considered in most cases, explicit expressions of the effective adiabatic potential-energy curves $V_{|j\Omega\rangle}$ are given in the following. They correlate with the different states of the open-shell atom, defined by the atomic total angular momentum j and by its projection, m_j, along the internuclear axis. These curves are labelled by j and Ω; at large internuclear separations Ω tends to the atomic sub-level projection $|m_j|$. For the interaction of a ^2P_j atom with a closed-shell particle the $V_{|j\Omega\rangle}$ interactions are:

$$\left.\begin{aligned}
V_{|3/2\,3/2\rangle} &= V_0-\tfrac{1}{3}V_2+\Delta \\
V_{|3/2\,1/2\rangle} &= V_0+\tfrac{1}{10}V_2+\tfrac{1}{2}\Delta\mp\tfrac{1}{2}(\tfrac{9}{25}V_2^2+\Delta^2+\tfrac{2}{5}\Delta V_2)^{1/2} \\
V_{|1/2\,1/2\rangle} &= V_0+\tfrac{1}{10}V_2+\tfrac{1}{2}\Delta\pm\tfrac{1}{2}(\tfrac{9}{25}V_2^2+\Delta^2+\tfrac{2}{5}\Delta V_2)^{1/2}
\end{aligned}\right\} \qquad (4)$$

and for a ^3P_j atom with a closed-shell particle they are:

$$\begin{aligned}
V_{|2\,2\rangle} &= V_0-\tfrac{1}{3}V_2+\Delta_2 \\
V_{|2\,1\rangle} &= V_0+\tfrac{1}{10}V_2+\tfrac{1}{2}(\Delta_1+\Delta_2)\pm\tfrac{1}{2}(\tfrac{9}{25}V_2^2+(\Delta_2-\Delta_1)^2)^{1/2} \\
V_{|2\,0\rangle} &= V_0+\tfrac{1}{10}V_2+\tfrac{1}{2}\Delta_2\pm\tfrac{1}{2}(\tfrac{9}{25}V_2^2+\Delta_2^2+\tfrac{2}{3}\Delta_2 V_2)^{1/2} \\
V_{|1\,1\rangle} &= V_0+\tfrac{1}{10}V_2+\tfrac{1}{2}(\Delta_2+\Delta_1)\mp\tfrac{1}{2}(\tfrac{9}{25}V_2^2+(\Delta_1-\Delta_2)^2)^{1/2} \\
V_{|1\,0\rangle} &= V_0-\tfrac{1}{3}V_2+\Delta_1 \\
V_{|0\,0\rangle} &= V_0+\tfrac{1}{10}V_2+\tfrac{1}{2}\Delta_2\mp\tfrac{1}{2}(\tfrac{9}{25}V_2^2+\Delta_2^2+\tfrac{2}{3}\Delta_2 V_2)^{1/2}.
\end{aligned} \qquad (5)$$

The different sign combination before the square roots in eqn (4) and (5) is due to the different sequence of fine-structure levels which are possible for open-shell atoms. The sign combination has to be selected to give asymptotically the right correlation with the related j energy values in the proper sequence. The Δ_i terms are the evaluated spin-orbit constants, with the appropriate sign, in all cases taking the atomic state with the lowest value of j as the zero energy level (see fig. 2). For example, when one considers the interaction between an alkali-metal atom at the first excited level, $^2P_{1/2,3/2}$, the spin-orbit constant Δ is positive and the sign before the square root in $V_{|3/2\,1/2\rangle}$ is positive, while that in $V_{|1/2\,1/2\rangle}$ is negative. For the ground-state halogen atoms, $^2P_{3/2,1/2}$, Δ is negative, the $\frac{3}{2}$ level being the lowest level here; the sign before the square root in $V_{|3/2\,1/2\rangle}$ is negative and that in $V_{|1/2\,1/2\rangle}$ positive. In the case of $Hg^*(^3P_{0,1,2})$[14] Δ_1 and Δ_2 are both positive and, respectively, given by the differences between $j=1$ and $j=0$ levels and $j=2$ and $j=0$ levels. Here the square roots in $V_{|2\,0\rangle}$ and $V_{|2\,1\rangle}$ are taken to be positive and those in $V_{|1\,1\rangle}$ and $V_{|0\,0\rangle}$ negative. In the case of a ^3P-state atom where the j levels are inverted, as in ground-state oxygen atoms, $^3P_{2,1,0}$, Δ_1 and Δ_2 are negative and the sign of the square roots are also inverted with respect to the previous case. General features of the effective potential-energy curves are shown in fig. 2.

Obviously Hund's cases (a), (c) and (e) are contained in limiting cases of the above adiabatic formulae. In fact when V_2 is negligible relatively to V_0 and Δ_i [Hund's case (e)], the various interactions have the form of the V_0 term and they are separated only by the spin-orbit constant. This situation occurs at large intermolecular distances. On the other hand, if $|V_2|<|\Delta_i|$, but not negligible, Hund's case (c) is operative. Finally, when $|V_2|>|\Delta_i|$, Hund's case (a) is obtained, and the various adiabatic interactions are described by V_Σ and V_Π potential-energy curves. The last two situations occur at intermediate and short distances, respectively.

The known cases of V_0 potentials will be shown to have the features of a typical van der Waals interaction correlating with properties of separated atoms (see next section). The anisotropy of interaction, V_2, most generally changes sign as a function of R because it is the sum of two contributions: the anisotropy of the long-range potential determined by the polarizability anisotropy of the open-shell atom, and the short-range repulsive anisotropy interaction which decays exponentially with distance.[15] These two interactions have different signs and give V_2 (or $-V_2$) the shape of a typical potential with an extremum.

For those atomic ions having ^2P or ^3P electronic configurations, the same previous equations (4) and (5) correctly describe their interactions with closed-shell particles.[16] For these systems the V_0 term is essentially due to the ion-induced dipole interaction (see Appendix) and the V_2 terms exhibit features similar to those for the neutral case.

An intermediate situation arises for the interaction of metastable rare-gas atoms with closed-shell atoms.[17] For instance the Xe^* $(^3P_{2,0})$ metastable atom interacts at long distance as a Cs atom in the ground state because it has an excited electron in the 6s orbital.[18] At shorter distances the effect of the $(5p^5)$ ionic core becomes important[19] both for the effective V_0 and the anisotropic V_2 term. Similarly, for the interaction between the metastable $Ne^*(^3P_{2,0})$ atom and a ground-state rare-gas atom (Ar, say)[17] the anisotropy is due mainly to the ionic core of Ne^*, which is shielded at long distance by the 3s electron, and the interaction is similar to that between Na and Ar. However, at short distances the ionic core strongly affects both the V_0 and V_2 component of the interaction, which then becomes similar to that between Ne^+ and Ar.

4. Size and Strength of the Spherical Component of Interactions

A comparison among van der Waals forces for a great number of systems is presently possible and allows us to obtain a physical picture of the effect of properties of separate atoms on these interactions. This is plausible since van der Waals interactions occur at

Table 1. Comparison between estimated and experimental potential parameters of the isotropic component V_0 of the interaction in open shell-closed shell systems

system	estimated[a]		experimental		
	ε/meV	R_m/Å	ε/meV	R_m/Å	ref.
O(^{3}P)-He	2.4	3.19	2.1	3.27	3a
O(^{3}P)-Ne	4.7	3.28	4.3	3.30	3a
O(^{3}P)-Ar	8.0	3.63	7.8	3.60	3a
O(^{3}P)-Kr	8.7	3.78	9.3	3.75	3a
O(^{3}P)-Xe	9.8	3.97	11.8	3.90	3a
O(^{3}P)-H$_2$[b]	4.3	3.43	4.7	3.49	3b
O(^{3}P)-CH$_4$[b]	8.7	3.79	9.3	3.75	3b
F(^{2}P)-Ar	6.9	3.57	6.8	3.50	2b
F(^{2}P)-Kr	7.2	3.73	7.2	3.65	2b
F(^{2}P)-Xe	7.8	3.94	8.1	3.78	2b
Hg*(^{3}P)-Ar	14.7	4.23	13.6	4.33	7

[a] From correlation formulae given in section 4. The values of atomic polarizabilities are: for rare gases from ref. (21), (22); for oxygen and fluorine from ref. (21a); for excited mercury from ref. (23). The values of molecular polarizabilities are from ref. (24) for H$_2$ and from ref. (25) for CH$_4$. [b] Averaged over molecular orientations.

distances such that the particles still retain their individual properties. Interestingly it has recently been shown[20] that both the atomic and molecular 'size' and the long-range attraction can be related to a single parameter such as the polarizability. Therefore correlation formulae have been proposed between the parameters of the potential and the polarizabilities of the interacting particles. These correlations allow reasonable estimates of the well depth, ε, and its location R_m for any pair considered.

Specifically, the size of the interaction between A and B, as measured by R_m, can be given by[20]

$$R_m = 1.767 \frac{\alpha_A^{1/3} + \alpha_B^{1/3}}{(\alpha_A \alpha_B)^\gamma}$$

where $\gamma = 0.095$. When polarizabilities α_A and α_B are in Å^3, R_m is in Å. This formula has been obtained through a statistical analysis over a large number of van der Waals systems.[20] The well depth, ε, as a measure of the strength of the interaction, is then estimated assuming attraction as given by a $-C_6 R^{-6}$ potential, obtaining C_6 again from α_A and α_B according to the Slater-Kirkwood formula, and by using the proportionality between εR_m^6 and C_6.[20]

In table 1 a comparison between the above parameters estimated from these correlations and those from the experimental V_0 interactions are shown for some open-shell systems. The satisfactory comparison confirms that the spherical interactions V_0 are amenable to being interpreted as typical van der Waals interactions.

5. Trends in the Anisotropic Component of Interatomic Forces

The halogen (^{2}P) and oxygen (^{3}P) atoms present low polarizability anisotropy[21] and are characterized by the highest electron affinity in the Periodic Table. For their interactions the anisotropy V_2 potentials can be essentially attributed to the ionic contribution from the excited ionic states.[15] This contribution, which is dominant at short range, increases as the interacting ionic and neutral states come closer. For example, for the O-rare-gas interactions the repulsive wall of the V_2 term shifts towards larger distance from He to Xe, causing an increase in the difference between the V_Σ and V_Π potentials:[3a] note that

the ionization potentials of rare-gas atoms decrease in the same direction. Similar results have been obtained for the F–rare-gas systems.[2b,26]

When a comparison is made between the fluorine[2b] and the oxygen[3a] systems, it can be observed that anisotropies decay faster in the first case because of the smaller size of fluorine but are stronger at shorter range because of higher contributions from the excited ionic states.

For the interaction of a rare-gas ion, A^+, with a rare-gas atom, B, the anisotropy contribution may be considered to be brought about by charge exchange to give $A + B^+$ or, in other words, by the strong interaction between electronic states of the same species corresponding to $A^+ + B$ and $A + B^+$ of the separated system.[10b,19a] Charge-exchange effects are akin to the previously considered ionic contributions in rare-gas halides and rare-gas oxides. For example for the XeF molecule the ionic contribution originates from the interaction between $Xe + F$ and $Xe^+ + F^-$. Naturally, charge exchange effects increase as the difference between the ionization energy of A and that of B decreases.

To understand the effect of the anisotropy term V_2 on the adiabatic $V_{|j\,\Omega\rangle}$ curves, it is necessary to consider the sign of V_2 and to compare this term to V_0 and Δ_i. For instance in the case of XeF^{2b} the highest and lowest well depths of the adiabatic curves $V_{|j\,\Omega\rangle}$ correlating with the $F(^2P)–Xe(^1S)$ are 145.4 and 6.8 meV, respectively, and their locations are 2.31 and 3.93 Å, respectively. In the case of XeO,[3a] these well depths are 17.3 and 9.2 meV, respectively, and the minimum distances are 3.69 and 4.00 Å, respectively. Moreover, the ground state in XeF has Σ symmetry, while in XeO it has Π symmetry. These differences are essentially due to the different behaviour of the V_2 interactions but also to the slightly different positions of the repulsive walls of the V_0 interactions (see table 1).

At a distance where Δ_i is of the order of V_2 the transition between Hund's case (c) and (a) occurs. Typical values are 3.25 Å for XeF^{2b} and 3.60 and 3.75 Å for XeO.[3a] Since the ground state of XeF is completely confined in Hund's case (a) at distances around the energy minimum, this state has a more prominent molecular character than the lowest states of the XeO molecule.

At distances where the transition between Hund's cases (a) and (c) occurs the elements of the P matrix [see eqn (3)] present maximum values. The explicit computations of the non-adiabatic coupling terms are reported elsewhere.[2b,3] These terms depend on the ratios between V_2 and its derivative, with respect to the intermolecular distance, and the spin–orbit splitting constant. They are especially useful in estimating non-adiabatic effects and are needed to compute intramultiplet mixing and orientation and alignment cross-sections.

6. Discussion and Conclusions

The present exploratory analysis of open-shell interatomic interactions that are being provided by molecular beams and other techniques shows the advantages of representing such interactions by a Legendre expansion. The atomic spin orbit is then added phenomenologically and effective adiabatic curves for the description of scattering and bound states are obtained.

For the cases analysed here the spherical component of the interaction, V_0, correlates with what is presently known about the size and strength of van der Waals forces. More is being learnt about the shape of these forces around minima, but simple correlation formulae are still to be found and tested (see, however, where interactions of atoms with surfaces are also considered[27]).

Although van der Waals forces, and therefore also our $V_0(R)$ potentials, are still elusive to quantum chemistry, some examples are available [HeO, ref. (28), and $HeAr^+$ and $NeAr^+$, ref. (16)] that anisotropic components $V_2(R)$, for which characteristics and trends are much less known, may nevertheless be anticipated by theoretical approaches.

Appendix

Correlation between Size and Strength of Interactions and Atomic Polarizabilities: Extension to Ion–Atom Systems

When the interaction between an ion A^+ with a closed-shell particle B is considered, it is interesting to maintain the same physical picture as in section 4 by modifying the previous correlation formulae considering that the size and strength of intermolecular forces are still due to a combined effect between a repulsive and an attractive contribution. However, in this case, while the repulsion is still related to the 'size' of the ion and of the neutral atom, the attraction depends asymptotically on the ion–induced dipole interaction, $-e^2\alpha_B/2R^4$. The following correlation formulae are proposed:

$$R_m = 1.647 \left(\frac{\alpha_{A^+}^{1/3} + \alpha_B^{1/3}}{\alpha_B^{\gamma'}} \right) \text{Å}$$

where $\gamma' = 0.143$ for all systems, and

$$\varepsilon = 6.36 \times 10^3 \frac{\alpha_B}{R_m^4} \text{ meV}.$$

The γ' coefficient is equal to $3/2 \cdot \gamma$, where γ is the exponent for neutral–neutral interaction[20] and the factor 3/2 takes into account the ratio between exponents for the different R dependence of the long-range attraction (R^{-6} and R^{-4}). The coefficients in the above formulae are obtained using as reference the potential for system K^+–Kr, for which various experimental and theoretical determinations agree satisfactorily.[29]

As in section 4 for neutral–neutral interactions, the above correlation formulae can be used to estimate potential parameters for ion–neutral interactions. In table 2 a comparison between these estimated values and the experimental determinations are reported for some ion–rare-gas systems. Only a few typical systems are listed. For cases involving rare-gas open-shell ions, again the isotropic V_0 potential parameters are compared with the estimated values. The comparison is satisfactory considering the overall uncertainties involved, and it suggests that also in the open-shell ion case the anisotropy generates a manifold of potential-energy curves bracketing the spherical component V_0 which, here too, retains the meaning of a typical ion–neutral interaction of van der Waals type.

Table 2. Comparison between estimated and experimental parameters for some ion-rare-gas interactions[a]

| system | estimated[b] | | experimental | | |
	ε/meV	R_m/Å	ε/meV	R_m/Å	ref.
Na^+–Ar	212	2.65	190	2.69	29
Rb^+–Xe	170	3.51	185	3.54	29
K^+–Ar	104	3.16	127	2.94	29
K^+–Kr[c]	144	3.24	144	3.24	29
He–Ar$^+$	20	2.83	20	2.87	10c, 16
Ne–Ar$^+$	39	2.85	47	2.95	16
He–Ne$^+$	45	2.31	47	2.33	10b, 30

[a] Ions and rare-gas atoms are in their ground states, and for open-shell rare-gas ions the V_0 interactions are considered. [b] From correlation formulae given in the Appendix. The polarizability values for the ions are obtained from ref. (31) and those for rare gas atoms from ref. (21), (22). [c] Reference system.

References

1 V. Aquilanti, G. Grossi and F. Pirani, *Electronic and Atomic Collisions*, Invited Papers XIII ICPEAC, ed. J. Eichler, I. V. Hertel and N. Stolterfoht (Berlin, 1983) p. 441; V. Aquilanti, F. Pirani, and F. Vecchiocattivi, *Structure and Dynamics of Weakly Bound Molecular Complexes*, ed. A. Weber (Plenum, New York, 1987), p. 423.

2 (a) V. Aquilanti, E. Luzzatti, F. Pirani and G. G. Volpi, *Chem. Phys. Lett.*, 1982, **90**, 382; (b) V. Aquilanti, E. Luzzatti, F. Pirani and G. G. Volpi, *J. Chem. Phys.*, in press.

3 (a) V. Aquilanti, R. Candori and F. Pirani, *J. Chem. Phys.*, in press; (b) V. Aquilanti, R. Candori, L. Mariani, F. Pirani and G. Liuti, *J. Phys. Chem.*, in press.

4 (a) V. Aquilanti, E. Luzzatti, F. Pirani and G. G. Volpi, *Gazz. Chim. Ital.*, 1980, **110**, 57; (b) V. Aquilanti, E. Luzzatti, F. Pirani and G. G. Volpi, *J. Chem. Phys.*, 1980, **73**, 1181.

5 V. Aquilanti, G. Liuti, F. Pirani, F. Vecchiocattivi and G. G. Volpi, *J. Chem. Phys.*, 1976, **65**, 4751; B. Brunetti, G. Liuti, E. Luzzatti, F. Pirani and F. Vecchiocattivi, *J. Chem. Phys.*, 1981, **74**, 6734; B. Brunetti, G. Liuti, E. Luzzatti, F. Pirani and G. G. Volpi, *J. Chem. Phys.*, 1983, **79**, 273; G. Liuti, E. Luzzatti, F. Pirani and G. G. Volpi, *Chem. Phys. Lett.*, 1985, **121**, 559.

6 I. V. Hertel and W. Stoll, *Adv. At. Mol. Phys.*, 1978, **13**, 113.

7. W. H. Breckenridge, M. C. Duval, C. Jouvat and B. Soep, *Structure and Dynamics of Weakly Bound Molecular Complexes*, ed. A. Weber (Plenum, New York, 1987), p. 213.

8 See, for example, R. Düren and E. Hasselbrink, *J. Chem. Phys.*, 1986, **85**, 1880.

9 M. J. Verheijen and H. C. W. Beijerinck, *Chem. Phys.*, 1986, **102**, 255.

10 (a) Y. Tanaka, K. Yoshino and D. E. Freeman, *J. Chem. Phys.*, 1975, **62**, 4484; I. Dabrowski and G. Herzberg, *J. Mol. Spectrosc.*, 1978, **73**, 183; I. Dabrowski, G. Herzberg and K. Yoshino, *J. Mol. Spectrosc.*, 1981, **89**, 491.

11 (a) V. Aquilanti and G. Grossi, *J. Chem. Phys.*, 1980, **73**, 1165; (b) V. Aquilanti, P. Casavecchia, G. Grossi and A. Laganà, *J. Chem. Phys.*, 1980, **73**, 1173; (c) V. Aquilanti, G. Grossi and A. Laganà, *Nuovo Cimento.*, 1981, **63b**, 7.

12 (a) R. H. G. Reid and A. Dalgarno, *Phys. Rev. Lett.*, 1969, **22**, 1029; R. H. G. Reid, *J. Phys. B*, 1973, **6**, 2018; (b) F. H. Mies, *Phys. Rev. A*, 1973, **7**, 942.

13 C. H. Becker, P. Casavecchia, Y. T. Lee, R. E. Olson and W. A. Lester Jr, *J. Chem. Phys.*, 1979, **70**, 5477.

14 For the interaction of this open-shell atom see also: A. I. Voronin and V. A. Kvlividze, *Theor. Chim. Acta*, 1967, **8**, 334.

15 (a) M. Krauss, *J. Chem. Phys.*, 1977, **67**, 1712; (b) T. H. Dunning Jr and P. J. Hay, *J. Chem. Phys.*, 1977, **66**, 3767; (c) T. H. Dunning Jr and P. J. Hay, *J. Chem. Phys.*, 1978, **69**, 134.

16 B. Brunetti, F. Vecchiocattivi, A. Aguilar-Navarro and A. Solé, *Chem. Phys. Lett.*, 1986, **126**, 245.

17 R. W. Gregor and P. E. Siska, *J. Chem. Phys.*, 1981, **74**, 1076; A. Aguilar-Navarro, B. Brunetti, S. Rosi, F. Vecchiocattivi and G. G. Volpi, *J. Chem. Phys.*, 1985, **82**, 773.

18 T. Krümpelmann and Ch. Ottinger, *Chem. Phys. Lett.*, 1987, **140**, 142.

19 (a) P. M. Dehmer, *Comm. At. Mol. Phys.*, 1983, **13**, 205; (b) G. Nowak and J. Fricke, *J. Phys. B*, 1985, **18**, 1355; (c) G. Nowak, L. Frey and J. Fricke, *J. Phys. B*, 1985, **18**, 2851.

20 G. Liuti and F. Pirani, *Chem. Phys. Lett.*, 1985, **122**, 245.

21 (a) H. J. Werner and W. Meyer, *Phys. Rev. A*, 1976, **13**, 13; (b) E. A. Reinsch and W. Meyer, *Phys. Rev. A*, 1976, **14**, 915.

22 H. Schumacher, R. B. Bernstein and E. W. Rothe, *J. Chem. Phys.*, 1960, **33**, 584.

23 E. C. Darwall, M. A. D. Fluendy and K. P. Lawley, *Mol. Phys.*, 1970, **19**, 673. For the long-range interaction between Hg*(^{3}P) and noble-gas atoms see also: H. A. Hyman, *Chem. Phys. Lett.*, 1975, **31**, 593.

24 *Handbook of Chemistry and Physics*, ed. R. C. Weast (CRC Press Inc., Boca Raton, Fla, 1986–87).

25 H. J. Werner and W. Meyer, *Mol. Phys.* 1976, **31**, 855; R. D. Amos, *Mol. Phys.*, 1979, **38**, 33.

26 For experimental studies about halogen–rare-gas interactions, see also: C. H. Becker, P. Casavecchia and Y. T. Lee, *J. Chem. Phys.*, 1978, **69**, 2377; C. H. Becker, J. J. Valentini, P. Casavecchia, S. J. Sibener and Y. T. Lee, *Chem. Phys. Lett.*, 1979, **61**, 1; C. H. Becker, P. Casavecchia and Y. T. Lee, *J. Chem. Phys.*, 1979, **70**, 2986; P. Casavecchia, G. He, R. K. Sparks and Y. T. Lee, *J. Chem. Phys.*, 1981, **75**, 710; P. Casavecchia, G. He, R. K. Sparks and Y. T. Lee, *J. Chem. Phys.*, 1982, **77**, 1878, and references therein.

27 G. Ihm, M. W. Cole, F. Toigo and G. Scoles, *J. Chem. Phys.*, 1987, **87**, 3995.

28 V. Staemmler and R. Jaquet, *Chem. Phys.*, 1985, **92**, 141; V. Aquilanti, R. Candori, E. Luzzanti, F. Pirani and G. G. Volpi, *J. Chem. Phys.*, 1986, **85**, 5377.

29 L. A. Viehland, *Chem. Phys.*, 1984, **85**, 291.

30 D. Hausamann and H. Morgner, *Mol. Phys.*, 1985, **54**, 1085.

31 S. H. Patil, *J. Chem. Phys.*, 1985, **83**, 5764.

M_j Selectivity in Collisional Energy Transfer between Alkali-metal Atoms

Masaaki Baba* and Hajime Katô

Department of Chemistry, Faculty of Science, Kobe University, Nada-ku, Kobe 657, Japan
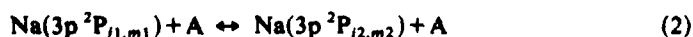
Na atoms in the magnetic field have been selectively excited to each Zeeman sub-level of either the $3p\,^2P_{1/2}$ or $3p\,^2P_{3/2}$ state by a tunable dye laser and the Zeeman spectra of the fluorescence from the collisionally populated $3p\,^2P$ levels have been measured. From the intensities of the Zeeman lines, the selectivity in the collisional transitions between the Zeeman sub-levels of the $3p\,^2P_{1/2}$ and $3p\,^2P_{3/2}$ states has been directly specified. The time evolution of the σ-polarized fluorescence intensity of the $\mathrm{Na}(3p\,^2P_{1/2} \rightarrow 3s\,^2S_{1/2})$ transition has been measured following the $\mathrm{Na}(3p\,^2P_{3/2} \leftarrow 3s\,^2S_{1/2})$ excitation by a σ-polarized short light pulse at $H = 129$ G. An amplitude modulation was found in the fluorescence from the collisionally energy transferred state $\mathrm{Na}(3p\,^2P_{1/2})$. This is the first observation of quantum beats in collision-induced fluorescence. The frequency of the modulation coincides very well with that of the quantum beats of the resonance fluorescence $\mathrm{Na}(3p\,^2P_{3/2} \rightarrow 3s\,^2S_{1/2})$, but the phases are opposite. These results are explained by assuming the conservation of the coherence during the collisional energy transfer.

When alkali-metal vapour is irradiated with either the $^2P_{3/2}-^2S_{1/2}\,D_2$ line or the $^2P_{1/2}-^2S_{1/2}\,D_1$ line, the fluorescence of both D lines are observed. The fluorescence, which is different from the exciting light, is caused by inelastic collisions between the excited alkali-metal atoms and the ground-state atoms. A number of studies on collisions in alkali-metal vapours and alkali-metal vapour–inert-gas mixtures have been reported.[1-3] With the advent of lasers it became possible to determine the accurate potential-energy curves of many excited states of alkali-metal diatomic molecules.[4-8] *Ab initio* molecular-orbital calculations of all excited states of Na_2 and NaK molecules, which decompose, respectively, into $\mathrm{Na}(3p\,^2P) + \mathrm{Na}(3s\,^2S)$ and $\mathrm{Na}(3p\,^2P) + \mathrm{K}(4s\,^2S)$, have been reported.[9-12] Hence, reasonably accurate potential-energy curves, which are necessary for studying the collisional energy transfer between alkali-metal atoms, are now available. We shall study the processes

$$\mathrm{Na}(3p\,^2P_{3/2}) + \mathrm{A} \leftrightarrow \mathrm{Na}(3p\,^2P_{1/2}) + \mathrm{A} \qquad (1)$$
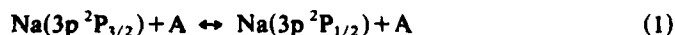
where A is an alkali-metal atom in the ground state. The energy difference between the sodium D_2 line at $16\,973.379\,\mathrm{cm^{-1}}$ and the D_1 line at $16\,956.183\,\mathrm{cm^{-1}}$ is interconverted by the kinetic energy of relative motion. This collisional energy transfer can occur because the energy difference, $17.196\,\mathrm{cm^{-1}}$, is small compared with the average kinetic energy $3k_B T/2$. The cross-sections of energy transfer in collisions between alkali-metal atoms of the same species were observed to be larger than those between dissimilar alkali-metal atoms.[13-16] Theoretical studies of the excitation transfer due to collisions between alkali-metal atoms have been reported.[17,18] The discrepancy between the experimental cross-section and the theoretical value was considerably large, and further experiments were desirable.

The present study is concerned with an orientation-dependent process:

$$\mathrm{Na}(3p\,^2P_{j1,m1}) + \mathrm{A} \leftrightarrow \mathrm{Na}(3p\,^2P_{j2,m2}) + \mathrm{A} \qquad (2)$$

where j and m are the quantum numbers of, respectively, the total internal angular momentum and its projection along the space-fixed z axis. By applying a strong magnetic field, one can excite a selected Zeeman sublevel. The m dependence and the depolarization induced in collision with inert gases have been studied extensively.[19-25] In the present investigation, the Na atoms in the magnetic field were excited to a selected Zeeman sub-level of either the $3p\,^2P_{1/2}$ or the $3p\,^2P_{3/2}$ state by a tunable dye laser. We measured the Zeeman spectra of the fluorescence from the collisionally populated $3p\,^2P$ levels. From the intensities of the Zeeman lines, we could directly specify the selectivity in collisional transitions between Zeeman sub-levels of the $3p\,^2P_{1/2}$ and the $3p\,^2P_{3/2}$ states. Further, we found Zeeman quantum beats in the collision-induced fluorescence $Na(3p\,^2P_{1/2} \rightarrow 3s\,^2S_{1/2})$ as well as the resonance fluorescence $Na(3p\,^2P_{3/2} \rightarrow 3s\,^2S_{1/2})$. These two patterns are very similar, which indicates that the coherence is conserved in the collisional energy-transfer process. These results will be reported and discussed in this article.

Experimental

A rectangular cell ($10 \times 10 \times 30$ mm) made of Pyrex with a side-arm reservoir was simultaneously baked at 800 K and evacuated at lower than 1×10^{-6} Torr† for several hours. Sodium metal or a sodium–potassium mixture was sealed *in vacuo* at a residual pressure lower than 1×10^{-6} Torr. The cell was surrounded by an oven and was placed in the centre of an electromagnet. In order to eliminate the effect of radiation trapping, the laser beam was collimated by a slit (0.2 mm) and passed close to the cell window. The vapour pressure was kept as low as possible within the sensitivity of our fluorescence detector. The temperature of the cell was maintained *ca.* 10 K above the temperature of the reservoir in order to prevent condensation on the cell window.

The experimental set-up to measure the Zeeman spectrum is as follows: the electromagnet had conical pole pieces tapered to 50 mm diameter. A maximum field of 20 kG could be obtained at a separation of 30 mm. The direction of the external magnetic field coincides with the laboratory-fixed Z-axis. A plane-polarized laser beam was propagated along the X axis with its electric vector E pointing along either the Z axis or Y axis, which was chosen to excite selectively either the π or σ component. A fluorescence detector was placed along the Y axis. The intensity, I_π, of the light polarized along the Z axis and the intensity I_σ of the light polarized along the X axis were observed separately through the polarization analyser followed by a polarization scrambler. A single component of the Zeeman levels was selectively excited by a single-mode dye laser (Coherent 699-29, linewidth 500 kHz) with an output power of 300 mW. The atomic fluorescence spectra were measured by a monochromator (Spex Model 1269) and a photon-counting detector with a cooled photomultiplier (RCA C31034). In order to observe well resolved Zeeman lines, the entrance and exit slits of the monochromator were fixed to 2 μm (spectral slit width of 0.2 cm^{-1}) and the magnetic field of 14.8 kG was applied.

The quantum beats were measured by the following set-up. The direction of magnetic field of a Helmholtz coil coincides with the Z axis. A plane-polarized laser beam was propagated along the Z axis with its electric vector E pointing along the X axis. The time-resolved fluorescence intensity polarized along the X axis was observed in the Y direction through the polarization analyser followed by a polarization scrambler. The laser used as an excitation source was a synchronously pumped cavity-dumped dye laser (Spectra Physics 375 and 344S) which was excited by a mode-locked YAG laser (Coherent Antares 76-s). The pulse duration was 10 ps (f.w.h.m.) and the linewidth was *ca.* 6 cm^{-1}. The fluorescence decay curves were obtained with a time-to-amplitude

† 1 Torr = 101 325/760 Pa.

converter and a multichannel pulse-height analyser. A microchannel plate photomulti-
plier (Hamamatsu R1564U-01) was used, and the instrumental response was 60 ps. The
time-resolved fluorescence intensity at a selected wavenumber was measured through a
monochromator (Nikon P250).

Results and Discussion

The Zeeman splittings of the $^2P_{3/2}$, $^2P_{1/2}$ and $^2S_{1/2}$ levels are shown schematically in fig.
1 (top). The relative strengths for observation perpendicular to the magnetic field are
indicated by the lengths of the lines in fig. 1 (bottom), using full lines for *perpendicular*
(σ) components ($\Delta m = \pm 1$) and broken lines for parallel (π) components ($\Delta m = 0$) as
given by Condon and Shortley.[26] When the Na($3p\,^2P_{3/2}$) atoms are equally populated
over the magnetic sublevels, the intensities of the transitions

$$Na(3p\,^2P_{3/2,1/2} \rightarrow 3s\,^2S_{1/2,-1/2}), \qquad Na(3p\,^2P_{3/2,3/2} \rightarrow 3s\,^2S_{1/2,1/2}),$$

$$Na(3p\,^2P_{3/2,-3/2} \rightarrow 3s\,^2S_{1/2,-1/2}) \quad \text{and} \quad Na(3p\,^2P_{3/2,-1/2} \rightarrow 3s\,^2S_{1/2,1/2})$$

will be in the ratio of $1:3:3:1$ for the σ polarization. When the Na($3p\,^2P_{1/2}$) atoms
are equally distributed over magnetic sub-levels, the intensities of the transitions
Na($3p\,^2P_{1/2,1/2} \rightarrow 3s\,^2S_{1/2,-1/2}$) and Na($3p\,^2P_{1/2,-1/2} \rightarrow 3s\,^2S_{1/2,1/2}$) will be in the ratio of
$1:1$ for the σ polarization.

At the applied magnetic field of 14.8 kG, the Zeeman splittings of the Na($3p\,^2P_{3/2}$)
and the Na($3p\,^2P_{1/2}$) levels are 2.76 and 1.84 cm^{-1}, respectively. These values are an
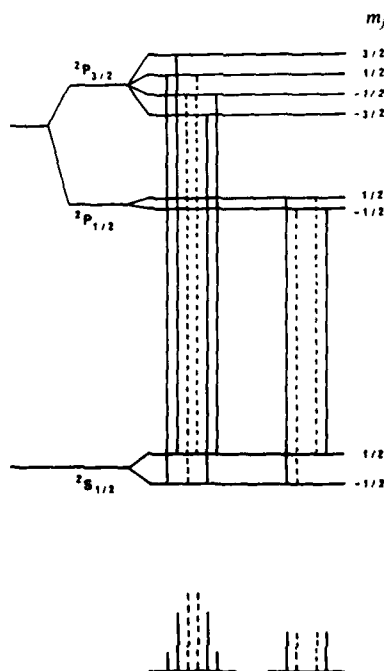
Fig. 1. Zeeman splittings of the $^2P_{3/2}$, $^2P_{1/2}$, and $^2S_{1/2}$ levels, and the *allowed transitions* [(——)
polarized perpendicular (σ) and (- - -) polarized parallel (π) to the magnetic field]. The bottom
part shows the relative transition probabilities by the lengths of the lines.

order of magnitude smaller than the fine-structure splitting of 17.196 cm^{-1}. Hence, the mixing of the Na(3p ^{2}P$_{3/2}$) and Na(3p ^{2}P$_{1/2}$) levels by the Zeeman interaction may be neglected. The hyperfine splittings of the $m_j = \frac{3}{2}$ level of Na(3p ^{2}P$_{3/2}$) and the $m_j = \frac{1}{2}$ level of Na(3s ^{2}S$_{1/2}$) are, respectively, 0.004 and 0.042 cm^{-1}, which are much smaller than the Zeeman splitting. Hence, the effect of the hyperfine interaction may be neglected in the present study of the collisional-energy transfer. The applied magnetic field of 14.8 kG is sufficient to produce a complete Paschen–Back effect of the hyperfine structure, and the nuclear spin angular momentum I and the total electronic angular momentum j are decoupled.

The observed Zeeman spectra of fluorescence from the collisionally populated Na(3p ^{2}P$_{1/2}$) level following the selective excitation to each magnetic sub-level of Na(3p ^{2}P$_{3/2}$) are shown in fig. 2 for Na vapour. The temperature of the reservoir was kept at 450 K, and the vapour pressure of Na atoms was 4×10^{-5} Torr.[27] The radiative lifetimes of the Na(3p ^{2}P$_{3/2}$) and Na(3p ^{2}P$_{1/2}$) states are reported to be 16.3 ns.[28,29] Hence, the effect of multiple collisions can be neglected. The intensity ratio of the transitions Na(3p ^{2}P$_{1/2,1/2} \rightarrow$ 3s ^{2}S$_{1/2,-1/2}$) and Na(3p ^{2}P$_{1/2,-1/2} \rightarrow$ 3s ^{2}S$_{1/2,1/2}$) gives directly the ratio of the collisional transitions,

$$\text{Na}(3p\ ^2P_{3/2,m}) + \text{Na}(3s\ ^2S_{1/2}) \rightarrow \text{Na}(3p\ ^2P_{1/2,1/2}) + \text{Na}(3s\ ^2S_{1/2}) \qquad (3)$$

and

$$\text{Na}(3p\ ^2P_{3/2,m}) + \text{Na}(3s\ ^2S_{1/2}) \rightarrow \text{Na}(3p\ ^2P_{1/2,-1/2}) + \text{Na}(3s\ ^2S_{1/2}) \qquad (4)$$
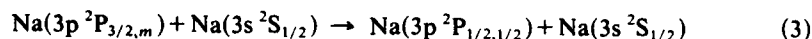
Fig. 2. Observed Zeeman spectra of the fluorescence, polarized perpendicular to the magnetic field (σ), from the collisionally populated levels Na(3p ^{2}P$_{1/2,m}$) following a selective excitation to each magnetic sub-level of Na(3p ^{2}P$_{3/2,m}$). The sample cell contains 4×10^{-5} Torr of Na atoms at 450 K.

because the probabilities of the radiative transitions $Na(3p\,^2P_{1/2,1/2} \rightarrow 3s\,^2S_{1/2,-1/2})$ and $Na(3p\,^2P_{1/2,-1/2} \rightarrow 3s\,^2S_{1/2,1/2})$ are the same. We express the transition probability of the process expressed by eqn (2) as $P_{\text{Na-A}}(j1, m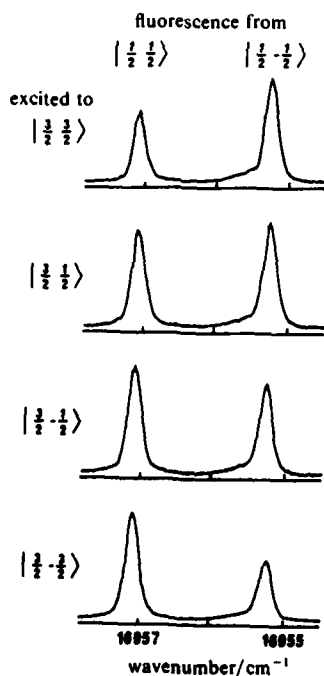1 \rightarrow j2, m2)$. The ratio of $P_{\text{Na-Na}}(\frac{3}{2}, m \rightarrow \frac{1}{2}, \frac{1}{2}) : P_{\text{Na-Na}}(\frac{3}{2}, m \rightarrow \frac{1}{2}, -\frac{1}{2})$ for the selective excitation to each magnetic sub-level $Na(3p\,^2P_{3/2,m})$ is listed in table 1, which shows that the ratio increases in the order $m = \frac{3}{2}, \frac{1}{2}, -\frac{1}{2}$ and $-\frac{3}{2}$. The Zeeman spectra of the fluorescence from the collisionally populated $Na(3p\,^2P_{3/2})$ level following the selective excitation to each magnetic sub-level of $Na(3p\,^2P_{1/2})$ are shown in fig. 3 for Na vapour. The ratios of the transition probabilities $P_{\text{Na-Na}}(\frac{1}{2}, m \rightarrow \frac{3}{2}, \frac{3}{2}) : P_{\text{Na-Na}}(\frac{1}{2}, m \rightarrow \frac{3}{2}, \frac{1}{2}) : P_{\text{Na-Na}}(\frac{1}{2}, m \rightarrow \frac{3}{2}, -\frac{1}{2}) : P_{\text{Na-Na}}(\frac{1}{2}, m \rightarrow \frac{3}{2}, -\frac{3}{2})$ for $m = \frac{1}{2}$ and $-\frac{1}{2}$ are listed in table 1. The probability increases in the order $P_{\text{Na-Na}}(\frac{1}{2}, m \rightarrow \frac{3}{2}, \frac{3}{2})$, $P_{\text{Na-Na}}(\frac{1}{2}, m \rightarrow \frac{3}{2}, \frac{1}{2})$, $P_{\text{Na-Na}}(\frac{1}{2}, m \rightarrow \frac{3}{2}, -\frac{1}{2})$ and $P_{\text{Na-Na}}(\frac{1}{2}, m \rightarrow \frac{3}{2}, -\frac{3}{2})$ for $m = \frac{1}{2}$, and in the opposite order for $m = -\frac{1}{2}$. The transition energies decrease as the transition probabilities increase for $m = \frac{1}{2}$, but the transition energies increase as the transition probabilities increase for $m = -\frac{1}{2}$. Hence, the energy difference seems to be unimportant in determining the transition probability. Similar experiments were performed for the Na+K system. The temperature of the reservoir was kept at 450 K and the vapour pressure of Na atoms and K atoms were, respectively, 4×10^{-5} and 2×10^{-3} Torr.[27] The results are similar to the Na+Na system, and they are listed in table 1.

The quantum-mechanical theories of fine-structure transition have been described and been applied to calculate the cross-sections for fine-structure transitions in collisions of Na with inert-gas atoms.[30-37] The total cross-section for the $j_1 m_1 \rightarrow j_2 m_2$ transition

Table 1. The observed ratios $P_{\text{Na-A}}(\frac{3}{2}, m \rightarrow \frac{1}{2}, \frac{1}{2}) : P_{\text{Na-A}}(\frac{3}{2}, m \rightarrow \frac{1}{2}, -\frac{1}{2})$ and $P_{\text{Na-A}}(\frac{1}{2}, m \rightarrow \frac{3}{2}, \frac{3}{2}) : P_{\text{Na-A}}(\frac{1}{2}, m \rightarrow \frac{3}{2}, \frac{1}{2}) : P_{\text{Na-A}}(\frac{1}{2}, m \rightarrow \frac{3}{2}, -\frac{1}{2}) : P_{\text{Na-A}}(\frac{1}{2}, m \rightarrow \frac{3}{2}, -\frac{3}{2})$ and the total cross-sections $\sigma(j_1 m_1; j_2 m_2)$ expressed by Grawert constants

m	$P_{\text{Na-Na}}(\frac{3}{2}, m \rightarrow \frac{1}{2}, \frac{1}{2}) : P_{\text{Na-Na}}(\frac{3}{2}, m \rightarrow \frac{1}{2}, -\frac{1}{2})$	$P_{\text{Na-K}}(\frac{3}{2}, m \rightarrow \frac{1}{2}, \frac{1}{2}) : P_{\text{Na-K}}(\frac{1}{2}, m \rightarrow \frac{1}{2}, -\frac{1}{2})$
$\frac{3}{2}$	0.71 : 1	0.76 : 1
$\frac{1}{2}$	0.88 : 1	0.91 : 1
$-\frac{1}{2}$	1.22 : 1	1.16 : 1
$-\frac{3}{2}$	1.78 : 1	1.59 : 1

A	m	$P_{\text{Na-A}}(\frac{1}{2}, m \rightarrow \frac{3}{2}, \frac{3}{2})$	:	$P_{\text{Na-A}}(\frac{1}{2}, m \rightarrow \frac{3}{2}, \frac{1}{2})$	:	$P_{\text{Na-A}}(\frac{1}{2}, m \rightarrow \frac{3}{2}, -\frac{1}{2})$	:	$P_{\text{Na-A}}(\frac{1}{2}, m \rightarrow \frac{3}{2}, -\frac{3}{2})$
Na	$\frac{1}{2}$	0.60	:	0.84	:	0.93	:	1.00
	$-\frac{1}{2}$	1.00	:	0.95	:	0.89	:	0.68
K	$\frac{1}{2}$	0.61	:	0.81	:	0.92	:	1.00
	$-\frac{1}{2}$	1.00	:	0.98	:	0.95	:	0.75

m	$\sigma(\frac{3}{2}, m; \frac{1}{2}, \frac{1}{2})$	$\sigma(\frac{3}{2}, m; \frac{1}{2}, -\frac{1}{2})$
$\frac{3}{2}$	$3B(1)/4 + B(2)/4$	$B(2)$
$\frac{1}{2}$	$B(1)/2 + B(2)/2$	$B(1)/4 + 3B(2)/4$
$-\frac{1}{2}$	$B(1)/4 + 3B(2)/4$	$B(1)/2 + B(2)/2$
$-\frac{3}{2}$	$B(2)$	$3B(1)/4 + B(2)/4$

where $B(1) = B(\frac{3}{2}\frac{1}{2}; 1)$ and $B(2) = B(\frac{3}{2}\frac{1}{2}; 2)$

m	$\sigma(\frac{1}{2}, m; \frac{3}{2}, \frac{3}{2})$	$\sigma(\frac{1}{2}, m; \frac{3}{2}, \frac{1}{2})$	$\sigma(\frac{1}{2}, m; \frac{3}{2}, -\frac{1}{2})$	$\sigma(\frac{1}{2}, m; \frac{3}{2}, -\frac{3}{2})$
$\frac{1}{2}$	$3A(1)/4 + A(2)/4$	$A(1)/2 + A(2)/2$	$A(1)/4 + 3A(2)/4$	$A(2)$
$-\frac{1}{2}$	$A(2)$	$A(1)/4 + 3A(2)/4$	$A(1)/2 + A(2)/2$	$3A(1)/4 + A(2)/4$

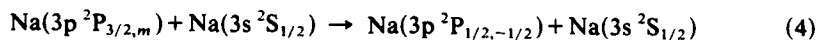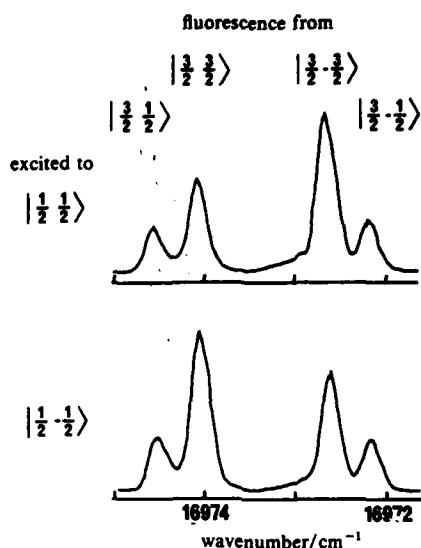where $A(1) = B(\frac{1}{2}\frac{3}{2}; 1)$ and $A(2) = B(\frac{1}{2}\frac{3}{2}; 2)$

Fig. 3. Observed Zeeman spectra of the fluorescence, polarized perpendicular to the magnetic field (σ), from the collisionally populated levels $Na(3p\ ^2P_{3/2,m})$ following a selective excitation to each magnetic sub-level of $Na(3p\ ^2P_{1/2,m})$. The sample cell contains 4×10^{-5} Torr of Na atoms at 450 K.

is given by

$$\sigma(j_1m_2; j_2m_2) = \sum_g \langle j_1j_2m_1 - m_2|gm_1 - m_2\rangle^2 B(j_1j_2; g) \qquad (5)$$

where $\langle j_1j_2m_1 - m_2|gm_1 - m_2\rangle$ is the Clebsch–Gordan coefficient. The dynamical parameters $B(j_1j_2; g)$ are specified by a close-coupled partial-wave calculation,[33,35] and we shall call these the Grawert constants. The coefficients are derived by considering the conservation of the angular momentum. For $j_1 = \frac{1}{2}$ and $j_2 = \frac{3}{2}$, the total cross-sections are expressed by two Grawert constants $B(\frac{1}{2}\ \frac{3}{2}; 1)$ and $B(\frac{1}{2}\ \frac{3}{2}; 2)$ (table 1). The observed results suggest that the value of $B(j_1j_2; 2)$ is larger than $B(j_1j_2; 1)$. The magnitude of $B(j_1j_2; g)$ depends on the interaction potentials, and further theoretical calculations of $B(j_1j_2; g)$ based on accurate potential-energy curves are desired.

When atomic or molecular states are coherently excited by an optical pulse, the emitted light may exhibit the spontaneous decay and an amplitude modulation called quantum beats at the frequency of the energy separation between the excited states.[38,39] We have observed hyperfine quantum beats and Zeeman quantum beats in the light emitted from the $Na(3p\ ^2P_{3/2})$ level after excitation by a short laser pulse.[40] The quantum beats observed at the external magnetic field of 129 G are shown in fig. 4.

The $Na(3p\ ^2P_{3/2})$ and $Na(3s\ ^2S_{1/2})$ levels are split by the Zeeman and hyperfine interactions. The Hamiltonian responsible for the hyperfine and Zeeman interactions is given by

$$H' = A_jI \cdot j + B_j[3(I \cdot j)^2 + (\tfrac{3}{2})I \cdot j - I(I + 1)j(j + 1)]/2I(2I - 1)j(2j - 1)$$
$$+ g_j\mu_Bj \cdot H - g_I\mu_BI \cdot H \qquad (6)$$

where A_j is the magnetic hyperfine structure constant, B_j is the electric quadrupole interaction constant, and the third and fourth terms represent, respectively, the interactions of the electronic and nuclear-magnetic moments with the external magnetic field.
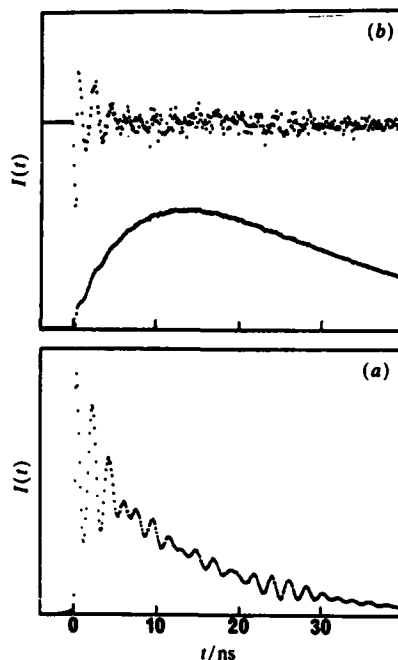
Fig. 4. Observed fluorescence intensities as a function of time following the excitation Na(3p $^2P_{3/2}$ ← 3s $^2S_{1/2}$) by a σ-polarized short light pulse in the presence of the external magnetic field, $H = 129$ G. (*a*) Fluorescence of the Na(3p $^2P_{3/2}$ → 3s $^2S_{1/2}$) transition with σ polarization. (*b*) Fluorescence of the Na(3p $^2P_{1/2}$ → 3s $^2S_{1/2}$) transition with σ polarization. The upper trace is the modulated part, which is obtained by subtracting the unmodulated part and the amplitude is expanded.

g_j and g_I are, respectively, the gyromagnetic ratios of the electron and nucleus, while μ_B is the Bohr magneton. The values of A_j, B_j, g_j and g_I are reported, respectively, to be 18.65 MHz, 2.82 MHz, 1.3344, and -0.0008 for Na(3p $^2P_{3/2}$), and 885.82 MHz, *ca.* 0 MHz, 2.0023, and -0.0008 for Na(3s $^2S_{1/2}$).[39,41] The energy levels at $H = 129$ G and the transition moments between these levels have been calculated, and the results are shown schematically in fig. 5. The pattern of the beats in fig. 4(*a*) was explained very well by a theoretical calculation.[40] The main pattern of the beats was explained as the overlap of two types of beats, which exhibit intensity modulations at frequencies corresponding to the energy separations between the levels of $m_j = \frac{3}{2}$ and $-\frac{1}{2}$, and $m_j = \frac{1}{2}$ and $-\frac{3}{2}$.

The time evolution of the σ-polarized fluorescence intensity of the Na(3p $^2P_{1/2}$ → 3s $^2S_{1/2}$) transition following the excitation Na(3p $^2P_{3/2}$ ← 3s $^2S_{1/2}$) by a σ-polarized short light pulse at $H = 129$ G is shown in fig. 4(*b*). This shows a rise, which corresponds to the production of the Na(3p $^2P_{1/2}$) atoms induced by collisions of the Na(3p $^2P_{3/2}$) atoms with the Na(3s $^2S_{1/2}$) atoms, and a decay, which occurs either radiatively or non-radiatively. It is very interesting to find an amplitude modulation in the fluorescence from the collisionally energy-transferred state Na(3p $^2P_{1/2}$). In order to enhance the modulated part, we have subtracted the unmodulated part by simulating the fluorescence rise and decay by least-squares fitting, and the modulated part is shown in the upper trace of fig. 4(*b*). That is, to our knowledge, the first observation of quantum
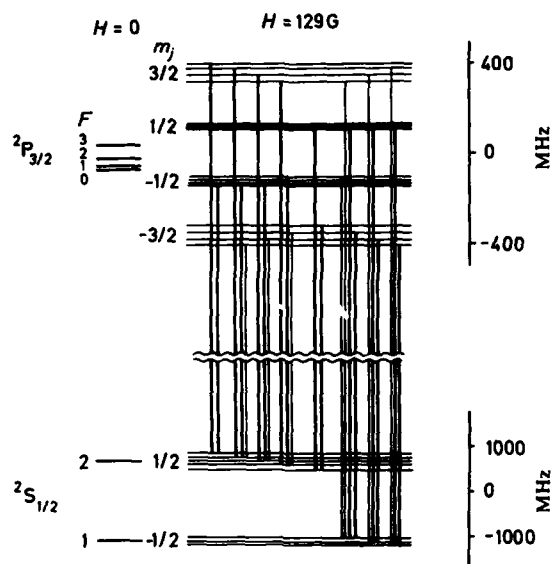
Fig. 5. Zeeman and hyperfine structure of the $Na(3p\,^2P_{3/2})$ and $Na(3s\,^2S_{1/2})$ levels at the magnetic field $H = 129\,G$. The allowed transitions of σ polarization are shown; thick lines are of predominant transition probabilities, and thin lines are of minor transition probabilities.

beats in collision-induced fluorescence. The frequency of the modulation coincides very well with that of the quantum beats of the resonance fluorescence $Na(3p\,^2P_{3/2} \rightarrow 3s\,^2S_{1/2})$, but the phases are opposite.

When the $Na(3s\,^2S_{1/2,1/2})$ atoms are coherently excited by a σ-polarized optical pulse of the Na D_2 line, the quantum beats of the resonance fluorescence are given by

$$\langle{}^2S\tfrac{1}{2}\tfrac{1}{2}|\mu_X|{}^2P\tfrac{3}{2}\tfrac{3}{2}\rangle^2\langle{}^2S\tfrac{1}{2}\tfrac{1}{2}|\mu_X|{}^2P\tfrac{3}{2}-\tfrac{1}{2}\rangle^2$$

$$\times \cos\left(E_{3/2,3/2} - E_{3/2,-1/2}\right)t/\hbar \exp\left(-\Gamma t\right) \tag{7}$$

where $\langle jm|\mu_X|j'm'\rangle$ is the transition moment of the $jm-j'm'$ transition and μ_X is the electric dipole moment along the X axis, E_{jm} is the energy of the jm level, and Γ is the decay rate of the excited state. If we assume that the coherence is conserved during the collisional energy transfer following the coherent excitation of the $Na(3s\,^2S_{1/2,1/2})$ atoms by a σ-polarized optical pulse of the Na D_2 line, then the intensity modulation of the fluorescence $Na(3p\,^2P_{1/2} \rightarrow 3s\,^2S_{1/2})$ is given by

$$[\langle{}^2S\tfrac{1}{2}\tfrac{1}{2}|\mu_X|{}^2P\tfrac{3}{2}\tfrac{3}{2}\rangle\langle{}^2S\tfrac{1}{2}\tfrac{1}{2}|\mu_X|{}^2P\tfrac{3}{2}-\tfrac{1}{2}\rangle$$

$$\times P(\tfrac{3}{2}\tfrac{3}{2} \rightarrow \tfrac{1}{2}\tfrac{1}{2})P(\tfrac{3}{2}-\tfrac{1}{2} \rightarrow \tfrac{1}{2}\tfrac{1}{2})\langle{}^2P\tfrac{1}{2}\tfrac{1}{2}|\mu_X|{}^2S\tfrac{1}{2}-\tfrac{1}{2}\rangle^2$$

$$+\langle{}^2S\tfrac{1}{2}\tfrac{1}{2}|\mu_X|{}^2P\tfrac{3}{2}\tfrac{3}{2}\rangle\langle{}^2S\tfrac{1}{2}\tfrac{1}{2}|\mu_X|{}^2P\tfrac{3}{2}-\tfrac{1}{2}\rangle$$

$$\times P(\tfrac{3}{2}\tfrac{3}{2} \rightarrow \tfrac{1}{2}-\tfrac{1}{2})P(\tfrac{3}{2}-\tfrac{1}{2} \rightarrow \tfrac{1}{2}-\tfrac{1}{2})\langle{}^2P\tfrac{1}{2}-\tfrac{1}{2}|\mu_X|{}^2S\tfrac{1}{2}\tfrac{1}{2}\rangle^2]$$

$$\times \cos\left(E_{3/2,3/2} - E_{3/2,-1/2}\right)t/\hbar \exp\left(-\Gamma t\right). \tag{8}$$

The frequency of the intensity modulation given by eqn (7) coincides with that of eqn (8). The coefficient of $\cos\left(E_{3/2,3/2} - E_{3/2,-1/2}\right)t/\hbar$ in eqn (7) is positive, but the corresponding coefficient in eqn (8) is negative, as can be seen easily. Hence, the phases of the intensity modulations expressed by eqn (7) and (8) are opposite. This character

holds also in the case of the coherent excitation of the Na($3p\,{}^2S_{1/2,-1/2}$) atoms. These results are in good agreement with the observed results. Therefore, the present experimental results give direct evidence of the conservation of coherence during the collisional energy transfer.

References

1 L. Krause, *Adv. Chem. Phys.*, 1975, **28**, 267.
2 L. Krause, *Appl. Opt.*, 1966, **5**, 1375.
3 E. E. Nikitin, *Adv. Chem. Phys.*, 1975, **28**, 317.
4 K. P. Huber and G. Herzberg, *Molecular Spectra and Molecular Structure, IV. Constants of Diatomic Molecules* (van Nostrand Reinhold, New York, 1979).
5 P. Kusch and M. M. Hessel, *J. Chem. Phys.*, 1978, **68**, 2591.
6 G. K. Chawla, H. J. Vedder and R. W. Field, *J. Chem. Phys.*, 1987, **86**, 3082.
7 M. E. Kaminsky, *J. Chem. Phys.*, 1977, **66**, 4951; 1980, **73**, 3520.
8 C. Effantin, O. Babaky, K. Hussein, J. d'Incan and R. F. Barrow, *J. Phys. B*, 1985, **18**, 4077.
9 D. D. Konowalow, M. E. Rosenkrantz and M. L. Olson, *J. Chem. Phys.*, 1980, **72**, 2612.
10 D. D. Konowalow and M. E. Rosenkrantz, *J. Phys. Chem.*, 1982, **86**, 1099.
11 A. Valance and O. N. Tuan, *J. Phys. B*, 1982, **15**, 17.
12 W. J. Stevens, D. D. Konowalow and L. B. Ratcliff, *J. Chem. Phys.*, 1984, **80**, 1215.
13 K. Hoffmann and R. Seiwert, *Ann. Phys.*, 1961, **7**, 71.
14 J. Pitre and L. Krause, *Can. J. Phys.*, 1968, **46**, 125.
15 R. Seiwert, *Ann. Phys.*, 1956, **18**, 54.
16 V. Stacey and R. N. Zare, *Phys. Rev. A*, 1970, **1**, 1125.
17 E. I. Dashevskaya, A. I. Voronin and E. E. Nikitin, *Can. J. Phys.*, 1969, **47**, 1237.
18 E. I. Dashevskaya, E. E. Nikitin, A. I. Voronin and A. A. Zembekov, *Can. J. Phys.*, 1970, **48**, 981.
19 A. C. G. Mitchell and M. W. Zemansky, *Resonance Radiation and Excited Atoms* (Cambridge University Press, Cambridge, 1961).
20 P. P. Feofilov, *The Physical Basis of Polarized Emission* (Consultants Bureau, New York, 1961).
21 W. Berdowski and L. Krause, *Phys. Rev.*, 1968, **165**, 158.
22 W. Berdowski, T. Shiner and L. Krause, *Phys. Rev. A*, 1971, **4**, 984.
23 J. C. Gay and W. B. Schneider, *Z. Phys. A*, 1976, **278**, 211.
24 M. Elbel and F. Naumann, *Z. Phys.*, 1967, **204**, 501.
25 A. Gallagher, *Phys. Rev.*, 1967, **157**, 68.
26 E. U. Condon and G. H. Shortley, *The Theory of Atomic Spectra* (Cambridge University Press, Cambridge, 1951).
27 A. N. Nesmeyanov, *Vapor Pressure of the Chemical Elements* (Elsevier, New York, 1963).
28 J. K. Link, *J. Opt. Soc. Am.*, 1966, **56**, 1195.
29 B. P. Kibble, G. Copley and L. Krause, *Phys. Rev.*, 1967, **153**, 9.
30 A. M. Arthurs and A. Dalgarno, *Proc. R. Soc. London, Ser. A*, 1969, **256**, 540.
31 R. H. G. Reid and A. Dalgarno, *Phys. Rev. Lett.*, 1969, **22**, 1029.
32 R. H. G. Reid and A. Dalgarno, *Chem. Phys. Lett.*, 1970, **6**, 85.
33 G. Grawert, *Z. Phys.*, 1969, **225**, 283.
34 F. H. Mies, *Phys. Rev. A*, 1973, **7**, 942.
35 R. H. G. Reid, *J. Phys. B*, 1973, **6**, 2018.
36 T. F. George and P. L. Devries, *Chem. Phys. Lett.*, 1983, **96**, 99.
37 E. E. Nikitin, *Commt. Atom. Mol. Phys.*, 1971, **3**, 7.
38 P. A. Franken, *Phys. Rev.*, 1961, **121**, 508.
39 A. Corney, *Atomic and Laser Spectroscopy* (Clarendon Press, Oxford, 1977).
40 M. Baba, K. Namba, N. Tamai and H. Katô, to be published.
41 E. Arimondo, M. Inguscio and P. Violino, *Rev. Mod. Phys.*, 1977, **49**, 31.

Determination of Molecular Orientation and Alignment from Polarized Laser Photofragmentation Measurements

Orientated CH_3I Molecular Beams

Richard B. Bernstein* and Seung E. Choi†

Department of Chemistry and Biochemistry, University of California, Los Angeles, California 90024, U.S.A.

Steven Stolte

Fysisch Laboratorium, Katholieke Universiteit, 6525 ED Nijmegen, The Netherlands

It is important to determine the degree of orientation and alignment of a given ensemble of molecules, whether they be reagents (prepared *via* hexapole focusing or laser excitation), or products from crossed-beam reactions or scattering from surfaces. In general, the orientational probability density function $P(\cos \theta)$, *i.e.* the spatial distribution function of the molecular framework, can be expressed as a Legendre expansion in $\cos \theta (= \rho)$, where the angle θ is defined with respect to the axis of a reference electric field. The first moment of $P(\rho)$, *i.e.* $\langle P_1(\rho) \rangle = \bar{P}_1$, is the average orientation, while the second moment, $\bar{P}_2$, is the average alignment. Unfortunately, because of hyperfine coupling effects (dependent upon the electric field strength and upon the time-dependence of the passage of the orientated molecules from strong to weak field, *e.g.* from the hexapole through guiding and orientation fields), it is not always possible to ascertain the actual $P(\rho)$. The present paper provides the methodology for inversion of experimental measurements of the asymmetry parameters, $\kappa_{\parallel}, \kappa_{\perp}$, from the polarized laser-induced photofragmentation of oriented symmetric-top molecules, to yield the first few Legendre moments of $P(\rho)$ and thus characterize a given ensemble of molecules in terms of its orientation and alignment. As an example, this method is applied to available experimental measurements on CH_3I in weak electric fields, for which computations dealing with certain limiting (adiabatic, sudden) hyperfine coupling cases have been carried out.

1. Introduction

A central issue in chemical reaction dynamics,[1] and especially in dynamical stereochemistry,[2] is the influence of the mutual orientation and alignment of the reagents upon their reactivity. Since the introduction of the electrostatic hexapole technique for the preparation of orientated molecule beams,[3,4] there have been a number of studies of the so-called reactive asymmetry effect in elementary bimolecular reactions using beams of (partially) orientated reagent molecules.[5-7] There have also been reports of the orientation dependence of photoionization,[8] of molecule-surface scattering[9] and the orientation of molecules desorbed from a surface.[10]

In all experiments with orientated molecules in the gas phase, an important question is the actual extent or degree of orientation of the molecular framework of the molecules under investigation. In many cases, although there is little doubt about the direction of the orientation ('heads' *vs.* 'tails'), there is considerable uncertainty about the shape,

† Present address: James Franck Institute, University of Chicago, Chicago, IL 60637, U.S.A.

or even the breadth, of the orientational distribution function $P(\cos \theta)$, where θ is the angle between the molecular dipole axis and the electric field ε.

For the simple case of symmetric-top molecules, the theory of hexapole focusing and state-selection *via* the first-order Stark effect is well developed.[3,11] Experiments with near-ideal hexapole lenses[12] confirmed key elements of the focusing theory for methyl halides and related molecules. For the prolate tops, single $|JKM_j\rangle$ states can be resolved, while for oblate tops[12b] and 'pseudo-symmetric' tops (such as t-butyl halides)[13] unstructured focusing curves of near-theoretical shape with proper threshold voltages are obtained.

For proper analysis of the reactive asymmetry experiments, one requires a knowledge of the overall orientational distribution function of the ensemble of states of the focused beam molecules entering the reaction zone. One can characterize this distribution in terms of its so-called Legendre moments,[14] *i.e.* $\langle P_1(\cos \theta) \rangle \equiv \bar{P}_1 \equiv \langle \cos \theta \rangle$, the average orientation, $\langle P_2(\cos \theta) \rangle \equiv \bar{P}_2 \equiv \frac{3}{2}\langle \cos^2 \theta \rangle - \frac{1}{2}$, the average alignment of the ensemble *etc.*

Until recently, it was necessary to use theoretical orientational distributions since there was no experimental way to measure them. (In exceptional cases, one can employ the observed electric-field dependence of the steric effect itself to check the calculated degree of orientation, as for oriented N_2O[7] and NO[15]). In many cases, such theoretical distributions are expected to be inaccurate, since they are calculated in the strong-field (spin-decoupled) limit in which the $|JKM_J\rangle$ representation is appropriate. Nuclear spin effects (hyperfine coupling) lead to a partial loss of spatial orientation[7,16] and alignment.[15,17] In particular, $|JKM_J\rangle$-selected molecules, after passing out of the strong-field region (*e.g.* $E = 10\ \mathrm{kV\ cm^{-1}}$) and entering the relatively weak 'orientation field' (*e.g.* $E = 50\ \mathrm{V\ cm^{-1}}$), used to preserve the quantization axis in the reaction zone, undergo recoupling of the nuclear spin(s), ($|IM_I\rangle$) with the rotational angular momentum ($|JKM_J\rangle$) to form a superposition of the hyperfine states ($|FM_F\rangle$) with a lower degree of orientation and alignment. An extensive theoretical treatment[16] of this 'weak-field' problem has provided expressions for the orientation probability distributions $P(\cos \theta)$ for all the methyl halides in the zero-field limit, but an analytical description of the electric-field E-dependence is not yet available. The treatment also has been carried out in both the adiabatic and sudden approximation, with distinguishable results. Fig. 1 shows some typical results,[16] to be discussed in section 3.

Experiments to demonstrate the E dependence have been carried out[18] for the 'worst-case' molecule, CH_3I (for which the nuclear spin of the halogen is $\frac{5}{2}$ and the nuclear quadrupole coupling constant $eqQ = 1940\ \mathrm{MHz}$), revealing the extreme field dependence: for low J states at low fields, the spatial disorientation effect of the spin-recoupling process is severe. Thus, as is well-known,[6,7,15] one cannot simply assume a theoretical knowledge of the shape of $P(\cos \theta)$, or its first moment $\langle \cos \theta \rangle = \bar{P}_1$, in view of the hyperfine effect. Even the influence of the details of the passage from strong to weak field upon the asymptotic, weak-field distribution $P(\cos \theta)$ must be taken into account. An objective measurement of the orientational distribution of an arbitrary ensemble of (partially) oriented molecules is therefore desirable, all the more so in the absence of detailed information on the method of preparation of the ensemble.

Gandhi *et al.*[19] have provided such an experimental method (albeit with certain limits of applicability) that makes use of polarized laser-induced photofragmentation of the ensemble of (oriented) molecules. The molecules are photodissociated within an orientation field, *i.e.* a vertical d.c. electric field $\mathscr{E}$ with the polarization of the laser vertical (or horizontal). In its simplest form, the experiment consists of a measurement of the photofragment signals S^+ and S^- in the $+z$ ('up') and $-z$ ('down') directions. Normally $\mathscr{E}$ is directed upward, *i.e.* from $-z$ to $+z$. The measured $\pm z$ asymmetry in the signal is an indicator of the degree of orientation of the 'parent' molecules prior to photodissociation. Provided that the optical transition is parallel in nature and the dissociation 'prompt' ($\tau \lesssim 1\ \mathrm{ps}$), as for CH_3I at *ca.* $280\ \mathrm{nm}$,[20] the analysis is
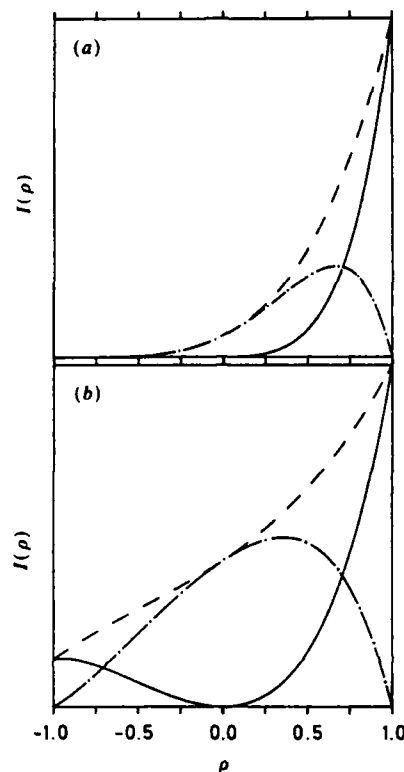
Fig. 1. Theoretical orientation probability density functions $P(\rho)$ and photofragment angular distributions $I(\rho)$ for CH_3I in the strong-field limit [ref. (23)] (*a*) and weak-field limit [ref. (16)] (*b*), the latter in the adiabatic approximation, all referring to the parent state $|JKM_J\rangle = |222\rangle$. (- - -) Normalized $P(\rho)$; (———) $S_\parallel(\rho)$; (— · —) $S_\perp(\rho)$. (All ordinates designated I; S curves not normalized.)

straightforward.[19,21] Given the functional form of $P(\cos\theta)$ characterizing the ensemble of molecules, one can calculate directly from $P(\cos\theta)$ the experimental ratio $\kappa = S^-/S^+$ ($0 \leqslant \kappa \leqslant 1$) for the normal experimental polarities. Comparison of experimental κ values for several different $|JKM_J\rangle$ parent states obtained with vertical laser polarization under weak-field conditions showed fair agreement[19] with the calculated[16] ('sudden-limit') values, but the conclusion was limited by the accuracy of the κ measurements. Measurement of κ with horizontal laser polarization gives some independent information of the degree of orientation of the ensemble.[18,21] Fig. 2 shows some typical experimental results,[21] to be discussed in more detail in section 5. In the Appendix, methods are suggested to obtain even more information from measurements as a function of laser polarization angle.

The goal of the present work is to develop useful relations to make it possible to determine the molecular orientation and alignment from such polarized laser photofragmentation measurements. It will be seen that such measurements of κ for both parallel and perpendicular polarizations can be used to evaluate the first two Legendre moments, $\bar{P}_1$ and $\bar{P}_2$ of the orientational distribution, and in certain cases, lead to an estimate of $\bar{P}_3$. The method is tested with several computer-simulated and experimental data sets.
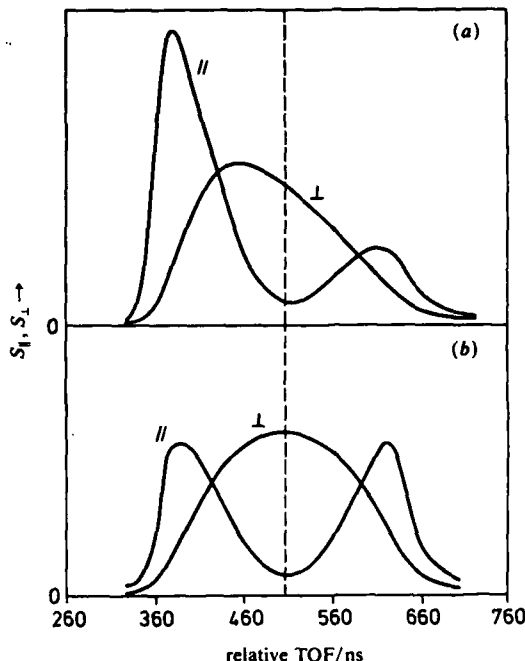
Fig. 2. Sample of experimental TOF distributions of the $I(^2P_{1/2})$ fragment from the polarized laser-photofragmentation of CH_3I (parent state $|JKM_J\rangle = |222\rangle$), using vertical ($\|$) and horizontal ($\perp$) laser polarizations as indicated, all in a weak field ($ca.$ 30 V cm^{-1}). (a) Orientated beam molecules; (b) 'unorientated' (but state-selected) beam molecules, same beam as in (a), but with orientation field set at zero to randomize M_P. Original data from ref. (21) (fig. 3), but smoothed and re-plotted (with a small shift in position of vertical 'dividing line' between the hemispheres). See text (section 5) for re-analysis of results.

2. Methodology

To avoid extensive duplication, we make use of much of the notation and assumptions of ref. (14) and (22), which dealt with the $Rb + CH_3I$ reaction, and the treatment of the theory of oriented symmetric-top molecules (in the strong-field limit) and their photofragmentation asymmetry.[23] We also assume familiarity with many of the relevant references to photofragmentation dynamics with emphasis on CH_3I.[24-32] For simplicity, we shall assume that the β parameter of the photofragment angular distribution $I(\theta) \propto 1 + \beta P_2(\cos\theta)$ is 2; $i.e.$ a pure parallel transition with prompt dissociation. (The more general results for $-1 \leqslant \beta \leqslant 2$ are presented in the appendix.)

The observable κ values (for $\|$ and $\perp$ laser polarizations) are given in terms of the photofragment intensities (the 'signals' $S^{\mp}$) in each hemisphere. Thus

$$\kappa_\| = S_\|^- / S_\|^+ = \int_{-1}^0 P(\rho)\rho^2\,d\rho \bigg/ \int_0^1 P(\rho)\rho^2\,d\rho \qquad (1a)$$

$$\kappa_\perp = S_\perp^- / S_\perp^+ = \int_{-1}^0 P(\rho)\tfrac12(1-\rho^2)\,d\rho \bigg/ \int_0^1 P(\rho)\tfrac12(1-\rho^2)\,d\rho \qquad (1b)$$

where $P(\rho)$ is the orientational probability density function (p.d.f.) of the oriented (selected) molecules, $e.g.$ from parent states JKM_J. Here, $\rho = \cos\theta$ and $\int_{-1}^1 P(\rho)\,d\rho = 1$ as usual;[22,23] $1 \geqslant \rho \geqslant -1$.

Expanding $P(\rho)$ in a Legendre series,

$$P(\rho) = \sum_{n=0}^{N} C_n P_n(\rho) \tag{2}$$

where $P_n(\rho)$ is the nth Legendre function and $N = 2J$. The coefficients C_n are closely related[14,22] to the Legendre moments of the p.d.f.:

$$C_n = \frac{2n+1}{2} \langle P_n(\rho) \rangle = \frac{2n+1}{2} \bar{P}_n. \tag{3}$$

We rewrite eqn (2) in terms of the Legendre moments:

$$P(\rho) = \sum_{n=0}^{N} \left(\frac{2n+1}{2} \bar{P}_n \right) P_n(\rho). \tag{4}$$

Thus, $S_{\parallel}^-$, $S_{\parallel}^+$, $S_{\perp}^-$, $S_{\perp}^+$ and $\kappa_{\parallel}$, $\kappa_{\perp}$ can be expressed in terms of simple series as follows. Write expressions for the signals in each hemisphere, $S_{\parallel}^{\mp}$ or $S_{\perp}^{\mp}$, in terms of hemisphere expansion coefficients, designated $s_{\parallel}^{\mp}$, $s_{\perp}^{\mp}$. Thus,

$$S_{\parallel}^{\mp} = \sum_{n=0}^{N} s_{\parallel n}^{\mp} \bar{P}_n \tag{5a}$$

$$S_{\perp}^{\mp} = \sum_{n=0}^{N} s_{\perp n}^{\mp} \bar{P}_n \tag{5b}$$

where

$$s_{\parallel n}^- = \int_{-1}^{0} \left(\frac{2n+1}{2} \right) \rho^2 P_n(\rho)\, d\rho; \qquad s_{\parallel n}^+ = \int_{0}^{1} \left(\frac{2n+1}{2} \right) \rho^2 P_n(\rho)\, d\rho \tag{5c}$$

and

$$s_{\perp n}^- = \int_{-1}^{0} \left(\frac{2n+1}{4} \right) (1-\rho^2) P_n(\rho)\, d\rho; \qquad s_{\perp n}^+ = \int_{0}^{1} (2n+1,4)(1-\rho^2) P_n(\rho)\, d\rho. \tag{5d}$$

These hemisphere expansion coefficients can be readily evaluated by (analytical) integration using known Legendre expressions $P_n(x)$.

Employing an expansion for the Legendre function $P_n(\rho)$ adapted from eqn (2.5.13) of Edmonds,[33] and carrying out the appropriate hemispheric integrations (ρ from -1 to 0 and from 0 to $+1$, as required), one obtains the desired expansion coefficients $s_{\parallel n}^{\mp}$ and $s_{\perp n}^{\mp}$ explicitly, in terms of simple series. For odd n, we find:

$$s_{\parallel n}^{\mp} = \mp \sum_{m=0}^{(n-1)/2} \left(\frac{(-)^m (2n-2m)!(2n+1)}{2^{n+1} m!(n-m)!(n-2m)!(n+3-2m)} \right) \tag{6a}$$

$$s_{\perp n}^{\mp} = \mp \sum_{m=0}^{(n-1)/2} \left(\frac{(-)^m (2n-2m)!(2n+1)}{2^{n+1} m!(n-m)!(n-2m)!(n+3-2m)(n+1-2m)} \right). \tag{6b}$$

(Thus, for odd n, $s_{\parallel n}^+ = -s_{\parallel n}^-$ and $s_{\perp n}^+ = -s_{\perp n}^-$).

For even n, the upper limit of the summations in eqn (6) is $n/2$, and all s_n coefficients are zero beyond $n = 2$. Explicit s_n coefficients for odd and even n are listed in table 1, for $0 \leqslant n \leqslant 6$.

Truncating the series at $n = 3$ yields the following explicit expressions for the hemispheric signals:

$$S_{\parallel}^{\mp} = \tfrac{1}{6} \mp \tfrac{3}{8} \bar{P}_1 + \tfrac{1}{3} \bar{P}_2 \mp \tfrac{7}{48} \bar{P}_3, \tag{7a}$$

$$S_{\perp}^{\mp} = \tfrac{1}{6} \mp \tfrac{3}{16} \bar{P}_1 - \tfrac{1}{6} \bar{P}_2 \pm \tfrac{7}{24} \bar{P}_3. \tag{7b}$$

Table 1. Hemispheric expansion coefficients $s_n{}^a$

n	$6s_{\|n}^-$	$6s_{\|n}^+$	$6s_{\perp n}^-$	$6s_{\perp n}^+$
0	1	1	1	1
1	$-\frac{9}{4}$	$\frac{9}{4}$	$-\frac{9}{8}$	$\frac{9}{8}$
2	2	2	-1	-1
3	$-\frac{7}{8}$	$\frac{7}{8}$	$\frac{7}{4}$	$-\frac{7}{4}$
4	0	0	0	0
5	$\frac{11}{64}$	$-\frac{11}{64}$	$-\frac{143}{384}$	$\frac{143}{384}$
6	0	0	0	0

^{a} Expansion coefficients, eqn (5), for signal in the indicated hemisphere $(-z, +z)$ for $\|$ and $\perp$ polarization of laser (see text). Thus:

$$S_\|^\mp = \sum_n s_{\|n}^\mp \bar{P}_n \,;\, \kappa_\| = S_\|^- / S_\|^+ \quad \text{and} \quad S_\perp^\mp = \sum_n s_{\perp n}^\mp \bar{P}_n \,;\, \kappa_\perp = S_\perp^- / S_\perp^+.$$

Note that

$$(S_\|^- + 2S_\perp^-) + (S_\|^+ + 2S_\perp^+) = 1. \tag{8}$$

Utilizing eqn (7), we obtain the so-called 'three-moment' approximation(s) for $\kappa_\|$, $\kappa_\perp$:

$$\kappa_\| = (1 - \tfrac{9}{4}\bar{P}_1 + 2\bar{P}_2 - \tfrac{7}{8}\bar{P}_3)/(1 + \tfrac{9}{4}\bar{P}_1 + 2\bar{P}_2 + \tfrac{7}{8}\bar{P}_3) \tag{9a}$$

$$\kappa_\perp = (1 - \tfrac{9}{8}\bar{P}_1 - \bar{P}_2 + \tfrac{7}{4}\bar{P}_3)/(1 + \tfrac{9}{8}\bar{P}_1 - \bar{P}_2 - \tfrac{7}{4}\bar{P}_3). \tag{9b}$$

Also utilizing eqn (7), we obtain a simple relation that yields the alignment $\bar{P}_2$ directly. We define R as the ratio of the total signal (both hemispheres) $\|$ *vs.* $\perp$:

$$R \equiv (S_\|^- + S_\|^+)/(S_\perp^- + S_\perp^+). \tag{10}$$

Using eqn (7), we find that

$$R = (1 + 2\bar{P}_2)/(1 - \bar{P}_2). \tag{11a}$$

Thus

$$\bar{P}_2 = (R-1)/(R+2) \tag{11b}$$

independent of $\kappa_\|$, $\kappa_\perp$. Combining eqn (9) and (10), we obtain explicit equations for $\bar{P}_1$, $\bar{P}_2$ and $\bar{P}_3$ from the observables $\kappa_\|$, $\kappa_\perp$ and R. [$\bar{P}_2$ from eqn (11b).]

$$\bar{P}_1 = \frac{16}{15}\left(\frac{R}{R+2}\right)\left[\left(\frac{1-\kappa_\|}{1+\kappa_\|}\right) + \frac{1}{2R}\left(\frac{1-\kappa_\perp}{1+\kappa_\perp}\right)\right] \tag{12a}$$

$$\bar{P}_3 = \frac{24}{35}\left(\frac{R}{R+2}\right)\left[\left(\frac{1-\kappa_\|}{1+\kappa_\|}\right) - \frac{2}{R}\left(\frac{1-\kappa_\perp}{1+\kappa_\perp}\right)\right]. \tag{12b}$$

[Note that $R/(R+2) = \tfrac{1}{3}(1 + 2\bar{P}_2)$, from eqn (11).]

Next, we consider a few special cases, approximations to the above treatment.

(1) $\bar{P}_2 = \bar{P}_3 = 0$ and $R = 1$, so

$$\frac{1-\kappa_\|}{1+\kappa_\|} = 2\left(\frac{1-\kappa_\perp}{1+\kappa_\perp}\right) \tag{13}$$

and

$$\bar{P}_1 = \frac{4}{9}\left(\frac{1-\kappa_\|}{1+\kappa_\|}\right) = \frac{8}{9}\left(\frac{1-\kappa_\perp}{1+\kappa_\perp}\right) \tag{14}$$

Eqn (14) is termed the 'one-moment approximation.'

(2) $\bar{P}_3 = 0$ and $R \neq 1$. Assume no measurement of R, so the evaluations of $\bar{P}_1$ and $\bar{P}_2$ must come from $\kappa_\parallel, \kappa_\perp$ only. From eqn (9) with $\bar{P}_3$ set at 0, we obtain explicit formulae for $\bar{P}_1$ and $\bar{P}_2$:

$$\bar{P}_1 = \frac{2}{3} \frac{(1-\kappa_\parallel)(1-\kappa_\perp)}{(1-\kappa_\parallel \kappa_\perp)} \tag{15a}$$

$$\bar{P}_2 = \frac{1}{4} \frac{[1-3(\kappa_\perp - \kappa_\parallel) - \kappa_\parallel \kappa_\perp]}{(1-\kappa_\parallel \kappa_\perp)}. \tag{15b}$$

Eqn (15) represents the 'two-moment approximation.' It will be seen in Sec. V that this approximation is useful, in the absence of further information beyond $\kappa_\parallel$ and $\kappa_\perp$.

(3) The next approximation is to assume $\bar{P}_2 = 0$ ($R = 1$), in the absence of direct measurements of R, and to use the three-moment approximation; *i.e.* eqn (12). Thus,

$$\bar{P}_1 = \frac{16}{45}\left[\left(\frac{1-\kappa_\parallel}{1+\kappa_\parallel}\right) + \frac{1}{2}\left(\frac{1-\kappa_\perp}{1+\kappa_\perp}\right)\right] \tag{16a}$$

$$\bar{P}_3 = \frac{8}{35}\left[\left(\frac{1-\kappa_\parallel}{1+\kappa_\parallel}\right) - 2\left(\frac{1-\kappa_\perp}{1+\kappa_\perp}\right)\right]. \tag{16b}$$

This approximation is termed '3-moment, with $\bar{P}_2 = 0$.' In section 5, we shall test the applicability of these various approximations to realistic examples.

3. Theoretical Calculations of $\kappa_s = , \kappa_\perp$

Next, we consider the role played by the Legendre moments in determining the observables $\kappa_\parallel, \kappa_\perp$. table 2 presents theoretical calculations of the κ values according to eqn (1) for six experimentally important[12,19] $|JKM_J\rangle$ parent states in the strong-field (spin-decoupled) and weak-field limits. The original calculations[16] of the $P(\rho)$ were carried out using a number of approaches to the hyperfine coupling problem. The hyperfine calculations were based on considerations of the nuclear spin of the iodine and of the three hydrogen nuclei and the coupling of each to the rotational angular momentum. In one of these, a sudden approximation was used [somewhat similar to the treatment of ref. (17)], assuming a sharp discontinuity in the field strength of the exit of the strong-field region. The resulting 'weak-field' $P(\rho)$ exhibits[16] a rapid oscillatory time

Table 2. Theoretical calculations of $\kappa_\parallel, \kappa_\perp$ for selected $|JKM_J\rangle$ parent states of CH_3I[a]

parent state $|JKM_J\rangle$	parallel			perpendicular		
	strong field (decoupled)	weak field[b]		strong field (decoupled)	weak field[b]	
		sudden	adiabatic		sudden	adiabatic
$|222\rangle$	0.003	0.285	0.266	0.067	0.528	0.541
$|111\rangle$	0.032	0.467	0.649	0.231	0.680	0.798
$|212\rangle$	0.067	0.528	0.470	0.293	0.699	0.744
$|313\rangle$	0.099	0.508	0.465	0.340	0.683	0.758
$|211\rangle$	0.293	0.700	0.836	2.015[c]	0.961	0.917
$|312\rangle$	0.293	0.550	0.626	1.753[c]	0.894	0.833

[a] Entries are κ values calculated for the indicated cases. [b] 'weak field' implies that $E \leqslant 1\ V\ cm^{-1}$ in the region of the orientation field probed by the laser. [c] Surprisingly, these entries are greater than unity, despite the fact that $\bar{P}_1 > 0$ (*i.e.* 'normal' direc of orientation). This is due to the $\sin^2\theta$ factor in the $\perp$-polarization probing by the laser.

Determination of Orientation and Alignment

Table 3. $\bar{P}_1$ and $\bar{P}_2$ for selected $|JKM_J\rangle$ parent states: adiabatic *vs.* sudden approximations[a]

	Set 1[a]			
	$\bar{P}_1$		$\bar{P}_2$	
parent state $|JKM_J\rangle$	A_1	S_1	A_1	S_1
$|222\rangle$	0.283 1	0.294 3	0.041 95	0.070 62
$|111\rangle$	0.107 1	0.185 7	0.035 71	0.022 16
$|212\rangle$	0.148 1	0.147 1	−0.015 87	−0.035 31
$|211\rangle$	0.059 70	0.735 7	0.046 48	0.017 65
$|312\rangle$	0.085 99	0.099 57	−0.012 14	0.000 00
	Set 2[b]			
	$\bar{P}_1$		$\bar{P}_2$	
	A_2	S_2	A_2	S_2
$|222\rangle$	0.273 3	0.272 0	0.040 0	0.056 14
$|111\rangle$	0.098 02	0.166 6	0.018 84	0.016 44
$|212\rangle$	.0.148 8	0.136 0	−0.018 74	−0.028 07
$|211\rangle$	0.042 00	0.067 90	0.044 70	0.013 11
$|312\rangle$	0.095 10	0.091 90	−0.011 09	−0.046 52

[a] Set 1: A_1 and S_1 denote adiabatic and sudden approximations, respectively, taking only I coupling into account. [b] Set 2: A_2 and S_2 denote adiabatic and sudden approximations, but now taking I and H couplings into account.

dependence, with an average asymptotic form expressible in terms of an expansion in ρ. [From the resulting $P(\rho)$, the κ values are calculated *via* eqn (1).]

In the other approach, the adiabatic approximation was used. Here it is assumed that there is a gradual rather than a sudden transition in field strength between the strong- and weak-field regions, *i.e.* the hexapole and the orientation field. Thus there is no time-dependence of the weak-field $P(\rho)$. The resulting orientational distribution function is also expressed explicitly in ρ and then the κ values are calculated as for the sudden approximation. The κ values appear in table 2; it is obvious that the disorientation effect of the nuclear spins (mainly due to that of the I) is severe, and that it should be possible to distinguish between the strong-field and the two weak-field approximations from κ measurements. Table 3 lists the theoretically calculated values of $\bar{P}_1$ and $\bar{P}_2$ for five selected $|JKM_J\rangle$ parent states.

Fig. 1 shows a graphic example of the loss in orientation due to the hyperfine recoupling problem. The strongly asymmetric $P(\rho)$ in the strong field (decoupled) limit (upper panel) is compared with the much less asymmetric $P(\rho)$ for the zero-field, *i.e.* the fully coupled adiabatic limit (lower panel).

4. Orientation and Alignment of Symmetric-top Molecules

In the strong-field limit in which the $|JKM_J\rangle$ representation is appropriate, expansions for $P(\rho)$ have been presented[23] for all $|JKM_J\rangle$ states for $J \leq 4$. From these, one can evaluate the Legendre moments $\bar{P}_1$, $\bar{P}_2$ *etc.* (Of course, $\bar{P}_1$ is simply $KM_J/(J^2+J) = \langle\cos\theta\rangle$,[3,11] for the symmetric-top). Table 4 lists these moments for all the symmetric-top states $|JKM_J\rangle$ for which $J \leq 3$.

Table 4. Legendre moments of $P(\rho)$ for symmetric tops (strong field, *i.e.* decoupled limit)

state $\|JKM_J\rangle$	Legendre moments							
	$\bar{P}_0$	$\bar{P}_1$	$\bar{P}_2$	$\bar{P}_3$	$\bar{P}_4$	$\bar{P}_5$	$\bar{P}_6$	$\bar{P}_7$ etc.
$\|111\rangle$	1	$\frac{1}{2}$	$\frac{1}{10}$	0	0	0	0	0
$\|222\rangle$	1	$\frac{2}{3}$	$\frac{2}{7}$	$\frac{1}{14}$	$\frac{1}{126}$	0	0	0
$\|221\rangle$	1	$\frac{1}{3}$	$-\frac{1}{7}$	$-\frac{1}{7}$	$-\frac{2}{63}$	0	0	0
$\|211\rangle$	1	$\frac{1}{6}$	$\frac{1}{14}$	$\frac{2}{7}$	$\frac{8}{63}$	0	0	0
$\|133\rangle$	1	$\frac{3}{4}$	$\frac{5}{12}$	$\frac{1}{6}$	$\frac{1}{22}$	$\frac{1}{132}$	$\frac{1}{1715}$	0
$\|332\rangle$	1	$\frac{1}{2}$	0	$-\frac{1}{6}$	$-\frac{7}{66}$	$-\frac{7}{33}$	$-\frac{1}{286}$	0
$\|331\rangle$	1	$\frac{1}{4}$	$-\frac{1}{4}$	$-\frac{1}{6}$	$\frac{1}{66}$	$\frac{5}{132}$	$\frac{5}{572}$	0
$\|322\rangle$	1	$\frac{1}{3}$	0	$\frac{1}{6}$	$\frac{49}{198}$	$\frac{4}{33}$	$\frac{3}{143}$	0
$\|321\rangle$	1	$\frac{1}{6}$	0	$\frac{1}{6}$	$-\frac{7}{198}$	$-\frac{5}{33}$	$-\frac{15}{286}$	0
$\|311\rangle$	1	$\frac{1}{12}$	$\frac{3}{20}$	$\frac{1}{6}$	$\frac{1}{198}$	$\frac{25}{132}$	$\frac{75}{572}$	0

In the interpretation of reactive asymmetry experiments with oriented symmetric-top molecules, one must take cognizance of the possible alignment, as well as orientation, of the (state-selected reagent) molecules. Then one will want to consider the possibility of both positive and negative alignments ('end-on' *vs.* 'broadside'), even with the same sign of the orientation.

Fig. 3 shows three examples of alignments of a molecular framework: vertical, horizontal and magic-angle, listing values of $\bar{P}_1$ and $\bar{P}_2$. At the magic angle, for which $\langle\cos^2\theta\rangle = \frac{1}{3}$, one has $\bar{P}_2 = 0$, but of course there are two distinct (opposite) orientations, *i.e.* $\bar{P}_1 = \pm 1/\sqrt{3}$. Thus, the two Legendre moments $\bar{P}_1$ and $\bar{P}_2$ appear to provide quite independent 'steric' information about the ensemble of molecules under consideration. However, upon closer examination, one notes a tendency for a correlation between them as the classical limit is approached. Note that in the limit of 'tight' precession, *i.e.* $K/(J^2+J)^{1/2} \to 1$, there is indeed a trivial relationship between the moments: $\bar{P}_2 = \frac{3}{2}\bar{P}_1^2 - \frac{1}{2}$. (In general, $\bar{P}_2 \geq \frac{3}{2}\bar{P}_1^2 - \frac{1}{2}$.)

Fig. 4 illustrates the relationship between $\bar{P}_2$ and $\bar{P}_1$ for each of the 20 unique states of interest up to $\|JKM_J\rangle = \|444\rangle$. The tight-precession 'limiting parabola' (above) is also plotted. In general, the greater the orientation $\bar{P}_1$, the greater the alignment $\bar{P}_2$.
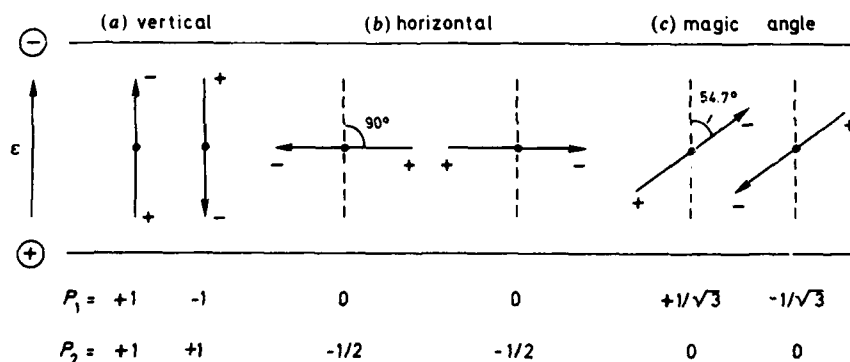

Fig. 3. Three special cases of alignment of classical electric dipoles within a homogeneous electric field $\mathcal{E}$ pointing up, toward the $+z$ direction. (a) Vertical alignment, 'up' *vs.* 'down'; (b) horizontal alignment, 'left' *vs.* 'right'; (c) 'magic angle,' *i.e.* precessing in a cone whose angle of generation (shown) is 54.7°, but with 'up' *vs.* 'down' orientation. Listed at bottom are the values of P_1 and P_2 for each arrangement.
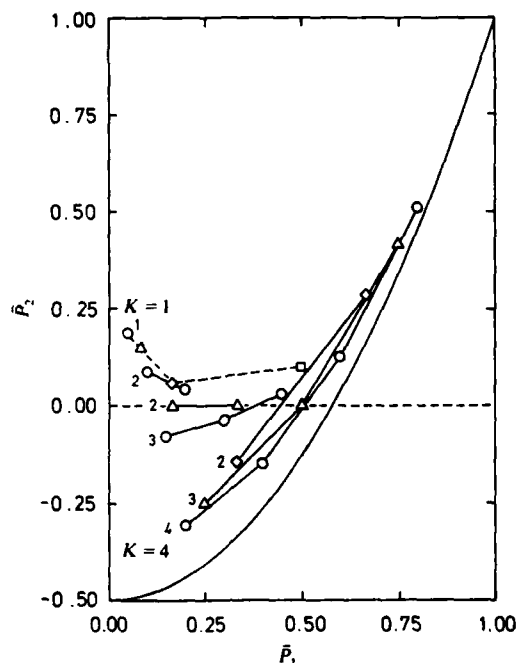
Fig. 4. Plot of $\bar{P}_2$ vs. $\bar{P}_1$ for $|JKM_J\rangle$ states of symmetric-top molecules in strong-field limit (values from table 4), for J states $(1 \leqslant J \leqslant 4)$: $\square$, $J = 1$; $\diamondsuit$, $J = 2$; $\triangle$, $J = 3$; $\bigcirc$, $J = 4$; K states $(1 \leqslant K \leqslant J \leqslant 4)$ as indicated. Individual M_J states not denoted; however, they are easily identified as follows: $M_J = 1$ has smallest $\bar{P}_1$ (leftmost), $M_J = 2$ next, ..., $M_J = 4$ greatest $\bar{P}_1$ (in each sequence, connected by solid lines). For $K = 1$ points, $M_J = 1$; dashed segments connect $J = 4, 3, 2, 1$ respectively. Solid curve: 'limiting parabola' $P_2 = \frac{3}{2}P_1^2 - \frac{1}{2}$. $\bar{P}_1$ is readily calculated *via* $KM_J/(J^2 + J)$; $\bar{P}_2$ from $P(\rho)$ expansions in ref. (23). An explicit formula for $\bar{P}_2$ is given in ref. 6(b):

$$\bar{P}_2 = \frac{[3M_J^2 - J(J+1)] \cdot [3K^2 - J(J+1)]}{[(2J+1)(2J-1)J(J+1)]}.$$

This is, in a sense, a cautionary note, since both orientation and alignment affect reactivity, and in different ways, and thus the attribution of an observed effect to orientation only is simplistic. [This problem has been addressed, in part, in earlier papers, *e.g.* ref. (7), (14) and (15), using theoretical moments as input.]

5. Inversion to the Legendre Moments from $\kappa_\parallel$, $\kappa_\perp$ and R

Based on the results presented in section 4, it is evident that orientation distributions $P(\rho)$ for a beam of orientated CH_3I molecules (and the observable photofragment asymmetry factors $\kappa_\parallel$, $\kappa_\perp$) are strongly dependent upon both the $\mathscr{E}$-field in the photodissociation (and/or reaction) zone and the details of the passage from the strong- to the weak-field regions. This has been confirmed by experiments.[18,19,21] Thus it will be important in the future to determine directly the actual orientation and alignment of the ensemble of molecules under study without 'theoretical prejudice.' The present inversion scheme, going from $\kappa_\parallel$, $\kappa_\perp$ and R to the moments $\bar{P}_1$, $\bar{P}_2$ and $\bar{P}_3$ of the distribution function $P(\rho)$, will now be illustrated with examples, some from hypothetical

pure parent-state beams, others for actual ensembles from oriented molecule beam experiments.

For the first example, we consider the performance of the one-moment and two-moment approximations, using eqn (14) and (15), respectively, for two realistic calculated cases. For this, we use the 'full' hyperfine coupling computations[16] of $P(\rho)$ for different parent $|JKM_J\rangle$ states (i.e. nuclear spin of the I and the spins of the H nuclei, coupled with the rotational angular momentum) in the two limiting weak-field cases: (a) sudden and (b) adiabatic approximation.

Table 2 has listed these calculated κ values for the experimentally relevant parent rotational states, which here form the simulated, error-free, data base for an inversion exercise.

Table 5 presents $\bar{P}_1$ values, the results of the two 'one-moment' approximations of eqn (14) and the 'two-moment' approximation of eqn (15), compared with the exact $\bar{P}_1$ values from table 3, for the fully coupled sudden and adiabatic cases. Of the two one-moment approximations, the one employing $\kappa_\perp$ data is less affected by the neglect of $\bar{P}_2$ than the one using $\kappa_\parallel$ values. In practice, however, $\kappa_\parallel$ is much more accurately measured experimentally since, for the $\kappa_\parallel$ configuration, there are fully resolved two peaks in the TOF spectrum (see fig. 2); thus, less reliable experimental information comes from $\kappa_\perp$.

The goodness of the one-moment approximation of eqn (14) can also be portrayed graphically. Fig. 5 is a plot of the theoretically calculated values of $\kappa_\perp$ vs. $\kappa_\parallel$ for the state-selected $|JKM_J\rangle$ parent states of table 5 (i.e. sudden and adiabatic weak-field approximations, the fully coupled case corresponding to set 2 of table 3). Also plotted in the fig. 5 is the implicit relation between $\kappa_\perp$ and $\kappa_\parallel$ demanded by the one-moment approximation, eqn (14). Deviations are significant, but the correlation is quite evident. (This is not the case in the strong-field, decoupled limit.)

Obviously, more reliable information on the moments of the orientational distribution function will require accurate experimental measurements of $\kappa_\parallel$, R and $\kappa_\perp$.

We shall now apply the various levels of the inversion approximations to the published experimental data, on differently prepared orientated molecule beams, usually parent states $|JKM_J\rangle = |222\rangle$, $|111\rangle$, as well as the control experiments on the unorientated but JK-selected beams, identified as $|22\rangle$ or $|11\rangle$, measured under rather weak-field conditions (typically 30 V cm^{-1}, but by no means in the 'zero-field' limit). Thus, we hope to learn how these and more accurate future experiments can be best interpreted in terms of low-order Legendre moments of the $P(\rho)$.

Table 6 summarizes all the available results,[19,21] including a reanalysis of the experimental data of ref. (21), in part to ascertain if more accurate moments could be gleaned

Table 5. $\bar{P}_1$ calculated from $\kappa_\parallel$, $\kappa_\perp$ using one- and two-moment approximations, vs. 'exact' $\bar{P}_1$

parent state $\|JKM_J\rangle$	sudden				adiabatic			
	1-moment, from		2-moment	exact[a]	1-moment, from		2-moment	exact[a]
	$\kappa_\parallel$	$\kappa_\perp$			$\kappa_\parallel$	$\kappa_\perp$		
$\|222\rangle$	0.247	0.275	0.265	0.272	0.258	0.265	0.262	0.273
$\|111\rangle$	0.161	0.169	0.167	0.167	0.095	0.100	0.098	0.098
$\|212\rangle$	0.137	0.157	0.150	0.136	0.160	0.125	0.135	0.149
$\|211\rangle$	0.078	0.018	0.024	0.068	0.040	0.038	0.039	0.042
$\|312\rangle$	0.129	0.050	0.063	0.092	0.102	0.081	0.087	0.095

[a] For the theoretically calculated $P(\rho)$ values taking into account both I and H coupling (from table 3).
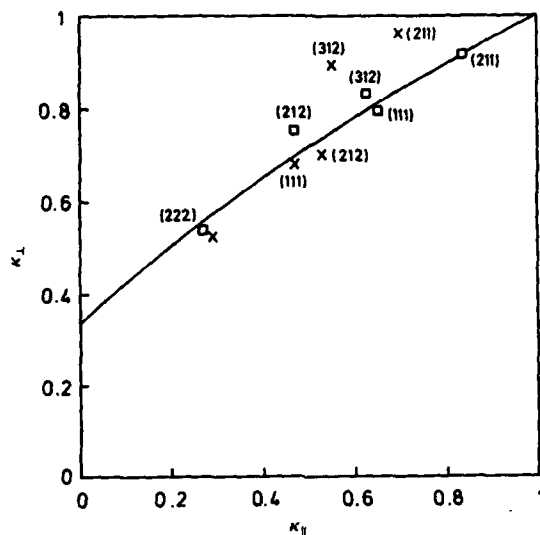
Fig. 5. Test of one-moment approximation, based on calculated results for CH_3I, taking into account the hyperfine coupling [ref. (16)], in the weak-field limit, in both the sudden and the adiabatic approximations. The parent $|JKM_J\rangle$ states are indicated. The coordinates of each point are $\kappa_{\parallel}, \kappa_{\perp}$. The solid curve is the relationship between $\kappa_{\perp}$ and $\kappa_{\parallel}$ implicit in the one-moment approximation, eqn (14);

$$i.e. \left(\frac{1-\kappa_{\perp}}{1+\kappa_{\perp}}\right) = \frac{1}{2}\left(\frac{1-\kappa_{\parallel}}{1+\kappa_{\parallel}}\right)$$

appropriate for the limiting case of $\beta = 2$.

from the data. Each entry (beam no.) is for a separate orientation-photofragmentation experiment. Although there had been some attempt at controlling the experimental conditions[19,21] (such as state-selection purity, correction for the direct beam contribution, electric field strength in the orientation/photofragmention region *etc.*), the experiments thus far have been somewhat crude. However, the results are suggestive of the level of reproducibility and accuracy necessary to obtain a given uncertainty in the derived orientation and alignment moments. Clearly, a major concern in the propagation of error from the measurements ($\kappa_{\parallel}$, R and/or $\kappa_{\perp}$) to the low-order moments. For example, there can be no physical interpretation to a non-zero $\bar{P}_3$ for the $|111\rangle$ parent state, or for a significant alignment $\bar{P}_2$ for the intentionally unorientated $|22'\rangle$ ensemble *etc.* Thus, examination of the tabulated results provides information on the 'leverage' of such measurements with respect to the desired moments.

Table 7 summarizes the most reliable results, for $\bar{P}_1$ and $\bar{P}_2$ only, based on reconsidering the entire body of experiments reported in table 6. Once again, the 'unorientated' molecule beams $|22\rangle$ and $|11\rangle$ are important benchmarks to test how well the inversion procedure works for these presumably known cases, for which $\bar{P}_1$ and $\bar{P}_2$ should be zero.

6. Discussion and Conclusions

Examination of table 7 shows that even the available 'first generation' measurements[19,21] of the asymmetry of the angular distribution of the polarized-laser photofragmentation suffice to demonstrate certain facts about the orientation and alignment of the molecular

Table 6. Analysis of experimental κ results for CH_3I

beam no.	parent state $\|JKM_J\rangle$	$\kappa_\parallel$	$\kappa_\perp$	R	$\bar{P}_1$	$\bar{P}_2$	$\bar{P}_3$	ref. (fig. no.)	comments
1	$\|222\rangle$	0.26	—	—	0.261	—	—	19 (1)	a
2	$\|111\rangle$	0.42	—	—	0.182	—	—	19 (2a)	a
3	$\|212\rangle$	0.37	—	—	0.204	—	—	19 (2b)	a
4	$\|211\rangle+\|312\rangle$	0.53	—	—	0.137	—	—	19 (2c)	a
5a	$\|'222'\rangle^h$	0.35	—	—	0.214	—	—	21 (3)	a
		0.35	0.59	—	0.224	0.023	—	21 (3)	b
		0.35	0.59	(1.0)	0.217	0	−0.006	21 (3)	c
6a	$\|'111'\rangle^h$	0.53	—	—	0.137	—	—	21 (4)	a
		0.53	0.61	—	0.181	0.161	—	21 (4)	b
		0.53	0.61	(1.0)	0.152	0	−0.041	21 (4)	c
6a	$\|111\rangle^i$	0.49	—	—	0.152	—	—	21 (4)	a
		0.49	0.57	—	0.203	0.167	—	21 (4)	b
		0.49	0.57	(1.0)	0.167	0	−0.047	21 (4)	c
7	$\|212\rangle$	0.37	—	—	0.204	—	—	21 (5)	a, g
		0.37	0.80	—	0.119	−0.208	—	21 (5)	b, g
		0.37	0.80	(1.0)	0.183	0	0.054	21 (5)	c, g
8	$\|211\rangle+\|312\rangle$	0.53	—	—	0.137	—	—	21 (5)	a, g
		0.53	0.81	—	0.104	−0.118	—	21 (5)	b, g
		0.53	0.81	(1.0)	0.128	0	0.022	21 (5)	c, g
6b	$\|11\rangle^j$	0.96	—	—	0.009	—	—	21 (4)	a, f
		0.96	0.90	—	0.020	[0.581]	—	21 (4)	b, e, f
		0.96	0.90	(0.1)	0.017	0	−0.019	21 (4)	c, f
		0.96	0.90	1.03	0.017	0.010	−0.019	21 (4)	d, f
6a	$\|111\rangle^i$	0.58	—	—	0.118	—	—	21 (4)	a, f
		0.58	0.62	—	0.166	[0.023]	—	21 (4)	b, e, f
		0.58	0.62	(1.0)	0.136	0	−0.047	21 (4)	c, f
		0.58	0.62	1.01	0.137	0.003	−0.046	21 (4)	d, f
5b	$\|'22'\rangle^{h,j}$	0.98	—	—	0.005	—	—	21 (3)	a, f
		0.98	1.01	—	−0.013	[−1.956]	—	21 (3)	b, e, f
		0.98	1.01	(1.0)	0.003	0	0.005	21 (3)	c, f
		0.98	1.01	0.83	0.002	−0.060	0.004	21 (3)	d, f
5a	$\|'222'\rangle^h$	0.38	—	—	0.200	—	—	21 (3)	a, f
		0.38	0.61	—	0.210	[0.025]	—	21 (3)	b, e, f
		0.38	0.61	(1.0)	0.203	0	−0.008	21 (3)	c, f
		0.38	0.61	1.06	0.208	0.020	−0.002	21 (3)	d, f

^{a} 1-moment approximation, using $\kappa_\parallel$. ^{b} 2-moment approximation. ^{c} 3-moment approximation, but fixing $\bar{P}_2 = 0$. ^{d} 3-moment approximation, no restriction on $\bar{P}_2$. ^{e} Values in brackets are dubious. ^{f} Data re-analysed (see section 5 and caption of fig. 2; preferred results). ^{g} $\kappa_\parallel$ from ref. (19). ^{h} Data uncorrected for direct beam contribution. ^{i} Data corrected for direct beam contribution. ^{j} Unorientated.

ensembles under observation. Detailed analysis of the 'lineshape', *i.e.* the $S(t)$ TOF curves [such as that carried out in ref. (29) and (30)] is unnecessary for this purpose.

It appears that the first-moment $\bar{P}_1$, *i.e.* the average molecular orientation, can be fairly well determined and, moreover, that the deduced values are in fair accord with the sudden approximation in the weak-field limit. (Distinction between the sudden and the adiabatic is best made on the basis of the $\|111\rangle$ parent state; see entries in tables 2 and 3.) As pointed out already in ref. (19), the experimental κ values clearly show the deleterious influence of the hyperfine coupling effect upon the degree of orientation of CH_3I in weak fields.

Table 7. Summary of best experimental values of $\bar{P}_1$ and $\bar{P}_2$, compared to theoretical calculations (sudden and adiabatic) in the weak-field limit

beam no.	parent state $|JKM_J\rangle$	$\bar{P}_1$ experi-mental[a]	$\bar{P}_1$ sudden	$\bar{P}_1$ adiabatic	$\bar{P}_2$ experi-mental[a]	$\bar{P}_2$ sudden	$\bar{P}_2$ adiabatic
5b	$|22\rangle$	0.00_2	0	0	-0.06	0	0
6b	$|11\rangle$	0.01_7	0	0	0.01	0	0
1	$|222\rangle$	0.26^b	0.27	0.27	—	0.056	0.040
5a	$|\text{'}222\text{'}\rangle$	0.21^c			0.02		
2	$|111\rangle$	0.18^b	0.17	0.098	—	0.016	0.019
6a	$|111\rangle$	0.14^c			0.00_3		
3	$|212\rangle$	0.20^b	0.14	0.15	—	-0.028	-0.019
4	$|211\rangle$	$0.14^{b,d}$	0.07	0.04	—	0.013	0.045
	$|312\rangle$		0.09	0.10		-0.047	-0.011

[a] Values from table 6, rounded to two significant figures. [b] From 1-moment approximation based on tabulated κ_1 [data of ref. (19)]. [c] Values from re-analysed data [ref. (21)]. [d] Admixture of $|211\rangle$ and $|312\rangle$ parent states, but predominantly $|211\rangle$.

The evaluation of the second-moment $\bar{P}_2$, *i.e.* the alignment of the molecules, has not been accomplished reliably in these experiments. The apparent values of $\bar{P}_2 = -0.06$ for the presumably unorientated $|22\rangle$ ensemble suggests that there was an experimental problem in determining the ratio R (which requires special attention regarding the polarizing optics, windows *etc.*, not yet taken into account). Of course, there is virtually no leverage to extract a meaningful $\bar{P}_3$ (*e.g.* note in table 6 the unphysical $\bar{P}_3$, deduced for the $|11\rangle$ state, for which $\bar{P}_3$ should be identically zero).

We return, then, to the main question; namely, can we measure the spatial orientation and alignment of an 'unknown' partially state-selected/orientated ensemble of molecules? The answer is clearly 'yes' for orientation and, very probably (in the second generation of experiments), 'yes' for alignment.

Appendix

In the treatment given in the main body of this paper (section 2), a restriction was imposed on the shape of the photofragment angular distributior, namely, that the β parameter is fixed at 2 (prompt dissociation and parallel-type transition) so that $I(\theta) \propto \cos^2 \theta$ *etc.* For the experiments of ref. (19) and (21) (the data base used here) involving low-J states of CH_3I, this is an excellent approximation. The 'valley' ($\leqslant 5\%$) between the two peaks of the doublet in the well resolved TOF spectra can be accounted for entirely from the known ($=96\%$) degree of polarization of the laser-beam polarizer.[18,19,21] Thus, for these low-J states, there is $\leqslant 1\%$ of any possible '$\perp$' contribution to the transition and, as shown by the real-time experiments of ref. (20), the dissociation is clearly prompt (*i.e.* sub-picosecond). (For thermal ensembles including high J states, this is not the case.)

In general, however,[25] β may assume any value within its allowed range $2 \geqslant \beta \leqslant -1$, and the present analysis needs to be extended to deal with arbitrary values of β. In what follows, we maintain the assumption of prompt dissociation but consider the β to be governed by the admixture of $\perp$ to $\parallel$ components of the transition dipole at the laser wavelength used, as well as the angle between the polarizer axis and the orientation field. We make use of (a rewritten form of) eqn (30) of ref. (23), interpreting β in terms of certain key angles.

The results thus obtained for the observable hemispheric signals $S^{\mp}$ are therefore β-dependent. They are linear combinations of the earlier ($\beta = 2$) ones [see section 2, preceding eqn (1)]. Thus, we now have

$$S_{\parallel}^{\mp}(\beta) = \left(\frac{1+\beta}{3}\right) S_{\parallel}^{\mp} + \left(\frac{2-\beta}{3}\right) S_{\perp}^{\mp} \tag{A1a}$$

and

$$S_{\perp}^{\mp}(\beta) = \left(\frac{4+\beta}{6}\right) S_{\perp}^{\mp} + \left(\frac{2-\beta}{6}\right) S_{\perp}^{\mp}. \tag{A1b}$$

One finds expressions for the hemispheric signals analogous to eqn (7):

$$S_{\parallel}^{\mp}(\beta) = \frac{1}{6} \mp \frac{1}{16}(4+\beta)\bar{P}_1 + \frac{\beta}{6}\bar{P}_2 \mp \frac{7}{48}(\beta-1)\bar{P}_3 \mp \left(\frac{3\beta+16}{78}\right)\bar{P}_5 + \cdots \tag{A2a}$$

$$S_{\perp}^{\mp}(\beta) = \frac{1}{6} \mp \frac{3}{16}\left(\frac{8-\beta}{6}\right)\bar{P}_1 - \frac{\beta}{12}\bar{P}_2 \pm \frac{7}{96}(2+\beta)\bar{P}_3 \mp \left(\frac{16-\frac{3}{2}\beta}{768}\right)\bar{P}_5 + \cdots. \tag{A2b}$$

Truncating at $\bar{P}_4$ leads to expressions for the κ values, analogous to eqn (9):

$$\kappa_{\parallel}(\beta) = \frac{1 - \frac{3}{8}(4+\beta)\bar{P}_1 + \beta\bar{P}_2 - \frac{7}{8}(\beta-1)\bar{P}_3}{1 + \frac{3}{8}(4+\beta)\bar{P}_1 + \beta\bar{P}_2 + \frac{7}{8}(\beta-1)\bar{P}_3} \tag{A3a}$$

$$\kappa_{\perp}(\beta) = \frac{1 - \frac{3}{16}(8-\beta)\bar{P}_1 - \frac{\beta}{2}\bar{P}_2 + \frac{7}{16}(2+\beta)\bar{P}_3}{1 + \frac{3}{16}(8-\beta)\bar{P}_1 - \frac{\beta}{2}\bar{P}_2 - \frac{7}{16}(2+\beta)\bar{P}_3}. \tag{A3b}$$

Analogous to eqn (10), we define the ratio R to be

$$R \equiv [S_{\parallel}^{-}(\beta) + S_{\parallel}^{+}(\beta)]/[S_{\perp}^{-}(\beta) + S_{\perp}^{+}(\beta)]. \tag{A4}$$

With this definition, one can relate R to $\bar{P}_2$ (analogous to eqn (11), but here with a β-dependence):

$$R = \frac{(1 + \beta\bar{P}_2)}{(1 - \frac{1}{2}\beta\bar{P}_2)}. \tag{A5a}$$

Thus,

$$\bar{P}_2 = \frac{(2/\beta)(R-1)}{(R+2)}. \tag{A5b}$$

Next, we evaluate two important ratios:

$$\frac{1 - \kappa_{\parallel}(\beta)}{1 + \kappa_{\parallel}(\beta)} = \frac{\frac{3}{8}(4+\beta)\bar{P}_1 + \frac{7}{8}(\beta-1)\bar{P}_3}{1 + \beta\bar{P}_2} \tag{A6a}$$

$$\frac{1 - \kappa_{\perp}(\beta)}{1 + \kappa_{\perp}(\beta)} = \frac{\frac{3}{16}(8-\beta)\bar{P}_1 - \frac{7}{16}(2+\beta)\bar{P}_3}{1 - (\beta/2)\bar{P}_2}. \tag{A6b}$$

16 *Determination of Orientation and Alignment*

Combining these results with eqn (A3a), one obtains the analogue to eqn (12) for $\bar{P}_1$ and $\bar{P}_3$:

$$\bar{P}_1 = \frac{8}{15}\left(\frac{2+\beta}{\beta}\right)\left(\frac{R}{R+2}\right)\left[\left(\frac{1-\kappa_{\parallel}(\beta)}{1+\kappa_{\parallel}(\beta)}\right) + \frac{2}{R}\left(\frac{\beta-1}{2+\beta}\right)\left(\frac{1-\kappa_{\perp}(\beta)}{1+\kappa_{\perp}(\beta)}\right)\right] \quad (A7a)$$

$$\bar{P}_3 = \frac{8}{35}\left(\frac{8-\beta}{\beta}\right)\left(\frac{R}{R+2}\right)\left[\left(\frac{1-\kappa_{\parallel}(\beta)}{1+\kappa_{\parallel}(\beta)}\right) - \frac{2}{R}\left(\frac{4+\beta}{8-\beta}\right)\left(\frac{1-\kappa_{\perp}(\beta)}{1+\kappa_{\perp}(\beta)}\right)\right]. \quad (A7b)$$

It is readily seen that eqn (A1)–(A7) all reduce properly to the analogous equations in the main body of the text (section 2) in the limiting case of $\beta = 2$ (there assumed).

Note also that, if the laser polarization is rotated from $0°$ ($\parallel$ to z axis) to $90°$ ($\perp$ to z axis), effectively converting $\beta = 2$ to $\beta = -1$ [via eqn (30) of ref. (23)], then eqn (A3a) takes the form

$$\kappa_{\parallel}(\beta = -1) = \frac{1 - \frac{9}{8}\bar{P}_1 - \bar{P}_2 + \frac{7}{4}\bar{P}_3}{1 + \frac{9}{8}\bar{P}_1 - \bar{P}_2 - \frac{7}{4}\bar{P}_3} \quad (A8)$$

which is identical to the right-hand side of eqn (9b) in the text. Thus,

$$\kappa_{\parallel}(\beta = -1) = \kappa_{\perp}(\beta = 2) \quad (A9)$$

as expected. [Eqn (A9) can also be obtained directly from eqn (A3).] However, $\kappa_{\perp}(\beta = -1) \neq \kappa_{\parallel}(\beta = 2)$. The analogy to the (preferred) one-moment approximation of eqn (14) is found, as in the earlier text [preceding eqn (13)], by taking $\bar{P}_2 = \bar{P}3 = 0$, so

$$\frac{1-\kappa_{\parallel}(\beta)}{1+\kappa_{\parallel}(\beta)} = 2\left(\frac{4+\beta}{8-\beta}\right)\left(\frac{1-\kappa_{\perp}(\beta)}{1+\kappa_{\perp}(\beta)}\right). \quad (A10)$$

After a little algebra, one obtains the one-moment approximation:

$$\bar{P}_1 = \frac{8}{3(4+\beta)}\left(\frac{1-\kappa_{\parallel}(\beta)}{1+\kappa_{\parallel}(\beta)}\right) = \frac{16}{3(8-\beta)}\left(\frac{1-\kappa_{\perp}(\beta)}{1+\kappa_{\perp}(\beta)}\right) \quad (A11)$$

which, of course, reduces to eqn (14) for $\beta = 2$.

In conclusion, from a practical viewpoint, if one has independent knowledge that the dissociation is prompt, then it is a relatively simple matter to use the directly measured β value (obtained from unorientated molecule experiments) together with eqn (A7) and (A8) to evaluate the desired Legendre moments $\bar{P}_1$, $\bar{P}_2$ and $\bar{P}_3$. At the very least, the one-moment approximation, eqn (A11), can be used to estimate the first moment with essentially the same reliability as the special case (for $\beta = 2$) in the text, via eqn (14).

Note that more experimental information than simply $\kappa_{\parallel}$, $\kappa_{\perp}$ and R could be readily available, since it is easy to carry out experiments varying the laser polarization angle. It has been pointed out by Gandhi[18] that $S(t)$ curves obtained with laser polarization set at the magic angle eliminate the influence of β and are governed entirely by the shape of $P(\rho)$ and the translational recoil energy distribution. Experiments that measure $S(t)$ TOF curves as a function of the laser polarization angle [see eqn (28a) of ref. (23)] can, in principle, yield the full $P(\rho)$, not simply its first few Legendre moments.

References

1 R. D. Levine and R. B. Bernstein, *Molecular Reaction Dynamics and Chemical Reactivity* (Oxford University Press, New York, 1987), and references cited therein.
2 R. B. Bernstein, D. R. Herschbach and R. D. Levine, *J. Phys. Chem.*, 1987, **91**, 5365 and references cited therein.
3 K. H. Kramer and R. B. Bernstein, *J. Chem. Phys.*, 1965, **42**, 767.
4 E. M. Jones and P. R. Brooks, *J. Chem. Phys.*, 1970, **53**, 55.
5 P. R. Brooks, *Science*, 1976, **193**, 11.

6 (a) S. Stolte, *Ber. Bunsenges. Phys. Chem.*, 1982, **86**, 413; (b) S. Stolte, in *Atomic and Molecular Beam Methods*, ed. G. Scoles (Oxford University Press, New York, 1988), Chap. 25, p. 631.

7 D. H. Parker, H. Jalink and S. Stolte, *J. Phys. Chem.*, 1987, **91**, 5427, and references cited therein.

8 S. Kaesdorf, G. Schönhense and U. Heinzmann, *Phys. Rev. Lett.*, 1985, **54**, 885.

9 E. W. Kuipers, M. B. Tenner, A. W. Kleyn and S. Stolte, *Nature (London)*, 1988, **334**, 420.

10 L. V. Novakoski and G. M. McClelland, *Phys. Rev. Lett.*, 1987, **59**, 1259.

11 R. B. Bernstein, *Chemical Dynamics* via *Molecular Beam and Laser Techniques* (Oxford University Press, New York, 1982), chap. 3.

12 (a) S. R. Gandhi, T. J. Curtiss, Q-X. Xu, S. E. Choi and R. B. Bernstein, *Chem. Phys. Lett.*, 1986, **132**, 6; (b) S. R. Gandhi, Q-X. Xu, T. J. Curtiss and R. B. Bernstein, *J. Phys. Chem.*, 1987, **91**, 5437.

13 Q-X. Xu, K-H. Jung and R. B. Bernstein, *J. Chem. Phys.*, 1988, **89**, 2099.

14 S. Stolte, K. K. Chakravorty, R. B. Bernstein and D. H. Parker, *Chem. Phys.*, 1982, **71**, 353.

15 D. van den Ende and S. Stolte, *Chem. Phys.*, 1984, **89**, 121.

16 S. E. Choi, *Ph.D. Dissertation* (University of California, Los Angeles, 1987).

17 R. Altkorn, R. N. Zare and C. H. Greene, *Mol. Phys.*, 1985, **55**, 1.

18 S. R. Gandhi, *Dissertation* (Univ. of California, Los Angeles, 1988).

19 S. R. Gandhi, T. J. Curtiss and R. B. Bernstein, *Phys. Rev. Lett.*, 1987, **59**, 2951.

20 J. L. Knee, L. R. Khundkar and A. H. Zewail, *J. Chem. Phys.*, 1985, **83**, 1966.

21 S. R. Gandhi and R. B. Bernstein, *Z. Phys. D* (Otto Stern Centennial Issue), 1988, in press.

22 S. E. Choi and R. B. Bernstein, *J. Chem. Phys.*, 1985, **83**, 4463.

23 S. E. Choi and R. B. Bernstein, *J. Chem. Phys.*, 1986, **85**, 150.

24 J. P. Simons, *J. Phys. Chem.*, 1987, **91**, 5378.

25 *Faraday Discuss. Chem. Soc.*, 1986, **82**.

26 S. J. Riley and K. Wilson, *Discuss. Faraday Soc.*, 1972, **53**, 132.

27 S. Yang and R. Bersohn, *J. Chem. Phys.*, 1974, **61**, 4400.

28 M. D. Barry and P. A. Gorry, *Mol. Phys.*, 1984, **52**, 461.

29 G. E. Hall, N. Sivakumar, R. Ogorzalek, G. Chawla, H-P. Haerri, P. L. Houston, I. Burak and J. W. Hepburn, *Faraday Discuss. Chem. Soc.*, 1986, **82**, 13.

30 P. L. Houston, *J. Phys. Chem.*, 1987, **91**, 5378; R. Ogorzalek Loo, G. E. Hall, H-P. Haerri and P. L. Houston, *J. Phys. Chem.*, 1988, **92**, 5.

31 (a) T. A. Spiglanin and D. W. Chandler, *Chem. Phys. Lett.*, 1987, **141**, 428; (b) D. W. Chandler and P. L. Houston, *J. Chem. Phys.*, 1987, **87**, 1445.

32 J. F. Black and I. Powis, *Chem. Phys. Lett.*, 1988, **148**, 479.

33 A. R. Edmonds, *Angular Momentum in Quantum Mechanics* (Princeton University Press, 1957), see also R. N. Zare, *Angular Momentum* (Wiley-Interscience, New York, 1988), chap. 3 and 6.

Products' Angular Distribution for Stereoselective Reactions

Simple Optical and Kinematic Considerations

I. Schechter and R. D. Levine*

*The Fritz Haber Research Center for Molecular Dynamics,
The Hebrew University, Jerusalem 91904, Israel*

The angular distribution of reactive (and also of non-reactive) scattering
has been shown to provide useful insights into the steric requirements of
chemical reactions. In a simple optical model, the differential scattering
cross-section, $d^2\sigma_R/d^2w$, and the differential orientation-dependent cross-
section $d\sigma_R/d \cos \gamma$ are both derived from a common opacity function. The
angle-dependent line-of-centre model has been used to compute both cross-
sections. For the $K + CH_3I$ reaction where the barrier, according to Bernstein,
is a linear function of the cosine of the approach angle, the two differential
cross-sections are closely related. Within the angle-dependent line-of-centres
model one can also re-examine the optical mode analysis of the non-reactive
scattering. This suggests a reinterpretation of the variable 'the potential at
the distance of closest approach' as 'the energy along the line of centres'.
With this interpretation, the systematics in the opacity functions, determined
from the observed non-reactive scattering, can be simply accounted for. In
particular, for several reactions [*e.g.* $K + CH_3Br$, $K + (CH_3)_3CBr$] the opacity
analysis provides evidence for a 'cone of non-reaction' of a primarily
geometrical nature reflecting presumably the steric hindrance of the organic
group.

In the analysis of the reactivity of orientated molecules it has been shown
to be necessary to distinguish carefully between the theoretical steric require-
ments, defined in the molecular frame and the operational orientation defined
in the laboratory frame. This distinction is readily implemented using a
kinematic model. It is thereby found that for $K +$ oriented CH_3I the reactivity
is strongly dependent on the experimental orientation for backwards scatter-
ing. This dependence diminishes for less backwards scattering and is practi-
cally unobservable for sideways scattering. This loss in selectivity is,
however, of purely kinematic origin: for higher impact parameters the
relation between a given experimental orientation angle and the theoretical
angle of attack is one-too-many. The kinematic model used incorporates
an impulsive release of the exoergicity *á là* the DIPR model. The impulse
is not directed along the old bond. A very definite polarization of the KI
angular momentum in the direction perpendicular to the plane of reaction
is noted.

Much recent effort[1-24] has led to a good understanding of the concept of cone of
acceptance for activated chemical reactions in the thermal and hyperthermal regimes:
the steric requirement of the reaction is essentially determined by the variation of the
height of the barrier to reaction with the orientation of the reagents *at the barrier*. More
work is required for activationless reactions such as[25-27] between ions and polar reagents.
It has, however, been proposed[24] that their steric requirements are due to the orientation-
dependence of the barrier in the 'effective potential' which is the sum of the anisotropic
long-range potential and the spherically symmetric centrifugal barrier. We mention as
an aside that reactions between neutral molecules are seldom activationless. Examination
of polar plots[28] of the potential-energy surfaces for such reactions show a rather sudden
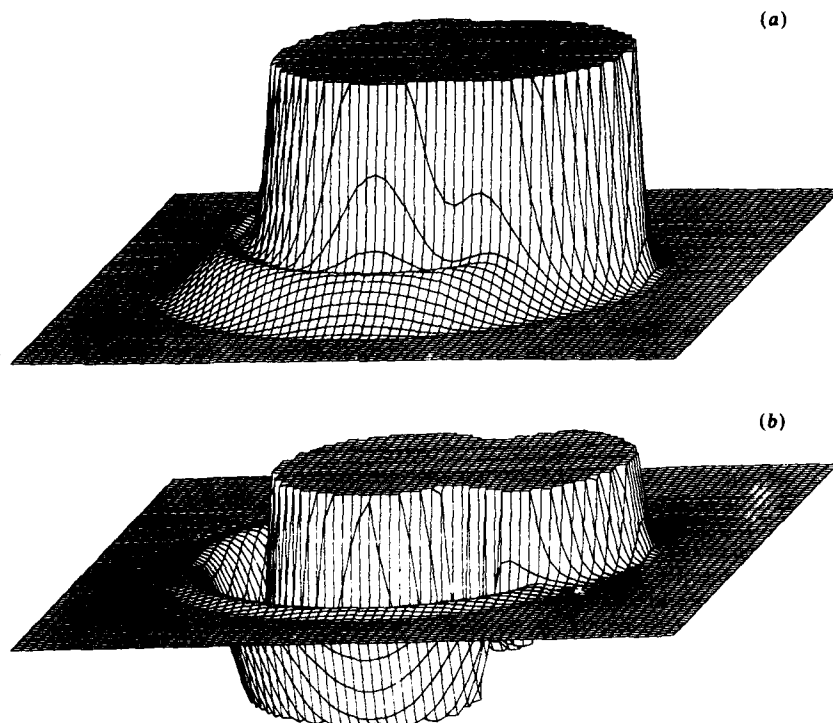
Fig. 1. Polar representations of the potential-energy surfaces for $K + CH_3I$ from ref. (21). The square grid is 14.4×14.4 Å and the vertical scale for the potential spans 1.8 eV. The asymptotic plateau is at zero. (a) The $CH_3 - I$ bond distance is constrained to its equilibrium value. (b) The $CH_3 - I$ bond distance is allowed to vary (at a given R and γ, $\cos \gamma = \hat{r} \cdot \hat{R}$) until the minimal value of the potential is reached. For further examples of such relaxed potentials see ref. (28).

onset of (typically, quite anisotropic) chemical forces which determine the stereochemistry. Using realistic but approximate potentials[21,29,30] an example of such polar plots for the canonical reaction[1,31-34]

$$K + CH_3I \rightarrow KI + CH_3$$

is shown in fig. 1. For this and other reactions, the long-range anisotropic potential has the form[24,35]

$$V(R) = C_6[1 + \kappa_{eff}P_2(\cos \gamma)]R^{-6} + C_7 \cos^3 \gamma R^{-7} \tag{1}$$

where κ_{eff} contains both inductive and dispersive contributions and is typically of the order of 0.1.[24] Hence the long-range R^{-6} potential term is not very anisotropic. Moreover, and unlike the conclusions of ref. (22), this term cannot distinguish the two ends of the CH_3I molecule. The reason is that $P_2(\cos \gamma) = P_2[\cos (\pi - \gamma)]$ so that the resulting effective potential barrier is symmetric about the molecular centre of mass. It is only the quadrupolar R^{-7} term that has an asymmetric dependence. For neutral molecules the quadrupole moments are seldom large enough to make this term significant. Hence for the $K + CH_3I$ system (which is known[36] to have an activation barrier), the stereochemistry is determined primarily by the orientation dependence of the barrier owing to the system-specific chemical forces.

A fuller understanding of the steric requirements of reactive collisions must, however, await the solution of at least three problems. The first is that of kinematic rotation. The theory specifies the cone of acceptance in terms of the relative orientation of the reagents at the barrier. Experimental results (and intuitive understanding) refer to the orientation of the well separated reagents. It is an essential (but sometimes overlooked) point that the term 'orientation' has two different technical definitions in the two preceding *sentences*. The potential energy is a function of the coordinates of the atoms. The barrier will therefore depend on the orientation as defined in the molecular framework. In other words, it will depend on the angle between the coordinates. Two possible angles that have been used are α and γ, which are the angle between the old and new bond and the angle between the approach direction and the reagent axis, respectively. $\cos \alpha = \hat{r} \cdot \hat{r}'$, where r and r' are the old and new bond coordinates (and the carat denotes a unit vector), and $\cos \gamma = \hat{r} \cdot \hat{R}$, where R is the vector from the reagent centre of mass to the attacking atom. Experiments are carried out in the laboratory framework. Hence the orientation is specified with respect to some space-fixed axis. Both the use of an inhomogeneous electrical field to orient the reagent[7] and the use of lasers to align the reagent[37] specify the distribution of the molecular axis. In a molecular-beam experiment one can also specify the (rather sharply peaked) distribution of the relative velocity $\dot{R}$. The orientation of the reagents is thus defined in terms of the angle ρ, $z \equiv \cos \rho = \hat{r} \cdot \hat{k}$, where $\hat{k}$ is a unit vector in the direction of $\dot{R}$. It is important to note that it is not only for purely experimental reasons that the angle ρ is distinguished. Even in the absence of any forces, *i.e.* for purely kinematic reasons, the angles α and γ will change with time in the course of the motion. We are so used to thinking about collinear collisions, when $\alpha = \gamma = \rho$, that we sometimes fail to note that, for finite impact parameters, a whole range of γ or α values corresponds to a particular value of ρ. The higher the impact parameter, the weaker is the correspondence between the experimental and theoretical definitions of 'orientation'.

It is important to emphasize that the 'smearing' of the theoretical orientation in higher-impact-parameter collisions is a purely kinematic effect which occurs even in the absence of any forces. The simplest way to account for this aspect is by a Monte Carlo simulation.[38,39] We have previously discussed this in some detail[39] and will here provide an explicit illustration involving the apparent reduction in steroselectivity in the $K + CH_3I$ reaction for non-backwards-scattered KI.

Over and above the purely kinematic problem of relating the experimental and theoretical orientations, there is a dynamical problem. The anisotropic long-range forces and the anisotropy of the chemical interaction can 'rotate' such vectors and v or† r whose direction is otherwise conserved. The effect of such 'reorientation' has been discussed by several authors.[8,10-12,15,19,20] In some models it is even assumed that the anisotropic forces are strong enough in the energy range of interest to specify the orientation at the barrier in a manner largely independent of the initial experimental orientation. It appears to us that while reorientation is no doubt important at low collision energies, its effect does diminish at higher energies. Trajectory computations[10,15,20,21] indeed establish a fairly close correspondence between the orientations at the barrier and as initially selected. The prime reason for loss of experimental orientation appears to us to be kinematic rather than dynamic, at all but the lowest energies.

For low-energy collisions there is now clear computational evidence[42-43] that for the same mass combination (*e.g.* $O + HCl$, $Cl + HCl$), modification of the longer-range potential while maintaining roughly the same barrier functionality, can lead to different dynamics. It is thus of interest to be able to assess simply the importance of reorientation

---

† In quantum mechanics there will always be a distribution of $\hat{r}$ values.[40,41] Even so, $\hat{r}$ is conserved along any classical trajectory for a spherical potential.

effects. Loesch[19] has shown how this can be done for $b = 0$ collisions using only two coordinates (R and γ). Using the same two coordinates, we[15] have shown how it can be done also for $b \neq 0$. Our approach is not equivalent to that of Loesch and we are in the process of comparing our approximation[15] to the results of exact trajectory computations.

The third aspect where further work is required is the role of reagent rotation.[3,15,19,44-48] Even for unexcited reagents this may be induced by the anisotropic forces, but even the purely kinematic implications of higher initial rotational angular momenta need be better understood.

The discussion has so far centred attention on the dependence of the reactivity on the orientation. Mathematically, this dependence is given by the partial or differential reaction cross-section† $d\sigma_R/d\cos\rho$ such that[8]

$$\sigma_R = \int_{-1}^{1} d\sigma_R/dz)\, dz \tag{2}$$

where $z = \cos\rho$. The differential cross-section is an integral over the opacity function for a given orientation

$$d\sigma_R/dz = 2\pi \int bP(b, z)\, db. \tag{3}$$

One could, instead, integrate over z first, leading to the familiar opacity function

$$P(b) = \int P(b, z)\, dz \tag{4}$$

which has the interpretation of the reaction probability for unoriented reagents. Integration of $P(b)$ over $d(\pi b^2)$ then leads to σ_R:

$$\sigma_R = \int_{o}^{\infty} P(b)\, d(\pi b^2). \tag{2'}$$

One has, therefore, two routes from $P(b, z)$, the reaction probability at a given b and orientation, to σ_R. The first is to integrate first over b and then over z, going through $\sigma_R(z)$ as the intermediate concept. The second route is to integrate over z leading to $P(b)$ and then to integrate over b. In schematic outline

$$
\begin{array}{ccc}
P(b, z) & \xrightarrow{\ (4)\ } & P(b) \\
\downarrow{\scriptstyle (3)} & & \downarrow{\scriptstyle (2')} \\
d\sigma_R/dz & \xrightarrow{\ (2)\ } & \sigma_R
\end{array}
$$

The first route has received much recent attention, as already discussed. For some reason, the second route has been somewhat neglected. This is perhaps due to the opacity function $P(b)$ having gone out of fashion. One needs to average over all orientations in order to get $P(b)$. However, part of the motivation for being interested in stereoselectivity is to understand better the reason for the magnitude of the reactivity of unoriented reagents. Indeed, the very early measurements by Greene and Ross and co-workers of values of $P(b)$ below unity were interpreted[32,49-51] as indirect proof for stereoselectivity. We shall discuss these pioneering results in more detail below. It will be shown that the systematics noted[32,50] in the $P(b)$ obtained from the analysis of angular

---

† Rather than ρ we could use γ as the variable. The whole point 1 above is, however, that $\sigma_R(z)$ is not necessarily equal to $\sigma_R(\cos\gamma)$.

distribution of non-reactive scattering can be accounted for. In particular these tend to support the general trends in the orientation dependence of the barrier to reaction. A cone of 'non-reaction' due to steric hindrance can also be inferred from the results for $K + CH_3I$ and other reactions [*e.g.* $K + CH_3Br$, $K + (CH_3)_3CBr$], where such hindrance is to be expected on classical stereochemical grounds.

The opacity function also serves as a useful guide to the angular distribution of the products.[7,52-54] For the canonical $K + CH_3I$ reaction we shall see below that even the simplest optical model generates quite realistic angular distributions of the reactively scattered KI product from the orientation dependence of the barrier to reaction, using $P(b)$ as a link between the two.

The optical model analysis suggests that there is a very useful route from the steric requirements of the reaction to the angular distribution of unorientated reagents. The latter is available for a number of reactions and exhibits clear systematics.[7,52,55] Some of these can be readily understood using the reduced variable[49,56] ('the energy along the line of centers') $E_T(1 - b^2/d^2)$. It is therefore of interest to further probe this connection. We do so using a DIPR[57-64] model modified as described below. The nature of the modification is that the repulsive impulse delivered past the barrier is taken to be directed not necessarily along the old bond. We suggest that the need for this modification can be seen already from earlier studies[59,61] of the $K + CH_3I$ reaction using the DIPR model.

The experimentally measurable [*e.g.* ref. (65)] double differential cross-section $d^3\sigma_R/d^2w dz$ cannot, however, be computed using only the optical model. The reason is the previously mentioned kinematic rotation relating the orientation variables ρ and γ, $z = \cos \rho$. The equivalence $\rho = \gamma$ is only strictly valid for $b = 0$. At other b values one needs to establish a correspondence between the two in order to relate $d^3\sigma_R/d^2w d \cos \gamma$, which can be computed in the optical model to the measurable $d^3\sigma_R/d^2w d \cos \rho$. One further requires a correspondence from b to the scattering angle. For off-collinear configurations at the barrier, this is not a simple relation. Hence we compute $d^3\sigma_R/d^2w dz$ by incorporating the modified DIPR assumption into the kinematic approach. This turns out to be a very natural refinement which does not complicate the kinematic approach, but enables it to provide realistic products' angular distributions for collisions of orientated (or unorientated, as the case may be) reagents. In particular, we recover the observed[65] trend towards reduced 'reactive asymmetry' as the products are monitored for less backwards directions in the $K + CH_3I$ reaction. The reduction is therefore largely due to the purely kinematic effect that at higher b values the relation between z and γ is one-too-many.

To avoid confusion between the many angles used in this paper we list below the four most common ones together with a short description:

bend angle at the barrier: $\cos \alpha = \hat{r} \cdot \hat{r}'$
theoretical orientation angle: $\cos \gamma = \hat{r} \cdot \hat{R}$
experimental orientation angle: $z = \cos \rho = \hat{r} \cdot \hat{k}$
scattering angle: $\cos \theta = \hat{k}' \cdot \hat{k}$.

Opacity Analysis

In the angle-dependent line-of-centres model,[5-7] reaction occurs with unit probability (*i.e.* $P(b, \gamma) = 1$) whenever the energy along the lines of centres exceeds the barrier height, $V_b(\cos \gamma)$, at the separation d

$$E_T(1 - b^2/d^2) \geq V_b(\cos \gamma). \tag{6}$$

The angle-averaged opacity function

$$P(b, E_T) = \tfrac{1}{2} \int_{-1}^{1} P(b, \gamma) \, d \cos \gamma \tag{7}$$

is thus the fraction of the range $(-1$ to $1)$ of $\cos \gamma$ for which condition (6) is satisfied. Whatever the angle dependence of the barrier may be, it is clear that $P(b, E_T)$ is not a function of b and E_T separately but only a function of the variable E'_T

$$E'_T \equiv E_T(1 - b^2/d^2) \tag{8}$$

which is the kinetic energy along the line of centres, at the barrier.

In the quite common case when the barrier is lowest for a collinear configuration $(\cos \gamma = 1)$, and monotonically increases with decreasing γ,

$$P(b, E_T) \equiv P(E'_T) = \tfrac{1}{2}\{1 + \cos [\gamma(E'_T)]\}. \tag{9}$$

Here, $\gamma(E'_T)$ is the solution of the implicit equation of

$$E'_T = V_b(\cos \gamma)|_{(\gamma = \gamma(E'_T))} \tag{10}$$

and eqn (9) is derived by performing the integral in eqn (7) over the range $\cos \gamma(E'_T)$ to unity for which $P(b, \gamma) > 0$.

Following Beck *et al.*[49] [in particular, their eqn (22)], we could also write the opacity function as a function of the barrier height $P_b(E'_T) \equiv P_b(V_b)$. Note, however, an essential difference. In the angle-dependent line-of-centres model ' variation of V_b is entirely due to the angle dependence of the barrier. In the optical model of Beck *et al.*, the entire variation of the barrier [denoted $V(y)$, where y is the relative separation, in ref. (49) and subsequent studies], is due to a variable distance of closest approach. In our kinematic model[39] (and also later below) we do allow the location d of the barrier to vary with γ. For many reactions, however, this is a secondary correction. The primary variation of the barrier is due to its orientation dependence at roughly constant distance. The work of Evans *et al.*[17] has established a useful correction for a non-spherical barrier in terms of an anisotropy parameter γ.

The opacity function (9), when plotted *vs.* b at constant E_T is monotonically diminishing with a cut-off at b_{max}

$$E_T(1 - b^2_{max}/d^2) = V_b(\cos \gamma = -1). \tag{11}$$

Note that at impact parameters at just below b_{max} only essentially collinear configurations lead to reaction, whereas near $b = 0$ the entire range of angles from $\cos \gamma = -1$ down to $E_T = V_b(\cos \gamma)$ can lead to reaction. In other words, $\cos \bar{\gamma}(E'_T)$ is the opening (half) angle of the cone of acceptance for reaction at the impact parameter b and initial kinetic energy E_T. When $P(E'_T)$ is integrated over b to yield $\sigma_R(E_T)$, it is found[6] that $P(E'_T = E_T) \equiv P(E_T, b = 0) = [1 + \cos \gamma(E_T)]/2$ plays the role of the 'steric factor', *i.e.*

$$\sigma_R(E_T) = P(E_T, b = 0)(1 - \langle V_b(\cos \gamma)\rangle / E_T) \tag{12}$$

where $\langle V_b(\cos \gamma)\rangle$ is the angle-averaged barrier height.

Fig. 2 shows the opacity function *vs.* b at four collision energies for the $K + CH_3I$ reaction. The barrier functionality is the linear one,

$$V_b(\cos \gamma) = V_0 + V_1(1 + \cos \gamma) \tag{13}$$

derived by Bernstein[13] on the basis of the experimental results on the reactive asymmetry by Parker *et al.*,[66] which were at an energy of $3.1 \text{ kcal mol}^{-1}$. A similar functional dependence of V_b on $\cos \gamma$ is found for the potential-energy surfaces shown in fig. 1. These surfaces provide one very important additional insight: the functional form (13) is valid only up to a barrier height of *ca.* $3.2 \text{ kcal mol}^{-1}$. For values of $\cos \gamma$ below *ca.* 0.65 the barrier height is *de facto* infinite. [See *e.g.* fig. $2(a)$ of ref. (21).] In principle one should distinguish between the dependence of the barrier on the angle γ, $\cos \gamma = \hat{r} \cdot \hat{R}$ and on the angle α, $\cos \alpha = \hat{r} \cdot$. Owing to the high mass of the I atom this distinction is of less importance in the present system. Note, however, that our angle γ is complementary to the one used in ref. (6), (7) and (13), hence the difference in sign in eqn (13).
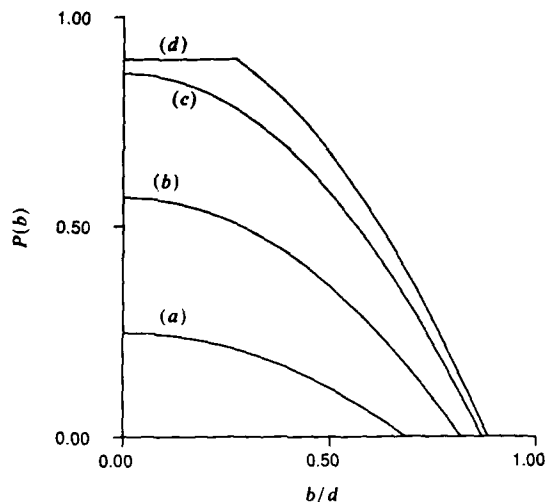
Fig. 2. The opacity function for $K+CH_3I$ computed, for a barrier linear in $\cos \gamma$ [cf. eqn (13)] up to $V_b = 0.139$ eV (corresponding to $\cos \gamma = 0.8$) and infinitely high thereafter, at four collision energies: (a) 0.062 eV, (b) 0.1 eV, (c) 0.135 eV, (d) 0.15 eV. For $E_T \geqslant 0.139$ eV $P(b)$ will show saturation. A more realistic barrier functionality will presumably be smoother and hence the break will be rounded. Compare with fig. 17 of ref. (69).

The collision energies chosen for plotting fig. 2 are in the range covered in the early non-reactive scattering experiments of Airey *et al.*[67] Their results were subjected to an optical model analysis[32,49,50] to yield the opacity function for reaction. Additional results are due to Harris and Wilson.[51] The lowest energy also corresponds to the experiments of Kinsey *et al.*[54] The functional form (21) for the barrier accounts well for the trends in the observed results: At energies just past the threshold the steric factor is quite low (*e.g.*[54,54] *ca.* 0.6 at 1.44 kcal mol^{-1}) and increases with energy. $P(b, E_T)$ remains, however, below unity even at higher energies. In other words, there is a cut-off to the increase of the steric factor with increasing collision energies. The decline of $P(bE_T)$ with increasing b is not sharp but occurs over the entire range of b values. The cut-off impact parameter, b_{max}, where $P(b, E_T)$ declines to zero initially increases with E_T. The dependence of b_{max} on E_T can be computed readily, since for a linear barrier function the explicit solution of eqn (10) is trivial, $\cos \gamma(E'_T) + 1 = (E'_T) = E'_T - V_0)/V_1$ or

$$P(b, E_T) = P(E'_T - V_0)/2V_1 \tag{14}$$

and

$$b^2_{max} = d^2((1 - V_0/E_T). \tag{15}$$

Eqn (14) and (15) are only valid for E_T up to 3.1 kcal mol^{-1}, which is the limit of the known validity of the linear barrier form (13). We can use the theoretical potential-energy surfaces (and the observed cone of non-reaction which corresponds[68] to $\cos \gamma \approx$ 0.6) to conclude that for $\cos \gamma$ somewhere past 0.6 the barrier dependence will rise sharply. Hence for E_T values above *ca.* 3.2 kcal mol^{-1}, the maximal opening angle $\gamma(E'_T)$ will no longer increase with E_T. Fig. 3 shows a plot of $P(E'_T)$ and of $\gamma(E'_T)$ *vs.* E'_T, demonstrating the onset of saturation.

The conclusion that $P(b, E_T)$ will rise linearly with E'_T (with a constant slope = $1/2V_1 = 1/2.7$ mol kcal^{-1} and then reach a plateau is borne out by the plots of Airey *et al.* [fig. 10 of ref. (67)]. Even the value of $P(^h, E_T)$ at the plateau, expected from our
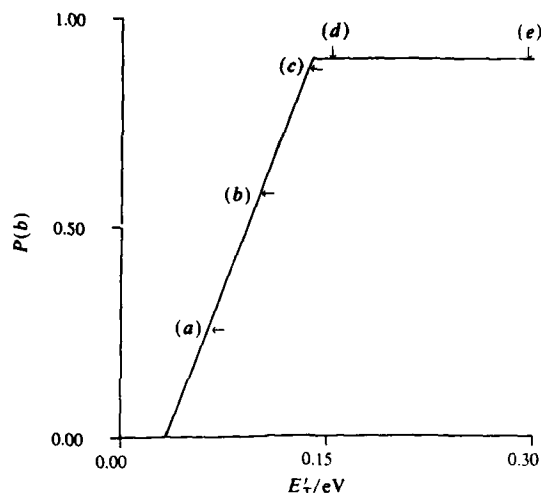
Fig. 3. The opacity function for $K + CH_3I$ plotted *vs.* the energy E'_T along the lines of centres, $E'_T = E_T(1 - b^2/d^2)$. For a given collision energy the plot terminates at $E'_T = E_T$ [shown as arrows for the energies used in fig. 2 and (*e*) 0.29 eV]. Compare with fig. 17 of ref. (69) and with fig. 19 of ref. (50) for $K + CH_3Br$. Also shown is the maximal angle of the cone of acceptance for reaction. Note the saturation for $E_T \geqslant 0.139$ eV.

considerations to be at *ca.* $(1 + 0.7)/2 = 0.85$ is in agreement with experimental results. Note, however, that the optical model assumes that every trajectory that can cross the barrier will proceed to react. For the $K + CH_3I$ reaction there is evidence from trajectory computations[30] that at higher energies trajectories can recross the barrier. Hence at higher values of E'_T, $P(E'_T)$ should be regarded as the probability of crossing the barrier rather than as the probability of reaction. It is interesting to note [*e.g.* fig. 16 and 18 of ref. (69)] that many other reactions show levelling-off of the $P(E'_T)$ *vs.* E'_T plots. At the E'_T value where $P(E'_T)$ becomes virtually saturated, it is equal to $(1 + \cos \gamma_{max})/2$, where γ_{max} is *de facto* the maximal opening angle of the cone of acceptance. The results of the optical-model analysis of experimental non-reactive scattering [fig. 18(*c*) of ref. (69) in particular] show clearly that the larger the steric hindrance, the lower is the value of $P(E'_T)$ at the onset of saturation. [Note in particular the large steric hindrance for $(CH_3)_3CBr$.] Hence the conclusions that a 'geometrical maximal angle' for reaction, experimentally uncovered for $K + CH_3I$,[66,68] will also be observed for many other systems.

Analysis of potential-energy surfaces has also suggested[29] that such steric hindrance will be the case *e.g.* for the $O + HCl$ and $Cl + HCl$ reactions. Here the bulky Cl group geometrically precludes the approach of the reagent over much of the angular ranch.

In general, a plot of $P(E'_T)$ *vs.* E'_T will show a threshold corresponding to the lowest value of E'_T for which reaction is possible. From eqn (6), this corresponds to $b = 0$ collisions and the threshold energy is minimal value of $V_b(\cos \gamma)$. If the barrier is lowest for collinear attack and increases monotonically thereafter, the threshold is at $E_0 = V_b(1)$ and the maximal possible impact parameter that can lead to reaction is

$$b_m^2 = b^2(1 - E_0/E_T). \tag{16}$$

Roberts[56] has derived the E'_T dependence of the opacity function from considerations based on an imaginary component for the elastic scattering potential.[70] When the imaginary (the, so-called, optical) potential is well localized in space, $P(b, E_T)$, will be a function of E'_T. Such a localized optical potential was shown[71] to reproduce the

energy dependence of the reaction cross-section for $K + CH_3I$. The picture of a localized optical potential is consistent with the line-of-centres model where the decision whether reaction takes place is taken at the barrier. When the opacity is a function of E'_T one can replace the integration in eqn (4) over b by an integration over E'_T, $dE'_T = E_T d(b^2/d^2)$. Hence from eqn (3') one obtains for the yield function[70,72,73] the following form:[56]

$$E_T \sigma_R = \pi d^2 \int_{E_0}^{E_T} P(E'_T) \, dE'_T. \tag{17}$$

This enables one to 'invert' the translational energy dependence of σ_R to obtain the opacity function[56]

$$P(E'_T) = \frac{d}{dE_T} (E_T \sigma_R / \pi d^2)|_{E_T = E'_T}. \tag{18}$$

The translational energy dependence of σ_R for $K + CH_3I$ and for $Rb + CH_3I$ has been directly measured.[36,74,75] In addition, it has been indirectly obtained[51,69] from the optical-model analysis of non-reactive scattering. There have also been numerous trajectory and model studies[30,53,71,76-83] of this dependence. The possibility of recrossing the barrier at higher collision energies back into the reagents region[10,30] implies that eqn (18) cannot be used well past the barrier. In the immediate post-threshold regime one can use for the yield function the ubiquitous form[73,83]

$$E_T \sigma_R = \pi d^2 A (E_T - E_0)^{s-1} \tag{19}$$

where A is a combination of constants. (It is $k^2 \sigma_R$ which is dimensionless,[7] where k is the wavevector corresponding to E_T). Using eqn (18), this leads to[56]

$$P(E'_T) = \begin{cases} sA(E'_T = E_0)^{s-1}; & E'_T \geqslant E_0 \\ 0; & \text{otherwise} \end{cases} \tag{20}$$

or, equivalently,

$$P(b, E_T) = sA(E_T - E_0)^{s-1}(1 - b^2/b_{max}^2)^{s-1}. \tag{21}$$

The linear barrier case as previously discussed corresponds to $s = 2$. A steeper dependence of $V_b (\cos \gamma)$ on $\cos \gamma$, say

$$V_b(\cos \gamma) = V_0 + V_1(1 + \cos \gamma)^n \tag{22}$$

lead to eqn (20) with $V_0 = E_0$ and $s - 1 = 1/n$. A parabolic dependence on $1 - \cos \gamma$ would yield exactly $s = 3/2$. The values of s reported by Roberts[56] from a fit of eqn (19) to various trajectory results range from $5/4$ to 2.

The plot of $P(E'_T)$ *vs.* E'_T shown in fig. 3 corresponds to $s = 2$ up to $E'_T = 3.2$ kcal mol^{-1}. The saturation seen therein is due to the rather sudden onset of very high barriers to reaction for $\cos \gamma$ below -0.6 or so. One could mimic this behaviour using eqn (20) with s just above unity. (Roberts[56] finds $s = 1.25$ for the trajectory computations[30] of $K + CH_3I$). The rather clear geometrical interpretation[34,68] of the change in the behaviour of $V_b(\cos \gamma)$ due to steric hindrance by the CH_3 group appears to us to be preferable. *In other words, the inversion (18) must be handled with care.*

The angular distribution of reactive scattering for rebound reactions[7] has been thoroughly discussed by Herschbach and co-workers[52,54,84] and by Hardin and Grice.[53] The one new point is that the input opacity function as used here takes into consideration the steric requirements of the reagents.

Starting from $d\sigma_R/d(\pi b^2) = P(b)$ one obtains[7,52-54]

$$d^2\sigma_R/d^2w = [d(\pi b^2) d^2w)]P(b)$$

$$= (d^2\sigma^o/d^2w)P(b). \tag{23}$$
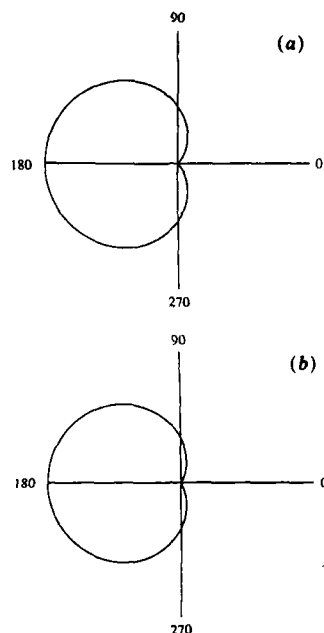
Stereoselective Reactions

Fig. 4. Polar plots of (a) $d\sigma_R/d \cos \gamma$ (the reactivity as a function of orientation) and (b) $d^2\sigma_R/d^2 w$ (the angular distribution of reactive collisions) kfor $K + CH_3I$ at $E_T = 0.135$ eV. In these plots the distance from the origin is the magnitude of the relevant cross-section, and the polar angle is ρ or γ, respectively. The plots are normalized to unity in the backwards direction. Note the similarity of the two polar plots.

Here, $d^2\sigma^o/d^2 w$ is the angular distribution computed for the assumed trajectories, which give rise to a mapping from the initial b to the final scattering angle. If that relation is one-too-many (or, more than one), t. e right-hand side of eqn (20) contains a sum over all b values that leads to a scattering into a given final angle. Since our interest here is in the qualitative features we shall make the simplest assumption, that of hard-sphere scattering, whence[7] $d^2\sigma^o/d^2 w = d^2/4$, and the scattering angle θ is related to b by[7]

$$b(\theta) = d \cos (\theta/2). \qquad (24)$$

The justification for this assumption for the $K + CH_3I$ reaction in particular[54] and for other reactions has been discussed before.[52,84] Hardin and Grice[53] provide a more accurate procedure.[53] Since we shall have to return to this topic below for the kinematic transformation from γ to z we shall then refine also the angular aspects of the scattering. Here we use eqn (24) which, together with eqn (23), leads to the simple result

$$d^2\sigma_R/d^2 w = (d^2/4) P[b(\theta), E_T]$$

$$= (d^2/4) P[E_T'(\theta)]. \qquad (25)$$

For the case of a linear barrier, eqn (13), we have, using eqn (14), the explicit result

$$d^2\sigma_R/d^2 w = \begin{cases} (d^2/4)(E_T(1 - \cos \theta) - 2V_0)/4V_1; & \sin^2(\theta/2) \leqslant V_0/E_T. \\ 0; & \text{otherwise} \end{cases} \qquad (26)$$

This simple result accounts for the essentially linear decline of the observed[85,86] reactive
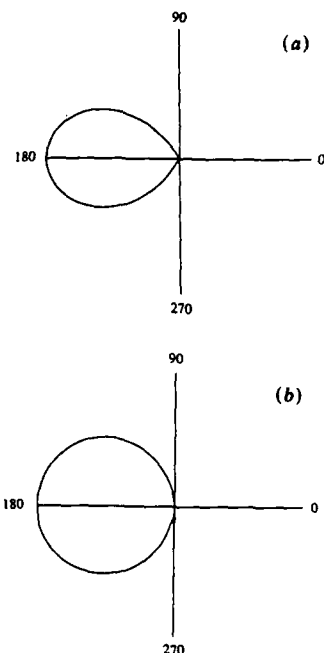
Fig. 5. As in fig. 4 for the lower energy $E_T = 0.062$ eV.

angular distribution from its value in the backwards direction. It also predicts a cut-off in the forward direction. For $V_0 = 0.76$ kcal mol^{-1}, the cut off is at θ *ca.* 60° [*cf. e.g.* with fig. 9 of ref. (86)].

A polar plot of $d^2\sigma_R/d^2w$ computed using eqn (26) at $E_T = 3.1$ kcal mol^{-1} is shown in fig. 4(*a*). This is to be compared with the plot of the observed result, fig. 2 of ref. (33). This computation is compared in fig. 4 with a polar plot of $d\sigma_R/d\cos\gamma$. For a linear barrier functionality, we have using eqn (4) and (13)

$$d\sigma_R/d\cos\gamma = \tfrac{1}{2}\pi d^2[1 - V_b(\cos\gamma)]/E_T$$

$$= \tfrac{1}{2}\pi d^2\left[\left(1 - \frac{V_0}{E_T}\right) - \frac{V_1(1+\cos\gamma)}{E_T}\right]. \tag{27}$$

The similarity in the two plots shown in fig. 4 is also evident in the comparison of the two experimental results. [*Cf. e.g.* fig. 2.18 and 3.25 of ref. (7).] The two plots show, however, quite distinct aspects, and their startling similarity is indeed somewhat accidental and reflects the special properties of a linear barrier function. In the polar plots both $d\sigma_R/d\cos\gamma$ and $d\sigma_R/d\cos\theta$ are normalized to unity at the maximum. At $E_T = 3.2$ kcal mol^{-1} the cut-off on cosγ is *ca.* 0.7. This corresponds to cos $\theta = 0.3$, which is the cut-off angle at $E_T = 2.2$ kcal mol^{-1}. Note, however, that the observed angular distribution[86] is less dependent on E_T than suggested by eqn (27). This perhaps is due to eqn (27) only being valid for $E_T \leqslant 3.1$ kcal mol^{-1}. At higher energies, as already discussed, the linear functionality will be misleading. For lower collision energies (*e.g.* 1.4 kcal mol^{-1}), the similarity between the two plots, fig. 5, would be less striking. Even so, it is a tribute to the linear barrier functional form[13] that it can simply and readily account for this unexpected[66] similarity.
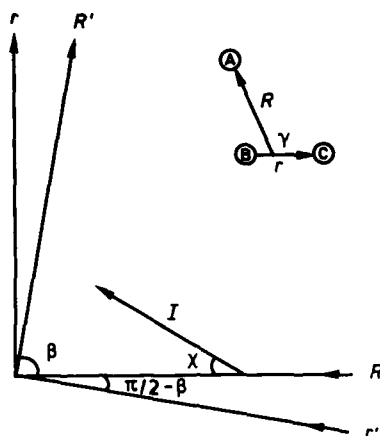
Fig. 6. The two sets of cartesian axes and the definition of the vectors and of the impulse I.

Kinematic Model

There are two aspects which opacity analysis does not address. One is the fate of the system past the barrier: how, say, is the total angular momentum partitioned between the orbital component of the relative motion and the rotational angular momentum of the product? We shall indeed be interested in an even more detailed question, namely how is this partitioning dependent on the scattering angle?[87] A second aspect is that in the optical model one cannot combine the experimental specification of the initial state (which is in terms of the distribution ρ, $z = \cos\rho = \hat{k} \cdot \hat{r}$) and the reaction criterion in terms of the relative orientation of the reagents at the barrier.

Both these aspects can be handled in the kinematic model, as has been discussed before[39] with special reference to laser-aligned reagents. Here, we shall be primarily concerned with orientated[34,65,66,88] CH_3I. In particular we shall show that purely kinematic effects can account for the observed[65] reduction in the role of reagent orientation for non back-scattered products.

The new feature of the model is that it is used to generate realistic angular distributions for rebound reactions by incorporating an impulsive release. There are therefore two separate lines of development that lead to the present version of the model. The first starts with the original DIPR model.[57,58,60,63] The model is augmented by (i) explicit account of the internal degree of freedom of the reagent (or, equibalently, of the product); (ii) a reaction criterion which derives from an angle-dependent barrier to reaction. Only those trajectories that can surmount the barrier lead to products, and (iii) the impulse is released not necessarily along the direction of the old bond.

Another route is to begin with the kinematic model of Elsum and Gordon.[89] One then incorporates a criterion for reaction which depends on the orientation at the barrier.[39] The second modification is that the final momenta are specified not only by kinematic considerations but also by an impulsive release. We shall present the model here along these lines.

The purely kinematic part is as before. One starts by a rotation[7,90,91] of the cartesian coordinate system $(r, -R)$ suitable for the reactants, by an angle $(\pi/2) - \beta$ to the cartesian system $(R', -r')$ suitable for the products (fig. 6),

$$\begin{pmatrix} R' \\ r' \end{pmatrix} = \begin{pmatrix} -m_A/(m_A + m_B) & \sin^2\beta \\ 1 & m_C/(m_B + m_C) \end{pmatrix} \begin{pmatrix} R \\ r \end{pmatrix}. \tag{28}$$

Here, as usual, $\cos^2 \beta = m_A m_C / (m_A + m_B)(m_B + m_C)$ and m_X is the mass of atom X. To see that eqn (28) is indeed a rotation, it is convenient to introduce the mass-scaled coordinates

$$Q = (\mu_{A-BC})^{1/2} R, \qquad q = (\mu_{BC})^{1/2} r$$

$$Q' = (\mu_{AB-C})^{1/2} R', \qquad q' = (\mu_{AB})^{1/2} r'$$

where the μs are the reduced masses. Then eqn (28) can be written[7]

$$\begin{pmatrix} Q' \\ q' \end{pmatrix} = \begin{pmatrix} -\cos \beta & \sin \beta \\ \sin \beta & \cos \beta \end{pmatrix} \begin{pmatrix} Q \\ q \end{pmatrix}. \tag{29}$$

The kinetic energy is

$$T = (\dot{Q}^2 + \dot{q}^w))/2; \qquad T' = (\dot{Q}'^2 + \dot{q}'^2)/2$$

where the dot denotes the time derivative. In the purely kinematic limit the velocities are computed from eqn (28)

$$\begin{pmatrix} \dot{Q}' \\ \dot{q}' \end{pmatrix} = U(\beta) \begin{pmatrix} \dot{Q} \\ \dot{q} \end{pmatrix} \tag{30}$$

where $U(\beta)$ is the rotation matrix in eqn (29).

When there is an impulsive release, there is an additional component to the velocities due to the impulse. We specify the impulse I by its magnitude and direction. To conform with previous usage[58-61] we define the magnitude in terms of a dimensionless parameter q:

$$I = [m_C / (m_B + m_C)] q P$$

$$= (m_C m_A / M) q \dot{R} \tag{31}$$

where M is the sum of the three masses and $P = \mu_{A-BC} \dot{R}$ is the initial momenta. We do allow, however, for the impulse to be at an angle χ with respect to the $-R$ axis (*i.e.* at an angle $\pi/2 - \chi$ with respect to the r axis). Hence the components of I along R and r are specified by the two components of I

$$I = \begin{pmatrix} -\cos \chi & \sin \chi \\ \sin \chi & \cos \chi \end{pmatrix} \begin{pmatrix} I \\ 0 \end{pmatrix} \tag{32}$$

while the two components of the impulse along R', r' are the two components of $I' = U(\beta) I$.

In the computation of $\dot{r}'$, $\dot{R}'$ we thus have

$$\begin{pmatrix} \dot{R}' \\ \dot{r}' \end{pmatrix} = \begin{pmatrix} -m_A / (m_A + m_B) & \sin^2 \beta \\ 1 & m_c / (m_B + m_C) \end{pmatrix} \left(\begin{pmatrix} \dot{R} \\ \dot{r} \end{pmatrix} + \begin{pmatrix} I_R / \mu_{A-BC} \\ I_r / \mu_{BC} \end{pmatrix} \right). \tag{33}$$

Otherwise, the comp ..tion follows the details presented in ref. (39).

In applications, we need to specify the values of q and χ. We used $q = 18$, which is in the range (*e.g.*[61] 15-20) recommended by previous applications to the $K + CH_3I$ reaction.[58-61] In his detailed study,[59] Knutz noted that to obtain broad products' translational energy distribution it is necessary to take q to be a function of the orientation angle, with q being largest for a collinear configuration. An examination of the potential-energy surfaces[21,29,30,76] suggests to us that the origin of the need to take the magnitude of the impulse along $\hat{r}$ to be a function of orientation is simply that the impulse is not directed along $\hat{r}$. In other words, we question the basic premise of the DIPR model. Inspection of all reasonable surfaces shows the impulse in $K + CH_3I$ to be delivered relatively early and to be much more in the direction of $\hat{R}$ than of $\hat{r}$. Hence, we agree with Kuntz[59] that the immpulse along $\hat{r}$ is maximal for a collinear configuration and
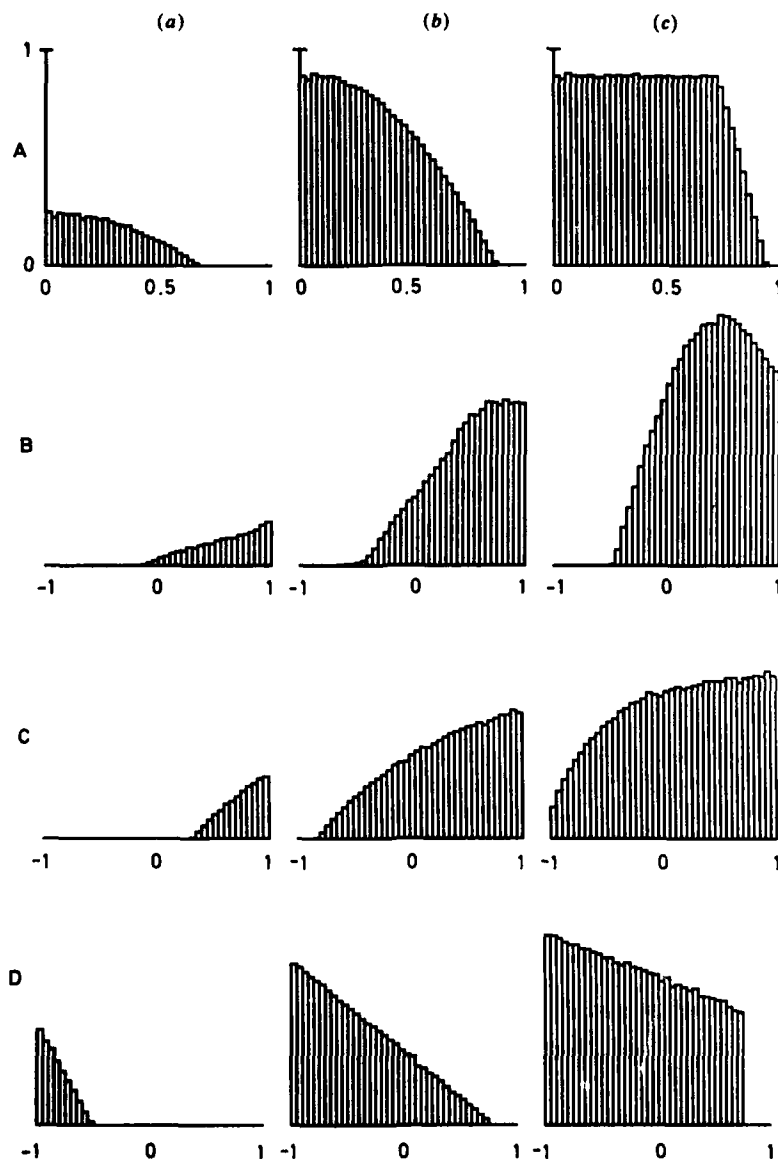
Stereoselective Reactions

Fig. 7. Kinematic model vcomputations for $K+CH_3I$. Shown are the (Λ) opacity function $P(b)$ vs. b/d, (B) the angular distribution $P(k' \cdot k) = (d^2\sigma_R/d^2w)/\sigma_R$ vs. $\cos\theta = \hat{k}' \cdot \hat{k}$, and the distributions of reactive reactants in $\hat{r} \cdot \hat{k} = \cos\rho$ (C) and in $\hat{r} \cdot \hat{R} = \cos$ (D) at three collision energies: (a) 0.062 eV, (b) 0.135 eV, (c) 0.290 eV. k At the highest energy there can be some recrossing of the barrier back into the reactants region. This is not incorporated in the model. Hence a strict interpretation of the results at the highest energy is that they are the distribution for those reactants that can cross the barrier. Note that at the highest energy, the distribution in cos γ is nearly that of a 'painted sphere',[88] namely, nearly constant reactivity within the cone of acceptance. Note also the shift to more forward scattering as the initial energy is increased. In this and all subsequent figures, the scalar product of unit vectors is denoted by a round bracket, *e.g.* $(k' \cdot k) = \hat{k}' \cdot \hat{k}$.
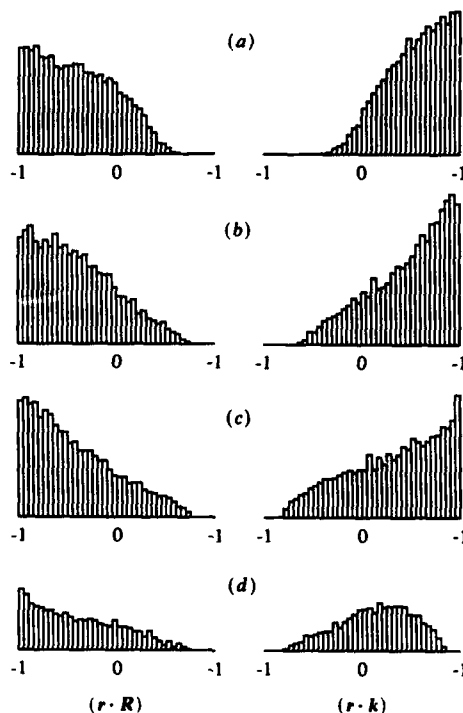
Fig. 8. Kinematic model computations of the distribution of initial orientations of those trajectories that lead to reaction *and* are scattered into the indicated angular ranges $[a, b]$, $a \leqslant \cos \theta \leqslant b$, at $E_T = 0.135$ eV, $j = 3$. Note that the distribution in $z = \cos \rho = \hat{r} \cdot \hat{k}$ is quite different for sideways scattering. It is the distribution in $\hat{r} \cdot \hat{k}$ of all reactants that can be selected using orientated reagents. $(k \cdot k)$: (a) [0.95, 1.00], (b) [0.80, 0.85], (c) [0.50, 0.55], (d) [0.00, 0.05].

diminishes with increasing angle of attack. In our approach, there is, however, a second component of the impulse, along $\hat{R}$. The skewing angle β for $K + CH_3I$ is quite large (*ca.* 80°) so that the r' axis is rotated with respect to the R axis by only a small $(\pi/2 - \beta)$ angle (fig. 6). The result is that the impulse I is nearly parallel to the r' axis. Another way of stating our approach is therefore that it corresponds to an early release. Owing to the low mass of the departing methyl group a significant fraction of the energy impulsively released ($ca.^{7,79,92} \sin^2 \beta$), will be available for the products' translation).

Fig. 7 shows a typical output from the kinematic model for $q = 18$ and $\chi = 2°$ at three collision energies. The opacity function is, as expected, monotonically declining (*cf.* the same two energies in fig. 2) and the angular distribution of the KI product is somewhat more realistic. It still shows the overall nearly linear decline ($vs. \cos \theta = \hat{k}' \cdot \hat{k}$) from its value in the backwards direction. Here, however, the initial decline is somewhat more rounded, as is observed.[86] Regarding the distribution of initial conditions for those reagents that do react (the so-called[7] reactive reactants): The distribution in $\hat{R} \cdot \hat{r}$ is that expected for the linear barrier function used in the computation. Note that when all products are collected (as is the case here but not in several figures below), the distribution in $\hat{r} \cdot \hat{k}$ is quite similar to that in $\hat{r} \cdot \hat{R}$. The reason is that most reactive collisions have k nearly (anti)parallel to R.

Note that in fig. 7 and all following figures, the cosine of the angle between two vectors a, b is denoted by $(a \cdot b)$. In other words, $\hat{a} \cdot \hat{b} = (a \cdot b)$.
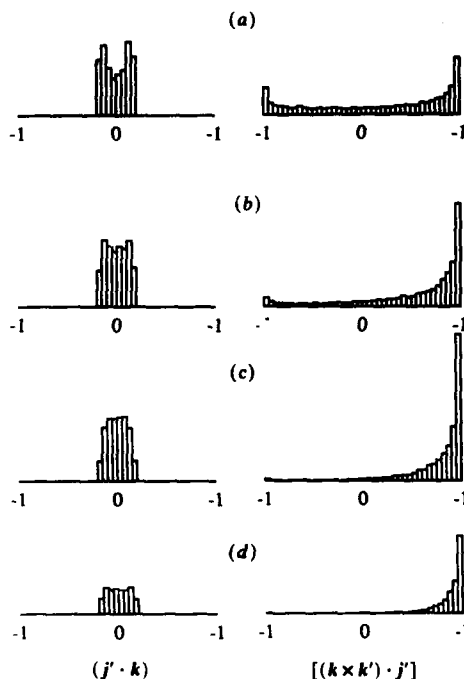
Fig. 9. Kinematic model computations of the correlation between products' angular momentum polarization and scattering angle. Shown are the distributions of the KI angular momentum j', along the direction $\hat{k}$ of the initial velocity and along the direction perpendicular to the plane of the collision $\hat{k} \wedge \hat{k}'$ for the same four angular ranges shown in fig. 8. Note that j' is essentially perpendicular to the plane of the collision.

In a crossed molecular beam experiment one typically collects only those products that have been scattered into a narrow angular range. Fig. 8 shows the distribution in initial conditions for those reactants that reacted *and* were detected at the indicated range of $\cos \theta = \hat{k}' \cdot \hat{k}$. The important point is the distribution in $\hat{r} \cdot \hat{k}$. Even for backwards scattering we find (not shown) contributions from the entire range of impact parameters. Hence the distribution in $\hat{r} \cdot \hat{k}$ is *not* uniform up to the cut-off (as would be the case if only $b \approx 0$ collisions contributed). Next, note the gradual shift in the $\hat{r} \cdot \hat{k}$ distribution as the distribution is examined for more forward scattering. While there is no one-to-one relation between the initial impact parameter and final scattering angle, sampling the $\hat{k}' \cdot \hat{k}$ distribution does probe the $\hat{r} \cdot \hat{k}$ distribution.

The angular momentum disposal in the products is shown in fig. 9 for the same conditions as in fig. 8. To compare with the discussion of Hsu *et al.*[87] [see also ref. (93) and (94)], note that their y axis is along $\hat{k}' \wedge \hat{k}$ and the z axis is along k. In general, and as expected for repulsive release,[3,7] the product KI angular momentum j' is perpendicular to the scattering plane and at lower collision energies is in the opposite direction to l'. Note, however, that the details *are* sensitive to the scattering angle. In the forward direction, j' is very preferentially parallel to l'. Of course, the scattering is predominantly backwards, but the width of the $\hat{k} \wedge \hat{k}' \cdot \hat{j}'$ [denoted $\langle \hat{J}_y^2 \rangle$ in ref. (87)] distribution is very strongly scattering-angle-dependent. The width of the $\hat{j}' \cdot \hat{k}$ distribution ($= \langle \hat{j}_z'^2 \rangle$) is far less variable. At higher collision energies, when the scattering is more forward, j' is preferentially oriented parallel to l'.
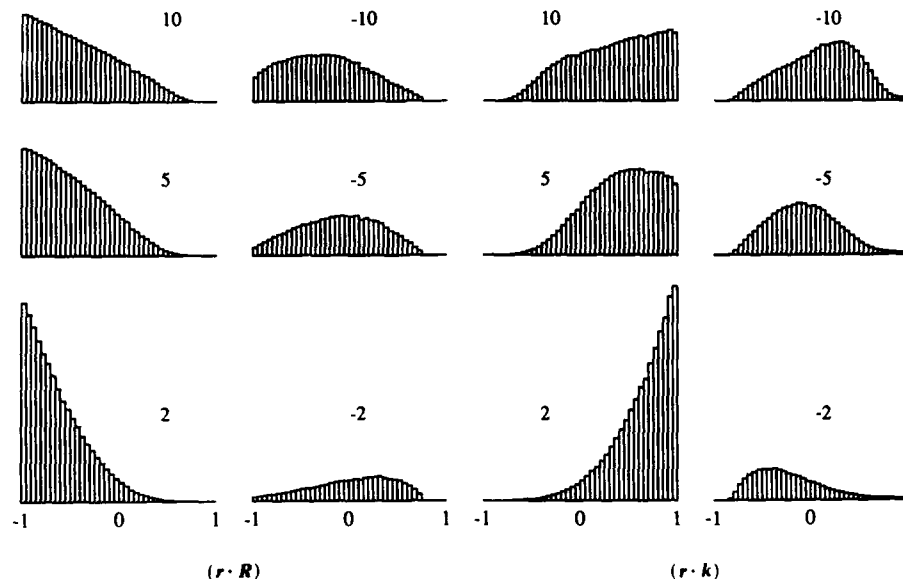
Fig. 10. Kinematic model computations of the distribution of initial orientations for those trajectories that lead to reaction at $E_T = 0.135$ eV for several field strengths, V_0. The field voltages (in kV) are those used in the experimental study[65,95] of K + orientated CH_3I.

We turn now to several aspects for the reaction of oriented[34,65,66,88,95] CH_3I. The distribution of all CH_3I molecules with respect to the direction $\hat{E}$ of the field $W(\cos p)$ was computed by a Legendre polynomial expansion.[95,96]

$$W(z) = \sum_n [(2n+1)/2]\langle P_n(z)\rangle P_n(z) \qquad (34)$$

where $z = \cos p$ and the numerical values of the Legendre moments $\langle P_n(z)\rangle$

$$\langle P_n(z)\rangle \equiv \int_{-1}^{1} W(z)P_n(z)\,dz \qquad (35)$$

are taken from table 1 of ref. (95). As in our previouis study,[39] of aligned reagents, we simulate the orientation of the reagents by weighting the trajectories in accordance with the distribution (34).

Fig. 10 shows the distribution of *reactive* reactants at several field values. We emphasize that in fig. 10, all reactive events are counted, irrespective of the final scattering angle. What the figure emphasizes is the essential distinction between the distribution of the reactive reactants in $\hat{r} \cdot \hat{k}$, which is subject to experimental control and the distribution in $\hat{r} \cdot \hat{R}$ which is of theoretical interest. It might appear at first glance that the distribution of reactive reactants in $\hat{r} \cdot \hat{R}$ should be governed only by the angular dependence of the barrier to reaction and hence independent of the field. This is not so because the field orientates the reactants. Hence the distribution of *all* reactants in $\hat{r} \cdot \hat{R}$ is no longer uniform as it would be in the absence of the field (*i.e.* for randomly oriented reagents).

We consider that fig. 10 is a clear demonstration of the importance of purely kinematic aspects.

The angular distribution of reactively scattered KI at different orienting fields is shown in fig. 11. The different plots are drawn to a common scale so that, for example, the cross-section is maximal for backwards scattering for $V_0 = 2$ kV and diminishes for
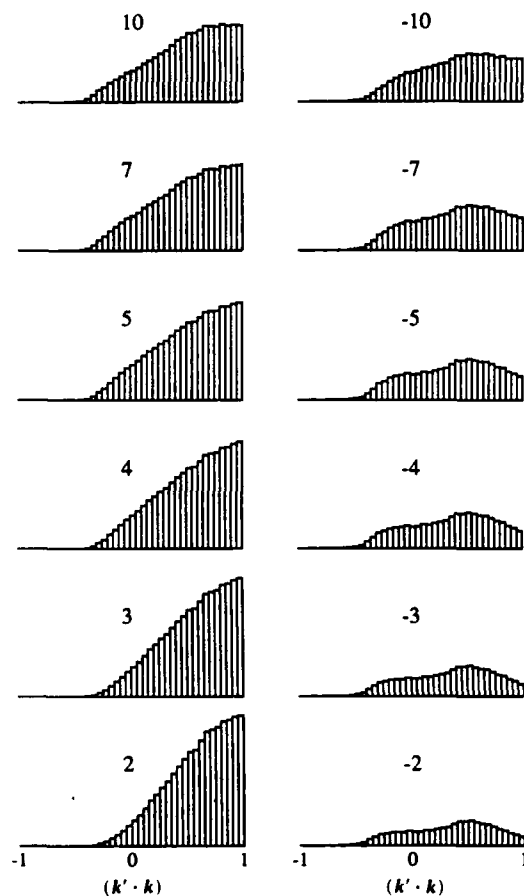
Fig. 11. Kinematic model computations of the angular distribution of KI vs. $\cos \theta = \hat{k}' \cdot \hat{k}$, for K+orientated CH_3I collisions at $E_T = 0.135$ eV. The initial distribution of all reactants is as in eqn (34) with weights appropriate to the experimental conditions[65,95] and to the indicated rod voltage, V_0 in kV). Note the loss of selectivity [i.e. compare the magnitude of the cross-section $d\sigma_R/d \cos \theta$ for favourable ($V_0 > 0$) vs. unfavourable ($V_0 > 0$) orientations] in the more forward direction.

higher fields. Since[65] $\langle \cos \rho \rangle = \langle P_1(z) \rangle$ is approximately proportional to $1/V_0$, fig. 11 shows that for the backwards direction the reactivity is monotonically increasing with the mean orientation.

As the scattering is monitored for more forward direction, the role of the experimental orientation diminishes, and the reactivity becomes less dependent on V_0. This is a purely kinematic effect. For backwards scattering, the reagent axis should be preferentially oriented along $\hat{k}$. More forward scattering receives contribution from a wider range of $\hat{r} \cdot \hat{k}$ values, fig. 8. As V_0 is varied, one can much more readily affect the distribution of reactive reactants that contribute to backwards scattering. In optical model terminology, at higher b values, corresponding to the more forward scattering, there is a wide range of $\hat{r} \cdot \hat{R}$ values that correspond to a given $\hat{r} \cdot \hat{k}$ value. A summary of our computations for orientated reagents drawn in the manner closest to experimental
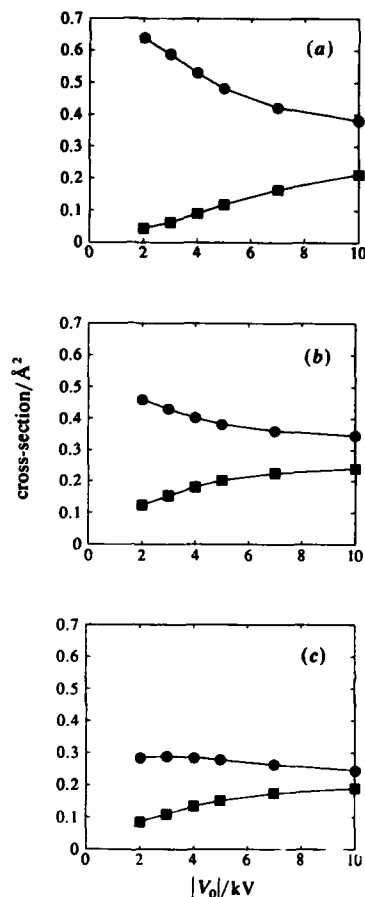
Fig. 12. Kinematic model computations of the reactivity for favourable *vs.* unfavourable orientation of CH_3I for different scattering directions. The angular range of $\cos \theta = \hat{k} \cdot \hat{k}'$ is (*a*) [0.95, 1.00], (*b*) [0.50, 0.55], (*c*) [0.25, 0.30]; ●, $V_0 > 0$; ■, $V_0 < 0$. The largest effect is for $V_0 = \pm 2$ kV. The mean orientation is roughly proportional to $1/V_0$). For backwards scattering, compare with fig. 3 of ref. (95). Note the loss of selectivity for more forward scattering.

results[88,95] is shown in fig. 12. Here, the reactivity is plotted for the 'favorable' *vs.* 'unfavorable' orientations as obtained by reversing the sign of the field. For backwards scattering, reversing the (mean) orientation makes much more of a difference.

Conclusions

Considerable insight into the steric requirements of the $K + CH_3I$ reaction was shown to be provided by the angular distribution in scattering experiments using unoriented reactants. There are several factors which make the $K + CH_3I$ system a particularly favorable example. Foremost is the simple orientation dependence of the barrier to reaction: it is essentially linearly increasing with $1 - \cos \gamma$ (the approach angle) up to a cut-off due to the sudden onset of the steric hindrance by the CH_3 group (fig. 1). There are many other systems with qualitatively similar features. $K + (CH_3)_3CBr$ is an

obvious example. Why the $K + CF_3I$ system[97] is possibly different remains to be better understood. Another class of systems predicted[28] to have strong steric hindrance is the H-atom transfer as in[98] $O + HBr$. Here too, we expect a primarily rebound mechanism. Even the $H + H_2$ exchange reaction has an angular distribution dominated[84] by hard-sphere scattering. Since also for this reaction, the opacity function is determined primarily by the steric requirements,[10] the measured[99] angular distribution should be amenable to similar considerations. It would be of particular interest to examine the reactive scattering of H or of D from HD [*cf.* fig. 4 of ref. (1)].

It is unfortunate that we know of no *ab initio* computation of the orientation dependence of the barrier for the $K + CH_3I$ reaction or any other reaction with steric hindrance. We would like to use this opportunity to invite such computations. On our part, we undertake to make good use of such input.

The examination of the dependence of the scattering cross-section on the orientation of the reagents has brought forth by a now familiar situation: experimentalists measure in the laboratory frame of reference while theorists compute in the molecular frame. The relation between the experimental orientation (measured by $\hat{r} \cdot \hat{k}$) and the theoretical one (measured by, say, $\hat{r} \cdot \hat{R}$) is not one-to-one at all but the lowest impact parameters. A Monte Carlo simulation is probably the simplest way of generating the distribution of theoretical orientations corresponding to a given experiment using oriented reagents. In this way, the apparent loss of steric selectivity[65] for those $K +$ orientated CH_3I collisions that lead to more forward-scattered KI could be accounted for.

References

1 R. B. Bernstein, D. R. Herschbach and R. D. Levine, *J. Phys. Chem.*, 1987, **91**, 5365.
2 M. Karplus and M. J. Godfrey, *J. Am. Chem. Soc.*, 1966, **88**, 5332.
3 N. H. Hijazi and J C. Polanyi, *Chem. Phys.*, 1978, **69**, 150.
4 A. Kafri, R. Kosloff, R. D. Levine and S. Alexander, *Chem. Phys.*, 1976, **13**, 323.
5 I. W. M. Smith, *J. Chem. Educ.*, 1982, **59**, 9; I. W. M. Smith, *Kinetics and Dynamics of Elementary Gas Reactions* (Butterworth, London, 1980).
6 R. D. Levine and R. B. Bernstein, *Chem. Phys. Lett.*, 1984, **105**, 467.
7 R. D. Levine and R. B. Bernstein, *Molecular Reaction Dynamics and Chemical Reactivity* (Oxford University Press, New York, 1987).
8 N. C. Blais, R. B. Bernstein and R. D. Levine, *J. Phys. Chem.*, 1985, **89**, 10.
9 I. Schechter, R. Kosloff and R. D. Levine, *Chem. Phys. Lett.*, 1985, **121**, 297.
10 I. Schechter and R. D. Levine, *Int. J. Chem. Kinet.*, 1986, **18**, 1023.
11 (*a*) N. Agmon, *Chem. Phys.*, 1981, **61**, 189; (*b*) N. Agmon, *Int. J. Chem. Kinet.*, 1986, **18**, 1047.
12 J. Jellinek and E. Pollak, *J. Chem. Phys.*, 1983, **78**, 3014; E. Pollak, *J. Chem. Phys.*, 1985, **82**, 106; N. Abu-Salbi, D. J. Kouri, Y. Shima and M. Baer, *J. Chem. Phys.*, 1985, **82**, 2650.
13 R. B. Bernstein, *J. Chem. Phys.*, 1985, **82**, 3656.
14 R. E. Wyatt, *J. Chem. Phys.*, 1969, **51**, 3489; J. N. L. Connor and M. S. Child, *Mol. Phys.*, 1970, **18**, 653; For the bending-corrected linear model see E. F. Hayes and R. B. Walter, *J. Phys. Chem.*, 1984, **88**, 3318, and references therein.
15 H. Kornweitz, A. Persky and R. D. Levine, *Chem. Phys. Lett.*, 1986, **128**, 443.
16 M. D. Pattengill, R. N. Zare and R. L. Jaffe, *J. Phys. Chem.*, 1987, **91**, 5489.
17 G. T. Evans, R. S. C. Che and R. B. Bernstein, *J. Chem. Phys.*, 1985, **82**, 2258; G. T. Evans, *J. Chem. Phys.*, 1987, **87**, 3865.
18 J. Alvarino and A. Lagana, *J. Phys. Chem.*, 1987, **91**, 5487.

19 H. Loesch, *Chem. Phys.*, 1986, **104**, 213; 1987, **112**, 85.
20 M. H. M. Janssen and S. Stolte, *J. Phys. Chem.*, 1987, **91**, 5480.
21 N. C. Blais and R. B. Bernstein, *J. Chem. Phys.*, 1986, **85**, 7030.
22 Y. R. Luo and S. W. Benson, *J. Phys. Chem.*, 1988, **92**, 1107.
23 J. N. L. Connor and W. Jakubetz, in *Selectivity in Chemical Reactions*, ed. J. C. Whitehead, D. Reidel, Dordrecht, 1988, p. 323
24 R. D. Levine and R. B. Bernstein, *J. Phys. Chem.*, in press.
25 T. Su and M. T. Bowers, *Gas Phase Ion Chemistry*, ed. M. T. Bowers (Academic Press, New York, 1979), Vol. 1, Chap. 3; T. Su and M. T. Bowers, *Int. J. Mass Spectrom. Ion Phys.*, 1975, **17**, 309.
26 R. A. Barker and D. P. Ridge, *J. Chem. Phys.*, 1976, **64**, 4411; D. P. Ridge, in *Structure/Reactivity and Thermochemistry of Ions*, ed. P. Ausloos and S. G. Lias (Reidel, Dordrecht, 1987).
27 D. C. Clary, *Mol. Phys.*, 1984, **53**, 2; 1985, **54**, 605.
28 I. Schechter, R. D. Levine and R. B. Bernstein, *J. Phys. Chem.*, 1987, **91**, 5466.
29 L. Raff and M. Karplus, *J. Chem. Phys.*, 1966, **44**, 1212.
30 R. A. LaBudde, P. J. Kuntz, R. B. Bernstein and R. D. Levine, *J. Chem. Phys.*, 1973, **59**, 6286.
31 M. Karplus, in *Structural Chemistry and Molecular Biology*, ed. A. Rich and N. Davidson (Freeman, 1968).
32 E. F. Greene and J. Ross, *Science*, 1968, **159**, 587.
33 R. B. Bernstein and A. M. Rulis, *Discuss. Faraday Soc.*, 1973, **55**, 293.
34 R. B. Bernstein, in *Recent Advances in Molecular Reaction Dynamics* (Aussois, France, 1985).
35 J. O. Hirschfelder, C. F. Curtiss and R. B. Bird, *Molecular Theory of Gases and Liquids* (Wiley, New York, 1964); See also in particular U. Buck, F. Gestermann and H. Pauly, *Chem. Phys.*, 1980, **50**, 217 and the appendix by W. H. E. Schwartz and B. Pittel therein.
36 (*a*) M. E. Gersch and R. B. Bernstein, *J. Chem. Phys.*, 1972, **56**, 6131; see also (*b*) K. T. Wu, *J. Phys. Chem.* 1979, **83**, 1043.
37 R. N. Zare, *Ber. Bunsenges, Phys. Chem.*, 1982, **86**, 422.
38 M. G. Prisant, C. T. Rettner and R. N. Zare, *J. Chem. Phys.*, 1981, **75**, 2222.
39 I. Schechter, M. G. Prisant and R. D. Levine, *J. Phys. Chem.*, 1987, **91**, 5472.
40 S. E. Choi and R. B. Bernstein, *J. Chem. Phys.*, 1985, **83**, 3656.
41 S. Kais and R. D. Levine, *J. Phys. Chem.*, 1987, **91**, 5462.
42 A. Persky and M. Broida, *J. Chem. Phys.*, 1984, **81**, 4352.
43 A. Persky and H. Kornweitz, *J. Phys. Chem.*, 1987, **91**, 5496.
44 N. Sathyamurthy, *Chem. Rev.*, 1983, **83**, 601.
45 H. R. Mayne, *Chem. Phys. Lett.*, 1986, **130**, 24.
46 H. R. Mayne and S. K. Minick, *J. Phys. Chem.*, 1987, **91**, 1940.
47 J. M. Alvariño and A. Lagana, *Chem. Phys. Lett.*, 1988, **144**, 558.
48 N. Sathyamurthy and J. P. Toennies, *Chem. Phys. Lett.*, 1988, **143**, 323.
49 D. Beck, E. F. Greene and J. Ross, *J. Chem. Phys.*, 1962, **37**, 2895.
50 E. F. Greene, A. L. Moursund and J. Ross, *Adv. Chem. Phys.*, 1966, **10**, 135.
51 R. M. Harris and J. F. Wilson, *J. Chem. Phys.*, 1971, **54**, 2088.
52 D. R. Herschbach, *Adv. Chem. Phys.*, 1966, **10**, 319.
53 R. Grice and D. R. Hardin, *Mol. Phys.*, 1971, **21**, 805.
54 J. L. Kinsey, G. H. Kewi and D. R. Herschbach, *J. Chem. Phys.*, 1976, **64**, 1914.
55 M. Karplus and M. Godfrey, *J. Chem. Phys.*, 1968, **49**, 3602.
56 R. E. Roberts, *J. Chem. Phys.*, 1976, **64**, 3311.
57 P. J. Kuntz, M. H. Mok and J. C. Polanyi, *J. Chem. Phys.*, 1969, **50**, 4623.
58 P. J. Kuntz, *Trans. Faraday Soc.* 1970, **66**, 576.
59 P. J. Kuntz, *Mol. Phys.*, 1972, **23**, 1035.
60 M. T. Marron, *J. Chem. Phys.*, 1973, **58**, 153.
61 M. T. Marron and R. B. Bernstein, *Impulsive Model for Reactive Collisions*, Madison, Wis. TCl report 470 (1972).
62 D. A. Case and D. R. Herschbach, *J. Chem. Phys.*, 1978, **69**, 150.
63 M. G. Prisant, C. T. Rettner and R. N. Zare, *J. Chem. Phys.*, 1984, **81**, 2699.
64 G. M. McClelland and D. R. Herschbach, *J. Phys. Chem.*, 1987, **91**, 5509.
65 D. H. Parker, K. K. Chakravorty and R. B. Bernstein, *Chem. Phys. Lett.*, 1982, **86**, 113.
66 D. H. Parker, K. K. Chakravorty and R. B. Bernstein, *J. Phys. Chem.*, 1981, **85**, 466.
67 J. R. Eirey, E. F. Greene, G. P. Reck and J. Ross, *J. Chem. Phys.*, 1967, **46**, 3295.
68 S. E. Choi and R. B. Bernstein, *J. Chem. Phys.*, 1985, **83**, 4463.
69 J. Ross and E. F. Greene, in *Molecular Reaction Kinetics*, ed. Ch. Schlier (Academic Press, New York, 1971).
70 R. D. Levine, *Quantum Mechanics of Molecular Rate Processes* (Clarendon Press, Oxford, 1969).
71 I. Rusinek and R. E. Roberts, *Chem. Phys.*, 1973, **1**, 392.
72 C. A. Coulson and R. D. Levine, *J. Chem. Phys.*, 1967, **47**, 1235.
73 R. D. Levine and R. B. Bernstein, *J. Chem. Phys.*, 1972, **56**, 2281.

74 H. E. Litvak, A. Gonzalez Ureña and R. B. Bernstein, *J. Chem. Phys.*, 1974, **61**, 4091.
75 K. T. Wu, H. F. Pang and R. B. Bernstein, *J. Chem. Phys.*, 1978, **68**, 1064.
76 D. L. Bunker and E. A. Goring-Simpson, *Faraday Discuss. Chem. Soc.*, 1973, **55**, 93.
77 R. M. Harris and D. R. Herschbach, *Faraday Discuss. Chem. Soc.*, 1973, **55**, 233.
78 B. C. Eu, *J. Chem. Phys.*, 1974, **60**, 1178; *Chem. Phys.*, 1974, **5**, 95.
79 H. Kaplan and R. D. Levine, *Chem. Phys. Lett.*, 1976, **39**, ███; *J. Chem. Phys.*, 1975, **63**, 5064.
80 A. Cabello and A. G. Ureña, *Chem. Phys. Lett.*, 1975, **35**, 255.
81 H. K. Shin, *Chem. Phys. Lett.*, 1975, **34**, 546.
82 M. Menendez, L. Bañares, J. Alonso and A. Gonzalez Ureña, *Chem. Phys.*, 1988, **120**, 273.
83 A. G. Ureña, *Adv. Chem. Phys.*, 1987, **56**, 213.
84 G. H. Kwei and D. R. Herschbach, *J. Phys. Chem.*, 1979, **83**, 1550.
85 G. H. Kwei, J. A. Norris and D. R. Herschbach, *J. Chem. Phys.*, 1970, **52**, 1317.
86 A. M. Rulis and R. B. Bernstein, *J. Chem. Phys.*, 1972, **57**, 5497.
87 D. S. Y. Hsu, G. M. McClelland and D. R. Herschbach, *J. Chem. Phys.*, 1974, **61**, 4927.
88 R. J. Beuhler Jr and R. B. Bernstein, *J. Chem. Phys.*, 1969, **51**, 5305.
89 I. R. Elsum and R. G. Gordon, *J. Chem. Phys.*, 1982, **76**, 3001.
90 F. T. Smith, *J. Chem. Phys.*, 1959, **31**, 1352.
91 J. O. Hirschfelder, *Int. J. Quant. Chem.*, 1969, **IIIS**, 17.
92 A. Kafri, E. Pollak, R. Kosloff and R. D. Levine, *Chem. Phys. Lett.*, 1975, **33**, 201.
93 C. Maltz, N. D. Weinstein and D. R. Herschbach, *Mol. Phys.*, 1972, **24**, 133.
94 D. A. Case and D. R. Herschbach, *Mol. Phys.*, 1975, **30**, 1537.
95 S. Stolte, K. K., Chakravorty, R. B., Bernstein and D. H. Parker, *Chem. Phys.*, 1982, **71**, 353.
96 S. Stolte, *Ber. Bunsenges. Phys. Chem.*, 1982, **86**, 413.
97 P. R. Brooks, *Science*, 1976, **193**, 11.
98 K. G. McKendrick, D. J. Rakestraw and R. N. Zare, *Faraday Discuss. Chem. Soc.*, 1987, **84**, ███.
99 R. Götting, H. R. Mayne and J. P. Toennies, *J. Chem. Phys.*, 1986, **85**, 6396.

Stereochemical Influences in Atom–Triatomic Collisions

Zeyad T. Alwahabi, Carmel G. Harkin, Anthony J. McCaffery*
and Benjamin J. Whitaker

School of Molecular Sciences, University of Sussex, Brighton BN1 9QJ

High-resolution dispersed fluorescence spectra from NH_2 in the electronically excited $\tilde{A}\,^2A_1$ state have been obtained. Single quantum-state excitation using a tunable ring dye laser was employed and rotational energy transfer (RET) in the excited vibronic manifold was studied. Analysis shows that angular momentum based propensity rules are much more successful at predicting RET relaxation rates than are those based on the energy transfer. The results are interpreted with reference to the molecule-fixed axis system, and this allows us to work backwards to the incoming particle trajectory. Thus we obtain information about the stereochemistry of the $NH_2\,(^2A_1)+H$ interaction.

Collisionally induced transitions between the rotational levels of small molecules, particularly diatomics, have been extensively studied in recent years.[1,2] Of particular interest to us have been the attempts to formulate simple expressions for rates of rotational energy transfer (RET).[3-6] The motivation for this lies in the ubiquitous nature of rotational relaxation in gas dynamics, and that an understanding of many important processes, for example cluster nucleation, requires the ability to calculate rotational relaxation rates quickly and efficiently. Full quantum-mechanical calculations are time-consuming and expensive, even for diatom–atom scattering, owing to the rapid computational explosion as the number of open rotational channels increases. Approximations, such as the infinite-order sudden (IOS), which decouple the scattering equations, have been very successful in predicting 'scaling' laws for RET.[7] More recently several semiempirical 'fitting' laws have been proposed,[3-6] and there has been considerable speculation as to their physical origin.[8] In particular it has been suggested that angular momentum constraints may be more important than energetic constraints.[9] In diatom–atom systems, however, this distinction is not clear cut since the transferred energy, $|\Delta E|$, scales as the transferred angular momentum, $|l|$, and thus the question was unresolved until now.

The study of atom–triatomic molecule collisions offers several interesting new possibilities which offset the obvious additional complexities in spectra and intermolecular potential. The most important of these is the existence of molecule fixed projections of the rotational angular momentum that are spectrally resolvable. In a bent triatomic or asymmetric-top molecule the rotational energy levels form stacks associated with the angular momentum, N, and its projection onto two of the molecular axes. Although the internal projections are not simultaneously rigorous quantum numbers, they do form a very valuable basis for spectroscopic identification and more relevantly here, for visualising the molecular dynamics of scattering experiments.

Using high-resolution spectroscopic selection and detection techniques it is straightforward to isolate collisional processes which change the angular momentum vector and only one of the internal projection quantum numbers. In this way one is in effect sampling planar slices of the intermolecular potential. Thus experimentally one may isolate different aspects of the intermolecular potential by the simple device of fully spectroscopically resolving the initial and final states.

The particular system we have chosen to study is that of $NH_2 + H$. Aside from the intrinsic interest in NH_2 for the role it plays in atmospheric, interplanetery and combustion chemistry the radical is also an archetype of the Renner–Teller interaction. Thus NH_2 is unusual and spectroscopically complicated. Two particular points are important here. First, because NH_2 is a radical, the electronic states involved in the transitions of interest are both doublets and thus each rotational level is split through the effect of the spin-rotation interaction. An important consequence is that for open-shell collision partners we are faced with scattering on two distinct surfaces (singlet and triplet). Secondly, NH_2 is an asymmetric rotor, and consequently, as briefly discussed above, the rotational levels are split into a number $(2N+1)$ of sub-levels which depend on the relative orientation of the angular momentum vector to the molecule-fixed axis system. These states are usually labelled $N_{k_a k_c}$, where k_a and k_c refer to the projection of the angular momentum (excluding spin) onto the a and c axes of the molecule. We will see later that this will have important consequences when we consider rotational energy transfer between these levels.

The difficult and complex problem of collisional energy transfer of an open-shell molecule with an open-shell atom was first tackled by Shapiro and Kaplan[11] for the $OH + H$ system, and for the $NH_2 + H$ system by Dixon and Field.[12] In the latter paper rotational relaxation rates were interpreted in terms of the distorted-wave Born approximation which gave a semiquantitative fit to their experimental data.[13] Rotationally resolved fluorescence intensities were used to obtain relative rates of transfer from initially populated levels. Propensities such as: $|\Delta N| \leqslant 2$, and $\Delta k_a = 0, 2$ (with $\Delta k_a = 0$ for $\Delta N = 2$) were observed for the $NH_2 + H_2/He$ system.† A correlation between the spin of the initially populated state and the collisionally populated state was observed for the *ortho* states, and consequently H atoms were thought by these authors to be the dominant collision partner. In contrast He atoms were thought to be responsible for collisional transfer between the *para* states. Subsequent time-resolved experiments,[14] verified the $|\Delta N| \leqslant 2$ propensity rule and suggested that cascading (multiple collisions) might be responsible for the larger ΔN changes.

Somewhat earlier Kroll[15] had also observed energy transfer between the rotational levels in the $^2A_1$ state of NH_2. Although the collision partner was unspecified, Kroll found a significant retention of molecular orientation, in the laboratory-axis frame, after RET. A more systematic study at higher resolution of this polarisation transfer was later undertaken in our laboratory,[16,17] the results of which were interpreted in terms of an extended version of the perturbation treatment proposed by Dixon and Field.[12]

Experimental

The experimental arrangement is illustrated in fig. 1. NH_2 (amidogen) radicals were produced in a flow-reactor following the reaction of H atoms with hydrazine (N_2H_4). The reaction chamber consisted of a quartz discharge tube and a Pyrex flow-line equipped with gas inlet jets and observation/excitation ports fitted with fused silica windows. The observation cell was arranged so that laser-induced fluorescence could be detected either orthogonally to, or coaxially with, the excitation axis. The discharge tube and flow-line were etched with *ca.* 15% hydrofluoric acid for *ca.* 25 min prior to use in order to diminish radical destruction on the walls. The reactor was pumped by means of a double-stage rotary pump with a displacement of $80 \, m^3 h^{-1}$ (Edwards model E2M 80). The H atoms were produced by microwave discharge at 2.45 GHz (Microtron model 200). In our initial experiments a gas mixture of H_2 in He (with a dilution of *ca.* 1:5) was used; however, in later experiments the H_2/He mix was replaced by water vapour, where it was found to produce more controllable experimental conditions and allowed

† NH_2 can be produced by the reaction of hydrazine with the products of a microwave discharge in H_2/He.
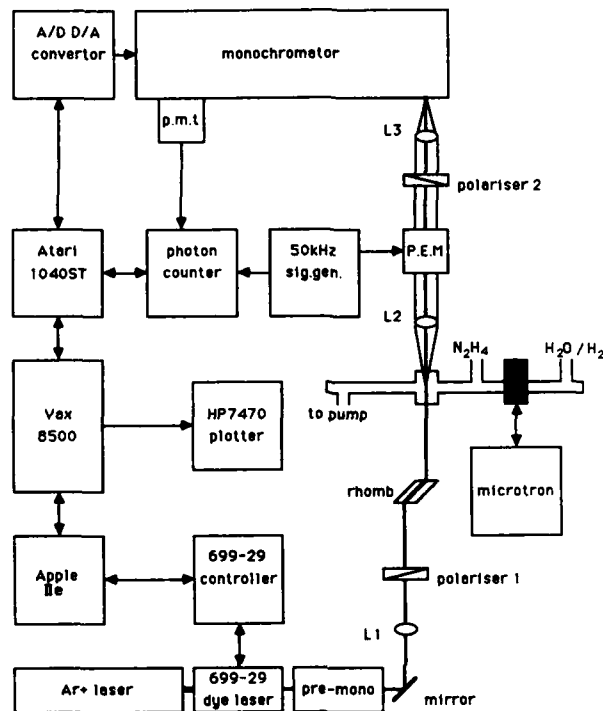
Fig. 1. The experimental set-up.

us to work at lower pressures. In both cases the total pressure in the flow line, as measured by a capacitance transducer downstream of the reaction zone (MKS Baratron model 222), was 1.5–2.0 Torr† for the H_2/He mix and *ca.* 0.6 Torr with water vapour. Hydrazine, 98% pure as supplied by Aldrich, was contained in a glass ampoule from where it was fed to the reactor inlet jet *via* PTFE tubing. The flow was controlled by a needle valve.

The reaction of H atoms with N_2H_4 results in hydrogen abstraction:

$$H + N_2H_4 \rightarrow H_2 + N_2H_3.\tag{1}$$

The NH_2 radicals are believed to be produced by subsequent reactions of the N_2H_3 radicals with H atoms.[18,19] A green flame is observed at the contact point which was found, on spectroscopic analysis, to be due to N_2^*, and probably arises from the recombination reaction of NH radicals. The NH radicals are in turn most probably the result of NH_2 recombination to yield NH and ammonia.

The output from a continuous-wave tunable dye laser (Coherent model 699-29) was directed so as to cross the flow tube *ca.* 10cm downstream of the hydrazine inlet jet. The dye laser is controlled by a microcomputer (Apple IIe) which is connected to an integral wave-meter assembly. Thus it is possible to control the absolute wavelength of the laser to 4 parts in 10^7 (±0.007 cm^{-1}). The spectral width of the dye laser (*ca.* 0.0003 cm^{-1}) was two orders of magnitude smaller than the Doppler width of NH_2

---

† 1 Torr = 101 325/760 Pa.

under our experimental conditions (0.054 cm^{-1} at 300 K). Transitions to the $(0, 9, 0)$ and $(0, 10, 0)$ vibrational manifolds of the $\tilde{A}\,^2A_1$ first electronically excited state from the $(0, 0, 0)$ manifold of the $\tilde{X}\,^2B_1$ ground state lie in the tuning range of rhodamine 6G. Excitations to individual rotation levels were assigned by monitoring the total laser-induced fluorescence using a photodiode attached to one of the optical windows of the observation cell, and scanning the frequency of the dye laser. Line positions were found to be in very good agreement with the published tables of Dressler and Ramsey.[20] The narrow linewidth of the laser allowed excitation into *each* spin component of any given rotational level, $J = N \pm 1/2$, in turn.

Once a transition had been assigned the fluorescent light was collected by a lens and dispersed through a $\frac{3}{4}$ m double-grating Czerny-Turner monochromator (Spex model 1402). The gratings of this instrument were replaced with ones of 1800 grooves mm^{-1} giving a dispersion of 4 Å mm^{-1}. The dispersed fluorescence fell onto a Peltier cooled photomultiplier turbe (EMI 9863B/100: S20 spectral response) and was detected by photon counting electronics (Brookdeal model 5C1). The photon counter and mono-chromator were interfaced to a micro-computer (Atari model 1040ST) which collected and stored the dispersed spectrum.

Two different experimental geometries were used in this study. In order to detect the degree of circular polarisation, $C = (I_+ - I_-)/(I_+ + I_-)$, the fluorescence was measured coaxially to the laser-beam propogation axis. In this case the output from the dye laser was first directed through a prism monochromator (Anaspec model 300S) to remove any background dye laser fluorescence before being passed through a linear polariser and then a Fresnel rhomb. The resultant circularly polarised light was then focused into the flow-reactor through one of the optical windows. The resultant fluores-cence was collimated with an $f\,1.5$ lens and passed through a photoelastic modulator (Morvue model PEMSF4) driven at 50 kHz and an analysing polariser before being focused onto the entrance slits of the monochromator. Further details can be found elsewhere;[21] however, the net result of this arrangement is to produce a modulated signal at the detector such that in one arm of the modulation cycle the signal is proportional to I_+, while in the other it is proportional to I_-. The photon counter can be operated in synchronous sampling mode so that these two signals could be recorded separately and the sum and difference easily computed and displayed.

In the second experimental arrangement the degree of linearly polarised fluorescence, $P = (I_\parallel - I_\perp)/(I_\parallel - I_\perp)$, could be obtained. In these experiments the Fresnel rhomb and premonochromator were removed from the optical train, and the fluorescence was collected orthogonally to the excitation axis. The driving frequency of the PEM was also changed to 100 kHz to provide full-wave polarisation modulation. An additional advantage of this optical arrangement was that it was possible to observe the resonance fluorescence.

One final experimental consideration is that as a free radical the molecular g factor is quite large and Hanle depolarisation of the fluorescent light by magnetic fields is easily observable for modest field strengths (*ca.* 0.5 mT).[22] In order to guard against these effects a set of three pairs of Helmholtz coils (average diameter 30 cm) were constructed around the observation cell. The field at the centre of the coils was measured with a magnetometer (Schonstedt Instruments model DRM1) and nulled to $\pm 1\,\mu\text{T}$ by varying the current in each pair of coils independently. In point of fact, for our particular laboratory orientation, the effects of the earth's magnetic field on the polarisation of the laser induced emission appear to be negligible.[23]

Results

We have studied rotational energy transfer between a large number of states in the $(0, 9, 0)$ and $(0, 10, 0)$ vibrational manifolds of the $\tilde{A}\,^2A_1$ state of NH_2 and NHD. Here

we wish to present results for excitation into the $(0, 9, 0)$ Σ stack (*i.e.* states with $k_a = 0$), where we have made a systematic study of the relative rates of population, orientation and alignment transfer as functions of initially excited quantum number (including electron spin), and nuclear-spin symmetry. A typical dispersed fluorescence spectrum is shown in fig. 2. The signal-to-noise ratio on some of the resonance lines is greater than $3000:1$. In general line strengths for excitation into the *ortho* levels are three times stronger than for the *para* levels because of the nuclear-spin statistics. As can be seen from the spectrum the spin-splitting in the Δ levels (*i.e.* $k_a = 2$) is well resolved, while for fluorescence from the Σ states, where the splitting is *ca.* $0.2\ \mathrm{cm}^{-1}$, typically only a single line is visible owing the limited instrument resolution (*ca.* $0.3\ \mathrm{cm}^{-1}$).

The results for population transfer are presented in tables 1–3. The tabulated results were divided into two sets according to whether the rotational transfer is to a state in the same k_a stack or crosses stacks. For each initial level $N_{k_a k_c}$ two sets of data are presented according to the initially excited spin component (except for the case of excitation into the 0_{00} level, where there is only one spin level). In order to obtain relative transfer rates from the fluorescence spectra the spectral line intensities must be taken into account. The computer program ASYMROT of Birss and Ramsey[25] was used to calculate the transition strengths, from which we deduced the relative populations of the collisionally excited levels.

The concurrent use of polarised light allows us to select simultaneously both space- and mole-fixed axes. This comes about because polarised light will selectively excite the (degenerate) magnetic sub-levels of the selected rotational state, creating a distribution which for single-photon excitation is completely described by its first three Legendre moments. The state multipole moments are known as population, orientation and
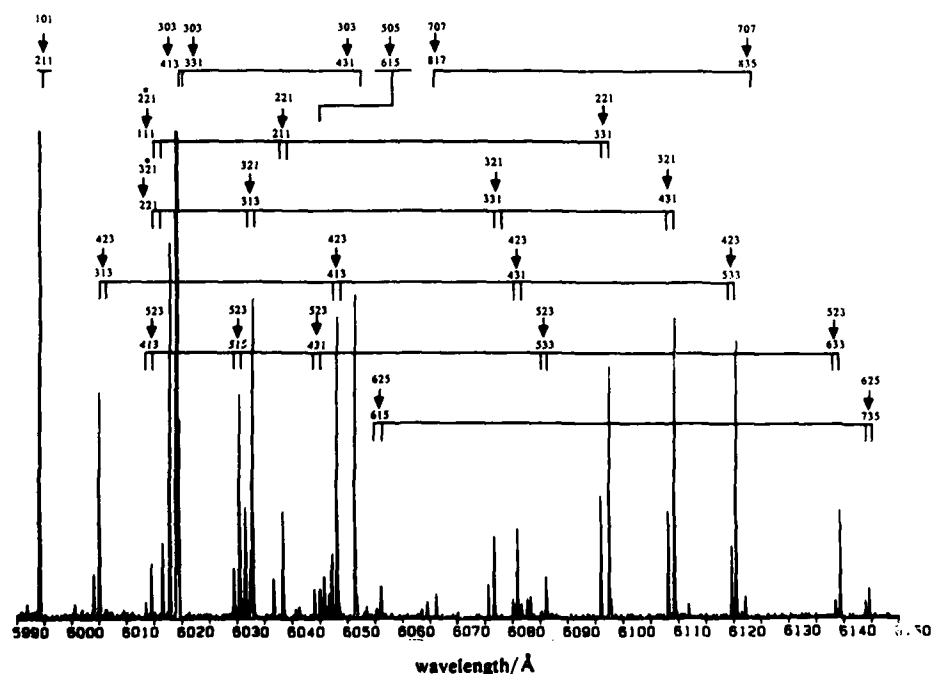
Fig. 2. Typical spectrum showing the dispersed fluorescence following excitation of the $(^2A_1)(0, 9, 0)3_{03}(J = 3.5)$ level from $(^2B_1)(0, 0, 0)3_{13}$.

Table 1. Relative populations for intra Σ stack and inter $\Sigma \rightarrow \Delta$ rotational energy transfer following P excitation of the 0_{00} level of the $^2A_1$ state

excitation $0_{00} \leftarrow 1_{10}$	radiative transition $^2A_1-^2B_1$	$\|l\|/\hbar$	$\Delta E/\mathrm{cm}^{-1}$	relative population $J_{ex} = 0.5$
Σ stack	$0_{00}-1_{10}$	0.00	0.00	1.000
	$2_{02}-3_{12}$	2.45	54.26	0.137
	$4_{04}-5_{14}$	4.47	181.78	0.018
Δ stack	$2_{20}-1^{10}$	2.45	−99.75	0.130
			−104.25	0.050
	$3_{22}-2_{12}$	3.46	−43.03	0.030
			−46.33	0.020
	$4_{22}-3_{12}$	4.47	30.36	0.025
			27.41	0.020

The relative populations of the collisionally populated states have been deduced from the line strengths of the observed transitions. Fitting these data against $|l|$ using eqn (3) gives: $a = 0.97$, $b = -0.97$, $R = -0.97$. The exponential-gap law, $k_{N'_{k_a k_c} \rightarrow N'_{k_a k_c}} = a \exp(-b|\Delta E|)$, gives: $a = 0.14$, $b = -0.011$, $R = -0.43$, where a and b are the free parameters and R is the correlation coefficient.

alignment. Experiments with circularly polarised light are mainly sensitive to the orientation, while linearly polarised light predominately probes the alignment. The linear polarisation ratios for transfer out of the 2_{02} state are given in table 4. In table 5 we show the results for circular polarisation following transfer out of the 3_{03} level.

Discussion

The rotational energy levels in the $(0, 9, 0)$ vibrational manifold of $^2A_1$ of NH_2 are shown schematically in fig. 3, in which the spin splittings have been much exaggerated, although the ordering of the states is correct. Now referring to fig. 3 it is apparent, for example, that the 5_{23} level lies close to the 3_{03} level, in fact the energy gap is only $14\ \mathrm{cm}^{-1}$. If

Table 2. As for table 1, but for Q excitation of 1_{01}

excitation $1_{01} \leftarrow 1_{11}$	radiative transition $^2A_1-^2B_1$	$\|l\|/\hbar$	$\Delta E/\mathrm{cm}^{-1}$	relative population $J_{ex} = 0.5$	relative population $J_{ex} = 1.5$
Σ stack	$1_{01}-2_{11}$	0.00	0.00	1.000	1.000
	$3_{03}-4_{13}$	2.13	90.75	0.084	0.080
Δ stack	$2_{21}-3_{31}$	2.00	−117.52	0.070	0.060
			−122.12	0.100	0.106
	$3_{21}-4_{31}$	2.60	−62.24	0.036	0.025
			−65.71	0.049	0.057
	$4_{23}-5_{33}$	3.27	13.79	0.011	0.015
			11.05	0.016	0.023
	$5_{23}-6_{33}$	4.21	106.17	0.009	0.005
			103.34	0.007	0.007

Fitting these data against $|l|$ using eqn (3) gives for $J_{ex} = 1.5$: $a = 1.01$, $b = -1.15$, $R = -0.99$, and for $J_{ex} = 0.5$: $a = 1.03$, $b = -1.20$, $R = -0.99$. The exponential-gap law gives for $J_{ex} = 1.5$: $a = 0.16$, $b = -0.014$, $R = -0.42$, and for $J_{ex} = 0.5$: $a = 0.15$, $b = -0.016$, $R = -0.44$.

Table 3. As for table 1, but for Q excitation of 3_{03}

excitation $3_{03} \leftarrow 3_{13}$	radiative transition ${}^2A_1-{}^2B_1$	$\|l\|/\hbar$	$\Delta E/\text{cm}^{-1}$	relative population $J_{ex} = 2.5$	relative population $J_{ex} = 3.5$
Σ stack	$1_{01}-2_{11}$	2.13	−90.75	0.270	0.250
	$3_{03}-4_{13}$	0.00	0.00	1.000	1.000
	$5_{05}-6_{15}$	2.21	164.37	overlapped	0.140
	$7_{07}-8_{17}$	4.10	405.57	0.002	0.003
Δ stack	$2_{21}-3_{31}$	2.92	−208.27	0.040	0.070
			−212.87	0.080	0.060
	$3_{21}-4_{31}$	2.97	−152.99	0.030	0.090
			−156.46	0.080	0.070
	$4_{23}-5_{33}$	2.20	−76.96	0.019	0.072
			−79.70	0.065	0.042
	$5_{23}-6_{33}$	3.11	15.42	0.009	0.023
			12.59	0.020	0.010
	$6_{25}-7_{35}$	4.5	136.37	0.001	0.009
			133.92	0.005	0.010

Fitting these data against $|l|$ using eqn (3) gives for $J_{ex} = 3.5$: $a = 1.10$, $b = -1.13$, $R = -0.90$, and for $J_{ex} = 2.5$: $a = 1.16$, $b = -1.21$, $R = -0.92$. The exponential-gap law gives for $J_{ex} = 3.5$: $a = 0.13$, $b = -0.006$, $R = -0.35$, and for $J_{ex} = 2.5$: $a = 0.12$, $b = -0.007$, $R = -0.34$.

energetic considerations were dominant one would expect efficient energy transfer on collision between these two states, since the cell temperature in our experiments, as determined from lineshape analysis, is 300 K. Examination of table 3, which presents the data for excitation into the 3_{03} spin doublets, shows that this is not the case. In fact the relative populations of the 5_{23} spin states are *ca.* a factor of four smaller than those of the 2_{21} states, which lie *ca.* 210 cm^{-1} from the laser-populated level. This is not simply an isolated example. Exponential-gap law[24] plots for all the population-transfer data presented in the tables show very poor linear correlation coefficients (see table captions), and clearly some other mechanism is at work.

Some insight into what is going on may be gleaned from the study of Orlikowski and Alexander of rotational energy transfer between the spin–orbit states of NO following collisions with Ar atoms.[26] As with NO in NH$_2$ one is faced with several stacks of rotational states within any given vibrational manifold; in the case of NO these are the

Table 4. Linear polarisation ratios following Q excitation of 2_{02}

excitation $2_{02} \leftarrow 2_{10}$	radiative transition ${}^2A_1-{}^2B_1$	$l/\hbar$	$\Delta E/\text{cm}^{-1}$	linear polarisation $J_{ex} = 1.5$	linear polarisation $J_{ex} = 2.5$
Σ stack	$0_{00}-1_{10}$	2.45	−54.26	0.25 ± 0.09	1.78 ± 0.05
	$2_{02}-2_{12}$	0.00	0.00	18.67 ± 0.84	24.25 ± 2.8
Δ stack	$2_{20}-2_{12}$	2.83	−154.00	2.25 ± 2.1	2.47 ± 2.3
	$3_{22}-3_{12}$	2.08	−97.29	0.86 ± 0.05	4.51 ± 1.4
	$3_{22}-3_{30}$	2.08	−98.49	4.25 ± 2.8	6.95 ± 2.2
	$4_{22}-4_{32}$	2.86	−22.46	6.24 ± 1.9	11.12 ± 2.4
	$4_{22}-4_{14}$	2.86	−23.90	6.27 ± 0.5	3.75 ± 1.6

Note that the ratios here are given in %, and not as defined in the text. Data are only presented for fluorescence from the same spin state as J_{ex}.

Stereochemical Influences in Atom-Triatomic Collisions

Table 5. Circular polarisation ratios for R excitation of 3_{03}

excitation $3_{03} \leftarrow 2_{11}$	radiative transition $^2A_1-^2B_1$	$l/\hbar$	$\Delta E/cm^{-1}$	circular polarisation $J_{ex} = 2.5$	circular polarisation $J_{ex} = 3.5$
Σ stack	$1_{01}-1_{11}$	2.13	-90.75	10.6 ± 2.50	15.2 ± 3.50
	$1_{01}-2_{11}$	2.13	-90.75	8.3 ± 2.00	11.6 ± 2.00
	$3_{03}-3_{31}$	0.00	0.00	16.6 ± 2.5	29.6 ± 4.0
	$3_{03}-4_{13}$	0.00	0.00	-13.1 ± 1.0	-10.4 ± 0.7
	$3_{03}-3_{13}$	0.00	0.00	16.8 ± 0.50	19.5 ± 0.50
Δ stack	$2_{21}-1_{11}$	2.92	-210.50	13.04 ± 2.0	23.6 ± 3.0
	$2_{21}-2_{11}$	2.92	-210.50	overlapped	20.6 ± 0.4
	$3_{21}-3_{13}$	2.97	-154.71	15.4 ± 0.2	13.5 ± 0.4
	$4_{23}-4_{13}$	2.20	-77.56	overlapped	15.2 ± 0.2
	$4_{23}-3_{13}$	2.20	-77.56	19.4 ± 2.5	24.2 ± 0.6

Ratios are given in %. Data are only presented for fluorescence from the same spin state as J_{ex}.

two spin-orbit states separated by 123 cm^{-1}, in NH_2 these are the Renner-Teller-coupled k_a states (Σ, Δ *etc.*). The authors were able to derive scaling laws for the intra- and inter-stack energy transfer in NO based on the properties of the angular momentum coupling coefficients which showed that for transfer between spin-orbit states, at least, vector-coupling considerations dominated energetic considerations.

For NH_2, as for any asymmetric rotor, the angular momentum vector of the nuclear frame can be projected onto any two of the molecular axes, and the magnitude of the angular momentum transferred on collision, $|l|$, will not scale simply with $|\Delta E|$ as it does in diatomic molecules. This is illustrated in fig. 4. The diagram illustrates the case
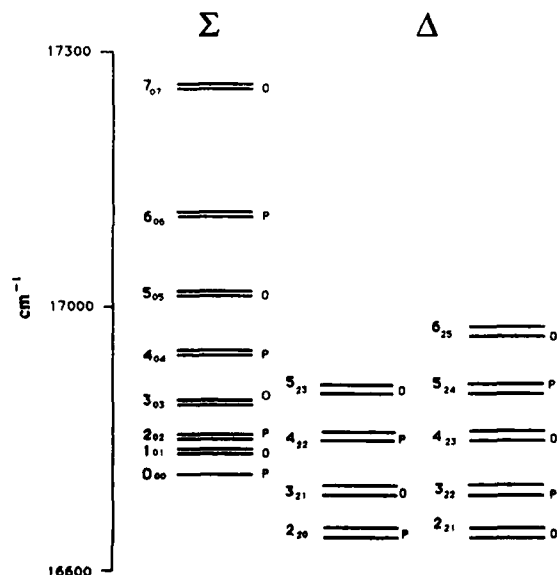
Fig. 3. Energy-level diagram for the Σ and Δ states of NH_2 in the $(0,9,0)$ vibrational manifold of the $^2A_1$ state.
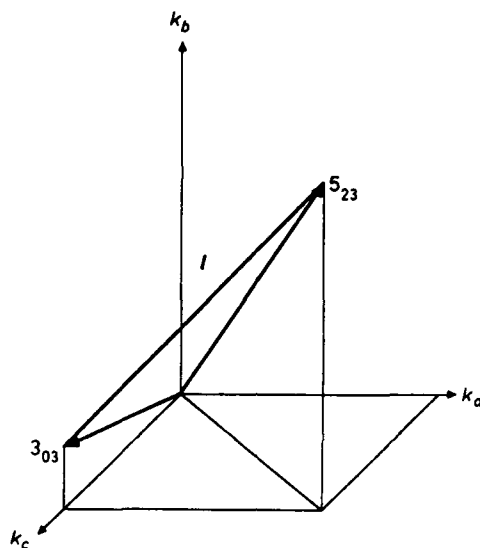
Fig. 4. The molecular-fixed projections of the 3_{03} and 5_{23} level. The vector l is the transferred angular momentum.

discussed above, that is collisional transfer from $3_{03} \rightarrow 5_{23}$. The collisionally transferred angular momentum can be obtained from geometrical considerations, and is given by:

$$l^2 = -2(N^2 + N - k_a^2 - k_c^2)^{1/2}(N'^2 + N' - k_a'^2 - k_c'^2)^{1/2}$$
$$+ N^2 + N - 2k_a k_a' - 2k_c k_c' + N'^2 + N'. \tag{2}$$

Since the energy-gap law gives a poor fit to rate constants for transferred population it is of interest to see how these scale with the transferred angular momentum, $|l|$. In contrast to the case for transferred energy, scaling with transferred angular momentum, according to an inverse exponential law,

$$k_{N_{k_a k_c} \rightarrow N'_{k_a' k_c'}} = a \exp{(-b|l|)} \tag{3}$$

is found to give an excellent fit to a wide range of data. The correlation coefficients for this law are given in the tables. All the data presented here can be accounted for with the parameters $a = 1.06 \pm 0.07$ and $b = 1.13 \pm 0.08$ with a reduced χ^2 of 0.3. However, an additional point needs to be made. In the analysis we have only considered data for like spin doublet components. That is if the state $J = N + \frac{1}{2}$ was excited we have tried only to fit data for transfer to the state $J' = N' + \frac{1}{2}$ and *vice versa* (for intra Σ stack transfer, where relative transfer rates of the spin components cannot be resolved, we have simply assumed that $\Delta M_S = 0$ makes the dominant contribution). When the electron spin is explicitly included the calculation of $|l|$ does not correctly predict the spin-branching transfer. This result can only be explained in terms of a spin-correlated interaction potential (*i.e.* an open-shell collision partner). The fact that the results are independent of the source H atoms indicates that hydrogen is the dominant collision partner in both *ortho* and *para* levels.

Using a hard-sphere approximation *ca.* 20 collisions would be expected during the radiative lifetime (*ca.* 10 μs^{27}) of excited NH_2; in fact, rather more than this are likely to occur since the cross-section for rotational de-excitation will be somewhat larger than

gas kinetic. It may therefore be argued that our experiment does not give nascent rotational distributions, but the result of cascading as suggested by Dearden *et al.*[14]

For a number of reasons we do not believe that we are observing multiple collisions. The first of these may be found by examing the NH_3 surface, illustrated in fig. 5. Recent calculations[28] are in very good agreement with experiment,[29] and the surface is believed to be very accurate. An important feature of the surface is the existence of a conical intersection for H atoms approaching along the b axis of $^2A_1$ NH_2. The N—H distance at which the cusp occurs is highly dependent on the H—N—H bond angle. The situation illustrated in fig. 5 is for HNH = 120°. For linear NH_2 the $^2A_1$ and $^2B_1$ states are degenerate (correlating to a $^2\Pi$ state) and the conical intersection occurs at $r_{N-H} = \infty$. The vibrational period of the $(0, 9, 0)$ states is estimated, assuming no anharmonicity, to be *ca.* 6 fs, which is two orders of magnitude smaller than the flight time of an H atom at 3 ·) K through a 1 nm diameter interaction zone (400 fs), so that during the interaction the H atom will sample many different forms of the surface, and is highly likely to meet the cusp. The rapidly changing topology of the $NH_2 + H$ surface is an unusual situation (quite unlike the interaction potential of a vibrating diatomic and an atom). Classical trajectory studies by Dixon[30] show efficient quenching on the $(^2A_1)NH_2 + H$ surface, so it is likely that the majority of collisions transfer molecules non-radiatively into ground-state species either reacting to form NH_3 or quenching to $(^2B_1)NH_2$. This would leave in the excited state just those molecules that have undergone essentially single-collision events.

Further evidence for this proposal comes from our polarisation data. The polarisation of the emitted light observed in the resonance lines is near to theoretical, and significant polarisation is observed in the transferred features (see tables 4 and 5). These observations are obviously inconsistent with a large number of collisions per excited state lifetime. Furthermore, the polarisation ratio appears to increase as the pressure in the cell increases.

What is unique about scattering studies of asymmetric rotors is the ability to back-project to the sub-set of trajectories, in the molecular frame, responsible for a

r_{N-H}/bohr
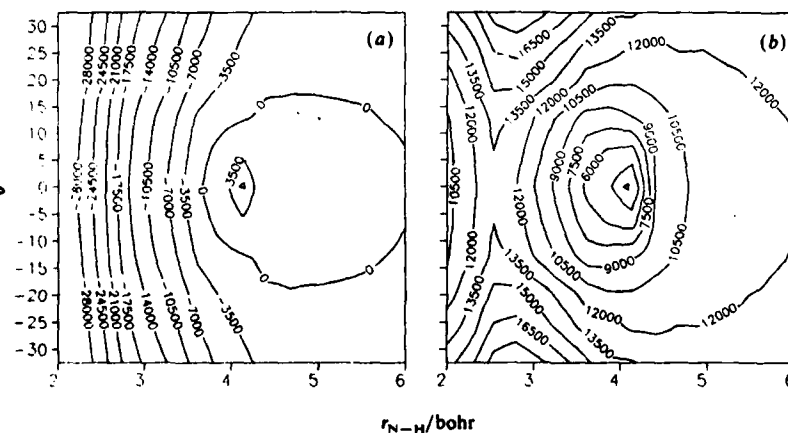
Fig. 5. The potential energy surfaces for the A (a) and X (b) states of ammonia. Contour levels are in cm^{-1} from the ground $(^2B_1)$ state of NH_2 drawn from the data of ref. (28). The NH_2 fragment is taken to have a bond angle of 120° and a bond length of 2.0 bohr. The angle θ is relative to the plane spanned by the NH_2 group. The triangle marks the point of conical intersection between the two surfaces.

particular transition. The correlation between l and the rotational relaxation rate is important because, being a vector quantity, the transferred angular momentum has direction as well as magnitude. Consequently in a collision between an H atom and an amidogen radical which results in RET with a given vector l a unique trajectory (or at least a sub-set of trajectories) can be ascribed to the incoming atom. Thus the experiment is capable of giving direct and accurate information on the fundamental stereochemistry of the interaction.

Molecules in the Σ stack are rotating about the c axis. Collisions with H atoms moving in the a-b plane will lead to intra-stack transfer, while collisions with atoms moving predominantly in the b-c plane will lead to inter-stack ($\Sigma \to \Delta$) transfer (see fig. 6). Unfortunately we do not know the topology of the surface for approach in the b-c plane. Some of our data, however, show that these latter collisions are more depolarising than those in the a-b plane, although not consistently so. The evidence from the population-transfer study indicates that there is essentially no difference between the rates of inter- and intra-stack transfer; however, there is some evidence to show that the spin-branching ratio is larger for inter-stack transfer, which we tentitively propose might be explained by the triplet surface lying closer to the singlet in the b-c plane. Further work is in progress, particularly with regard to the interpretation of the polarisation data.
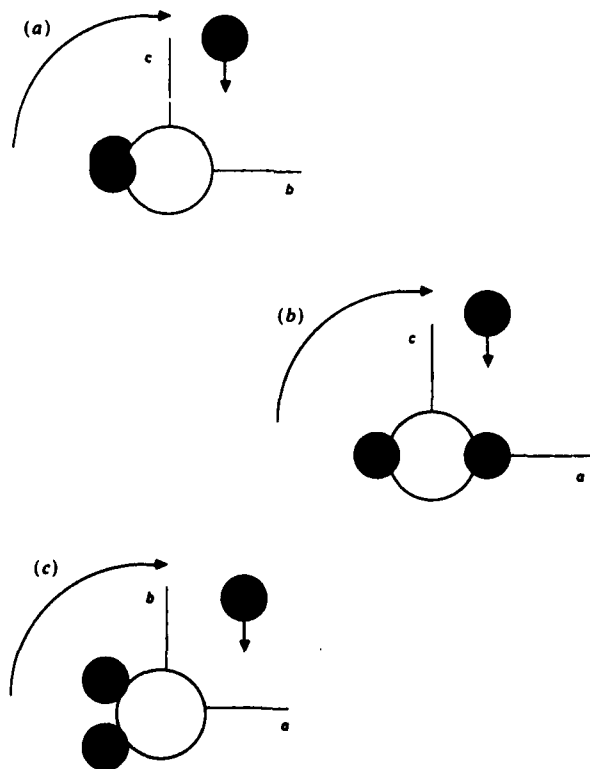
Fig. 6. The stereochemistry of the $(^2A_1)NH_2 + H$ as probed by laser-induced fluorescence. (a) N, k_a-changing collisions (rotation in the b-c plane about the a axis). (b) N, k_a, k_c-changing collisions (rotation in the a-c plane about the b axis). (c) N, k_c-changing collisions (rotation in the a-b plane about the c axis).

Conclusions

Asymmetric-top molecules have a unique role to play in collision dynamics by virtue of the rotational levels possessing molecule-fixed projections of the angular momentum vector. In cases where the quantum states are spectroscopically resolvable, laboratory-fixed axes may be unambiguously tied to those fixed on the molecule by o_..ical excitation and then identified after collision by high-resolution spectroscopic detection.

A study of energy transfer in $(^2A_1)$ $NH_2 + H$ collisions has been presented and a feature of this molecule is that full spectroscopic resolution of quantum levels, including spin, is feasible. A wide range of rotational energy-transfer results have been obtained and it is clear that by comparison with diatomics, the behaviour is anomalous with no apparent scaling relationship for rotational relaxation rates to transferred energy. However, the relationship with transferred angular momentum is very close and a momentum-gap law provides a quantitative fit to all our data. The key parameter in this law is the angular momentum transferred on collision. The magnitude and direction of l may be calculated from simple geometric considerations given values of N, k_a, and k_c for the initial and final states. Specific values of l can only arise from a limited set of H-atom trajectories and thus the possibility arises that sets of $N_{k_a k_c}$-resolved collision dynamic data may be used in conjunction with simple trajectory calculations to build up an intermolecular potential in at least two orthogonal planes, giving genuine stereochemical information.

Polarisation data augment this treatment and yield greater insight through the retention or loss of correlation by collision. Furthermore, spin-branching ratios are an indicator of the importance of the triplet surface. Both of these aspects of this problem will be addressed in forthcoming publications.

References

1 A. J. McCaffery, M. J. Proctor and B. J. Whitaker, *Annu. Rev. Phys. Chem.*, 1986, **37**, 223.
2 M. Faubel and J. P. Toennies, *Adv. At. Mol. Phys.*, 1977, **13**, 229.
3 T. A. Brunner and D. E. Pritchard, in *Dynamics of the Excited State*, ed. K. P. Lawley (John Wiley, Chichester, 1982).
4 C. Nyeland, *Chem. Phys. Lett.*, 1984, **109**, 603.
5 J. Derouard, *Chem. Phys.*, 1984, **84**, 181.
6 B. J. Whitaker and Ph. Bréchignac, *Laser. Chem.*, 1986, **6**, 61.
7 A. E. DePristo and H. Rabitz, *Chem. Phys.*, 1977, **24**, 2014.
8 N. Smith and D. E. Pritchard, *J. Chem. Phys.*, 1981, **74**, 3939.
9 B. J. Whitaker and Ph. Bréchignac, *Chem. Phys. Lett.*, 1983, **95**, 407.
10 M. A. Hoffbauer, S. Burdenski, C. F. Giese and W. R. Gentry, *J. Chem. Phys.*, 1983, **78**, 3832.
11 M. Shapiro and H. Kaplan, *J. Chem. Phys.*, 1979, **71**, 2182.
12 R. N. Dixon and D. Field, *Proc. R. Soc. (London), Ser. A*, 1979, **366**, 225.
13 R. N. Dixon and D. Field, *Proc. R. Soc. (London), Ser. A*, 1979, **366**, 247.
14 S. J. Dearden, R. N. Dixon and D. Field, *J. Chem. Soc., Faraday Trans. 2*, 1982, **78**, 1423.
15 M. Kroll, *J. Chem. Phys.*, 1975, **63**, 319.
16 B. J. Whitaker and A. J. McCaffery, *Chem. Phys. Lett.*, 1981, **86**, 185.
17 B. J. Whitaker and A. J. McCaffery, *J. Chem. Phys.*, 1983, **78**, 3857.
18 M. Gehring, K. Hoyerman, H. G. Wagner and J. Wolfrum, *J. Chem. Phys.*, 1971, **75**, 1287.
19 M. Arvis, C. Devillers, M. Gillois and M. Curtat, *J. Phys. Chem.*, 1974, **78**, 1356.
20 K. Dressler and D. A. Ramsey, *Philos. Trans. R. Soc. London, Ser. A*, 1959, **251**, 553.
21 R. A. Shatwell and A. J. McCaffery, *J. Phys. E*, 1974, **7**, 297.
22 M. Kroll, *J. Chem. Phys.*, 1975, **63**, 1803.
23 C. G. Harkin, A. J. McCaffery and B. J. Whitaker, unpublished results.
24 J. C. Polanyi and K. P. Woodall, *J. Chem. Phys.*, 1972, **56**, 1563.
25 F. W. Birss and D. A. Ramsey, *Comp. Phys. Comm.*, 1984, **38**, 83.

26 T. Orlikowski and M. H. Alexander, *J. Chem. PHys.*, 1983, **79**, 6006.

27 S. Mayama, S. Hiraoka and K. Obi, *J. Chem. Phys.*, 1984, **80**, 7.

28 M. I. McCarthy, P. Rosmus, H. J. Werner, P. Botchwina and V. Vaida, *J. Chem. Phys.*, 1987, **86**, 6693.

29 V. Vaida, M. I. McCarthy, P. C. Engelking, P. Rosmus, H. J. Werner and P. Botchwina, *J. Chem. Phys.*, 1987, **86**, 6669; M. N. R. Ashfold, C. L. Bennet, K. N. Rosser, R. J. Stickland and C. M. Western, *Chem. Phys.*, 1986, **101**, 467.

30 R. N. Dixon, personal communication.

Orbital Orientation in van der Waals Reactions

C. Jouvet, M. C. Duval, B. Soep,* W. H. Breckenridge and C. Whitham
*Laboratoire de Photophysique Moléculaire du CNRS, Bat. 213, Université de Paris sud,
91405 Orsay Cedex, France*

J. P. Visticot
Service des Atomes et des Surfaces, C.E.N. Saclay, 91191 Gif sur Yvette Cedex, France

Excited-state metal-molecule reactions [$Hg(^3P_1) + H_2$, $Ca(^1P_1) + HCl$] have
been studied within the complexes formed by the reactants. Under these
conditions specific aspects of orbital orientation within the molecular frame
are exemplified.

The reactivity of aligned atoms or oriented molecules is expected to depend strongly
upon the direction of the orientation with respect to the intermolecular axis.[1,2] In
addition when there exists more than one exit channel for the reaction, changing this
orientation can also change the branching ratio to these various exit channels. Rettner
and Zare, in a beam-gas experiment, have shown an important effect of the laser
polarisation in the reaction of $Ca(4s4p^1P_1)$ with HCl;[3,4] the laser polarisation orientates
the Ca 4p orbital in the calcium beam with respect to the target HCl gas. Specifically
they have shown that the perpendicular alignment of the Ca 4p orbital perpendicular
to the direction of approach ($p\pi$) enhances the production of the $CaCl(A^2\Pi)$ state,
while the $CaCl(B^2\Sigma^+)$ product is favoured by a parallel approach ($p\sigma$). The memory
of this preparation will, however, be best conserved in the case of collisions with impact
parameters close to zero.

In turn we have chosen to proceed to excited-state reactions where the orientating
field is the molecular field induced by the van der Waals interaction of the reactants,
i.e. generating an orientation in the molecular frame of the complex. The principle of
the experiment is to form a metal-molecule complex in a supersonic expansion, in a
state which correlates with the ground state of the metal. Then the complex is promoted
to the reactive surface by a tunable laser in the vicinity of the atomic transition, the
metal being considered as the chromophore. The dynamical evolution of the excited
complex on a definite excited surface leads to the formation of the products. The optical
excitation will select out a surface of a given symmetry, thus influencing directly the
course of the reaction. Moreover, the selection obtained of the initial geometry may
lead to an important change in the product-energy distribution.[5] Another aspect of the
selectivity as offered by van der Waals complex reactions, the mechanical orientation
of the reactants, has been developed by Wittig and co-workers.[5]

In the $Hg(^3P_1)$-H_2 system the reaction rate depends strongly upon the accessed state
corresponding to a different Hg(6p) configuration ($^3\Sigma$ or $^3\Pi$) and this behaviour has
been confirmed by theoretical calculations.[7]

The $Ca(4s4p^1P_1)$-HCl system has also been studied in a complex, in the optical
domain close to the calcium $^1P_1$ line, but no marked effect of the optical preparation
has been observed on the chemiluminescent state A or B of CaCl. This is explained
using the model of Rettner and Zare[3,4].

Experimental

The technique uses laser spectroscopy in a supersonic jet, which was developed ten

years ago by Smalley *et al.*[8] Briefly, the reaction partners are expanded with a rare gas in a supersonic expansion. A cold complex is obtained after a few millimetres in the expansion, in a collision-free region. This complex is then excited with a tunable laser to the reactive surface. The chemical reaction occurs and the products are detected and analysed by their chemiluminescence spectra (CaCl), or by laser-induced fluorescence of the product (HgH).

In the case of the Ca-HCl complex the preparation of the complex is more involved and the experiment (fig. 1) consists of a supersonic pulsed beam coupled to a laser vaporisation source of the type described by Smalley *et al.*[8,9] When the valve opens, a mixture of argon and HCl(1%) starts to flow into a 1 mm diameter channel. *Ca.* 5 mm downstream, it reaches a rotating calcium rod where the beam of the second harmonic of a YAG laser is focused. The laser pulse evaporates the calcium *ca.* 1 ms after the opening of the valve at the maximum of the gas flux. Then a short channel, 2 mm long, leads to the chamber evacuated by a Roots pump (1000 m^3 h^{-1}) and the Ar, HCl, Ca mixture is expanded into the vacuum, producing condensation of Ca and HCl in a complex. A second tunable laser crosses the molecular jet *ca.* 15 mm downstream and excites the complexes. This second laser is delayed by 30 μs with respect to the first, which corresponds to the time taken by the metal flow to reach the observation region. The chemiluminescence induced by the second laser is analysed by a small mono-chromator followed by a red-sensitive phototube and a boxcar integrator.

In the case of mercury-hydrogen complexes the rotational envelope of the excitation spectrum ensures that 1/1 Hg-H$_2$ species are observed. In the Ca-HCl case it is not so straightforward to ascertain the exact composition of the complex, hence we have chosen the mildest expansion conditions where the total pressure does not exceed 2 atm† and the evaporation laser power is smallest. When the evaporation laser intensity is increased
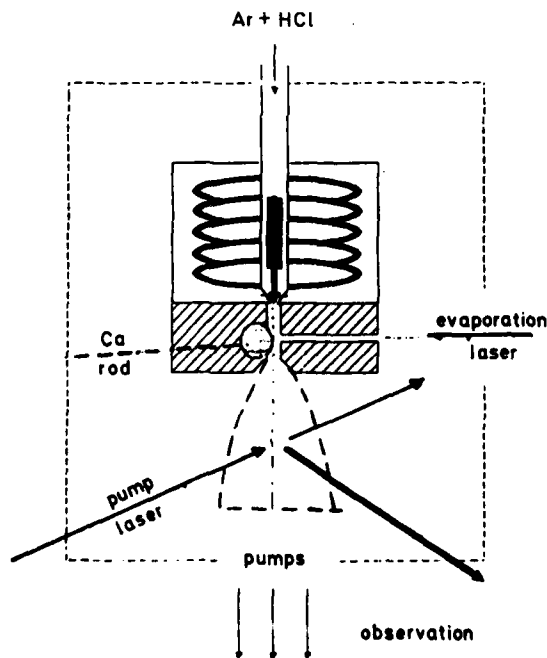
Fig. 1. Schematic diagram of the laser evaporation in the Ca-HCl experiment.

† 1 atm = 101 325 Pa.

the calcium pulse broadens temporally owing to higher metallic cluster formation. We thus infer that under mild conditions the Ca–HCl complex is the dominant calcium complex.

Moreover cold CaCl molecules are present in the X state owing to the reaction of metastable calcium atoms resulting from the evaporation process with HCl in the channel prior to the expansion. However, owing to the chemiluminescent nature of the reaction these CaCl molecules can easily be discriminated from those issued from the reaction.

Orbital Selectivity in the Hg–H$_2$ van der Waals Complex Reaction

It is known that, in the gas phase, excitation of the resonant $Hg(^1S_0-^3P_1)$ transition in presence of H_2 leads to the formation of $HgH(^2\Sigma^+)$ through a direct mechanism.[10,11] The quenching cross-section of $Hg(^3P_1)$ by H_2 (30 Å^2) suggested that the reaction in the complex should be slow enough for a structured intermediate state to be observed in the region accessible from the ground-state complex.

The reactivity of $Hg(^3P_1)$ within the Hg–H$_2$ complex depends crucially upon the mercury 6p orbital orientation with the complex axis as we have demonstrated.[12,13] The pπ preparation of the reaction provokes a rapid direct insertion of Hg in the H—H bond, while in the pσ preparation the reaction is much slower and is indirect.

It is important to mention how straightforwardly the orbital orientation may be achieved in a complex of a p-excited atom. The combination of the attractive and repulsive forces between the metal and the molecule result in the formation of two different electronic states of different energies, depending upon the orbital orientation of the atomic orbital with respect to the intermolecular axis. On the other hand, in collisions where rotational momentum is important, as at room temperature, the distinction between the pπ and pσ excitations may be reduced. Hence reactions within complexes provide a good and simple means to study orbital stereoselectivity. In the very simple case of the diatomic Hg–rare gas complexes we have observed these states on both sides of the $Hg(^3P_1)$ line, the pπ state being the deepest state. In Hund's case c for mercury complexes the p orbital is not as well aligned as it would be in case a; the $\Omega = 0$ state corresponds to a $^3\Pi$ state, while the $\Omega = 1$ state is a $^3\Sigma + ^3\Pi$ combination, which corresponds to a more on-axis average alignment. In both cases the rotation of the complex may destroy the orbital orientation. This Coriolis effect will vary with the ratio of the rotational spacing ($2BJ$) with the Ω state separation. At the very low rotational temperatures achieved in our experiments (*ca.* 3 K) the coriolis coupling is much smaller than the electronic gap.

The reaction of $Hg(^3P_1)$ within the $Hg-H_2(^3P_1)$ complex is a good example (fig. 2). The action spectrum shown measures the production of the HgH molecule as a function of the exciting frequency: the rapid reaction in the $^3\Pi$ ($\Omega = 0$) potential region is shown by a continuous spectrum, while the structure in the $^3\Sigma$ ($\Omega = 1$) region indicates a process slower than 3 ps.[13] Moreover, a low barrier to reaction is observed in the entrance valley of the $^3\Sigma$ approach, amounting at least to 100 cm^{-1}.[13] This barrier is manifest by a direct dissociation of the complex into $Hg(^3P_1) + H_2$ when the exciting photon provides greater energy than the Hg–H$_2$ $^3\Sigma$ well. These results have been confirmed by the *ab initio* calculations of Bernier and Millé.[6] They also found that the Π surface in the $Hg(^3P_1) + H_2$ is attractive and that the reaction proceeds through the lengthening of the H—H bond followed by mercury insertion at a distance close to 1.5 Å, as we observed.[13] Furthermore a barrier is also calculated in the other configuration $^3\Sigma$ ($\Omega = 1$) but can be traversed by tunnelling to another surface, leading to the HgH product.

This example shows that the use of the van der Waals technique sorts out the different potential-energy surfaces corresponding to the 6p orbital orientations, yielding strong differences in reactivity. We have sought with the same ideas to investigate the influence of the orbital orientation on the product state formation in the Ca–HCl system.
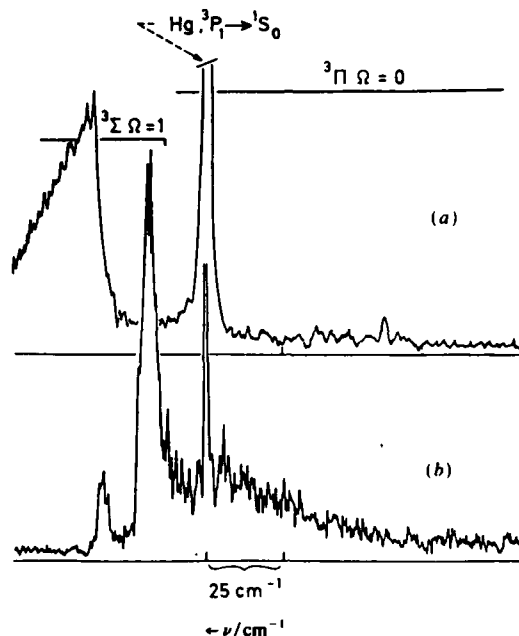
Fig. 2. (*a*) Fluorescence excitation spectrum of the $Hg-H_2$ complex. (*b*) Action spectrum of the $Hg-H_2$ complex: the pump laser is scanned while the probe laser is maintained tuned to the bond head of the 0-0 transition in $Hg-H(^2\Pi_{1/2}\leftarrow{}^2\Sigma^+)$. The blue domain ($\Omega = 1$) in (*b*) extends into the continuum as observed in (*a*) and the red domain, right of the mercury, line corresponds to the $\Omega = 0$ excitation.

The Ca–HCl ($^1P_1$) van der Waals Reaction

This reaction is observed in the apparatus described in fig. 1 and the preliminary results are reported in the following. The efficiency for the tunable laser to produce CaCl* by excitation of the complex in the spectral domain of the calcium $^1P_1$ line is shown in fig. 3. The resulting chemiluminescence is observed in the red (around 600 nm). The fluorescence spectrum resulting from the excitation of the complex at 430 nm is given
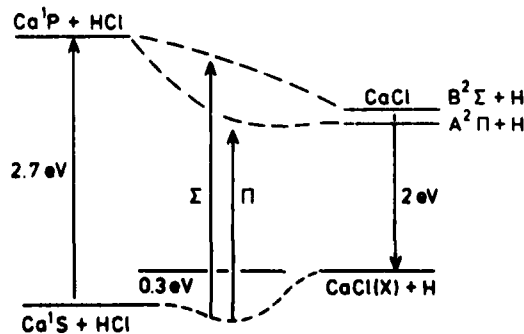
Fig. 3. Energy diagram along the reaction coordinate of the $Ca(^1P_1) + HCl$ system.

in fig. 4. It is compared to the laser induced chemiluminescence spectrum due to the reaction between $Ca(4s4p^1P_1)$ and HCl obtained in a beam-gas configuration. The two spectra present the two characteristic maxima at 620 and 595 nm, corresponding to the emission of the two states A and B of CaCl.[3,4,14-16] The emission recorded with the laser at 430 nm presents all the characteristics of a chemiluminescence resulting from the excitation of a Ca-HCl complex. First, the intensity increases with the Ar/HCl pressure and disappears instantaneously when the valve opening is blocked. Moreover, no difference is found between the time dependence of this signal and the time evolution observed when doing direct laser-induced fluorescence of CaCl. This last point is not only a further proof that the emitting product is CaCl, but it also indicates that this product is formed instantaneously.

It is important to stress that in order to observe the emission resulting from the excitation of the Ca-HCl complex the experimental conditions have to be carefully controlled. The evaporation laser produces not only neutral calcium atoms but also other species which can absorb and re-emit light. For too large an intensity on the vaporisation laser, other fluorescent signals are observed which can be discriminated from the known CaCl chemiluminescence displayed in fig. 4. These spurious signals increase when the background pressure in the main chamber is increased from 10^{-2} to 10 mbar. Their origin is believed to be collisions with background gas. This is confirmed by looking at the time evolution, which shows a slower rise-time than the laser. Moreover, these signals are maximal for a delay of *ca.* 50 μs instead of 30 μs for the 1:1 complex, suggesting another heavier precursor. Consequently, in order to see the signal of the Ca-HCl complex, the laser vaporisation power as well as the delay between the two
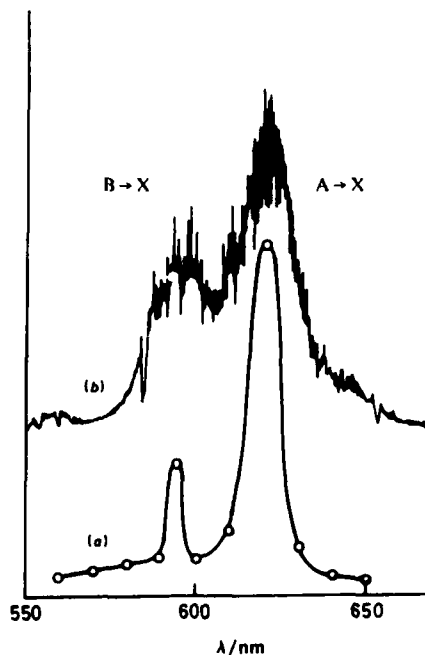
Fig. 4. Chemiluminescence spectra of CaCl. (*a*) The points correspond to the excitation of the Ca-HCl complex excited by a laser out of resonance of the Ca line ($\lambda = 430$ nm). The second spectrum (*b*) results from the reaction of a calcium atom excited in the $4s4p^1P_1$ state with HCl.

laser pulses has to be carefully chosen to minimise the contribution of these spurious signals to the Ca-HCl complex chemiluminescence.

Fig. 5 shows the action spectrum of the Ca-HCl complex obtained by tuning the excitation laser in the vicinity of the resonance line of Ca and recording at the emission maximum at 620 nm, corresponding to the emission from the A $^2\Pi$ state. This spectrum, extending over ca. 1000 cm^{-1}, appears as a broad structureless continuum. No important differences were observed when monitoring the fluorescence coming from either the A or B state.

Such a wide structureless spectrum has been observed in the excitation of the Hg-Cl$_2$ van der Waals complex.[17-19] It has been interpreted as a fast reaction without any activation barrier. This is likely to be the case here considering the large cross-section of 68 Å^2 which has been measured for the chemiluminescence reaction of Ca(4s4p^{1}P$_1$) with HCl.[4]

Such a large cross-section has led Rettner and Zare to interpret the reaction between excited Ca and HCl by a harpooning mechanism.[4] Nevertheless, it has been shown[20,21] that attachment of an s electron to HCl results in dissociation into Cl$^-$ + H$^+$. The net effect of this attachment will be the same as for the harpooning reaction, but selective for the s or pσ electron. In the interpretation of Rettner and Zare [see ref. (4)], the covalent Ca(^{1}P) + HCl($^1\Sigma^+$) surface crosses successively the Ca$^+$(^{2}S, ^{2}D, ^{2}P) + HCl$^-$($^2\Sigma^+$) ionic surfaces for decreasing Ca-HCl distances. The first crossing, at ca. 3.5 Å, is responsible for the large cross-section. It ends on a symmetrical Ca$^+$(^{2}S) + HCl$^-$($^2\Sigma^+$) ionic intermediate which cannot retain the memory of the initial polarisation. The conclusion was that the effect of the polarisation on the A/B branching ratio could only originate from inner crossings in the entrance channel.

If we now consider the excitation of the Ca-HCl van der Waals complex, this process derives its oscillator strength from the close Ca(^{1}S-^{1}P) transition and the direct excitation of the ionic species should be much weaker owing to the small ionic character of the ground-state Ca-HCl complex. The absorption of a photon thus excites the complex to a covalent potential-energy surface [Ca(^{1}P) + HCl($^1\Sigma^+$)], and because the surfaces corresponding to the various orbital orientations are no longer degenerate, the different
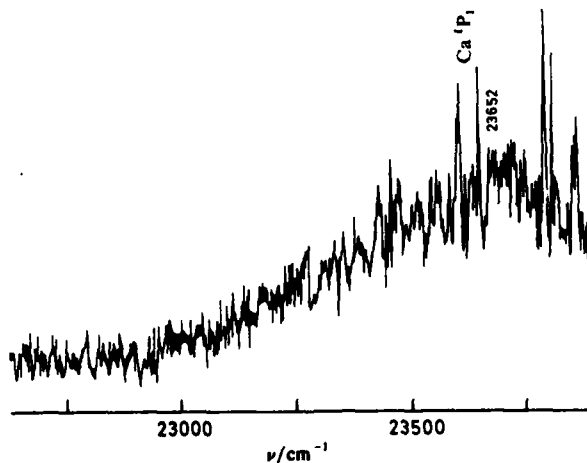
Fig. 5. Action spectrum of the Ca-HCl complex obtained by monitoring the fluorescence of the A $^2\Pi$ state of CaCl (λ = 620 nm) while scanning the laser wavelength. The position of the Ca (4s^2 ^{1}S$_0$-4s4p^{1}P$_1$) resonance line is also indicated.

orientations will correspond to different laser frequencies (fig. 3). As the typical equilibrium distance for such a complex would be of the order of 3-4 Å, the laser absorption occurs close to the crossing with the $Ca^+(^2S) + HCl^-(^2\Sigma^+)$ ionic surface and the reaction is expected to proceed predominantly *via* crossing. In this interpretation, whatever the orientation of the state populated by the laser or, equivalently, whatever the laser wavelength, no difference is expected in the branching ratio between the A and B states of CaCl because there is only one symmetrical ionic intermediate. Consequently the observation of a constant A/B branching ratio as a function of the laser wavelength is consistent with the interpretation of Rettner and Zare.[4] Furthermore, the complex is very likely to possess a linear Ca-HCl structure in comparison with the similar HgHCl[23] system. Thus the $p\pi$ and $p\sigma$ orientations yield Π and Σ states in the complex, and the fact that the orbital orientation has no effect on the A/B branching ratio does not mean that the reactivity is the same for σ or π orientations. Considering the Σ symmetry of the ionic surface for a linear Ca-HCl complex, the ionic covalent coupling should be maximum for the $p\sigma$ orientation,[21] producing a more intense Σ transition in the action spectrum. The coupling of the $p\pi$ orientation with the ionic surface should then occur through the large-amplitude excursions on the resulting A' surfaces. On the other hand, weaker transitions to a delocalised Ca^+HCl^- ionic state will be searched for in a wide frequency domain. This may show evidence of a stretched HCl transition state in the Franck-Condon envelope of the resulting action spectrum. Work is also in progress to detect other products of the half-collision, such as metastable calcium atoms competing with the reaction, possibly with different efficiency for the different accessible surfaces (orbital orientations).

Conclusion

Two examples of the influence of the orbital orientation on the reactivity of metal-molecule complexes have been discussed and in one of them ($Hg + H_2$) the Π/Σ orientation modifies the reactivity in an exemplary manner. In the Ca-HCl experiment no effect is observed in the domain of the calcium $^1P_1$ transition in agreement with Rettner and Zare.[4]

We have also explored different portions of the reactive surface: far from the transition state in the $Hg-H_2$ case, very close to in the Ca-HCl case, which will lead to further developments.

References

1 R. B. Bernstein, D. R. Herschbach, R. D. Eyring and X. X. Levine, *J. Phys. Chem.*, 1987 **91**, 5637.
2 J. P. Simons, *J. Phys. Chem.*, 1987, **91**, 5365.
3 C. T. Rettner and R. N. Zare, *J. Chem. Phys.*, 1981, **75**, 3636.
4 C. T. Rettner and R. N. Zare, *J. Chem. Phys.*, 1982, **77**, 2416.
5 S. Buelow, M. Noble, G. Radhakrishnan, H. Reisler, G. Wittig and G. Hancock, *J. Phys. Chem.*, 1986, **90**, 1015.
6 C. Jouvet, M. Boivineau, M. C. Duval and B. Soep, *J. Phys. Chem.*, 1987, **91**, 5416.
7 A. Bernier and P. Mille, *J. Chem. Phys.*, 1988, **88**, 4843.
8 R. E. Smalley, D. H. Levy and L. Wharton, *J. Chem. Phys.*, 1976, **64**, 3264.
9 R. E. Smalley, *Laser Chem.*, 983, **2**, 167.
10 A. B. Callear and J. C. McGurk, *J. Chem. Soc., Faraday Trans. 2*, 1972, **68**, 289.
11 A. C. Vikis and D. J. le Roy, *Can. J. Chem.*, 1973, **51**, 1207; and references cited therein.
12 C. Jouvet and B. Soep, *Chem. Phys. Lett.*, 1983, **96**, 426.
13 (a) C. Jouvet and B. Soep, *Laser Chem.*, 1985, **5**, 157;
   (b) W. H. Breckenridge, C. Jouvet and B. Soep, *J. Chem. Phys.*, 1986, **84**, 1443.
14 U. Brinkmann and H. Telle, *J. Phys. B*, 1977, **10**, 133.
15 U. Brinkmann, V. H. Schmidt and H. Telle, *Chem. Phys. Lett.* 1980, **73**, 530.
16 H. Telle and U. Brinkmann, *Mol. Phys.*, 1980, **39**, 361.
17 C. Jouvet and B. Soep, *Chem. Phys. Lett.*, 1983, **96**, 426.

18 C. Jouvet, *Thèse* (Université de Paris-sud, 1985).
19 C. Jouvet and B. Soep, *J. Phys. (Paris)*, 1985, **46** (C1), 313.
20 S. V. O'Neil, P. Rosus, D. W. Norcross and H. J. Werner, *J. Chem. Phys.*, 1986, **85**, 7232.
21 J. P. Gauyacq, *Europhys. Lett.*, 1986, **1**, 287.
22 R. Grice and D. H. Herschbach, *Mol. Phys.*, 1974, **27**, 159.
23 J. A. Shea and E. J. Campbell, *J. Chem. Phys.*, 1984, **81**, 5236.

24/13

Orbital Polarization and Fine-structure Effects in Time-resolved Cooperative Fluorescence from Dissociating Alkali–metal Diatoms

Gershon Kurizki

Chemical Physics Department, Weizmann Institute of Science, 76100 Rehovot, Israel

Gabriel Hose

Theorie III, IFF DER KFA, Postfach 1913, D-5170 Jülich, Federal Republic of Germany

Abraham Ben-Reuven*

School of Chemistry, Raymond and Beverly Sackler Faculty of Exact Sciences, Tel-Aviv University, 69978 Ramat Aviv, Tel-Aviv, Israel

Time-resolved cooperative fluorescence (TRCF) from electronically excited dissociating homonuclear diatoms is suggested as a new technique for studying orbital and spin-polarization effects in fragmented diatoms. The method is based on a theoretical prediction of a novel feature named here 'superbeats'. This feature results from a combination of two oscillatory effects, namely, the ringing oscillations caused by the time variation of the interference phase between the receding atoms during emission (P. Grangier, A. Aspect and J. Vigué, *Phys. Rev. Lett.*, 1985, **54**, 418) and the quantum beats associated with the fine-structure splitting. The time-resolved superbeat pattern is shown to be sensitive to the amplitudes and phases of the superposed states, with different orbital polarization and spin, mixed by adiabatic and non-adiabatic couplings in the outcome of the dissociation process. Qualitative estimates are made, based on a detailed analysis, for the photodissociation of Li_2. Under conditions in which rotational effects can be neglected, the two states $^1\Sigma_{u(g)}$ and $^3\Pi_{u(g)}$ of Li_2 are superposed in the final outcome of the reaction. This should lead to a superbeat pattern dependent on the amplitude and phase of the superposition. Conditions for the experimental observability of these features have been studied, showing that a time resolution of $\leqslant 0.1$ ns is required.

1. Introduction

An electronically excited homonuclear diatom dissociating into a pair of open-shell atoms undergoes a transition from the region of medium-range internuclear separations (Just above a few Å), where the electronic potential-energy curves are dominated by resonant dipole–dipole interactions, to the long-range region where fine-structure splitting predominates. The transition from one region to the other occurs in an interval of separations that will be denoted by $R_c (\leqslant 20$ Å in Na_2 and $\leqslant 200$ Å in Li_2), where most of the non-adiabatic dynamics take place.[1] These dynamics determine the asymptotic amplitudes and relative phases of the superposition of fine-structure states into which the dissociating diatom evolves from a given dipole–dipole eigenstate prepared by the excitation.

Since most of the fluorescence is emitted long after the fragments have receded away from the transition region (unless their dissociation velocity is very low), its spectrum only yields the branching ratios (squared amplitudes) of the different fine-structure

1

states in the asymptotic superposition. In order to obtain information on the relative phases too, and thereby gain more insight into the dynamics, one must resort to measurements sensitive to the coherent interference between the emitting states. As shown here, time-resolved fluorescence can be the source of such information.

One aspect of the potential usefulness of time-resolved fluorescence was revealed in an experiment by Grangier *et al.*[2] on photodissociated Ca_2, in which the rate of fluorescence exhibited a 'ringing' oscillatory pattern. In this case the Ca_2 diatom is excited to a dissociative state of *ungerade* parity ($^1\Pi_u$) and evolves into an *ungerade*-symmetrized superposition in which one atom is in the excited ^1P state while the other is in the ground ^1S state, or *vice versa*. As the two fragments fly apart, the emission of this superposition alternates between constructive and destructive interference with an angular frequency kv, where k is the emission wavevector and v is the separation velocity, thus forming the temporal ringing pattern. The sensitivity of such patterns to the orbital polarization and parity of the dissociative state and to separation velocity can be deduced from a theory of cooperative fluorescence based on a generalized master-equation approach.[3-5]

The temporal patterns obtained for dimers of closed-shell atoms such as Ca_2 are due to emission from one dissociative state only, correlated to one ($^1P + {}^1S$) atomic-limit state, so that no dynamics are involved in the process. In contrast, when Ca_2 is replaced by dimers of open-shell atoms, such as Na_2 or Li_2 dissociated by one or two photons, the atoms evolve into an *ungerade* or *gerade* superposition of several doublet states of the form $^2P_j + {}^2S_{1/2}$, with $j = \frac{3}{2}$ or $\frac{1}{2}$ values of the angular momentum and $\Omega = 0, \pm 1, \pm 2$ values of its projection onto the inter-nuclear axis. In such systems, the interatomic *ungerade* or *gerade* ringing pattern will interfere with quantum beats at the doublet splitting frequency, δ, associated with the superposed doublet states. The resultant time-resolved pattern will contain 'superbeat' frequencies $\delta \pm ky$, in addition to the pure ringing frequency kv. The sensitivity of this pattern to the amplitudes and phases of the emitting doublet states and the relationship of these parameters to the dissociation dynamics is the key point of our work.[6]

The choice of an atomic system for the demonstration of such effects is dictated primarily by the ability to resolve the beats in time. This makes Li particularly attractive, because its doublet splitting is so small ($\delta \approx 10^{10} \, s^{-1}$), 50 times smaller than that of Na. Whereas δ is fixed for each system, the ringing frequency kv can be modified by using different wavelengths for the photodissociating radiation. High velocities ($v \gtrsim 10^4 \, cm \, s^{-1}$ in Li_2) are preferable for two reasons: (i) the interesting superbeat features become more distinct as the ringing and beating frequencies become comparable and (ii) the ringing period becomes much shorter than radiative lifetime, allowing the observation of several ringing peaks before the signal disappears. At such velocities the system evolution can be divided into two distinct stages: *the preparation stage* leading to the asymptotic superposition state (at separations beyond R_c), followed by *the emission stage*, extending up to separations of several wavelengths.

2. The Preparation Stage

As an illustration of the ideas discussed above, we consider the photodissociation of a homonuclear diatom through the $\Omega = 0^+$ channel: $^1\Sigma_{u(g)}^* \rightarrow {}^2P_j^* + {}^2S_{1/2}$ ($j = \frac{3}{2}, \frac{1}{2}$). In order to keep to the selected single channel, two conditions must prevail: (*a*) Coriolis coupling ($\Delta\Omega = 1$) to other excited electronic states must be precluded. This is achieved by cooling the diatomic beam so that low values of nuclear angular momentum predominate. For sufficiently large velocities ($v \gtrsim 10^3 \, cm \, s^{-1}$ in Li_2) the Coriolis coupling is then negligible compared to the radial non-adiabatic coupling.[1] (*b*) The $\Omega = 1$ dissociation channel $^1\Pi_{u(g)}^* \rightarrow {}^2P_j + {}^2S_{1/2}$ should be avoided by selecting $^1\Sigma_{u(g)}^*$ excitation only. The $1\,^1\Sigma_u^+$ state in Li_2 is uniquely selected in the Francke-Condon region upon exciting the ground

rovibronic state by a photon whose energy lies between 2.879 and 3.154 eV. In this excitation range the 1 $^1\Pi_u$ state can decompose only very slowly via tunnelling, as seen from the potential-energy curves.[7,8] The separation velocities attainable in this range are $\leqslant 5 \times 10^5$ cm s^{-1}. Higher velocities can be accessed by exciting the 2 $^1\Sigma_g^+$ state *via* simultaneous absorption of two counter-polarized photons.

Under the conditions specified above, the $^1\Sigma_{u(g)}^+$ state excited in the Franck-Condon region is mixed subsequently (by spin-orbit coupling) with the $\Omega = 0^+$ component of the $^3\Pi_{u(g)}$ triplet, forming two adiabatic states outside the domain of short-range forces ($R \geqslant 1$ nm). These states have the form

$$|\pm\rangle = \alpha_\pm(R)|I\rangle + \beta_\pm(R)|II\rangle \tag{1}$$

using as a basis

$$|I\rangle = {}^1\Sigma_w^+$$

$$|II\rangle = 2^{-1/2}[{}^3\Pi_w(\Lambda = -1, S_z = 1) - {}^3\Pi_w(\Lambda = 1, S_z = -1)] \tag{2}$$

with w = u or g as the parity. The coefficients $\alpha_\pm(R)$, $\beta_\pm(R)$, and energies $\varepsilon_\pm(R)$ of the adiabatic states, are obtained by diagonalizing the Hamiltonian matrix[9]

$$H_w(\Omega = 0^+) = \begin{pmatrix} V_\Sigma(R) & \sqrt{2}\delta/3 \\ \sqrt{2}\delta/3 & V_{II}(R) - \delta/3 \end{pmatrix} \tag{3}$$

where $V_{\Sigma(II)}(R)$ is the dipole-dipole interaction in the $|I\rangle(|II\rangle)$ state and δ is the fine-structure splitting. One can easily show that at separations where the dipole-dipole interaction dominates the $|-\rangle(|+\rangle)$ state is selectively populated for u(g) parity in the Franck-Condon region. In the asymptotic range (where the fine-structure splitting dominates), the adiabatic states attain the limiting forms

$$|-\rangle \rightarrow 3^{-1/2}(|I\rangle - \sqrt{2}|II\rangle); \; (j = \tfrac{1}{2})$$

$$(R \gg R_c) \tag{4}$$

$$|+\rangle \rightarrow 3^{-1/2}(\sqrt{2}|I\rangle + |II\rangle); \; (j = \tfrac{3}{2})$$

which are, respectively, the lower and higher doublet states.

The internuclear radial motion causes time-dependent mixing of the adiabatic $|\pm\rangle$ states in the region extending beyond R_c. The non-adiabatic character of the wavefunction formed by this mixing

$$|\Psi\rangle = b_+(t)|+\rangle + b_-(t)|-\rangle \tag{5}$$

depends strongly on the separation velocity v. We calculated this wavefunction by the approximate semiclassical model of radial coupling[10] (neglecting Coriolis coupling as discussed above), in which the Schrödinger equation can be brought to the form

$$\dot{\rho}^{++} = f(\rho_{+-} + \rho_{-+}) = -\dot{\rho}_{--}$$

$$\dot{\rho}_{+-} = \dot{\rho}_{-+}^* = i\varepsilon\rho_{+-} - f(\rho_{++} - \rho_{--}) \tag{6}$$

where

$$\varepsilon = \varepsilon_+(R) - \varepsilon_-(R)$$

$$f = -[\alpha_+(R)\dot{\alpha}_-(R) + \beta_+(R)\dot{\beta}_-(R)]. \tag{7}$$

Here $\rho_{ij} = b_i b_j^*$ are the density-matrix elements (in the Schrödinger picture) with $i, j = +$ or $-$.
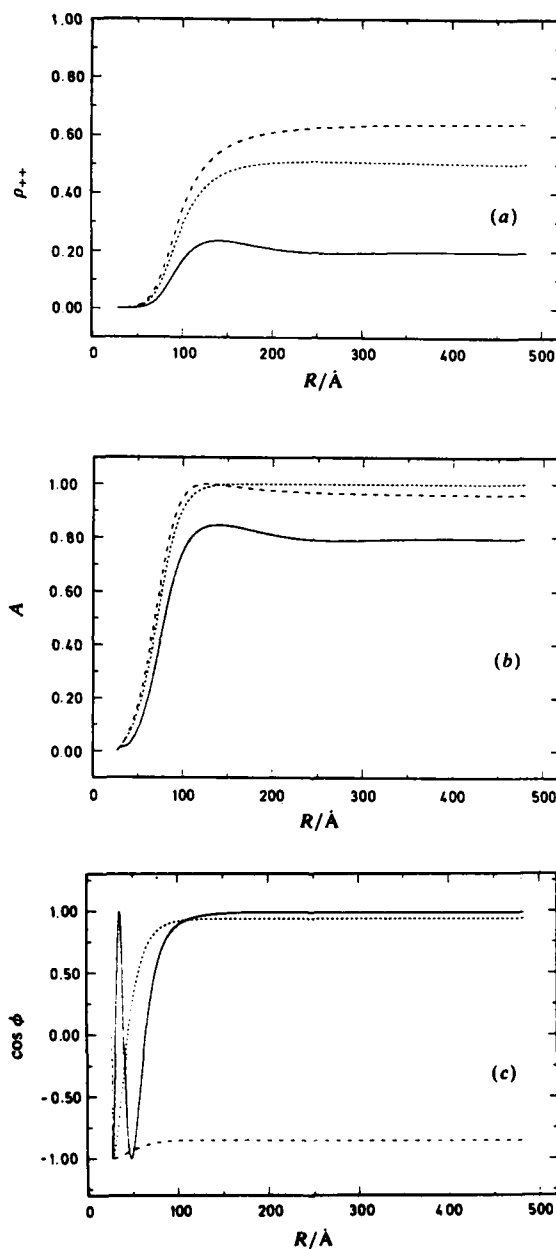
Fig. 1. Dependence of non-adiabatic state parameters (see text) on internuclear separations for three dissociation velocities of Li_2, corresponding to wavelengths λ_{ex} of photoexcitation to the continuum of the $1\ ^1\Sigma_u^+$ state. (——) $v = 22\,900$ cm s^{-1} ($\lambda_{ex} = 4304.56$ Å), (- - -) $v = 71\,300$ cm s^{-1} ($\lambda_{ex} = 4292.23$ Å), (— · —) $v = 346\,500$ cm s^{-1} ($\lambda_{ex} = 4003.32$ Å).

Fig. 1 shows the separation dependence (or, equivalently, time dependence) of the parameters completely specifying the non-adiabatic wavefunction: (*a*) the population of the initially unexcited state ρ_{++} (in the *ungerade* case), (*b*) the amplitude of the coherent mixture $A = 2|\rho_{+-}|$ and (*c*) the cosine of the non-adiabatic phase $\phi(t) = \arg(b_+/b_-) - \int_0^t \varepsilon \, dt'$.

The results drawn for three different velocities indicate the gradual transition from adiabatic to strongly non-adiabatic behaviour as the velocity increases. At the largest velocity (dash–dot curve) the 'sudden collision' limit is reached. In this limit the character of the $^1\Sigma_u^+$ state does not change when passing through the region of dynamical coupling, because spin does not have enough time to couple to the orbital momentum. Then $\rho_{++} \approx |\langle + |^1\Sigma_u^+ \rangle|^2 \approx \frac{2}{3}$. Fig. 1(*a*)–(*c*) demonstrates that the dynamical parameters rapidly approach their asymptotic values beyond $R \approx 20$ nm, a separation that is much smaller than the emission wavelength and (for the velocities considered) corresponds to times too short for significant emission to occur. We can therefore use these asymptotic values as initial conditions for the emission stage, which we examine after a time delay $t_D = R_D/v$ chosen at will for any R_D well beyond R_c (here $R_D = 50$ nm).

3. The Emission Stage

The system is now in a coherent superposition with time-independent amplitudes (for $t > t_D$) of the two adiabatic states $|\pm\rangle$, which are correlated to different doublet levels and symmetrized in accord with their parity and $\Omega = 0^+$ projection. This superposition oscillates at the frequency ε [eqn (6)] which is now close to the doublet splitting δ, with a weak time-dependent perturbation owing to the long-range (retarded) dipole–dipole coupling. Since this coupling is also part of the cooperative emission process,[4] one can make a smooth transition from the equations of motion (6), upon setting $f \approx 0$ at $t > t_D$, to the corresponding equations for a radiatively coupled pair of atoms whose cooperative excitation energies are split by $\varepsilon(t)$. Such equations are obtainable using a generalized master-equation approach developed by Agarwal.[11] In ref. (4) a master equation is derived for the density operator of many radiatively coupled identical multilevel fragments, taking account of their motion. This equation is then solved exactly for a pair of two-level atoms (which is an appropriate model for dissociating Ca_2). In the present case the master equation is cast into a set of equations for a pair of three-level atoms (doublet and ground states). They are then solved approximately, by using a multiple time-scales expansion[12] in the small parameter $\gamma/\varepsilon(t) \lesssim \gamma/\delta$, with the $|\pm\rangle$ states as the basis.

The total (spectrally unresolved) emission rate obtained from this solution for the *ungerade* case varies with $\tilde{t} = t - t_D$ as follows:[6]

$$\dot{P}(\tilde{t} = t - t_D) \approx \sum_{\pm} \rho_{\pm\pm}(t_D)(\gamma + \Gamma_{\pm}) \exp\left[-\int_0^{\tilde{t}} (\gamma + \Gamma_{\pm}) \, d\tilde{t}' \right]$$

$$+ A(t_D)\Gamma_c \cos(\delta\tilde{t} + \phi) \exp\left[-\int_0^{\tilde{t}} (\gamma + \Gamma_+ - \Gamma_-) \, d\tilde{t}' \right] \qquad (8)$$

where $A = 2|\rho_{+-}|$ and

$$\Gamma_{\pm} \approx \pm(\tfrac{2}{3}\Gamma_\Pi + \tfrac{1}{3}\Gamma_\Sigma)$$

$$\Gamma_c \approx \sqrt{\tfrac{2}{3}}(\Gamma_\Pi + \Gamma_\Sigma). \qquad (9)$$

Here $\Gamma_\Lambda[R(t)]$ (with $\Lambda = \Sigma$ or Π) are the modifications of the atomic emission rate owing to the radiative coupling. They exhibit oscillatory variation with $R(t)$ responsible for

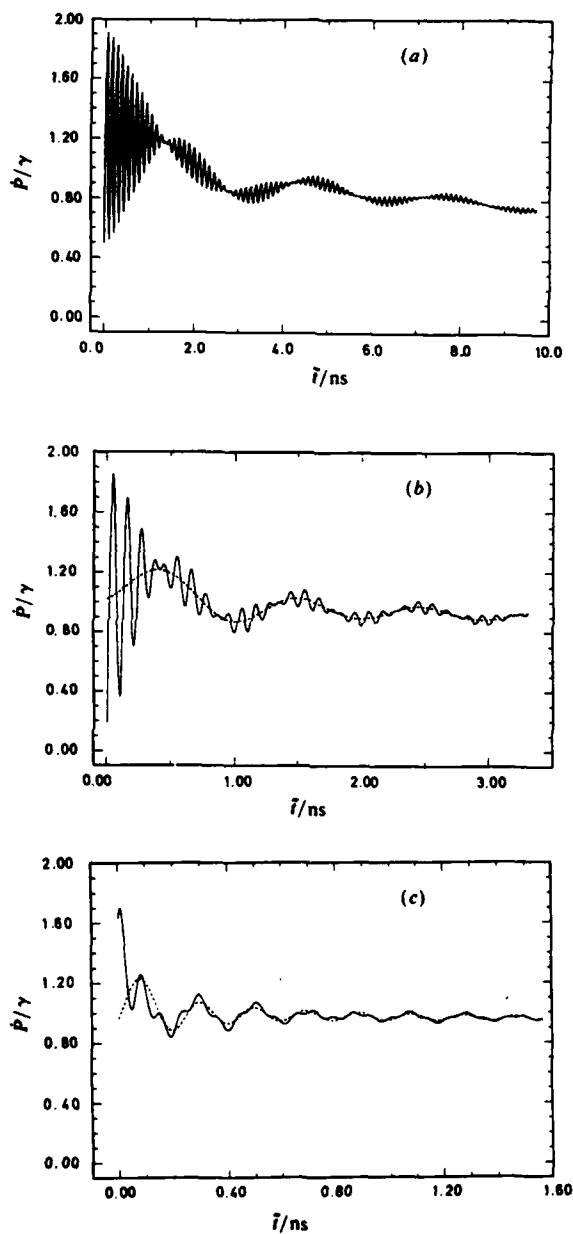**Fig. 2.** Temporal dependence of the emission rate (——) normalized to the atomic emission rate. The emission rates are calculated for the velocities and non-adiabatic state parameters of fig. 1. (- - -) The decay rates of adiabatic state populations.

ringing patterns of the kind observed by Grangier *et al.*[2] for a single excited $^1\Lambda_u$ state, whose emission rate has the form[3,4]

$$\dot{P}_\Lambda(\tilde{t}) \approx \rho_\Lambda(t_D)[\gamma + \Gamma_\Lambda(\tilde{t})] \exp\left[-\int_0^{\tilde{t}} (\gamma + \Gamma_\Lambda)\, d\tilde{t}' \right]. \tag{10}$$

The pattern in eqn (8), valid for a superposition of two symmetrized excited states at different energies, is more complex than that of eqn (10), not only owing to the mixture of ringing decays of the populations $\rho_{\pm\pm}$, but also due to the term expressing the interference of the $|\pm\rangle$ states, which is proportional to their coherence amplitude A. In this term, the ringing rate Γ_c is modulated by the asymptotic quantum beating $\cos{(\delta\tilde{t} + \phi)}$ and is the source of the superbeat frequencies $\delta \pm kv$.

Emission patterns calculated from eqn (8), using the same three velocities as in fig. 1 along with the corresponding asymptotic values of ρ_{++}, A and ϕ, are displayed in fig. 2. The broken line describes the ringing population-decay terms. Their rapid superbeat modulations are clearly discernible at low velocities. At the highest velocity used [fig. 2(c)] the quantum-beat and ringing frequencies become almost equal. The ringing population-decay terms have an initial value shifted by $(\frac{1}{3})$ $(\rho_{++} - \rho_{--})$ from 1 (the normalized atomic rate). The separation between its maxima and minima diminishes as $(kR)^{-1}(\rho_{++} + \frac{1}{2}\rho_{--})$. The envelope of superbeating oscillations is symmetrically positioned about the population-decay terms and diminishes as $(2^{3/2}A/kR)$. The dynamical phase shift ϕ can be deduced from the number and location of superbeat peaks, the maxima of

$$\cos{(\delta\tilde{t} + \phi)} \sin{kv\tilde{t}} = \tfrac{1}{2}\{\sin{[(\delta - kv)\tilde{t} + \phi]} + \sin{[(\delta + kv)\tilde{t} + \phi]}\} \tag{11}$$

within a period of $2\pi/kv$. A similar calculation for the *gerade* case yields reversed superbeats with $\phi \to \phi + \pi$. One may conclude from the figures that temporal patterns detected with sufficient accuracy and time resolution can disclose all the dynamical parameters of the non-adiabatic process.

4. Discussion

The major conclusion of this work is that time-resolved emission stores valuable information on the coherent character of non-adiabatically dissociating open-shell atomic pairs, notably on the phase of superposed fine-structure states emerging from the reaction. Such information can be used, *e.g.* to determine the orbital polarization of the spin–orbit products as a function of non-adiabaticity. It is also important as an experimental test of the simplified semiclassical model[9,10] used in section 2 *versus* fully quantal calculations.[13] The phase is much more sensitive to the accuracy of the calculation than the populations, as it accumulates as a function of $R(t)$ over several multiples of 2π at certain velocities [fig. 1(c)].

The observation of such effects in Li_2 at any dissociation velocity requires a temporal resolution better than *ca.* 30 ps (3 points per beating period). The weakness of the detectable signal from a molecular beam poses a greater difficulty as the radiative lifetime of the emitting atomic transition in Li(6407 Å) is rather long $(1.6 \times 10^{-7}$ s). Enhancement of the emission rate within sufficiently short time intervals ($\leqslant 30$ ps) may be the clue to the detection problem.

References

1 E. E. Nikitin, *Adv. Chem. Phys.*, 1975, **28**, 317; E. I. Dashevskaya, A. I. Voronin and E. E. Nikitin, *Can. J. Phys.*, 1975, **17**, 317.

2 P. Grangier, A. Aspect and J. Vigué, *Phys. Rev. Lett.*, 1985, **54**, 418; P. Grangier and J. Vigué, *J. Phys. (Paris)*, 1987, **48**, 781.
3 G. Kurizki and A. Ben-Reuven, *Phys. Rev. A*, 1985, **32**, 2560.
4 G. Kurizki and A. Ben-Reuven, *Phys. Rev. A.* 1987, **36**, 90.
5 A. Ben-Reuven and G. Kurizki, *J. Phys. Chem.*, 1987, **91**, 5422.
6 G. Kurizki, G. Hose and A. Ben-Reuven, in *Advances in Laser Science III* (Proc. of ILS III Conference, Atlantic City, Nov. 1987) (AIP, in press).
7 D. D. Konowalow and K. L. Fish, *Chem. Phys.*, 1983, **77**, 435.
8 I. Schmidt-Mink, W. Müller and W. Meyer, *Chem. Phys.*, 1985, **92**, 263.
9 M. Ya, Ovchinnikova, *Theor. Expt. Chem.*, 1965, 1, 12 (*Theor. Eksp. Khim.*, 1965, 1, 22).
10 See, for example, A. Salin, in *Physics of Ion-Ion and Electron-Ion Collisions*, ed. F. Brouillard and J. W. McGowan (Plenum Press, New York, 1983), p. 325.
11 G. S. Agarwal, *Quantum Statistical Theories of Spontaneous Emission* (Springer, Berlin, 1974).
12 A. Nayfeh, *Perturbation Methods* (Wiley, New York, 1973).
13 F. H. Mies, P. S. Julienne, Y. B. Band and S. J. Singer, *J. Phys. B*, 1986, **19**, 3249.

Coherence Effects in the Polarization of Photofragments

M. Glass-Maujean

Laboratoire de Spectroscopie Hertzienne de l'Ecole Normale Supérieure,† Université Pierre et Marie Curie, 4 Place Jussieu, 75252 Paris Cedex 05, France

J. Alberto Beswick*

LURE,‡ Université de Paris Sud, 91405 Orsay, France

The general quantum-mechanical treatment of coherence effects in the polarization of the fluorescence, as well as in the orientation of photofragments, is reviewed. They are the result of simultaneous excitatin of dissociative electronic states with different symmetry correlating to the same limit. The coherent excitation produces interferences which depends both on the photoabsorption probability amplitudes as well as on the relative phases of the continuum vibrational wavefunctions at large distances. Oscillations in the polarization degree of photofragments fluorescence as a function of the photon energy are predicted. Examples are presented in the case of direct dissociation of diatomic molecules. The case of slow predissociation is also analysed. Finally, possible extensions to the photodissociation of polyatomic molecules are considered.

1. Introduction

The ultimate goal of photofragmentation studies is to obtain the most detailed state-to-state cross-sections. These include final electronic, vibrational and rotational branching ratios and also vector properties such as alignment and orientation of photofragments.[1-6] The degree of alignment and orientation in turn determines the polarization of photofragments fluorescence and effects laser-induced measurements. Since the pioneering theoretical prediction by van Brunt and Zare[7] in 1968, several experimental and theoretical studies have dealt with polarization of the light emitted by photofragments.[8-24] Recently, the importance of coherence effects on the degree of polarization has been emphasized.[17-20,25,26] One particularly striking example is the anomalous polarization rate of the Ca*(P) fluorescence observed in the photodissociation of Ca$_2$.[18] This effect is due to the interference between the emission from the magnetic sub-levels ±1 coherently populated in the dissociation of a II molecular state. Consider a diatomic molecule AB excited by photon absorption to a dissociative $^1\Pi$ state, leading to A*(^{1}P) + B(^{1}S) fragments. Since $\Lambda = \pm 1$ for a Π state, the excited A*(^{1}P) fragment is populated in the magnetic sub-levels $m_{L_A} = \pm 1$ only (the internuclear vector being the quantization axis). Thus A* is aligned.[6] In addition, photodissociation in general creates a coherent superposition of the $m_{L_A} = \pm 1$ atomic magnetic sub-levels. For linearly polarized light, the degree of polarization of the atomic fluorescence defined by:

$$p = \frac{I_\parallel + I_\perp}{I_\parallel + I_\perp}$$

(where $I_{\parallel}$ and $I_{\perp}$ refer to the direction of the incident polarization) is dramatically affected by this coherence.[18,19] In the Ca_2 case, for example, a degree of polarization of $P = 0.64$ has been measured[18] which is larger than the maximum allowed polarization ($p = 0.5$) predicted by the classical theory as well as by the quantum theory when coherence is ignored.

Other coherences can be produced in the populations of the magnetic sub-levels.[17,23] Consider, for example, the case discussed above, namely the AB molecule dissociating into $A^*(^1P) + B(^1S)$ fragments. Two molecular singlet states ($^1\Pi$ and $^1\Sigma$) are correlated to this limit. They can both be populated by optical absorption from the $^1\Sigma$ ground state and therefore they will be coherently excited. Since the $^1\Pi$ state is correlated to $A^*(^1P, m_{L_A} = \pm 1)$ fragments and the $^1\Sigma$ state to $A^*(^1P, m_{L_A} = 0)$ fragments, the photodissociation will induce an additional coherence between the $m_{L_A} = 0$ and the $m_{L_A} = \pm 1$ magnetic sub-levels. As opposed to the former, this coherence depends on the ratio of photoabsorption amplitudes for excitation of the $^1\Sigma$ and $^1\Pi$ dissociative states as well as on the relative phases of their corresponding vibrational continuum wavefunctions.

Recently,[26] a quantum-mechanical calculation of the degree of polarization of Ly_α emission in the photodissociation of H_2, leading to $H(1s) + H(2p)$ fragments, has been completed. The calculation of the photodissociation amplitudes was performed by integration of the time-independent close-coupled Schrödinger equations for the $B(^1\Sigma)$, $B'(^1\Sigma)$ and $C(^1\Pi)$ electronic states of H_2, using the existing *ab initio* potential-energy curves,[28-31] adiabatic corrections,[32-35] non-adiabatic couplings[36] and transition dipole moments.[37-39] The photodissociation amplitudes were in turn used to calculate the polarization degree of the Ly_α fluorescence. It was shown that coherence effects can produce pronounced oscillations of the fluorescence polarization as a function of the photon energy, and that these effects are amenable to experimental evidence.

The polarization of photofragments fluorescence was calculated[26] using the density-matrix formalism in the molecular frame and within the axial recoil approximation. This is usually valid in the case of direct dissociation, but definitely does not apply for slow predissociation. In some recent experiments,[27] the degree of orientation of the fragments in the dissociation of a triatomic molecule has been measured directly by laser-induced fluorescence. It thus seems important to have a general formalism which not only provides the degree of polarization of photofragments fluorescence including all effects due to rotation, but which also gives directly the alignment and orientation of the products.

In this paper, we review the general theory of molecular photodissociation into two fragments using the density-matrix formalism in the laboratory frame and apply it to the cases studied before as well as to the case of slow predissociation. The presentation follows the general lines of Vasyutinskii's work[17] on orientation of atoms in the photodissociation of diatomic molecules. Particular attention is paid to the proper description of the vibrational continuum wavefunctions in the case where non-adiabatic transitions take place. We also show how this general treatment can be applied to polyatomic photodissociation.

The paper is organized as follows. In section 2 we present the general formalism. Section 3 is devoted to the case of direct dissociation, while section 4 deals with predissociation. Finally, in section 5 we discuss the application to polyatomic molecules.

2. General Quantum-mechanical Treatment

(A) Photofragments Fluorescence Cross-section

We are interested in describing a process in which a molecular system initially in a discret state $|\alpha_i\rangle$ is excited by photon absorption to a coherent superposition of a set of continuum eigenstates $|\alpha_d, \varepsilon_d\rangle$, where ε_d is the relative kinetic energy of the fragments in channel

d, which subsequently decay into some final continuum states $|\alpha_f, \varepsilon_f\rangle$ by photon emission (see fig. 1). The partial-differential cross-section for this process is given by:

$$\frac{\partial^2 \sigma}{k_f^2 \, \partial d_f \, \partial \hat{\Omega}_f} = (\hbar c k_i (\sum_{\alpha_f} \int_0^\infty k_f \, d\varepsilon_f$$

$$\times \left| \sum_{\alpha_d} \int_0^\infty d\varepsilon_d \frac{\langle \alpha_f, \varepsilon_f | \boldsymbol{D} \cdot \boldsymbol{e}_f | \alpha_d, \varepsilon_d \rangle \langle \alpha_d, \varepsilon_d | \boldsymbol{D} \cdot \boldsymbol{e}_i^* | \alpha_i \rangle}{E - \varepsilon_d - W_d + i\Gamma_d} \right|^2 \delta(E - \varepsilon_f - W_f - \hbar c k_f) \tag{1}$$

where k_i and k_f are the wavevectors of the incident absorbed and the final emitted photons, respectively, while $\boldsymbol{e}_i$ and $\boldsymbol{e}_f$ are the corresponding polarizations. W_d and W_f are the asymptotic (*i.e.* for infinite fragment separation) energies for channels d and f, and Γ_d is the radiative linewidth of the emitting state. Finally, $\boldsymbol{D}$ is the transition dipole operator and E is the total initial energy of the system, $E = E_i - \hbar c k_i$.

We now invoke the usual assumptions concerning dissociation, namely that photon emission during the fragmentation is negligible. In this case the main contribution to the matrix elements $\langle \alpha_f, \varepsilon_f | \boldsymbol{D} \cdot \boldsymbol{e}_f | \alpha_d, \varepsilon_d \rangle$ comes from the asymptotic region (the photon emission occurs at very large R). In that region the continuum wavefunctions can be written in terms of incoming and outgoing spherical free waves. Since we are interested here in a dissociating event, we choose the particular asymptotic form denoted by $|\alpha_d, \varepsilon_d^{(-)}\rangle$ having incoming waves in all channels and a single outgoing wave in channel d. Hence, for energy-normalized eigenstates,

$$\langle R | \alpha_d, \varepsilon_d^{(-)} \rangle_{R \to \infty} \simeq \left(\frac{\mu}{2\pi K_d \hbar^2} \right)^{1/2} \left[\frac{\exp(iK_d R)}{R} |\alpha_d\rangle + \sum_{\tilde{\alpha}_d} \left(\frac{K_d}{\tilde{K}_d} \right)^{1/2} S^*_{\alpha_d \alpha_d} \sim \frac{\exp(-i\tilde{K}_d R)}{R} |\tilde{\alpha}_d\rangle \right] \tag{2}$$

where $K = (2\mu\varepsilon)^{1/2}/\hbar$, μ being the reduced mass for the relative motion of the fragments, is the de Broglie wavevector associated with the dissociation coordinate R. In eqn (2),
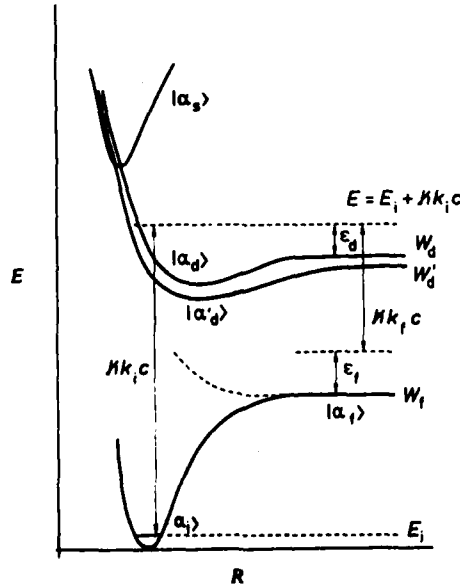
Fig. 1. Schematic potential-energy curves for photodissociation of a diatomic molecule.

$|\alpha\rangle$ are eigenvectors for all other degrees of freedom of the system: orientation of the recoiling axis as well as all the internal degrees of freedom of the fragments. Since $|\alpha\rangle$ channels are usually coupled at finite R, the asymptotic behaviour of $|\alpha_d, \varepsilon_d^{(-)}\rangle$ involves a linear combination of all $|\alpha_d\rangle$ channels as expressed in eqn (2). The coefficients of this expansion are related to the matrix elements $S_{\alpha_d\bar{\alpha}_d}$ of the scattering S matrix. The same asymptotic form applies to the continuum final state $|\alpha_f, \varepsilon_f^{(-)}\rangle$.

Using eqn (2) into the matrix elements $\langle \alpha_f, \varepsilon_f | D \cdot e_f | \alpha_d, \varepsilon_d \rangle$ in eqn (1), and performing the integrations over ε_d, ε_f and R, one obtains (see Appendix):

$$\frac{\partial^2\sigma}{k_f^2 \partial k_f \partial\hat{\Omega}_f} - hc \sum_{\alpha_f} k_f k_i \sum_{\alpha d} \left| \frac{\langle \alpha_f | D \cdot e_f | \alpha_d \rangle \langle \alpha_d, \varepsilon_d^{(-)} | D \cdot e_i^* | \alpha_i \rangle}{\hbar c k_f - (W_d - W_f) + i\Gamma_d} \right|^2 \tag{3}$$

which is sum of Lorentzian functions having widths Γ_d and centred on the fragments' transition energies $(W_d - W_f)$. Finally, after integration of eqn (3) over k_f we find

$$\frac{\partial\sigma}{\partial\hat{\Omega}_f} = 4\pi k_i \sum_{\alpha_d\alpha'_d} \rho_{\alpha_d\alpha'_d} D_{\alpha'_d\alpha_d} = 4\pi k_i \, \text{Tr}\,(\rho D) \tag{4}$$

where

$$\rho_{\alpha_d\alpha'_d} = \langle \alpha_d, \varepsilon_d^{(-)} | D \cdot e_i^* \, \alpha_i \rangle \langle \alpha_i | D \cdot e_i | \alpha'_d, \varepsilon_d^{\prime(-)} \rangle \tag{5}$$

is the excitation density matrix, while

$$D_{\alpha'_d\alpha} - \sum_{\alpha_f} \left(\frac{k_i^2 + k_f^{\prime 3}}{2} \right) \frac{\langle \alpha'_d | D \cdot e_f^* | \alpha_f \rangle \langle \alpha_f | D \cdot e_f | \alpha_d \rangle}{(\Gamma'_d + \Gamma_d) - i(W'_d - W_d)} \tag{6}$$

with $\hbar c k_f = W_d - W_f$, $i\Gamma_d = W_d - W_f$ and $\hbar c k_f' = W'_d - W_f + i\Gamma'_d \approx W'_d - W_f$, is the detection matrix. It is clear from eqn (6) that only terms with $|W'_d - W_d| \leq (\Gamma'_d + \Gamma_d)$ are significant. Therefore, in addition to the diagonal terms, the only off-diagonal terms which need to be retained are those corresponding to degeneracies since (except for H) fine and hyperfine structure levels have energy spacings which are generally large as compared to the radiative width.

Notice that the partial-differential cross-sections defined in eqn (1) and (4) correspond to excitation from a well defined initial state $|\alpha_i\rangle$. In the usual situation an ensemble of $|\alpha_i\rangle$ states are incoherently populated in the initial state. The excitation matrix ρ should then be calculated using eqn (5) multiplied by the population of $|\alpha_i\rangle$ and sum over all initial states.

(B) Rotational Basis Sets

We now turn to the specification of the basis sets used to describe the overall rotation of the molecule and the internal degrees of freedom of the fragments. Two obvious choices are possible: the molecular or 'body-fixed' basis set and the 'space-fixed' basis set. In the body-fixed system we write the wavevectors as:

$$|j\Omega JM\rangle = |\varphi_{j\Omega}\rangle|\Phi^J_{M\Omega}\rangle \tag{7}$$

with:

$$\langle \hat{R} | \Phi^J_{M\Omega} \rangle = \sqrt{\left(\frac{2J+1}{4\pi}\right)} D^{J*}_{M\Omega}(\phi_R, \theta_R, 0) \tag{8}$$

where the $D^J_{mn}(\alpha, \beta, \gamma)$ are the rotational Wigner functions. In eqn (7) and (8) J denotes the quantum number associated with the total angular momentum J, M the projection of J on the laboratory z axis, and Ω its projection on the molecular axis R. The polar angles θ_R and ϕ_R specify the orientation of the molecular axis R in the laboratory system of reference (see fig. 2). Finally, $|j\Omega\rangle$ are the eigenvectors describing all internal
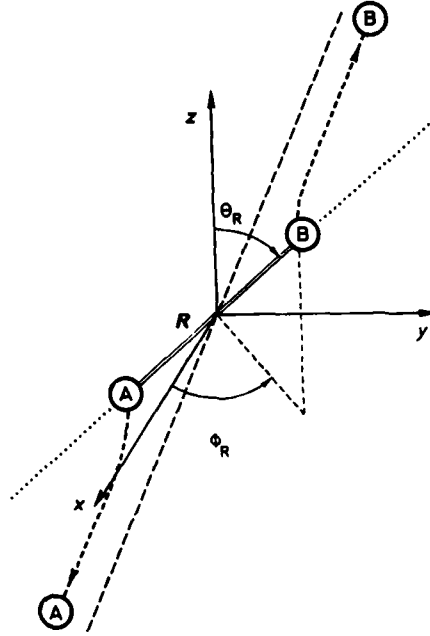
Fig. 2. Coordinate system used in the calculations.

degrees of freedom of the fragments, $j = j_A + j_B$ being the fragment's total angular momentum. We have $J = j + l$, l being the orbital angular momentum associated with the relative motion of the fragments. We notice that since J and M are good quantum numbers, the scattering matrix S in eqn (2) is diagonal with respect to them. On the other hand, Ω is a good quantum number for $R \rightarrow \infty$, but only an approximate one for finite R.

In the space-fixed system we write instead:

$$|jlJM\rangle = \sum_{m_j m_l} (-)^{j-l+M} (2J+1)^{1/2} \begin{pmatrix} j & l & J \\ m_j & m_l & -M \end{pmatrix} |\varphi_{jm_j}\rangle |Y_{lm_l}\rangle \qquad (9)$$

where

$$\langle \hat{R} | Y_{lm_l}\rangle = Y_{lm_l}(\theta_R, \phi_R) \qquad (10)$$

are the spherical harmonics. In eqn (9), the internal eigenstates $|jm_j\rangle$ refer now to the space-fixed system. Between the two basis sets there is the transformation:

$$|j\Omega JM\rangle = \sum_l t_{\Omega,l}^{(jJ)} |jlJM\rangle = \sum_{m_j l m_l} T_{\Omega JM, m_j l m_l}^{(j)} |\varphi_{jm_j}\rangle |Y_{lm_l}\rangle \qquad (11)$$

with

$$t_{\Omega,l}^{(jJ)} = (-)^{j-l+\Omega} (2l+1)^{1/2} \begin{pmatrix} j & l & J \\ \Omega & 0 & \Omega \end{pmatrix} \qquad (12)$$

and

$$T_{\Omega JM, m_j l m_l}^{(j)} = (-)^{M-\Omega} (2l+1)^{1/2} (2J+1)^{1/2} \begin{pmatrix} j & l & J \\ \Omega & 0 & \Omega \end{pmatrix} \begin{pmatrix} j & l & J \\ m_j & m_l & -M \end{pmatrix}. \qquad (13)$$

Since we are interested not only in the calculation of the fluorescence cross-section but also in the degree of alignment and orientation of the fragments, it is more convenient to express ρ and D in the laboratory frame. On the other hand, ρ is much more easily calculated in the body-fixed frame. Using the transformation (11) we can write:

$$\frac{\partial \sigma}{\partial \hat{\Omega}_f} = 4\pi k_i \, \mathrm{Tr} \, (\rho^{(sf)} D^{(sf)}) = 4\pi k_i \, \mathrm{Tr} \, (T^{-1} \rho^{(bf)} T D^{(sf)}). \qquad (14)$$

(C) Excitation Density Matrix in the Body-fixed Frame

We begin by the calculation of $\rho^{(bf)}$. The dissociative eigenstates $|\alpha_d, \varepsilon_d^{(-)}\rangle$ can be written:

$$|\alpha_d, \varepsilon_d^{(-)}\rangle = \sum_{j_d \tilde{\Omega}_d} \left|\varphi_{j_d \tilde{\Omega}_d, j_d \tilde{\Omega}_d}^{J_d, \varepsilon_d}\right) |\tilde{\Omega}_d J_d M_d\rangle \qquad (15)$$

where, according to eqn (2),

$$\langle R | \varphi_{j_d \tilde{\Omega}_d, j_d \tilde{\Omega}_d}^{J_d, \varepsilon_d(-)} \rangle_{R \to \infty} \approx \left(\frac{\mu}{2\pi K_d \hbar^2}\right)^{1/2}$$

$$\times \left[\frac{\exp(iK_d R)}{R \, \delta_{\Omega_d \tilde{\Omega}_d} \delta_{j_d \tilde{j}_d}} + \left(\frac{K_d}{\tilde{K}_d}\right)^{1/2} S_{j_d \tilde{\Omega}_d, j_d \tilde{\Omega}_d}^{J_d \bullet} \frac{\exp(-i\tilde{K}_d R)}{R}\right] |\tilde{j}_d \tilde{\Omega}_d\rangle. \qquad (16)$$

Similarly, it is convenient to expand the initial eigenstate $|\alpha_i\rangle$ in terms of the body-fixed rotational basis set. Hence, we write:

$$|\alpha_i\rangle = \sum_{\Omega_i} |\varphi_{\Omega_i}^{J_i}\rangle |\Omega_i K_i M_i\rangle. \qquad (17)$$

Using eqn (16) and (17), the matrix elements of the electric dipole operator are given by

$$\langle \alpha_i | D \cdot e | \alpha_d, \varepsilon_d^{(-)}\rangle = \sum_p (-)^{J_i - M_i + p} \left(\frac{2J_i + 1}{2J_d + 1}\right)^{1/2} (e)_{-p}$$

$$\times \begin{pmatrix} J_d & 1 & J_i \\ M_d & p & M_i \end{pmatrix} \langle J_i \| D \| j_d \Omega_d J_d, \varepsilon_d^{(-)}\rangle$$

where we have defined the reduced matrix elements:

$$\langle J_i \| D \| h_d \Omega_d J_d, \varepsilon_d^{(-)}\rangle = \sum_q \sum_{\Omega_i, j_d \tilde{\Omega}_d} (-)^{J_i - \Omega_i} (2J_d + 1)$$

$$\times \begin{pmatrix} J_d & 1 & J_i \\ \tilde{\Omega}_d & q & -\Omega_i \end{pmatrix} \langle \varphi_{\Omega_i}^{J_i} | (D)_q | \varphi_{j_d \tilde{\Omega}_d, j_d \tilde{\Omega}_d}^{J_d, \varepsilon_d(-)}\rangle. \qquad (19)$$

In eqn (18),

$$(e)_0 = (e)_z; \qquad (e)_{\pm 1} = \mp \frac{1}{\sqrt{2}}[(e)_x \pm i(e)_y] \qquad (20)$$

are the tensorial components of the polarization vector in the space-fixed system, while in eqn (19),

$$(D)_0 = (D)_{z'}; \qquad (D)_{\pm 1} = \mp \frac{1}{\sqrt{2}}[(D)_{x'} \pm i(D)_{y'}] \qquad (21)$$

where $z \| R$, are the components of the electric dipole operator in the body-fixed system.

Using eqn (18) and after averaging over M_i, assuming the molecule is initially randomly orientated, one obtains:

$$\rho^{(bf)}_{j_d\Omega_dJ_dM_d,j_d\Omega_d'J_d'M_d'} = \sum_{KQ} (-)^{K-Q-J_i-M_d'} \frac{2K+1}{\sqrt{[(2J_d+1)(2J_d'+1)]}} F_{KQ}(e_i)$$

$$\times \begin{Bmatrix} 1 & 1 & K \\ J_d' & J_d & J_i \end{Bmatrix} \begin{pmatrix} J_d & J_d' & K \\ M_d & -M_d' & -Q \end{pmatrix}$$

$$\times \langle J_i \| D \| j_d\Omega_dJ_d, \varepsilon_d^{(-)} \rangle^* \langle J_i \| D \| j_d'\Omega_d'J_d', \varepsilon_d'^{(-)} \rangle \tag{22}$$

where K can only take the values 0, 1 and 2, and

$$F_{KQ}(e) = \sum_{pp'} (-)^p (e)^*_{-p}(e)_{-p'} \begin{pmatrix} 1 & 1 & K \\ -p' & p & Q \end{pmatrix} = \sum_{pp'} (e)_p(e^*)_{p'} \begin{pmatrix} 1 & 1 & K \\ p & p' & Q \end{pmatrix} \tag{23}$$

is a function which depends only on the polarization vector e. For linearly polarized light along z, for example, $Q=0$ and F_{KQ} is different from zero only for $K=0$ and $K=2$.

(D) Excitation Density Matrix in the Space-fixed Frame

The next step is to transform $\rho^{(bf)}$ to the space-fixed frame using:

$$\rho^{(sf)}_{j_dm_{j_d}lm_l,j_d'm_{j_d'}l'm_l'} = \sum_{\Omega_dJ_dM_d} \sum_{\Omega_d'J_d'M_d'} T^{(j_d)}_{\Omega_dJ_dM_d,m_{j_d}lm_l} \rho^{(bf)}_{j_d\Omega_dJ_dM_d,j_d'\Omega_d'J_d'M_d'} T^{(j_d')}_{\Omega_d'J_d'M_d',m_{j_d'}l'm_l'} \tag{24}$$

with the transformation matrix T being defined by eqn (12). Actually, since the detection matrix D is independent of the orbital angular momentum l and we have assumed that different j_d have spacings larger than their radiative widths, we are only interested in the reduced density matrix $\rho^{(j)}_{m_j,m_j} = \sum_{lm_l} \rho^{(sf)}_{jm_jlm_l,jm_j'lm_l}$. Using eqn (24), (22) and (12) and performing the sum over l and m_l, one obtains:

$$\rho^{(j_d)}_{m_{j_d}',m_{j_d}} = \sum_{KQ} (-)^{j_d+m_{j_d}}(2K+1) \begin{pmatrix} j_d & j_d & j_d & K \\ m_{j_d}' & -m_{jd} & -m_{jd} & Q \end{pmatrix} P^{(j_d)}_K F_{KQ}(e_i) \tag{25}$$

with

$$P^{(j_d)}_K = \sum_{\Omega_dJ_d} \sum_{\Omega_d'J_d'} \sum_{Q'} (-)^{j_d+J} \begin{pmatrix} J_d & J_d' & K \\ \Omega_d & -\Omega_d' & -Q' \end{pmatrix} \begin{pmatrix} j_d & j_d & K \\ -\Omega_d' & \Omega_d & -Q' \end{pmatrix}$$

$$\times \begin{Bmatrix} 1 & 1 & K \\ J_d' & J_d & J_i \end{Bmatrix} \langle J_i \| D \| j_d\Omega_dJ_d, \varepsilon_d^{(-)} \rangle^* \langle J_i \| D \| j_d\Omega_d'J_d', \varepsilon_d^{(-)} \rangle \tag{26}$$

which, using eqn (19), can be explicitly written as:

$$P^{(j_d)}_K = \sum_{\Omega_dJ_d} \sum_{\Omega_d'J_d'} \sum_{qq'Q'} \sum_{\Omega_i\Omega_i'} \sum_{j_d\tilde\Omega_d} \sum_{j_d\tilde\Omega_d'} (-)^{j_d-J_i-\Omega_i-\Omega_i'}(2J_d+1)(2J_d'+1)$$

$$\times \begin{pmatrix} J_d & J_d' & K \\ \Omega_d & -\Omega_d' & -Q' \end{pmatrix} \begin{pmatrix} j_d & j_d & K \\ -\Omega_d' & \Omega_d & -Q' \end{pmatrix} \begin{pmatrix} J_d & 1 & J_i \\ \tilde\Omega_d & q & -\Omega_i \end{pmatrix} \begin{pmatrix} J_d' & 1 & J_i \\ \tilde\Omega_d' & q' & -\Omega_i' \end{pmatrix}$$

$$\times \begin{Bmatrix} 1 & 1 & K \\ J_d' & J_d & J_i \end{Bmatrix} \langle \varphi^{J_i}_{\Omega_i} | (D)_q | \varphi^{j_d,\varepsilon_d^{(-)}}_{j_d\Omega_d,J_d\tilde\Omega_d} \rangle^* \langle \varphi^{J_i}_{\Omega_i'} | (D)_{q'} | \varphi^{j_d,\varepsilon_d^{(-)}}_{j_d\Omega_d',J_d\tilde\Omega_d'} \rangle. \tag{27}$$

Note at this point that with the definition given by eqn (25), the product $P^{(j_d)}_K F_{KQ}(e_i)$ is directly related (for $Q=0$) to the population ($K=0$), orientation ($K=1$), and alignment ($K=2$) of the fragments. Some well known[17] general conclusions can be made by inspection of eqn (23) and (26). First, orientation cannot be obtained with linearly polarized light since in that case $F_K0=0$ for $K=1$. On the other hand, orientation of a fragment can be obtained with circularly polarized light except for a dissociative Σ state (one of the 3-j coefficients in eqn (26) is zero in that case).

Polarization of Photofragments

It is clear from eqn (26) how coherence effects in the alignment and orientation of the fragments (and hence in the fluorescence polarization) will appear. They come from the terms in the sum involving $\Omega_d \neq \Omega_d'$. They are of two types. The first involves terms with $\Omega_d = \pm1$, $\Omega_d' = \mp1$, i.e. for II *states*. They were discussed in detail[18,19,25] in connexion with the anomalous degree of polarization found in the photodissociation of Ca_2. It corresponds to $Q' = \Omega_d - \Omega_d' = \pm2$ and therefore it will only show in the alignment ($K = 2$) and not in the orientation ($K = 1$) of the photofragments. The other possible coherence effect arises when two states of different symmetry ($\Omega_d = 0$ and $\Omega_d' = \pm1$, for instance) are excited simultaneously.[25] In the particular case of $Q' = \Omega_d - \Omega_d' = \pm1$, it is possible to observe this coherence in the alignment but also in the orientation of the fragments. It is obvious from eqn (26) and (27) that coherence effects involving states with different symmetry will depend not only on the absolute value of the dissociation amplitudes $\langle \varphi_{\Omega_i}^{j_i} | (D)_q (\varphi_{\Omega_d}^{j_d}) \rangle$ but also on the *relative phases of the vibrational continuum wavefunctions*. In general the amplitudes are slowly varying functions of the energy while the phases are more rapidly changing. Therefore an oscillating behavior of all vector properties (alignment, orientation, polarization) is expected.[25]

(F) Fragments' fluorescence intensity

We turn now to the calculation of the fluorescence cross-section, eqn (4), which will be given by:

$$\frac{\partial \sigma}{\partial \hat{\Omega}_f} = 4\pi k_i \mathrm{Tr}(\rho^{(sf)} D^{(sf)}) = 4\pi k_i \sum_{m_{j_d} m_{j_d}'} \rho^{(j_d)}_{m_{j_d} m_{j_d}'} D^{(j_d)}_{m_{j_d}' m_{j_d}} \tag{28}$$

with

$$D^{(j_d)}_{m_{j_d}' m_{j_d}} = \frac{k_f^3}{2\Gamma_d} \sum_{m_{j_f}} \langle j_d m_{j_d}' | \boldsymbol{D} \cdot \boldsymbol{e}_f^* | j_f m_{j_f} \rangle \langle j_f m_{j_f} | \boldsymbol{D} \cdot \boldsymbol{e}_f | j_d m_{j_d} \rangle. \tag{29}$$

Using

$$\langle j_f m_{j_f} | \boldsymbol{D} \cdot \boldsymbol{e}_f | j_d m_{j_d} \rangle = \sum_p (-)^{j_f - m_{j_f} + p} \left(\frac{2j_f + 1}{2j_d + 1} \right) (\boldsymbol{e}_f)_{-p}$$

$$\times \begin{pmatrix} j_d & 1 & j_f \\ m_{j_d} & p & -m_{j_f} \end{pmatrix} \langle j_f \| \boldsymbol{D} \| j_d \rangle \tag{30}$$

we finally obtain

$$\frac{\partial \sigma}{\partial \hat{\Omega}_f} = \frac{2\pi k_i k_f^2}{\Gamma_d} \sum_K (-)^{j_f - j_d - K} \frac{(2j_f + 1)}{(2j_d + 1)} P_K^{(j_d)} F_K(\boldsymbol{e}_i, \boldsymbol{e}_f)$$

$$\times \begin{Bmatrix} 1 & 1 & K \\ j_d & j_d & j_f \end{Bmatrix} |\langle j_f \| \boldsymbol{D} | j_d \rangle \|^2 \tag{31}$$

where

$$F_K(\boldsymbol{e}_i, \boldsymbol{e}_f) = (2K + 1) \sum_Q F_{KQ}(\boldsymbol{e}_i) F_{KQ}^*(\boldsymbol{e}_f). \tag{32}$$

Eqn (27) provides the density matrix for the production of fragments in states $|j_d m_{j_d}\rangle$ specified by an angular momentum j_d. In the general case the fragments will both have angular momenta j_A and j_B different from zero, and $j_d = j_A + j_B$. Since we are interested here in the emission from one of the fragments (say A), the detection matrix D factorizes in a product of two matrices one for fragment A and another (diagonal and unity) for fragment B. It will then be more convenient to work with the product basis set $|j_A m_{j_A}\rangle |j_B m_{j_B}\rangle$ instead of $|j_d m_{j_d}\rangle$.

(E) Angular Momenta of the Fragments

The transformation between the two basis sets is simply given by

$$|j_d m_{j_d}\rangle = \sum_{m_{j_A} m_{j_B}} C(j_A m_{j_A}, 4j_B m_{j_B}; j_d m_{j_d}) |j_A m_{j_A}\rangle |j_B m_{j_B}\rangle \qquad (33)$$

with

$$C(j_A m_{j_A}, j_B m_{j_B}; j_d m_{j_d}) = (-)^{j_A - j_B + m_{j_d}} (2j_d + 1)^{1/2} \begin{pmatrix} j_A & j_B & j_d \\ m_{j_A} & m_{j_B} & -m_{j_d} \end{pmatrix}. \qquad (34)$$

The elements of the excitation density matrix in which we are interested, will then be given by

$$\rho^{(j_A)}_{m_{j_A}, m_{j_A}} = \sum_{m_{j_B}} \sum_{m_j} \sum_{m_{j_d}} C(j_A m_{j_A}, j_B m_{j_B}; j_d m_{j_d}) \rho^{(j_d)}_{m_{j_d}, m_{j_d}} C(j'_A m'_{j_A}, j_B m_{j_B}; m'_{j_d})$$

$$= \sum_{KQ} (-)^{j_A + m_{j_A}} (2K + 1) \begin{pmatrix} j_A & j_A & K \\ m'_{j_A} & -m_{j_A} & Q \end{pmatrix} \bar{P}^{(j_A j_B j_d)}_K F_{KQ}(e_i) \qquad (35)$$

with

$$\bar{P}^{(j_A j_B j_d)}_K = (-)^{j_A - j_B + j_d + K} (2j_d + 1) \begin{Bmatrix} j_A & j_A & K \\ j_d & j_d & j_B \end{Bmatrix} P^{(j_A j_B j_d)}_K \qquad (36)$$

with

$$P^{(j_A j_B j_d)}_K = \sum_{\Omega_d J_d} \sum_{\Omega'_d J'_d} \sum_{Q'} (-)^{j_d + J_i} \begin{pmatrix} J_d & J'_d & K \\ \Omega_d & -\Omega'_d & -Q' \end{pmatrix} \begin{pmatrix} j_d & j_d & K \\ -\Omega'_d & \Omega_d & -Q' \end{pmatrix}$$

$$\times \begin{Bmatrix} 1 & 1 & K \\ J'_d & J_d & J_i \end{Bmatrix} \langle J_i \| D \| j_A j_B j_d \Omega_d J_d, \varepsilon_d^{(-)} \rangle^* \langle J_i \| D \| j_A j_B j_d \Omega'_d J'_d, \varepsilon_d^{(-)} \rangle$$

$$= \sum_{\Omega_d J^d} \sum_{\Omega'_d J'_d} \sum_{qq'Q'} \sum_{\Omega_i \Omega_i} \sum_{J_d \Omega_d} \sum_{J'_d \Omega_d} \sum_{\bar{J}_A \bar{J}_B} \sum_{\bar{J}_A \bar{J}_B} (-)^{j_d - J_i - \Omega_i - \Omega'_i} (2J_d + 1)(2J'_d + 1)$$

$$\times \begin{pmatrix} J_d & J'_d & K \\ \Omega_d & -\Omega'_d & -Q' \end{pmatrix} \begin{pmatrix} j_d & j_d & K \\ -\Omega'_d & \Omega_d & -Q' \end{pmatrix} \begin{pmatrix} J_d & 1 & J_i \\ \Omega_d & q & -\Omega_i \end{pmatrix} \begin{pmatrix} J'_d & 1 & J_i \\ \tilde{\Omega}_d & q' & -\Omega_i \end{pmatrix}$$

$$\times \begin{Bmatrix} 1 & 1 & K \\ J'_d & J_d & J_i \end{Bmatrix} \langle \varphi^{J_i}_{\Omega_i} | (D)_q | \varphi^{J_d, \varepsilon_d^{(-)}}_{j_A j_B j_d \Omega_d, \bar{J}_A \bar{J}_B \bar{J}_d \tilde{\Omega}_d} \rangle^* \langle \varphi^{J_i}_{\Omega_i} | (D)_{q'} | \varphi^{J'_d, \varepsilon_d^{(-)}}_{j_A j_B j_d \Omega_d, \bar{J}_A \bar{J}_B \bar{J}_d \tilde{\Omega}_d} \rangle \cdot \qquad (37)$$

which has essentially the same form as $P^{(j_d)}_K$ given in eqn (26) and (27), except for the explicit dependence of the dissociation matrix elements on j_A and j_B. Note that $\bar{P}^{(j_A j_B j_d)}_K$ reduces to $P^{(j_d)}_K$ when $j_B = 0$.

By the same calculation conducting to eqn (31) it is possible to write the fluorescence cross-section as:

$$\frac{\partial \sigma}{\partial \hat{\Omega}_f} = \frac{2\pi k_i k_f^3}{\Gamma_d} \sum_K (-)^{j'_A - j_A - K} \frac{(2j'_A + 1)}{(2j_A + 1)} \bar{P}^{(j_A j_B j_d) K}_K F_K (e_i, e_f)$$

$$\times \begin{Bmatrix} 1 & 1 & K \\ j_A & j_A & j'_A \end{Bmatrix} |\langle j'_A \| D \| j_A \rangle|^2 \qquad (38)$$

where we have denoted by j'_A the angular momentum quantum number for fragment A in the final state after photon emission.

Eqn (35)–(38) together with the definitions of F_K and F_{KQ} given in eqn (23) and (32), constitute our general expressions for the excitation density matrix of the photofragments in the laboratory frame $\rho^{(j_A)}_{m_{j_A}, m_{j_A}}$, the alignment and orientation degrees given by $\bar{P}^{(j_A j_B j_d)}_K F_{KQ}(e_i)$, and the fluorescence cross-section provided by eqn (38). They can be applied to any photofragmentation process involving a molecular system breaking into two fragments induced by electric dipole transitions.

3. Direct Dissociation for Diatomic Molecules

A. Axial Recoil Approximation

Eqn (37) can be simplified in the axial recoil approximation in which one assumed that the dissociation matrix elements are slowly varying functions of the total angular momentum and that Ω_d is a good quantum number. Therefore:

$$\langle \varphi^{J_i}_{\Omega_i} |(D)_q| \varphi^{J_d,\varepsilon_d(-)}_{j_A j_B j_d \Omega_d, j_A j_B j_d \Omega_d'} \rangle = \delta_{\Omega_d,\Omega_d'} \langle \varphi^{J_i}_{\Omega_i} |(D)_q| \varphi^{J_i,\varepsilon_d(-)}_{j_A j_B j_d \Omega_d, j_A j_B j_d \Omega_d'} \rangle \qquad (39)$$

where $J_d = J_i$, $J_i \pm 1$ have been replaced by the average $J_d = J_i$ value. Using this equation in eqn (37) one finally obtains

$$P^{(j_A j_B j_d)}_K = \sum_{\Omega_d \Omega_d'} \sum_{\Omega_i} (-)^{j_d + \Omega_i - \Omega_d - \Omega_d'} \begin{pmatrix} 1 & 1 & K \\ (\Omega_i - \Omega_d') & (\Omega_d - \Omega_i) & (\Omega_d' - \Omega_d) \end{pmatrix}$$
$$\times \begin{pmatrix} j_d & j_d & K \\ -\Omega_d' & \Omega_d & (\Omega_d' - \Omega_d) \end{pmatrix} M^*_{\Omega_i, j_A j_B j_d \Omega_d} M_{\Omega_i, j_A j_B j_d \Omega_d'} \qquad (40)$$

where we have defined

$$M_{\Omega_i, j_A j_B j_d \Omega_d} = \sum_{j_A j_B} \langle \varphi^J_{\Omega_i} |(D)_{(\Omega_i - \Omega_d)}| \varphi^{J_i,\varepsilon_d(-)}_{j_A j_B j_d \Omega_d, j_A j_B j_d \Omega_d} \rangle. \qquad (41)$$

We notice from eqn (4) that in the axial recoil approximation orientation ($K = 1$) cannot be obtained for a parallel transition; i.e. for $\Omega_i - \Omega_d = \Omega_i - \Omega_d' = 0$.

(B) Application to a Simple Case

As an example of application let us consider the simple photodissociation event:

$$AB(^1\Sigma) \xrightarrow{h\nu_i} AB^*(^1\Sigma, {}^1\Pi) \longrightarrow A^*(^1P) + B(^1S) \xrightarrow{h\nu_f} A(^1S) + B(^1S) \qquad (42)$$
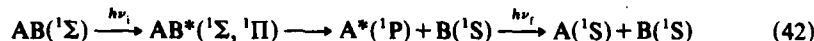
where a diatomic molecule in an initial state $^1\Sigma$ state is excited simultaneously to a $^1\Sigma$ and a $^1\Pi$ state, both correlating to the same limit with atom A being in an excited ^1P electronic state from which emits a photon to a final ^1S state. We further assume that non-adiabatic couplings can be neglected and that the axial recoil approximation is adequate. In our notation we then have: $j_A = 1$, $j_A' = 0$, $j_B = 0$, $\Omega_i = 0$, $\Omega_d = 0, \pm 1$. Since the atom B is produced with total angular momentum zero we shall have $j_d = j_A = 1$, $j_f = j_A' = 0$ and we can use eqn (31) with

$$P^{(j_d)}_K = \sum_{\Omega_d \Omega_d'} (-)^{j_d + \Omega_i - \Omega_d - \Omega_d'} \begin{pmatrix} 1 & 1 & K \\ (\Omega_i - \Omega_d') & (\Omega_d - \Omega_i) & (\Omega_d' - \Omega_d) \end{pmatrix}$$
$$\times \begin{pmatrix} j_d & j_d & K \\ -\Omega_d' & \Omega_d & (\Omega_d' - \Omega_d) \end{pmatrix} M^*_{\Omega_i, j_d \Omega_d} M_{\Omega_i, j_d \Omega_d'}. \qquad (43)$$

Using the explicit values of the $3 - j$ coefficients we obtain

$$P^{(1)}_0 = -\tfrac{1}{3}\{|M_\Sigma|^2 + 2|M_\Pi|^2\}$$
$$P^{(1)}_1 = \tfrac{1}{2}\{|M_\Pi|^2 - (M^*_\Sigma M_\Pi + M_\Sigma M^*_\Pi)\} \qquad (44)$$
$$P^{(1)}_2 = +\tfrac{1}{13}\{2|M_\Sigma|^2 + 7|M_\Pi|^2 + 3(M^*_\Sigma M_\Pi + M_\Sigma M^*_\Pi)\}$$

where we have denoted by M_Σ and M_Π the dissociation matrix elements into the Σ and Π states, respectively. As expected, $P^{(1)}_1$ is zero for a pure $\Sigma \to \Sigma$ transition. Using these values of P in eqn (31) the fluorescence intensity for given incident e_i and final e_f polarizations can be computed and the degree of polarization can be obtained by the

use of eqn (1). For linearly incident polarization (chosen along the laboratory z axis) and parallel (z) and perpendicular (x) polarizations of the emitted photon, we have:

$$(F_0)_\| = \tfrac{1}{3}; \qquad (F_1)_\| \approx 0; \qquad (F_2)_\| = +\tfrac{2}{3}$$
$$(F_0)_\perp = \tfrac{1}{3}; \quad \phi(F_1)_\perp \approx 0; \qquad (F_2)_\perp = -\tfrac{1}{3} \tag{45}$$

and

$$\left(\frac{\partial\sigma}{\partial\hat{\Omega}_f}\right)_\| \propto \tfrac{1}{15}\{3|M_\Sigma|^2 + 8M_\Pi|^2 - 2(M_\Sigma^* M_\Pi + M_\Sigma M_\Pi^*)\}$$

$$\left(\frac{\partial\sigma}{\partial\hat{\Omega}_f}\right)_\perp \propto \tfrac{1}{15}\{|M_\Sigma|^2 + |M_\Pi|^2 + (M_\Sigma^* M_\Pi + M_\Sigma M_\Pi^*)\}. \tag{46}$$

In order to make contact with earlier calculations, we have to denote differently the dissociation matrix elements. In ref. (17), (19) and (25), the continuum wavefunctions were taken to be of the form:

$$\chi_{\Omega_d}^{\varepsilon_d}(R)_{R\to\infty} \approx \left(\frac{2\mu}{2\pi K_d\hbar^2}\right)^{1/2} \sin\left(K_d R - \phi_{\Omega_d}\right) \tag{47}$$

where ϕ_{Ω_d} is the asymptotic phase which is related to the scattering matrix S (which in this case is diagonal) by $S_{\Omega_d,\Omega_d} = -\exp(2i\phi_{\Omega_d})$. Comparing now eqn (16) and (47), we shall then have:

$$|\varphi_{\Omega_d}^{\varepsilon_d(-)} = i \exp\left(i\phi_{\Omega_d}\right)\frac{\chi_{\Omega_d}^{\varepsilon_d}(R)}{R}|\Omega_d\rangle \tag{48}$$

and

$$M_\Sigma = i \exp\left(\phi\Sigma\right)M_\Sigma; \qquad M_\Pi = -i \exp\left(\phi\Pi\right)M_\Pi \tag{49}$$

where M_Σ and M_Π are the real dissociation matrix elements using the vibrational continuum wavefunctions χ defined asymptotically by eqn (47). The minus sign in the definition of M_Π corresponds to the usual phase choice for the electronic wavefunction of a Π state. With these definitions we find:

$$P = \frac{(\partial\sigma/\partial\hat{\Omega}_f)_\| - (\partial\sigma/\partial\hat{\Omega}_f)_\perp}{(\partial\sigma/\partial\hat{\Omega}_f)_\| + (\partial\sigma/\partial\hat{\Omega}_f)_\perp}$$

$$= \frac{2M_\Sigma^2 + 7M_\Pi^2 + 6M_\Sigma M_\Pi \cos\left(\phi_\Sigma - \phi_\Pi\right)}{4M_\Sigma^2 + 9M_\Pi^2 + 2M_\Sigma M_\Pi \cos\left(\phi_\Sigma - \phi_\Pi\right)} \tag{50}$$

which is the result obtained earlier. In particular for a pure $\Sigma \to \Sigma$ transition ($M_\Pi = 0$) we obtain:

$$P_{\Sigma-\Sigma} = \tfrac{1}{2} \tag{51}$$

while for a pure $\Sigma \to \Pi$ transition ($M_\Sigma = 0$):

$$P_{\Sigma-\Pi} = \tfrac{7}{9} \approx 0.78 \tag{52}$$

which as has been fully discussed before[18,19] is much larger than the maximum classical value of 0.5. It should be emphasized that although it is not clearly seen in eqn (50), this result also arises from a coherence effect involving $\Omega_d = \pm1$ states. If in the calculation of P, eqn (43), these terms are not included the result given in eqn (52) to $P = 1/7 \approx 0.14$, which is much smaller than the result when coherence effects are included.

(C) Fine Structure

In the preceding example we have considered the case where the two atomic fragments where in singlet states and the atom B had total angular momentum zero. Let us consider now the case where the two fragments have non-zero momentum:

$$AB(^1\Sigma) \xrightarrow{h\nu_i} AB^*(^1\Sigma,^1\Pi) \longrightarrow A^*(^2P) + B(^2S) \xrightarrow{h\nu_f} A(^2S) + B(^2S). \tag{53}$$
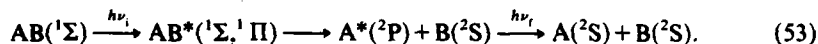
In this case we apply eqn (36) and (40) with $j_A = 1/2$, $3/2$, $j'_A = 1/2$, $j_B = 1/2$. The function P_K has exactly the same expression as before [eqn (44)] except that the dissociation matrix elements M_Σ and M_Π will in general be different for different values of j_A. Their actual values will, of course, depend on the dissociation dynamics. However, for kinetic energies larger than the fine-structure splitting the dissociation occurs faster than the coupling of the spin to the orbital angular momentum. In these conditions the dissociation probability for obtaining a particular fine-structure limit will be given simply by the weight of that fine-structure component in the excited molecular wavefunction. For molecular wavefunctions in Hund's case (a) giving fragments with orbital angular momenta L_A, L_B and spin angular momenta A_A, S_B, we have:[20]

$$|\Lambda S\Sigma\Omega\rangle_{R\to\infty} = \sum_{\Lambda_A\Lambda_B} C_{\Lambda_A\Lambda_B\Lambda}|L_A\Lambda_A\rangle|L_B\Lambda_B\rangle|S\Sigma\rangle$$

$$= \sum_{j_Aj_Bj_d}\sum_{\Lambda_A\Lambda_B}\sum_L |j_Aj_Bj_d\Omega\rangle A_{\Lambda_A\Lambda_B\Lambda S\Sigma\Omega j_Aj_Bj_d}$$

with

$$A_{\Lambda_A\Lambda_B\Lambda S\Sigma\Omega j_Aj_Bj_d} = (-)^{L_A-L_B+L-S+\Lambda+\Omega}(2S+1)^{1/2}(2j_A+1)^{1/2}(2j_B+1)^{1/2}(2L+1)^{1/2}$$

$$\times C_{\Lambda_A\Lambda_B\Lambda}\begin{pmatrix} L & L_B & L \\ \Lambda_A & \Lambda_B & \Lambda \end{pmatrix}\begin{pmatrix} \Lambda & S & j_d \\ \Lambda & \Sigma & \Omega \end{pmatrix}\begin{Bmatrix} L_A & S_A & j_A \\ L_B & S_B & j_B \\ L & S & j_d \end{Bmatrix} \tag{55}$$

where the coefficients $C_{\Lambda_A\Lambda_B\Lambda}$ are determined by the electrostatic interaction at large distances. If one of the atoms is in an S state ($L_B = 0$ for instance) then the sum reduces to only one term and the coefficient is unity. Furthermore, if the total spin is zero ($S = 0$) eqn (55) reduces to:

$$A_{\Lambda 0\Lambda 00\Omega j_Aj_Bj_d} = \frac{\sqrt{(2j_A+1)}}{\sqrt{[(2S_A+1)(2j_d+1)]}}(-)^{j_A-S_A-j_d}\delta_{j_dL_A}\delta_{S_AS_B}\delta_{Sj_B} \tag{56}$$

and the coefficients A are independent of Λ. Using these coefficients we write for our particular case:

$$M_{j_A\Omega_d} = (-)^{j_A-3/2}\sqrt{\left(\frac{2j_A-1}{6}\right)}M_{\Omega_d} \tag{57}$$

where the M_{Ω_d} are the M_Σ and M_Π defined in eqn (49). Using the fact that the emission matrix elements from the two fine-structure components are realted by: $\langle j'_A = 1/2\|D\|j_A = 3/2\rangle = 2\langle j'_A - 1/2\|D\|j_A = 1/2\rangle$, we finally obtain for excitation with linearly polarized light:

$$(\partial\sigma/\partial\hat{\Omega}_f)_\parallel^{(1/2)} = (\partial\sigma/\partial\hat{\Omega}_f)_\perp^{(1/2)} \propto \tfrac{1}{45}(5M_\Sigma^2 + 10M_\Pi^2) \tag{58}$$

and

$$(\partial\sigma/\partial\hat{\Omega}_f)_\parallel^{(3/2)} \propto \tfrac{1}{45}(14M_\Sigma^2 + 34M_\Pi^2 + 4M_\Sigma M_\Pi \cos(\phi_\Sigma - \phi_\Pi))$$

$$(\partial\sigma/\partial\hat{\Omega}_f)_\perp^{(3/2)} \propto \tfrac{1}{45}(8M_\Sigma^2 + 13M_\Pi^2 - 2M_\Sigma M_\Pi \cos(\phi_\Sigma - \phi_\Pi)). \tag{59}$$

The polarization of the fragments' fluorescence will then be given by:[20,25]

$$P^{(1/2)} = 0$$

$$P^{(3/2)} = \frac{6M_\Sigma^2 + 21M_\Pi^2 + 18M_\Sigma M_\Pi \cos(\phi_\Sigma - \phi_\Pi)}{22M_\Sigma^2 + 47M_\Pi^2 + 6M_\Sigma M_\Pi \cos(\phi_\Sigma - \phi_\Pi)}$$

(60)

which show the effect of depolarization due to the fine structure. Actually, although the fine structure is resolvable in principle, in some experiments the two emissions are not resolved and the detected intensities are just the incoherent sum of the emissions given by eqn (58) and (59). The degree of polarization is in that case:[20,25]

$$P = \frac{6M_\Sigma^2 + 21M_\Pi^2 + 18M_\Sigma M_\Pi \cos(\phi_\Sigma - \phi_\Pi)}{32M_\Sigma^2 + 67M_\Pi^2 + 6M_\Sigma M_\Pi \cos(\phi_\Sigma - \phi_\Pi)}$$

(61)

which is of course lower than the polarization of the $j_A = 3/2$ component since the $j_A = 1/2$ component is unpolarized.

(D) Effect of Non-adiabatic Coupling

When coupling occurs between the continua, it is no longer possible to write the dissociation matrix elements as in eqn (49). Instead a full close-coupling calculation of the $\varphi^{(-)}$ wavefunctions has to be conducted and eqn (61) should be written:

$$P = \frac{6|M_\Sigma|^2 + 21|M_\Pi|^2 + 9(M_\Sigma M_\Pi^* + M_\Sigma^* M_\Pi)}{32|M_\Sigma|^2 + 67|M_\Pi|^2 + 3(M_\Sigma M_\Pi^* + M_\Sigma^* M_\pi)}.$$

(62)

An interesting situation involving such a case is constituted by H_2 in the region above the threshold for production of $H(1s) + H(2p)$ fragments. Since the potential-energy curves,[28,31] adiabatic corrections,[32-35] electronic couplings[36] and the transitions dipole moments[37-39] are well known in this energy region, accurate calculations can be performed. In addition, with the development of synchrotron radiation sources and vacuum u.v. (v.u.v.) lasers, it will be possible to compare theory and experiment in great detail. Thus H_2 provides a particularly stringent test for the predicted coherence effects. If H_2 is initially in its ground state, several dissociative excited electronic states can be populated through electric dipole transitions in this energy region: B, B', and C. Adiabatically, the B' state correlates to $H(1s) + H(2s)$ fragments. Therefore, in the adiabatic approximation, only the $B(^1\Sigma)$ and the $C(^1\Pi)$ states, which correlate both to $H(1s) + H(2p)$ fragments, are relevant for determining the degree of polarization of the Ly_α emission. The adiabatic approximation, however, does not hold for the $B(^1\Sigma)$ and the $B'(^1\Sigma)$ states in H_2. They are coupled by radial non-adiabatic terms which induce transitions between the two states at large internuclear distances $(R_0 \approx 15 \, a_0)$.[40,41] Therefore, the three states B, B' and C have to be considered when treating direct dissociation in this energy region.

In ref. (42) we have shown that the amplitude M_Σ can be very accurately analysed in terms of the half-collision scattering matrix and that it can be written:

$$M_\Sigma \propto M_B(1-P)^{1/2} \exp(i\phi_B - M_{B'}^{1/2}P^{1/2}) \exp(i\phi_{b'})$$

(63)

where M_B and $M_{B'}$ are the adiabatic photodissociation matrix elements for the B and B' states, respectively, ϕ_B and $\phi_{B'}$ are their phases and P is the probability of a non-adiabatic transition between the two states during the half-collision after photon absorption. For the C state, which can be considered to be uncoupled, we can write:

$$M_\Pi \propto M_C \exp(i\phi_C).$$

(64)

Using eqn (63) and (64) in eqn (62), we finally obtain

$$P = \frac{(\partial\sigma/\partial\hat{\Omega}_r)_\parallel - (\partial\sigma/\partial\hat{\Omega}_r)_\perp}{(\partial\sigma/\partial\hat{\Omega}_r)_\parallel + (\partial\sigma/\partial\hat{\Omega}_r)_\perp} = N/D$$

(65a)

with

$$N = 21M_C^2 + 6M_B^2(1-P) + 6M_{B'}^2 P - 12M_B M_{B'}[P(1-P)]^{1/2} \cos(\phi_B - \phi_{B'})$$
$$+ 18M_C M_B(1-P)^{1/2}\cos(\phi_C - \phi_B) - 18M_C M_{B'}P^{1/2}\cos(\phi_C - \phi_{B'}) \quad (65b)$$

and

$$D = 67M^2 + 32M_B^2(1-P) + 32M_{B'}^2 P - 64M_B M_{B'}[P(1-P)]^{1/2}\cos(\phi_B - \phi_{B'})$$
$$+ 6M_C M_B(1-P)^{1/2}\cos(\phi_C - \phi_B) - 6M_C M_{B'}P^{1/2}\cos(\phi_C - \phi_{B'}). \quad (65c)$$

It is clear from an inspection of eqn (65) that P depends in a rather complicated manner on the phase differences between the three dissociative states. This is due to the contribution of the two completely different effects, namely: the oscillating behaviour of the photodissociation cross-section $\sigma_\Sigma = |M_\Sigma|^2$ due to the non-adiabatic coupling between the B and B′ states and the coherence effect between the Σ and the Π states. The oscillation of σ_Σ is the result of a quantum interference effect between two different paths, leading to the same final state of the fragments.[42,43] Consider, for example, the final state H(1s) + H(2p) we are interested in here. There are two paths which lead to this final state: excitation of the B electronic excited state followed by an adiabatic dissociation, or excitation of the B′ state followed by a non-adiabatic transition to the B state. The partial photodissociation cross-section into the H(1s) + H(2p) channel will then be the square of the sum of the two quantum-mechanical amplitudes associated to each one of those paths as expressed in eqn (63). Hence the interference effect. Ignoring the non-adiabatic coupling between the B and B′ states and assuming an incoherent excitation with linearly polarized light of the B and C states, the polarization rate would be nearly constant.

4. Predissociation

(a) Isolated Resonance

In the case of predissociation the axial recoil approximation is no longer valid and the general equations (33) to (37) have to be used. On the other hand, for slow predissociation (*i.e.* when the rotational spacings are larger than the predissociation widths) it is possible to excite one particular transition $J_i \to J_d$, and the sum over J_d and J'_d reduce to only one term. More precisely, let us assume that a bound electronic state $|\alpha_s\rangle$ (see fig. 1) predissociates to a set of dissociative continua $|\alpha_d, \varepsilon_d^{(-)}\rangle$. For slow predissociation, the isolated resonance approximation is valid and the eigenstate $|\alpha_d, \varepsilon_d^{(-)}\rangle$ can be written:

$$|\alpha_d, \varepsilon_d^{(-)}\rangle = a_{\alpha_d,\alpha_s}^{\varepsilon_d(-)}|\alpha_s^{(0)}\rangle + \sum_{\alpha_d'}\int d\varepsilon_d' b_{\alpha_d,\alpha_d'\varepsilon_d'}^{\varepsilon_d(-)}|\alpha_d'^{(0)}, \varepsilon_d'^{(-)}\rangle \quad (66)$$

where $|\alpha_s^{(0)}\rangle$ and $|\alpha_d'^{(0)}, \varepsilon_d'^{(-)}\rangle$ are the zero-order eigenfunctions for the bound and the (prediagonalized) continuum states in the absence of the perturbation V, which induced the predissociation. The coefficients a and b in eqn (66) are given by

$$a_{\alpha_d,\alpha_s}^{\varepsilon_d(-)} = \frac{V_{\alpha_s,\alpha_d}^{\varepsilon_d(-)}}{\varepsilon_d - \varepsilon_s - i\Gamma_s}$$

$$b_{\alpha_d,\alpha_d'\varepsilon_d'}^{\varepsilon_d(-)} = \lim_{\eta \to 0} \frac{V_{\alpha_s,\alpha_d'}^{\varepsilon_d'(-)*}}{\varepsilon_d - \varepsilon_d' - i\eta}\frac{V_{\alpha_s,\alpha_d}^{\varepsilon_d(-)}}{\varepsilon_d - \varepsilon_s - i\Gamma_s} \quad (67)$$

with

$$\Gamma_s = \pi \sum_{\alpha_d}|V_{\alpha_s,\alpha_d}^{\varepsilon_d(-)}|^2 \quad (68)$$

and $V_{\alpha_s,\alpha_d}^{\varepsilon_d(-)} = \langle \alpha_s^{(0)}|V|\alpha_d^{(0)}, \varepsilon_d^{(-)}\rangle$ being the discrete-continuum matrix elements of the interaction V. The energy ε_s gives the positions of the bound levels of the $|\alpha_s\rangle$ electronic state with respect to the dissociation threshold of $|\alpha_d\rangle$. Assuming that only the $|\alpha_s^{(0)}\rangle$ state has oscillator strength from the ground state, the matrix elements of the electric dipole operator between the initial state $|\alpha_i\rangle$ and the dissociative eigenstate $|\alpha_d, \varepsilon_d^{(-)}\rangle$ will be given by:

$$\langle \alpha_i|D \cdot e|\alpha_d, \varepsilon_d^{(-)}\rangle = a_{\alpha_d,\alpha_s}^{\varepsilon_d(-)}\langle \alpha_i|D \cdot e|\alpha_s^{(0)}\rangle \tag{69}$$

which, according to eqn (67), is a Lorentzian centered at ε_s with half-width at half-maximum equal to Γ_s. Just as for $|\alpha_i\rangle$ [see eqn (17)], the zero-order wavefunctions $|\alpha_s^{(0)}\rangle$ can be expanded in terms of the body-fixed rotational wavefunctions:

$$|\alpha_s^{(0)}\rangle = \sum_{\Omega_s} |\varphi_{\Omega_s}^{J_{r_s}}\rangle|\Omega_s J_s M_s\rangle. \tag{70}$$

Substituting eqn (70) into eqn (69) we obtain for the matrix elements of the electric dipole operator, an equation similar to eqn (18) with the new reduced matrix elements:

$$\langle J_i\|D\|j_A h_B j_d \Omega_d J_d, \varepsilon_d^{(-)}\rangle = \sum_q \sum_{\Omega_i} \sum_{\Omega_s} (-)^{J_i-\Omega_i}(2J_d+1)\begin{pmatrix} J_d & 1 & J_i \\ \Omega_s & q & -\Omega_i \end{pmatrix}$$
$$\times \langle \varphi_{\Omega_i}^{J_i}|(D)_q|\varphi_{\Omega_s}^{J_d}\rangle \frac{V_{\Omega_s,j_A j_d \Omega_d}^{J_d \varepsilon_d(-)}}{\varepsilon_d - \varepsilon_s - i\Gamma_s} \tag{71}$$

where

$$V_{\Omega_s,j_A j_B j_d \Omega_d}^{J_d \varepsilon_d(-)} = \sum_{j_A j_B j_d \Omega_d} \langle \varphi_{\Omega_s}^{J_d}|V|\varphi_{j_A j_B j_d \Omega_d, j_A j_B j_d \Omega_d}^{J_d \varepsilon d(-)}\rangle. \tag{72}$$

In eqn (71) and (72) we have used the fact that $J_s = J_d$ for an intramolecular coupling. Substituting now eqn (71) into eqn (37) with $J_d = J'_d$, we finally obtain

$$P_K^{(j_A j_B j_d)} = \sum_{\Omega_d \Omega_d'} \sum_{Q'} (-)^{j_d + J_i}\begin{pmatrix} J_d & J_d & K \\ \Omega_d & -\Omega_d' & -Q' \end{pmatrix}\begin{pmatrix} J_d & j_d & K \\ -\Omega_d' & \Omega_d & -Q' \end{pmatrix}$$
$$= \begin{Bmatrix} 1 & 1 & K \\ J_d & J_d & J_i \end{Bmatrix}\Phi_{j_A j_B j_d \Omega_d \Omega_d'}^{J,J_d \varepsilon_d(-)}$$

with

$$\Phi_{j_A j_B j_d \Omega_d \Omega_d'}^{J,J_d \varepsilon_d(-)} = \sum_{\Omega_s \Omega_i'} \sum_{\Omega_i \Omega_i} \frac{(V_{\Omega_s,j_A j_B j_d \Omega_d}^{J_d \varepsilon_d(-)})^*(V_{\Omega_s,j_A j_B j_d \Omega_d'}^{J_d \varepsilon_d(-)})}{(\varepsilon_d - \varepsilon_s)^2 + \Gamma_s^2} \langle \Omega_i J_i\|D\|\Omega_s J_d\rangle^*\langle \Omega_i' J_i\|D\|\Omega_s' J_d\rangle \tag{74}$$

and

$$\langle \Omega_i J_i\|D\|\Omega_s J_d\rangle = \sum_q (-)^{J_i-\Omega_i}(2J_d+1)\begin{pmatrix} J_d & 1 & J_i \\ \Omega_s & q & -\Omega_i \end{pmatrix}\langle \varphi_{\Omega_i}^{J_i}|(D)_q|\varphi_{\Omega_s}^{J_d}\rangle. \tag{75}$$

(B) Application to some Simple Cases

As an example of the above, let us consider a simple case of slow predissociation, namely:

$$AB(^1\Sigma) \xrightarrow{h\nu_i} AB^*(^1\Pi) \xrightarrow{\Gamma_s} AB^*(^1\Sigma) \longrightarrow A^*(^1P) + B(^1S) \xrightarrow{h\nu_f} A(^1S) + B(^1S) \tag{76}$$
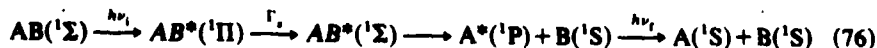
where $j_d = 1$, $j_r = 0$ and $\Omega_d = \Omega_d' = 0$. Since, in addition, $j_B = 0$, we can use eqn (31) to calculate the fluorescence cross-sections with:

$$P_K^{(j_d)} = (-)^{j_d + J_i}\begin{pmatrix} J_d & J_d & K \\ 0 & 0 & 0 \end{pmatrix}\begin{Bmatrix} j_d & j_d & K \\ 0 & 0 & J_i \end{Bmatrix}\Phi_{j_d 00}^{J,J_d \varepsilon_d(-)} \tag{77}$$

and

$$\frac{\partial \sigma}{\partial \hat{\Omega}_f} = \frac{2\pi k_i l_f^3}{9\Gamma_d} |\langle j_f = 0 \| D \| j_d = 1\rangle|^2 \sum_K P_K^{(j_d)} F_K(e_i, e_f) \qquad (78)$$

from which we obtain

$$r = P_0^{(1)}/P_2^{(1)} = 5(-)^{J_i - 1} \times \begin{cases} (2J_i + 1)/(J_i + 2) & \text{for } R(J_i) \text{ transitions} \\ 1 & \text{for } Q(J_i) \text{ transitions} \\ (2J_i + 1)(J_i - 1) & \text{for } P(J_i) \text{ transitions.} \end{cases} \qquad (79)$$
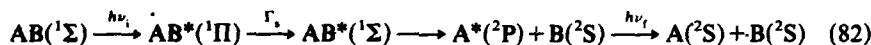
With the use of eqn (78) and (79) we can calculate the polarization degree of the photofragments fluorescence. For incident linearly polarized light we shall have:

$$P = \frac{(\partial \sigma/\partial \hat{\Omega}_f)_\parallel - (\partial \sigma/\partial \hat{\Omega}_f)_\perp}{(\partial \sigma/\partial \hat{\Omega}_f)_\parallel + (\partial \sigma/\partial \hat{\Omega}_f)_\perp} = \frac{3}{2r - 1} \qquad (80)$$

which, in the case of an $R(1)$ transition for instance, gives:

$$P = 3/11. \qquad (81)$$

If again we consider the case where the fragments have fine structure:

$$AB(^1\Sigma) \xrightarrow{h\nu_i} AB^*(^1\Pi) \xrightarrow{\Gamma_s} AB^*(^1\Sigma) \longrightarrow A^*(^2P) + B(^2S) \xrightarrow{h\nu_f} A(^2S) + B(^2S) \qquad (82)$$

we have from eqn (36), (38) and (73):

$$\frac{\partial \sigma^{(j_A)}}{\partial \hat{\Omega}_f} \propto (2j_A + 1)^{-1} |\langle j_A' = 1/2 \| D \| j_A \rangle|^2 \sum_K \begin{Bmatrix} j_A & j_A & K \\ 1 & 1 & 1/2 \end{Bmatrix}^2 P_K^{(j_A)} F_K(e_i, e_f) \qquad (83)$$

with

$$P_K^{(j_A)} = (-)^{J_i + 1} \begin{pmatrix} J_d & J_d & K \\ 0 & 0 & 0 \end{pmatrix} \begin{pmatrix} 1 & 1 & K \\ 0 & 0 & 0 \end{pmatrix} \begin{Bmatrix} 1 & 1 & K \\ J_d & J_d & J_i \end{Bmatrix} \Phi_{j_A 1/2 100}^{J_i J_d e_d(-)}. \qquad (84)$$

From eqn (83) and (84) we finally obtain for linearly polarized incident light:

$$P^{(1/2)} = 0 \qquad (85)$$

$$P^{(3/2)} = \frac{3}{4r + 1}$$

r being defined by eqn (79). Eqn (85) shows, just as in the direct photodissociaton case, the depolarization effect due to the spin coupling. In particular, for an $R(1)$ transition:

$$P^{(3/2)} = 1/7. \qquad (86)$$

The case studied here actually applied to H_2 in the region of the $D(^1\Pi)$ state. This state is coupled by rotational interactions to the $B'(^1\Sigma)$ state, which correlated to $H(2p) + H(1s)$ fragments. If the fine-structure components are not resolved in the experiment we have to add the intensities of the two components. Using the fact that $\Phi_{3/2} = 2\Phi_{1/2}$ [see section 3(C)] and that $|\langle j_A' = 1/2 \| D \| j_A = 3/2 \rangle|^2 = 4 |\langle j_A' = 1/2 \| D \| j_A = 1/2 \rangle|^2$, we obtain

$$P = \frac{3}{6r + 1} \qquad (87)$$

and for an $R(1)$ transition $P = 3/31$, which, as expected, is much smaller than $P^{(3/2)}$.

5. Photodissociation of Polyatomics

The general expressions eqn (35)-(37) can be used in the case of polyatomic molecules with j_A and j_B being the total angular momenta of the fragments (electronic plus rotational). What remains to be done is to express the initial wavefunction $|\alpha_i\rangle$ in terms of the body-fixed frame with z' in the direction of R, which in this case is the vector going from the centre of mass of A to that of B. Usually, R does not constitute a principal axis of inertia for the bound molecule, so that a transformation is needed in order to express the asymmetric rotor wavefunctions describing the initial state in the reference system of the principal axes of inertia in terms of the symmetric-top wavefunctions $|\Omega JM\rangle$ referred to the body-fixed frame used in our calculations. To illustrate this point, let us consider the triatomic case with no electronic angular momentum. The ABC molecular dissociating into an atom A and a diatomic molecule BC will be described by the R vector going from A to the centre of mass of BC and the r vector of BC. If both fragments have zero electronic angular momentum, the body-fixed wavefunctions $|j\Omega JM\rangle$ will be given by

$$\langle \hat{r}\hat{R} | j\Omega JM\rangle = Y_{j\Omega}(\theta, \phi)\langle \hat{R} | \Phi^J_{M\Omega}\rangle \tag{88}$$

with $\langle \hat{R}|\Phi^J_{M\Omega}\rangle$ being the symmetric-top wavefunctions defined in eqn (8). The polar angles θ and ϕ correspond to r in the body-fixed frame.

Using eqn (8), eqn (88) can be written

$$\langle \hat{r}\hat{R} | j\Omega JM\rangle = Y_{j\Omega}(\theta, 0)\left(\frac{2J+1}{4\pi}\right)^{1/2} D^{J*}_{M\Omega}(\phi_R, \theta_R, \phi). \tag{89}$$

The initial wavefunction $|\alpha_i\rangle$, on the other hand, is usually given in terms of the symmetric-top wavefunctions in the reference system of the principal axes of inertia:

$$|\alpha_i\rangle = \sum_{K_i} |\varphi^{(J_i)}_{K_i}\rangle \left(\frac{2J_i+1}{8\pi^2}\right)^{1/2} D^{J*}_{M_iK_i}(\alpha, \beta, \gamma) \tag{90}$$

where (α, β, γ) are the Euler angles specifying the orientation of the principal axes of inertia with respect to the laboratory frame. Between the two body-fixed frames there will be a rotation of angles (δ, η, ξ) which can be calculated knowing the equilibrium geometry of the molecule. We shall then have the transformation:

$$D^J_{MK}(\alpha, \beta, \gamma) = \sum_{\Omega} D^J_{M\Omega}(\phi_R, \theta_R, \phi) D^J_{\Omega K}(\delta, \eta, \xi) \tag{91}$$

and therefore $|\alpha_i\rangle$ can be written as in eqn (17) with

$$|\varphi^J_{\Omega i}\rangle = \sum_{K_i} D^{J*}_{\Omega_i K_i}(\delta, \eta, \xi)\frac{1}{\sqrt{2\pi}}|\varphi^J_{K_i}\rangle. \tag{92}$$

Using eqn (92) in eqn (27) provides the final expressions for the dissociation of a triatomic molecule. For direct dissociation, the axial recoil approximation is usually valid for the dissociative state $|\alpha_d, \varepsilon^{(-)}_d\rangle$. In that case, eqn (40) can be used.

6. Conclusions

We have revisited the general theory of fluorescence polarization of photofragments in the framework of the density-matrix formalism. The excitation density matrix was first calculated in the molecular frame and then transformed to the laboratory system of axes to obtain both the alignment and the orientation of the fragments. In the laboratory frame, the excitation density matrix clearly shows the coherence effects which are the result of simultaneous excitation of dissociative electronic states with different symmetries correlating to the same limit. We have paid particular attention to the proper

treatment of the asymptotic behaviour of the dissociative wavefunction in the multichannel case. This allows us to treat correctly the case of non-adiabatic transitions occurring during the half-collision after photon absorption.

We have also studied the case of slow predissociation and shown how this general treatment can be applied with some minor addition calculations to the dissociation of polyatomic molecules.

Appendix

Substituting eqn (2) into the matrix elements $\langle \alpha_f, \varepsilon_f | D \cdot e_f | \alpha_d, \varepsilon_d \rangle$ for both $|\alpha_d\rangle$ and $|\alpha_f\rangle$, the integral over ε_d in eqn (1) will involve integrals of the form:

$$z = \int_0^\infty dK_d f(K_d) \int_0^\infty dR \frac{\exp(-iK_dR)}{K - K_d + i\gamma_d} \exp(\pm iK_fR) \qquad (A.1)$$

where $K = (2\mu E)^{1/2}/\hbar$, $\gamma_d = 2\mu\Gamma_d/\hbar^2(K + K_d)$ and where $f(K_d)$ is a smooth function. Interchanging the integrals, one obtains

$$z = \begin{cases} 0, & \text{for the integrals involving } \exp(-iK_dR); \\ 2\pi f(K)/(K \pm K_f + i\gamma_d), & \text{for the integrals involving } \exp(iK_dR). \end{cases} \qquad (A.2)$$

and neglecting the non-resonant terms involving $(K + K_f + i\gamma_d)^{-1}$ one finally obtains, for $K \approx K_f$, eqn (3) of section 2(A).

References

1 *Molecular Photodissociation Dynamics, Adv. Gas-phase Photochemistry and Kinetics*, ed. M. N. R. Ashfold and J. E. Baggott (Royal Society of Chemistry, London, 1987).
2 *Faraday Discuss. Chem. Soc.*, 1986, **82**.
3 G. G. Balint-Kurti and M. Shapiro, *Chem. Phys.*, 1981, **61**, 137; *Adv. Chem. Phys.*, 1985, **60**, 403.
4 G. G. Balint-Kurti, *J. Chem. Phys.*, 1986, **84**, 4443.
5 J. P. Simons, *J. Phys. Chem.*, 1984, **88**, 1287.
6 C. H. Greene and R. N. Zare, *Annu. Rev. Phys. Chem.*, 1982, **33**, 119; *J. Chem. Phys.*, 1983, **78**, 6741.
7 R. J. van Brunt and R. N. Zare, *J. Chem. Phys.*, 1968, **48**, 4304.
8 G. A. Chamberlain and J. P. Simons, *Chem. Phys. Lett.*, 1985, **32**, 355; *J. Chem. Soc., Faraday Trans. 2*, 1975, **71**, 2043.
9 M. J. MacPherson, J. P. Simons and R. N. Zare, *Mol. Phys.*, 1979, **38**, 2049.
10 M. MacPherson and J. P. Simons, *J. Chem. Soc., Faraday Trans. 2*, 1979, **75**, 1572.
11 E. D. Poliakoff, S. H. Southworth, D. A. Shirley, K. H. Jackson and R. N. Zare, *Chem. Phys. Lett.*, 1979, **65**, 407.
12 J. Husain, J. R. Wiesenfeld and R. N. Zare, *J. Chem. Phys.*, 1980, **72**, 2479.
13 E. W. Rothe, U. Krause and R. Duren, *Chem. Phys. Lett.*, 1980, **72a**, 100.
14 G. W. Loge and R. N. Zare, *Mol. Phys.*, 1981, **43**, 1419.
15 G. W. Loge and J. R. Wiesenfeld, *Chem. Phys. Lett.*, 1981, **78**, 32.
16 E. D. Poliakoff, J. L. Dehmer, D. Dill, A. C. Parr, K. H. Jackson and R. N. Zare, *Phys. Rev. Lett.*, 1981, **46**, 907.
17 O. S. Vasyutinskii, *Sov. Phys. JETP*, 1981, **54**, 855; *Zh. Eksp. Teor. Fiz.*, 1981, **81**, 1608; *Khim. Phys.*, 1986, **5**, 768.
18 J. Vigué, P. Grangier, G. Roger and A. Aspect, *J. Phys. (Paris) Lett.*, 1981, **42**, L-531.
19 J. Vigué, J. A. Beswick and M. Broyer, *J. Phys. (Paris)*, 1983, **44**, 1225.
20 S. J. Singer, K. F. Freed and Y. B. Band, *J. Chem. Phys.*, 1983, **79**, 6060.
21 H. Hemmati, W. M. Fairbank Jr, P. K. Boyer and G. J. Collins, *Phys. Rev. A*, 1983, **28**, 567.
22 J. Vigué, P. Grangier and A. Aspect, *Phys. Rev. A*, 1984, **30**, 3317.
23 J. A. Guest, M. A. O'Halloran and R. N. Zare, *Chem. Phys. Lett.*, 1984, **103**, 261.
24 M. Lambert, B. Callen, H. Dugan, S. V. Filseth, F. J. Morgan and C. M. Sadowski, *Chem. Phys. Lett.*, 1987, **139**, 45.
25 M. Glass-Maujean and J. A. Beswick, *Phys. Rev. A*, 1987, **36**, 1160.
26 M. Glass-Maujean and J. A. Beswick, to be published.
27 E. Hasselbrink, J. R. Waldeck and R. N. Zare, to be published.
28 W. Kolos and L. Wolniewicz, *Can. J. Phys.*, 1975, **53**, 2189.
29 W. Kolos and J. Rychlewski, *J. Mol. Spectrosc.*, 1976, **62**, 109.

30 W. Kolos, *J. Mol. Spectrosc.*, 1976, **62**, 429.
31 W. Kolos and L. Wolniewicz, *J. Mol. Spectosc.*, 1975, **54**, 303.
32 W. Kolos and L. Wolniewicz, *J. Chem. Phys.*, 1966, **45**, 509.
33 A. L. Ford, E. M. Greenawalt and J. C. Browne, *J. Chem. Phys.*, 1977, **67**, 983.
34 W. Kolos and R. Rychlewski, *J. Mol. Spectrosc.*, 1981, **88**, 1.
35 L. Wolniewicz, *J. Chem. Phys.*, 1983, **78**, 6173.
36 F. Borondo, J. R. Eguiagaray and A. Riera, *J. Phys. B*, 1982, **15**, 899.
37 W. Kolos and L. Wolniewicz, *J. Chem. Phys.*, 1969, **51**, 5002.
38 L. Wolniewicz, *Chem. Phys. Lett.*, 1975, **31**, 248.
39 A. L. Ford, J. C. Browne, E. J. Shipsey and P. Devries, *J. Chem. Phys.*, 1975, **63**, 362.
40 D. R. Bates and J. T. Lewis, *Proc. Phys. Soc. A*, 1955, **68**, 173.
41 I. V. Komarov and V. N. Ostrovsky, *J. Phys B*, 1979, **12**, 2485.
42 J. A. Beswick and M. Glass-Maujean, *Phys. Rev. A*, 1987, **35**, 3339.
43 M. Glass-Maujean, H. Frohlich and J. A. Beswick, *Phys. Rev. Lett.*, 1988, **61**, 157.

Vector and Product Quantum-state Correlations for Photografmentation of Formaldehyde

Thomas J. Butenhoff, Karen L. Carleton, Mie-Chen Chuang and C. Bradley Moore*

Department of Chemistry, University of California, Berkeley, California 94720, U.S.A.

The vector correlations of para-H_2 ($v = 1$, $J = 0$–8) produced from H_2CO photolysis on the $rR_0(0)e$ line of the $2^1 4^1$ $S_1 \leftarrow S_0$ transition have been measured by analysing Doppler-resolved laser-induced fluorescence lineshapes. The correlations of the H_2CO transition dipole moment μ with the H_2 recoil velocity v and μ with the angular momentum J are small, probably because H_2CO rotates many times between excitation and fragmentation. The correlation of v with J has been found to be between the limiting cases of $v \| J$ and $v \perp J$. In addition, the $H_2(v, J)$ linewidths have been used to measure the product state correlation. H_2 fragments in high vibrational states correlate with CO fragments in low rotational states.

Formaldehyde is an excellent molecule for the study of photofragmentation for a variety of reasons.[1,2] Its well resolved $S_1 \leftarrow S_0$ spectrum allows excitation to single rovibronic levels. The photodissociation mechanism for the molecular channel has been well established:[1] the excited molecule internally converts to high vibrational levels of the ground electronic state and then dissociates to form H_2 and CO.

Past studies of the photofragmentation have concentrated on energy disposal in the products. The product translational energy distribution has been measured by time-of-flight mass spectroscopy,[3] the CO(v, J) distribution has been measured by laser-induced fluorescence (LIF),[2] and the ortho-H_2 (v, J) distribution has been measured with coherent anti-Stokes Raman spectroscopy (CARS).[4] These experiments have yielded a wealth of information about the dissociation dynamics. The high rotational excitation of the CO corresponds to an impact parameter of ca. 0.9 Å, which implies that the H_2 is repelled by the charge distribution outside of the carbon nucleus of the CO.[2] The large impact parameter is consistent with the bent planar ab initio transition-state geometry and reaction coordinate.[5,6]

To date, the experiments on H_2CO have measured scalar properties of the photodissociation process. Recently, it has become possible to determine vector correlations from the analysis of the fragment LIF Doppler profiles.[7,8] The vectors involved are the photolysis laser polarization ε_p, the transition dipole moment of the parent molecule μ, the velocity of the fragment v, and the angular momentum of the fragment J. The excitation laser preferentially excites parent molecules whose transition dipole moments are along the polarization axis of the laser. If the parent dissociates on a timescale short compared to its rotational period, the parent anisotropy is carried over to the fragment's translational recoil direction and rotation which results in $\langle \mu \cdot v \rangle$ and $\langle \mu \cdot J \rangle$ correlations. In addition, the repulsive force of the dissociation can result in a $\langle v \cdot J \rangle$ correlation, which, unlike the other correlations, is not smeared out by parent rotation. The magnitudes of these vector correlations are sensitive to the photofragmentation dynamics and should provide good tests of dynamical models.

The Doppler profiles provide fragment translational energies, which can be used to measure product quantum-state correlations.[9] None of the previous work has measured state-resolved velocities. In the case of CO, the bandwidth of the probe laser was larger than the Doppler width of the peaks; in the CARS work, the H_2 was translationally

cooled by collisions with helium to reduce the Doppler width and increase the detection sensitivity. The $CO(v, J)$ and $H_2(v, J)$ populations together with the measured translational energy distribution suggest that there may be a correlation between the CO rotational state and the H_2 vibrational state.[4]

This paper reports the initial results of vector and product quantum-state correlation measurements from Doppler-resolved LIF lineshapes of the $H_2(v, J)$ fragment.

Experimental

Formaldehyde was photolysed on the $rR_0(0)e$ line of the $2^1 4^1$ $S_1 \leftarrow S_0$ transition in a pulsed supersonic free jet. The nascent $H_2(v, J)$ product was probed on the $C\,^1\Pi_u \leftarrow X\,^1\Sigma_g^+$ or $B\,^1\Sigma_u^+ \leftarrow X\,^1\Sigma_g^+$ transition by vacuum-ultraviolet (v.u.v.) laser-induced fluorescence (110-116 nm). Fig. 1 shows the three experimental geometries employed in this experiment. The jet axis was mutually orthogonal to both the laser-propagation direction and the fluorescence-detection direction. The polarizations of both the photolysis and probe lasers were linear, as measured by a Glan-Thompson polarizer.

The photolysis laser consisted of a Nd:YAG pumped dye laser (Quantel TDL50, LDS-698/DCM dye mixture, 10 Hz) doubled in a static KDP crystal. Typical characteristics were 5-7 mJ per pulse, 10 ns pulse length and 0.3 cm^{-1} bandwidth at the 339 nm photolysis wavelength. The 0.5 cm diameter laser beam intersected the jet 1.5 cm below the nozzle. H_2CO fluorescence was collected with a photomultiplier (PMT) which was mutually orthogonal to both the jet and laser propagation axes. During the photofragmentation experiment, the H_2 product signals were normalized by the H_2CO fluorescence to reduce fluctuations from photolysis laser intensity and H_2CO number density.

The products were probed 100 ns after photolysis. The probe laser consisted of a Nd:YAG pumped dye laser (Quantel, LDS-698/DCM dye mixture) which was
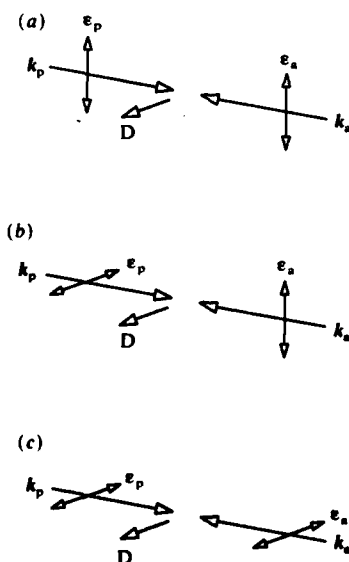
Fig. 1. The photolysis (k_p, ε_p) and probe (k_a, ε_a) laser-beam geometries (k and ε are the laser propagation directions and polarizations) are shown with the detector axis D. All polarizations are detected. Case (*a*) is a mutually orthogonal geometry, case (*b*) is the coaxially detected geometry with $\varepsilon_a \| \varepsilon_p$.

frequency-doubled in an autotracking KDP crystal (Inrad). The ultraviolet output pulse (*ca.* 7 mJ per pulse, 10 ns) was focussed with a 15 cm lens into the centre of a 10 cm long krypton tripling cell to generate the v.u.v. Typical krypton pressures were 50–300 Torr,† depending on wavelength. The v.u.v. and residual u.v. light excited the tripling cell through a v.u.v.-grade lithium fluoride (LiF) window directly into the vacuum chamber. The v.u.v beam diameter was estimated to be 0.4 cm in the probe region.

V.u.v. power fluctuations were monitored by measuring the v.u.v.'s specular reflection from a LiF flat with a solar blind PMT (EMR 542G-08-19, LiF window). The LiF flat was placed in the vacuum chamber between the jet and the entrance window for the photolysis laser. To avoid saturation of the PMT, the reflected v.u.v. was attenuated with fine nickel mesh. The difference in LiF reflectivity for the two probe laser polarizations was accounted for in the peak intensity measurements.

Undispersed, unpolarized H_2 fluorescence was detected with a solar-blind PMT (EMR 542G-09-19, MgF_2 window) mounted in the vacuum and situated mutually orthogonal to the jet axis and the laser beam—propagation directions. The 2.9 cm diameter cathode of the PMT was 5 cm from the jet axis. When probing the $C\,^1\Pi_u \leftarrow X\,^1\Sigma_g^+\,H_2$ transition, a 2 mm thick v.u.v.-grade MgF_2 flat was placed in front of the PMT to filter out scattered v.u.v. laser light. When probing the $B\,^1\Sigma_u^+ \leftarrow X\,^1\Sigma_g^+\,H_2$ transition, a 2.2 cm diameter $f/1$ CaF_2 lens collected and focussed the fluorescence onto the PMT as well as filtered scattered v.u.v. laser light. The PMT signals were amplified, boxcar-averaged, digitized and stored in a personal computer. The same computer was used to trigger the pulsed nozzle, trigger the Nd:YAG lasers and scan the probe dye laser.

H_2CO was made in the usual manner.[10] The sample mixture was prepared by flowing He (550 Torr) over liquid H_2CO ($T = -89\,°C$, $P_{vapour} = 8.7\,Torr$[11]) and expanded into the vacuum chamber through the 0.8 mm diameter orifice of the pulsed nozzle (General Valve).

Various transitions were used to probe the H_2. $H_2(v=1)$ was probed on the $B\,^1\Sigma_u^+ \leftarrow X\,^1\Sigma_g^+$ (2, 1) and (3, 1) bands, $H_2(v=3)$ on the $C\,^1\Pi_u \leftarrow X\,^1\Sigma_g^+$ (1, 3) band and $H_2(v=2)$ on the $C\,^1\Pi_u \leftarrow X\,^1\Sigma_g^+$ (0, 2) and $B\,^1\Sigma_u^+ \leftarrow X\,^1\Sigma_g^+$ (6, 2) bands.

Analysis and Results

Vector Correlations

The correlations between the parent dipole moment, μ, the H_2 rotational vector, *J*, and the product velocity vector, *v*, are extracted using Dixon's lineshape analysis.[7,12] If the product is assumed to have a single recoil velocity *v*, then the spectral rovibrational line profile is given by

$$g(\chi) = \frac{I}{2\Delta\nu_D}\,[1 + \beta_{eff}P_2(\cos\theta)P_2(\chi)] \tag{1}$$

where $\Delta\nu_D = \nu_0 v/c$ is the maximum Doppler shift (ν_0 is the line centre), χ is the ratio of the Doppler shift to the maximum Doppler shift [$\chi = (\nu - \nu_0)/\Delta\nu_D$], I is proportional to the integrated intensity of the transition, $P_2(x) = (3x^2 - 1)/2$ is the second Legendre polynomial, θ is the angle between the photolysis polarization and the probe-laser propagation axis and β_{eff} is the effective lineshape parameter. The effective lineshape parameter, as expressed by Dixon, is

$$\beta_{eff} = \left(\frac{b_2\beta_0^2(20) + b_3\beta_0^0(22) + b_4\beta_0^2(22)}{b_0 + b_1\beta_0^2(02)}\right). \tag{2}$$

† 1 Torr = 101 325/760 Pa.

Formaldehyde Photofragmentation
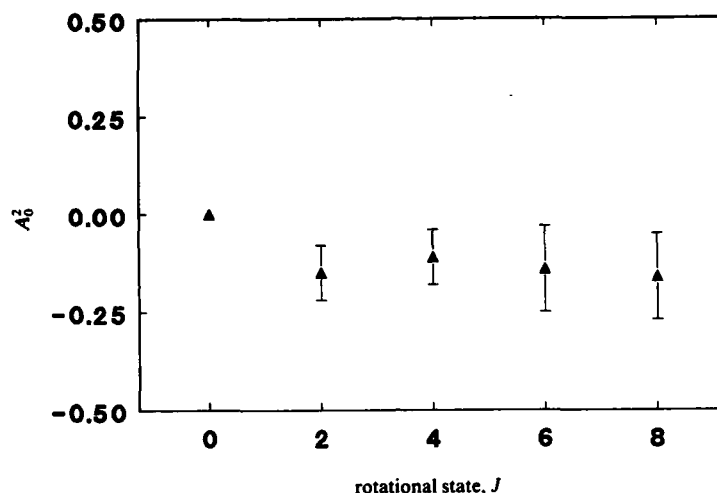
Fig. 2. Alignment for $H_2(v=1)$ as a function of rotational state from photolysis of 2^14^1 H_2CO on the $rR_0(0)e$ line.

Here, $b_0 \ldots b_4$ are calculated constants for a given rovibrational transition and geometry, and each of the β parameters is related to a vector correlation. The alignment of the J vector in the laboratory frame is typically given by A_0^2,[13] which is equal to $\frac{4}{5}\beta_0^2(02)$ in Dixon's analysis. The spatial anisotropy, often referred to as β,[14] is equal to $2\beta_0^2(20)$. The other correlations in this analysis are the vJ correlation, $\beta_{vJ} = \beta_0^0(22)$ and the multiple correlation, $\beta_{\mu vJ} = \beta_0^2(22)$.

Both a P- and an R-branch for each $H_2(v=1, J)$ state were measured at least twice for three combinations of photolysis and probe-laser polarizations. The line profiles were least-squares fitted to the lineshape function (which was convoluted to a 1.0 cm^{-1} f.w.h.m. Gaussian to account for initial parent velocities and the probe-laser bandwidth) to determine the intensity, maximum Doppler shift and lineshape parameter. Since our detection is unpolarized, each geometry is the average of two of Dixon's standard cases.[7] The geometries shown in fig. 1 correspond to his cases 1 and 2, 9 and 10, and 11 and 12.

The most reliable method to evaluate the alignment is to analyse the integrated peak intensities as a function of branch and geometry. The integrated peak intensity, I, is related to A_0^2 by[13]

$$I = CSG(b_0 + \tfrac{5}{4}b_1 A_0^2) \tag{3}$$

where C is proportional to the population, S is the absorption line strength, G accounts for geometric experimental differences (laser-beam overlap, H_2CO fluorescence signals *etc.*), and b_0 and b_1 are the same as in eqn (2). In a given geometry, b_1/b_0 is similar for P- and R-branches which necessitates the use of multiple geometries. The experimental geometry factor G is determined from the R(0) line intensities: for R(0), b_1 (as well as A_0^2) is zero, and C does not vary with geometry, so G is proportional to I/b_0. The R(0) line was measured ten times for each geometry in order to determine G accurately. The least-squares fit to the plot of $I/(SGb_0)$ *vs.* $5b_1/4b_0$ yields an intercept equal to C and a slope equal to A_0^2C. Fig. 2 shows the alignment measured for $H_2(v=1)$.

After the alignment has been determined, the denominator of eqn (2) is known and a least-squares fit of the β_{eff} measurements is used to determine the other three correlations, β, β_{vJ} and $\beta_{\mu vJ}$. The measured spatial anisotropy, vJ, and μvJ correlations for $H_2(v=1)$ are shown in fig. 3. Sample data are shown in fig. 4. The simulated line profile
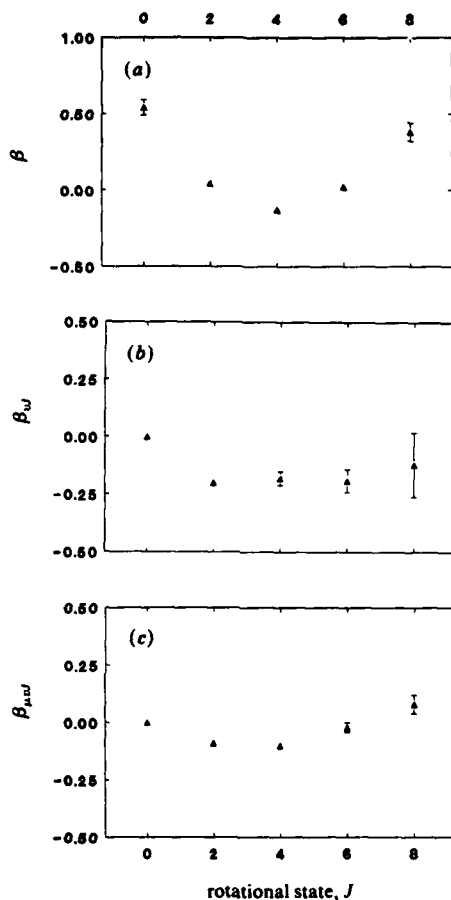
Fig. 3. Vector correlations for $H_2(v=1)$ as a function of rotational state from photolysis of $2^1 4^1$ H_2CO on the $rR_0(0)$ line. (a) spatial anisotropy, $\langle \mu \cdot v \rangle$, (b) vJ correlation, $\langle v \cdot J \rangle$ and (c) multiple correlation, $\langle \mu \cdot v \cdot J \rangle$.

has a β_{eff} calculated with eqn (2), using the measured values of β, β_{vJ} and $\beta_{\mu vJ}$. The calculated β_{eff} agree quite well with the β_{eff} obtained by finding the best-fit parameters for each individual line.

Product Quantum-state Correlations

The average velocity for a particular $H_2(v, J)$ state is determined from the H_2 maximum Doppler shift, $\Delta \nu_D$. The corresponding CO average velocity and the total average translational energy in the products is calculated using conservation of linear momentum. The distribution of these average translational energies is calculated by scaling each value by the corresponding $H_2(v, J)$ population; the H_2 vibrational state populations have previously been measured by CARS[4] and the rotational state populations were measured by LIF.[15] Fig. 5 shows the result and compares it with the translational energy distribution measured by time-of-flight mass spectroscopy.[3] In making fig. 5, the average

Doppler shift/cm^{-1}
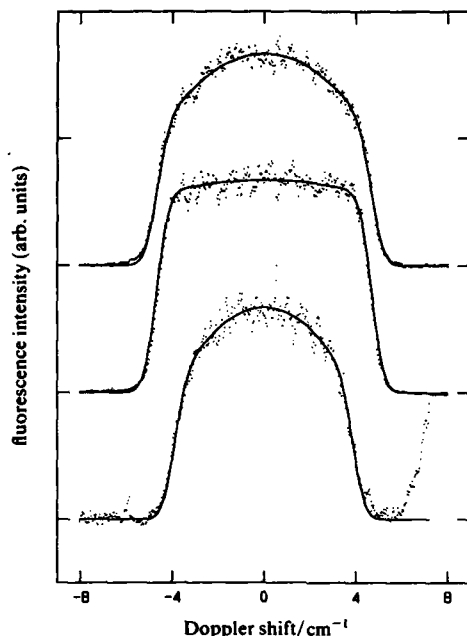
Fig. 4. $H_2(J = 2)$ line profiles for the coaxially detected geometry with $\varepsilon_a \perp \varepsilon_p$. The simulations assume a single fragment recoil velocity v and include a convolution with a $1.0\ \mathrm{cm}^{-1}$ f.w.h.m. Gaussian to account for the probe-laser bandwidth and initial parent velocities. The top trace is the $B\ ^1\Sigma_u^+ \leftarrow X\ ^1\Sigma_g^+$ (3, 1) P(2) line; the simulated lineshape has $\beta_{eff} = 0.577$ and $v = 1.57 \times 10^6\ \mathrm{cm\ s}^{-1}$. The middle trace is the $B\ ^1\Sigma_u^+ \leftarrow X\ ^1\Sigma_g^+$ (3, 1) R(2) line; $\beta_{eff} = 0.096$ and $v = 1.57 \times 10^6\ \mathrm{cm\ s}^{-1}$. The bottom trace is the $C\ ^1\Pi_u \leftarrow X\ ^1\Sigma_g^+$ (1, 3) R(2) line; $\beta_{eff} = 0.580$ and $v = 1.31 \times 10^6\ \mathrm{cm\ s}^{-1}$. The three peaks are not drawn on the same scale.

translational energy was calculated and plotted for each $H_2(v, J)$ line measured; the fact that some $H_2(v, J)$ lines were measured more than others was considered when scaling the populations. It is clear, and not surprising, that lower H_2 vibrational states correspond to higher average translational energies.

The average CO rotational state that corresponds to a given $H_2(v, J)$ state can also be determined by conservation of energy:

$$E_{Rot}(CO) = BJ(J + 1) = E_{avl} - E_{int}[H_2(v, J)] - E_{trans}(H_2 + CO) \qquad (4)$$

where B is the CO rotational constant, E_{avl} is the total energy available to the products, E_{int} is the vibrational and rotational energy of the H_2 product ard E_{trans} is the total translational energy of the products. The CO is considered to be in its ground vibrational state (experimentally only 14% is measured in $v = 1$).[2] The porobability of a calculated CO rotational state is proportional to the corresponding $H_2(v, J)$ population. Fig. 6 shows the CO rotational distribution calculated from $H_2(v, J)$ Doppler widths and populations, and the CO rotational populations measured directly by Bamford *et al.*[2] As in fig. 5, J_{CO} was calculated and plotted for each $H_2(v, J)$ line measured. As previously predicted,[4] higher vibrational states of H_2 are correlated with lower rotational states of CO.
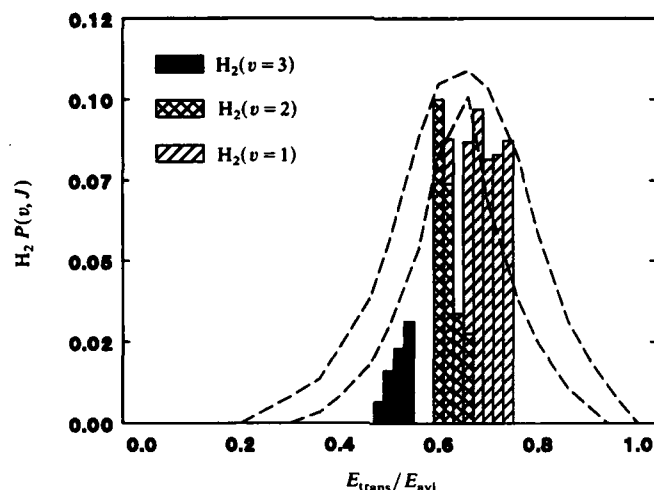
Fig. 5. The product translational energy distribution calculated from $H_2(v, J)$ Doppler widths and populations. The dashed lines give the error limits on the measured translational energy distribution [ref. (3)].
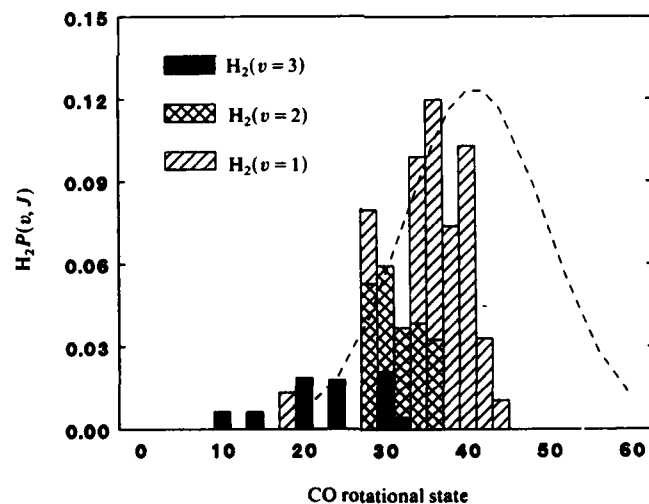
Fig. 6. The Co rotationa state distribution calculated from $H_2(v, J)$ Doppler widths and populations. The dashed line is the measured $CO(v = 0)$ distribution [ref. (2)].

Discussion

Vector Correlations

Vector correlations offer new information and insights on photofragmentation dynamics. Dixon discusses the limiting values for vector correlations in the case of no parent rotation and high-J products $(-0.4 \leqslant A_0^2 \leqslant 0.8, -1 \leqslant \beta \leqslant 2$ and $-0.5 \leqslant \beta_{vJ} \leqslant 1)$.[7] Unfortunately, formaldehyde is not the simplest case of fragmentation since the dissociation
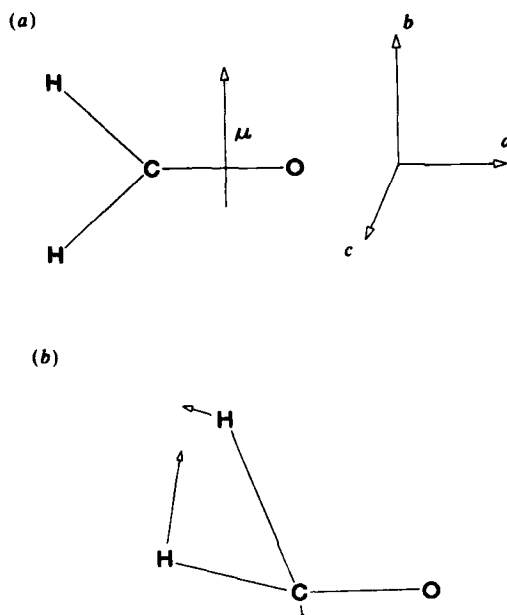
Fig. 7. ₍a₎ Molecule-fixed axes and dipole moment in the ground state of H_2CO and (b) the *ab initio* transition-state geometry and reaction coordinate vectors.

occurs predissociatively from a long-lived excited state (50 ns lifetime). This causes some averaging of the initial correlations owing to the many excited-state parent molecule rotations prior to dissocia. ion. It is therefore not surprising that the laboratory-frame correlations measured in these experiments, the spatial anisotropy and the rotational alignment, are small. However, theoretical work suggests that these correlations are not totally destroyed. Yang and Bersohn have shown that the spatial anisotropy for a symmetric top is reduced by a factor of 4–5 as the parent-state lifetime becomes large.[16] Nagata has shown that the alignment is greatly reduced by parent rotations, but is does not necessarily become zero.[17]

Formaldehyde is approximately a symmetric top ($A \approx 9.406\ cm^{-1}$, $B = 1.295\ cm^{-1}$, $C = 1.134\ cm^{-1}$),[18] which in these experiments is excited to the $J = 1$, $K_a = 1$, $K_c = 1$) state by a b-type transition. The dipole moment along the b axis is in the molecular plane, perpendicular to the CO axis (see fig. 7). The measured spatial anisotropy of the H_2 ($J = 2, 4, 6$) product is small; however, $J = 0$ and $J = 8$ have β values near the expected upper limit of 0.5 for a symmetric top. This suggests that the H_2 product velocity vector is mostly parallel to the parent dipole moment for $J = 0$ and $J = 8$.

We can qualitatively understand these results in terms of an impulsive model where the peak of the H_2 product-state distribution is determined by the transition-state geometry and the width arises from motions in the transition-state normal modes (similar to the effects of parent molecular motions in a direct dissociation process).[19] This is consistent with the observed Boltzmann-like rotational distribution which peaks at $J = 3-4$.[15] The $J = 0$ and $J = 8$ populations are small since there are only a few special transition-state geometries and momenta which produce H_2 in low or high rotational states. The H_2 products from these special geometries must have a large $\langle \mu \cdot J \rangle$ correla-

tion and a positive anisotropy. However, the populations in $J(H_2) = 2$–6 are considerable larger. There are many transition-state geometries which lead to intermediate rotational states with a corresponding distribution of recoil velocity directions. This causes a reduction of the observed anisotropy. As a result, the anisotropy is larger for the extremes of the distribution and reduced for the majority of the rotational product states.

The measured H_2 alignment is small, but negative. Unfortunately, as shown by Nagata, a b-type parent excitation followed by rotation drastically reduces the alignment and may even cause it to change sign.[17] It is therefore difficult to draw conclusions from the alignment parameters in this case. Since both the alignment and the anisotropy are small, the triple vector correlation is almost negligible. Parent molecule rotation makes interpretation of the the laboratory-frame correlations difficult. Experiments are now underway to measure the *ortho*-H_2 vector correlations produced from the rotationless parent excited state.

Unlike the spatial anisotropy and the alignment, the vJ correlation should be unaffected by parent rotation and should be easier to interpret. This correlation occurs at the instant of dissociation in the molecular frame of reference, independent of the laboratory frame. Dixon has given the high-J limits of the vJ correlations: $\beta_{vJ} = 1.0$ for $v\|J$, and $\beta_{vJ} = -0.5$ for $v\perp J$. Although most of the H_2 data are not in the high-J limit, the $J = 6$ and $J = 8$ data suggest that v is intermediate between being parallel and perpendicular to J. This may result from a vJ correlation at some intermediate angle or a distribution of vJ correlations in between parallel and perpendicular orientations. It is not clear how to interpret β_{vJ} for very low J values, and it is not known whether the β_{vJ} values for $J = 2$ or $J = 4$ are closer to one extreme or the other, but they are most likely also intermediate in value.

One explanation for the observed vJ correlation is that the final H_2 v and J vectors are influenced by out-of-plane motions in the formaldehyde transition state. In the out-of-plane normal mode, the two H-atom motions are out of phase, one moving up while the other moves down.[5] The H_2C—O angle at the turning point of this floppy zero-point motion (900 cm^{-1} frequency) is 30° (similar to the angle in the H_2CO excited state). Previously, it was believed that the H_2CO dissociation occurred in the plane of the transition state, which would result in v being perpendicular to J. However, transition-state motions could easily contribute to a non-planar dissociation. In addition, excitation of the low-frequency transition-state vibrations, in particular the out-of-plane bend, would increase the non-planar character of the transition state. Experimentally, the $2^1 4^1$ $rR_0(0)$ S_1 excitation prepares the H_2CO molecule with 1140–2225 cm^{-1} of energy above the barrier on the S_0 surface.[20] This excess energy should result in one or two quanta of vibrational excitation in the transition state which would cause J to be less perpendicular to v.

We have also measured the vector correlations for $H_2(v = 3)$ using the $C\ ^1\Pi_u \leftarrow X\ ^1\Sigma_g^+$ transition. Although they show qualitatively similar behaviour to the $H_2(v = 1)$ correlations, there is the possibility of competition between LIF and 1 v.u.v. + 1 u.v. multiphoton ionization which becomes accessible for the $C\ ^1\Pi_u \leftarrow X\ ^1\Sigma_g^+$ transitions. This should negligibly effect the linewidths, but might alter the peak shapes.[21] Future experiments will measure the $H_2(v = 3)$ correlations through the $B\ ^1\Sigma_u^+ \leftarrow X\ ^1\Sigma_g^+$ transition where ionization (1 v.u.v. + 1 u.v.) is not a problem.

Preliminary studies of other H_2CO excitations suggest that the vector correlations are quite sensitive to the initial H_2CO rovibrational state. This contrasts with the rotational distributions which change little with differences in parent excitations.[2,15] Fig. 8 shows $H_2(v = 3, J = 2)$ line profiles for two different 4^3 S_1 H_2CO rotational levels. The line profiles are markedly different. The change in line profiles is most likely caused by a change of the fragment anisotropies. Excitation of parent states with $K_c = 0$ may produce fragments that are more anisotropic than those with $K_c > 0$ because of a better preservation of the initial parent molecule orientation when $K_c = 0$. When H_2CO is
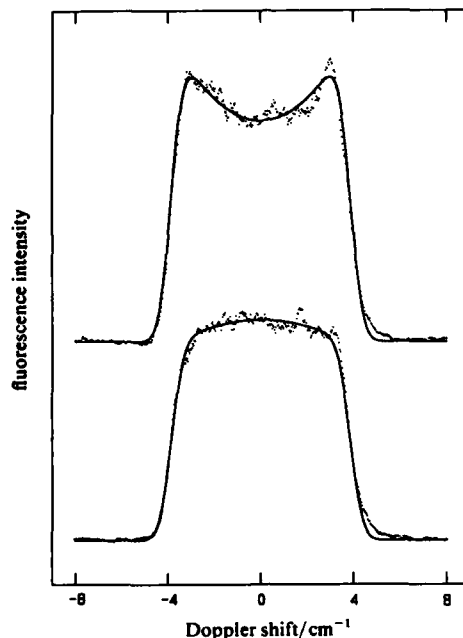
Formaldehyde Photofragmentation

Fig. 8. The effect of rotational state in the 4^3 S_1 H_2CO band. Both spectra show the C $^1\Pi_u \leftarrow$ X $^1\Sigma_g^+$ (1, 3) Q(3) line taken with the mutually orthogonal geometry. (*a*) $rR_1(1)o$ line photolysis (S_1 H_2CO $J = K_a = 2$, $K_c = 0$); the simulated lineshape has $\beta_{eff} = -0.433$ and $v = 1.29 \times 10^6$ s^{-1}. (*b*) $rR_1(1)e$ line photolysis (S_1 H_2CO $J = K_a = 2$, $K_c = 1$); $\beta_{eff} = 0.105$ and $v = 1.29 \times 10^6$ cm s^{-1}.

excited to the same rotational line of a different vibrational band, the H_2 lineshape parameters, β_{eff}, are also different (fig. 9). A given $H_2(v, J)$ line is more dipped for H_2CO excited to its 4^3 band than to its 2^14^1 band (for the mutually orthogonal geometry). The 4^3 H_2CO excitation is 600 cm^{-1} below the 2^14^1 band and may lead to less excitation in the transition-state vibrations. We are in the process of studying these effects with a full quantitative analysis.

Product Quantum-state Correlations

The measured product-state correlations show a striking dependence of the CO J-state distribution on the H_2 rovibrational state. As more of the available energy is put into H_2 internal excitation, the CO rotational energy decreases. As shown in fig. 6, more energy in H_2 vibration correlates with less CO rotation. The calculated CO rotational distribution does not exactly agree with that previously measured.[2] Computer simulations were employed to study the effect of fitting lineshapes with a single recoil velocity when undoubtedly the H_2 fragments have a distribution of velocities. A velocity distribution was constructed by assuming a particular $H_2(v, J)$ state correlated with a Gaussian distribution of $CO(v = 0)$ J states. Doppler profiles that included the fragment velocity distribution as well as a 1.0 cm^{-1} Gaussian laser bandwidth convolution were calculated with various values of β_{eff} and then least-squares fitted to the single fragment velocity Doppler lineshape function. For J_{CO} distributions with f.w.h.m. < 5, the single fragment velocity fits reproduce the average fragment velocity and the J_{CO} peak. For J_{CO}
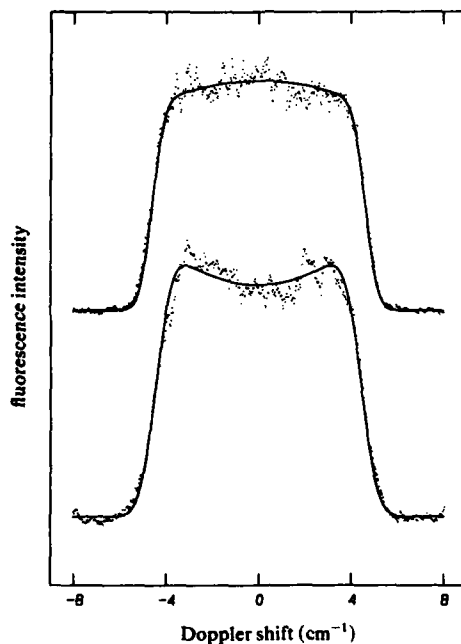
Fig. 9. The effect of the S_1 H_2CO vibrational state. Both spectra show the B $^1\Sigma_u^+ \leftarrow$ X $^1\Sigma_g^+$ (2, 1) P(2) line taken with the mutually orthogonal geometry. (a) The 2^14^1 $rR_0(0)e$ photolysis; the simulated lineshape has $\beta_{eff} = 0.145$ and $v = 1.57 \times 10^6$ cm s^{-1}. (b) The 4^3 $rR_0(0)e$ photolysis; $\beta_{eff} = -0.242$ and $v = 1.57 \times 10^6$ cm s^{-1}.

distributions with an f.w.h.m. of 10, the single-velocity fits systematically produce a $\Delta\nu_D$ and a fragment velocity that is a few per cent too large. This causes the calculated J_{CO} to be 2-5 quanta lower than the peak J_{CO}. This shows that the distribution of velocities for each $H_2(v, J)$ can account for the discrepancy between the measured J_{CO} distribution and that calculated from the measured H_2 Doppler widths. The H_2 $v = 0$ states were not measured, but they are expected to fill in the high-J_{CO} part of the distribution.

The correlation of product quantum states was predicted in previous H_2CO studies.[4] Their CO rotational distribution was highly inverted and best explained by a large dissociation impact parameter (0.8-0.9 Å).[2] Constraining the impact parameter distribution about some large value would produce the observed correlation as follows. Conservation of angular momentum requires that

$$J_{tot} = J_{H_2CO} = L + J_{CO} + J_{H_2} \tag{5}$$

where L is the orbital angular momentum of the separating products and the J_s are rotational vectors. The initial parent angular momentum is essentially zero ($J_{H_2CO} = 1$) so that

$$L = \mu v b \approx |J_{CO} + J_{H_2}| \tag{6}$$

where μ is the H_2—CO reduced mass, v is the relative velocity of the products and b is the impact parameter. Most of the internal angular momentum of the products is in J_{CO}. As more energy is put into internal product excitation, the translational energy and therefore the velocity, v, must decrease. Since b is constrained, a lower velocity

Table 1. Product correlations and impact parameters

H_2 state		average H_2 velocity $/10^6$ cm s^{-1}	J_{CO}	impact parameter^a/Å		
v	J			$J_{CO}+J_{H_2}$	J_{CO}	$J_{CO}-J_{H_2}$
1	0	1.57 ± 0.02	42 ± 4	0.86	0.86	0.86
	2	1.57	40	0.87	0.82	0.77
	4	1.54	40	0.92	0.83	0.74
	6	1.51	38	0.94	0.81	0.67
	8	1.49	30	.0.83	0.65	0.47
2	2	1.45 ± 0.04	35 ± 9	0.83	0.77	0.73
	4	1.43	33	0.84	0.75	0.64
	6	1.45	17	0.52	0.38	0.24
3	0	1.33 ± 0.04	32 ± 8	0.77	0.77	0.77
	2	1.31	33	0.87	0.81	0.76
	4	1.32	25	0.72	0.62	0.50
	6	1.30	18	0.61	0.45	0.29

^{a} The H_2 and CO J vector combinations correspond to: corotation $(J_{CO}+J_{H_2})$, counter-rotation $(J_{CO}-J_{H_2})$, and the rotational vectors perpendicular to each other (J_{CO}).

and therefore the velocity, v, must decrease. Since b is constrained, a lower velocity results in less orbital angular momentum and therefore less CO rotational angular momentum. The constrained impact parameter causes internally excited H_2 states to correlate with CO states in lower rotational levels.

The impact-parameter disributions can be calculated from the product correlation data using eqn 6. In order to do so, however, some assumption must be made about the relation of the H_2 and CO rotation vectors. The impact parameter as a function of H_2 J state is given in table 1 for several combinations of these vectors. The limiting cases are J_{H_2} parallel to J_{CO} (corotation), J_{H_2} perpendicular to J_{CO}, and J_{H_2} antiparallel to J_{CO} (counter-rotation). As suggested by the vJ correlation, the situation may be intermediate between the parallel and antiparallel extremes owing to the non-planar motions of the transition state. At this time, the experimental evidence does not discriminate between corotation or counter-rotation. The only firm conclusion is that the calculated impact parameters are large and outside the centre of the carbon nucleus as previously suggested.

Conclusions

We have seen strong evidence for correlations of the $CO(v, J)$ and $H_2(v, J)$ product states from formaldehyude photofragmentation. H_2 states with more internal excitation correlate with CO states with less rotation. These correlations can be explained by the constrained impact parameter distribution. The observed H_2 vector correlations are diminished by the long lifetime of the excited H_2CO parent state. However, the vJ correlation which should be unaffected by parent rotations suggests that v is intermediate between being parallel and perpendicular to J. This is most easily understood in terms of the large out-of-plane motions of the H_2CO transition state. Preliminary evidence suggests that the vector correlations depend strongly on the initial parent quantum state.

References

1 C. B. Moore and J. C. Weisshaar, *Annu. Rev. Phys. Chem.*, 1983, **34**, 525.
2 D. J. Bamford, S. V. Filseth, M. F. Foltz, J. W. Hepburn and C. B. Moore, *J. Chem. Phys.*, 1985, **82**, 3032.
3 P. Ho, D. J. Bamford, R. J. Buss, Y. T. Lee and C. B. Moore, *J. Chem. Phys.*, 1982, **76**, 3630.
4 D. Debarre, M. Lefebvre, M. Péalat, J-P. E Taran, D. J. Bamford and C. B. Moore, *J. Chem. Phys.*, 1985, **83**, 4476.
5 J. D. Goddard and H. F. Schaefer, *J. Chem. Phys.*, 1979, **70**, 5117.
6 J. D. Goddard, Y. Yamaguchi and H. F. Schaefer, *J. Chem. Phys.*, 1981, **75**, 3459.
7 R. N. Dixon, *J. Chem. Phys.*, 1986, **85**, 1866.
8 P. L. Houston, *J. Phys. Chem.*, 1987, **91**, 5388.
9 K-H. Gericke, *Phys. Rev. Lett.*, 1988, **60**, 561.
10 R. Spence and W. Wild, *J. Chem. Soc.*, 1935, 338.
11 R. Spence and W. Wild, *J. Chem. Soc.*, 1935, 506.
12 K-H. Gericke, S. Klee, F. J. Comes and R. N. Dixon, *J. Chem. Phys.*, 1986, **85**, 4463.
13 C. H. Greene and R. N. Zare, *J. Chem. Phys.*, 1983, **78**, 6741.
14 R. Schmiedl, H. Dugan, W. Meier and K. H. Welge, *Z. Phys. A*, 1982, **304**, 137.
15 T. J. Butenhoff, K. L. Carleton and C. B. Moore, to be published.
16 S. Yang, and R. Bersohn, *J. Chem. Phys.*, 1974, **61**, 4400.
17 T. Nagata, T. Kondow, K. Kuchitsu, G. W. Loge and R. N. Zare, *Mol. Phys.*, 1983, **50**, 49.
18 D. J. Clouthier and D. A. Ramsay, *Annu. Rev. Phys. Chem.*, 1983, **34**, 31.
19 H. B. Levene and J. J. Valentini, *J. Chem. Phys.*, 1987, **87**, 2594.
20 D. R. Guyer, W. F. Polik and C. B. Moore, *J. Chem. Phys.*, 1986, **84**, 6519.
21 D. C. Jacobs and R. N. Zare, *J. Chem. Phys.*, 1986, **85**, 5457.

Vector Correlations from Doppler-broadened Lineshapes

State-selected Dissociation of Methyl Nitrite

Michael P. Docker, Anton Ticktin, Ueli Brühlmann and J. Robert Huber*

Physikalisch-Chemisches Institut der Universität Zürich, Winterthurerstrasse 190, CH-8057 Zürich, Switzerland

The theoretical framework needed to analyse sub-Doppler lineshapes obtained by 2+1 LIF spectroscopy is outlined and applied to data for the state-selected photodissociation of *cis*-methyl nitrite (CH_3ONO). Excitation into the second overtone of the terminal N=O stretch ($v' = 2$) produces NO fragments with zero, one or two vibrational quanta and a highly correlated set of vector properties. These vector properties can be quantified in terms of five bipolar moments, which include the rotational alignment, the translational anisotropy parameter, the second Legendre moment of the (v, j) correlation and two moments which characterise the three-vector (μ, v, j) correlation [$\beta_0^2(22)$ and $\beta_0^2(24)$]. In principle, these bipolar moments can be used to separate the dissociation dynamics in to the influence of a *dissociation lifetime* and a *dissociation geometry*. The experimental evidence for the photolysis of methyl nitrite implies an essentially planar dissociation geometry leading to a strong perpendicular (v, j) correlation [$\beta_0^0(22) = -0.34 \pm 0.05$]. The slight deviation from complete planarity is probably caused by torsional forces. The dissociation lifetime derived from the value of the translational anisotropy parameter appears to be a function of the fragment vibrational level. A simple model which explains many of the observations is presented and discussed in the light of preliminary classical trajectory calculations.

Molecular photodissociation is a primary chemical process for which a wealth of dynamical and stereochemical information is now available.[1,2] One reason for this progress is the combination of detailed experimental measurements of fragment scalar and vector properties[1-5] together with the insight afforded by modern quantum (and classical) calculations using realistic *ab initio* potential-energy surfaces.[6,7]

In the present paper we concentrate on the dissociation of methyl nitrite into methoxy and nitric oxide fragments following excitation into the vibrationally structured first absorption continuum.

$$CH_3ONO(S_0) + h\nu \rightarrow CH_3ONO(S_1) \rightarrow CH_3O + NO(X\,^2\Pi) \qquad (1)$$
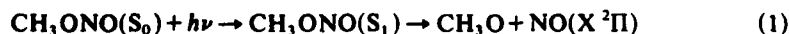
This system has several interesting features amenable to experimental[8-10] and theoretical attack,[11-13] including a prompt vibrational predissociation on a well characterised and isolated potential-energy surface, which leads to an anisotropic angular distribution of fragments with markedly non-statistical properties.

The scalar properties and some vector properties of the fragments have been discussed in detail elsewhere.[8-10] Here we present new results covering the correlations between the vectors μ, v and j, where μ is the parent molecular transition dipole moment, v is the NO fragment velocity vector and j is the fragment rotational angular momentum. We outline the theory required to analyse Doppler profiles obtained using 2+1 LIF spectroscopy and use the resulting bipolar moments to discuss the vibrational state-selected dissociation dynamics of methyl nitrite in terms of an essentially planar dissociation geometry and a possible fragment state-dependent dissociation lifetime.

1

Experimental

The experimental set-up and technique was similar to that described previously.[8,14] The laser beams were generated from two dye lasers (a home-made Hänsch type for photolysis and a Lambda Physik FL2002E for analysis) pumped by the same excimer laser (Lambda Physik EMG 101MSC) which was operated at 308 nm with a 10 Hz repetition rate. The pulse energy of the photolysis laser was maintained at <2 mJ in order to avoid unwanted multiphoton effects, whilst the two-photon absorption of the NO fragment ($X\,^2\Pi \rightarrow A\,^2\Sigma^+$) was achieved using a pulse energy of <1 mJ and a laser linewidth of *ca.* 0.05 cm^{-1}, determined by measuring the line profile of a thermal NO sample, and monitored continuously using a thermally stabilised confocal etalon (Tecoptics, finesse 20–30, 400–500 nm) mounted behind the sample cell. A 10 ns optical delay and an operating pressure of $\leqslant 150$ mTorr† ensured that collisional effects could be ignored on the timescale of the experiment. Both laser beams were linearly polarised and the plane of polarisation could be rotated by Fresnel rhombs (Suprasil, Steeg and Reuter) mounted in front of the cell. The various experimental geometries used are depicted in fig. 1.

The NO fragment was detected by $2+1$ LIF using an unpolarised detector (Hamamatsu R166UH and Schott UV-R-250 filter set) which collected the undispersed fluorescence collinear to the analysis electric vector (ε_a). The signals were stored and digitised by a boxcar integrator (SRS, SR250) linked to a Digital Minc 11 computer. The computer also controlled the excimer laser repetition rate, the Fresnel rhomb rotator and the tuning of the dye laser in addition to correcting the signals for shot-to-shot intensity fluctuations.
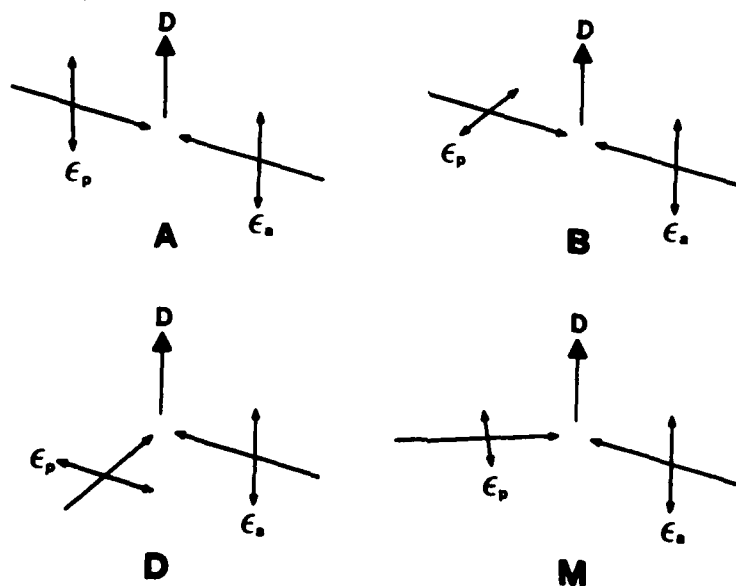
Fig. 1. Alternative experimental geometries (A, B, D and M) for $2+1$ LIF spectroscopy. Note that in each case the ε vector of the analysis beam (ε_a) points towards the detector (D) which accepts unpolarised light. The laboratory-frame z axis is always parallel to the ε-vector of the photolysis beam (ε_p). At the magic-angle geometry (M) the beams cross at 35.3°, the angle between ε_p and k_a is 54.7° and the two electric vectors are at 90°.

† 1 Torr = 101 325/760 Pa.

Theory and Analysis

The derivation of the lineshape function for $2+1$ LIF is analogous to that described by Dixon.[15] We start with the general expression for the LIF signal as a function of the symmetrised and re-scaled alignment parameters

$$I = CS \sum_{k,q} Z_{kq+} A_{q+}^{(k)}; \qquad q \geqslant 0 \tag{2}$$

where C is a constant (including the population), S is a line strength factor and Z_{kq+} is a coefficient dependent on the experimental geometry, the transition type and the number of photons involved in the absorption/emission sequence.

The main step in the derivation involves re-writing the re-scaled alignment parameters as a function of the Doppler shift, the angle θ_a (between k_a and ε_p) and the bipolar moments which characterise the correlated (μ, v, j) distribution in the molecular frame. The transformation used is specific to one-photon dissociation by linearly polarised light.[15] The result is a series of expressions (one for each bipolar moment) depending on the Z_{kq+} coefficients and some Legendre polynomials of the Doppler shift which can be conveniently re-written as

$$g(\nu) = \frac{1}{2\Delta\nu_D} [g_0 + g_2 P_2(x_D) + g_4 P_4(x_D) + g_6 P_6(x_D) + g_8 P_8(x_D)] \tag{3}$$

where the g_i coefficients are functions of the experimental geometry, including θ_a and the bipolar moments.[15]

The structure due to the $P_4(x_D)$, $P_6(x_D)$ and $P_8(x_D)$ terms will, in general, be smoothed away more efficiently by the laboratory-frame–molecule-frame transformation (convolution) and the integration over the spread of fragment translational energies than the structure due to the $P_2(x_D)$ term. Consequently, we ignore all but the first two terms in eqn (3). This assumption can be partially justified by adding weighted sums of various lineprofiles to eliminate the influence of the $P_2(x_D)$ term and hence confirm the negligible contribution of the $P_4(x_D)$ term (see later).

The full expressions for the g_0 and g_2 coefficients are

$$g_0 = b_0 + b_1 \beta_0^2(02) \tag{4}$$

$$g_2 = b_2 \beta_0^2(20) + b_3 \beta_0^0(22) + b_4 \beta_0^2(22) + b_5 \beta_0^2(24) \tag{5}$$

where the form of the b_i coefficients is given in table 1. The appealing simplicity of table 1 arises from the fact that for all the experimental geometeries studied here the axial symmetry of the final fluorescence step is preserved, *i.e.* we collect unpolarised light which travels parallel to the electric vector of the analysis beam. Furthermore, the expressions in terms of the $q^{(k)}$ factors are still quite general, and the only difference between the equations for $1+1$ LIF and $2+1$ LIF is in the form of the $q^{(k)}$ factors. For

Table 1. The b_i coefficients

geometry	b_0	b_1	b_2	b_3	b_4	b_5
A	$q^{(0)}$	$\frac{4}{7}q^{(2)}$	$-q^{(0)}$	$-q^{(2)}$	$\frac{2}{7}q^{(2)}$	$-\frac{3}{7}q^{(4)}$
B	$q^{(0)}$	$-\frac{2}{7}q^{(2)}$	$-q^{(0)}$	$-q^{(2)}$	$-\frac{5}{7}q^{(2)}$	$\frac{1}{14}q^{(4)}$
D	$q^{(0)}$	$-\frac{2}{7}q^{(2)}$	$2q^{(0)}$	$-q^{(2)}$	$\frac{2}{7}q^{(2)}$	$\frac{3}{14}q^{(4)}$
$\frac{1}{3}$(A+B+D)	$q^{(0)}$	0	0	$-q^{(2)}$	0	0
M	$q^{(0)}$	$-\frac{2}{7}q^{(2)}$	0	$-q^{(2)}$	$-\frac{4}{7}q^{(2)}$	$\frac{5}{42}q^{(4)}$

2 + 1 LIF these are given in terms of the $\bar{\alpha}'$ factors of ref. (16) by

$$q^{(0)} = 1 - \tfrac{1}{2}\bar{\alpha}'_{022} \tag{6}$$

$$q^{(2)} = \bar{\alpha}'_{202} - \tfrac{1}{2}\bar{a}'_{220} - \tfrac{1}{2}\bar{\alpha}'_{222} - \tfrac{1}{2}\bar{\alpha}'_{224} \tag{7}$$

$$q^{(4)} = \bar{\alpha}'_{404} - \tfrac{1}{2}\bar{\alpha}'_{422} - \tfrac{1}{2}\bar{\alpha}'_{424}. \tag{8}$$

The high-J_i limit of these $q^{(k)}$ factors is given in table 2. Note that the large values of the $q^{(4)}$ factors for 2 + 1 LIF contrast strongly with the values found for 1 + 1 LIF. As a consequence it is not possible to neglect the influence of the $\beta_0^2(24)$ term as is normally the case in the analysis of Doppler profiles obtained using 1 + 1 LIF.

Also note that the use of the 'magic angle' between the k vector of the analysis laser and the laboratory-frame Z axis ($\|\varepsilon_p$) does not result in an appreciable simplification of the lineshape as claimed by some authors[17,18] since only the term in $\beta_0^2(20)$ vanishes. Consequently, we only use magic-angle measurements to supplement the normal right-angled geometries and not to provide any additional insight into the details of the dissociation dynamics. It is possible to simplify further the lineshape function by setting other angles to 54.7 °, *e.g.* the influence of the emitted photon in an $n + 1$ LIF sequence can be removed by collecting polarised emission with its ε vector at 54.7 ° to the z axis. The usefulness of such an approach will be discussed in more detail in a subsequent publication.[19]

The analysis of the Doppler profiles was similar to that described before.[14] The line profiles were fitted using a non-linear least-squares routine, where the trial function was of the form

$$g(\nu) = \int_{\nu_{\min}}^{\nu_{\max}} \frac{W(v)}{2\Delta\nu_D} [1 + \beta_{\text{eff}} P_2(x_D)] \, dv \tag{9}$$

where ν is the frequency, v is the fragment velocity and $\Delta\nu_D = \nu_0 v/c$ is the Doppler width. The relative Doppler shift is given by $x_D = (\nu - \nu_0)/\Delta\nu_D$ and the parameter β_{eff} is equal to the ratio of the g coefficients described above ($\beta_{\text{eff}} = g_2/g_0$). The distribution of fragment recoil velocities is represented by $W(v)$. We include the effect of the laboratory-frame–molecule-frame transformation and the finite resolution of the analysis laser by convoluting the trial function with a Gaussian function. Note that, in principle, the parameter β_{eff} can be a function of the fragment velocity v, but that for experimental convenience we assume that β_{eff} and v are not correlated. We also assume that the (unknown) functional form of the $W(v)$ distribution can be approximated by a Gaussian in energy units $[P(E_t)]$,[14] where the two distributions are related as follows:[20]

$$W(v) = mvP(E_t) \tag{10}$$

and the Gaussian distribution has the following form

$$P(E_t) = \frac{1}{\delta_E \sqrt{\pi}} \exp\left[-(E_t - \bar{E}_t)^2/\delta_E^2\right]. \tag{11}$$

Table 2. High J_i limit of the $q^{(k)}$ factors

transition	$q^{(0)}$	$q^{(2)}$	$q^{(4)}$
O, S	$\tfrac{15}{14}$	$-\tfrac{45}{56}$	$\tfrac{45}{77}$
P, R	$\tfrac{17}{28}$	$\tfrac{15}{56}$	$-\tfrac{291}{154}$
Q	$\tfrac{13}{14}$	$\tfrac{45}{56}$	$\tfrac{171}{77}$

The mean of the Gaussian is $\bar{E}_t$ and the f.w.h.m. is given by

$$\Delta E_t = 2(\ln 2)^{1/2} \delta_E \qquad (12)$$

where the quantity δ_E is just $\sqrt{2}$ times the standard deviation of the Gaussian distribution.

It should be noted, however, that the Doppler profile fits are relatively insensitive to the functional form of $W(v)$ and that either a Gaussian in velocity or a rectangular function in energy fit the data equally well. To minimise distortion of the results due to the spread in the fragment translational energy we used a global fitting procedure whereby 1–4 profiles (corresponding to the four possible geometries) were fitted simultaneously using a single value of $\bar{E}_t$ and ΔE_t, but with a difference β_{eff} for each profile. Furthermore, by generating composite profiles which correspond to a β_{eff} of zero (and can be simulated with one less parameter) it was possible to provide an additional check for the ΔE_t values.

Results

All of the results described below were obtained by exciting the methyl nitrite parent molecule at 350.8 nm in to the $v' = 2$ band (two quanta of the terminal $N = O$ stretch) and monitoring nascent $NO(X\,^2\Pi)$ produced in $v'' = 0, 1$ or 2 and with a rotational quantum number of $j = 33.5$. Thus we start with a well characterised initial state from which dissociation may occur via one of three (vibrational) exit channels. Since we monitor the same j value in all three cases the additional complication of disentangling j-dependent dissociation dynamics from j-dependent alignment values, degree of electron alignment (D_{EA}) values or bipolar moments can be safely ignored.

The Doppler lineshapes for the $v'' = 1$ exit channel are shown in fig. 2 and 3. The general shape is well represented by the functional form $1 + \beta_{eff} P_2(x_D)$, but we can make an additional test to justify the neglect of the $P_4(x_D)$ (and higher-order terms). From table 1 it follows that a sum of three line profiles for geometries A, B and D (see fig. 4) will depend only on the (v, j) correlation [i.e. on moments of the form $\beta_0^0(kk)$] and is independent of any correlations involving μ. This allows the immediate qualitative conclusion that v and j are perpendicular [i.e. $\beta_0^0(22)$ is negative] since β_{eff} is positive for the R line (very small dip) and negative for the S line (small bump), whilst the $q^{(2)}/q^{(0)}$ ratio is positive for the R line and negative for the S line. Note that this conclusion is independent of any fit to the data and is thus also independent of our assumption of a Gaussian spread of fragment translational energies.

The pair of composite line profiles can be further weighted and added in such a way as to remove the influence of the $\beta_0^0(22)$ term but to still leave behind the terms in $\beta_0^0(44)$ and $\beta_0^0(66)$.[19] Clearly, these higher-order terms make a negligible contribution since the final composite lineshape is flat-topped (see fig. 4) and well represented by the simple functional form described earlier. Admittedly, this test is not conclusive since, we have not justified the neglect of the bipolar moments which represent the higher-order components of the three-vector correlation but we feel that these approximations should not distort the remainder of the analysis.

The set of eight Doppler lineshapes for $v'' = 1$ and the corresponding data for $v'' = 0$ and 2 yield eight separate values of β_{eff} which can be converted (via the solution of a set of over-determined simultaneous equations) into four bipolar moments [$\beta_0^2(20), \beta_0^0(22), \beta_0^2(22)$ and $\beta_0^2(24)$] (see table 3). Following previous practice[15] the value of $\beta_0^2(02)$ [equal to $\frac{5}{4}A_0^{(2)}$] was determined from integrated line intensities and used as an input parameter in the extraction of the bipolar moments from the set of values of β_{eff}.

The Doppler lineshape analysis also yields two scalar properties of the photofragments (see table 4), namely, $\bar{E}_t$, the average translational energy and ΔE_t, the f.w.h.m. of the translational energy distribution, which also characterises the spread in the internal
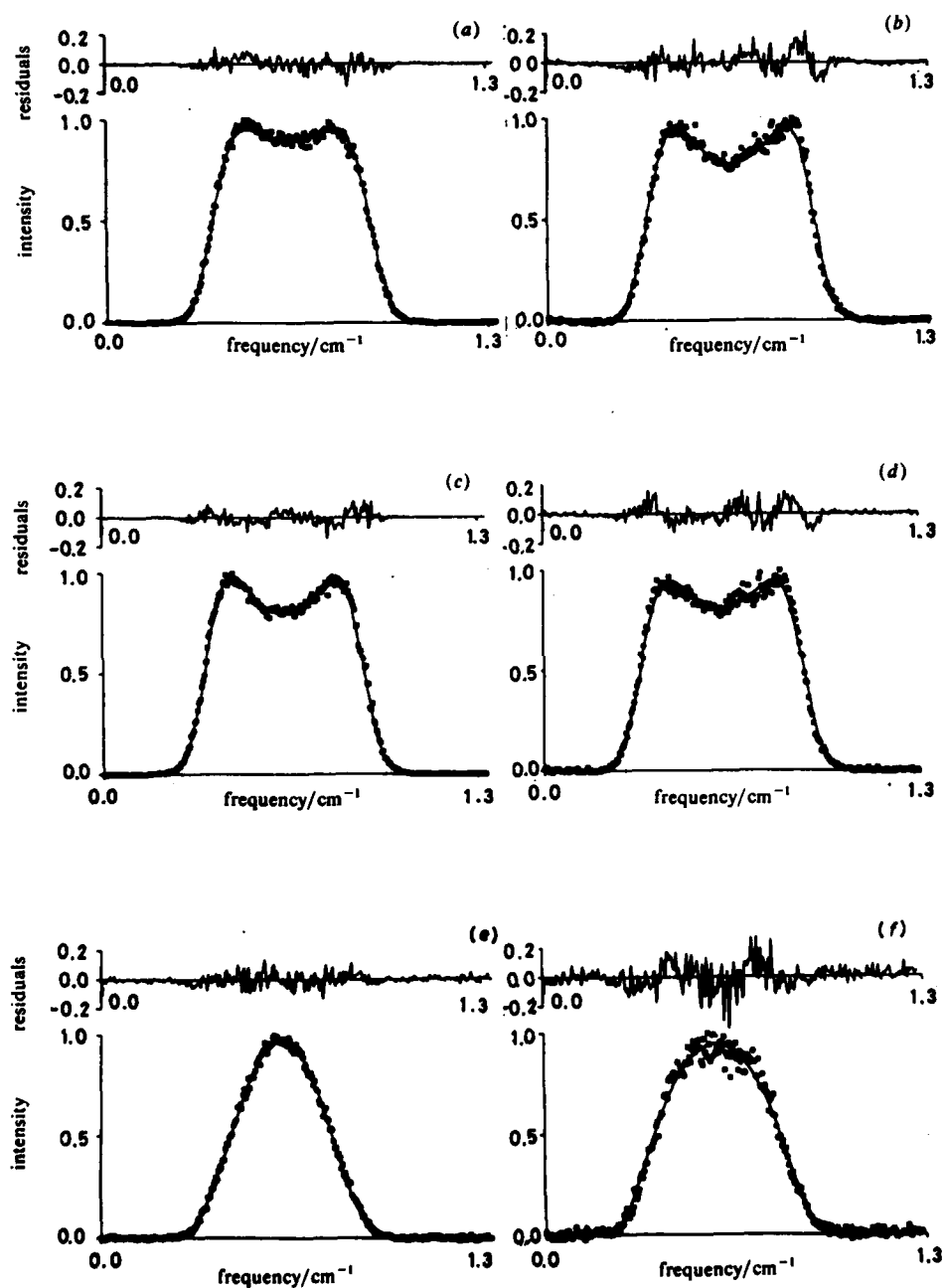
Fig. 2. Doppler profiles for the S_{22} [(a)-(c)] and R_{12} [(d)-(f)] transitions originating in a level with $j = 33.5$ for the geometries A [$(a), (d)$], B [$(b), (e)$] and D [$(c), (f)$] portrayed in fig. 1.
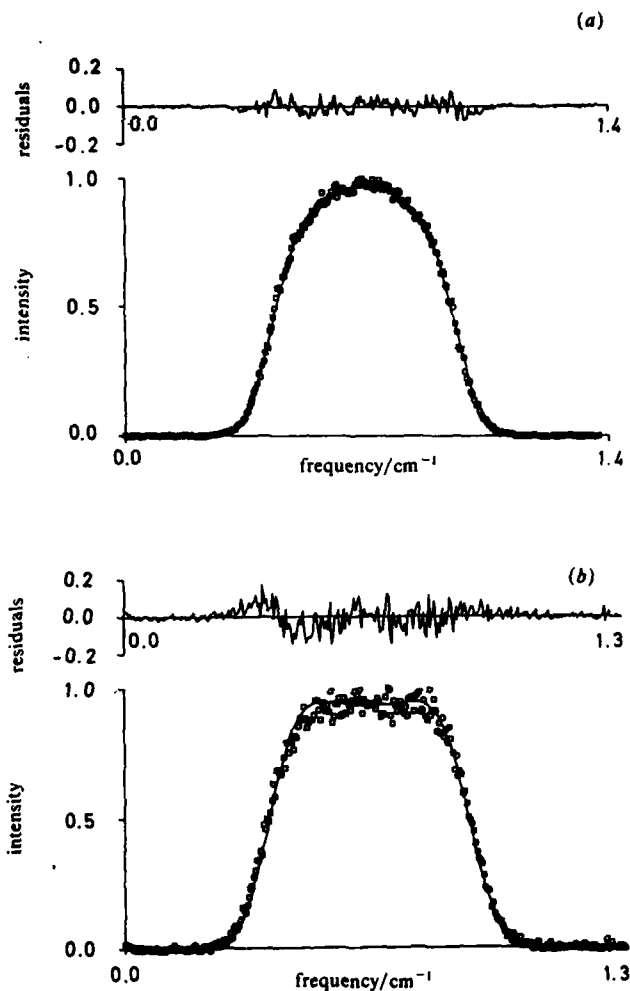
Fig. 3. As for fig. 2, but using the magic-angle geometry (M).

energy of the sister methoxy fragment. The latter values should be regarded with some caution since the simulations are relatively insensitive to ΔE_t.

Discussion

The main features of the dissociation dynamics of methyl nitrite are well understood.[8,12,21] The C—O—N=O group of the parent molecule is approximately planar in both the *cis* and *trans* conformers of methyl nitrite.[22] Excitation in the first absorption continuum $(S_0 \rightarrow S_1)$ corresponds to an $n \rightarrow \pi^*$ transition originating in the lone-pair orbitals of *the terminal oxygen and nitrogen atoms and terminating in the delocalised* π^* *orbital* which involves the three atoms of the O—N=O moiety. The transition is $A' \rightarrow A''$ in character and is associated with a transition dipole moment perpendicular to the plane defined by the O—N=O group. This simplifies the interpretation of the results compared
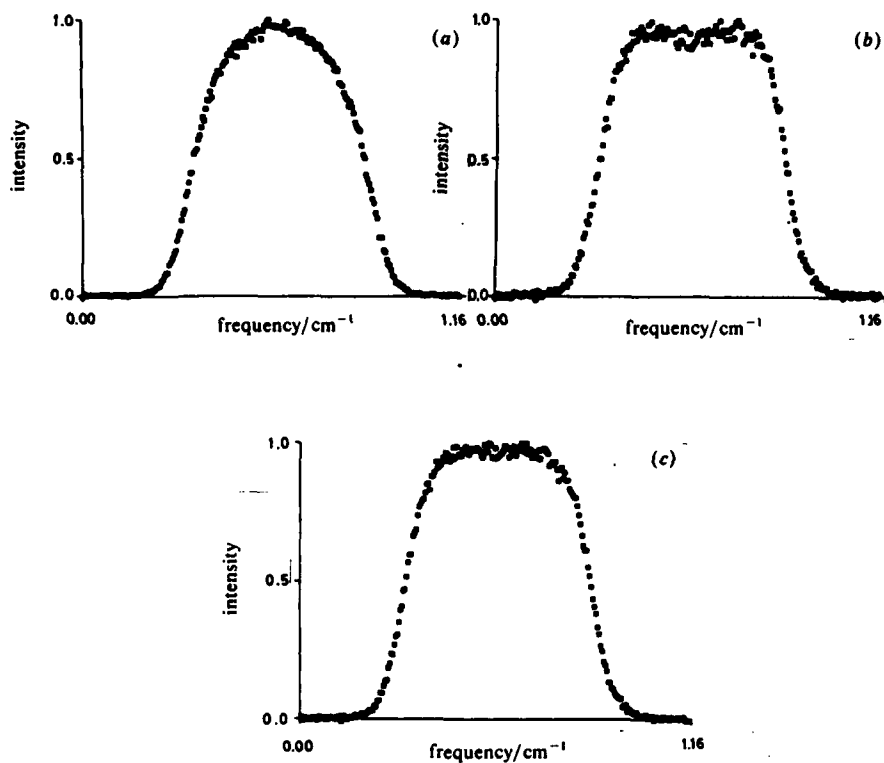
Fig. 4. $(a), (b)$ Composite profiles formed by adding the lineshapes for geometries A, B and D $[(a)$ is $S_{22}(33.5)]$. (c) Weighted sum of the R and S transitions (see text).

Table 3. Vector properties

	$v'' = 0$	$v'' = 1$	$v'' = 2$	planar[a]
β	−0.54	−0.82	−0.95	−1.0
$A_0^{(2)}$	0.31	0.39	0.52	0.8
$5A_0^{(2)}/2\beta$	−1.44	−1.19	−1.37	−2.0
D_{EA}	0.33	0.32	0.28	0.67[b]
$\beta_0^0(22)$	−0.30	−0.30	−0.41	−0.5
$\beta_0^2(22)$	0.34	0.32	0.34	0.5
$\beta_0^2(24)$	−0.26	−0.27	−0.15	−0.5

[a] For a hypothetical planar dissociation. [b] Upper limit for NO(X $^2\Pi$) in $j = 33.5$ (see text).

Table 4. Scalar properties

	$v'' = 0$	$v'' = 1$	$v'' = 2$
$\phi_{vib}{}^a$	0.2	0.5	0.3
β	−0.54	−0.82	−0.95
lifetime/fs[b]	340 ± 100	170 ± 60	0–80
lifetime/fs[c]	320 ± 100	120 ± 50	0–50
$\bar{E}_t$	5450	4580	3490
ΔE_t	2500	1950	800
$\Delta E_t / \bar{E}_t$	0.46	0.43	0.23
f^d	0.92–0.95	0.92–0.97	0.93–0.97

[a] Vibrational quantum yield derived from the data of ref. (30).
[b] Using the quasi-diatomic model[23,24] (see fig. 5 in Felder *et al.*[29])
and assuming an uncertainty of 10% in β. [c] As for (*b*), but including
the effect of parent-molecule rotation as the fragments separate
(*see text*). [d] Range calculated from the f.w.h.m. of the Gaussian
distribution.

with the situation for a parallel transition since there is no uncertainty about the position
of the molecular frame reference axis and it follows that the initial molecule-frame-
laboratory-frame transformation is unambiguous. Dissociation of the S_1 state occurs
via vibrational predissociation. The two-dimensional potential-energy surface involving
the coordinates $r(N=O)$ and $R(O-N)$ is characterised by a shallow well which
introduces a small barrier along the reaction coordinate. The potential well can support
quasi-bound levels which give rise to vibrational structure in the $S_0 \rightarrow S_1$ absorption
spectrum.

The decay of the excited parent molecule occurs by one of two routes, namely, by
tunnelling (a vibrationally adiabatic process) and/or by coupling vibrational modes to
the reaction coordinate (a non-adiabatic process). The most efficient decay channel is
promoted by coupling of the $N=O$ stretching mode (which supplies one quantum) to
the reaction coordinate. This gives rise to the propensity rule $v'' = v' - 1$.[12]

It has been accepted for some time[8] that the positive alignment, negative β and
perpendicular (v, j) correlation (see table 3) are firm evidence for the nature of the
electronic transition and the planar character of the dissociation process. This picture
is further confirmed by the values of the two additional bipolar moments presented here
for the first time. $\beta_0^2(22)$ is positive and $\beta_0^2(24)$ is negative, in keeping with a model
where $\mu \parallel j$ and v is perpendicular to both [see table 3 and ref. (15)].

However, the dissociation of methyl nitrite can be examined in further detail since
we have the possibility of vibrational-state selection in the parent molecule and rovibra-
tional-state selection in the NO fragment, which leads naturally to the question; how
does the fine detail of the dissociation dynamics depend on these three quantum numbers?
We shall concentrate here on the influence of the fragment vibrational level and address
the following question; is the dissociation lifetime for the dissociation geometry a
function of the NO fragment vibrational level?

In order to separate the influence of parent rotation before dissociation from the
molecule frame dissociation dynamics we consider photodissociation to occur by a
sequence of separate steps

$$M + h\nu \rightarrow M^* \tag{13}$$

$$M^* \rightarrow M^\ddagger \tag{14}$$

$$M^\ddagger \rightarrow A + B \tag{15}$$
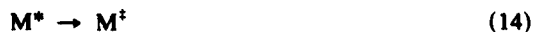
where the first step (photoexcitation) prepares the excited state in a more or less well defined distribution of quantum states. The subsequent evolution of the excited parent molecule may lead to direct or indirect (pre)dissociation, and may possibily involve a change of molecular geometry and the rotation of the whole molecule in space. Note that the theories used to disentangle the influence of a finite dissociation lifetime from the effect of a non-limiting dissociation geometry[23,24] are based on the simplification that at some critical time the molecule arrives at the 'dissociation geometry' and the fragments begin to separate. Thus the ill defined concept of the 'dissociation lifetime' includes a time before the molecule has started to fragment, when the parent-molecule geometry is approximately conserved (*i.e.* no appreciable bond stretching has occured and the three moments of inertia are approximately constant) and a time during which the fragments are separating.

In the present case of vibrational predissociation the excited methyl nitrite molecule is prepared within the Franck–Condon region in the shallow well of the two-dimensional potential-energy surface. The trajectory evolves within this well until it passes over the dissociation barrier. The residence time of the trajectory in the well represents the dissociation lifetime and the top of the barrier determines the dissociation geometry. Once the barrier has been crossed the strong repulsive forces lead to a very fast separation of the fragments.

This model allows us to separate the influence of parent rotation in the laboratory frame (prior to dissociation) from the remainder of the molecule frame dissociation dynamics. The reason that such a separation is non-trivial arises from the indirect nature of the photodissociation experiment, where state selection and production of the initially anisotropic distribution of parent molecules occurs at time $t = 0$, but the measurement of the fragment vector and scalar properties occurs at a time long after the fragmentation is complete. However, we can make progress by exploiting the vector properties of molecular photodissociation, especially the distinction between vector correlations involving only molecular frame quantities and the other correlations that link the molecular and laboratory frames.

The vector correlations which contain a component from the molecule-frame–laboratory-frame transformation are those involving μ (the parent-molecule transition dipole moment) and are represented by the bipolar moments $\beta_0^K (k_1 k_2)(K \neq 0)$. These include the rotational alignment [related to $\beta_0^2(02)$] and the translational anisotropy parameter [related to $\beta_0^2(20)$] as well as the moments which describe the three vector (μ, v, j) correlation of which only $\beta_0^2(22)$ and $\beta_0^2(24)$ have been measured.

We shall consider three quantities which are independent of the molecule-frame–laboratory-frame transformation (and hence the dissociation lifetime), namely $\beta_0^0(22)$, the degree of electron alignment (D_{EA}) and the ratio of the alignment to the translational anisotropy parameter. Each of these terms warrants further comment.

The term $\beta_0^0(22)$ represents the second Legendre moment of the (v, j) correlation

$$\beta_0^0(22) = \langle P_2(v, j)\rangle = \langle P_2 \cos \omega'_{tr}\rangle \tag{16}$$

and is independent of the laboratory frame since the vectors v and j are only produced at the moment of dissociation. It reflects the tendency of v and j to lie parallel (positive value) or perpendicular (negative value) and lies in the range $-\frac{1}{2} \leqslant \beta_0^0(22) \leqslant +1$.

The degree of electron alignment is related to the population of the Λ-doublet sub-levels of the $NO(X\,{}^2\Pi)$ fragment as follows

$$D_{EA} = \frac{\pi(A'') - \pi(A')}{\pi(A'') + \pi(A')}. \tag{17}$$

It reflects the alignment of the unpaired $p\pi$ electron in the ${}^2\Pi$ NO molecule with respect to the plane of molecule rotation.[25,26] D_{EA} is a symmetrical function ranging from -1 to $+1$ but is, in general, more strongly constrained by the j-dependent mixing of the

Λ-doublet sub-levels so that for NO in the $j = 33.5$ state D_{EA} lies between -0.67 and $+0.67$. The relevant limit for the planar dissociation of methyl nitrite considered in this work is $+0.67$.

Another vector property which is (approximately) independent of the dissociation lifetime is the ratio of the alignment to the translational anisotropy parameter. Following Dixon[15] we write the alignment and β as

$$A_0^{(2)} = \tfrac{4}{5}\langle P_2[\mu(t=0) \cdot j(t=\infty)]\rangle \tag{18}$$

$$\beta = 2\langle P_2[\mu(t=0) \cdot v(t=\infty)]\rangle \tag{19}$$

where $\mu(t=0)$ represents the parent molecule transition dipole moment in the laboratory frame at the moment of absorption and the vectors $j(t=\infty)$ and $v(t=\infty)$ represent the final positions of the fragment vectors after dissociation is complete. Next we use the azimuthally averaged addition (AAA) theorem described by Herschbach and co-workers:[27]

$$\langle P_n(a \cdot b)\rangle = \langle P_n(a \cdot c)P_n(c \cdot b)\rangle \tag{20}$$

to separate the problem into two parts, one part before dissociation has started (up to time t) and the other part after dissociation has begun. Hence

$$A_0^{(2)} = \tfrac{4}{5}\langle P_2[\mu(t=0) \cdot \mu(t=t)]P_2[\mu(t=t) \cdot j(t=\infty)]\rangle \tag{21}$$

$$\beta = 2\langle P_2[\mu(t=0) \cdot \mu(t=t)]P_2[\mu(t=t) \cdot v(t=\infty)]\rangle. \tag{22}$$

If we now assume that the 'dissociation geometry' is independent of the 'dissociation lifetime' then the quantities in angular brackets can be factorised into two separate averages. Finally, we take the ratio of the two expressions and cancel the lifetime factor giving

$$\frac{5A_0^{(2)}}{2\beta} = \frac{\beta_0^2(02)}{\beta_0^2(20)} = \frac{\langle P_2[\mu(t=t) \cdot j(t=\infty)]\rangle}{\langle P_2[\mu(t=t) \cdot v(t=\infty)]\rangle} \tag{23}$$

which we shall call the 'geometry index'.

We now return to the dissociation of methyl nitrite, for which the evidence is as follows. The vector properties that depend mainly on the dissociation geometry [$\beta_0^0(22)$, the D_{EA} and the 'geometry index'] are approximately constant (see table 3), whereas the alignment and β (both of which depend on the dissociation lifetime) change considerably with the fragment vibrational level. However, the two terms that characterise the (μ, v, j) correlation, and would be expected to be more sensitive to the influence of parent rotation than β or the alignment, are approximately constant.

This apparent contradiction prompted us to examine closely the data for all the combinations of parent and fragment vibrational levels which we had measured. This amounts to eight sets of data with the additional values being for the following combinations of v' and v'' (0, 0), (1, 0), (1, 1), (3, 1), (3, 2).

The average values for some of the bipolar moments together with their standard deviations (σ_n) are as follows:

$$\beta_0^0(22) = -0.32 \pm 0.07; \qquad \beta_0^2(22) = 0.29 \pm 0.05; \qquad \beta_0^2(24) = -0.15 \pm 0.11.$$

The comparatively small level of scatter for $\beta_0^0(22)$ and $\beta_0^2(22)$, and to a lesser extent $\beta_0^2(24)$, confirms the pattern of results seen for the $v' = 2$ data. The second moment of the (v, j) correlation is approximately constant and so is the moment $\beta_0^2(22)$. However, for all these cases the alignment[9] and the translational anisotropy parameter[28] are a function of the fragment vibrational level, such that the smallest (magnitude) of the alignment and β corresponds to fragments which differ most from the parent state in their vibrational quantum numbers (v'' compared with v').

We also re-examined the analysis procedure by which the bipolar moments were extracted from the experimental data. This procedure rests upon two assumptions, namely that the fragment translational energy distribution can be approximated by a Gaussian distribution and that the bipolar moments do not depend on the fragment translational energy.

The assumption of a Gaussian spread can be justified on the grounds that the quality of the fit is relatively insensitive to the form of the $W(v)$ distribution and that the time-of-flight profiles for CH_3O fragments produced in the dissociation of methyl nitrite are approximately Gaussian when plotted as a function of translational energy.[29]

The validity of assuming that the bipolar moments are independent of the fragment translational energy is more questionable, since it is quite possible for a more 'violent' fragmentation to produce faster more anisotropic fragments than a fragmentation in which more of the available energy ends up in the unobserved degrees of freedom of the sister fragment. Furthermore, the speed of separation of the two fragments in the dissociation of methyl nitrite which is also a function of the $W(v)$ distribution means that parent-molecule rotation during fragment separation can influence the observed laboratory-frame anisotropy. This point can be illustrated by regarding methyl nitrite as a quasi-diatomic molecule. Note that this approximation is probably more valid for the *trans* conformer since this species is closer to the prolate-top limit (cigar-shaped) than is the *cis* conformer. However, it is the *cis* conformer which predominates (by a ratio of 2:1) in a room-temperature sample, and is selectively excited ($\geqslant 90\%$) in the absorption step. We pursue the model to make the more general point that a spread of fragment translational energies can produce a corresponding spread in the translational anisotropy parameter or even in some of the other bipolar moments.

The effect of parent molecule rotation whilst two fragments are separating is to produce a tangential velocity component in addition to the axial-velocity component produced by the diatomic recoil.[23,24] The result is a reduction in the magnitude of beta by a factor (f) which can be approximated for a small deflection of the original velocity vector by

$$f = 1 - 3\sqrt{2}k_B T/2E_{rel} \tag{24}$$

where E_{rel} is the recoil energy of the two fragments (approximately equal to twice $E_t(NO)$ for the quasi-homonuclear methyl nitrite). The f factors for the three vibrational exit channels of interest here are given in table 4. It is clear that this mechanism does not produce very much distortion in the value of β; however, if the effect acts on several of the bipolar moments simultaneously then the result could be a systematic error in the final bipolar moments since these are extracted from the set of values of β_{eff}, each of which is a complicated function of the individual bipolar moments. Model calculations are in hand to assess the quantitative influence of such systematic errors. Also note that it is possible for a more general exit-channel interaction involving some of the vibrational modes of methyl nitrite to produce a tangential velocity component and reduce the observed laboratory-frame anisotropy in an analogous way to the effect of parent-molecule rotation as described above.

An alternative way to rationalise the apparently contradictory pieces of evidence is to postulate a slight change in the distribution of dissociation geometries which has no significant effect on the second moment of the (v, j) correlation, the D_{EA} or the geometry index but which alters the values of the other bipolar moments. The plausibility of such an assumption is probably best examined by means of classical trajectory calculations and we defer further discussion of this point to a subsequent publication.[28]

The rest of this section is based on the assumption of an approximately planar dissociation geometry and a dissociation lifetime which is a function of the fragment vibrational level. The relationship between the translational anisotropy parameter and the dissociation lifetime has been considered in detail by Yang and Bersohn.[24] We

follow their formulation of the quasi-diatomic model which assumes a Poisson distribution of dissociation lifetimes and a Boltzmann distribution for the rotation of the parent molecule. The resulting lifetimes, which strictly speaking are upper limits based on the assumption of a limiting dissociation geometry, are shown in table 4.

We quote two sets of lifetimes, one set based on a model which only includes parent-molecule rotation before fragment separation commences and another set which allows for the tangential velocity component produced by parent-molecule rotation as the breaking bond continues to stretch. The difference between these models is only significant for values of β close to the theoretical limit. Table 4 indicates that the dissociation lifetimes associated with fragments produced in $v'' = 2$ are only of the order of 1-2 O—NO vibrational periods, suggesting that the vibrational predissociation is virtually direct for this particular exit channel.

The simplest kinetic scheme suitable to describe the state-to-state dissociation of methyl nitrite is shown below:

$$CH_3ONO(v'=2) \xrightarrow{k_0} NO(v''=0)$$

$$CH_3ONO(v'=2) \xrightarrow{k_1} NO(v''=1)$$

$$CH_3ONO(v'=2) \xrightarrow{k_2} NO(v''=2).$$
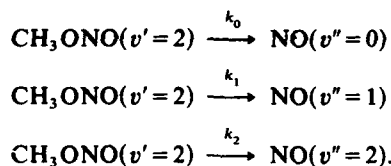
The overall dissociation rate is $k_{total} = k_0 + k_1 + k_2$ and the quantum yields for the three exit channels are given by $\phi_0 = k_0/k_{total}$ etc. This simple model predicts a direct correlation between the state-to-state rate constant for a particular exit channel (inversely proportional to the dissociation lifetime) and the quantum yield. The experimental values of the quantum yield based on the vibrational populations measured by Lahmani and co-workers[30] are shown in table 4 together with the upper limits for the dissociation lifetimes derived from the values of the translational anisotropy parameter.

The uncertainty in the values of the bipolar moments prevents a distinction between the translational anisotropy parameter for $v'' = 1$ and $v'' = 2$, but both are clearly different from the value for $v'' = 0$. However, this trend is not observed in the vibrational quantum yields where the channel leading to NO in $v'' = 1$ dominates over the other two channels and would therefore be expected to correlate with the fastest dissociation in contrast to the prediction of the simple model. However, a slightly refined model is able to explain the observed trends.

Suppose that the initial distribution of excited parent molecules is divided in to several sub-sets of molecules, each of which is predisposed to dissociate along a particular exit channel. Thus the exit-channel branching ratio is determined at the moment of absorption (presumably by the phase of the various parent internal motions) and the evolution of the parent molecule in to separating fragments (governed by the dissociation lifetime) is now independent of the vibrational quantum yield.

This model provides two possible explanations for the change of β with fragment vibrational level. The three exit channels can correlate with different sub-sets of the parent molecules that consist of molecules in different phases of their internal motions (giving rise to different dissociation lifetimes) or the three exit channels can correlate with parent molecules in different rotational states. These molecules could dissociate at the same (or at a different) rate and the change in the translational anisotropy parameter could be due to a different dissociation lifetime or a different rotational period.

The predictions of this model could be tested by multi-dimensional classical trajectory calculations which include the influence of the C—O—N=O torsional mode and the vibrations of the methyl group. Although each of these motions may be expected to have only a slight influence on the rate of escape from the flat region of the excited-state potential-energy surface accessed by photo-excitation, it is still possible for the combined

effect of these neglected motions to have an influence on the dynamics. Unfortunately, calculations of this sophistication are impracticable at the present time.

Preliminary classical calculations[31] based on a three-dimensional potential-energy surface $E[R, r, \theta(ONO)]$ suggest that the dissociation lifetime should be independent of the fragment vibrational level. However, it should be stressed that this result could change when the dynamics in the critical region of the potential-energy surface near the small dissociation barrier are treated quantum-mechanically.

A further test of the tentative conclusions reached here may be provided by direct measurements of the dissociation lifetime made possible by the recent advances in femtosecond laser technology.[32,33]

We conclude this section by considering the reasons for the slight non-planarity of the dissociation process. This effect is most apparent in the value of the moment $\beta_0^0(22)$ which loosely corresponds to an angle between v and j of ca. 65-75°. In addition, the effect is also apparent in the values of the translational anisotropy parameter and the alignment, since for fragments in $v'' = 2$ the translational anisotropy parameter is close to the theoretical maximum for a perpendicular recoil, but the alignment is still significantly short of its limiting value of 0.8. This observation is equivalent to noting that the geometry index is not equal to its limiting value of -2.0 for a planar dissociation following a perpendicular transition.

An explanation for these observations can be obtained using the treatment described by Gericke et al.,[34] which enables us to transform the values of $\beta_0^0(22)$, $\beta_0^2(22)$ and the alignment into expectation values for the square of the angular momentum projection along cartesian axes in the molecular frame. This approach rests on the assumption of pure perpendicular recoil ($v \perp \mu$) which allows the expressions quoted by Dixon[15] for some of the bipolar moments to be re-written as follows:

$$\langle j_z^2 \rangle = \{[2\beta_0^2(02)+1]/3\}j(j+1) \tag{25}$$

$$\langle j_x^2 \rangle = \{[2\beta_0^0(22)+1]/3\}j(j+1) \tag{26}$$

$$\langle j_z^2 \rangle = \{[1-2\beta_0^0(22)-2\beta_0^2(22)]/3\}j(j+1) \tag{27}$$

where the fragment velocity is parallel to the x axis and μ is parallel to the z axis. Applying these equations to the results for NO in $v'' = 0, 1$ and 2 yields the following average values:

$$\langle j_z^2 \rangle/[j(j+1)] \approx 0.6$$

$$\langle j_y^2 \rangle/[j(j+1)] \approx 0.1$$

$$\langle j_x^2 \rangle/[j(j+1)] \approx 0.3.$$

The relatively large component of j along the x axis, which is greater than the possible contribution from rotation of the parent molecule ($k_B T/2 \approx 100 \text{ cm}^{-1}$),[34] suggests that the main reason for the slight non-planarity in the dissociation process is due a contribution from some torsional force which tips the fragment j vector away from being perpendicular to the molecular plane and towards the fragment recoil direction (v). This is analogous to the result observed in the photodissociation of hydrogen peroxide.[34,35] However, the effect is (not unexpectedly) much smaller in the present case than that observed for hydrogen peroxide, indicating that the torsional forces involved are much less significant. The most likely cause of this effect is the $C-O-N=O$ torsional vibration of the methyl nitrite parent molecule. This conclusion reinforces the intuitive feeling that in order to improve the classical dynamical treatment of the dissociation of methyl nitrite[12] it will be necessary to include the effect of torsional forces.

Conclusion

We have considered the utility and the drawbacks of using sub-Doppler spectroscopy to probe the vector properties of fragments produced by the photodissociation of polyatomic molecules and have illustrated the argument with data for the state-selected dissociation of *cis*-methyl nitrite. Much useful qualitative information can be obtained, but the quantitative treatment of the results suffers from the need to make several simplifying assumptions about the spread of the fragment translational energy distribution and whether this spread is associated with a change in the microscopic dynamics and hence the bipolar moments which characterise the dissociation.

We conclude that the dissociation of methyl nitrite occurs via a predominantly planar dissociation geometry which is independent of the fragment vibrational level, but the dissociation lifetime may be a function of the fragment vibrational level. We suggest that this problem provides an interesting example for direct measurements of photodissociation lifetimes using femto second photolysis and probe pulses.

References

1 J. P. Simons, *J. Phys. Chem.*, 1987, **91**, 5378.
2 *Faraday Discuss. Chem. Soc.*, 1986, **82**.
3 *Molecular Photodissociation Dynamics*, ed. J. E. Bagott and M. N. R. Ashfold (Royal Society of Chemistry, London, 1987).
4 P. L. Houston, *J. Phys. Chem.*, 1987, **91**, 5388.
5 J. P. Simons, *J. Phys. Chem.*, 1984, **88**, 1287.
6. V. Engel, R. Schinke and V. Staemmler, *J. Chem. Phys.*, 1988, **88**, 129.
7 R. Schinke, V. Engel, S. Hennig, K. Weide and A. Untch, *Ber. Bunsenges, Phys. Chem.*, 1988, **92**, 295.
8 U. Brühlmann, M. Dubs and J. R. Huber, *J. Chem. Phys.*, 1987, **86**, 1249.
9 U. Brühlmann and J. R. Huber, *Z. Phys. D*, 1987, 7, 1.
10 U. Brühlmann and J. R. Huber, *Chem. Phys. Lett.*, 1988, **143**, 199.
11 M. Nonella and J. R. Huber, *Chem. Phys. Lett.*, 1986, **131**, 376.
12 S. Hennig, V. Engel, R. Schinke, M. Nonella and J. R. Huber, *J. Chem. Phys.*, 1987, **87**, 3522.
13 S. Hennig, A. Untch, R. Schinke, M. Nonella and J. R. Huber, *Chem. Phys.*, in press.
14 M. Dubs, U. Brühlmann and J. R. Huber, *J. Chem. Phys.*, 1986, **84**, 3106.
15 R. N. Dixon, *J. Chem. Phys.*, 1986, **85**, 1866.
16 M. P. Docker, *Chem. Phys.*, in press.
17 K-H. Gericke, *Phys. Rev. Lett.*, 1988, **60**, 561.
18 K-H. Gericke, A. U. Grunewald, S. Klee and F. J. Comes, *J. Chem. Phys.*, 1988, **88**, 6255.
19 M. P. Docker, in preparation.
20 G. E. Busch and K. R. Wilson, *J. Chem. Phys.*, 1972, **56**, 3626.
21 J. R. Huber, *Pure Appl. Chem.*, 1988, **60**, 947.
22 P. Tarte, *J. Chem. Phys.*, 1952, **20**, 1570.
23 G. E. Busch and K. R. Wilson, *J. Chem. Phys.*, 1972, **56**, 3638.
24 S-c. Yang and R. Bersohn, *J. Chem. Phys.*, 1974, 61, 4400.
25 M. H. Alexander and P. J. Dagdigian, *J. Chem. Phys.*, 1984, **80**, 4325.
26 P. Andresen and E. W. Rothe, *J. Chem. Phys.*, 1985, **82**, 3634.
27. J. D. Barnwell, J. G. Loeser and D. R. Herschbach, *J. Phys. Chem.*, 1983, **87**, 2781.
28 U. Brühlmann, A. Ticktin, M. P. Docker and J. R. Huber, in preparation.
29 P. Felder, B. A. Keller and J. R. Huber, *Z. Phys. D*, 1987, **6**, 185.
30 O. Benoist D'Azy, F. Lahmani, C. Lardeux and D. Solgadi, *Chem. Phys.*, 1985, **94**, 247.
31 A. Untch, R. Schinke, M. Nonella and J. R. Huber, unpublished results.
32 T. S. Rose, M. J. Rosker and A. H. Zewail, *J. Chem. Phys.*, 1988, **88**, 6672.
33 M. Dantus, M. J. Rosker and A. H. Zewail, *J. Chem. Phys.*, 1987, **87**, 2395.
34 K-H. Gericke, S. Klee, F. J. Comes and R. N. Dixon, *J. Chem. Phys.*, 1986, **85**, 4463.
35 M. P. Docker, A. Hodgson and J. P. Simons, *Faraday Disscuss. Chem. Soc.*, 1986, **82**, 25.

Vector Correlations in the 157 nm Photodissociation of OCS and the 266 nm Photodissociation of Methyl Iodide

R. Ogorzalek Loo,† C. E. Strauss, H-P. Haerri,‡ G. E. Hall§ and P. L. Houston*

Department of Chemistry, Cornell University, Ithaca, New York 14853, U.S.A.

I. Burak

School of Chemistry, Tel Aviv University, Tel Aviv, Israel

J. W. Hepburn

Department of Chemistry, University of Waterloo, Waterloo, Ontario, Canada

The photodissociations of OCS at 157 nm and of $CH_3I(CD_3I)$ at 266 nm have been investigated by using tunable vacuum ultraviolet laser-induced fluorescence and multiphoton ionization to probe the CO or S and the $CH_3(CD_3)$ or I photoproducts, respectively. In the OCS dissociation, sulphur is produced almost entirely in the $S(^1S)$ state, while CO is produced in its ground electronic state and in vibrational levels $v = 0$-3 in the approximate ratio $(v=0):(v=1):(v=2):(v=3) = (1.0):(1.0):(0.5):(0.3)$. The rotational distribution for each vibrational level is found to be near-Boltzmann, with temperatures that decrease from 1350 K for $v = 0$ to 770 K for $v = 3$. Measurements of the CO Doppler profiles demonstrate that the dissociation takes place from a transition of predominantly parallel character ($\beta > 1.3$) and that the CO velocity and angular momentum vectors are perpendicular to one another. In the CD_3I dissociation, the ratio of CD_3 $(v=0)/(v=2)$ was estimated to be *ca.* 1.1, with multiple determinations in the range 0.47-2.1. A value for the CH_3 $(v=0)/(v=2)$ ratio from dissociation of CH_3I could not be estimated, although it was clearly larger than that for CD_3. The CH_3 $(v''=0)$ and CD_3 $(v''=0)$ products from this dissociation are fitted by 120 ± 30 K and 105 ± 30 K rotational distributions, respectively. The dissociation mechanism produces alignment in the molecular frame such that there is a strong preference for $K = 0$. Assuming that the relative velocity vector lies along the CH_3 C_3 axis, then the velocity and rotation vectors tend to be perpendicular.

1. Introduction

Vector correlations are playing an increasingly important role in the elucidation of molecular dynamics in general, and of photodissociative events in particular.[1,2] The principal vectors involved in these latter processes are the transition dipole moment μ of the parent compound, which can be aligned by the polarization vector $\hat{E}$ of the dissociating light, the rotational vector J of (one of) the fragments, and the relative velocity vector v between the recoiling photofragments. The angular correlation between μ and v gives rise to the anisotropic laboratory distribution of laboratory recoil velocities; observation of this anisotropy provides information about the alignment of the transition dipole in the molecular frame and about the timescale for dissociation.[3] The correlation

between μ and J gives rise to rotational alignment, as characterized by emission or absorption of light of a preferred polarization; observation of alignment provides information similar to that obtained from observation of anisotropy.[4-7] The correlation between v and J, or the 'triple correlation' between all three vectors μ, v and J, gives rise to complex structure in the Doppler profiles of photofragments; such structure provides a glimpse of the transition state of the parent compound at the moment of bond rupture.[8-10] The v, J correlation is independent of the timescale of dissociation. This paper provides two examples of how vector correlations may be used in the elucidation of photofragment dynamics.

Doppler-profile measurements on the CO produced in the 157 nm photodissociation of OCS are reported below and reveal (1) that v is nearly parallel to $\mu(\beta > 1.3)$ and (2) that, as expected for a triatomic dissociation, v and J are aligned perpendicular to one another. The dissociation of OCS from the excited $^1\Sigma$ state has been previously investigated utilizing the 157 nm radiation of the F_2 laser. Black and Sharpless[11,12] studied the emission from the ^1S metastable state of the sulphur atom. A value of 0.80 ± 0.05 was determined for the $S(^1S)$ formation in the 157 nm dissociation. Ondrey *et al.* performed time-of-flight measurements on the S-atom product and interpreted them to indicate that the CO vibrational distribution was highly inverted, with a peak in the vibrational distribution at the $v = 5$ level and progressively less population in lower levels.[13] Our findings demonstrate that $S(^1S)$ is indeed the principal sulphur product, but that the CO fragment is much less vibrationally excited than previously suggested. The near-parallel nature of the transition confirms that absorption is predominantly to the $^1\Sigma$ state.

Multiphoton ionization (MPI) spectroscopy of the methyl product from the 266 nm dissociation of rotationally cooled CH_3I and CD_3I is reported below; the results demonstrate alignment in a different manner. The spectra show that there is a preference for low values of K, the projection of the methyl rotation vector N onto the top axis. In other words, the methyl fragment preferentially rotates about a C_2 axis rather than about the C_3 axis, in contrast to the recent observation of Black and Powis[14] concerning the dissociation of room-temperature CH_3I. The explanation for the difference between these two experiments appears to involve the rotational motion of the parent compound. Our results also suggest tht the methyl fragment has far less vibrational excitation in the ν_2 'umbrella' mode than that found in the earlier experiments of Sparks *et al.*[15]

2. Experimental

(A) Tunable V.U.V. LIF of CO from the 157 nm Dissociation of OCS

Sample concentrations of 10, 5, 2 and 0.5% OCS seeded in helium were supersonically expanded through a pulsed beam valve (Newport BV-100) with a 0.5 mm orifice at 25 psi† stagnation pressure into a background chamber pressure of *ca.* 5×10^{-5} Torr.‡ The molecular beam was intersected *ca.* 20–30 nozzle diameters downstream of the orifice by both the photolysis beam and the probe beam, each propagating at right angles to one another and to the molecular beam. Laser-induced fluorescence (LIF) was collected through an LiF window at 45° to the laser beams using a single $F/1$ lens (MgF_2). This technique was used to probe the vibrational and rotational populations of the CO product on the A $^1\Pi \leftarrow$ X $^1\Sigma^+$ system and to probe the sulphur (^1S, ^1D, ^3P) products on a variety of atomic transitions. The v.u.v. required for these measurements was generated by two-photon resonantly enhanced four-wave sum-mixing in magnesium vapour,[16] a technique which has been used by our groups in a variety of experiments.[17-19]

† 1 psi =
‡ 1 Torr = 101 325/760 Pa.

For Doppler-profile measurements, air-spaced intracavity etalons narrowed both of the dye lasers used to generate the v.u.v, and the tuned dye laser was scanned by ramping the pressure of N_2 in the grating/etalon housing. The etalon-narrowed v.u.v. linewidth was $0.16\,\text{cm}^{-1}$ f.w.h.m.

Unpolarized photolysis radiation at 157 nm was produced with an excimer laser (Lambda Physik, EMG-101) using a mixture of fluorine and neon in a 3 bar helium buffer. The energy output was 1–5 mJ per pulse at 50 Hz. A 1 m (nominal f1 for visible light) LiF lens focused the light; small displacements of this lens allowed a 4 mm lateral shift of the focus. The F_2 spot interesecting the beam was rectangular with *ca.* 4:1 aspect ratio; the long axis lay along the probe-beam direction.

The 157 nm intensity was monitored by visible fluorescence induced on the nearly resonant $B'\,{}^2\Delta \leftarrow X\,{}^2\Pi$ transition in NO.[20,21] The v.u.v passed first through the molecular beam chamber and entered unfocussed into the NO cell containing 400 Torr. A 4 in$\dagger$ f1 lens gathered fluorescence perpendicular to the laser-beam direction onto a photo-multiplier (Hammamatsu 1P120) after the laser had traversed a 3 in path through the NO. A 555–565 nm bandpass filter and temporal discrimination allowed rejection of the scattered red laser emission and the white-light laser discharge arc.

Fluorescence detection of the S and CO photofragments was accomplished using a solar-blind photomultiplier tube (EMR 541G-09-17). Signals from the photomultipliers averaged for typically ten shots by gated integrators (SRS, model SR150) with apertures similar in time duration to the fluorescence signals. A computer (IMB PC or DEC LSI-11) collected the digitized data and controlled the dye-laser wavelength scanning. For Doppler profiles, a custom-built (Quanta Ray) servo was used to ramp the nitrogen tuning pressure. For each Doppler profile, many spectral scans were taken rapidly in succession without averaging and then later combined so that as many as 100 shots per point could be averaged while drifts in the photolysis laser power could be minimized.

(B) MPI Spectra of CH_3 following the 266 nm Photodissociation of CH_3I

Our MPI apparatus, similar to that of Dietz *e al.*[22] consists of a supersonic molecular beam source, three differentially pumped chambers, and a home-built time-of-flight (TOF) mass spectrometer. The first chamber, pumped by a 6 in diffusion pump, houses the molecular beam valve[23] and a 1 mm diameter skimmer located 3 cm from the nozzle. A second 1 nm diameter skimmer, located in the second chamber at a distance of 40 cm from the first skimmer, collimates the molecular beam so that when it reaches the laser interaction region in the third chamber, another 40 cm downstream, the molecular beam is under 2 mm in diameter. The mass spectrometer, also housed in the third chamber, has a vertical flight tube jacketed by a liquid-nitrogen Dewar to enhance the vacuum by cryopumping.

A quadrupled Nd:YAG (Quanta-Ray DCR-1) was used as the dissociating (pump) laser, providing 266 nm light, while the frequency-doubled output from a Nd:YAG pumped dye-laser system (Quanta-Ray DCR-1A or DCR-2A, PDL, WEX) served as the ionizing (probe) laser. In the experimental geometry used for this work, the pump and probe lasers passed through the third chamber nearly counter-propagating with respect to each other, and perpendicular both to the molecular beam and to the vertical axis of the flight tube. The pump beam (*ca.* 3 mJ per pulse) was used either focussed with a 300 mm lens or collimated with a 3.3:1 telescope, while the probe laser (*ca.* mJ per pulse) was focussed with a 7.5 cm lens mounted inside the chamber on a linear motion feedthrough. This arrangement simplified the laser alignment and allowed for fine control of the probe-laser focus.

$\dagger$ 1 in $= 2.54 \times 10^{-2}$ m.

The TOF mass spectrometer is of the two-stage Wiley-McLaren[24] design, utilizing an extraction region and an acceleration region. The extraction region consists of a 3.5 in diameter stainless-steel repeller plate biased at +2090 V and spaced 2.54 cm away from a grid 1, itself composed of a 3.5 in diameter stainless-steel ring supporting a 90% transmissive stainless-steel mesh and biased at +1533 V. The acceleration region, defined by grids 1 and 2, is 1.27 cm in length. Grid 2 is also composed of the 90% transmissive mesh and is held at ground potential. Upon emerging from the extraction and acceleration regions, the ions travel through the 105 cm long, 2.0 in inner diameter flight tube and are subsequently detected by a Johnston MM-1 particle multiplier[24] (10^7 gain at 3 keV) with a 1.3 in diameter active area.

A modular home-built pulse generator/delay unit controlled the synchronization of the pulsed nozzle, lasers and data acquisition hardware. Our TOFMS operates in two modes, a mass-scan mode and a wavelength-scan mode. The mass-scan mode was used for discrete wavelength work, where the laser wavelength was fixed and either the full mass spectrum or the ion arrival time distribution for a particular mass was collected with every laser shot. For this mode of operation, the signal from the particle multiplier was amplified by a ×10 preamp,[26] digitized and averaged using a LeCroy 9400 digital storage oscilloscope[27] or a LeCroy TR8828C transient digitizer, and was then transferred to an IBM PC computer. Alternatively, digitization and averaging were accomplished using a Biomation 8100 waveform recorder[28] and a home-built interface with data transfer to an LSI 11/23 minicomputer. In the wavelength-scan mode of operation, the amplified particle multiplier signal was averaged in a Stanford Research Systems SR250 Gated Integrator/Boxcar Averager unit,[29] digitized, and transferred to an LSI-11/23 computer for data storage and analysis. For TOF wavelength scans under traditional conditions, where the desired information is 'mass n ion signal vs. wavelength', boxcar gates were positioned at the arrival times of the individual masses of interest.

The dye-laser power was monitored during wavelength scans. A dye cell containing a Rhodamine 6G solution was positioned so that the dye would be excited by a back-reflection from a probe-laser beam steering prism. The emitted dye fluorescence was monitored by a photodiode and served as a measure of the relative laser power during the experiment. Generally, one channel of data taken by the computer was reserved for the photodiode signal, while one or two additional channels recorded the ion signal data. In this way, ion signals having an n-photon probe laser power dependence could be normalized by (photodiode signal)^n. The pump laser power was periodically measured using a power meter, rather than by the photodiode/dye cell fluorescence method because its power remained relatively constant throughout experiments.

3. Results

(A) OCS

1. *The Relative Yield of* S(^{1}S)

The relative amounts of S(^{1}S), S(^{1}D) and S(^{3}P) formed in the 157 nm photodissociation of OCS were determined by comparing the strengths of the LIF signals for the corresponding atomic resonance lines: ^{1}P ← ^{1}S at 1688 Å, ^{1}P ← ^{1}D at 1448 Å and ^{3}D ← ^{3}P at 1484 Å. Measurements following dissociation in the molecular beam showed the S(^{3}P) signal to be as small or smaller than the S(^{1}D) signal, and both were much smaller than the S(^{1}S) signal. A possible source for the S(^{3}P) signal is dissociation of an OCS cluster. To eliminate the possible interference caused by clusters in the supersonic jet, measurements on the S(^{1}D) and S(^{1}S) were carried out in a flowing gas cell at a pressure of 10 m Torr. The S(^{1}S) signal was greater than 30 times stronger than the S(^{1}D) signal. Some difficulty in measuring the ratio of S(^{1}S) to S(^{1}D) signal strengths was caused by

the necessity of using different dyes to reach the two transitions and different photomultiplier bias voltages to observe the signals. The factor of 30 should be regarded as a minimum value; the actual value may be as large as 1000. From these observations, we conclude that the atomic S product is formed almost exclusively in the ^1S state, with less than 3% in the ^1D state.

2. CO *Vibrational and Rotational Distributions*

The internal energy distribution of the CO $(X\ ^1\Sigma^+)$ photofragment was determined by analysing the LIF spectra. To prove the various CO product vibrational levels, the (0, 0), (1, 1), (3, 2) and (5, 3) bands of the A $^1\Pi \leftarrow X\ ^1\Sigma^+$ system were recorded and analysed. A small region of the spectra, showing portions of the (0, 0), (3, 2) and (5, 3) bands, is reproduced in fig. 1. The observed spectra were normalized by the measured v.u.v. probe-laser power, and the intensities for the unperturbed rotational lines in the spectra were measured and divided by the appropriate Hönl–London factors to obtain the relative populations in the various product rotational states for each CO vibrational level. The measured population distributions based on Q-branch transitions are shown as Boltzmann plots in fig. 2 for $v = 0$, 1, 2 and 3. In every case the $P(J)$ distribution was well represented by a single rotational temperature, but that temperature was found to be different for the different CO vibrational levels. The full data set provided the following rotational temperatures:

$$v = 0,\ T_{rot} = 1350\ K;\ v = 1,\ T_{rot} = 1300\ K;\ v = 2,\ T_{rot} = 980\ K;\ and\ v = 3,\ T_{rot} = 770\ K.$$

The CO product vibrational distribution was obtained by comparing the relative intensities for the CO (A $^1\Pi \leftarrow X\ ^1\Sigma$) bands detected, normalizing these by the probe-laser power and correcting for the detector response. These corrected relative LIF intensities were converted into overall band intensities using the known rotational temperatures
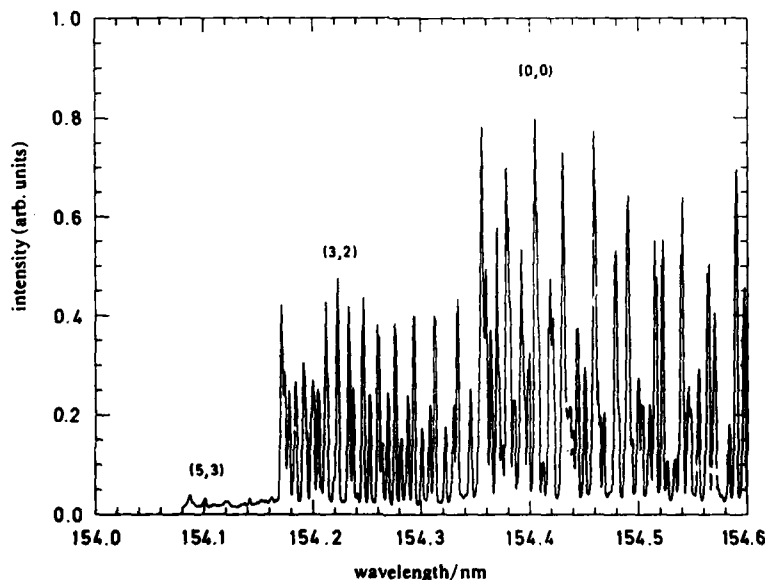
Fig. 1. Laser-induced fluorescence spectrum of the CO product of the 157 nm OCS photodissociation showing the regions of the (5.3), (3, 2) and (0, 0) bands.
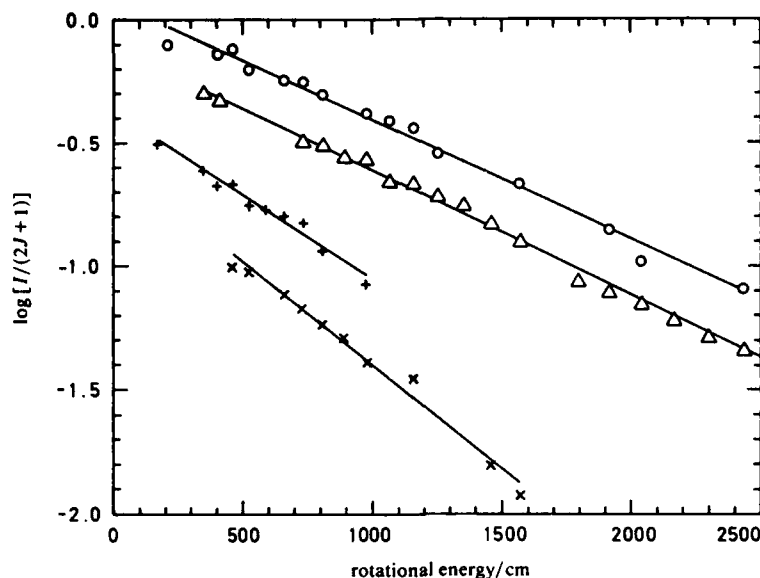
Fig. 2. Normalized population of Q-branch transitions as a function of rotational energy for the CO(v) product of the 157 nm OCS photodissociation. Analysis of the full data set provided the temperatures quoted in the text. The vertical offset of each data set has been adjusted for clarity of presentation. 0, $v = 0$; $\triangle$, $v = 1$; +, $v = 2$; ×, $v = 3$.

in each vibrational level to calculate the integrated intensity for each band. In order to obtain relative vibrational populations from these data, the integrated band intensities were then divided by the appropriate Franck-Condon factors, calculated by Waller and Hepburn.[30] The relative populations found were $(v = 0):(v = 1):(v = 2):(v = 3) = (1.0):(1.0):(0.5):(0.3)$.

Attempts were made to detect $v = 4$ and $v = 5$ products by recording spectra in the region of the (3, 4) and (5, 5) bandheads (1648 and 1630 Å). No signal was observed from these bands, in spite of good v.u.v. intensity and Franck-Condon factors. From this observation we conclude that the population in $v = 4$ and $v = 5$ is less than 5% of the $v = 0$ product population.

3. Doppler Profiles of CO Lines

High-resolution Doppler spectra of the CO fragment were recorded for several rotational lines in the (0, 0), (3, 0) and (1, 1) vibrational bands. Typical results are shown in fig. 3 for the Q(19) line of the (0, 0) band and the R(25) lines of the (3, 0) band. The calculated Doppler lineshapes are superimposed on the data and will be discussed in section 4 (A)3. Shapes qualitatively similar to that for the Q(19) line were observed for a wide range of Q-branch transitions in all vibrational levels, and shapes similar to that for the R(24) line were observed for a wide range of P- and R-branch transitions in all vibrational levels. To model the lineshapes, the CO velocity was selected to correspond to the CO($v = 0$, J) + S(^{1}S) channel, and the vector correlation assumed was $v \perp J$. The data shown are best described by a β parameter of 1.3, although the actual value could be somewhat higher, as discussed in section 4 (A)3.
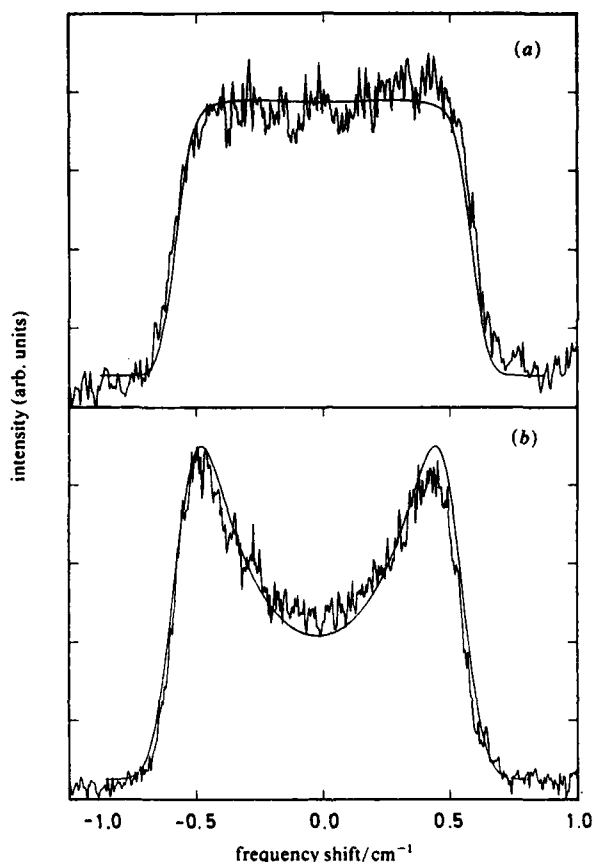
Fig. 3. Doppler scans of the CO product of the 157 nm photodissociation. Shown are the R(25) line (*a*) and the Q(19) line (*b*) of the CO ($v = 0$) product. The difference in Doppler profiles indicates that the vectors *v* and *J* are aligned perpendicular to one another.

(B) Methyl Iodide

The methyl radical products from the one-photon $\tilde{A}$-band dissociation of CH_3I or CD_3I were probed using $2 + 1$ MPI with the goal of obtaining product rotational and vibrational energy distributions. The types of measurements are reported in this section: (1) probe-laser wavelength scans in pump/probe experiments and (2) pulsed field mass spectrometry.

The background ion signals observed with either pump or probe laser alone in the molecular beam need to be either eliminated or understood in order to study the intended photodissociation process. In the pump/probe spectra, we have eliminated the background by moving the probe laser outside the molecular beam, where only recoiling photoproducts are ionized. In the pulsed-field mass spectral measurements, the pump and probe beams must be overlapped in the molecular beam, requiring a more serious investigation of the background ionization processes. Fortunately, information on the kinetic energy and angular distributions contained in he pulsed-field mass spectral data has allowed us to identify and minimize the background interferences. In many cases,

the background arises only from dimers and higher methyl iodide clusters. Thus, it serves as a cluster diagnostic and also highlights the differences in dynamics between monomers and clusters.

Iodine atoms in either their ground ($^3P_{3/2}$) or spin–orbit-excited ($^3P_{1/2}$) states have also been probed using 2+1 MPI, but with the goal of obtaining information about angular and translational energy distributions. The iodine measurements have been presented in previous papers[31,32] and are used in this work primarily as a diagnostic for the presence of methyl iodide dimers or higher clusters.

1. *Pump/Probe Results*

The pump/probe experiments used a 266 nm pump laser to dissociate CH_3I or CD_3I and a tunable probe laser to ionize the photoproducts outside the molecular beam. The resulting CD_3 spectra, obtained using the two-photon 3p $^2A_2'' \leftarrow$ 2p $^2A_a''$ transition[33] are displayed in fig. 4, while spectra of similar quality were obtained for CH_3. Several previously unreported hot bands appear in these spectra. Most of the vibrational activity observed in these spectra can be assigned to the out-of-plane bending mode, ν_2. Hudgens *et al.*[33] observed the same preponderance of ν_2 bands in their methyl spectra obtained from the pyrolyses of dimethyl sulphoxide and di-t-butyl peroxide. Rotational structure is quite evident in a number of these bands, particularly the 0_0^0, 2_2^0 bands; however, individual rotational levels and their spin sub-levels were not resolved. Acquisition of higher-resolution spectra was prevented by predissociation and a strong intensity-dependent broadening.

(*a*) *Vibrational Populations.* A serious concern in obtaining vibrational population ratios is that different rates of intermediate-state predissociation can change the ionization efficiency; consequently, our intensity comparisons were limited to v'' progressions, *i.e.* transitions which access the same intermediate-state vibrational level. We compared the 0_0^0 band with the 2_2^0 band and the 2_1^1 band with the 2_3^1 band. For CH_3 and CD_3, the $\Delta v =$ even selection rule for antisymmetric vibrations prevents direct comparisons between fragments with even and odd numbers of quanta in umbrella mode vibrations. Bands such as the 2_0^1 band are forbidden, and so cannot be compared to bands such as the 2_1^1 band to obtain the $(v = 0):(v = 1)$ population ratio.
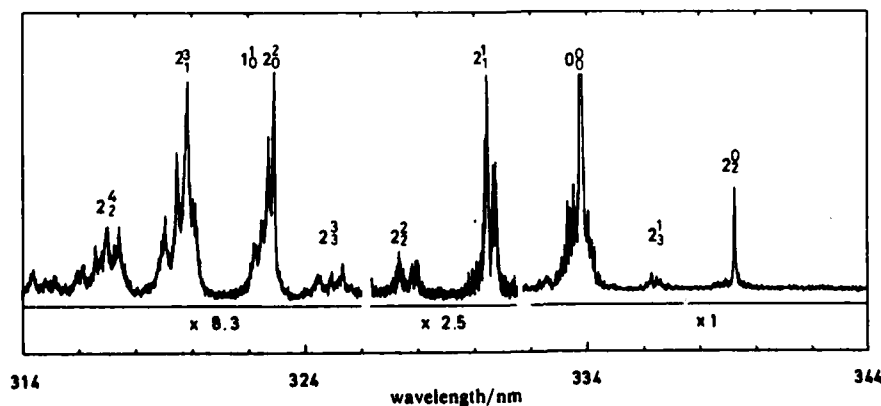
Fig. 4. Two-photon resonant, three-photon ionization spectrum of the CD_3 3p $^2A_2'' \leftarrow ^2A_2''$ transition. The CD_3, generated from the one-proton dissociation of CD_3I at 266 nm, is probed off-axis. This spectrum has not been corrected for dye-laser power. The peak intensity of the 0_0^0 band is off-scale in this figure.

Franck–Condon factors were calculated using one-dimensional wavefunctions for umbrella-mode transitions in CH_3 and CD_3.[34] The similar geometry of the $2p\,^2A_2''$ Rydberg states favours sequences over progressions. Because poor Franck–Condon factors limit the number of observed $\Delta v > 2$ transitions, and intermediate-state predissociation in the higher vibrational levels limits the total number of v'' progressions observed, the task of obtaining complete vibrational populations is a difficult one.

Spectra of the 0_0^0, 2_2^C, 2_1^1 and 2_3^1 bands were corrected for their observed quadratic laser power dependence, integrated and divided by their respective Franck–Condon factors. Fourteen different determinations of the CD_3 $(v = 0):(v = 2)$ vibrational populations yield an average ratio of 1.1, ranging in the extreme from 0.47 to 2.1. We place more faith in the larger-valued ratios, because of problems with dynamic range in this measurement; it is easy to saturate the stronger 0_0^0 band. The $(v = 1):(v = 3)$ vibrational population ratio can be obtained from the 2_1^1 and 2_3^1 bands, although the ratio has larger uncertainty. The $(v = 1):(v = 3)$ ratios ranged in the extreme from 1.2 to 10, so that the dissov ation definitely produces more $v = 1$ than $v = 3$. For CH_3, the ratio of 0_0^0 to 2_2^0 band intensities was even larger than for CD_3; consequently it was difficult to obtain an accurate value for the $(v = 0):(v = 2)$ ratio, although it is clearly larger than that for CD_3. We could not observe the 2_3^1 band in CH_3, so a comparison of $v = 1$ to $v = 3$ populations was not possible.

(b) *Rotational Temperatures.* Eqn (1) provides an expression for the rotational energy levels of oblate symmetric-top molecules in non-degenerate vibrational levels of non-degenerate electronic states:[35]

$$F_{[v]}(J, K) = B_{[v]}J(J+1) - (B_{[v]} - C_{[v]})K^2. \tag{1}$$

This expression assumes unresolved spin-rotational interaction and neglects centrifugal stretching terms. For planar symmetric tops, $C_e = \tfrac{1}{2}B_e$. From the rotational energy expression, one can see that for parallel bands $(\Delta K = 0)$ having similar values for the initial- and final-state rotational constants, all K components will fall at nearly the same frequency for each J, resulting in simple O, P, R and S branches and a very strong Q branch. The 0_0^0 bands of CH_3 and CD_3 and the 2_2^0 band of CD_3 are each dominated by a sharp Q branch, consistent with their similar values for B'' and B'.

Rotational structure simulations were completed for the CH_3 and CD_3 $3p\,^2A_2'' \leftarrow 2p\,^2A_2''\,0_0^0$ bands. These simulations, shown in fig. 5 and 6, were based on the rotational energies of eqn (1), the rotational constants of table 1 and the linestrength formulae from the literature.[35] Nuclear-spin statistics were taken into account, and some excess $K = 0$ population was introduced [see section 4(B)]. The Q branch is 'anomalously large' in linear polarization, and we did not attempt to match its intensity in the simulations. Because of spectral line-broadening mechanisms such as predissociation[14,37-39] and the AC Stark effect,[40] linewidths greater than either the laser linewidth ($ca.$ 0.4 cm^{-1}) or the Doppler width of fast nascent methyl radicals (up to 1 cm^{-1}) were used to fit the data. For the CD_3 spectrum, the Q branch was excessively broadened relative to the other branches, and so a 10 cm^{-1} linewidth was used for the Q branch, while 5 cm^{-1} linewidths were used for the O, P, R and S branches. The CH_3 spectrum was fitted with a 10 cm^{-1} linewidth for all branches. Rotational temperatures of 120 ± 30 K and 105 ± 30 K were fit to the CH_3 and CD_3 0_0^0 bands, respectively.

2. Pulsed-field Mass Spectrometry Results

Kinetic-energy measurements on selected internal states of methyl photoproducts have been made, using the 'core sampling' variant of the pulsed-field mass-spectrometric method described in a preliminary communication.[31] The internal state of the probed fragment is chosen by tuning the wavelength of the resonant ionizing laser, while the
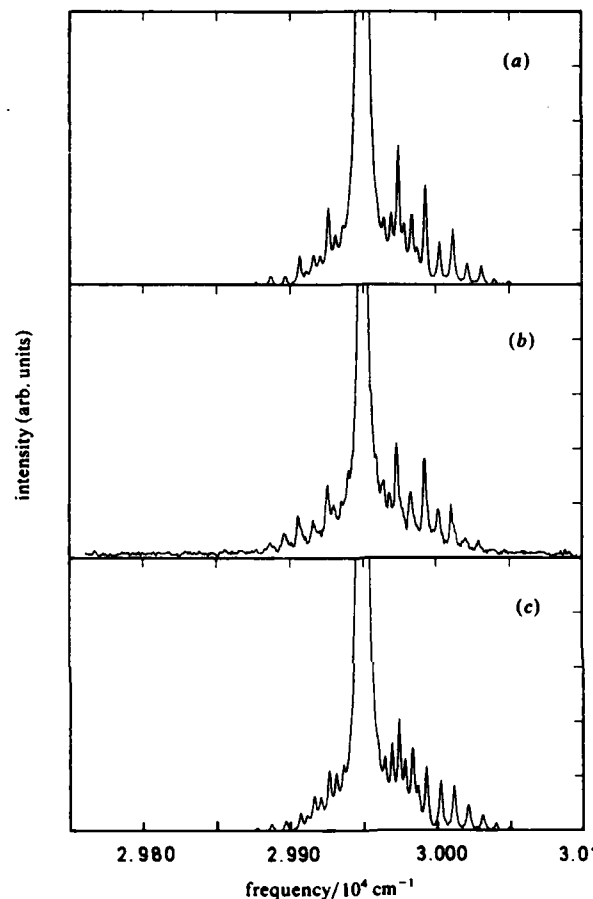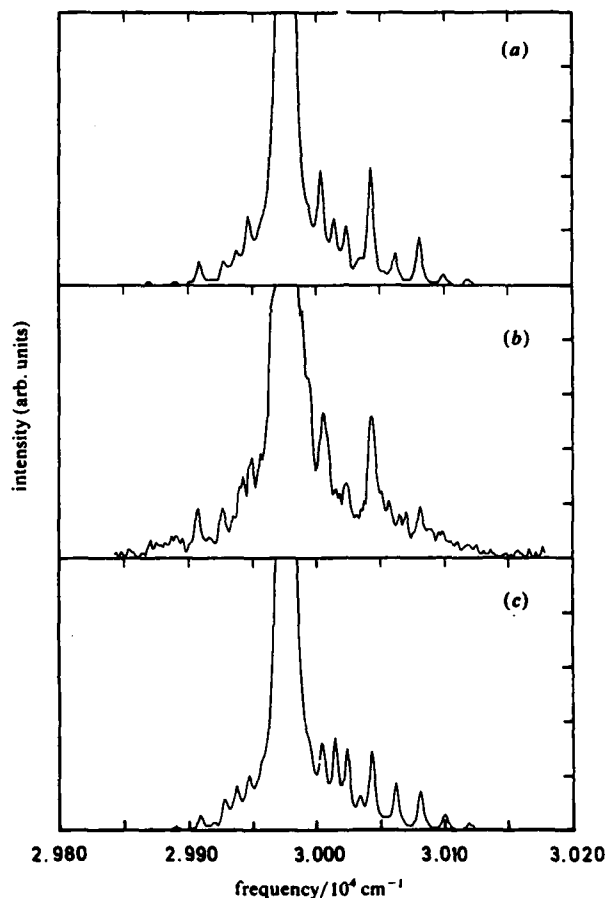
Photodissociation Vector Correlations

Fig. 5. A comparison of the fits to the 0_0^0 band of the CD_3 $3p\,^2A_2'' \leftarrow 2p\,^2A_2''$ transition. The simulations modeled either a Boltzmann distribution of K levels or a preference for $K = 0$. A rotational temperature of 105 K and linewidths of $5\,cm^{-1}$ were used. (*a*) In this simulation, $K = 0$ alignment was modelled by multiplying the $K = 0$ contribution from a Boltzmann distribution by a factor of 6. (*b*) Observed CD_3 0_0^0 band spectrum. (*c*) Boltzmann simulation.

fragment velocity is determined from the arrival time distribution of the corresponding ions at the detector. Data for CD_3 have been shown in an earlier communication,[31] while data for CH_3 will be presented elsewhere.[34]

The most obvious feature of these arrival time distributions is the ratio of methyl formed in coincidence with I to methyl formed in coincidence with I* increases with the number of quanta of umbrella-mode excitation in the methyl radical for both CH_3 and CD_3.[31] To obtain numerical values for the I/I* ratios at a fixed probe wavelength, the peak areas were corrected for the slight measured differences in β,[9] [$\beta(I) = 1.7$, $\beta(I^*) = 1.8$] and for differences in ion-collection solid angle for methyl fragments arising from the I and I* channels, we have assumed that any velocity-dependent ionization probability effects arising from v, J correlations[1,2] are the same for both I and I* channels. The ratios listed in tables 2 and 3 were obtained from measurements on the

Fig. 6. A comparison of the fits to the 0_0^0 band of the CH_3 $3p$ $^2A_2'' \leftarrow 2p$ $^2A_2''$ transition. The simulations modeled either a Boltzmann distribution of K levels or a preference for $K = 0$. A rotational temperature of 120 K and linewidths of 10 cm^{-1} were used. (*a*) In this simulation, $K = 0$ alignment was modelled by mutlif lying the $K = 0$ contribution form a Boltzmann distribution by a factor of 5. (*b*) Observed CH_3 0_0^0 band spectrum. (*c*) Boltzmann simulation.

Q-bench maxima of CH_3 and CD_3 bands indicated. Based on multiple determinations, we estimate th. uncertainties to be ± 0.05 for CH_3 $v = 0$ and CD_3 $v = 0, 1$ and ± 0.1 for CH_3 $v = 1, 2$ and CD_3 $v = 2, 3$. We note that for the same number of quanta of umbrella-mode excitation, CH_3 shows a larger I/I^* ratio than does CD_3, as has been previously observed in the 248 nm methyl iodide dissociation.[41]

We observed a strong wavelength dependence on the I/I^* ratios within individual vibronic bands, which we believe arises from two sources: a variation in ratio with rotational level and a variation arising from the effect of overlapping vibronic bands. The task of obtaining I/I^* ratios for individual vibrational levels is complicated by these wavelength dependences. However, comparisons of I/I^* ratios at discrete wavelengths in the CH_3 and stronger CD_3 bands listed in tables 2 and 3 did show consistently that the smallest I/I^* ratios were obtained at the wavelengths of peak intensity in each

Table 1 Methyl rotational constants for ν_2 excitation

CH_3[a] $2p\,^2A_2''$	CH_3 $3p\,^2A_2''$	CH_3[b] $4p\,^2A_2''$	CD_3[c] $2p\,^2A_2''$	CD_3 $3p\,^2A_2''$	CD_3[b] $4p\,^2A_2''$
$B_0 = 9.57789\,(16)$	$B_0 = 9.55$	$B_0 = 9.75$	$B_0 = 4.80198\,(11)$	$B_0 = 4.764$	$B_0 = 4.8202$
$B_1 = 9.25814\,(16)$			$B_1 = 4.706848\,(90)$		
$B_2 = 8.93320\,(22)$			$B_2 = 4.61046\,(14)$		
$B_3 = 8.60974\,(28)$			$b_3 = 4.50688\,(22)$		

[a] C. Yamada, E. Hirota and K. Kawaguchi, *J. Chem. Phys.*, 1981, **75**, 5256. [b] For the CH_3 $4p\,^2A_2'' \leftarrow ^2A_2''$ transition, Black and Powis [J. F. Black, *Ph.D Thesis* (University of Nottingham, 1987)] used a value of $\Delta C - \Delta B = -0.005$, and they used -0.075 for the value in the analogous CD_3 transition. We used $\Delta C - \Delta B = -0.075$ for the CD_3 $3p\,^2A_2 \leftarrow 2p\,^2A_2''$ and 0.15 for the corresponding CH_3 transition. We did not optimize our values for $\Delta C - \Delta B$. [c] J. Frye, T. J. Sears and D. Leitner, *J. Chem. Phys.*, 1988, **88**, 5300.

The CH_3 $3p\,^2A_2 \leftarrow 2p\,^2A_2''$ 0_0^0 band was not very sensitive to rotational constant value. The error limit could be as large as $\pm 0.1\ \mathrm{cm}^{-1}$. For CD_3, the eror limit is *ca.* $\pm 0.01\ \mathrm{cm}^{-1}$.

Table 2. CH_3 Bands

wavelength/nm	band	I/I* ratios	I* quantum yield
340.8	2_2^0	—	—
333.5	0_0^0	0.08	0.92
329.4	2_1^1	0.30	0.77
325.8	2_2^2	1.1	0.47
319.1	2_0^2	—	—
317.9	1_0^1	—	—
315.5	2_1^3	—	—

Table 3. CD_3 bands

wavelength/nm	band	I/I* ratio	I* quantum yield
339.3	2_2^0	0.19	0.84
336.2	2_3^1	0.64	0.61
333.8	0_0^0	<0.05	>0.95
330.5	2_1^1	0.09	0.92
327.8	2_2^2	0.25	0.80
324.5[a]	2_3^3	0.74	0.57
322.9[a]	$1_0^1, 2_0^{2b}$	0.11	0.90
319.8[a]	2_1^3	0.10	0.9'.
317.0[a]	2_2^4	0.21	0.83
314.4[a]	2_3^5	0.69	0.59
312.6[a]	$2_0^4, 2_4^6$	0.52[c]	0.66

[a] I/I* ratios for these bands may be affected by overlapping vibronic bands. [b] There may also be a contribution from the 2_4^2 band. [c] Assuming $v'' = 0$ recoil velocities. If $v'' = 4$ recoil velocities are assumed, the ratio is 0.57.

vibronic band. Consequently, it was possible to obtain lower limits for vibrational level I/I* ratios, as are quoted in those tables, by taking measurements at the wavelengths of peak intensity. As the wavelength was changed to probe higher rotational levels, the I/I* ratio increased, often from 2 to 4 times. For some of the weaker bands poorer signal levels prevented I/I* measurements away from the band maxima. The greater chance of overlapping vibronic bands in the region at wavelengths shorter than 326 nm also reduces our confidence in the attribution of these measured I/I* ratios to a specific vibrational state.

4. Discussion

(A) OCS

1. *The Quantum Yield of* S(^{1}S)

Our results indicate that >97% of the sulphur product from the 157 nm OCS photodissociation is S(^{1}S). This conclusion is supported both by the small magnitude of the LIF signals for the S(^{3}P) and S(^{1}D) species relative to that for S(^{1}S) and by the widths of the Doppler profiles obtained for the various CO LIF lines, all of which were consistent with a single S(^{1}S) dissociation channel. The absolute quantum yield for the S(^{1}S) production was found by Sharples *et al.* to be 0.80 ± 0.05.[11,12] Since our results indicate that the S(^{3}P) and S(^{1}D) species are produced in less than 3% yield, either the absolute quantum yield measured by Sharples *et al.* is low by *ca.* 0.17 or there is significant dissociation through a channel which does not produce sulphur atoms, *e.g.* OCS → CS + O. Our detection system is insensitive to the possibility of this second channel.

2. *Internal Energy Distribution*

The rotational distribution of the CO fragment of 157 nm OCS dissociation can be characterized as Boltzmann for each vibrational level with a temperature which varies from 1350 K for $v = 0$ to 780 K for $v = 3$. Such high rotational temperatures cannot be predicted for a sudden dissociation from a linear state. As discussed elsewhere,[42] sudden approximations to a dissociation from a linear state predict much lower rotational temperatures in models based on (1) an impulse approximation, (2) a Franck-Condon approximation and (3) the 'rotational reflection principle.' It thus appears that the rotational excitation is caused by final-state interactions induced by non-linearity in the exit channel of the dissociative state. The variation of rotational temperature with vibrational level is consistent with a statistical model: the rotational surprisal is nearly constant for all vibrational levels, so that a single dynamical constraint appears to be responsible for the distributions.

The vibrational distribution was found by summing line intensities over the appropriate bands and correcting the ratios so obtained by the Franck-Condon factors and the photomultiplier response function. Nearly equal populations were found in $v = 0$ and $v = 1$, with *ca.* half as much population in $v = 2$ and *ca.* one third as much in $v = 3$.

A theoretical prediction of the vibrational distribution requires a complete knowledge of the excited-state potential-energy surface. This information is not available. However, a Franck-Condon calculation[43] which takes into account the overlap between the OCS molecular ground-state wavefunction and that of the excited state, as approximated by an Airy function, yields a distribution in reasonable agreement with observation:[42] $(v = 0):(v = 1):(v = 2):(v = 3) = (1.0):(1.0):(0.6):(0.17)$. In this calculation the C—O bond distances in the CO and OCS molecules were taken at 1.128 and 1.160 Å, respectively, while the excited-state potential was approximated by an exponential repulsion in the dissociation coordinate characterized by a slope of 0.0025 dyn at the ground-state

geometry and a range parameter of 1.2 bohr^{-1}. However, this potential overestimation the OCS absorption bandwidth.[42]

It is interesting to note that no vibrational excitation is found in the 222 nm OCS dissociation through the fiest excited $^1\Delta$ state.[44] In this case the energy available for the nuclear r ntion is comparable to that available in the 157 nm dissociation, where vibrational excitation of the molecular fragment is observed. This different behaviour is due to the torque exerted on the CO when the OCS molecule is excited to the highly bent Δ state. As a result of this torque, 50% of the available energy is deposited into the CO rotational degree of freedom, resul†ing in a highly inverted rotational distribution.[44]

The vibrational distribution found in this work differs substantially from that found by Ondrey *et al.*[13] In their work, pure OCS was expanded through a pulsed nozzle into the dissociation chamber. The molecular beam was then irradiated with pulsed light at 157 nm, and the velocity of the sulphur atom was determined by a time-of-flight technique. The high vibrational excitation of the CO fragments was inferred from the observed slow velocity distribution of the sulphur-atom products. One potential problem with this work is that the authors hae ignored cluster formation in cooled beams. It has been previously demonstrated that dissociation of OCS clusters results in translationally cold fragments.[44] Moreover it is expected from previous results[44] that a supersonic expansion of pure OCS will produce a high degree of clustering. Even with a beam of 10% OCS in He, based on the Doppler profiles we observe at least a 10% contribution from slow CO molecules product from photodissociation of clusters. The problem is likely to be much worse in a beam of pure OCS.

More than half of the 110.8 kcal mol^{-1} of the available energy for the CO + S channel in the 157 nm photodissociation is utilized for the 63.4 kcal·mol^{-1} excitation of the S(^{1}S) state, leaving 46.9 kcal mol^{-1} available for the internal and recoil degrees of freedom. *Ca.* 5.9 kcal mol^{-1} or 12% of this available energy is deposited in vibrational excitation of the CO fragment, while another 1.9 kcal mol^{-1} or 4% of the available energy is deposited into CO rotational excitation. Thus, *ca.* 84% of the energy available to nuclear motion is deposited in the relative translational recoil of the two fragments, and the Doppler widths are quite broad.

3. Vector Correlations

Calculated and observed Doppler profiles of the Q(19) line and he R(25) line of the CO ($v = 0$) recorded following 157 nm photolysis of a 0.5% mixture of OCS in helium are displayed in fig. 3. Reasonable agreement is obtained if the CO ($v = 0, J = 19$) or ($v = 3, J' = 25$) velocity is assumed to be that which would be produced for dissociation in coincidence with a S(^{1}S) sibling photofragment, if the vector correlation between v and J is assumed to be a perpendicular one, and if the recoil anisotropy is assumed to be described by $\beta = 1.3$. That the dip in the Q(19) line appears to be rather more shallow than might be expected for this value of β is a consequence of the fact that the F$_2$ laser is unpolarized in the plane perpendicular to its propagation direction, which decreases the Doppler profile modulation by a factor of four. We have accounted for this reduction in our analysis. Even so, we regard the value of $\beta = 1.3$ to be a lower limit. CO Doppler profiles obtained from this photodissociation can be influenced by at least three experimental artifacts: dissociation of clusters, reduced detectivity because of molecular motion on the timescale of detection and saturation of the dissociation. Our attempts to evaluate these factors are described below.

We know from our previous work at 222 nm that OCS expansions can produce dimers and higher clusters.[44] Profiles obtained following the 157 nm dissociation of a beam of 10% OCS in helium showed that all transitions had excess intensity in the centre of the Doppler profile, which we attribute to slower fragments produced in the

dissociation of clusters. This feature was reduced in 5% mixtures and was absent in mixtures containing less than 2%.

A second artifact appeared even for the more dilute mixtures when highly focussed pump and probe beams were employed: the intensity in the centre of all transitions was somewhat reduced. We attribute this effect to the rapid motion of CO fragments out of the probe beam on the timescale of the detection, *ca.* 100 ns. The use of larger pump, probe, and detection volumes eliminated this effect.

A third possible problem is that the F_2 laser may saturate the OCS dissociation so that the initial alignment is less polarized than that expected in the weak-field limit. Attempts to obtain sufficient signal-to-noise ratios at lower dissociation intensities are in progress, and it may be that weaker fields will produce larger modulation of the Doppler profiles, *i.e.* larger values of β. Thus, $\beta = 1.3$ should be taken as a lower limit.

Fortunately, the above effects do not have a substantial influence on our measurement of the *v*, *J* correlation, since this correlation is obtained from the difference between the Q- and P- or R-branch transitions.[2,8-10] Our finding of a perpendicular correlation is consistent with angular momentum conservation. Since the angular momenta of the parent compound and the photon are all quite small compared to the angular momentum of the CO, conservation requires that $J = -L$, where $L = \mu(v \times b)$, is the orbital angular momentum of the half-collision. Since L is perpendicular to *v*, we conclude that *J* must also be perpendicular to *v*.

(B) Methyl Iodide

1. *Rotational Energy Distributions*

Fits to the methyl rotational distributions observed following dissociating methyl iodide cooled to near 15 K in our supersonic beam are shown in fig. 5 and 6 and indicate rotational temperatures of 120 ± 30 K for CH_3 $v = 0$ and 105 ± 30 K for CD_3 $v = 0$. These fits have assumed some excess population in $K = 0$ levels, to be discussed below. Using $E_{rot} = (3/2)k_B T$, we find the average rotational excitation to be 125 or 109 cm^{-1} for CH_3 or CD_3, respectively. Limitations on these measurements due to alignment effects on the two-photon line-strength formulae and due to predissociation in the methyl 3p $^2A_2''$ Rydberg state have been discussed elsewhere.[32]

The only previous study of dissociation of supersonically cooled methyl iodide was reported by Sparks *et al.*,[15] who used a 300 cm^{-1} wide rotational distribution in order to fit a vibrational distribution to their time-of-flight data. If 300 cm^{-1} is taken as the average rotational energy in a Boltzmann distribution, the rotational temperature would be 286 K. Our more direct measurement of 120 K indicates that less energy is disposed into rotation.

A number of workers have studied the photodissociation of room-temperature methyl iodide. Hermann and Leone[45] used the spectrum of infrared fluorescence from the methyl radical to learn about the vibrational distribution, but they intentionally relaxed the rotational distribution by use of a buffer gas. Preliminary results from recent diode-laser absopriton *vs.* gain experiments show high rotational excitation,[46,47] but it is likely that translation-to-rotation excitation on the timescale of observations precludes a determination of the nascent rotational distribution. Welge and coworkers[48] used two-colour MPI to probe the methyl 3s $^2A_1' \leftarrow 2p$ $^2A_2''$ transition in an effusive beam. From their fit to the CD_3 rotational profile, they estimated *ca.* 175 cm^{-1} of rotational excitation, corresponding to a rotational temperature of 170 K, but the CH_3 3S $^2A_1'$ state was too heavily predissociated for them actually to resolve any rotational structure. Recently, Black and Powis[14] have fitted a 200 K rotational distribution to their effusive-beam data for CH_3, probed by 2+1 MPI on the 4p $^2A_2'' \leftarrow 2p$ $^2A_2''$ Rydberg transition. The mid-section of their CD_3 Boltzmann plots was fitted by a 140 K rotational distribution. Thus, in the two effusive-beam/MPI experiments, where the initial temperatur of

the CH_3I was *ca.* 300 K, the rotational temperature of the methyl product was found to be lower than that of the parent compound, whereas in our experiments on a rotationally cooled beam, the methyl-product temperature was found to be *higher* than that of the parent compound. A close examination of the source product rotation is called for. One source might be that initial parent rotation, while a second might be $I-C-H_3$ bending.

(*a*) *Initial Parent Rotation.* We consider first the role of parent rotation and whether it could cause the methyl fragments appear to be warmer than the parent methyl iodide. Conservation of angular momentum in this dissociation may be stated as

$$J_{CH_3} + J_{h\nu} = J_{CH_3} + J_1 + L \tag{2}$$

where L is the orbital angular momentum of the half-collision, $J_{h\nu}$ is the unit angular momentum of the photon and J_1 is the angular momentum of the iodine atom, which is equal to $\frac{1}{2}$ for I^*. In a collinear dissociation, the impact parameter, b, would be equal to 0, and since $L = \mu(v \times b)$, L would also be equal to 0, so that J_{CH_3} would need to be approximately equal to J_{CH_3I}.

Is there any way by which a collinear of dissociation could result in a higher rotational temperature for the CH_3 than for the CH_3I? At first it might seem possible. Since both $k_B T$ and the product of $J(J+1)$ times hcB are proportional to the rotational energy (and hence to each other), it is clear that, for a conserved J, the rotational temperature is expected to increase if the rotational constant increases in going from parent to products. Methyl iodide indeed has two rather small rotational constants, those about the two principal axes perpendicular to the C_3 axis $[B_0(CH_3I) = C_0(CH_3I) = 0.250\ 217\ cm^{-1}]$,[49] whereas the corresponding rotational constants in the CH_3 fragment are rather large $[A_0(CH_3) = B_0(CH_3) = 9.57\ cm^{-1}]$.[50,51] If most of the rotational angular momentum about these two CH_3I axes were retained by the CH_3 fragment, the difference in rotational constants between the parent and fragment would result in greatly increased rotational energy.†

However, a closer examination shows that only the CH_3I rotations about the C_3 axis will be retained by the CH_3, while the rotations about the other two principal axes of the parent molecule will be converted almost entirely to the orbital angular momentum of the half-collision. The main reason for this high conversion to orbital angular momentum is that the CH_3I centre of mass is so close to the iodine. A detailed treatment of the partitioning of rotation about the axes perpendicular to the C_3 axis shows that $J_{frag}/J_{parent} = 0.4\%$.[32] Thus, we see that if this dissociation can be treated as a linear one, little of the initial parent rotation about the non-top axes will be retained as fragment rotation. Instead, essentially all of it will emerge as the orbital angular momentum of the half-collision.

It remains for us to consider the fate of the parent angular momentum about he top axis. The constants for rotation about the C_3 axis of the fragment and the parent $[C_0(CH_3) \approx 4.785\ cm^{-1}$ and $A_0(CH_3I) \approx 5.119\ cm^{-1}]$[49,50] are quite similar; in fact the rotational constant is actually smaller for CH_3 than for CH_3I. Thus, if the angular momentum about the C_3 axis is conserved, the rotational temperature should actually decrease. We conclude that parent rotations about the top axis cannot account for the observation that the rotational energy of the fragment is larger than that of the parent.

(*b*) $I-C-G_3$ *Bending.* Rotational excitation could be the consequence either of conversion of the zero-point $I-C-H_3$ bending vibrational into rotation or of dissociation through a non-linear intermediate, particularly in the case of the I channel, where a

---

† Accepted nomenclature[51] assigns the C axis as the top axis for an oblate symmetric top, such as CH_3, while the A axis is assigned as the top axis for a prolate symmetric top, such as CH_3I.

curve-crossing is assumed to occur. Measurements of the anisotropy parameter demonstrate that the primary absorption leading to formation of ground-state I is $A_1(^3Q_{0+}) \leftarrow {}^1A_1$, just as for formation of I*. Ground-state I atoms must arise from a curve-crossing to a state of E symmetry. Previous authors[41,52,53] have suggested that this curve-crossing can be made allowed by an e-type vibration, such as the methyl iodide ν_6 rocking mode. Such parent vibrational excitation would impart a torque in the dissociation leading to fragment rotation about a C_2 axis. Although such a torque would not be required in the case of dissociation to the I* channel, it might nevertheless be a consequence of either the shape of the dissociative potential-energy surface or the zero-point bending motion. Arguments against the former cause come from the absence of bending activity in the Raman spectrum of dissociating CH_3I.[54] In either case, the I—C—H_3 bending will produce methyl radicals which should be (1) rotationally hotter than expected from a purely collinear dissociation and (2) aligned in the molecular frame such that their axis of rotation is perpendicular to the top axis. In addition, since rotation about the C_2 axis is required in the case of dissociation *via* the I channel, it is expected (3) that the methyl radicals produced in coincidence with I will be rotationally hotter than those produced in coincidence with I*.[54] Data supporting prediction (3) comes from our core-sampling results. Comparisons of I/I* ratios at discrete wavelengths in the CD_3 0_0^0, 2_1^1 and 2_2^2 bands showed consistently that the smallest I/I* ratios were obtained at the wavelengths of peak intensity in each vibronic band, and that as the wavelength was tuned to higher rotational transitions, the I/I* ratio increased. Data supporting prediction (1) have been discussed above; for dissociation of rotationally cold parent molecules, we observe that the fragment rotational energy is higher than expected on the basis of a collinear dissociation. Data supporting prediction (2) will be discussed in the next section. There is indeed strong evidence that the methyl fragment is rotating preferentially, though not exclusively, about an axis perpendicular to the C_3 top axis.

We conclude by postulating a possible scenario for the dissociation. Rotationally cold parent molecules dissociate to produce minor rotational excitation of the fragments, in agreement with predictions (1)-(2) above. The rotation imparted to the fragment is due to I—C—H_3 bending and should be about an axis perpendicular to the C_3 top axis. For parent molecules which are rotating substantially (*e.g.* those starting at 300 K), the rotation imparted by the dissociation is completely masked by the rotation carried over by conservation into the fragment from the parent. While parent rotation about the axes perpendicular to the C_3 top axis mostly converted to orbital angular momentum, rotation about the top axis is converted to fragment rotation, also about the top axis. Because the rotational constant for the fragment about this axis is smaller than that of the parent, and because two parent rotational degrees of freedom have been lost to orbital angular momentum, the fragment rotational temperature is colder than that of the parent. Fragment rotation following dissociation of rotationally excited CH_3I should be aligned along the top axis.

2. Alignment in the Molecular Frame.

Fragment alignment has proven to be extremely useful in revealing the mechanism of photodissociation.[1,2] For diatomic fragments, alignment information has been extracted from polarization measurements, from correlations between the fragment velocity, v, and its rotational angular momentum, J, and from the triple correlation between v, J, and the parent transition dipole, μ. For polyatomic fragments information concerning alignment in the molecular frame is available in other ways, in particular from K, the projection of the total angular momentum onto the top axis. In the present case, $K = 0$ indicates that the methyl is rotating about a C_2 axis, while $K = \pm N$ indicates that it is rotating about its C_3 axis. For a collinear dissociation, fragment rotation results only

from parent rotation about the C_3 axis, as discussed above, so that we would expect $K = \pm N$. For a non-linear dissociation of a rotationally cold CH_3I parent, particularly one induced by an e-type vibration, we expect that the fragment will be rotating about a C_2 axis so that $K = 0$.

Conveniently, the two-photon spectroscopy is quite different for these two limiting cases. For $K = \pm N$, O and P branches are inconsistent with the $\Delta K = 0$ selection rule, so only Q, R and S branches are allowed. In contrast, for $K = 0$, the selection rule $\Delta N = 0, \pm 2$ holds, allowing only O, Q and S branches. Furthermore, the nuclear-spin statistics enhance the alignment effects: for CD_3, $K \neq 0$ levels display slight intensity variations with a weighting of $11:8:8$ for $K = 3N : K = 3N + 1 : K = 3N + 2$, while for CH_3, the variation is $4:2:2$. The spin statistics are much more pronounced for $K = 0$ levels where there is an $N = \text{odd} : N = \text{even}$ weighting of $10:1$ and CD_3 and $0:4$ in CH_3. Hence, a strong preference for $K = \pm N$ would be evident from the relative dominance of the Q, R and S branches, while preference for $K = 0$ would be evident from the enhanced odd or even N lines of the O, Q and S branches.

The CD_3 0_0^0 band rotational structure shows, indeed, that the odd-N'' O- and S-branch lines are enhanced; the dissociation mechanism seems strongly to favour $K = 0$ population. Fig. 5(a) shows a 105 K simulation with the $K = 0$ contribution multiplied by a factor of 6, while Fig. 5(c) shows an unaligned simulation. Fig. 5(b) is the experimenal spectrum, which agrees very nicely with fig. 5(a). A CH_3 0_0^0 band spectrum is displayed in fig. 6(b) and simulated in fig. 6(a) and (c). Once again, alternate lines of the O and S branches are enhanced in intensity, ut in this case the enhanced lines correspond to even-N''. Again, the experimental spectrum agrees best with $K = 0$ enhancement.

The alternating intensities make a particularly strong case for a dissociation mechanism which favours $K = 0$ alignment in the molecular frame. We have found no other dynamical arguments capable of explaining odd-N'' enhancement in CD_3 and even-N'' enhancement in CH_3. Other types of alignment can explain enhancement of individual branches, but not of alternating lines. Only $K = 0$ nuclear-spin statistics result in the enhancement of every *other* line, instead of every *third* line. It is likely that there is enhancement for other low-K values, but our spectrum, which does not resolve the individual K-components, is sensitive only to the $K = 0$ component through its influence on the nuclear-spin statistics.

The recent report by Black and Powis[14] of a preference for CD_3 $K = \pm N$ levels in the I^* channel of the methyl iodide dissociation at first appears to be at variance with the above observations, but in fact the two experiments are complementary. The effusive-beam experiment relied upon resolution of individual Ks to provide direct evidence of alignment. This experiment is most sensitive to the observation of $K = \pm N$ levels; the $K = \pm N$ lines are best resolved since the K splittings increase as $2K + 1$. As mentioned above, our experiment is most sensitive to $K = 0$ molecular frame alignment because this alignment can be observed by the effect of the CD_3 and CH_3 spin statistics on odd or even rotational lines, respectively. Furthermore, while their experiment was performed in an effusive beam with non-negligible parent rotation, ours was performed in a supersonic jet to minimize contributions from initial parent rotation. For a rotationless parent molecule eqn (2) suggests that J_{CH_3} should be nearly equal to $-L$, so that the recoil velocity, v, should be perpendicular to the CH_3 rotation axis. Both the Black and Powis results and ours are consistent with the scenario postulated above in which $K = \pm N$ molecular frame alignment arises from initial parent rotation and $K = 0$ alignment arises from $I-C-H_3$ bending. Once the parent has been cooled enough to reduce the alignment due to initial rotation, the alignment due to $I-C-H_3$ bending is unmasked.

The observed rotational excitation and the $K = 0$ molecular frame alignment have important implications for the I^* channel. The I channel of the dissociation cannot entirely account for the observed rotational excitation of the $v = 0$ methyl radicals

because the measured I/I^* ratios indicate that little of the $v = 0$ methyl ion signal arises from methyl formed in coincidence with I. Similarly, the amount of $K = 0$ alignment observed (particularly at low N) is too large to be accounted for solely by the I channel. It seems that the I^* channel of this dissociation must also contribute to the alignment, either through the zero-point $I—C—H_3$ bending or through bending induced by a non-linear dissociative surface.

While we have described the alignment of methyl radical rotation with respect to its C_3 axis and have tacitly assumed the recoil velocity to be parallel to this axis, we have ignored more complicated effects of the correlation between v and J. We expect from these results that for non-rotating parent molecules v should be perpendicular to J, while for strongly rotating parent molecules v should be parallel to J. Under these conditions, the probe-laser polarization will clearly affect the detection efficiency for particular dissociation channels and rotational branches. In light of the evidence for alignment shown in these experiments and in those of Black and Powis, further efforts to determine the contributions of v, J correlations to the methyl iodide dissociation will certainly be important.

3. *Vibrational Distributions and* I/I^* *Ratios.*

By far the most disconcerting results in this work are those for the methyl radical $(v = 0):(v = 2)$ vibrational population measurements. In 1981 Sparks *et al.*[15] derived vibrational distributions from their time-of-flight data that showed *ca.* 14 times as much CH_3 $(v = 2)$ as CH_3 $(v = 0)$ and indicated that the I^* channel vibrational distribution peaks at $v = 2$, while that for the I channel peaks at $v = 3$ or 4. Several theoretical calculations[55-59] used potential-energy surfaces based on these measurements. The infrared fluorescence measurements of Hermann and Leone,[45] while not providing populations for $(v = 0)$ CH_3, appeared to confirm the measurements of Sparks *et al.* for the other vibrational levels. We find, instead, that the CD_3 $(v = 0):(v = 2)$ ratio is *ca.* $(1.1):(1.0)$ (multiple determinations ranged from 0.47 to 2.1), while that for CH_3 is even larger.

We are satisfied that the discrepancies between our $(v = 0):(v = 2)$ ratio and that of Sparks *et al.* do not arise from problems with the Franck–Condon factors used in our analysis. *Our core-sampling measurements of* I/I^* *ratios are independent of the Franck–*Condon factors, yet they are still inconsistent with a combination of the vibrational populations of Sparks *et al.* and the overall I/I^* ratio for the methyl iodide dissociation.[60] That is, if we apply the CH_3 $(v = 0):(v = 1):(v = 2)$ vibrational population ratio of $(1.0):(4.4):(14.6)$ measured by Sparks *et al.* to our CH_3 $v = 0$, $v = 1$ and $v = 2$ I^* quantum yields of 0.92, 0.77 and 0.47, respectively, an overall I^* quantum yield of *ca.* 0.56 is obtained: $[(1.0)(0.92) + (4.4)(0.77) + (14.6)(0.47)]/[1.0 + 4.4 + 14.6] = 0.56$. (We have not included contributions from vibrational levels higher than $v = 2$ in this calculation, but because the I^* quantum yields decrease with increasing vibrational excitation, the additional contributions would lower the overall I^* quantum yield still further.) Leone and colleagues[61] have measured a quantum yield of 0.73 ± 0.04 for the 266 nm dissociation of CH_3I, in agreement with the value of Riley and Wilson of 0.76.[52] Photolysis experiments performed at nearby wavelengths or with broadband sources[61-68] have provided similar, or even larger values for the quantum yield. In light of those results, an I^* quantum yield of 0.56 is not reasonable.

Instead, if we assume vibrational populations in keeping with our MPI measurements: CH_3 $(v = 0):(v = 1):(v = 2) = 1.1:1.0:1.0$, and neglect higher vibrations, then an I^* quantum yield of 0.73 is obtained, in agreement with the accepted value. Of course, larger populations of $v \geq 2$ than assumed will lower the quantum yield slightly, while larger populations of $v = 0$ will increase it. We know that the CH_3 ratio of $(v = 0):(v = 2)$ is larger than 1.1 and that the vibrational populations for $v > 2$ are not negligible. The

$v = 1$ population has little effect, since its I* quantum yield is 0.76, very close to the value for the overall yield. Probably any increase in quantum yield from the underestimate of the $v = 0$ population is counteracted by the decrease from the underestimate of the $v > 2$ populations. Such an argument would explain the superb agreement of our overall quantum yield estimate with the measured yield of Leone and co-workers.[61]

For CD_3, a $(v = 0):(v = 1):(v = 2)$ ratio of $1.1:1:1$ and neglect of $v > 2$ provides an I* quantum yield of 0.90. It is quite likely, however, that the populations of vibrational levels $v > 2$ are substantial, and because those levels have significantly smaller quantum yields the overall quantum yield will probably be smaller than 0.90. To our knowledge, no quantum-yield measurements of the 266 nm CD_3I dissociation exist for comparison, although broad-band photolysis[66-68] and 274 nm photoacoustic measurements[69] have provided values of 0.99 and 0.73, respectively. (Note that these two techniques yielded values of 0.92 and 0.76 for CH_3I quantum yield.)

The source of the discrepancy between our measurements and those of Sparks *et al.* apparently lies in an experimental problem encountered by the latter group. Recent as yet unpublished reports[69] indicate that a reinvestigation of the photodissociation of CH_3I, though at 248 nm, has shown that the data of Sparks *et al.* were contaminated by vibrationally excited CH_3I which produced a faster CH_3 $(v = 0)$ than the CH_3 $(v = 0)$ from vibrationally cold CH_3I. This led to an incorrect bond energy and misassignment of the time-of-flight peaks, so that the vibrational level at the maximum of the distribution is, in fact, $v'' = 0$, with comparable but smaller amounts of $v'' = 1$ and 2. The new data also show some $\nu_1 = 1$ population. These data are in much better agreement with those found in our own study.

5. Conclusions

Vector correlations have been used to elucidate the photodissociations of a CH_3I at 266 nm and of OCS at 157 nm. In the OCS dissociation, sulphur is produced almost entirely in the $S(^1S)$ state, while CO is produced in its ground electronic state and in vibrational levels from $v = 0$–3 in the approximate ratio $(v = 0):(v = 1):(v = 2):(v = 3) = (1.0):(1.0):(0.5):(0.3)$. The rotational distribution for each vibrational level is found to be near-Boltzmann, with temperatures that decrease from 1350 K for $v = 0$ to 780 K for $v = 3$. Measurements of the CO Doppler profiles demonstrate that the dissociation takes place from a transition of predominantly parallel character $(\beta > 1.3)$ and that the CO velocity and angular-momentum vectors are perpendicular to one another.

Our experiments have provided new and unexpected results for the 266 nm methyl iodide dissociation in a supersonic molecular beam. We have found that the CH_3 $(v'' = 0)$ and CD_3 $(v'' = 0)$ products from this dissociation are fitted by 120 ± 30 K and 105 ± 30 K rotational distributions, respectively. The dissociation mechanism produces alignment in the molecular frame such that there is a preference for $K = 0$. The $K = \pm N$ preference observed in the effusive-beam results of Black and Powis[14] is due to the initial CH_3I rotation. It is likely that photodissociation through both the I and I* channels is responsible for the observed $K = 0$ preference, perhaps due to e-type vibrations of the parent.

The ratio of CD_3 $(v = 0)/(v = 2)$ was estimated to be *ca.* 1.1, with multiple determinations ranging from 0.47 to 2.1. A value for the CH_3 $(v = 0):(v = 2)$ ratio could not be estimated, although it was clearly larger than that for CD_3. These vibrational ratios disagree strongly with the reported measurements of Sparks *et al.*,[15] which suggested CH_3 $(v = 0)/(v = 2)$ ratios *ca.* 0.07, but they are in much better agreement with an unpublished reinvestigation for the same laboratory.[70] Our core-sampling measurements, showing nearly equal amounts of I and I* for CH_3 $(v'' = 2)$ and primarily I* for CH_3 $(v'' = 0)$, support our measured vibrational population ratio.

References

1 J. P. Simons, *J. Phys. Chem.*, 1987, **91**, 5378.
2 P. L. Houston, *J. Phys. Chem.* 1987, **91**, 5388.
3 R. N. Zare and D. R. Herschbach, *Proc. IEEE*, 1963, **51**, 173.
4 R. J. Van Brunt and R. N. Zare, *J. Chem. Phys.*, 1968, **48**, 4304.
5 G. Gouedard and J. C. Lehmann, *J. Phys.*, 1973, **34**, 693.
6 U. Fano and J. H. Macek, *Rev. Mod. Phys.*, 1973, **45**, 553.
7 C. H. Greene and R. N. Zare, *J. Chem. Phys.*, 1983, **78**, 6741; *Annu. Rev. Phys. Chem.*, 1982, **33**, 119.
8 G. E. Hall, N. Sivakumar, P. L. Houston and I. Burak, *Phys. Rev. Lett.* 1986, **56**, 1671.
9 R. N. Dixon, *J. Chem. Phys.*, 1986, **85**, 1866.
10 G. E. Hall, N. Sivakumar, D. Chawla, P. L. Houston and I. Burak, *J. Chem. Phys.*, 1988, **88**, 3682.
11 G. Black, R. L. Sharpless, T. G. Slanger and D. C. Lorents, *J. Chem. Phys.*, 1975, **62**, 4274.
12 G. Black and R. L. Sharpless, *J. Chem. Phys.*, 1979, **70**, 5567.
13 G. S. Ondrey, S. Kanfer and R. Bersohn, *J. Chem. Phys.*, 1983, **79**, 179.
14 J. F. Black, *Ph.D. Thesis* (University of Nottingham, 1987).
15 R. K. Sparks, K. Shobatake, L. R. Carlson and Y. T. Lee, *J. Chem. Phys.*, 1981, **75**, 3838.
16 A. C. Provorov, B. P. Stoicheff and S. C. Wallace, *J. Chem. Phys.* 1977, **67**, 5393.
17 I. M. Waller and J. W. Hepburn, *J. Chem. Phys.*, 1987, **87**, 3261
18 N. Sivakumar, I. Burak, W-Y. Cheung, J. W. Hepburn and P. L. Houston, *J. Phys. Chem.*, 1985, **89**, 3609.
19 N. Sivakumar, G. E. Hall, P. L. Houston, J. W. Hepburn and I. Burak, *J. Chem. Phys.*, 1988, **88**, 3692.
20 M. R. Taherian and T. G. Slanger, *J. Chem. Phys.*, 1984, **81**, 3796.
21 M. R. Taherian and T. G. Slanger, in *Photophysics and Photochemistry Above 6 eV*, 1985, p. 387.
22 T. G. Dietz, M. A. Duncan, M. G. Liverman, and R. E. Smalley, *J. Chem. Phys.*, 1980, **73**, 4816.
23 T. E Adams, B. H. Rockney, R. J. S. Morrison and E. R. Grant, *Rev. Sci. Instrum.*, 1981, **52**, 1469; The beam valve used by us is a forerunner of the BV-100 pulsed valve marketed by Newport Research Corporation, 18235 Mt. Baldy Circle, Fountain Valley, CA 92728-8020.
24 W. C. Wiley and I. H. McLaren, *Rev. Sci. Instrum.*, 1955, **26**, 1150.
25 MM-1 Focussed mesh electron multiplier, Johnston Laboratories, Cockeyesville, MD 21030.
26 CLC100 Video Amplifier, Comlinear Corporation, 4800 Wheaton Drive, Fort Collins, CO 80525.
27 LeCroy, 700 South Main Street, Spring Valley, NY 10977.
28 Gould, Inc., 3631 Perkins Ave., Cleveland, OH 44114.
29 Stanford Research Systems, Inc, 460 California Ave., Palo Alto, CA 94306.
30 I. M. Waller and J. W. Hepburn, *J. Chem. Phys.*, 1988, **88**, 6658.
31 R. Ogorzalek Loo, *Ph.D. Thesis* (Cornell University, 1988).
32 R. Ogorzalek Loo, *Ph.D. Thesis* (Cornell University, 1988).
33 J. W. Hudgens, T. G. DiGiuseppe and M. C. Lin, *J. Chem. Phys.* 1983, **79**, 571.
34 R. Orgorzalek Loo, H-P. Haerri, G. E. Hall and P. L. Houston, in preparation.
35 G. Herzberg, *Molecular Spectra and Molecular Structure III. Electronic Spectra and Electronic Structure of Polyatomic Molecules* (Van Nostrand, Princeton, 1966), p. 84.
36 K. Chen and E. S. Yeung, *J. Chem. Phys.*, 1978, **69**, 43.
37 P. Chen, S. D. Colson, W. A. Chupka and J. A. Berson, *J. Phys. Chem.*, 1986, **90**, 2319.
38 M. N. R. Ashfold, *Mol. Phys.*, 1986, **54**, 1.
39 M. N. R. Ashfold, R. N. Dixon, K. N. Rosser, R. J. Stickland and C. M. Western, *Chem. Phys.*, 1985, **101**, 476.
40 R. E. Demaray, C. Otis, K. Aron and P. Johnson, *J. Chem.*, 1980, **72**, 5772; C. E. Otis and P. M. Johnson, *Chem. Phys. Lett.*, 1981, **83**, 73; P. M. Johnson and C. E. Otis, *Annu. Rev. Phys. Chem.*, 1981, **32**, 139; P. J. H. Tjossem and T. A. Cool, *Chem. Phys. Lett.*, 1983, **100**, 479; L. Li, R. N. Porter and P. Johnson, *Phys. Rev. Lett.*, 1984, **53**, 1336.
41 G. N. A. van Veen, T. Baller, A. E. de Vries and N. J. A. van Veen, *Chem. Phys.*, 1984, **87**, 405.
42 C. E. Strauss, P. L. Houston, I. Burak and J. W. Hepburn, in preparation.
43 M. D. Morse and K. F. Freed, *J. Chem. Phys.*, 1981, **74**, 4395.
44 N. Sivakumar, G. E. Hall, P. L. Houston, J. W. Hepburn and I. Burak, *J. Chem. Phys.*, 1988, **88**, 3692.
45 H. W. Hermann and S. R. Leone, *J. Chem. Phys.*, 1982, **76**, 4766.
46 J. Frye, T. J. Sears and D. Leitner, *J. Chem. Phys.*, 1988, **88**, 5300; J. Frey, G. E. Hall and T. J. Sears, *J. Chem. Phys.*, submitted.
47 S. Leone, personal communication.
48 J. Danon, H. Zacharias, H. Rottke and K. C. Welge, *J. Chem. Phys.*, 1982, **76**, 2399.

49 G. Herzberg, *Molecular Spectra and Molecular Structure II. Electronic Spectra and Electronic Structure of Polyatomic Molecules* (Van Nostrand, Princeton, 1966), p. 621.

50 Ref. (49), p. 609.

51 R. S. Mulliken, *J. Chem. Phys.*, 1955, **23**, 1997.

52 S. J. Riley and K. R. Wilson, *Discuss. Faraday Soc.*, 1972, **53**, 132.

53 M. D. Barry and P. A. Gorry, *Mol. Phys.*, 1984, **52**, 461.

54 D. Imre, J. L. Kinsey, A. Sinha and J. Krenos, *J. Phys. Chem.*, 1984, **88**, 3956; M. O. Hale, G. E. Galica, S. G. Glogover and J. L. Kinsey, *J. Phys. Chem.*, 1986, **90**, 4997; R. L. Sundberg, D. Imre, M. O. Hale, J. L. Kinsey and R. D. Coalson, *J. Phys. Chem.*, 1986, **90**, 5001.

55 M. Shapiro, *J. Phys.Chem.*, 1986, **90**, 3644.

56 S.-Y. Lee and E. J. Heller, *J. Chem. Phys.*, 1982, **76**, 3035.

57 S. K. Gray and M. S. Child, *Mol. Phys.*, 1984, **51**, 189.

58 N. E. Henriksen, *Chem. Phys. Lett.*, 1985, **121**, 139.

59 G. D. Billing and G. Jolicard, *J. Phys. Chem.*, 1984, **88**, 1820.

60 W. P. Hess, S. J. Kohler, H. K. Haugen and S. R. Leone, *J. Chem. Phys.*, 1986, **84**, 2143.

61 P. Brewer, P. Das, G. Ondrey and R. Bersohn, *J. Chem. Phys.*, 1983, **79**, 720.

62 F. G. Goodwin, P. A. Gorry, P. M. Hughes, D. Raybone, T. M. Watkinson and J. C. Whitehead, *Chem. Phys. Lett.*, 1987, **135**, 163.

63 S. L. Baughcum and S. R. Leone, *J. Chem. Phys.*, 1980, **72**, 6531.

64 W. H. Pence, S. L. Baughcum and S. R. Leone, *J. Phys. Chem.*, 1981, **85**, 3844.

65 T. Donohue and J. R. Wiesenfeld, *J. Phys. Chem.*, 1976, **80**, 437.

66 T. Donohue and J. R. Wiesenfeld, *Chem. Phys. Lett.*, 1975, **33**, 176.

67 T. Donohue and J. R. Wiesenfeld, *J. Phys. Chem.* 1975, **63**, 3130.

68 T. F. Hunter, S. Lunt and K. Kristjansson, *J. Chem. Soc., Faraday Trans. 2*, 1983, **79**, 303.

69 Y. T. Lee, Personal commun.

Photofragment Vector Correlations in Vibrationally Mediated Photodissociation

A New Angle on Intramolecular Vibrational Redistribution

Mark Brouard, Maria T. Martinez, John O'Mahony and John P. Simons*

Chemistry Department, The University, Nottingham, NG7 2RD

Vector correlations in OH fragments, generated through vibrationally medi-
ated two-photon photodissociation of H_2O_2 at *ca.* 750 nm, have been deter-
mined through Doppler-resolved LIF spectroscopy. The new measurements,
together with a knowledge of the photofragment quantum-state distributions
and an understanding of the dynamics of the direct *single*-photon dissoci-
ation, have allowed a detailed insight into the intramolecular dynamics in
the vibrationally excited ground state. In particular, it has been possible to
estimate the average vibrational mode composition after IVR over a
nanosecond period. Both angle bending and torsion, as well as large-
amplitude O—O stretching motions, are found to be excited. Extension of
this experiment into the picosecond or sub-picosecond timescale should
offer the opportunity of monitoring IVR processes in real time.

Steric indicators of intermolecular reaction dynamics, *e.g.* differential cross-sections,
product polarizations, sensitivity to reagent polarization, are increasingly valued by
students of reactive and inelastic collisions, both at surfaces and in the gas phase. They
provide a three-dimensional image of the 'shape' of the interaction potentials in both
the entrance and the exit channels, a measure of structure and its reorganization in the
course of atomic and molecular collisions.[1]

Measurements of product polarizations and translational anisotropies following
'half-collision' events such as molecular photodissociation are equally valued since they
either supplement structural information derivable from analysis of the molecular
absorption or emission spectrum or, much more commonly, they provide unique evidence
of structural changes in the electronically excited molecule when fast dissociation has
broadened its excited state(s) into a continuum.[2-7]

Studies of state-resolved intramolecular processes in isolated electronically excited
polyatomic molecules have also benefited from measurements of the polarization of
their spectroscopically resolved fluorescent decay; loss of polarization reflects
intramolecular vibrational–rotational energy transfer (IVRET) promoted through
Coriolis or centrifugal effects.[8,9] Steric indicators have not yet been used, however, to
probe the dynamics of intramolecular vibrational redistribution (IVR) in the ground
electronic state. One of the great unknowns in this process is the changing vibrational
composition of the excited molecules as they evolve for example, from an initial high
energy 'local-mode overtone' state into a mix of bond-stretching and angle-bending
modes.

The development of vibrationally mediated photodissociation by Crim and co-
workers[10-14] offers a new method of probing this evolution. Unlike conventional single-
photon excitation which proceeds through a vertical excitation near the ground-state
equilibrium geometry, vibrationally mediated photodissociation accesses the dissociation
continuum through a double-resonance pathway proceeding *via* the intermediate excita-
tion of a local-mode X—H overtone state. Its subsequent evolution through IVR can

allow Franck-Condon excitation to occur at geometries distorted far beyond the ground-state equilibrium dimensions.[10-14] This is most pronounced when the total absorbed photon energy is not very far above threshold and when the electronically excited continuum state is strongly repulsive. Under these conditions, photofragment separation begins at a range where any angular anisotropies associated with bending or torsion about the dissociating bond will already have been greatly weakened. Polarization of the photofragments' rotational angular momenta, if observed, should be dominated by contributions from angular motions in the intermediate level.

This strategy has been employed in a series of experiments using H_2O_2 as the exemplary molecule[15] since it has already been used as a bench-mark system (a) to probe the dynamics of vibrationally state-selected predissociation out of the ground electronic state on both nanosecond[14] and picosecond[16] timescales, (b) to probe the stereochemical dynamics of its direct photodissociation following single-photon excitation into low-lying electronic continua at 266.[17,18] 248[19-21] and 193 nm[22,23] and (c) to demonstrate the occurrence of vibrationally mediated photodissociation.[10-15] Using single-colour excitation (in the first instance) at ca. 750 nm, sequential two-photon absorption leads to dissociation of the HO—OH bond, via the intermediate excitation of the third O—H stretching overtone, $4\nu(O-H)$.[10,12-15] The energy absorbed, 26 666 cm^{-1} is not too far above the HO—OH bond-dissociation energy, $D_0(HO-OH) = 17\,300$ cm^{-1}, and this, together with the Franck-Condon constraint restricts secondary photon absorption to molecules for which the HO—OH distance has increased from 1.45 to ca. 1.8-2.0 Å. Comparison between the final photofragment quantum-state distributions and their recoil velocity-rotational angular momentum $[\epsilon(\mu), v, j]$ vector correlations generated under direct and under vibrationally mediated conditions has allowed (i) assignment of the electronic continuum states accessed at long range (where the lower-lying interfragment repulsive potential-energy surfaces are approaching degeneracy), (ii) assessment of the separate contributions made by torsional and angle-bending vibrations to the rotational excitation of the recoiling OH fragments and (iii) determination of the average mode composition of the vibrationally excited molecules dissociated by secondary absorption out of the overtone state.

Experimental

Two pulsed, tunable dye lasers, each pumped by the same excimer laser (XeCl), generated the photolysis (750 nm) and detection (310 nm) beams. The frequency spread of the latter was narrowed to a bandwidth of ca. 0.08 cm^{-1} by insertion of an etalon in the laser cavity, and the pulse was optically delayed by ca. 10 ns. The polarization of the two (necessarily identically polarized) photons absorbed at 750 nm, could be rotated to lie either parallel or perpendicular to that of the probe allowing the co-axial counter-propagating photolysis (p) and probe (a) beams to be aligned with $\epsilon_a\|(\epsilon p_1\|\epsilon p_2)$ (case A) or $\epsilon_a\perp(\epsilon p_1\|\epsilon p_2)$ (Case B) (p_1 is the overtone-pumping photon and p_2 is the photolysis photon). The laser-induced OH (A-X) photofragment fluorescense (LIF) was collected without polarization analysis, along an axis parallel to ϵ_a. In order to avoid saturation and any complications arising from photodissociation at the probe laser frequency, the detection beam was first expanded by a factor of ca. 100, then attenuated and finally collimated to a beam of 1 mm diameter. The overtone pumping/photolysis radiation (<5 mJ per pulse in 20 ns) was focussed into the centre of the cell by a 30 cm focal-length lens, while H_2O_2 vapour was flowed slowly through the cell at pressures in the range 10-20 mTorr.† Photofragment LIF signals were integrated on a boxcar system, transfer-

---

† 1 Torr = 101 325/760 Pa.

red on a shot-by-shot basis to a microcomputer where they were normalized to the probe laser power, averaged and finally stored on disc for subsequent data-processing. The LIF signal intensity increased with the square of the photolysis laser energy, exponent $n = 2.12 \pm 0.18$: neither the overtone pumping nor the subsequent photolysis step were saturated at the laser fluences employed (*ca.* 1 GW cm^{-2}). When the photolysis wavelength was scanned across the spectral region occupied by the overtone band $4\nu(O-H)$, the OH(A-X) LIF intensity faithfully followed the rotational contours of the overtone spectra recorded previously by Crim and co-workers.[24,25].

Data Analysis

Excitation into the symmetric and antisymmetric local-mode states $(4, 0)^{\pm}$, $4\nu(O-H)$ will be associated with transitions polarized perpendicular to the O—O axis, either type B or type C; the rotational contour of the overtone band has been analysed by Dübal and Crim in terms of a perpendicular transition in a very near symmetric, prolate top.[24,25] Necessarily, the overtone pumping will initially generate an aligned population of vibrationally excited molecules. However, given the laser fluences employed and assuming a cross-section for secondary photon absorption $\leqslant 10^{-19}$ cm^2 (*cf.* the value estimated for the equivalent step in HONO$_2$[26]) the average interval between primary and secondary excitation will be $\geqslant 2$ ns. This is long enough to allow the parent molecular rotation to destroy most if not all of the alignment initially present.[27] At 300 K, the most probable rotational angular momentum $J(H_2O_2) = 10\text{-}11$.

Suppose, for the sake of argument, that it were possible for the absorbed frequency to select a population of H_2O_2 molecules with $J(H_2O_2) \approx 0$. Angular momentum conservation would require

$$J(H_2O_2) = j_1 + j_2 + l \approx 0 \tag{1}$$

where j_1, j_2 and l are, respectively, the internal and orbital angular momenta of the two OH fragments. When the fragments were monitored *via* the $R_2(1)\uparrow$ feature in the OH(A-X) LIF spectrum (corresponding to $j_1 = \frac{1}{2}$), the Doppler-broadened spectral width indicated an average rotational angular momentum for the sister, 'unobserved' OH fragment of $j_2 = 9$. Conservation of angular momentum would necessarily require $l \approx 9$ also if $J(H_2O_2) \approx 0$. Orbital angular momentum can be acquired through the tangential motion imparted by parent molecular rotation perpendicular to the recoil axis and/or by HOO angle bending. The latter contribution will be very minor since it is the O—O bond rather than the H—O bond that breaks, so in fact $J(H_2O_2)$ must be greater than zero, confirming the argument for rotational scrambling. This allows us to neglect higher-order terms [$O(\cos^4 \theta)$ in the high-j limit] in the photofragment anisotropies, referenced to the molecule-fixed frame and the use of the analyses of Greene and Zare[28] and of Dixon[29] to estimate the final photofragment velocities and vector correlations from the Doppler-resolved LIF spectral lineshapes.

The OH Doppler-resolved rotational profiles were non-linearly least-squares fitted to the lineshape function[15,29]

$$g(\bar{v}) = \sum_i \frac{W(v_i)}{2\Delta v_D^i} (1 + \beta_{eff} P_2(\cos \theta_a) P_2) \chi_D^i) \tag{2}$$

after its convolution with a Gaussian (f.w.h.m. = 0.1 cm^{-1}) to accommodate the finite laser resolution (0.08 cm^{-1}) and the velocity spread associated with parent molecular motion. β_{eff} represents the 'effective' (velocity-averaged) translational anisotropy and θ_a is the angle between the vectors $\varepsilon_{p_2}(\|\varepsilon_{p_1})$ and k_a, the probe laser propagation axis. $W(v_i)$ is the probability that the observed OH fragment [OH(1), say] is born with a velocity v_i; Δv_D^i and χ_D^i are the corresponding maximum Doppler shifts and relative displacements from the line centre.

The distribution $W(v_i)$ of recoil velocities v_i reflects the spread of internal energies in the 'unobserved' OH(2) fragments, E_{int}^i,

$$v_i = \left(\frac{2(E_{avl} - E_{int}^i)}{M_{OH}}\right)^{1/2} \tag{3}$$

(where E_{avl} is the maximum energy available for kinetic energy release). The experimental probabilities $W(v_i)$ may lie between two limiting forms: (*a*) the states populated in OH(1) and OH(2) are completely correlated, in which case eqn (2) reduces to the single recoil velocity form[29] and the profiles may be fitted with Δv_D and β_{eff} as the optimized parameters, or (*b*) the OH(1) and OH(2) quantum states are completely uncorrelated. In this case $W(v_i)$ may be determined directly from the experimentally observed OH rovibrational populations[10,12,13] and the Doppler lineshapes fitted with E_{avl} and β_{eff} as the optimized parameters. As described elsewhere,[29] these two sets of β_{eff} values [determined from pairs of $Q(N'')\uparrow$ and $P(N'')\uparrow$ transitions in at least two geometries] are employed in the least-squares solution of the simultaneous equations

$$\beta_{eff} = \frac{b_2\beta_0^2(20) + b_3\beta_0^0(22) + b_4\beta_0^2(22)}{b_0 + b_1\beta_0^2(02)} \tag{4}$$

where $\beta_0^2(20) \equiv \frac{1}{2}\beta$, the translational anisotropy; $\beta_0^0(22)\langle P_2(\hat{j}_{OH} \cdot \hat{v}_{OH})\rangle$, the v, j correlation; $\beta_0^2(22) \equiv$ the $\varepsilon(\mu)$, v, j correlation; $\beta_0^2(02) \equiv 5/4A_0^{(2)}$, the rotational alignment; and b_0–b_4 are the angular momentum and geometrical coupling factors listed by Dixon.[29] Rotational alignments (and Λ-doublet population ratios) were obtained separately from the measurement of the integrated intensity ratios for $P\uparrow$- and $Q\uparrow$-branch lines in geometries A and B. Data analysis of the Doppler broadened profiles generated two sets of bipolar moments, $\beta_0^k(k_1, k_2)$, corresponding to the two limiting approximations for the velocity distribution $W(v_i)$ (see later, table 2). The returned values of E_{avl}, resulting from the analysis which assumed uncorrelated fragment pair distributions, were found to depend somewhat on the probed OH rotational level, implying that *this* limiting assumption was not correct.† The true values of the bipolar moments probably lie somewhere between the two data sets, but the main conclusions to be presented and discussed below are common to both.

Results and Discussion

Doppler-resolved spectral profiled have been recorded for OH photofragment rotational levels $N = 1, 2, 3, 6, 10$ and 14, using a selection of $P\uparrow$, $Q\uparrow$, $R\uparrow$ and satellite features. The results were independent of the choice of F_1 or F_2 spin–orbit states: some typical contours recorded for case A and case B excitation–detection geometries are shown in fig. 1–3. Rotational alignments and Λ-doublet ratios were measured from the relative integrated intensities of $P(N)\uparrow$ and $Q(N)\uparrow$ features, recorded under the two alternative geometries: the rotational population distributions reproduced those reported earlier by Crim and co-workers.[10,12,13] Tables 1 and 2 summarize the complete set of scalar and vector data for the two-photon vibrationally mediated dissociation at 750 nm: they also include corresponding data for the single-photon dissociation at 248,[19-21] 266[17,18] and 355 nm[13] for comparative purposes.

---

† A more detailed discussion of the fragment pair correlations will be given elsewhere.
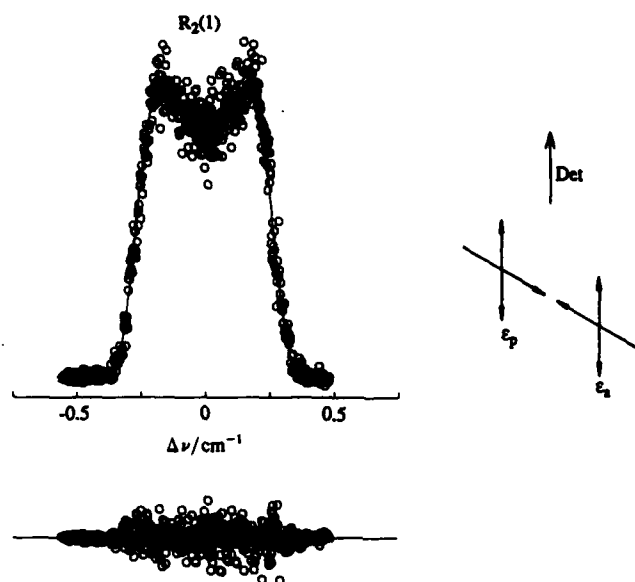
Fig. 1. The $R_2(1)$ Doppler-resolved profile [from the 0-0 band of the OH (A-X) transition] obtained after vibrationally mediated photodissociation of H_2O_2 at 750 nm. The least-squares fit and residuals correspond to data analysis using eqn (2), assuming an uncorrelated *distribution* function for $W(v_i)$ (see text).

The Translational Anisotropy

Single-photon, direct dissociation in the ultraviolet leads to fragment recoil with an anisotropy parameter β close to the limiting value $\beta = -1$. This corresponds to fast recoil perpendicular to the parent molecular transition dipole and is consistent with dissociation *via* the lowest-lying dissociation continuum $H_2O_2(\tilde{A}\ ^1A)$.[17-21] In contrast, under vibrationally mediated conditions, β, while still negative, is considerably smaller than its limiting value. The reduced magnitude could arise, in principle, through a number of possible causes, including delayed dissociation, parent molecular rotation, internal vibrational motions and overlapping transitions into two neighbouring continua associated with opposite polarizations. Of these, the first seems unlikely in view of the repulsive nature of the excited continua and the greatly increased rotational period of the 'stretched' molecule. The excitation of large-amplitude antisymmetric vibrations, to be effective, would require an extension of the O—H bond distance to more than five times its normal equilibrium value! Molecular rotation about the b or c inertial axes near-perpendicular to the dissociating bond would only deflect the terminal recoil velocity vector by *ca.* 8° and reduce β by 6% at most. Overlapping transitions into the $\tilde{A}\ ^1A$ and $\tilde{B}\ ^1B$ electronically excited continuum states, *via* transitions polarized either perpendicular ($\tilde{A} \leftarrow \tilde{X}$) or near-parallel to the O—O axis ($\tilde{B} \leftarrow \tilde{X}$) are left as the most acceptable interpretation for $\beta_K -0.4$. Two factors would encourage such behaviour: the steadily decreasing separation of the $\tilde{A}\ ^1A$ and $\tilde{B}\ ^1B$ continua as the HO—OH distance increases, and their intersection when the torsion angle φ is reduced to *ca.* 90°.[30] When the absorbed energy is restricted to two photons of wavelength 750 nm the constraints of energy conservation and the operatin of the Franck-Condon principle limit secondary excitation *to molecules in which the* HO—OH distance has been extended to 1.8-2.0 Å (see fig. 4). Torsion about the O—O bond, between the preferred *trans*-planar geometry
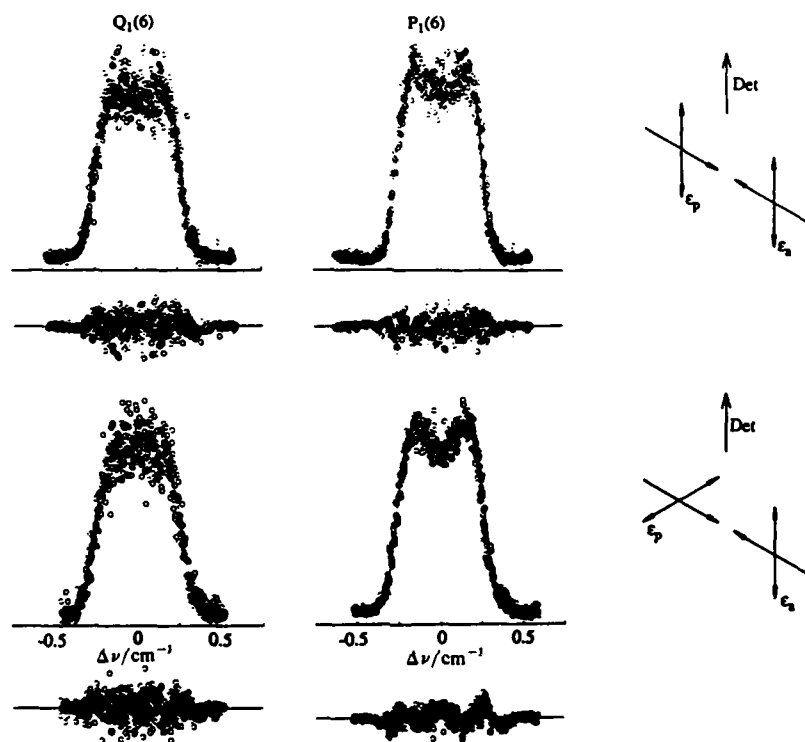
Fig. 2. The $Q_1(6)$ and $P_1(6)$ Doppler-resolved profiles in geometries A and B (see caption to fig. 1).

of the $\tilde{A}\,^1A$ state ($\varphi = 180°$) and the *cis*-planar geometry of the $\tilde{B}\,^1B$ state ($\varphi = 0°$) allows the two states to intersect when $\varphi = 90°$.[31] Strong excitation of the torsional mode will be identified as an important consequence of IVR in the intermediate overtone state in later discussion.

The Source of OH Photofragment Rotational Excitation

When hydrogen peroxide is excited directly into the dissociation continuum by absorption of an ultraviolet photon at 248 or 266 nm, the strong positive (v, j) correlation in the rotationally excited OH fragments $\langle P_2(\hat{v}_{OH} \cdot \hat{j}_{OH}) \rangle \leq +0.4$, identifies torsion about the O—O axis as a major dynamical feature.[17-21] At the short internuclear distances, $r(O—O) \approx r_{eq}(HO—OH)$ dictated by the Franck-Condon principle, the excited potentials $V^A(\varphi)$ [and $V^B(\varphi)$] each display a strong torsional angular dependence:[30] both experiment and theory[20,31,32] have converged in assigning torsional motion on the excited potential-energy hypersurface as a major source of the observed rotational excitation. The zero-point motion in the ground state is expected to play only a minor role and the parent molecular rotation is unlikely to be effective in view of the inertial properties of H_2O_2, $I_a \ll I_b \approx I_c$.

When the photodissociation is vibrationally mediated *via* the overtone state $4\nu(O—H)$, the upper state preparation is quite different. Now, the electronically excited molecules are generated with highly extended O—O distances, where the torsional
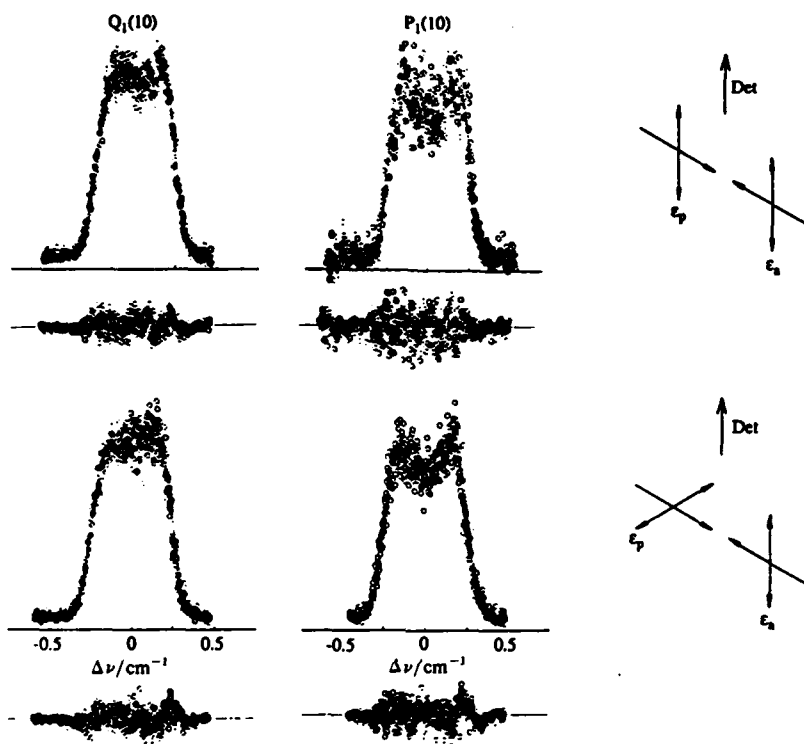
Fig. 3. The $Q_1(10)$ and $P_1(10)$ Doppler-resolved profiles in geometries A and B (see caption to fig. 1).

Table 1. Average energy disposals for vibrationally mediated and direct photodissociation of H_2O_2 (energies in cm^{-1})

		E_{ROT}	E_{VIB}	E_{TRANS}[a]
2×750 nm	OH($v=0$) (89%)	1624[b]	0	8335 ± 400
	OH($v=1$) (11%)	1077[b]	7136	6539 ± 300
	average$_c$	1564	785[b]	8137 ± 390
248 nm[d]	average	2500	0	20 850
266 nm[e]	average	2100	0	20 000
355 nm[f]	average	790	0	not measured

[a] From Doppler profiles analysed assuming a single recoil velocity. [b] Calculated from the rotational and vibrational populations reported by Crim and co-workers.[13] [c] These energy-disposal data imply $\Delta H_0^0 = 16\,680\ cm^{-1}$, slightly below the accepted value of $17\,300\ cm^{-1}$. This discrepancy may reflect the failings of the single recoil analysis of the Doppler profiles. [d] Ref. (19)–(21). [e] Ref. (17) and (18). [f] Ref. (13).

Table 2. OH photofragment Λ-doublet populations and bipolar moments generated *via* two-photon photodissociation of H_2O_2 at $\lambda = 747.7$ nm

N''	$\dfrac{\pi(A'')}{\pi(A')}$	$(\epsilon, \hat{j})$ $\beta_0^2(02)$ $(=\tfrac{5}{4}A_0^{(2)})$	$(\varepsilon, \hat{v})^a$ $2\beta_0^2(20)$ $(\equiv\beta)$	$(\hat{v}, \hat{j})^a$ $\beta_0^0(22)$	$(\varepsilon, \hat{v}, \hat{j})^a$ $\beta_0^2(22)$
1	—	—	-0.25 ± 0.15 -0.47 ± 0.14	—	—
6	1.12 ± 0.10	-0.05 ± 0.05	-0.14 ± 0.08 -0.29 ± 0.05	$+0.09 \pm 0.02$ $+0.08 \pm 0.03$	-0.04 ± 0.02 -0.05 ± 0.05
10	1.20 ± 0.07	-0.06 ± 0.09	-0.21 ± 0.03 -0.52 ± 0.06	$+0.19 \pm 0.02$ $+0.23 \pm 0.04$	$+0.09 \pm 0.03$ $+0.09 \pm 0.04$

[a] The first entry for each rotational state corresponds to analysis assuming a single recoil velocity and the second to analysis assuming an uncorrelated distribution function for $W(v_i)$ (see text). The correct values lie somewhere between the bipolar moments obtained with these two limiting assumptions.
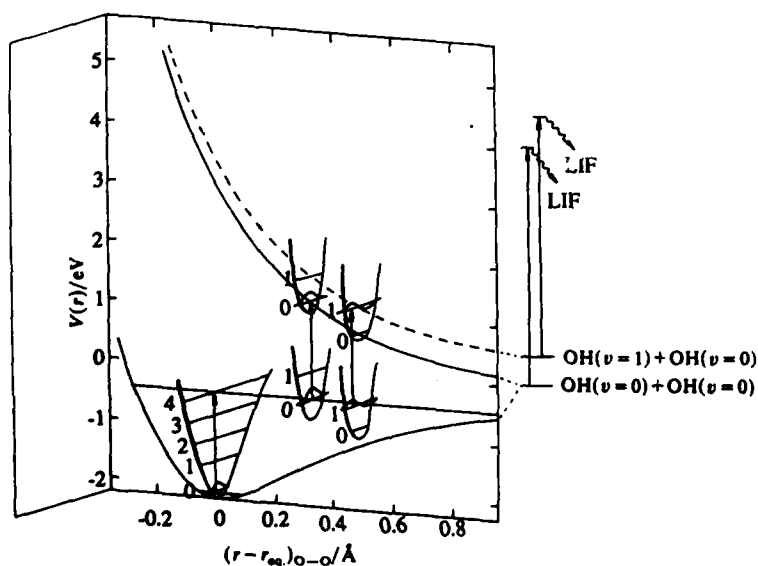
Fig. 4. Schematic of the H_2O_2 vibrationally mediated photodissociation leading to generation of (rotationless) OH $v=0$ and $v=1$ fragments. The ground-and-excited-state potentials (drawn approximately to scale) are taken, respectively, as a Morse curve[17] and from the *ab initio* Ã-state surface ($\varphi = 180°$) reported by Schinke and Staemmler.[30] The O—O bond separations at which secondary photon absorption takes place are shown as the minimum necessary to fulfil energy-conservation and Franck–Condon restrictions.

angular dependencies $V^{\tilde{A}}(\varphi)$, $V^{\tilde{B}}(\varphi)$ are very greatly weakened (see fig. 5); however, the fractional energy conversion into photofragment rotation is far more efficient, with $\langle f_R \rangle \approx 0.17-0.18$ at 2×750 nm, *cf.* $\langle f_R \rangle = 0.11$ (248 nm), 0.10 (266 nm) or 0.07 (355 nm). The much higher levels of rotational excitation under vibrationally mediated conditions must reflect the prior excitation of angular motions in the intermediate overtone level through IVR in the ground electronic state. The comparison with single-photon excitation at 355 nm[12,13] is particularly striking since the total energy absorbed is not very different from that at 2×750 nm. The decreasing rotational excitation with decreasing (single)-photon energy parallels the Franck-Condon requirement for photon absorption by molecules with increasingly extended O—O distances, where there is a corresponding weakening in the angular dependence of the electronically excited-state potential(s), particularly at 355 nm. At this wavelength, direct excitation requires thermal population of (or possibly Raman pumping into) highly excited vibrational levels and an extension of the O—O distance to $r(O-O) \approx 1.7$ Å. (The very low absorption cross-section at 350 nm, $\sigma(300 \text{ K}) = 4.8 \times 10^{-22}$ cm^2,[33] reflects the very low Boltzmann population factor). The very much lower rotational excitation of the OH fragments generated at 355 nm compared with 2×750 nm also implies a very different vibrational-mode composition in the photoselected ground-state population, when the overtone levels are populated through IVR rather than by thermal means.

Vibrational-mode Composition in H_2O_2 following IVR in the Overtone Level, $4\nu(O-H)$

While single-photon dissociation generates OH fragments exclusively in the zero vibrational level, vibrational mediation *via* $4\nu(O-H)$ excites a small fraction (11%) into the level $v = 1$.[10,12,13] The Doppler widths of rotational lines in the OH (A-X), 0,0 and 1,1
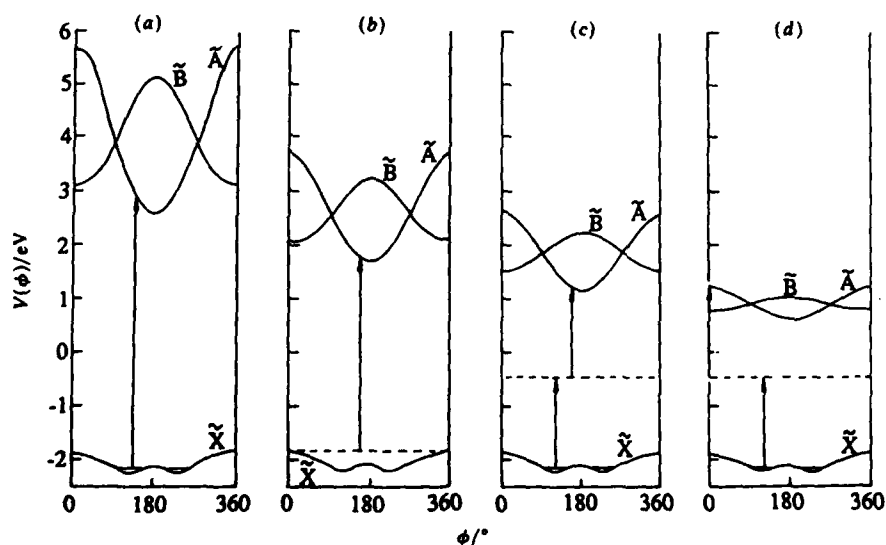
Fig. 5. Slices through the $\tilde{X}$-,[15] $\tilde{A}$- and $\tilde{B}$-[30] state torsional potentials at r_{O-O} separations appropriate for excitation at (*a*) 248 nm ($r_{O-O} = 1.54$ Å), (*b*) 355 nm ($r_{O-O} \approx 1.68$ Å), (*c*) and (*d*) 2×750 nm ($r = 1.8$ and 2.0 Å), respectively; these represent the minimum and maximum O—O bond extensions necessary to generate vibrationless OH fragments, as dictated by Franck-Condon and energy-conservation requirements.

transitions (respectively, $\Delta\nu_D \approx 0.6$ and $0.5\,\text{cm}^{-1}$), monitored *via* LIF, indicate the dominance of $OH(v=0)$ as the 'unobserved' partner in each case. Since the Franck-Condon factors for transitions between 'bound' OH [in $H_2O_2(\tilde{X})$] and 'free' OH [in $H_2O_2(\tilde{A}$ or $\tilde{B})$] will favour $\Delta v(OH)=0$ only, the vibrational excitation created un `··-vibrationally mediated conditions must reflect a residual level of O—H vibration in the subset of parent molecules which dissociate to $OH(v=1)+OH(v=0)$, but a complete redistribution for the major fraction dissociating into $2OH(v=0)$. The energy conservation/Franck-Condon restrictions on the two photodissociation channels are depicted in fig. 4. The potential-energy curves are calculated assuming a Morse function for the ground electronic state, with $D_e = 17\,790\,\text{cm}^{-1}$, $\beta = 2.38\,\text{Å}^{-1}$ and $r_e = 1.47\,\text{Å}$,[17] and the *ab initio* potentials are calculated for $V^A(r)$ by Staemmler and co-workers, and reported by Schinke and Staemmler.[30] In the first case, where both fragments are generated in $v=0$, all of the energy of $13\,333\,\text{cm}^{-1}$, deposited initially through the O—H local-mode transition, is redistributed through IVR. In the second case, the redistributed energy is reduced to $13\,333 - \Delta E[OH(v=1) - OH(v=0)] = 9766\,\text{cm}^{-1}$. Assuming approximately half the vibrational energy distribution into angle-bending and torsional modes is channelled into rotation in the separated fragments,[23,34,35] the $\nu(O—O)$ stretching mode will accept *ca.* $10\,130\,\text{cm}^{-1}$ [$2OH(v=0)$] or *ca.* $7600\,\text{cm}^{-1}$ [$OH(v=1)+OH(v=0)$], just sufficient to allow Franck-Condon access into the vibrationally adiabatic potential correlating with $OH(v=1)+OH(v=0)$ (fig. 4). Generation of *both* fragments in $OH(v=1)$, or either fragment in the level $v=2$ is impossible for two-photon dissociation at 750 nm, despite their energetic accessibility.

The Bending and Torsional Modes

The relative energies absorbed by the angle-bending and torsional modes can be estimated through consideration of the three photofragment vector correlations, the rotational alignment $A_0^{(2)}$ [$\equiv \frac{4}{5}\beta_0^2(02)$] the (v,j) correlation $\beta_0^0(22)$, and the translational anisotropy [$\equiv \beta_0^2(20)$]. In the classical, high-j limit the photofragment rotational angular momentum components j_x (taken parallel to the O—O axis in H_2O_2), j_y (taken perpendicular to the O—O axis) and j_z (taken parallel to the twofold symmetry axis) are

$$\langle j_z^2 \rangle \approx \left(\frac{2\beta_0^2(02)+1}{3} \right) j(j+1) = +0.3j(j+1) \tag{5a}$$

$$\langle j_y^2 \rangle \approx \left(\frac{1-2(\beta_0^0(22)+\beta_0^2(02))}{3} \right) j(j+1) = +0.2j(j+1) \tag{5b}$$

$$\langle j_x^2 \rangle \approx \left(\frac{1+2\beta_{0(22)}^0}{3} \right) j(j+1) = +0.5j(j+1) \tag{5c}$$

where recoil is assumed to be directed perpendicular to the symmetry axis. Rotational angular momentum about the O—O axis, j_x, can only be generated through torsion and, given the very small lever arm about the centre of mass of OH and the reduced energy available for photofragment repulsion, virtually all the angular momentum about y, z can be associated with transfer from the bending motion.

Thus

$$\frac{\langle E_{\text{torsion}} \rangle}{\langle E_{\text{bend}} \rangle} = \frac{\langle j_x^2 \rangle}{\langle j_y^2 \rangle + \langle j_z^2 \rangle} \approx 1. \tag{6}$$

The final-mode compositions for the populations of vibrationally excited H_2O_2 generating $2OH(v=0)$ or $OH(v=1)+OH(v=0)$ after photodissociation are shown in table 3.

Table 3. Estimates of the average vibrational energy distributions following excitation of the overtone level $4\nu(OH)$ in H_2O_2

energy/cm^{-1}	dissociation channel	
	$2OH(v=0)$	$OH(v=1)+OH(v=0)$
O—H stretch	0	3567
O—O stretch	10 130	7600
HOO bend	1600	1080
torsion	1600	1080

The relative values of $\langle j_y^2 \rangle^{1/2}:\langle j_z^2 \rangle^{1/2}$ also provide a means of estimating the average parent molecular torsion angle at the instant of electronic excitation out of the intermediate overtone state. A *trans*-planar configuration, with $\varphi = 180°$ would give $\langle j_y^2 \rangle = 0$; a *cis*-planar configuration, with $\varphi = 0°$, would give $\langle j_z^2 \rangle = 0$; in practice the average configuration clearly has a torsion angle near mid-way between the two extremes, close to the angle $\varphi = 90°$, at which the torsional potentials $V^A(\varphi)$ and $V^B(\varphi)$ intersect. This strengthens the interpretation of the reduced value for the translational anisotropy, $\beta = -0.4$ for $OH(v=0)$ to overlapping excitation into the two near-degenerate electronically excited continua: a ratio $(\tilde{A}\leftarrow\tilde{X}):(\tilde{B}\leftarrow\tilde{X}) \approx 4:1$ would accommodate the observed anisotropy. Large-amplitude torsional vibrations are also consistent with the high concentration of vibrational energy, ca. 1600 cm^{-1}, into the torsional mode. For H_2O_2 molecules with an equilibrium O—O distance the barrier to free internal rotation is ca. 2500 cm^{-1}; this will decrease at extended O—O distances and many of the excited molecules must behave as hindered internal rotors, necessarily with average dihedral angles $\leq 90°$.

Intramolecular Vibrational Redistribution

The long time interval between the initial preparation of the vibrationally excited overtone level and its subsequent excitation into the dissociative continuum in a two-photon process allows more than ample time for the completion of intramolecular energy flow in the vibrational excited overtone state. When the O—H local mode is sufficiently excited $(6\nu(O—H)]$ to allow *single*-photon unimolecular decomposition in the *ground* electronic state, the need for redistribution into large [indeed infinite (!)]-amplitude motion in the O—O stretch is self-evident.[14] A number of classical trajectory calculations[36-38] and a recent quantal calculation[39] all suggest that the redistribution is mediated *via* weak coupling into the OOH bend: the subsequent transfer into the low-frequency O—O stretching motion occurs on a picosecond timescale. The quantal calculation[39] identifies two component vibrational states which are coupled into the ground-state dissociation continuum, rationalizing the bi-exponential rate of appearance of the OH fragments found by Scherer and Zewail.[16] One state accommodates only a single quantum in the torsional mode, while the other accommodates none at all, but has two quanta in the OOH bend. This absence of torsional excitation parallels the results of the classical trajectory calculations, where redistribution into torsional motion is predicted to be slow despite the relatively high density of torsional states.[40]

Under vibrationally mediated conditions, where the intermediate overtone level $[4\nu(O—H)]$ would persist indefinitely, were it not for the advent of the second photon (or another molecule), the timescale is extremely long, ca. 2 ns in this experiment. Redistribution into the torsional mode would thus have ample opportunity to play a role, as indicated by the positive $v_{OH}, j_{OH})$ correlation in the recoiling fragments.

The two different patterns of behaviour suggest that a study of the vibrationally mediated photodissociation using picosecond or femtosecond laser pulses and delay times would be particularly rewarding, offering the opportunity to monitor IVR in real time, through changes in the photofragment quantum-state distributions and their vector correlations. Sensitivity to the laser pulse *duration* can also be anticipated[41] on femtosecond timescales.

Conclusions

Determination of the vector correlations and the quantum-state distribution in the OH fragments recoiling from H_2O_2 following both direct and vibrationally mediated electronic excitation has been given detailed insights into the intramolecular dynamics, both in the vibrationally excited ground state and the electronically excited continuum. The average vibrational mode composition in H_2O_2 molecules initially excited into the O—H, local-mode state, $4\nu(O-H)$ and allowed to evolve over a nanosecond timescale has been determined for the first time. There is clear evidence for excitation of both the torsional and OOH bending, as well as the O—O stretching modes, through intramolecular vibrational redistribution. In addition, there is strong evidence for excitation into both the first *and* the second excited electronic continua, $\tilde{A}\,^1A$ and $\tilde{B}\,^1B$, which approach degeneracy as the interfragment distance increases and the dihedral torsional angle approaches $\varphi = 90°$.

Future experiments should include picosecond or sub-picosecond time resolution to allow the evolution of the overtone state to be followed in real time; the use of two colours to allow 'Franck–Condon' scanning of the long-range part of the electronically excited potential-energy hypersurfaces; velocity-aligned Doppler spectroscopy[42,43] to clarify the inter-fragment correlations; and the extension to HOOD to distinguish between the two fragments.

References

1 Dynamical Stereochemistry Issue, *J. Phys. Chem.*, 1987, **91**, 5365–5515.
2 C. H. Greene and R. N. Zare, *Annu. Rev. Phys. Chem.*, 1982, **33**, 119.
3 J. P. Simons, *J. Phys. Chem.*, 1987, **91**, 5378.
4 P. L. Houston, *J. Phys. Chem.*, 1987, **91**, 5388.
5 G. E. Busch, R. T. Mahoney, R. I. Morse and K. R. Wilson, *J. Chem. Phys.*, 1969, **51**, 449; 837.
6 R. Schmiedl, H. Dugan, W. Meier and K. H. Welge, *Z. Phys. A*, 1982, **304**, 137.
7 I. Nadler, D. Margarefteh, H. Reisler and C. Wittig, *J. Chem. Phys.*, 1985, **82**, 3885.
8 G. M. Nathanson and G. M. McClelland, *J. Chem. Phys.*, 1984, **81**, 629; 1986, **84**, 3170.
9 N. Ohta and H. Baba, *Chem. Phys. Lett.*, 1988, **146**, 410.
10 T. M. Ticich, M. D. Likar, H-R. Dübal, L. J. Butler and F. F. Crim, *J. Chem. Phys.*, 1987, **87**, 5820.
11 A. Sinha, R. L. Vander Wal, L. J. Butler and F. F. Crim, *J. Phys. Chem.*, 1987, **91**, 4645.
12 M. D. Likar, A. Sinha, T. M. Ticich, R. L. Vander Wal and F. F. Crim, *Ber. Bunsenges. Phys. Chem.*, 1988, **92**, 289.
13 M. D. Likar, J. E. Baggott, A. Sinha, T. M. Ticich, R. L. Vander Wal and F. F. Crim, *J. Chem. Soc., Faraday Trans. 2*, 1988, **84**, in press.
14 F. F. Crim, in *Molecular Photodissociation Dynamics, Adv. Gas Phase Photochemistry and Kinetics*, M. N. R. Ashfold and J. E. Baggott (Royal Society of Chemistry, London, 1987), p. 177.
15 M. Brouard, M. T. Martinez, J. O'Mahony and J. P. Simons, *Chem. Phys. Lett.*, 1988, in press.
16 N. F. Scherer and A. H. Zewail, *J. Chem. Phys.*, 1987, **87**, 97.
17 K. H. Gericke, S. Klee, F. H. Comes and R. N. Dixon, *J. Chem. Phys.*, 1986, **85**, 4463.
18 F. J. Comes, K. H. Gericke, A. U. Grünewald and S. Klee, *Ber. Bunsenges. Phys. Chem.*, 1988, **92**, 273.

19 M. P. Docker, A. Hodgson and J. P. Simons, *Faraday Discuss. Chem. Soc.*, 1986, **82**, 25.
20 J. August, M. Brouard, M. P. Docker, A. Hodgson, C. J. Milne and J. P. Simons, *Ber. Bunsenges. Phys. Chem.* 1988, **92**, 264.
21 M. P. Docker, *PhD Thesis* (University of Nottingham, 1987).
22 A. U. Grünewald, K. H. Gericke and F. J. Comes, *J. Chem. Phys.*, 1987, **87**, 5709.
23 K. H. Gericke, A. U. Grünewald, S. Klee and F. J. Comes, *J. Chem. Phys.*, 1988, **88**, 6255.
24 H-R. Dübal and F. F. Crim, *J. Chem. Phys.*, 1985, **83**, 3863.
25 L. J. Butler, T. M. Ticich, M. D. Likar and F. F. Crim, *J. Chem. Phys.*, 1986, **85**, 2331.
26 J. August, M. Brouard and J. P. Simons, *J. Chem. Soc. Faraday Trans. 2*, 1988, **84**, 587.
27 T. Nagata, T. Kondow, K. Kuchitsu, G. W. Loge and R. N. Zare, *Mol. Phys.*, 1983, **50**, 49.
28 C. H. Greene and R. N. Zare, *J. Chem. Phys.*, 1983, **78**, 6741; see also D. A. Case, G. W. McClelland and D. R. Herschbach, *Mol. Phys.*, 1978, **35**, 541; A. J. Bain and A. J. McCaffery, *J. Chem. Phys.*, 1985, **83**, 2627.
29 R. N. Dixon, *J. Chem. Phys.*, 1986, **85**, 1866; see also A. C. Kummel, G. O. Sitz and R. N. Zare, *J. Chem. Phys.*, 1988, **88**, 7357; M. P. Docker, *Chem. Phys.*, 1988, in press.
30 R. Schinke and V. Staemmler, *Chem. Phys. Lett.* 1988, **145**, 486.
31 R. Schinke, *J. Phys. Chem.*, 1988, **92**, 4015.
32 R. Schinke, *Annu. Rev. Phys. Chem.*, 1988, **39**, in press.
33 D. L. Baulch, R. A. Cox, R. F. Hampson Jr, J. A. Kerr, J. Troe and R. T. Watson, *J. Phys. Chem. Ref. Data*, 1984, **13**, 1259.
34 R. Vasudev, R. N. Zare and R. N. Dixon, *J. Chem. Phys.*, 1984, **80**, 4863.
35 M. D. Morse and K. F. Freed, *J. Chem. Phys.*, 1983, **78**, 6045; M. D. Morse, Y. B. Band and K. F. Freed, *J. Chem. Phys.*, 1983, **78**, 6066.
36 T. Uzer, J. T. Hynes and W. P. Reinhardt, *J. Chem. Phys.*, 1986, **85**, 5791.
37 B. G. Sumpter and D. L. Thompson, *J. Chem. Phys.*, 1987, **86**, 2805.
38 J. Santamaria, C. Getino-Gonzalez and G. S. Ezra, *J. Chem. Soc.*, *Faraday Trans. 2*, 1988, **84**, in press.
39 K. Nishikawa and S. H. Lin, *Chem. Phys. Lett.*, 1988, **149**, 243.
40 M. S. Child, *J. Chem. Soc.*, *Faraday Trans. 2*, 1988, **84**, in press.
41 J. S. Hutchinson and K. T. Marshall, *J. Chem. Soc.*, *Faraday Trans. 2*, 1988, **84**, in press.
42 Z. Xu, B. Koplitz, S. Buelow, D. Baugh and C. Wittig, *Chem. Phys. Lett.*, 1986, **127**, 534.
43 R. N. Dixon, J. Nightingale, C. M. Weston and X. Wang, *Chem. Phys. Lett.*, 1988, in press.

Femtochemistry: The Role of Alignment and Orientation

Ahmed H. Zewail†

Arthur Amos Noyes Laboratory of Chemical Physics‡ California Institute of Technology, Pasadena, California 91125, U.S.A.

Some aspects of alignment and orientation have been considered for femtochemistry experiments. Elementary theoretical descriptions of the time evolution of alignment and angular momenta have been discussed and related to the radial and angular parts of the potential-energy surface. Applications to ICN unimolecular dissociation, $H + CO_2$ 'oriented' bimolecular reaction, and crossings between different potential-energy curves in alkali-metal halide reactions $(M + X)$ are given. Emphasis is on the femtosecond dynamics of the transition-state region and the clocking of fragment separation in real time.

1. Introduction

In femtochemistry, chemistry on the femtosecond timescale, one monitors the reaction using two laser pulses of different colours. The first pulse initiates the reaction and sets the zero of time (clocking). The second pulse probes the fragments as they separate from each other or as they form new bonds. Because of the time resolution and sensitivity, the separation can be viewed with sub-Ångstrom resolution. Elsewhere,[1-7] the concept of the experiments has been discussed in relation to the potential-energy surfaces (PES) of the reaction, and applications to a number of reactions hae been detailed. Here, we shall address the role of alignment and orientation in these femtochemical experiments.

On the femtosecond timescale, the fragments are in close proximity and the time evolution of coherence, angular momenta and possibly trapping resonances is expected to be important. Hence, borrowing from techniques used to study alignment of fragments at asymptotic distance separations[8] (*i.e.* time → ∞) one can perhaps observe the 'during' alignment of the reaction if femtosecond pulses are used. These studies should help in answering some new questions about the ephemeral transition-states orientation and population, and the angular dependence of the PES.

Some elementary theoretical descriptions of these time-dependent processes are given here. Comparison with experiments involving dissociation reactions will be made and extension to 'orientated' bimolecular reactions (collision complexes) will be discussed. We will first briefly highlight the experimental methodology and results.

2. The FTS Technique and Some Applications

The main technique described here is femtosecond transition-state spectroscopy (FTS) which is a pump-probe method that allows us to obtain snapshots of reactions while fragments are separating, or encountering each other. If ultrashort pulses are employed, the sensitivity of the detection is enhanced by a factor of 10^4–10^6 when compared with time-integrated, steady-state experiments. Essentially all molecules traversing the transition states can be detected, and this is a key feature of femtochemistry. The difficulty,

however, comes in generating pulses and in developing the techniques for observing changes on the femtosecond timescale.

The FTS signal recorded will be some measure of the absorption by the fragment of the probe pulse at wavelength λ_2 as a function of the time-delay τ between pump and probe. This could be accomplished, for instance, by measuring the change in the transmission of the probe. Since the experiment would not be background-free, far better sensitivity can be obtained through, for instance, the detection of the laser-induced fluorescence (LIF), or the multiphoton ionization (MPI) generated by the probe. Typically, we measure the FTS signal when λ_2 is tuned to the absorption wavelength of the free fragment, λ_2^∞ (where ∞ denotes that $R \to \infty$), and at a number of wavelengths absorbed by the transition states, λ_2^* (where $*$ denotes the transition-state region of R). Then a surface of measurements $A(t; \lambda_{2(a)}^*, \lambda_{2(b)}^*, \dots, \lambda_2^\infty)$ is constructed. This surface is related to the dynamics and to the PES of the reaction, as we will discuss below. The experiments are then repeated for different pump wavelengths (λ_1).

(a) Unimolecular Reactions

In the simplest FTS experiment (clocking), the probe is centred at an absorption of one of the free fragments. In this case, the absorption of the probe will initially be negligible and will only become substantial when the fragments achieve large internuclear distance and are therefore (essentially) non-interacting. The delay at which the probe absorption 'turns on,' $\tau_{1/2}$, is therefore a direct measurement of the time required for complete (or nearly complete) internuclear separation. In other words, FTS provides a 'clock' of the time required to break the bond and, thus, is a fundamental measurement.

The experiment can be pictured simply as a measure of the femtosecond 'time-of-flight' on the excited-state PES from the initially excited configuration at R_0 to the free fragment configuration, where the probe opens a 'window' on the PES. If the experiment is performed for various probe spectral widths, then additional information on the asymptotic shape of the potential can be obtained. Additionally, the clocking experiment offers significant practical advantages which have been discussed by Rosker *et al.*[3] Such clocking experiments have been performed on the dissociation reaction of ICN,

$$\text{ICN}^* \to [\text{I} \cdots \text{CN}]^{\ddagger *} \to \text{I} + \text{CN} \tag{1}$$
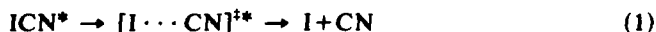
and provide $\tau_{1/2} = 205 \pm 30$ fs (see fig. 1).

FTS experiments can also be made by tuning λ_2 away from the transition of the free fragment. The final products will thus not absorb the probe wavelength, but instead the transition states of the reaction may do so. The FTS transient will therefore be expected to build-up, as the molecules enter the optically coupled region of the probe, and then subsequently decay, as the molecules move on to final products (see fig. 2). By obtaining FTS transients for various values of λ_2^*, information on the shapes of the PESs involved can be obtained. These experiments have been detailed elsewhere by Roster *et al.*[3] and discussed in relation to the PESs.

To relate these measurements to a dissociation time and to the characteristics of the PES, we first consider for repulsion between the I and the CN fragments a potential of the form:[9]

$$V(R, \theta) = V_0 \exp(-R/L_1) f(R, \theta) \tag{2}$$

where L_1 is the repulsion length parameter and $f(R, \theta)$ describes the angular part. The classical equation of motion for this system, without $f(R, \theta)$, can be integrated to give analytically the internuclear separation of the fragments as a function of time, $R(t)$, and the corresponding potential as a function of time, $V(t)$.

We then ask, what defines a dissociation time? If it were defined as the time for the two fragments to reach a separation at which their interaction energy is negligible, the dissociation time would depend on the sensitivity with which the energy can be measured;
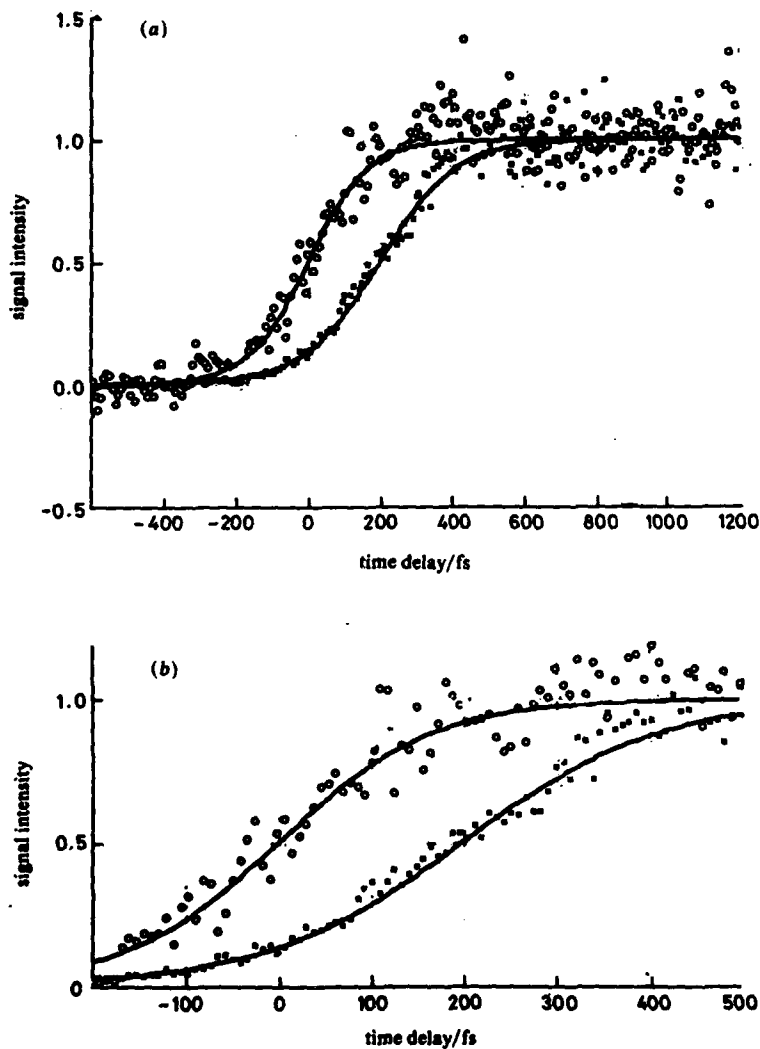
Fig. 1. Typical on-resonant FTS results for the ICN reaction. (a) O, the MPI calibration signal, which gives the detection-response function and the zero of time;[3] □, the FTS data for ICN, taken with $\lambda_2 = \lambda_2^\infty$. Note the time delay between these traces, $\tau_{1/2}$ (b) The same data, shown on an expanded scale.

an infinite time is required to reach infinite separation. A more invariant definition is obtained as follows: consider the difference between the time taken for the fragments to separate from R_0, the separation at the instant of photoexcitation, to R (as they travel along the actual potential) minus the time which would be required had the fragments travelled at the terminal velocity (v). Then τ_d is defined as the limit of this difference as $R \rightarrow \infty$. For the potential described above (with no anisotropy), one obtains: $\tau_d = (L_1/v) \ln 4$. While it is well defined, this τ_d is obtainable only from a
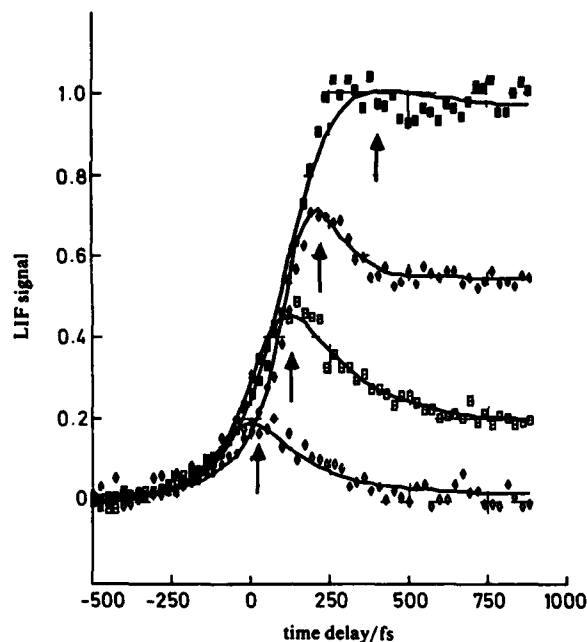
Fig. 2. Typical off-resonant FTS results for the ICN reaction. ■, $\lambda_2 = 389.7$ nm; ●, $\lambda_2 = 389.9$ nm; □, $\lambda = 390.4$ nm; ◇, $\lambda_2 = 391.4$ nm The zero of time is determined separately for each data set. Comparison with theory is discussed in ref. (3).

hypothetical experiment requiring the measurement of minute differences in long arrival times (see fig. 3).

A more useful description of bond breaking has been recently developed[3,10] to consider the time dependence of fragment separation and te absorption by fragments during this separation. When the fragments develop to be spectroscopically free, the absorption achieves a maximum. Dissociation can be spectroscopically free, the absorption achieves a maximum. Dissociation can be defined as the time delay when the mid-point of the absorption is reached:

$$\tau_{1/2} = (L_1/v) \ln(4E/\gamma). \tag{3}$$

Here, γ is the half-width of the energy distribution of the probe pulse and E is the energy available above dissociation ($E \gg \gamma$). An important observation is contained within this analysis: the probe spectral width determines a 'window' through which the free CN is viewed, and so affects $\tau_{1/2}$. Since we have both γ (40 cm^{-1}) and E (6000 cm^{-1}), the above expression yields for the repulsion length parameter $L_1 = 0.8$ Å, for the exponential potential discussed above. A similar procedure can be used to calculate length parameters of other potential shapes, e.g. R^{-n}. According to the above analysis, the potential falls to $1/e$ of its initial value in 0.8 Å, but the distance corresponding to $\tau_{1/2}$ (the time taken for the potential to drop to γ) is 4 Å.

There are several points to be made regarding this reaction. First, the PES of ICN dissociation is more complex than that illustrated here because there are two channels (with possible crossings) for dissociation involving the production of iodine either in its ground or its excited spin-orbit states (fig. 4). However, at 306 nm our available energy is just below the excited I* state channel, and it is known experimentally that
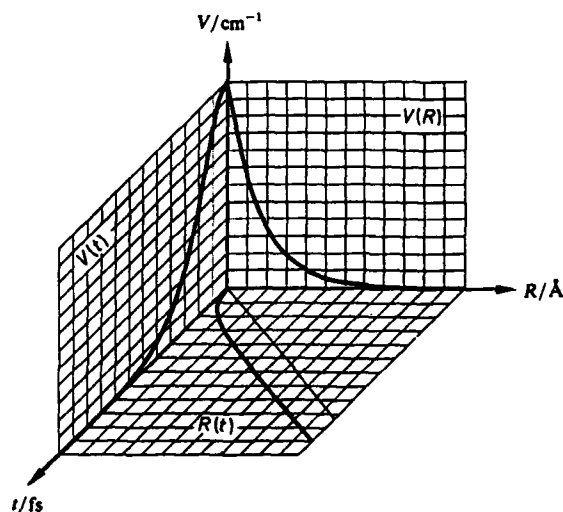
Fig. 3. A potential-energy surface as a function of the parameter t (time), with 25 fs per division, and as a function of the parameter R (internuclear distance), with 0.5 Å per division. An exponential shape is assumed and the initial potential energy at $t = 0$ and ($R = 0$) is 6000 cm^{-1} (17.2 kcal mol^{-1} above dissociation). Note that the recoil velocity, given by the instantaneous slope of $R(t)$ vs. t, rapidly achieves the terminal value. The difference between $R(t)$ and the straight line (which is determined by the terminal velocity) approaches a constant at long time; this difference represents the invariant τ_d defined in the text.

at this excitation wavelength the reaction is to the ground-state channel, which correlates with a bent state. The measurements reported here clock the dynamics of I—CN recoil and the development of free CN. As pointed out by several authors,[9,11,12] the dynamics that produce rotational excitation are due to bending, and could be on a shorter timescale. Time-resolved alignment experiments (discussed below) should aid us in resolving this bending dynamics. At our wavelength of excitation, the product rotational-state distribution of the nascent CN was explained by nearest-neighbour repulsion effects exclusively.[13] This is consistent with the picture here of repulsion between CN and iodine. Secondly, the absorption measurement depends also on the characteristics of the upper-state (I+CN*) potential. However, in the asymptotic limit ($R \to \infty$), $\tau_{1/2}$ is described, for the shape of the transients, the direction of the probe wavelength shifts and the effect of tuning the pump wavelength can separate V_1 and V_2 dynamics. Finally, we assumed here a repulsive potential, but there exists a method to invert the data to give the shape of the PES and to account for the attractive terms in the potential.[15] What about the angular part $f(R, \theta)$ of the PES? This we address below in section 3.

Theoretically, these observations are reproduced using classical-mechanical[3] as well as quantum-mechanical[16] treatment of the dissociation (see fig. 5). Even kinetics can describe the general behaviour of the transients as shown in ref. (3). From these results we determine that the transition states en route to dissociation live for only 50–20 fs, depending on the R region probed.

(c) Extension to Bimolecular Reactions

An important new issue arises for bimolecular reactions that is not a concern in the unimolecular case. For a unimolecular reaction, the reaction begins when the laser
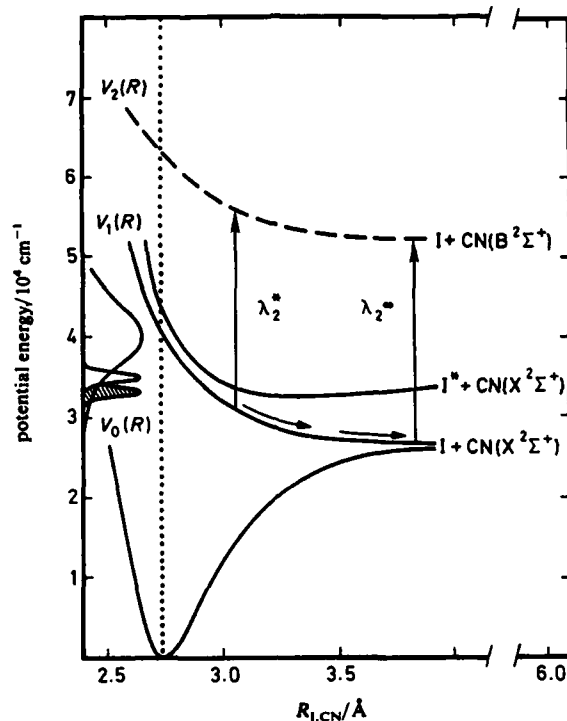
Fig. 4. The (typical) potential-energy surfaces of ICN and the concept of FTS experiments at $\lambda_2^{\ddagger}$ and λ_2^{∞}. The pump pulse causes a vertical transition from V_0 to V_1, and the subsequent motion on this surface is indicated. The transition-state is probed by $\lambda_2^{\ddagger}$, or the final state by λ_2^{∞}, which are shown by the respective arrows from V_1 to V_2. The absorption spectrum of ICN and the pump energies used are sketched on the left. Note that the difference between $\lambda_2^{\ddagger}$ and λ_2^{∞} is not to scale and that the van der Waals wells are not shown.

pulse initiates excitation and subsequent dissociation. Thus, the interval between the firing of this laser pulse and the subsequent probe laser pulse represents the actual amount of time that the reaction has been taking place. However, for a bimolecular reaction, whether in bulk or in crossed beams, there is no comparable way to establish the beginning point for the reaction. So there would appear to be no hope of determining the time of formation and decay of transient collision complexes with lifetimes of only femtoseconds to picoseconds.

However, a special trick enables one to establish the zero of time within an uncertainty governed by the laser pulse duration only, for a whole class of bimolecular reactions. This has now made it possible to study real-time dynamics of these bimolecular reactions. The first of these experiments by Scherer *et al.*,[17] in collaboration with Bernstein, has been conducted in the picosecond, rather than femtosecond, time domain, but the principle is the same. The method involves the use of a beam of a van der Waals 'precursor molecule' and containing the potential reagents in close proximity. Here, we make use of the approach of weak molecular complexes, as pioneered by the groups of Wittig and Soep to study product-state distributions,[18,19] so we can establish the zero of time and hence follow the course of the reaction in real time. For the reaction studied,

$$H + OCO \rightarrow [HOCO]^{\ddagger} \rightarrow OH + CO \qquad (4)$$
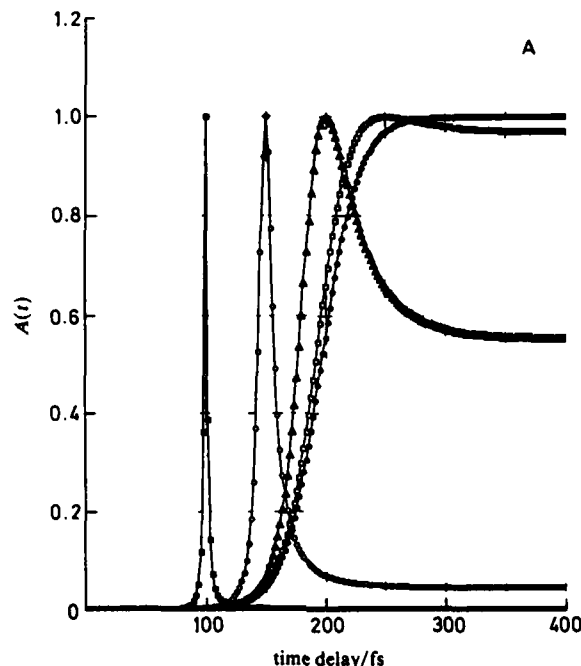
Fig. 5. (A) Predicted FTS results from classical mechanical calculation (see text): parameters are $L_1 = 0.8$ Å, $v = 0.026$ Å fs^{-1}, $E = 6000$ cm^{-1}, and $\gamma = 40$ cm^{-1} (representative for ICN). The curves shown are for (from left-to-right) $t^* = 100, 150, 200, 250$ and 1000 fs. The peak amplitude of each data set has been normalized to one and the calculation does not take into account the finite temporal width of the pulses. [For more details see ref. (3). Note the delay of the free fragment absorption, by 200 fs, and the build-up and decay of absorption of fragments in the transition region (λ_2^*).

The precursor molecule was IH$\cdots$OCO, formed in a free-jet expansion of a mixture of HI and CO$_2$ in an excess of helium carrier gas. Such van der Waals complexes have favourable geometry which limits the range of impact parameters and angles of attack of the H on the OCO.[18]

To clock the reaction, an ultrashort laser pulse initiates the experiment by photodissociating the HI, ejecting a translationally hot H atom in the general direction of the nearest-neighbour O atom in the CO$_2$. A probe laser pulse tuned to a wavelength suitable for detection of the OH was delayed relative to the photolysis pulse using a Michelson interferometer. The OH appeared after a delay of a few picoseconds from the initiation pulse. This delay represents a direct measure of the lifetime of the [HOCO]‡ collision complex at the available energy of the collision. The lifetime changes with translational energy. A new series of experiments using femtosecond pulses is being undertaken in order to follow the formation and decay of the collision complex in the femtosecond region, and to study the effect of limited impact parameter (orientation), an important feature of this approach, on the reaction dynamics. Comparison with classical trajectory calculations,[20] based upon the *ab initio* calculated PES, will be important.

It is probable that this technique will be applicable to a wide variety of bimolecular reactions, including not only those involving long-lived collision complexes that last for
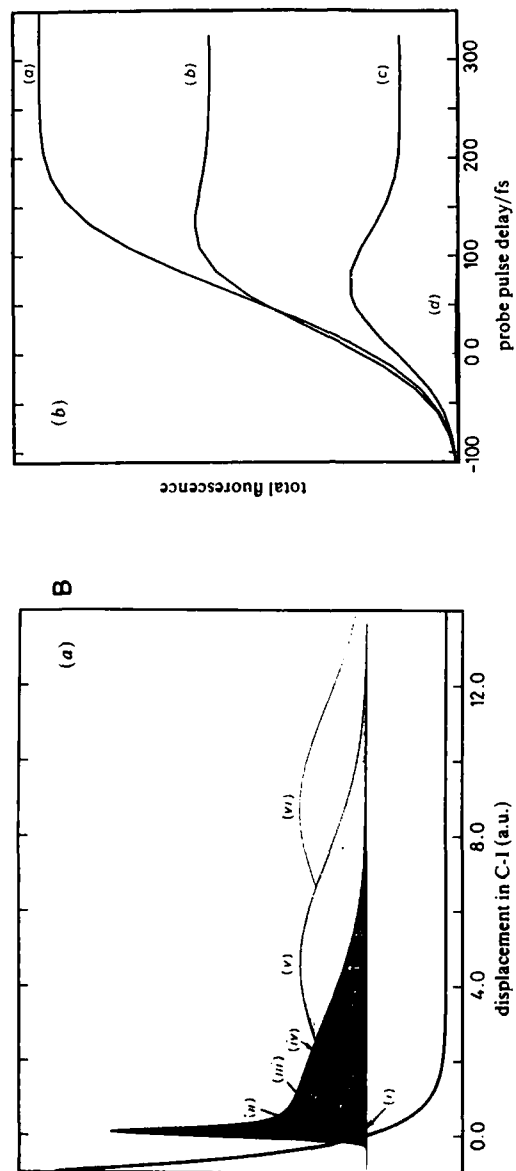
Fig. 5. (B) Predicted FTS results (b) from quantum calculation of the wavepacket propogation (a) for the ICN dissociation, using 125 fs pulses. The general agreement with experiment and with the classical model is good. Taken from ref. (16).

picoseconds, but also direct-mode reactions with transition-state lifetimes in the fem-tosecond range. As with unimolecular reactions, off-resonance detection should allow detailed measurements of the build-up and decay of the transition states with the zero of time for the bimolecular reaction being known to fs time resolution. The fact that the reagents are orientated (at least to some extent) also makes the alignment experiment described below of particular interest.

(c) Reactions from the 'Alkali-metal Age': Covalent to Ionic Crossings

The femtochemistry discussed thus far for unimolecular elementary reactions [section 2(a)] involves the process of bond breaking on dissociative potential-energy surfaces. The molecules are in 'transition' for only 50 fs or so, as evidenced by the rise and decay observed in the ICN experiments and confirmed by theory. If, however, in the process of falling apart, the system encounters a well in the potential-energy surface, or if there is more than one degree of freedom involved, the system cn be 'trapped' and thus exhibit behaviour indicative of quasi-bound states, or resonances. In real time, manifestation of these resonances would be a slow-down in the appearance of free fragments and possibly the appearance of oscillations reflecting the vibrational resonance frequency of the wavepacket of the dissociating fragments.

The classic reactions of alkali-metal–halogen are prototype systems for such studies. This class of reactions has been studied before in the 'alkali-metal age' of molecular-beam scattering of alkali metal (M) and halogen (X)[21-24] and observing their real-time behaviour will be of great interest to current studies in the 'femto age.' Because of the ionization potential of M and the electron affinity of X, the energy of $M^+ + X^-$ is higher than that of $M + X$. In the ground state the molecule is ionic M^+X^-, and this state correlates with $M^+ + X^-$ (see fig. 6). Hence, the covalent potential-energy curve $(M + X)$
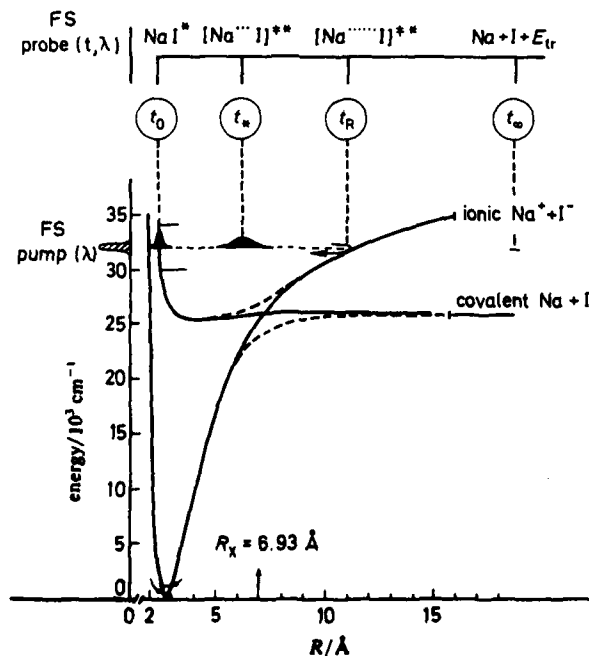
Fig. 6. The PES of an alkali-metal halide (NaI) reaction, and the concept of FTS experiments at λ_2^∞ and $\lambda_1^\ddagger$.

crosses the ionic (Coulombic) curve. Because of this crossing (or avoided crossing) at certain $M \cdots X$ separation (R_x), electron harpooning takes place. The potential-energy surfaces for such important processes have been described in a classic series of papers by Berry, and the reader is referred to the review article which also describes many of the experiments done on these systems[25]

In the femtosecond experiments by Rose *et al.* and Rosker *et al.*,[4,5] the initial pulse at λ_1 takes the molecule from the M^+X^- ground state to the covalent surface MX*. The second pulse probes the reaction at λ_2^* (transition-state region) and at λ_2^∞ (final product; in this case Na):

$$MX^* \rightarrow [M \cdots X]^{\ddagger *} \rightarrow M + X \qquad (M = Na; \; X = I, \, Br). \qquad (5)$$
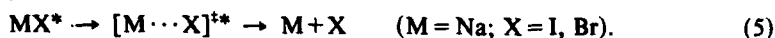
En route to products, the $[M \cdots X]^{\ddagger *}$ transition-state molecules 'decide' between ionic and covalent paths; either the packet of MX* will be trapped on the adiabatic potential-energy curve or it will dissociate by following the non-adiabatic curve. The two cases have entirely different temporal behaviour and, if there is trapping, the frequency and amplitude of the oscillations will provide details of the nature of the surfaces and the strength of the coupling. Comparison with theory[26] can then be made.

The experiments show (fig. 7) a striking oscillatory behaviour (when probing at λ_2^*) that persists for picoseconds (*cz.* 10 oscillations) in the case of NaI, and for less time (*ca.* 2 oscillations) for the NaBr case. Probing on-resonance (at λ_2^∞) gives a rise with plateaux separated by the same oscillation frequency. This on-resonance 'integration' of the trajectories is a clear demonstration of the concept of FTS, discussed earlier. The average period for NaI reaction is 1.25 ps, which corresponds to a frequency of 27 cm^{-1}. It is concluded that the packet for NaI is effectively trapped in the adiabatic well *en route* to products, and that the observed oscillations represent 'pulses of Na atoms' leaving the well. Since the oscillation damping time for NaI is *ca.* 10 ps, one crossing on the
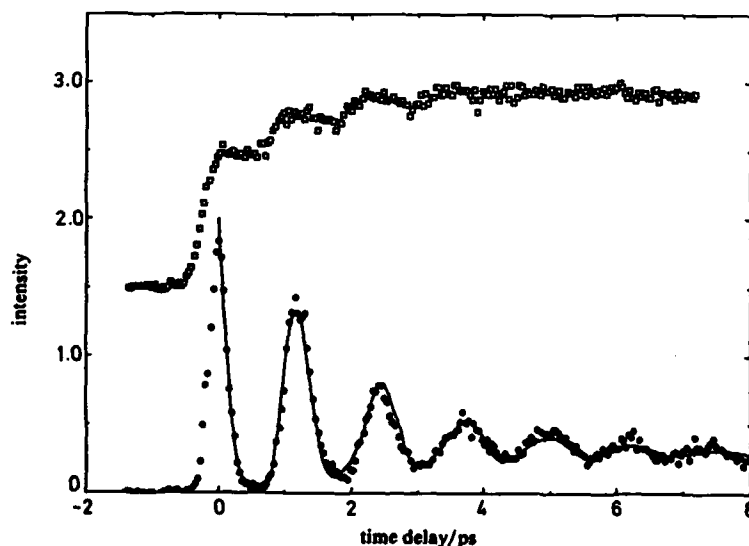
Fig. 7. Experimental FTS results obtained at λ_2^* and λ_2^∞ (589 nm) for the reaction: Na I* → [Na $\cdots$ I]$^{\ddagger *}$ → Na + I. The oscillatory (resonance) behaviour at the bottom is obtained $(\lambda_1 = 310 \, nm)$ when probing at λ_2^*, while the transient at the top was obtained by probing the free fragment (Na). Note that when probing the free fragment the signal shows an 'integration' which results in plateaux separated by exactly the resonance frequency. The NaBr reaction was also studied and results are discussed in ref. (4) and (5).
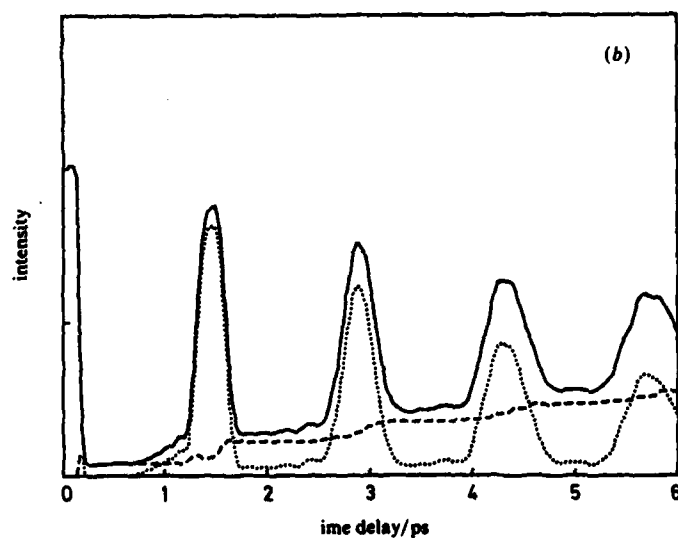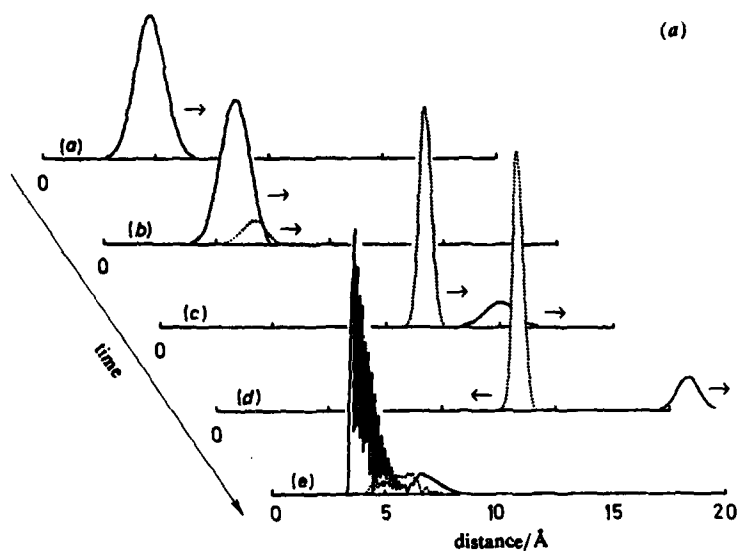
Fig. 8. (a) The quantum mechanical time evolution of the wave packet in the reaction of NaI. Note the 'splitting' of the packet into ionic and neutral states and their separate time evolutions. These results are typical for the different λ_1 values studied. (b) The simulated FTS transients for $\lambda_2^{\ddagger}$ and λ_2^{∞} probings and the total signal (—). $\lambda_1 = 300$ nm. Note the similarity to the experimental results in fig. 7. The calculations are detailed in ref. (27) by Engel et al.

outward phase per oscillation (*ca.* 1 ps) has a probability of *ca.* 0.1 to escape from the well. For NaBr, the frequency of oscillation is similar in magnitude, but severe damping is observed. Thus, the crossing for NaBr is much more facile than for NaI, consistent with theoretical expectation. In ref. (4) and (5) we compared theory with experiments and obtained the Landau–Zener probability of escape, the anharmonicity of the PES, and the coupling between the covalent and ionic curves. An interesting question is how the 'dephasing' and spread of the wavepacket influences the dissociation rate, as determined by the decay of the oscillations. The experiments do show manifestations of this decay and spreading, and theoretical modelling of the wavepacket dynamics in these prototype systems is important. Very recently, quantum and semiclassical calculations (fig. 8) have been performed[27] and agreement with the experiment is good.

Real-time observations of the dynamics at different λ_1 and λ_2^* should now allow one to view the motion of the wavepacket under different conditions from the Franck–Condon excitation region all the way to 'infinite separation,' or fragmentation, making contact with absorption spectroscopy, atomic beam scattering experiments promise to provide rich information bearing upon the shape of the PES, curve crossings and interactions among different degrees of freedom in many other reactions. In future publications,[28] we will detail these findings and relate to studies using wing emission spectra by Polanyi's group.[29]

3. Femtosecond Alignment and the Angular Part of PES

To this point, we have discussed the reaction $ABC^* \rightarrow A + BC$ as if its configuration space were one-dimensional (with no centrifugal contribution), the only parameter being the distance of A from the centre of mass of BC. However, the angular part of the potential may be important. As an example, the repulsion of bending ABC will generate a torque during the reaction . This time-dependent evolution of angular momentum is related to the alignment, which can be studied using FTS by polarizing the fs pulses. Transients taken with parallel pump and probe polarizations can be compared with those taken with perpendicular polarizations, as done in time-integrated experiments,[30] to probe the evolution on the femtosecond timescale.

The time dependence of alignment and angular momenta are reflected in two types of measurements. First, the angular part of the potential might lead to different $\tau_{1/2}$ values, depending on the final angular momentum state of the BC fragment. Secondly, the loss of alignment at early times will reflect the degree of the torque which leads to rotations in the BC fragment. Because the BC fragment most probably will be produced in a distribution of angular momentum states, the coherence time is expected to be short. These points are discussed next.

(a) Time Evolution of Alignment and Coherence

Here, we shall consider a triatomic molecule (*e.g.* ICN) with two coordinates, R and θ. R is the distance between the I atom and the centre of mass of the CN. The angle between r (the CN direction) and R is θ. Using the well known formula[31] for the angular dependence of the signal, and transforming from the space-fixed coordinate system to the molecule-fixed axes system, one obtains expressions for measurements of the signal when the E vector of the probing pulse is parallel, $I_{\parallel}(t)$, or perpendicular, $I_{\perp}(t)$, to the E vector of the pump pulse:

$$I_{\parallel}(t) = 1 + \frac{\beta}{10} + \frac{3\beta}{10} \cos(2j\omega_0 t) \qquad (6a)$$

$$I_{\perp}(t) = 1 - \frac{\beta}{20} - \frac{3\beta}{20} \cos(2j\omega_0 t). \qquad (6b)$$

In these equations, an overall constant is neglected and ω_0 is the fundamental rotational angular frequency. $j\hbar$ is the angular momentum of the fragment (CN), and β, as usual, is equal to 2 for a parallel transition (the CN B $\leftarrow$ X transition is parallel).

From the above expressions we note several points. First, in this case, the alignment of the CN (in a given j) generated by the dissociation impulse is periodic. Secondly, $I_\parallel(t)$ and $I_\perp(t)$ have identical periodicity but they are out of phase. The period of the oscillation is determined by $2\omega_0$. At $t = 0$ the ratio of the two absorptions is 3. For the ICN dissociation, we can obtain the expected time evolution. Since $j\hbar = \omega I$, one obtains for $j = 5$ that the CN will execute a revolution in *ca.* 1.7 ps. For $j = 25$, it will spend *ca* 340 fs in one revolution.† Accordingly, the transients will be periodic with the time constants determined by the characteristic j-state dynamics.

The problem is that the dissociation impulse does not produce the CN in one j state. Instead, because of the distribution in the torque (in this case, the bending angles) many j states are produced in the course of dissociation. For ICN, *e.g.* at 308 nm excitation, the average CN rotational energy is *ca.* 1200 cm^{-1} (the average j is 25) and the distribution is very wide. As a result of this distribution, the 'discrete coherence' described above will be replaced by 'dephasing,' and the question is then: what is the dephasing time, and what is the expected $I_\parallel(t)$ and $I_\perp(t)$ in the course of dissociation?

To handle these questions, we will assume a distribution of j states produced by dissociation. For simplicity, we take this distribution, $P(j)$, to be a Gaussian (centred at $j = 0$), and separate the alignment and population dynamics. Then, we can average the above equations over this distribution and obtain:

$$\langle I_\parallel(t)\rangle = \left(1 + \frac{\beta}{10} + \frac{3\beta}{10}\exp(-t^2/\tau_c^2)\right) A(t) \tag{7a}$$

$$\langle I_\perp(t)\rangle = \left(1 - \frac{\beta}{20} - \frac{3\beta}{20}\exp(-t^2/\tau_c^2)\right) A(t) \tag{7b}$$

where τ_c is the dephasing time given by $(\omega_0\Delta_j)^{-1}$ being the half-width of the distribution in j. $A(t)$ is the usual population ('incoherent') transient function (build-up of free fragment absorption or build-up and decay of transition-state absorption). We note that the ratio at $t = 0$ is again 3. However, the limiting values at long times will be 1.2/0.9 (and not 1) for exponential $A(t)$. The transients in this case will show decay in $I_\parallel$ experiments and a build-up in the $I_\perp$ experiments with a time constant τ_c. This is reminiscent of the problem of rotational diffusion of molecules in liquids.

To see the connection, we write the expressions for the case of liquids:[32]

$$I_\parallel^L(t) = \frac{I_0}{3}[1 + 2r(t)]\exp(-t/\tau_f) \tag{8a}$$

$$I_\perp^L(t) = \frac{I_0}{3}[1 - r(t)]\exp(-t/\tau_f) \tag{8b}$$

where τ_f is the incoherent fluorescence decay, and $r(t)$ describes the rotational diffusion, usually given as $r_0\exp(-t/\tau_r)$. According to these expressions, when $\tau_f > \tau_r$, then the ratio of $I_\parallel$ and $I_\perp$ at $t = 0$ is $(1 + 2r_0)/(1 - r_0)$. For a dipole transition, $r_0 = 0.4$ and this ratio is again 3! The signal will show the expected decay behaviour for $I_\parallel$ and build-up for $I_\perp$, and as $t \to \infty$, the ratio is 1 (not 1.2/0.9). On the other hand, if $\tau_f < \tau_r$, then the ratio is simply $(1 + 2r_0)/(1 - r_0)$ at all times. The same kind of behaviour can be seen from eqn (7a) and (7b) in the case of dissociation if we take $A(t)$ to be an exponential decay, representing, *e.g.* the decay of the transition states.

† For simplicity of notation we shall use j to denote the angular momentum of the CN fragment, although more conventionally we should use N.

To compare theory [eqn (7)] with experiments, we take $A(t)$ to be the absorption of fragments *during* dissociation. The model for this $A(t)$ has been developed elsewhere,[3,10] and here for illustration we consider the simplest case of a one-dimensional PES. Then,

$$A(t) = \frac{C}{Y^2 + W^2(t, t^*)} \qquad (9a)$$

where

$$W(t, t^*) = E(\text{sech}^2 x - \text{sech}^2 x^*). \qquad (9b)$$

The total energy is E and x and x^* are simply $vt/2L$ and $vt^*/2L$; v is the recoil velocity, L is the potential repulsion parameter [*i.e.* L_1 in eqn (3)], t^* is the time for maximum absorption by the probe and C is a constant. The model explains well the observed transients when $t^* \rightarrow \infty$ (free fragment detection) and for finite t^* values (transition states detection), and is consistent with quantum calculations as described above and shown in fig. 5.

We now use eqn (7) and simulate the expected behaviour for $\langle I_{\parallel} \rangle$ and $\langle I_{\perp} \rangle$ for different τ_c and t^*. Fig. 9 shows these calculations. It is interesting to note that the anisotropy becomes more pronounced as t^* becomes shorter. This is expected since the dephasing time is finite, and if we probe at early times on the PES we have a better chance for observing the large differences between $I_{\parallel}$ and $I_{\perp}$. Note that if the rotational distribution of the fragment $P(j)$ is shifted from $j = 0$, as in this case, then the coherence decay of eqn (7) will be modulated by $\cos(2\omega_0 j_{max} t)$. For $j_{max} = 25$, the period of the oscillation is 170 fs, longer than τ_c and hence is relatively unimportant.

The dephasing time can be estimated for the ICN dissociation. Since ω_0 for the CN is known and Δj of the rotational distribution is also known, $\tau_c \approx 40$ fs. The calculation of this dephasing time due to an 'impulse' of dissociation has direct analogy to dephasing
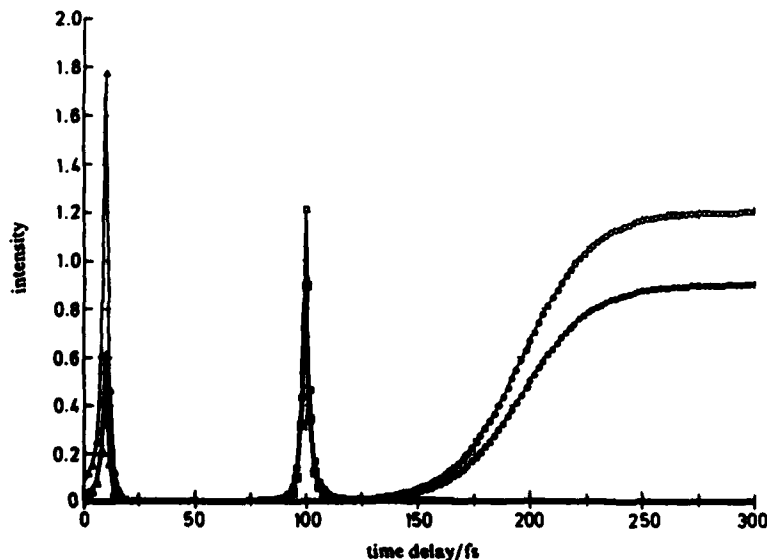
Fig. 9. The calculated $\langle I_{\parallel}(t) \rangle$ and $\langle I_{\perp}(t) \rangle$, showing the effect of t^* (10 fs, 100 fs and 1 ps) and τ_c (50 fs). The transients show the decrease of the anisotropy as t^* increases. Note that the initial ratio is 3, and at long time delays it becomes 1.2/0.9 (see text).

of molecules excited coherently into a distribution of rotational levels by a laser pulse.[33] In this case one obtains an initial dephasing and then recurrences at long times (determined by the rotational constant of the molecule), as verified experimentally.[34] If we apply this analogy to the problem at hand we obtain the following simple expression for τ_c:

$$\tau_c \approx 2.2[B\langle E_R\rangle]^{-1/2} \tag{10}$$

where τ_c is in ps and both the rotational constant B and the average rotational energy $\langle E_R\rangle$ are in cm^{-1}. At 306 nm of pump excitation $\langle E_R\rangle$ is known (see section 2) and this gives $\tau_c \approx 44$ fs according to this model. The experimental data in fig. 10 show the similarity of the $I_\parallel$ and $I_\perp$ transients, consistent with the analysis in fig. 9, and we will attempt an improvement of the S/N to permit extraction of an accurate τ_c. It is now clear that interesting new effects regarding temporal and spatial alignment can be searched for as we systematically change t^* and make the pulse duration even shorter.

In the above treatment we did not consider the effect of parent rotation. This may be incorporated in β, but for the ICN it is known that parent rotation is not what determines the rotational distribution of the CN.[34] Finally, it will be interesting to compare the above theoretical calculations, based on the separation of coherent (alignment) and incoherent (population) dynamics, with 'exact' dynamical calculations on PESs of different angular forms.[14] This will help us understand the different time scales involved and their relevance to the separability question, since the R and θ 'motions' are expected to be coupled.

(b) Time Evolution of Angular Momenta

The LIF spectrum of free CN exhibits the many transitions of the P and R branches. For 308 nm excitation, the R branch is fully resolved and extends to 381.5 nm. These transitions to the blue of the bandhead are associated with different rotational quantum numbers of the CN fragment.

The spectral width of the femtosecond probe is broad, so that the excitation of a single rotational level is impossible. However, we have attempted to probe regions selectively within the P branch of the CN spectrum which are associated with either high or low rotational quantum states. For example, the region near the bandhead is associated with high rotational states ($\leqslant 20$), and near the start of the P branch at 387.5 nm, with lower quantum numbers.

The clocking experiment was performed at various probe wavelengths between 388.7 and 387.4 nm The vaues of $\tau_{1/2}$ determined from these measurements[3] are shown in fig. 11 for both 306 and 285 nm pump wavelengths. At the bandhead as previously discussed, this experiment yields a time delay of $\tau_{1/2} \approx 200$ fs. However, a substantial decrease in $\tau_{1/2}$ was observed as the probe was shifted towards shorter wavelengths.

An obvious possible cause for this observation is due to the change in the translational energy with rotational excitation of the CN. For 7000 cm^{-1} of total available energy, the low-angular-momentum states will be produced with essentially all this energy in translation. However, for high-angular-momentum states the translational energy will be less than the available energy; for $j = 25$, $E_R = 1250$ cm^{-1}, and the translational energy becomes 5750 cm^{-1} (vibrational excitation is assumed to be negligible).[13] In the centre-of-mass frame, v is proportional to $E^{1/2}$, and $\tau_{1/2}$ at most should change from *ca.* 200 to *ca.* 180 fs. This is a much smaller effect than the data in fig. 11 show.

Probing the different rotational states of the CN is sensitive to a more interesting dependence, namely, the angular part of the potential. In general, the PES is not only radial but it has an angular dependence described by the angle (θ) between l and the centre-of-mass of the CN. For ICN, the potential has been postulated and used to fit the product state distribution, *e.g.* as done by Goldfield *et al.*[9] A form that is discussed
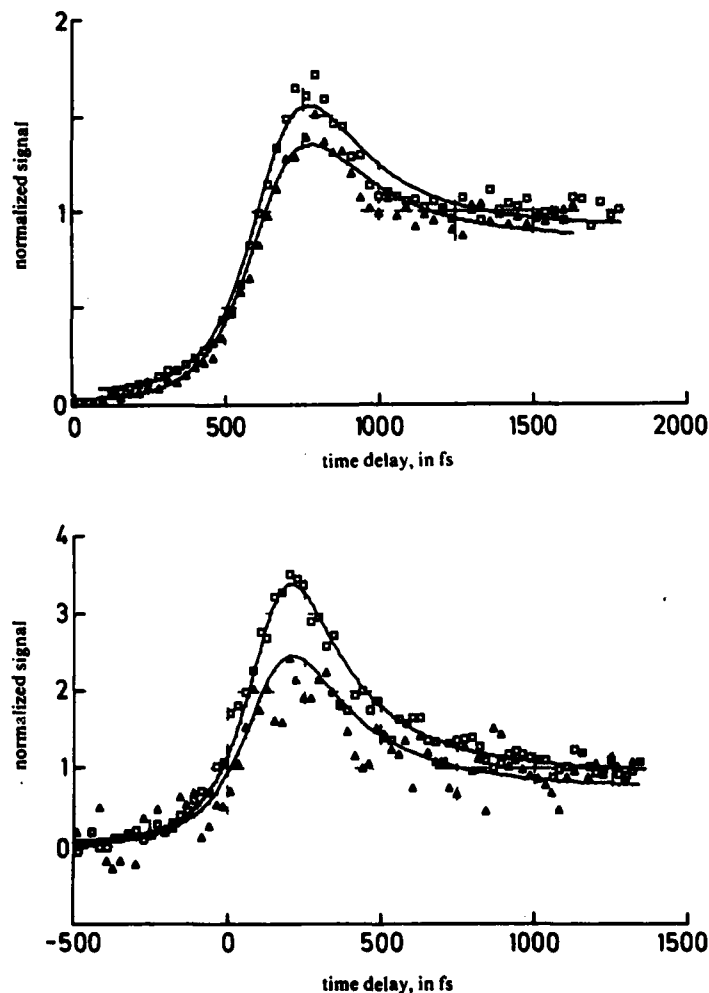
Fig. 10. Results of femtosecond alignment experiments. FTS data taken off-resonance, with either parallel (□) or perpendicularly polarized (▲) pump and probe beams. The probe polarization was kept parallel to the detection axis. Two data sets are shown, taken under different experiental conditions. Note that the time delay in (*a*) curve is arbitrary (the zero-of-time was not determined for this set). The data is normalized to unity at long time delays.[3]

by Schinke and others is generally written as:[35]

$$V(R, \theta) = A \exp\left(-\frac{R - R_0}{L}\right) \exp\left(-\frac{\varepsilon(\cos^2 \theta - 1)}{L}\right) \tag{11}$$

where ε/L is a measure of the anisotropy of the potential. When $\varepsilon = 0$, one recovers the single radial potential (isotropic). However, for negative ε, the potential describes a bent excited state which has a minimum at $\theta = 90°$ and a maximum at $\theta = 0$. Dugan[13] has discussed this bending (of CN relative to I) at the 308 nm excitation and obtained a bending angle of $\theta_0 = 18°$. Basically, if the molecule were linear ($\theta_0 = 0$, on the average),
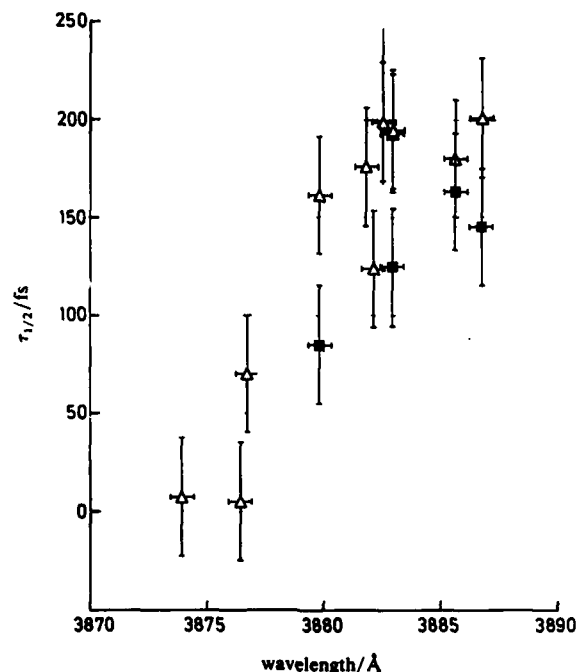
Fig. 11. Fragment delay time, $\tau_{1/2}$, as a function of probe wavelength. The values of $\tau_{1/2}$ obtained are shown for a pump wavelength of *ca.* 306 nm ($\triangle$) and 285 nm ($\blacksquare$). The FWHM of the probe was *ca.* 60 cm^{-1} in each case.

then the rotational distribution would show a maximum at $j \approx 0$; instead, the maximum seen in these experiments is at higher j values for this wavelength of excitation. As he pointed out, at these long wavelengths there are one or two quanta of bending vibration (ground state), and their classical turning points are at 14 and 19°. We will not attempt to quantify the angle here, but the important points are that the bent state produces a range of torques and that there is time evolution of j.

From the potential, one can calculate the torque and hence $j(t)$:

$$\text{torque} = \mathrm{d}j/\mathrm{d}t = R \times F = R \times [-\nabla V(R, \theta)]. \tag{12}$$

For illustration, we used Schinke's potential and calculated (using a simple torque) the evolution of $j(t)$. This is shown in fig. 12. The angular momenta evolve in very short, but finite times (*ca.* 50 fs or so) on the scale of femtochemistry experiments. The simple evolution shown here indicates that at shorter times the distribution is biased toward lower j states and these states evolve to their final j values at longer times. We calculated snapshots of the rotational distribution at steps of 10 fs and confirmed this picture.

It appears that probing different CN rotational states is monitoring different trajectories (reflecting the degree of the torque and the steepness of the PES along θ) of different reaction times. To see this in real time and compare with experiments, we are currently examining trajectory calculations on PESs of different forms. For example, for the potential in fig. 13 (Goldfield *et al.* type[9]) we ran trajectories (fig. 14) and observed different times. We also observed more complex evolution for $j(t)$ than the one shown in fig. 12. (This is because, as mentioned above, we simplified the nature of the torque for the sake of illustration). These calculations are in progress for different
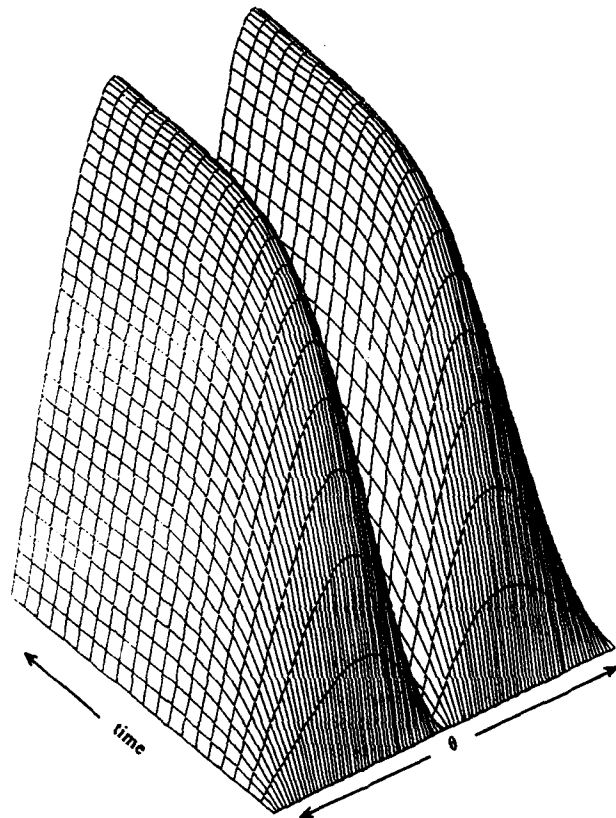
Fig. 12. Angular momentum as a function of time and angle, using Schinke-type potential (see text) and $\varepsilon < 0$. The time (10 fs steps) is from 0–200 fs and the angle is from $-\pi/2$ to $+\pi/2$. Note that when starting at the maxima and minima of the potential along θ $(0, \pm\pi/2, \ldots)$ no angular momentum is generated since $(\nabla V)_\theta = 0$ and hence the torque is zero; see eqn 11 and 12. We have also calculated snapshots of the rotational distribution and found that at 10 fs, the distribution cuts off at $j \sim 10$ while for 55 fs it cuts off at $j \sim 40$, assuming a simple torque.

parameters and potentials to compare with experimental findings and examine the promise for probing the angular part of the dynamics. Much more will be learned in the coming years about these problems. We have considered here the simple cases but there are other possibilities and interpretations as yet unexplored. Hopefully as we gain more experience with these new findings we will be able to address these and other problems of the PESs involved, like the effect of centrifugal barriers, van der Waals wells and crossings on V_1 and V_2 PESs.

(c) Half-collision vs Full-collision

The above discussions describe features of alignment, coherence and time evolution of angular momenta expected in reactions involving a half-collision. There are two points that should be made regarding other types of reactions which are bimolecular in nature, or exhibit resonance characteristics.
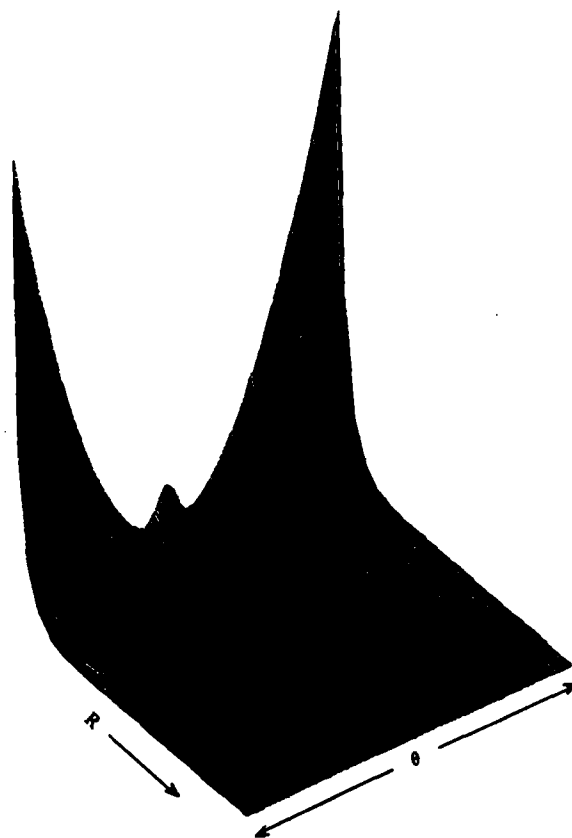
Fig. 13. A three-dimensional plot of a Goldfield *et al.* - type PES (see text) for ICN. The angle θ is from $-\pi$ to $+\pi$ and R is taken up to 6.7 Å ($R_0 = 2.7$ Å). The double well along θ describes the bent configurations.

In cases where there is crossing (or avoided crossing) between different potential-energy curves, as in the case of NaI, the temporal behaviour shown in fig. 7 suggests that alignment experients should be of great interest. In this case, there is no torque, but the initial alignment of the parent should play a role depending on the time for the wavepacket oscillatory propagation and the rotation time of the parent molecule. Thus, probing at different t^* should show he interplay between the two. For NaI, *e.g.* the rotation time of the molecule in the covalent excited state is 3.6 ps rad^{-1} for $j = 30$. This means that during one crossing from the covalent to the ionic curve, the molecule rotates an angle of 9.7°. Hence, measurements of $I_\parallel$ and $I_\perp$ should show anisotropy that changes with the number of crossings. Such behaviour will be interesting to observe and relate to the dynamics of wavepacket dephasing.

In the other class of reactions discussed in this paper, namely orientated bimolecular reactions, *e.g.* $H + CO_2$, these alignment experiments will be valuable. As shown[36] by Herschbach many years ago, the mean time, τ_d, for the decomposition of the collision complex can be estimated from knowledge of the angular distribution (direct *vs.* complex mode reaction) and the rotational period of the complex,

$$\tau_r = 2\pi(I/L). \tag{13}$$
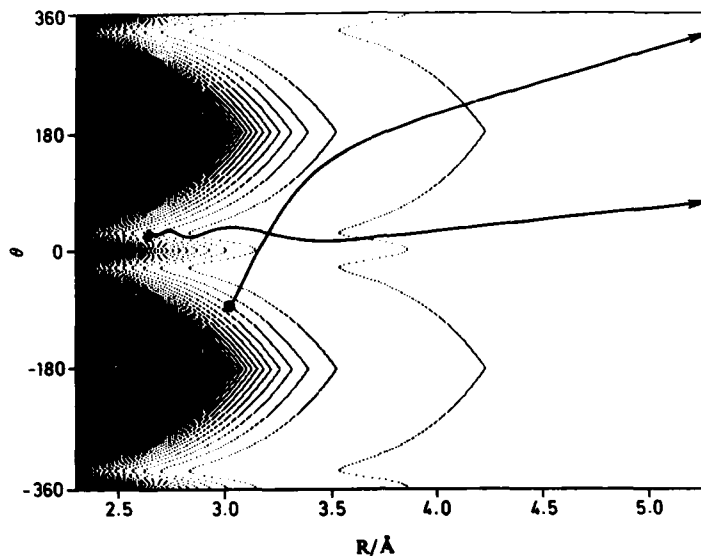
Fig. 14. A contour map of the PES of Goldfield *et al.*[9] Using a computer algorithm, for the classical dynamics,‡ two trajectories on this surface are displayed. These calculations in fig. 12-14, when completed, will be detailed in a separate publication.

For example, for RbKCl, $I \approx 500$ amu Å^2 and for $L < 500$ ℏ, $\tau_r > 1\text{-}2$ ps (τ_r is still long compared to vibrational time). The symmetry in the angular distribution thus indicates that τ_d is longer than 1-2 ps for this class of reactions.

Real-time studies can now be made to obtain direct information on τ_r and τ_d. If we monitor the collision complex (*e.g.* HOCO‡) in real time and study the loss of the alignment then we will know τ_r and, as discussed above, the time for he formation of the products can be measured directly to give τ_d. This will give the different timescales involved in the dynamics and allow one to examine the effect of limited impact parameter (stereospecificity) on the statistical or non-statistical behaviour of the reaction. There is a wealth of experiments to be performed in this direction to study the effect of available energy, orientation *etc.* As with our attempt to investigate the alkali-metal age reactions of MX in the femto age, we also plan to extend these types of experiments to the bimolecular femto age.

4. Conclusions

In this paper we presented some theoretical descriptions relating to the role of alignment and orientation in femtochemistry experiments. The experimental technique of femtosecond transition-state spectroscopy (FTS) is described and some applications to unimolecular, 'oriented' bimolecular, and 'alkali-metal age' reactions are presented. We did not detail other transition-state spectroscopies[29,37-41] or reaction rate measurements,[42,43] but these were discussed in ref. (1).

A key feature here is that because of the time resolution and sensitivity one is able to view the dynamics with a resolution that is sub-Ångstrom.[1] With polarized femtosecond pulses an additional dimension can now be explored, and this allows one to

probe both the coherent (alignment) and incoherent (population) parts of the dynamics, as they evolve on the femtosecond timescale. The applications presented are just the beginning and the future is very promising as we hope we and others will be able to study many other reactions in their transition-states, the 'during phase' of the reaction,[44] and obtain characteristics of the PES in real time.

References

1 A. H. Zewail, *Science*, submitted; and references therein to work on transition-state spectroscopy.
2 M. J. Rosker, M. Dantus and A. H. Zewail, 1988, **241**, 1200.
3 M. J. Rosker, M. Dantus and A. H. Zewail, *J. Chem. Phys.*, in press; M. Dantus, M. J. Rosker and A. H. Zewail, *J. Chem. Phys.*, in press.
4 T. S. Rose, M. J. Rosker and A. H. Zewail, *J. Chem. Phys.*, 1988, **88**, 6672.
5 M. J. Rosker, T. S. Rose and A. H. Zewail, *Chem. Phys. Lett.*, 1988, **146**, 175.
6 M. Dantus, M. J. Rosker and A. H. Zewail, *J. Chem. Phys.*, 1987, **87**, 2395.
7 N. F. Scherer, J. L. Knee, D. D. Smith and A. H. Zewail, *J. Phys. Chem.*, 1985, **89**, 5141.
8 J. Chem., Faraday Trans. 2, 1989, 85, issue 9, there are a number of papers concerning this subject in this issue.
9 E. M. Goldfield, P. L. Houston and G. S. Ezra, *J. Chem. Phys.*, 1986, **84**, 3120
10 R. Bersohn and A. H. Zewail, *Ber. Bunsenges Phys. Chem.*, 1988, **92**, 373.
11 M. A. O'Halloran, H. Joswig and R. N. Zare, *J. Chem. Phys.*, 1987, **87**, 303; and references therein.
12 I. Nadler, D. Mahgerefteh, H. Reisler and C. Wittig, *J. Chem. Phys.*, 1985, **82**, 3885.
13 C. H. Dugan and D. Anthony, *J. Phys. Chem.*, 1987, **91**, 3929; 1988, **92**, 720; and references therein.
14 M. Dantus and A. H. Zewail, to be published.
15 R. B. Bernstein and A. H. Zewail, *J. Chem. Phys.*, submitted.
16 S. O. Williams and D. G. Imre, *J. Phys. Chem.*, in press.
17 N. F. Scherer, L. R. Khundkar, R. B. Bernstein and A. H. Zewail, *J. Chem. Phys.*, 1987, **87**, 1451; N. F. Scherer, C. Sipes, R. B. Bernstein, A. H. Zewail, to be published.
18 G. Radhakrishnan, S. Buelow and C. Wittig, *J. Chem. Phys.*, 1986, **84**, 727.
19 C. Jouvet and B. Soep, *J. Chem. Phys.*, 1984, **80**, 2229.
20 G. Schatz and M. S. Fitzcharles, submitted for publication; G. Schatz, M. S. Fitscharles and L. B. Harding, submitted for publication.
21 D. R. Herschbach, *Le Prix Nobel, 1986* (Elsevier Publishing Co., Amsterdam, 1987).
22 Y. T. Lee, *Science*, 1987, **236**, 793.
23 J. C. Polanyi, *Science* 1987, **236**, 680.
24 R. D. Levine and R. B. Bernstein, *Molecular Reaction Dynamics and Chemical Reactivity* (Oxford University Press, NY, 1987) and references therein.
25 R. S. Berry, in *Alkali Haide Vapors*, ed. P. Davidovits and D. L. McFadden (Academic Press, NY, 1979) and references therein.
26 R. Grice and D. R. Herschbach, *Mol. Phys.*, 1974, **27**, 159; S. A. Adelman and D. R. Herschbach, *Mol. Phys.*, 1977, **33**, 793.
27 V. Engel, H. Metiu, R. Almeida, R. A. Marcus and A. H. Zewail, *Chem. Phys. Lett.*, submitted.
28 T. S. Rose, M. J. Rosker and A. H. Zewail, to be published.
29 H. J. Foth, J. C. Polanyi and H. H. Telle, *J. Phys. Chem.* 1982, **86**, 5027; see also ref. (1) for more discussion.
30 See the special issue of Dynamical Stereochemistry, *J. Phys. Chem.*, *J. Phys. Chem.*, 1987, **91**. This issue has many excellent articles on the subject.
31 See *e.g.*: R. Bersohn, in *Molecular Photodissociation Dynamics*, ed. M. N. R. Ashford and J. E. Baggott (Royal Society Chemistry, London, 1987), p. 1.
32 See: K. B. Eisenthal, *Acc. Chem. Res.*, 1975, **8**, 118.
33 P. M. Felker and A. H. Zewail, *J. Chem. Phys.*, 1987, **86**, 2460; J. S. Baskin, P. M. Felker and A. H. Zewail, *J. Chem. Phys.*, 1987, **86**, 2483.
34 W. J. Marinelli, N. Sivakumar and P. L. Houston, *J. Phys. Chem.* **88**, 6685.
35 R. Schinke, *J. Phys. Chem.*, 1988, **92**, 3195.

36 W. B. Miller, S. A. Safron and D. R. Herschbach, *Discuss. Faraday Soc.*, 1967, **44**, 108.
37 D. Imre, J. L. Kinsey, A. Sinha and J. Krenos, *J. Phys. Chem.* 1984, **88**, 3956.
38 P. R. Brooks, R. F. Curl and T. C. Maguire, *Ber. Bunsenges. Phys. Chem.*, 1982, **86**, 401.
39 R. B. Metz, T. Kitsopoulos, A. Weaver and D. Neumark, *J. Chem. Phys.*, 1988, **88**, 1463.
40 J. C. Nieh and J. J. Valentini, *Phys. Rev. Lett.*, 1988, **60**, 519.
41 P. D. Kleiber, A. M. Lyyra, K. M. Sando, S. P. Heneghan and W. C. Stwalley, *Phys. Rev. Lett.*, 1985, **54**, 2003.
42 L. R. Khundkar, J. L. Knee and A. H. Zewail, *J. Chem. Phys.*, 1987, **87**, 77. N. F. Scherer and A. H. Zewail *J. Chem. Phys.*, 1987, **87**, 97; J. L. Knee, L. R. Khundkar and A. H. Zewail *J. Chem. Phys.*, 1987, **87**, 115.
43 For a recent review see: J. L. Knee and A. H. Zewail, *Spectroscopy*, 1988, **3**, 44; and references therein.
44 I. W. M. Smith, *Nature (London)*, 1987, **328**, 760.

Rotational Alignment of NO from Pt(111): Inelastic Scattering and Molecular Desorption

Dennis C. Jacobs,*† Kurt W. Kolasinski, Robert J. Madix and Richard N. Zare

Department of Chemistry, Stanford University, Stanford, California 94305, U.S.A.

The rotational alignment distribution of NO has been measured subsequent to the molecule's interaction with a well characterized Pt(111) surface. Internal state distributions have been probed using $1+1$ resonance-enhanced multiphoton ionization (REMPI) spectroscopy in which lines of the NO $A\,^2\Sigma^+$-$X\,^2\Pi$ (0, 0) band constitute the resonant transition. NO/Pt(111) scattering has been studied in two distinct regimes: inelastic scattering and trapping/desorption. In both cases, there is relatively no preferential alignment of rotation for $J < 12.5$. However, molecules with higher rotational angular momentum show a marked increase in alignment. Inelastically scattered molecules prefer to rotate in a plane normal to the surface ('cartwheel' motion), whereas desorbing molecules prefer to rotate in a plane parallel to the surface ('helicopter' motion). These measurements provide new insight into momentum transfer at surfaces and the nature of the transition state which leads to molecular desorption.

Rotational dynamics at the gas–surface interface reveal unique information about the molecule–surface potential. A molecule passing from the constrained two-dimensional environment of a solid surface lattice into a three-dimensional vacuum has the potential for exhibiting strong rotational polarization.

Here, we investigate the rotational alignment of NO after it interacts with a Pt(111) surface. We examine experimentally two distinct dynamical regimes, inelastic scattering and trapping/desorption. The first refers to a collision of short duration (one or a few bounces) between the molecule and the surface. This scattering event leaves the molecule with an energy distribution characteristic of both the molecule's initial conditions and the nature of the surface. The second involves a relatively long surface residence time in which the molecule completely loses 'memory' of its initial conditions. In this latter case, the desorbed molecule's energy distribution is characterized solely by the conditions of the surface and the molecule–surface potential.

There have been only two prior studies in which rotational alignment has been measured for gas–surface scattering: NO/Ag(111)[1-3] and N_2/Ag(111).[4-6] These experiments both probed the regime of direct inelastic scattering by impinging an energetic supersonic molecular beam (10–90 kJ mol^{-1}) on a relatively cold Ag(111) surface. Kleyn and co-workers[1-3] measured a preference for NO to scatter from Ag(111) with its rotational motion resembling that of a 'cartwheel' (fig. 1). This behaviour is reconciled with a simple hard-cube model which permits forces only along the surface normal. These forces deliver an anisotropic torque on the molecule, causing an observed preference for cartwheel motion. Zare and co-workers[4-6] found a similar result for N_2/Ag(111). Additionally, they measured the rotational orientation resulting from surface scattering. They observed a strong correlation between rotational orientation, rotational quantum number and scattering exit angle.

Electric-field deflection techniques have probed surface scattering dynamics through the observation/preparation of molecular orientation. Novakoski and McClelland[7]
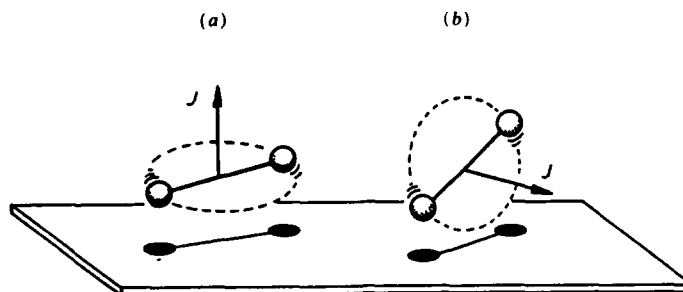

(a)   (b)

Fig. 1. Rotational alignment relative to the surface plane. The helicopter motion (a) is preferred for $A_0^{(2)} > 0$; the cartwheel motion (b) is favoured for $A_0^{(2)} < 0$.

measured a preferential molecular orientation for the desorption of CHF_3 from Ag(111), *i.e.* CHF_3 tends to desorb with its hydrogen atom orientated toward the surface. Additionally, they found that scattering leaves the molecule with a weak orientation in the opposite sense. More recently, Kuipers *et al.*[8] observed the scattering angular distribution of NO from Ag(111), where the incident NO was orientated in predominantly two opposite directions relative to the surface. There appeared to be a greater loss in normal translational energy when the oxygen atom, rather than the nitrogen atom, was directed toward the surface.

The present study represents the first observation of rotational alignment in desorption. Additionally, it reports the rotational alignment of scattered NO in a previously unexplored regime, one in which the molecule's final rotational energy exceeds the initial energy of the incident molecular beam. Here, surface vibration–rotational energy transfer is the operative mechanism. The experiment utilizes $1 + 1$ REMPI through the NO A $^2\Sigma^+$-X $^2\Pi$ (0,0) band to measure rotational alignment distributions in a state-specific manner. The quantitative reduction of $1 + 1$ REMPI spectra to alignment moments requires inclusion of both saturation in the resonant transition as well as incorporation of the symmetry character of the ionization transition. We present a brief summary of the methodology employed for the extraction of the quadrupole moment of the rotational alignment distribution from $1 + 1$ REMPI spectral intensities.

Experimental

The experiment utilizes an ultra-high vacuum (u.h.v.) scattering chamber, a tunable u.v. laser source and a variety of support electronics, all of which are described in detail elsewhere.[9] A schematic diagram of the apparatus is shown in fig. 2. In short, the u.h.v. chamber is equipped with a sample manipulator (to facilitate sample translation rotation, surface heating and cooling), LEED and Auger surface diagnostics (to monitor surface order and cleanliness), a pulsed molecular beam source, a port for entry of a laser beam and ion time-of-flight tube. The main chamber is pumped by a $220\,\mathrm{dm^3\,s^{-1}}$ ion pump, a titanium sublimation pump, a liquid-nitrogen cryopanel and a $1500\,\mathrm{dm^3\,s^{-1}}$ turbo-molecular pump (base pressure 2×10^{-10} Torr†).

A differentially pumped invaginated source chamber houses the pulsed valve/skimmer assembly. The supersonic beam (50 psi‡ neat expansion through a 0.1 mm nozzle orifice) is collimated with a 0.3 mm skimmer so that the beam strikes only a 5 mm

† 1 Torr = 101 325/760 Pa.
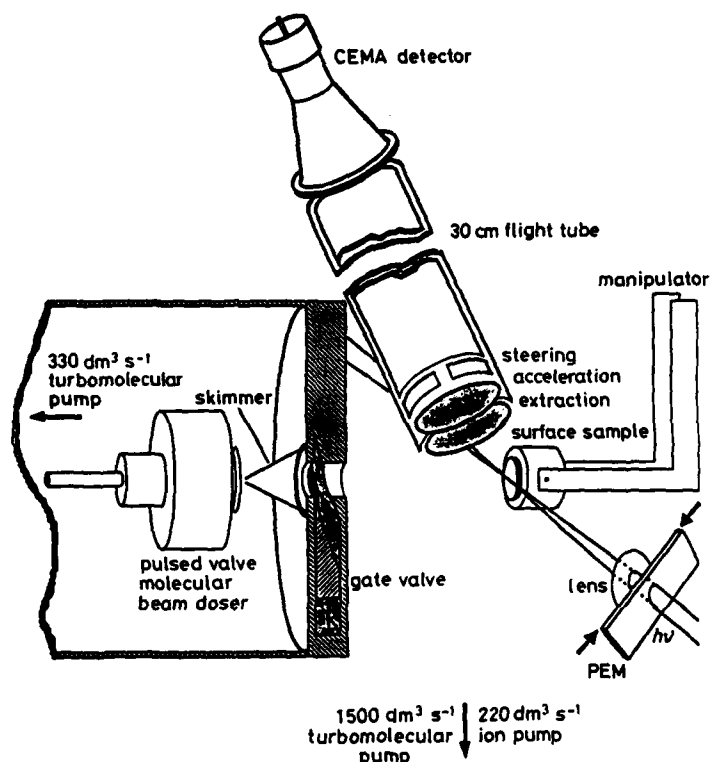‡ 1 psi = 6.894 76 × 10³ Pa.

Fig. 2. Experimental Apparatus. A differentially pumped pulsed valve doses the Pt(111) crystal. Laser radiation is focussed 2 mm above the surface. Ions produced in the REMPI process are accelerated through the time-of-flight tube and collected by the CEMA charged particle multiplier. The crystal can be rotated in order to face LEED and Auger diagnostics. Not shown are Helmholtz coils which cancel the earth's magnetic field and leave a residual magnetic field in the direction of the surface normal.

diameter region of the surface. The 10 cm nozzle–surface distance allows instantaneous pulsed molecular beam fluxes as high as 10^{17} molecule $cm^{-2} s^{-1}$. The rotational temperature of the neat beam is measured at 40 K and the beam translational energy is estimated to be 9 kJ mol^{-1}.[10] A 330 $dm^3 s^{-1}$ turbomomecular pump establishes a base pressure of 1×10^{-8} Torr in the source chamber.

The generation of tunable ultraviolet laser radiation relies on a commercial 10 Hz Quantel Nd:YAG system. The output of the dye laser (0.08 cm^{-1} bandwidth) is frequency-doubled and Raman shifted (second order anti-Stokes) in H_2. This system creates 6 ns pulses at 224 nm with *ca.* 200 μJ per pulse. A portion of the resulting laser beam is loosely focussed into the chamber (10 mJ cm^{-2} fluence). The direction of linear polarization is selected, on a shot-to-shot basis, by a photoelastic modulator (PEM) interfaced to a DEC PDP 11/23 computer. The energy of each laser pulse is measured by a pyroelectric detector and stored in the computer.

The laser light runs parallel to and passes 2 mm above the surface. A fraction of the molecules leaving the surface pass through the laser interaction region and become ionized by the laser radiation *via* the REMPI process. The resulting ions are accelerated through a time-of-flight tube and collected by a charged particle multiplier (CEMA

multichannel plates). The ion signal is digitized by a CAMAC charge-sensitive gated integrator and passed to the computer for storage.

Owing to the $^2\Pi$ symmetry of the NO ground state, stray magnetic fields can scramble the rotational alignment of the product distribution during the molecule's 1 μs flight time from the surface to the laser ionization region. In order to minimize stray magnetic fields,[11] Helmholtz coils are installed around the exterior of the main chamber. The regulated currents flowing through these coils are adjusted so that a small field, pointing along the surface normal, remains in the ionization region.† In addition, the filament current used to heat the surface is turned off for 10 ms during the laser pulse.

The dynamical regimes of direct inelastic scattering and trapping/desorption are differentiated according to their characteristic surface residence times. The residence time for direct inelastic scattering is infinitesimal on the microsecond timescale of the molecular-beam pulse. However, the trapped state will exhibit a half-life on the surface which is inversely proportional to the desorption rate constant. For our temperature regime, the half-life is estimated to be 2-2000 ms. Synchronizing the laser to fire during the nozzle pulse discriminates in favour of those molecules which have inelastically scattered. Conversely, firing the laser 200 μs after the 90 μs nozzle pulse precludes inelastic scattering contributions and permits only detection of those molecules which have trapped and subsequently desorbed. The surface coverage at which these experiments are performed is less than 3% of a monolayer.

Analysis

The accurate analysis of $1+1$ REMPI spectra of NO through the $A\,^2\Sigma^+$-$X\,^2\Pi$ $(0,0)$ band requires characterization of both the extent of saturation in the resonant step as well as the M_J-dependence of the ionization step. There are two stages in which the $1+1$ REMPI data are treated. First, the data are power-normalized to account for variations in the laser power arising from shot-to-shot fluctuations and changes in the laser gain across the dye curve. In real time, the computer corrects the ion signal for variations in the laser energy through a least-squares fitting routine described elsewhere.[12] Secondly, the normalized data are reduced to population and alignment distributions while considering saturation of the resonant step and variations in the ionization probability with M_J (the projection of J on the laser polarization direction).[12]

Our findings indicate that for our required sensitivity range, partial saturation is unavoidable. Complete saturation, however, eliminates all chances of measuring rotational alignment. Therefore we choose to work in a regime of moderately weak saturation and take great care in the reduction of population and alignment moments to remove the detrimental effects of saturation.

The second photon absorbed in a $1+1$ REMPI scheme excites a continuum transition in the molecule. The dipole moment of ths transition points in some direction relative to the internuclear axis. The limiting direction of the transition dipole moment is either parallel or perpendicular to the internuclear axis. The projection of the dipole transition moment onto the internuclear axis directly determines the M_J-dependent transition probability for the ionization step. This is required because different branch excitations in the resonant step create different alignment distributions in the intermediate level. The probability for ionization from the intermediate level is a function of both the intermediate-state alignment created by resonant excitation and the fraction of parallel *versus* perpendicular character in the ionization transition.

Fortunately, rotational populations extracted from different branch excitations reveal redundant information. Additionally, different branches saturate at different laser power

---

† A magnetic field along the cylindrical symmetry axis will not affect the observed alignment. Instead, it will ensure that stray transient fields will be insufficient to alter the net field direction.

levels because of variations in the rotational line strength with branch excitation. Calibration spectra of NO in a room-temperature bulb are utilized to determine both the extent of saturation and the M_J-dependent ionization probability in the $1+1$ REMPI process. This information is then used to analyse nascent distributions arising from NO molecules which have scattered and desorbed from the Pt(111) surface.

The experimentally measured M_J-dependent ionization probability is shown in fig. 3,[12] which reveals a relatively slight variation in the ionization transition probability with the quantum number, M_J. This has the consequence of limiting the amount of rotational alignment information which can be extracted from $1+1$ REMPI of NO. Rotational alignment is conveniently described by the even moments of the rotational angular distribution. In the case of cylindrical symmetry, $1+1$ REMPI through the NO A–X(0, 0) band will only be sensitive to the population and the quadrupole moment, $A_0^{(2)}$.[11,12] Because of the ionization dynamics, the $A_0^{(4)}$ moment cannot be extracted with any sensitivity. The value of the quadrupole moment ranges from $+2$ to -1,[13] where these limits correspond to the molecule rotating in a plane parallel to the surface ('helicopter' motion) or in a plane perpendicular to the surface ('cartwheel' motion), respectively (see fig. 1). A quadrupole moment of zero suggests no preferential alignment of rotation, i.e., an isotropic distribution.

Extraction of the population and quadrupole alignment moments requires that the ion signal be recorded for only two independent planes of linearly polarized light. In the laboratory, we record spectra under conditions where the polarization direction of the laser is either parallel or perpendicular to the surface normal. This is performed by
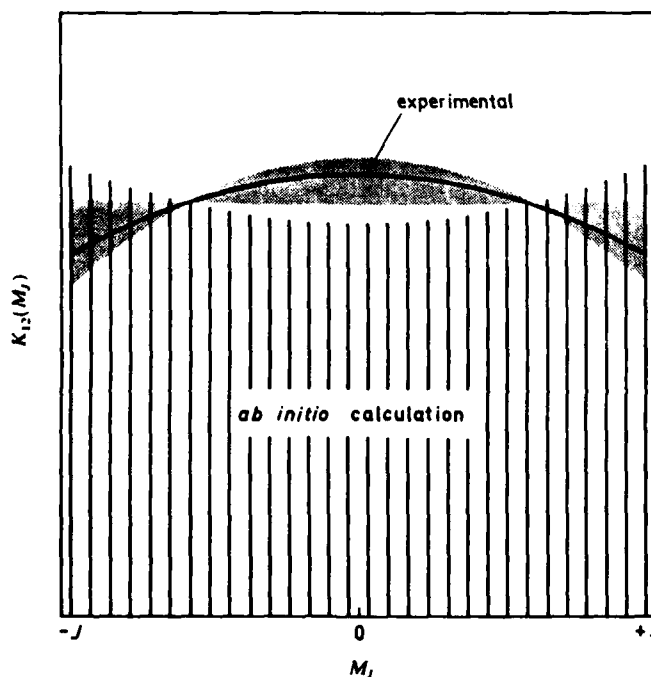
Fig. 3. The M_J-dependence of the ionization step in $1+1$ REMPI of NO through the A $^2\Sigma^+$–X $^2\Pi$ (0, 0) band. The solid curve and shaded region represent the best fit and corresponding uncertainty in the experimental measurement.[12] The vertical lines are calculated theoretically by *ab initio* methods.[21]

alternating the polarization between these two directions throughout an entire wavelength scan. For a given rotational transition out of a rotational state J, we identify $I_{\parallel}$ and $I_{\perp}$ as the integrated ion intensities for which the laser polarization was parallel or perpendicular to the surface normal (the cylindrical symmetry axis), respectively. The quadrupole alignment moment $A_0^{(2)}(J)$ is related to these measured intensities by

$$A_0^{(2)}(J) = \frac{2\{I_{\parallel} - I_{\perp}\} \sum\limits_{M_J} F_{\text{sat}}[k_{01}(M_J), k_{12}(M_J), I\Delta t]}{\{I_{\parallel} + 2I_{\perp}\} \sum\limits_{M_J} \left(3\dfrac{M_J^2}{J(J+1)} - 1\right) F_{\text{sat}}[k_{01}(M_J), k_{12}(M_J), I\Delta t]} \tag{1}$$

where M_J is the quantum number representing the projection of J on the cylindrical symmetry axis, $k_{01}(M_J)$ is the M_J-dependent transition probability for the resonant photon step, $k_{12}(M_J)$ is the M_J-dependent transition probability for the ionization step, $I\Delta t$ is the measured laser fluence and F_{sat} is a function which calculates the overall $1+1$ REMPI ionization probability while including the effects of saturation and intermediate-state alignment. The analytical form of F_{sat}, as well as $k_{01}(M_J)$ and $k_{12}(M_J)$, have been worked out previously.[11,12]

Results

Inelastic Scattering

The dynamical regime of inelastic scattering is selectively explored by firing the laser synchronously with the rising edge of the nozzle gas pulse.† A typical spectrum of NO scattered at normal incidence from a 400 K Pt(111) surface is shown in fig. 4. This
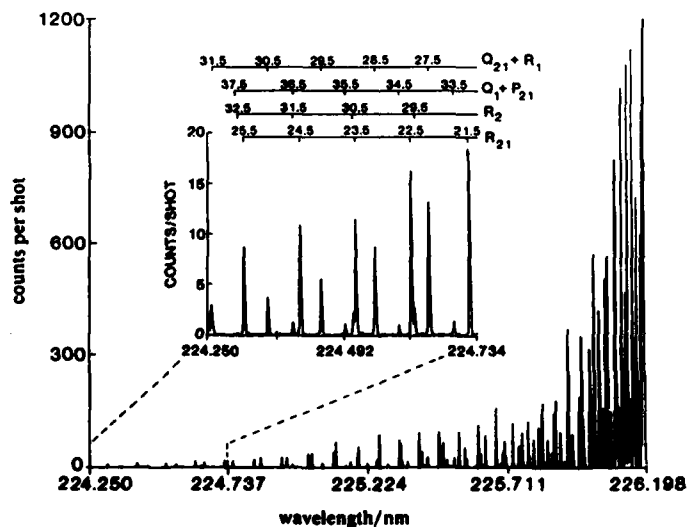
Fig. 4. *Spectrum of* NO *scattering from a* Pt(111) *surface at 400 K. The inset provides an expanded view of the high-J region. The rotational transitions of the resonant excitation step are assigned.*

† Normal incidence/normal detection prohibits angular discrimination against the incident molecular beam. Temporal discrimination is also impossible because of the slow falling edge on the molecular-beam pulse relative to the flight time of the molecules (0.5 mm μs^{-1}). However, owing to the low rotational temperature of the beam, interference from the beam will affect only the states $J < 7.5$.

portion of the spectrum contains predominantly branches originating from the $^2\Pi_{1/2}$ ground spin–orbit state. A section of the figure is expanded to illustrate the high signal-to-background ratio that is routinely realized with $1+1$ REMPI.

The spectra, recorded at orthogonal laser polarizations, are reduced to population and alignment distributions. The population distributions show considerable rotational excitation and are reported elsewhere.[9] Fig. 5 shows the quadrupole alignment moment for the scattered molecules *versus* their rotational quantum number *J*. For $J < 12.5$ there is no appreciable alignment. Of course, interference by the incident beam will dilute the amount of observable alignment in this region. Beyond $J = 12.5$ there is a steady rise in the rotational alignment until it peaks near $J = 25.5$. The maximum alignment observed corresponds to a quadrupole moment of -0.5. Recall that $A_0^{(2)}$ has a limiting value of -1, which occurs when all the molecules rotate with a cartwheel-type motion. For $J > 25.5$, the alignment appears to decrease slightly.

For clarity, fig. 5 includes only the quadrupole moment values measured for the $^2\Pi_{1/2}(A'')$ state. Here, the A'' notation refers to the symmetry of the ground-state Λ-doublet.[14] Measurement of the rotational alignment in the A' state of the $^2\pi_{1/2}$ level is difficult because of congestion in one branch and branch-mixing in the other. However, the two Λ-doublets of opposite symmetry in the $^2\Pi_{3/2}$ state exhibit similar rotational alignment distributions.

Trapping/desorption

The desorption regime is isolated by firing the laser 200 μs after the completion of the nozzle pulse,† thus eliminating contributions from inelastic scattering channels. The Pt(111) sample is held at 553 K, while the molecular beam delivers pulses of NO to the
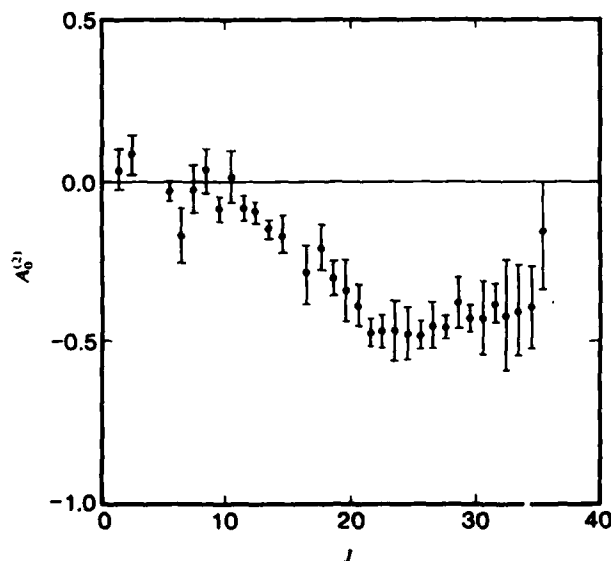
Fig. 5. Quadrupole moment alignment distribution as a function of the rotational quantum number *J* plotted for the case of inelastic scattering of NO from Pt(111) at 400 K.

† The nozzle pulse is characterized by a fast rising edge and a relatively slow tailing edge. Care is taken to ensure that the laser fires well after the visible tail of the pulse.
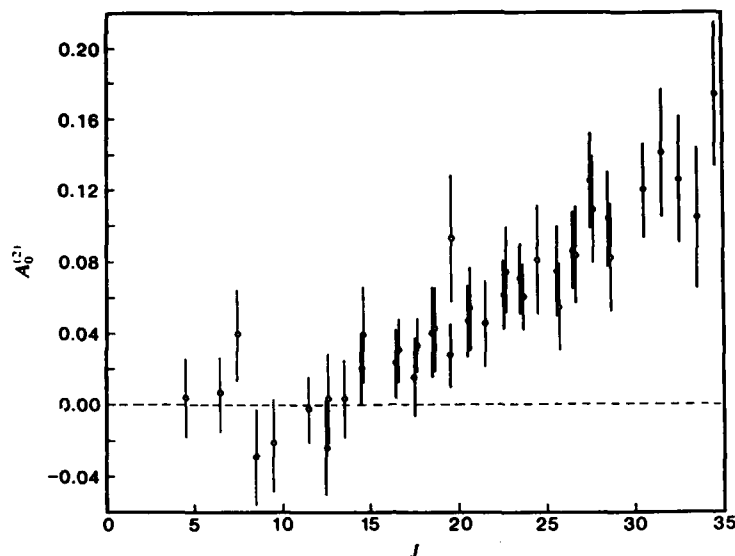
Fig. 6. Quadrupole moment alignment distribution for NO desorption plotted against rotational quantum number J. The Pt(111) surface temperature is 553 K. O, R_{21} branch member; ●, $Q_1 + P_{21}$ branch member.

surface at 10 Hz. Because of the low signal intensity in this operating regime, accurate alignment moments cannot be extracted during the course of a wavelength scan. Therefore, the laser is tuned to a specific rotational transition and ions are collected for 1000–10 000 laser shots at alternating laser polarization directions. The measured intensities are analysed using eqn. (1).

Fig. 6 shows the quadrupole moment, $A_0^{(2)}(J)$, as calculated from two different rotational branches of the same $^2\Pi_{1/2}$ Λ-doublet state.[15] There is little to no rotational alignment for $J < 12.5$, while higher rotational levels show increasing values of the quadrupole moment. A positive quadrupole moment indicates a preference for rotational motion similar to that of a helicopter (see fig. 1). As in the case of direct inelastic scattering, the Λ-doublet states in both spin–orbit levels exhibit similar degrees of alignment.

Discussion

The technique of 1 + 1 REMPI spectroscopy successfully probed rotational alignment in NO, subsequent to its interaction with a Pt(111) surface. The extraction of alignment information from 1 + 1 REMPI spectra requires a methodology which incorporates the effects of saturation in the resonant step and intermediate state alignment in the ionization step. As a check, the quadrupole moment was reduced from the polarization dependence of both R_{21} and $Q_1 + P_{21}$ branch members. While the polarization ratios of these two branches show opposite preferences, they reduce to the same values of the quadrupole moment for each rotational level J.

These experiments cover new ground in the field of gas–surface dynamics. They represent the first observation of rotational alignment in molecular desorption. Additionally, this marks the first study of inelastic scattering in which rotational levels up

to three times more energetic than the incident-beam energy are examined in a state-selective manner. Although significant surface to rotational energy transfer is responsible for populating states with rotational energy exceeding the beam energy, rotational alignment is created in these states and is preserved in the final distribution. The observation of opposite preferences for rotational alignment in desorption and inelastic scattering further exemplifies the interesting dynamics at work in this chemical system.

Both inelastic scattering and trapping/desorption regimes yield little rotational alignment for the levels, $J < 12.5$, while higher rotational levels show a monotonic increase in the magnitude of the quadrupole moment. For the case of desorption the alignment distribution implies a preference for helicopter motion. In contrast, the inelastic scattering process produces an alignment distribution which is indicative of cartwheel motion. Although both types of gas–surface interactions involve the same molecule–surface potential, their dynamics differ because of the way the molecule enters and exits the potential well. The following interpretations are supported by classical trajectory calculations which were performed to simulate the dynamics of the NO/Pt(111) interaction.[16]

In the case of inelastic scattering, the quadrupole moment shows a similar preference toward cartwheel motion as that seen for the scattering of NO[1-3] and N_2[4-6] from Ag(111). The preference for cartwheel motion in inelastic scattering arises from the predominantly out-of-plane forces that the molecule experiences during the impulsive surface collision. These forces torque the molecule such that it rotates in a plane normal to the surface. For NO/Pt(111), the observed quadrupole moment peaks at a value of -0.5.

There are four possible reasons why the quadrupole moment might not reach its limiting value of -1. First, corrugation in the surface potential introduces tangential forces that are not present on a flat surface. Hence, on a corrugated surface the molecule can receive torques which induce rotational motion in a plane other than the pure cartwheel limit predicted for a flat surface. Secondly, multiple bounces on the surface will scramble alignment, as demonstrated by the trajectory model presented elsewhere.[16] This effect potentially differentiates direct inelastic scattering from indirect inelastic scattering. Thirdly, the low populations in the highest rotational levels are susceptible to a weak but non-negligible contribution from trapping/desorption. This contribution would most likely have the opposite sense of alignment (as seen in the desorption results reported here) and thus affect the observed alignment more dramatically. Fourthly, breaking cylindrical symmetry in the system introduces new non-vanishing moments to the measured alignment distribution. The consequence of this effect is that measurement is made of the 'apparent' quadrupole moment rather than the true quadrupole moment.[17] However, we believe that deviations from cylindrical symmetry are minimal for this system.

The quadrupole moment distribution measured for the case of molecular desorption is quite surprising. For rotational states with $J > 12.5$ a positive quadrupole moment is observed. The maximum measured quadrupole moment ($+0.15$) implies that 1.2–1.5†times as many molecules desorb with their plane of rotation resembling that of a helicopter as those resembling a cartwheel motion. The observed alignment cannot be reconciled with the simple picture of a direct transition from the known low-temperature equilibrium position (NO bound normal to the surface) to the gas-phase free rotor without the existence of an intermediate state occupied immediately prior to desorption. Our measurements are sensitive to the last few interactions the molecule makes with the surface before desorbing, *i.e.* the nature of the molecule–surface potential near the

---

† The limiting values of this range assume that the rotational alignment distribution is best described by either an ellipsoid or a function which contains a linear combination of $\cos^2 \theta$ and $\sin^2 \theta$, respectively. The trajectory calculations suggest that the latter function provides a more accurate description of the distribution. In any case, these two functional forms probably represent the limiting cases for the alignment distribution.

transition state. Rotation in the plane of the surface is less hindered than rotation in a plane normal to the surface because the former motion never forces the repulsive O end of the molecule closer to the surface than the attractive N end. This implies that there exists a higher density of rotational states associated with helicopter motion on the surface than those associated with a cartwheel motion. Thermal population of these surface hindered-rotor states[18] followed by cleavage of the molecule–surface bond will leave the desorbed molecule with a preference toward helicopter motion (fig. 7).

The observed rotational alignment distribution for molecular desorption is not inconsistent with the NO/Pt(111) measurements of Ertl and co-workers[19] and Mantell *et al.*[20] The first group measured no detectable change in the populations extracted from Q-branch excitations relative to those of P and R branches.[19] This is a relatively insensitive measure of rotational alignment and the magnitude of their error bars precludes a quantitative determination of the quadrupole moment. Additionally, the maximum rotational quantum state which they were able to observe was $J = 23.5$. The latter study of Mantell *et al.* imposed the following limit on the quadrupole moment: $A_0^{(2)}(J) < |0.1|$ for $J = 4.5$ and $J = 12.5$.[20] This agrees well with our reported value of $A_0^{(2)}(J) = 0.0 \pm 0.04$ for these two quantum levels. Additionally, the experiments of Mantell *et al.*[20] were performed at a much higher coverage and lower temperature than those reported here. At higher coverages, lateral interactions become important and these may inhibit rotational motion in the plane parallel to the surface.
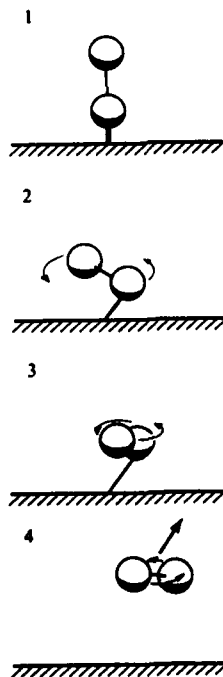
Fig. 7. Proposed mechanism for desorption. Frame 1 shows the low-temperature equilibrium geometry for NO on Pt(111). Rotation on the surface is less hindered in the plane parallel to the surface. Frames 2 and 3 show a rotationally excited species on the surface. Cleavage of the chemisorption bond (frame 4) leads to a preference for 'helicopter' motion in the escaping NO molecule.

In conclusion, the ability to make quantitative measurements of the polarization dependence of 1 + REMPI allows us to determine rotational alignment. Such rotational alignment measurements provide new insight into the highly anisotropic processes of inelastic scattering and trapping/desorption of molecules on surfaces.

References

1 A. Luntz, A. Kleyn and D. Auerbach, *Phys. Rev. B*, 1982, **25**, 4273.
2 A. Kleyn, A. Luntz and D. Auerbach, *Surf. Sci.*, 1983, **117**, 33.
3 A. Kleyn, A. Luntz and D. Auerbach, *Surf. Sci.*, 1985, **152**, 99.
4 G. O. Sitz, A. C. Kummel and R. N. Zare, *J. Vac. Sci. Technol. A*, 1987, **5**, 513.
5 G. O. Sitz, A. C. Kummel and R. N. Zare, *J. Chem. Phys.*, 1987, **87**, 3247.
6 G. O. Sitz, A. C. Kummel and R. N. Zare, *J. Chem. Phys.*, in press.
7 L. V. Novakoski and G. M. McClelland, *Phys. Rev. Lett.*, 1987, **59**, 1259.
8 E. W. Kuipers, M. G. Tenner, A. W. Kleyn and S. Stolte, *Nature* (London), in press.
9 D. C. Jacobs, K. W. Kolasinski, S. F. Shane and R. N. Zare, *J. Chem. Phys.*, submitted.
10 J. A. Serri, M. J. Cardillo and G. E. Becker, *J. Chem. Phys.*, 1982, **77**, 2175.
11 D. C. Jacobs and R. N. Zare, *J. Chem. Phys.*, 1986, **85**, 5457.
12 D. C. Jacobs, R. J. Madix and R. N. Zare, *J. Chem. Phys.*, 1986, **85**, 5469.
13 C. H. Greene and R. N. Zare, *J. Chem. Phys.*, 1983, **78**, 6741.
14 M. Alexander, P. Andreson, R. Bacis, R. Bersohn, F. Comes, P. Dagdigian, R. Dixon, R. Field, G. Flynn, K. Gerecke, E. Grant, B. Howard, J. Huber, D. King, J. Kinsey, K. Kleinermanns, K. Kuchitsu, A. Luntz, A. McCafferty, B. Pouilly, H. Reisler, S. Rosenwaks, E. Rothe, M. Shapiro, J. Simons, R. Vasudev, J. Wiesenfeld, C. Wittig and R. Zare, *J. Chem. Phys.*, in press.
15 D. C. Jacobs, K. W. Kolasinski, R. J. Madix and R. N. Zare, *J. Chem. Phys.*, 1987, **87**, 5038.
16 D. C. Jacobs and R. N. Zare, *J. Chem. Phys.*, submitted.
17 A. C. Kummel, G. O. Sitz and R. N. Zare, *J. Chem. Phys.*, in press.
18 Hindered rotation of chemisorbed molecules has been directly observed. See for example, M. D. Alvey, J. T. Yates Jr and K. J. Uram, *J. Chem. Phys.*, 1987, **87**, 7221.
19 J. Segner, H. Robota, W. Vielhaber, G. Ertl, F. Frenkel, J. Häger, W. Krieger and H. Walther, *Surf. Sci.*, 1983, **131**, 273.
20 D. A. Mantell, R. R. Cavanagh and D. S. King, *J. Chem. Phys.*, 1986, **84**, 5131.
21 S. N. Dixit, D. L. Lynch and W. M. Huo, *Phys. Rev. A*, 1985, **32**, 1267.

Steric Effects in Scattering and Adsorption of NO at Ag(111)

A. W. Kleyn*, E. W. Kuipers and M. G. Tenner
*FOM-institute for Atomic and Molecular Physics, Kruislaan 407, 109SJ Amsterdam,
The Netherlands*

S. Stolte
*Physics Department, Catholic University Nijmegen, Toernooiveld, 6525ED Nijmegen,
The Netherlands*

Scattering experiments have been performed using orientated beams of NO
molecules in the $\Pi_{1/2}$-electronic ground state and $J = M_J = \frac{1}{2}$. In direct
inelastic scattering we observe that with the O-end of the molecule preferen-
tially orientated towards the surface, the angular distribution shifts away
from the specular direction towards the surface. In the experiments on
trapping/desorption it appears that trapping is enhanced for the O-end
towards the surface. Both results can be interpreted in terms of larger
rotational excitation of the molecule with the O-end down than in case of
the N-end down. Since the rotational excitation will mainly occur at the
expense of the normal component of the incident velocity, this can easily
explain the experimental results. This is confirmed using classical trajectory
calculations. The interaction between NO and Ag(111) seems therefore to
be governed by the anisotropy of the repulsive interaction, which is stronger
for the O-end region.

Molecules tend to be adsorbed on a surface with preferential orientations. For example,
simple diatomic molecules like CO and NO are bound at several crystal surfaces with
the molecular axis orientated more or less perpeneicular to the surface.[1,2] In these
studies the preferential orientation of NO and CO are such that the molecules are bound
to the surface by, respectively, the N-atom end or the C-atom end. In addition, for *e.g.*
CO on Ni(110) the perpendicular orientation is known to be quite well defined.[3]

The fact that the molecules when adsorbed exhibit a preferred orientation with
respect to the surface, does not necessarily imply that the dynamics of gas–surface
interactions are governed by the initial molecular orientation in the gas phase. For
example, at very low velocities during its approach to the surface the molecule might
be able to achieve its optimum orientation adiabatically. Also the approach to the
orientated chemisorption state on the surface might be preceded by trapping into a
precursor state, a process which may not show significant orientational preference. The
dependence of the scattering dynamics on molecular orientation can also be degraded
due to *e.g.* surface structure and surface vibrations.

In recent years, however, there have been experimental studies that suggest the
possibility of orientational or steric effects in gas–surface scattering.[4-7] For example
promises for the presence of such effects come from the observations of rotational
excitation in direct inelastic scattering of notably NO from Ag(111), *e.g.* see ref. (4),
(7)–(10) and references cited therein. Theoretical analysis of NO scattering from Ag(111)
indicates that the rotational excitation can be induced by the anisotropy of the repulsive
wall of the molecule surface interaction potential.[11-16] Namely, the dominant feature
of rotational excitation for NO scattering from Ag(111) is the occurrence of rotational

rainbows, which are signatures of the maximal rotational excitation in the system and thus related directly to the form of the interaction.[11-16] A careful analysis of the rotational excitation spectra led Voges and Schinke to the conclusion that in fact two rotational rainbows occur, meaning that there are two orientations of the molecule for which the rotational excitation is extremal.[13] This in turn implies that the two ends of the molecule interact differently with the surface. From these theoretical studies it could not be established which end of the molecule yields, when scattered, the largest rotational excitation. Also other studies give indications for the importance of steric effects, but until now no direct experimental proof was available. The present experiments on collisions of orientated NO from Ag(111) demonstrate the occurrence of a steric effect in the direct inelastic scattering, as detected in the angular distribution of scattered particles.[17,18]

Even when indirect inelastic scattering steric effects occur this does not mean that also for trapping steric effects will be prominent. A direct experimental determination is required. At translational energies around 100 meV *ca.* 40% of the NO molecules have been observed to be trapped on Ag(111).[19] Because of its low binding energy, the molecule will desorb after having fully accommodated to the surface, but instantaneously on the time resolution of the experiment (*ca.* 10^{-5} s). Desorbed molecules therefore can be detected outside the angular domain of direct inelastic scattering and in this way one can obtain trapping probabilities from a scattering experiment.[19] Although the adsorption geometry of this system is not known, from analogy with other systems, we infer that the NO will be adsorbed also in an upright position with the N-end pointing towards the surface. We orientate the NO in the molecular beam just before it collides with the Ag(111) crystal and measure the relative difference in the intensity of the trapping-desorption scattering as function of the molecular orientation.[20] The results give us directly the more favourable end of the molecule for trapping at the surface. The results can be interpreted in terms of classical trajectory calculations.[21]

In a beautiful set of experiments Zare and co-workers have observed alignment and orientation of N_2 after direct inelastic scattering from Ag(111).[5] In this case the word orientation is used in a slightly different sense, namely that the average final angular momentum J for a given $|J|$ shows a preferential orientation in space; in other words, all molecules are spinning in the same direction. Clearly these experiments show evidence for a strong dependence of the gas–surface interaction on the initial direction of the molecular axis, but this is measured in the final state and not by selecting an initial state as is done in the experiments to be discussed here. In addition, these experiments show evidence for a kind of microcorrugation that couples to rotation *via* the parallel velocity. In the present system NO on Ag(111) corrugation is mostly neglected, which is not entirely correct.[22] Alignment means that J shows a preferred direction but that the sign of J is both positive and negative with equal probability. Alignment has also been observed for NO scattered from Ag(11) and is interpreted as evidence for the relative flatness of the surface.[23]

For the desorption of CHF_3 from Ag(111) the experimental observation of an orientational effect has been claimed by Novakoski and McClelland.[6] CHF_3 is believed to be more likely to desorb with the fluorine end directly pointing away from the surface. They concluded out of their measurements, that most probably the H-end will be more attracted by the surface, than the F_3-end.

Experimental

A detailed description of the experimental set-up will be given elsewhere; a schematic diagram of the apparatus is shown in fig. 1.[18,24] In brief, we use a pulsed supersonic molecular beam of a mixture of NO seeded in a mixture of He and Ne to prevent dimerisation in the expansion and to control the incident translational energy. Because
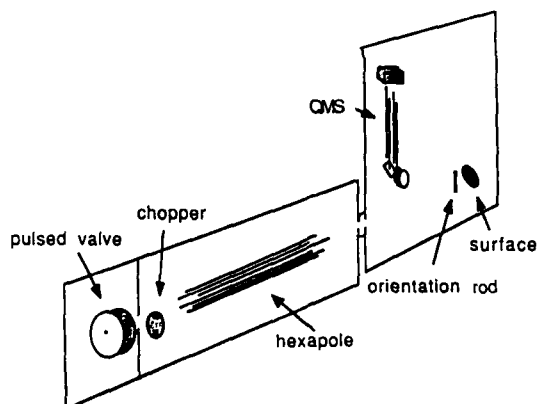
Fig. 1. Schematic diagram of the experimental arrangement.

of the low rotational temperatures (4 K) in these beams nearly all molecules will be in the lowest rotational level of the $\Pi_{1/2}$ electronic ground state of NO. At electric fields strong enough for λ-decoupling ($E > 12\,\mathrm{kV\,cm^{-1}}$) the orbital motion of the unpaired electron spin induces an essentially linear Stark effect for all M_J components of the $J = \frac{1}{2}$ rotational ground state.[25] Owing to this Stark effect the electric hexapole focusing technique can be used to produce a beam of state-selected and oriented NO molecules in an electric guiding field normal to the Ag(111)-surface.[26-29] The guiding field is generated by placing a 3 mm diameter rod, at a high d.c. voltage, parallel to the face of the grounded crystal. The probability distribution of the specific orientation γ_E of the molecular axis, pointing from O to N, with respect to the electric field direction E can be calculated for molecules in the $^2\Pi_{1/2}(J = \frac{1}{2}, \Omega = \frac{1}{2}, M_J = \frac{1}{2})$ state selected and is given by the expression $W(\cos \gamma_E) = 0.5 + 0.5 \cos \gamma_E$.[28,29] A polar plot of this distribution is shown in fig. 2. From this diagram it can be seen that by choosing a positive rod voltage the N-end of the molecule can be preferentially aimed at the surface. A negative
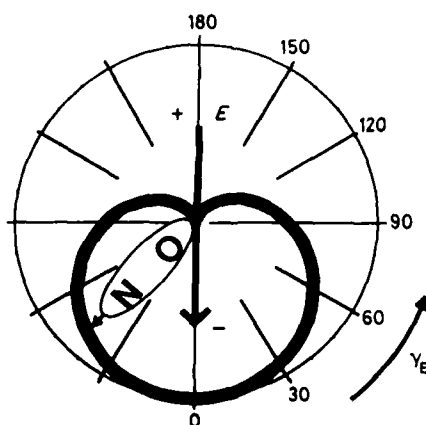
Fig. 2. Polar plot of the probability distribution for the angle γ_E between the molecular axis of NO[$^2\Pi_{1/2}(J = \frac{1}{2}, \Omega = \frac{1}{2}, M_J = \frac{1}{2})$] with respect to an external electrostatic field high enough for λ-decoupling ($E > 12\,\mathrm{kV\,cm^{-1}}$).

rod voltage causes an orientational distribution with mostly the O-end towards the surface.

The scattered molecules are detected with a quadrupole mass spectrometer. The crystal was mounted on a goniometer and the mass spectrometer was turned around the crystal. In this way both the detection angle Θ_f as well as the angle of incidence Θ_i, both measured with respect to the surface normal, can be varied.

Direct Inelastic Scattering

We have measured, for negative, zero and positive rod voltages, the relative intensity of the in-plane reflected molecules as a function of Θ_f at an incident translational energy, $E_i = 200$ meV, at an angle of incidence $\Theta_i = 37°$ and at a surface temperature, $T_s = 600$ K. In-plane scattering was chosen because it probes essentially only those molecules that are reflected directly from the crystal and have not been desorbed after trapping.[19,22] In fig. 3 we plot $[I_+(\Theta_f) - I_0(\Theta_f)]/I_0(\Theta_f)$ and $[I_-(\Theta_f) - I_0(\Theta_f)]/I_0(\Theta_f)$ as a function of Θ_f. Here $I_+(\Theta_f)$ is the scattered intensity measured at Θ_f with a positive rod voltage (thus with the N-end preferentially pointing towards the surface before the collision). For $I_-(\Theta_f)$ and $I_0(\Theta_f)$, respectively, the rod voltage was negative (with the O-end preferentially towards the surface) and zero (random orientation). Note, that from $W(\cos \gamma_E) = 0.5 + 0.5 \cos \gamma_E$ one expects, as confirmed by the data collected in our experiment, that the plotted ratios are exactly symmetric to one another. From this figure we see that the rod voltage influences the direct scattering of NO from Ag(111). For small scattering angles one observes $I(\Theta_f) < I_0(\Theta_f) < I_+(\Theta_f)$, whereas for large scattering angles the reverse is seen. This means that for the 'N-end collision', the preferred scattering angle is smaller while for the 'O-end collision' it is larger than for a 'random orientation collision'. Assuming the angular distribution for direct inelastic
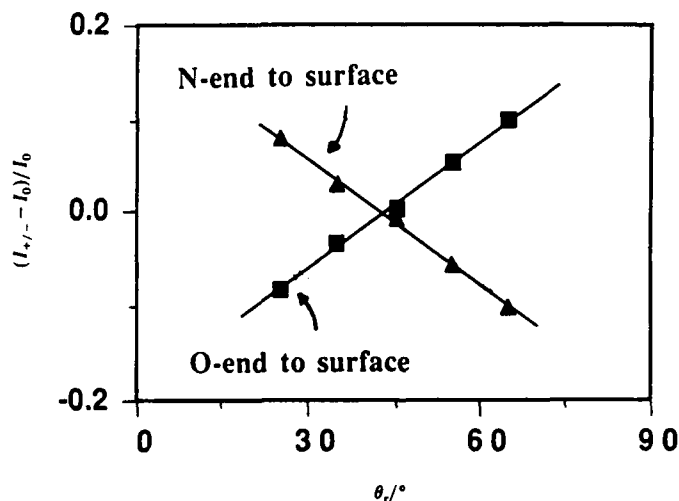

Fig. 3. Results of the measurements of NO $[^2\Pi_{1/2}(J = \frac{1}{2}, \Omega = \frac{1}{2}, M_J = \frac{1}{2})]$ direct scattering from an Ag(111) surface without guiding field and with an electric guiding field of 15 kV cm^{-1} for $\Theta_i = 35°$, $E_i = 200$ meV and $T_s = 600$ K. In the figure is plotted the relative change between the intensity scattered under the reflection angle Θ_f with an electric guiding field, $I_{+/-}(\Theta_f)$, and without an electric guiding field, $I_0(\Theta_f)$. The squares are the measurements done with negative rod voltage, E pointing towards the surface, and the triangles are the measurements for a positive rod voltage, E pointing away from the surface. The line through the points are drawn to guide the eye.

scattering for 'random orientation' can be parameterized by $I_0(\Theta_r) = \cos^{10}(\Theta_r - \Theta_i - 5°)$,[9,22] we obtain the angular distributions for positive and negative rod voltages (fig. 4). These angular distributions have been calculated by increasing or decreasing $I_0(\Theta_r)$ by the percentages shown in fig. 3. The shift between the angular distributions can be explained in the following way.

Near-specular scattering indicates that the surface used in our experiments is almost flat and structureless.[8,22] Indeed, in many theoretical studies of this system a flat surface is assumed.[11-16] Thus, the component of the molecular momentum parallel to the surface is expected to remain practically unchanged by the collision. This means that rotational excitation can only occur at the expense of the normal component of the incident momentum. The resulting loss of this normal momentum component implies an inclination of Θ_r towards the surface. Such an increase in inclination as a function of the final rotational state has been measured for NO–Ag(111) with state-specific detection.[4,8] Numerical scattering calculations on highly anisotropic interaction potentials could essentially reproduce the rotational excitation spectra observed.[12-16,30] The highest rotational excitation or lowest rotational rainbow was found to occur for an incoming orientation of the molecular axis of about 45°,[13] and the most anisotropic end of the molecule pointed towards the surface.[30] Combining the information from these theoretical studies and the present experiments, we conclude that the more anisotropic end of NO is the O-end. Conversely, the rotational excitation with the same 45° orientation, but with the other end in front, was calculated to be much less. This is in complete agreement with our results shown in fig. 4 and tells us that the N-end is the least anisotropic. Very recent calculations by Holloway and Halstead using propagation of semiclassical wavepackets on the potential by Voges and Schinke confirm that the rotational excitation will be different for NO beams orientated with their N-end preferentially towards the surface from those pointing with their O-end preferentially towards the surface.[31] Although more complex models including energy transfer to phonons and a structured surface may change the detailed shape of the angular distributions, we believe that the physical picture presented here will remain unchanged.
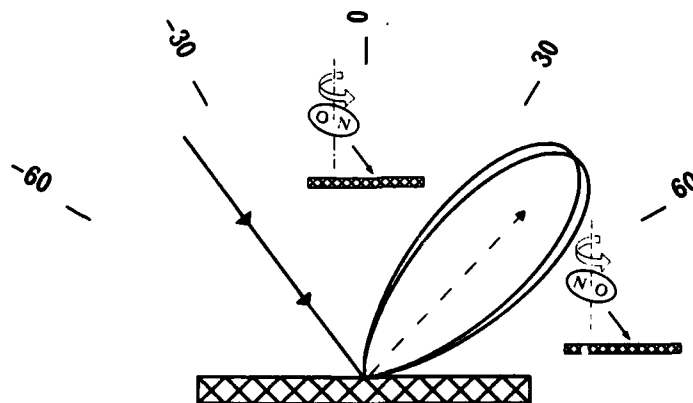

Fig. 4. Angular distributions, $I_+(\Theta_r)$ and $I_-(\Theta_r)$, for direct scattering of NO from Ag(111) presented in a polar plot for positive and negative rod voltage, i.e. for two different orientation distributions of the NO molecular axis with respect to the Ag(111) surface ($\Theta_i = 35°$, $E_i = 200$ meV, $T_s = 600$ K). The angular distributions, $I_+(\Theta_r)$ and $I_-(\Theta_r)$, are deduced as described in the text. The dotted arrow gives the direction for specular scattering. Note, that although the angular shifts might seem small, it is quite a noticeable effect in the energy loss. Moreover since the preferential orientation of the incoming molecular is not very large.

Trapping Desorption

In the experiments on trapping followed by desorption the total reflection angle, $\Theta_t = 180° - \Theta_i - \Theta_f$, was fixed to 160° to be sure that only molecules scattered *via* trapping-desorption scattering are detected.[19,22] The angle of incidence Θ_i has been varied between 30 and 80° with respect to the surface normal. The incident energy E_i was 100 meV. The surface temperature was held constant at 600 K, to keep the residence time of the NO molecule at the surface negligibly small on an experimental time resolution ($>10 \mu$s).[22] We record the intensity of the scattered molecules in the desorption channel for the two opposite incident orientational distributions alternatively. In fig. 5 we show the relative difference R between the trapped – desorbed intensity for an incoming molecular beam with preferentially the O-end in front and the one for the N-end in front, divided by the trapped – desorbed intensity for an unorientated beam, as a function of E_n, as before $E_n = E_i \cos^2 \Theta_i$ stands for the energy associated with the perpendicular velocity component. The intensity for the preferentially orientated molecules with the O-end towards the surface is larger causing a positive R. From this we conclude the molecules in this orientation have a larger trapping probability. In addition, R increases with increasing E_n also.[20]

These experimental results are very surprising. Intuitively one might think that molecules with the stronger bonding end will be trapped more easily. Their larger potential wells enhance the energy transfer from translation to other degrees of freedom. This idea is supported by classical trajectory calculations by Muhlhausen *et al.*[30] However, the experiments show the opposite. A possibility to explain our results may be found in the orientational dependence of energy transfer from translation to rotation. This dependence has been calculated by Voges and Schinke and shows a strong anisotropy in the repulsive part of the interacting potential.[13] The molecules preferentially oriented with the O-end in front gain more rotation. The rotational excitation will be gained at the expense of the translational energy, as we deduced from the studies
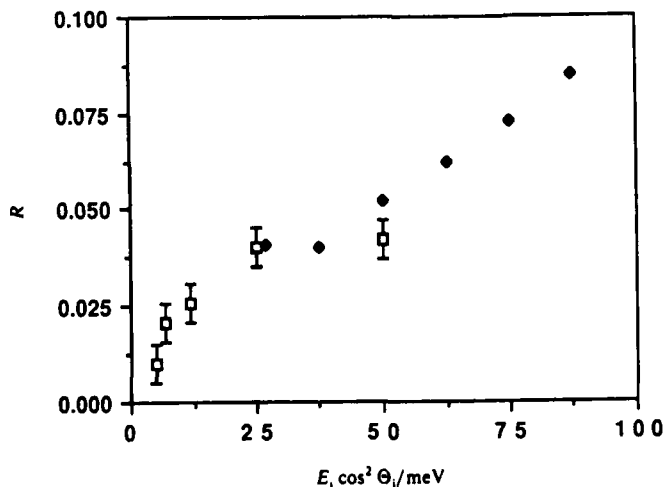

Fig. 5. The relative difference R, defined as the difference of the trapping desorption intensity for an incoming beam of NO molecules in the $(J, \Omega, M) = (\frac{1}{2}, \frac{1}{2}, \frac{1}{2})$ state with preferentially the O-end and with preferentially the N-end pointing towards the surface divided by the trapping-desorption signal from an unorientated molecular beam is plotted as a function of E_n. For the experimental points ($\square$) $E_n = E_i^* \cos^2 \theta_i$ with $E_i = 100$ meV. The filled dots give the results of classical trajectory calculations.

on direct inelastic scattering. Therefore, the higher excited molecules will possess less translational energy and may more easily get trapped. The present experiments suggest the same process of a strong orientational dependence of converting translational energy in rotational excitation in the impulsive molecule surface collision to explain the steric effect, on the trapping probability. This is substantiated in the following section. From the experiments we can clearly conclude that the trapping probability of NO on Ag(111) is larger for the orientation with the O-end pointing towards the surface than with the N-end pointing towards the surface.

Trajectory Study of Trapping

Trapping is due to the effect that molecules can transfer enough energy from translation into other degrees of freedom so they can no longer escape the potential well in front of the surface. For a weakly interacting system it has been established that the first collision with the surface is essential in determining whether or not trapping occurs.[19,32] This suggests that if sufficient energy is transferred to internal excitation of either molecule or lattice it is unlikely that this energy is converted again into 'normal' translational energy in a subsequent encounter with the repulsive wall of the surface. Using this assumption, simple classical trajectory calculations can reveal the essential physics of the trapping process. In the system under consideration, NO on Ag(111), two channels for transfer of translational energy are available, rotational excitation and substrate (phonon) excitation. One can imagine two limiting cases: the first occurs when the binding energy is small, the surface rigid and the repulsive part of the potential anisotropic, the energy transfer from translation to rotation will be the cause of trapping. The second occurs when the binding energy is large and strongly dependent on the molecular orientation and the surface non-rigid, the orientation dependent acceleration and subsequent phonon excitation will determine the trapping probability. A potential of the first case is assumed by Voges and Schinke.[13] The latter has been elucidated by Muhlhausen *et al.* in a classical trajectory study of the NO/Ag(111) interaction.[30]

The orientation-dependent trapping probability is computed by classical trajectory calculations[21] using the cube model[33] and the model potential of Voges and Schinke.[13] A surface cube mass of 240 amu was taken. Since the molecule surface interaction potential is assumed to be perfectly flat, only the normal components play a role in the calculations. The calculated overall trapping probability for an unorientated NO beam is in good agreement with the experimental results.[19] Fig. 6 shows the results as a function of γ, where γ is defined as the angle between the molecular axis, pointing from O to N, and the surface normal. Thus $\gamma = \gamma_E$ for positive rod voltage and $\gamma = -\gamma_E$ for negative rod voltage (*i.e.* the N-end in front). According to these calculations there should be a steric effect in the adsorption. However, in the case of the most attractive incoming orientation ($\gamma = 90°$) the adsorption probability is almost the lowest, which is in contrast to the result obtained by the calculations of Muhlhausen *et al.*,[30] but supports the experimental observation.[20] The reason for this is that the anisotropy in the repulsion has a much stronger steric effect in the rotational excitation and 'anticorrelated' with it is a steric effect in the phonon excitation. The 'anticorrelation' is not perfect and in our case the anisotropy in the rotational excitation over-rules the anisotropy in the phonon excitation.[8,21] In this way orientations leading to the largest rotational excitation will also have the largest energy transfer from translation to both rotation and phonons, and this results in the highest adsorption probability. In case of the present potential the orientations feeling stronger attraction are only marginally more accelerated towards the surface. Therefore the effect of the anisotropy in attraction is not visible. The anisotropy in the attraction of the potential used by Muhlhausen *et al.*[30] is much larger
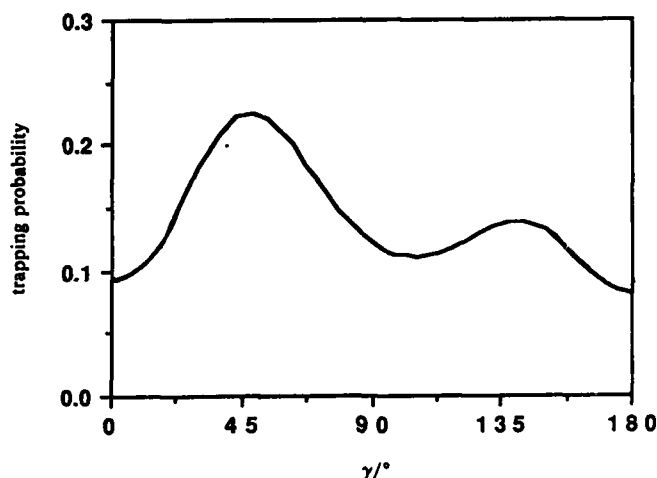
Fig. 6. The calculated trapping probability of NO with $E_n = 200$ meV on a 600 K Ag(111) surface as a function of the incoming molecular orientation, γ.

than the one we used. These authors find that the most attractive orientation adsorbs the best. However, their anisotropy is most probably exaggerated since it is based on a binding energy, that is much too strong. The present results are reminiscent of rotationally mediated selective adsorption.[34] The change in measured desorption flux for the two different preferential orientations in the experiment agrees surprisingly well with the results obtained from the classical trajectory calculations as shown in fig. 5.

Conclusions

We have observed that the angular distribution of NO directly scattered from Ag(111) depends on the initial orientation of the molecular axis. We attribute this to the different rotational excitation for the two ends of the molecule. In addition, we have observed that the trapping probability is larger in case the O-end of the molecule approaches the surface. From molecular-dynamics calculations, using the anisotropic interaction potential of Voges and Schinke,[13] together with the cube model[33] we can conclude that rotational excitation, phonon excitation and the trapping probability are dependent on the initial molecular orientation. The dependence on the initial molecular orientation of the rotational excitation is determined by the anisotropy in the repulsive part of the potential.

Steric effects have been found to govern the mechanism of purely gas-phase reactions.[35,36] In the present study a first experimental proof is given, that effects of molecular orientation also play an important role in gas–surface collisions. Orientated molecule scattering from surfaces offers a way for future determinations of molecule surface anisotropic potentials.[37]

References

1. H. Conrad, G. Ertl, J. Küppers and E. E. Latta, *Surf. Sci.*, 1977, **65**, 235.
2. H. Ibach and D. L. Mills, *Electron Energy Loss Spectroscopy and Surface Vibrations* (Academic Press, New York, 1982); H. Ibach and S. Lehwald, *Surf. Sci.*, 1978, **76**, 1.
3. D. A. Wesner, F. P. Coenen and H. P. Bonzel, *Surf. Sci.*, 1988, **199**, L419.
4. A. W. Kleyn, A. C. Luntz and D. J. Auerbach, *Phys. Rev. Lett.*, 1981, **47**, 1169; *Surf. Sci.*, 1982, **117**, 33.
5. G. O. Sitz, A. C. Kummel and R. N. Zare, *J. Vac. Sci. Technol. A*, 1987, **5**, 513; G. O. Sitz, A. C. Kummel, R. N. Zare and J. C. Tully, *J. Chem. Phys.*, in press; D. C. Jacobs, K. W. Kolasinski, R. J. Madix and R. N. Zare, *J. Chem. Phys.*, 1987, **87**, 5038.
6. L. V. Novakoski and G. M. McClelland, *Phys. Rev. Lett.*, 1987, **59**, 1259.
7. G. M. McClelland, G. D. Kubiak, H. G. Rennagel and R. N. Zare, *Phys. Rev. Lett.*, 1981, **46**, 831; G. D. Kubiak, J. E. Hurst, H. G. Rennagel, G. M. McClelland and R. N. Zare, *J. Chem. Phys.*, 1983, **79**, 5163.
8. J. Kimman, C. T. Rettner, D. J. Auerbach, J. A. Barker and J. C. Tully, *Phys. Rev. Lett.*, 1986, **57**, 2053.
9. C. T. Rettner, J. Kimman, F. Fabre, D. J. Auerbach, J. A. Barker and J. C. Tully, *J. Vac. Sci. Technol. A*, 1987, **5**, 508.
10. C. T. Rettner, F. Fabre, J. Kimman and D. J. Auerbach, *Phys. Rev. Lett.*, 1985, **55**, 1904; C. T. Rettner, J. Kimman, F. Fabre, D. J. Auerbach and H. Morawitz, *Surf. Sci.*, 1987, **192**, 107.
11. J. E. Hurst, G. D. Kubiak and R. N. Zare, *Chem. Phys. Lett.*, 1982, **93**, 235.
12. J. A. Barker, A. W. Kleyn and D. J. Auerbach, *Chem. Phys. Lett.*, 1983, **97**, 9.
13. H. Voges and R. Schinke, *Chem. Phys. Lett.*, 1983, **100**, 245; 1983, **95**, 221.
14. S. Tanaka and S. Sugano, *Surf. Sci.*, 1984, **136**, 488.
15. W. Brenig, H. Kasai and H. Müller, *Surf. Sci.*, 1985, **161**, 608.
16. J. E. Smedley, G. C. Corey and M. H. Alexander, *J. Chem. Phys.*, 1987, 3218.
17. E. W. Kuipers, M. G. Tenner, A. W. Kleyn and S. Stolte, *Nature (London)*, 1988, **334**, 420.
18. M. G. Tenner, E. W. Kuipers, W. Langhout, A. W. Kleyn and S. Stolte, to be published.
19. E. W. Kuipers, M. G. Tenner, M. E. M. Spruit and A. W. Kleyn, *Surf. Sci.*, 1988, xx, xxx.
20. M. G. Tenner, E. W. Kuipers, A. W. Kleyn and S. Stolte, submitted.
21. E. W. Kuipers, M. G. Tenner, A. W. Kleyn and S. Stolte, *Surf. Sci.*, in press.
22. E. W. Kuipers, M. G. Tenner, M. E. M. Spruit and A. W. Kleyn, *Surf. Sci.*, 1987, **189/190**, 669.
23. A. C. Luntz, A. W. Kleyn and D. J. Auerbach, *Phys. Rev. B*, 1982, **25**, 4273.
24. M. E. M. Spruit, E. W. Kuipers, M. G. Tenner, J. Kimman and A. W. Kleyn, *J. Vac. Sci. Technol. A*, 1987, **5**, 496.
25. S. Stolte, *Thesis* (Nijmegen, 1972).
26. K. H. Kramer and R. B. Bernstein, *J. Chem. Phys.*, 1965, **42**, 767.
27. D. van den Ende and S. Stolte, *Chem. Phys. Lett.*, 1980, **76**, 13; *Chem. Phys.*, 1984, **89**, 121.
28. S. Stolte, K. K. Chakravorty, R. B. Bernstein and D. H. Parker, *Chem. Phys.*, 1982, **71**, 353.
29. S. E. Choi and R. B. Bernstein, *J. Chem. Phys.*, 1986, **85**, 1.
30. C. W. Muhlhausen, L. R. Williams and J. C. Tully, *J. Chem. Phys.*, 1985, **83**, 2594.
31. S. Holloway and D. Halstead, submitted.
32. J. A. Barker and D. J. Auerbach, *Faraday Discuss. Chem. Soc.*, 1985, **80**, 277.
33. E. K. Grimmelmann, J. C. Tully and M. J. Cardillo, *J. Chem. Phys.*, 1980, **72**, 1039.
34. J. P. Cowin, C. F. Yu, S. J. Sibener and J. E. Hurst, *J. Chem. Phys.*, 1981, **75**, 1033; K. B. Whaley, J. C. Light, J. P. Cowin and S. J. Sibener, *Chem. Phys. Lett.*, 1982, **89**, 89; R. Schinke, *Surf. Sci.*, 1983, **127**, 283.
35. Special issue on dynamical stereochemistry, *J. Phys. Chem.*, 1987, **91**.
36. R. D. Levine and R. B. Bernstein, *Molecular Reaction Dynamics and Chemical Reactivity* (Oxford University Press, New York, 1987).
37. D. A. King, *Nature (London)*, 1988, **334**, 379.

Application of Translational Spectroscopy to the Study of Reactive Collisions of Molecules with Surfaces

Kenneth J. Snowdon

Fachbereich Physik, Universität Osnabrück, D-4500 Osnabrück, Federal Republic of Germany

The techniques of translational spectroscopy and glancing-incidence molecular ion beam–surface scattering have been combined to study reactive collisions of molecules with surfaces. A clear correlation between the results and known adsorption and reaction behaviour at thermal energies has been established. The similarity between the collision and molecular vibration times permits the identification and investigation of reaction intermediates which may not be detectable by conventional spectroscopies. The technique, which can in principle also measure the molecular orientation to the surface during scattering, should provide valuable insights into the dynamics of adsorption and reaction, both molecular and dissociative, on surfaces. Explicit results for the interaction of N_2 with Ni(110) and (111), O_2 with Ag(111) and Ni(110), and CO and CO_2 with Ni(110) surfaces are presented.

Atomic and molecular scattering experiments have long been used to probe the characteristics and resilience of chemical bonds, and the dynamics of individual reactive collision events.[1] Such experiments provide valuable insight because the energy dissipation mechanisms and potential-energy surfaces (PES) for low-energy scattering and chemical reactions are identical. Indeed, translational kinetic energy is often required to surmount activatio.. ﹃iers. Both gas-phase and gas-surface chemical processes have been studied in this way. In this paper results of the application of translational spectroscopy to study of chemical reactions at single crystal metal surfaces are described.

To place these and related studies in context, we must mention that both thermal and hypothermal beam–surface scattering are long-established techniques of surface science. They have been used as a diagnostic to provide surface structural information. More importantly here, they have also been used to determine the topography of gas–surface potentials, the energy dissipation mechanisms, and the residence times and sticking probabilities of gas atoms and molecules on surfaces.[2] We wish in this paper to explore the possibility of extracting chemical information from yet higher energy beam–surface scattering experiments.

The kinetic-energy region 1–10 eV is clearly in the activation- or 'chemical-energy' regime. Several groups have performed scattering experiments at these energies.[3] The interpretation of these experiments, however, is complicated by the difficulty of efficiently detecting neutral reaction products. Furthermore, sticking probabilities can be quite high. Increasing the collision energy can potentially remove both difficulties; however, additional complications arise. If the projectile energy is too high, surface damage, and penetration of the beam may occur. Furthermore, the relevance of such high-energy collisions to the interaction between the same reactants at 'chemical energies' may be questioned.

Aiding such 'high-energy' (tens of eV so several keV) investigations[4,5] is the apparent lack of strong coupling between the components of the projectile motion perpendicular and parallel to the surface, for small angles of incidence of the beam to the surface.[5] At sufficiently small angles, the surface corrugation is hardly visible, 'shadowing' prevents
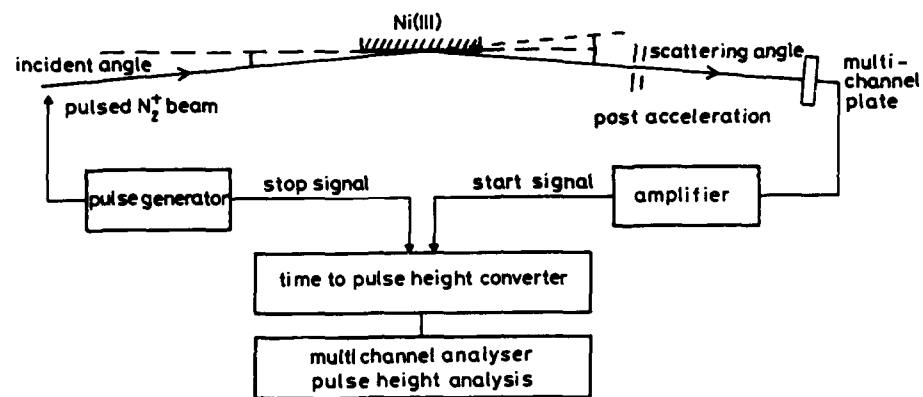
Fig. 1. Schematic diagram of the time-of-flight spectrometer [shown for an N_2^+ beam and an Ni(111) target].

damage and penetration of the surface layer, and variation of this incidence angle permits us to approach, arbitrarily closely, thermal velocities or chemical energies in that component of the projectile motion perpendicular to the surface.[6]

Experimental

Experiments were performed under ultra-high-vacuum conditions, using a pulsed mass-analysed molecular ion beam of either reactive or non-reactive gas species. This beam is incident at a small angle (typically 5°) to the surface of a single crystal. Crystals were spark cut, aligned and mechanically polished, then mounted in the vacuum chamber and further polished to atomic flatness by sputtering with a low-energy inert-gas beam (typically 1 keV Ne$^+$) incident at a glancing angle to the surface. The surface flatness can be monitored by observing the angular distribution of scattered particles. Initially, a very broad angular distribution is observed, owing to scattering from steps and defects. After several hours to days of sputtering and annealing, a sharply peaked angular distribution, indicative of an atomically flat surface, can generally be obtained.[7] The cleanliness of the surface is monitored by low-energy ion scattering[8] or recoil[9] spectroscopy.

Scattered 'reaction products' are currently analysed using a time-of-flight spectrometer with an acceptance cone angle of 1.2° at a fixed scattering angle of 10°. Scattered ions are accelerated in the 1.2 m flight-tube (fig. 1). This permits both their separation from the neutral products in the detected time-of-flight distribution and their mass identification. The flight-time resolution is typically 0.2%. The vibrational and rotational temperatures of molecular ions extracted from the plasma ion source are presently unknown.

Results

We have measured the velocity distributions of the products of small-angle scattering of (variously) H_2^+, H_3^+, N_2^+, O_2^+, CO$^+$ and CO$_2^+$ from Ni(111), Ni(110), Al(110), Ag(111) and Si(100) surfaces[5,10-16] in the projectile energy range 100-3000 eV. As an example, the product energy spectrum for 990 eV N_2^+ scattered from Ni(111) is shown in fig. 2. Clearly, N_2^+ can survive the collision without dissociating. The high dissociation energy
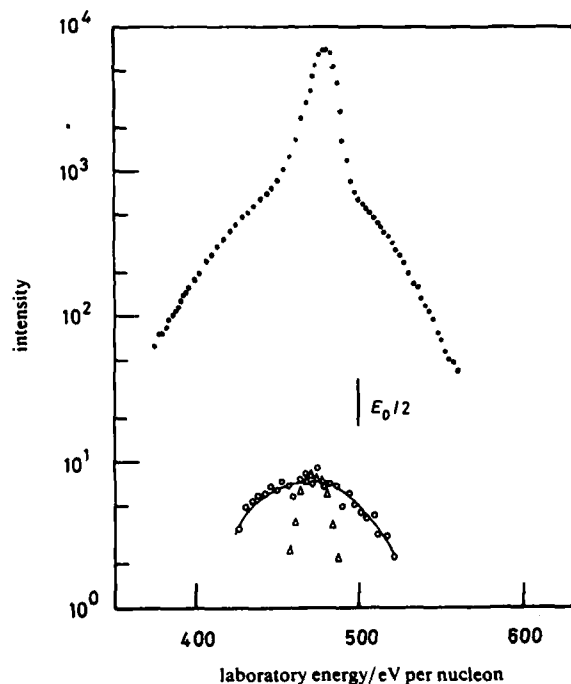
Fig. 2. Kinetic-energy distributions of neutral and ionized products of the scattering of 990 eV N_2^+ from an Ni(111) surface.[13] Scattering angle 10°, incidence angle 5°. ●, Neutrals $(N + N_2)$; ○, N^+; △, N_2^+.

of N_2^+ can survive the collision without dissociating. The high dissociation energy of N_2^+ (8.7 eV), or of N_2 (9.7 eV), however, does not preclude accompanying high vibrational or rotational excitation. That this does not in fact necessarily accompany all collisions is dramatically obvious from fig. 3, where the time-of-flight spectrum of the products of 1000 eV O_2^+ scattering from Ag(111) is reproduced. Here, a significant yield of O_2^- is observed. This ion is, however, stable against autodetachment only in its lowest vibrational states ($v = 0-2$). Furthermore, we can see from fig. 2 and 3 that charge exchange occurs in these collisions with high efficiency. In fig. 2, the ratio of neutral to positive ionic products is of the order of 104, while for the O_2^+/Ag(111) interaction (fig. 3), this ratio is greater than 2×10^3, and in addition, a second charge-transfer step occurs, leading to negative-ion formation. The yield ratio $(O_2^- + O^-)/(O_2 + O)$ is 0.01, with the degree of dissociation being large for the neutrals $[O/(O + O_2) = 0.9]$, and small for the negative ions $[O^-/(O^- + O_2^-) = 0.1]$. All ratios have been computed using integrated peak yields.

The projectile energy dependence of the O^- yield, normalized to the total number of nuclei scattered into the solid angular range of the detector, is shown in fig. 4.[6] The O^- yield exhibits a definite threshold at *ca.* 2400 eV projectile energy, whereas the O-atom yield increase at this energy is barely perceptible. The explanation for this behaviour is presented in the Discussion.

Fragmentation spectra corresponding to the scattering of 480 eV CO^+, N_2^+, CO_2^+ and O_2^+ from an Ni(110) surface are summarized in fig. 5.[14] The anticipated positions of possible negative ion species are shown. If we assign the peaks superimposed on the
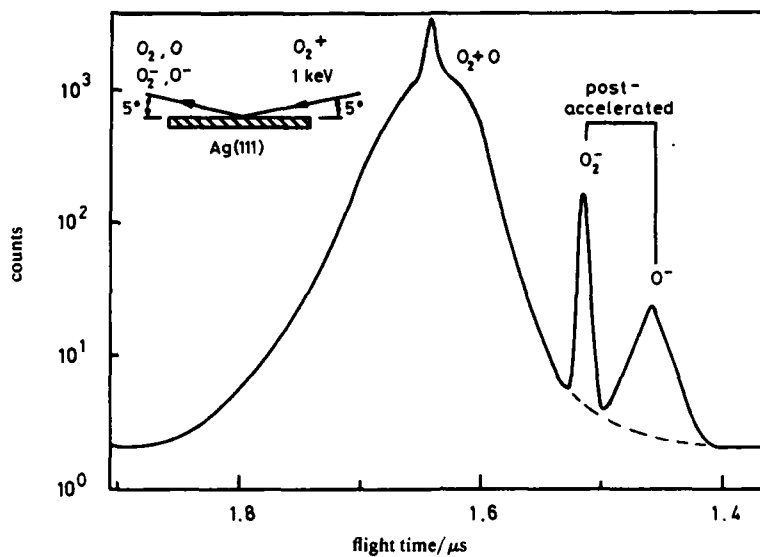
Fig. 3. Time-of-flight distribution of neutral and negative products of the scattering of 1000 eV O_2^+ from an Ag(111) surface.[6] Scattering angle 10 °, incidence angle 5 °.
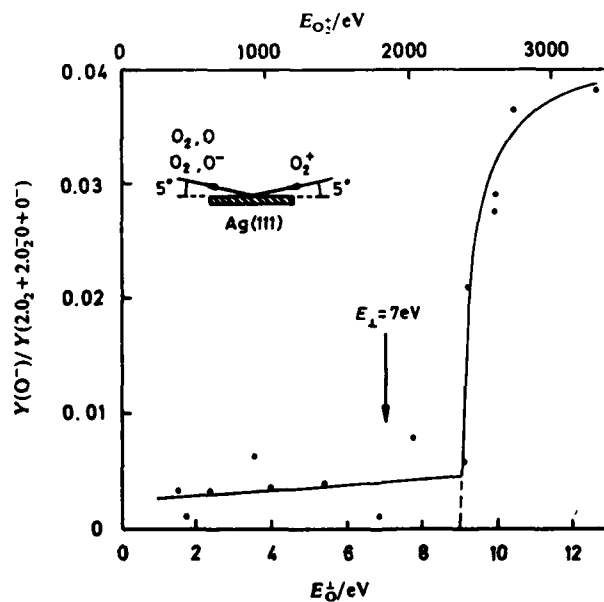

Fig. 4. Dependence of the normalized yield of O^- on O_2^+ beam energy $E_{O_2^+}$ for the interaction of O_2^+ with an Ag(111) surface.[16] Scattering angle 10 °, incidence angle 5 °, $E_O^\perp$ is the effective energy of the O^- particles normal to the surface.
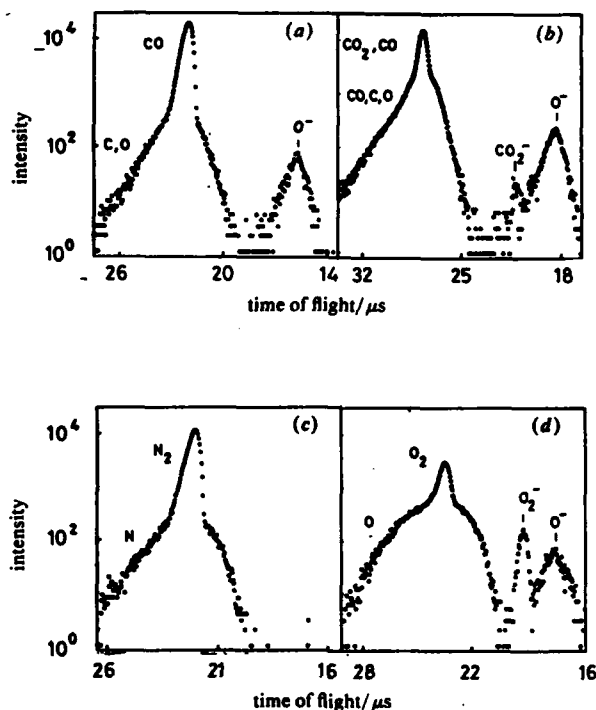
Fig. 5. Time-of-flight spectra of the products of specular scattering of 480 eV CO^+ (a), 480 eV CO_2^+ (b), 480 eV N_2^+ (c), and 490 eV CO_2^+ (d), from an Ni(110) surface.[14] The anticipated positions of CO_2^-, O^- and O_2^- are indicated.

broad distribution of the neutral species to surviving molecules, we conclude that N_2 and CO undergo negligible dissociation. The ratio $N_2/(N_2 + 0.5N) = 0.94$ and $CO/(CO + 0.5C + 0.5O^-) = 0.96$. This is in contrast to CO_2 and O_2, which predominantly dissociate. Clearly, the electronic structure or configuration of the molecule strongly influences the outcome of its interaction with a given surface.

Discussion

Central to any attempt to relate the results of these experiments to our understanding of adsorption and reaction at surfaces is the question of the influence of the beam energy. This differs by 2–3 orders of magnitude from that conventionally associated with adsorption and reaction studies. We have already briefly addressed the apparent lack of strong coupling between the components of the projectile-motion perpendicular and parallel to the surface. In addition, recent molecular dynamics calculations[17] have shown that the hard-cube model of scattering[18] is more appropriate at keV energies and glancing-incidence scattering geometries than for the thermal and hyperthermal energies (and non-glancing-incidence scattering geometries) for which it was developed. Furthermore, we have recently observed the transient adsorption of a keV atomic ion beam (incident at glancing angles) on crystal surface.[19] The mechanism of adsorption does not appear to differ in essence from that responsible for adsorption at thermal energies.[20]

The energy dissipated by the projectile appears primarily in excitation of the substrate (electron-hole pair, plasmon and phonon excitation). As a consequence, a large part of the topography of the interaction potential-energy surface may be probed during the scattering event, including that portion corresponding to adsorption or reaction equilibrium.

The collision time is large compared to the timescale for electronic processes. We therefore expect that we can both establish and access the various adiabatic electronic states of the collision system. The collision time is, however, comparable to molecular vibration times. We therefore expect that we can probe in such collision experiments intermediate states which may be dissociative or short-lived on the timescale of 10^{-14} s.

The data of fig. 2-5 exemplify these ideas. Both N_2 and CO, for example, are known to adsorb molecularly on Ni(110).[21,22] We observe negligible dissociation in our scattering experiments (fig. 5). Static adsorption and hyperthermal molecular-beam studies of the interaction of CO_2 with Ni(110) implicate a CO_2^- intermediate in the dissociative (CO+O) chemisorption of CO_2 on Ni(110).[23] We clearly observe significant dissociation, and clear evidence for the CO_2^- intermediate (fig. 5). Oxygen is known to adsorb atomically on Ni(110),[24] but no O_2^- intermediate has been identified in static experiments, even at low temperatures. We observe significant dissociation and O_2^- in our product distribution (fig. 5). We suggest[14] that dissociative chemisorption of O_2 on Ni(110) indeed proceeds *via* an O_2^- intermediate. To explain the discrepancy between the scattering and low-temperature adsorption results, the activation barrier between the O_2^- and $O^- + O^-$ regions of the potential-energy surface must be either non-existent, or of the order of the vibrational energy of the O_2^- ($v = 0$) species.

Molecular oxygen is known to be adsorbed molecularly on Ag(111) at thermal energies,[25] yet our scattering data (fig. 3), differ little from those obtained for Ni(110) (fig. 5), where oxygen is adsorbed atomically. This shows one influence of the high beam energies normal to the surface. We can always choose conditions such that we have sufficient energy available to surmount any or all activation barriers.

We observe O^- in fig. 3. The dependence of the O^- yield on incident O_2^+ beam energy was shown in fig. 4. Below $E_{O_2^+} \approx 2400$ eV, little O^- is observed. The neutral O atoms we observe at all energies (fig. 4) appear to arise from charge capture by the dissociative O_2 Π states.[5] It is energetically unfavourable for molecules possessing this electron configuration to capture a second electron. The O^- ions arise from capture of a second electron by molecules in the neutral ground-state configuration. The threshold we observe corresponds to the threshold for collisional dissociation of such molecules.[16,17] We attribute the small O^- yield below $E_{O_2^+} \approx 2400$ eV to collisional dissociation at defects on the surface. We conclude that we either do not efficiently access that region of the potential-energy surface corresponding to dissociative chemisorption, or that if we do, the probability of remaining in that channel is exceedingly small. Which (if any) of these possibilities is correct might be answered by performing trajectory calculations on the interaction PES. A model PES for the $O_2/Ag(111)$ interaction has recently been constructed.[26]

The neutral component of the product distributions (fig. 2, 3, 5) certainly contain atoms, since particles are observed at velocities exceeding the velocity of the incident beam. In the above analysis, we tentatively associated the sharp peak on the broad atom distribution with neutral molecules. We also attributed the formation of netural atoms (at least at low incident energies) to dissociative attachment reactions. Similar reactions in the gas phase often produce double-peaked atom time-of-flight or kinetic-energy distributions.[27] Our distributions may also have a double-peaked structure, which is masked by the neutral molecule peak. Other explanations, such as overlap with a third component (owing, for example, to collisional dissociation of neutral molecules), broadening of the distributions caused by inelastic and elastic losses, and orientation and apparatus function effects are under investigation.
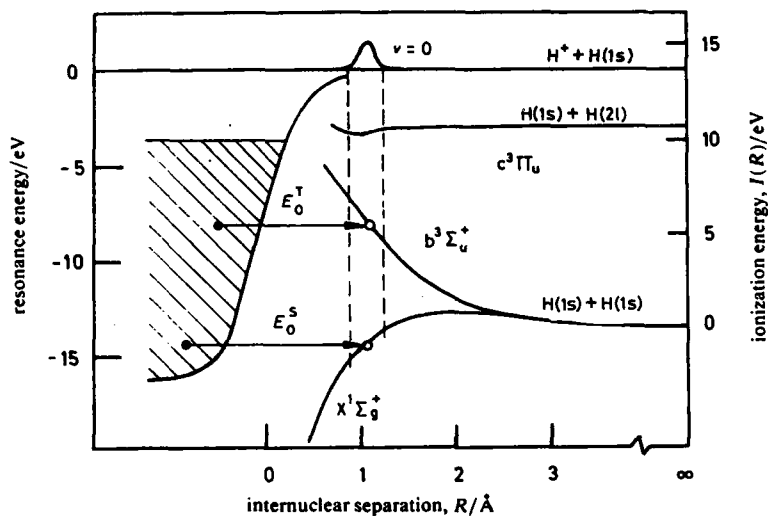
Fig. 6. Ionization potential curves of the lowest-lying electronic states of the H_2 molecule compared with a simplified Al(100) density of states. Electron capture from the metal to both the $X\,^1\Sigma_g^+$ and $b\,^3\Sigma_u^+$ states of the molecule is allowed over a wide range of internuclear separations, R. The distribution in R values in experiments of the type described here is determined by the vibrational population distribution in the H_2^+ ion. The approximate range for the $v = 0$ vibrational state is indicated by the dashed vertical lines.[28]
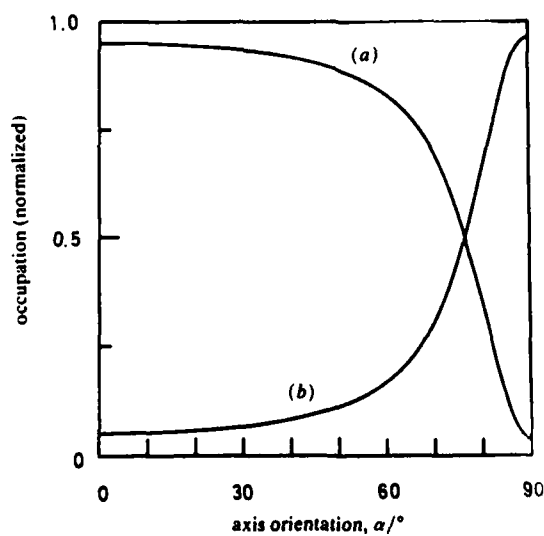
Fig. 7. Dependence on H_2 molecular-axis orientation to the surface normal of an Al(110) surface of charge capture and exit in the $X\,^1\Sigma_g^+$ and $b\,^3\Sigma_u^+$ channels[29] (perpendicular component of the beam energy, $E_\perp = 1$ eV; initial internuclear separation in H_2^+, $R_i = 2$ a.u.). (a) P_T ($E_\perp = 1$ eV), (b) $P_s(E_\perp = 1$ eV).

The surface in our experiments defines an axis which can strongly influence the probability of charge transfer to energetically accessible electronic states of different symmetry.[28] The interaction of H_2^+ with Al(110) provides a simple example (fig. 6). The dependence on the molecular-axis orientation of the probability of exciting in either the $X\,^1\Sigma_g^+$ (bound) or $b\,^3\Sigma_u^+$ (dissociative) state is shown in fig. 7.[29] For molecular-axis orientations parallel to the surface, exit in the dissociative channel is strongly depressed. Such effects should be easily measurable directly using position sensitive coincidence detection techniques. These effects can also strongly influence the interpretation of experimental results obtained with apparatus such as that illustrated in fig. 1, which selects only a limited range of molecular axis orientations.[27,29]

Conclusions

A correlation between the results of glancing incidence, energetic molecular ion beam–surface scattering experiments and adsorption and reaction phenomena at thermal and hyperthermal energies has been established. The effective energy of the beam perpendicular to the surface can be tuned easily to overcome activation energy barriers. In future, measurements using orientated beams, or experiments which measure (after scattering) the molecular-axis orientation during scattering, should be feasible. Using these techniques, both energetic and orientational barriers to adsorption and reaction on surfaces may be investigated in detail. Furthermore, the similarity of the collision and molecular vibration times permits the identification and investigation of reaction intermediates which may not be detectable by static spectroscopies. Combined with trajectory calculations on model potential-energy surfaces, we expect energetic beam–surface scattering techniques to provide significant and valuable insights into the dynamics of adsorption and reaction, both molecular and dissociative, on surfaces.

References

1 J. P. Toennies, *Annu. Rev. Phys. Chem.*, 1976, 27, 225; J. Ioup and A. Russek, *Phys. Rev. A*, 1973, 8, 2898.
2 J. A. Barker and D. J. Auerbach, *Surf. Sci. Rep.* 1985, 4, 1; H. Hoinkes, *Rev. Mod. Phys.*, 1980, 52, 933.
3 H. F. Winters, *J. Chem. Phys.*, 1966, 44, 1472; J. A. Taylor and J. W. Rabalais, *J. Chem. Phys.*, 1981, 75, 1735; H. Akazawa, I. Kusunoki and Y. Murata, *Surf. Sci.*, 1986, 177, 577.
4 P. Haochang, T. C. M. Horn and A. W. Kleyn, *Phys. Rev. Lett.*, 1986, 57, 3035.
5 P. H. F. Reijnen, A. W. Kleyn, U. Imke and K. J. Snowdon, *Nucl. Instr. Meth. B*, in press.
6 K. J. Snowdon, *Nucl. Instr. Meth. B.* in press.
7 U. von Gemmingen and R. Sizmann, *Surf. Sci.*, 1982, 114, 445.
8 D. P. Smith, *Surf. Sci.*, 1971, 25, 171.
9 D. J. O'Connor, R. J. MacDonald, W. Eckstein and P. R. Higginbottom, *Nucl. Instr. Meth. B*, 1986, 13, 235.
10 B. Willerding, W. Heiland and K. J. Snowdon, *Phys. Rev. Lett.*, 1984, 53, 2031.
11 U. Imke, S. Schubert, K. J. Snowdon and W. Heiland, *Surf. Sci.*, 1987, 189/190 960.
12 B. Willerding, K. J. Snowdon and W. Heiland, *Z. Phys. B*, 1985, 59, 445.
13 B. Willerding, K. J. Snowdon, U. Imke and W. Heiland, *Nucl. Instr. Meth. B*, 1986, 13, 614.
14 S. Schubert, U. Imke, W. Heiland, K. J. Snowdon, P. H. F. Reijnen and A. W. Kleyn, *Surf. Sci. Lett.*, in press.
15 J. H. Rechtien, P. H. F. Reijnen, A. Namiki, A. W. Kleyn and K. J. Snowdon, to be published.

16 P. H. F. Reijnen, A. W. Kleyn, U. Imke and K. J. Snowdon, to be published.
17 P. J. van den Hoek and A. W. Kleyn, to be published.
18 F. O. Goodman, *J. Phys. Chem. Solids*, 1965, **26**, 85.
19 K. J. Snowdon, D. J. O'Connor, R. J. MacDonald, *Appl. Phys. A*, in press.
20 K. J. Snowdon, D. J. O'Connor, R. J. MacDonald, to be published.
21 K. Horn, J. Dinardo, W. Eberhardt, H-J. Freund and E. W. Plummer, *Surf. Sci.*, 1982, **118**, 465.
22 Ya-po Hsu, K. Jacobi and H. H. Rotermund, *Surf. Sci.*, 1982, **117**, 581.
23 B. Bartos, H-J. Freund, H. Kuhlenbeck, M. Neumann, H. Lindner and K. Müller, *Surf. Sci.*, 1987, **179**, 59.
24 D. F. Mitchell, P. B. Sewell and M. Cohen, *Surf. Sci.*, 1977, **69**, 310.
25 C. T. Campbell, *Surf. Sci.*, 1986, **173**, L641.
26 M. E. M. Spruit and A. W. Kleyn, submitted.
27 J. Los and T. R. Govers, in *Collision Spectroscopy*, ed. R. G. Cooks (Plenum, New York, 1978).
28 K. J. Snowdon, B. Willerding and W. Heiland, *Nucl. Instr. Meth. B*, 1986, **14**, 467.
29 U. Imke, K. J. Snowdon and W. Heiland, *Phys. Rev. B*, 1986, **34**, 41.